

**Interface Design of Polymer Matrix
Composites - Mechanics, Chemistry,
Modelling and Manufacturing**

Copyright 2007 Risø National Laboratory
Roskilde, Denmark

ISBN 978-87-550-3626-0

ISSN 0907-0079

Interface Design of Polymer Matrix Composites – Mechanics, Chemistry, Modelling and Manufacturing

Proceedings of the 28th Risø International Symposium
on Materials Science

3 – 6 September 2007

Editors

B. F. Sørensen L. P. Mikkelsen H. Lilholt
S. Goutianos F. S. Abdul-Mahdi

RISØ NATIONAL LABORATORY
ROSKILDE, DENMARK

Risø International Symposium on

Interface Design of Polymer Matrix Composites - Mechanics,
Chemistry, Modelling and Manufacturing

INTERNATIONAL ADVISORY COMMITTEE

Anthony Bunsell, France

Ignazio Crivelli-Visconti, Italy

Anthony G. Evans, USA

Klaus Friedrich, Germany

Costas Galiotis, Greece

Axel Hermann, Germany

Ryszard Pyrz, Denmark

Philip J. Withers, UK.

LOCAL ORGANISING COMMITTEE

Kristoffer Almdal

Tom Løgstrup Andersen

Povl Brøndsted

Stergios Goutianos

Dorte Juul Jensen

Hans Lilholt

Aage Lystrup

Bo Madsen

Lars Pilgaard Mikkelsen

Leon Mishnaevsky Jr.

David Plackett

Bent F. Sørensen

Ann Gaust Thomsen

Erik Vogeley

Rasmus C. Østergaard

PREFACE

Polymer matrix composites are increasingly used in large load-carrying structures, such as aircraft structures, wind turbine blades, trains, boats and bridges, because they possess high stiffness and strength relative to weight. Yet, higher strengths are desired, so that future structures can be made larger and slimmer, saving material resources and costs. It is therefore of interest to develop composite materials with optimised properties.

The fibre/matrix interface is a key parameter controlling overall macroscopic composite properties, such as strength and fracture toughness. The Symposium addresses the understanding and methods for controlling the fibre/matrix interface. This covers the development of new experimental and modeling approaches, such as methods for surface modification, methods for surface characterisation, methods for mechanical characterisation of interfaces, as well as micromechanical and macroscale modeling. Furthermore, the Symposium covers application of such methods in the studies of topics like fibre/matrix debonding, crack bridging in composites, the effect of the fibre/matrix interface on fracture resistance of composites, tensile and compressive strength of composites, as well as hole and notch sensitivity. The integration of fibre surface modification methods into manufacturing of composite structures is also an important topic for the Symposium. The Symposium addresses the whole range from fundamental understanding to industrial applications.

The Risø Symposium and the Proceedings contain 8 key note presentations, and 20 contributed presentations, covering a large selection of the above topics.

The Risø Symposium was organized by the Materials Research Department and the Polymer Department of Risø National Laboratory.

We thank all those at Risø who have assisted in the preparations for the Symposium. We gratefully acknowledge the financial support received from Civilingeniør Frederik Leth Christiansens Almennyttige Fond.

Kristoffer Almdal, Tom Løgstrup Andersen, Povl Brøndsted,
Stergios Goutianos, Dorte Juul Jensen, Hans Lilholt, Aage Lystrup,
Bo Madsen, Lars Pilgaard Mikkelsen, Leon Mishnaevsky Jr.
David Plackett, Bent F. Sørensen, Ann Gaust Thomsen,
Erik Vogeley, Rasmus C. Østergaard

CONTENTS

Invited Papers

Natural fibre composites – with special emphasis on effects of the interface between cellulosic fibres and polymers E. K. Gamstedt, K. M. Almgren	1
The chemical aspects of fibre surfaces and composite interfaces and interphases, and their influence on the mechanical behaviour of interfaces F. R. Jones	21
Controlling fiber/matrix adhesion with binary self-assembled monolayers K. M. Liechti, W. D. Tandy, Jr.	45
From interface laws to composite behaviour B. F. Sørensen, L. P. Mikkelsen, R. C. Østergaard, S. Goutianos	55
Interfaces and interfacial effects in glass reinforced thermoplastics J. L. Thomason	75
Mixed-mode cohesive-zone models for delamination and deflection in composites M. D. Thouless, J. P. Parmigiani	93
Cohesive models for interface debonding V. Tvergaard	113
The importance of interfaces in thermoplastic matrix composites and their tailoring during manufacture R. P. Wool	125

Contributed Papers

Influence of temperature on cohesive parameters for adhesives A. Biel, T. Carlberger	143
Influence of polymer grade and compatibilizer concentration on the interfacial shear strength in sisal fibre polypropylene composites C. Burgstaller, W. Stadlbauer	149
The effect of cure cycle heating rate on the fibre/matrix interface V. Coenen, A. Walker, R. Day, A. Nesbitt, J. Zhang, B. L. Fox	157
Pulsed plasma deposited maleic anhydride thin films as functionalised surfaces in composite materials J. Drews, S. Goutianos, K. West, S. Hvilsted, K. Almdal	165
Microfractographic aspects of interfaces in CFRP under fatigue loading W. Förtsch, H. E. Franz, K. Friedrich	173
Estimation of interface cohesive laws by digital image correlation S. Goutianos, J. Drews	181
Surface characterization using Hansen Solubility (cohesion) Parameters C. M. Hansen	191
Interfacial properties of carbon fibre – epoxy composites under fatigue loading L. R. Jensen, J. C. Rauhe, R. Pyrz	199
Adhesion improvement of carbon fibres by plasma surface modification Y. Kusano, T. L. Andersen, B. F. Sørensen, P. K. Michelsen	207
Applications of solid state nuclear magnetic resonance to probe the interphase in natural fiber reinforced composites M. - P. G. Laborie	213
Hansen Solubility Parameters for a carbon fiber/epoxy composite H. Launay, C. M. Hansen, K. Almdal	221

Weak solutions in elasticity of dipolar materials with stretch M. Marin	227
Length-scale dependent crack-growth L. P. Mikkelsen	235
Software for automatic generation of 3D microstructural models of fiber reinforced composites with damageable elements L. Mishnaevsky Jr, P. Brøndsted	241
The influence of fiber waviness on the critical buckling load of multilayered composites H. G. Rai, E. V. Honein, R. A. Dibo, P. N. Ayoub	249
Strain sensing in carbon fiber reinforced materials using electromechanical measurements J. C. Rauhe, L. R. Jensen, R. Pyrz	257
On the apparent influence of the adherends on the fracture toughness of adhesive layers K. Salomonsson, U. Stigh	265
A strong toughening mechanism in an elastic plastic laminate P. Stähle, C. Bjerken, J. Tryding, S. Kao-Walter	273
On the simulation of kink bands in fiber reinforced composites K. D. Sørensen, L. P. Mikkelsen	281
Effect of acidic conditions on interface and strength of cellulose fibres A. Thygesen, B. Madsen, A. B. Thomsen, H. Lilholt	289
Previous Publications	297
Author Index	301

NATURAL FIBRE COMPOSITES – WITH SPECIAL EMPHASIS
ON EFFECTS OF THE INTERFACE BETWEEN CELLULOSIC
FIBRES AND POLYMERS

E. K. Gamstedt^{*,**} and K. M. Almgren^{**}

^{*} Department of Fibre and Polymer Technology, Royal Institute of
Technology, KTH, S-100 44 Stockholm, Sweden

^{**} STFI-Packforsk AB, P.O. Box 5604, S-114 86 Stockholm, Sweden

ABSTRACT

Natural fibres are finding increased use in composite applications, for e.g. packaging, decking, interior panels and furniture. The most widely used type of natural fibre is cellulosic fibres. These generally come from annual crops, e.g. hemp, flax and sisal, or from wood. A useful characteristic of natural cellulose fibres is that they can be more easily modified than the relatively inert carbon, aramid and glass fibres. This characteristic stems from the abundance of reactive functional groups on the surface of cellulosic fibres, as well as in the interior bulk of the fibre cell wall. It opens up opportunities to modify cellulosic fibres for improved mechanical properties. Since the microstructure in natural-fibre composites is far more complex than in e.g. laminated composites based on glass or carbon fibres, the influence of the fibre-matrix interface on key engineering properties is still far from understood. Natural-fibre composites usually have a distribution of fibre orientation, and the fibres are relatively short with varying properties. For instance, micrographs of fracture surfaces for wood-fibre composites with various fibre orientations show that the role of the interface depends on the local fibre orientation. In general, this kind of complexities calls for experimental work to quantify how the fibre-matrix interface controls properties such as strength, fracture toughness and moisture uptake/swelling in the natural-fibre composite. With the resulting understanding, it would be possible to chemically tailor the interface for optimal mechanical performance. This paper gives a number of recent experimental examples how the interfacial adhesion affects strength, stiffness and hygroexpansion in wood-fibre composites. Two alternative macroscopic techniques to quantify the interfacial stress-transfer ability are presented, one based on dynamic mechanical testing and another based on dynamic Fourier transform infrared analysis.

1. INTRODUCTION

1.1 Motivation. Natural-fibre composite materials are finding increased use during the last decade. Environmental concerns have led to replacement of synthetic composites and plastics with natural-fibre composites. Many natural-fibre composites are biodegradable and come from a renewable resource. Other advantages are that they are lightweight and relatively inexpensive. Drawbacks include a propensity to moisture uptake resulting in property degradation, and a large variation in fibre properties. The geometry and properties of natural fibres depend e.g. on the species, growing conditions, cambium age, harvesting, defibration and processing conditions. This variation makes it more difficult to analyse the effects of the fibres and their interfaces on the mechanical properties of the composite material. These difficulties call for development of new strategies to assess the mechanical influence of the interface. Most methodologies have been developed for glass- and carbon-fibre systems. These fibres generally have a well-defined geometry, with an extended prismatic cylindrical shape with circular cross-section. Natural fibres from annual crops or wood have a much more complex structure. If test methods developed for synthetic fibres are to be used for natural fibres, care must therefore be taken to account for the geometrical particularities of the natural fibres if the measurements should be interpreted with any confidence.

Natural lignocellulosic fibres have surfaces covered with accessible hydroxyl and also carboxyl end groups. These functional groups can be used as handles to bond the fibres more firmly to the polymer matrix. The surfaces of carbon and glass fibres are relatively inert. Graphite and silica surfaces contain relatively few functional groups. The lignocellulosic fibres therefore show more versatility, where the interface may be tailored to achieve an optimal interface with regards to an important engineering property for a given application. This opens opportunities to link micromechanics with constructive material synthesis to optimize the material performance with a more rational materials development. George et al. (2001) and Mohanty et al. (2001) have compiled reviews on interfacial modifications in natural-fibre composites and their effects on the composite properties.

The question ‘What is a good interface?’ can be raised. What is ‘good’ depends on which desired property that is aimed at for a given application. In a non-woven tissue where thermoplastic is used to make the loose cellulosic fibres adhere to one another without dispersing into air, a poor and sparse bonding between fibres is desired to make the material absorb a lot of moisture. If a laminated floor is considered, where a high concentration of wood fibres is bonded with a phenol formaldehyde resin, a strong interfacial bond is strived for to obtain a hard and scratch-resistant surface. Since cellulose fibres have the possibility to show a wide range with both poor and strong bonding to polymer matrix materials, depending on fibre-matrix modification and compatibility, the optimal interface is typically somewhere between the two extreme cases. For instance, if the interface is too strong, the composite material can become too brittle, resulting in a notch-sensitive material with low strength, since stress concentrating defects are inevitable. If the interface is too weak, the fibres are easily pulled out of the matrix, which also results in a weak material with low strength. An intermediate interface is therefore expected to be optimal in terms of strength, if all other microstructural parameters remain unaltered. It should however be recognized, that the fibre-matrix interface is seldom the most important feature to be addressed in materials development of high-strength composites. The effects of the interface may be well masked by the effects of fibre dispersion. Concentrations of transverse bundles are likely to have a greater impact on the strength properties. In any case, when other well-controlled microstructural parameters have been exhausted, it can be useful to focus on interfacial design to improve the desired mechanical property even further under given cost constraints.

From a mechanistic viewpoint, materials development with regard to how the fibre-matrix interface influences a certain mechanical property can be divided into two steps. The first step is to devise test methods to quantify the efficiency of the interface. The second step is model how the interfacial efficiency together with other microstructural parameters, such as fibre orientation and dispersion, affect the mechanical properties. The second step could potentially be used as a simulation tool for materials optimization. The first step, characterization of interfacial stress-transfer, is necessary input to the model, and can be used to rank different surface modifications to identify the optimal treatment for improved properties.

1.2 Effects on engineering properties. The fibre-matrix interface does not only influence strength in natural-fibre composites. Tuning of the interfacial properties can also be used to control other macroscopic composite properties. Temperature, moisture content, strain rate etc. will naturally affect to which degree the interface influences the mechanical properties, but these conditions are considered to be constant and not discussed in detail here. Some examples of interfacial influences on engineering properties are given in the list below:

- *Strength:* For wood-plastic composites with wood particles used as fillers, the composite strength is frequently used as a measure of the interfacial strength (e.g. Oksman 1996) since the wood particles act as stress raisers. For particle composites, it can be assumed that the strength improves with stronger fibre-matrix interfaces, provided that all other material parameters remain unchanged. For fibre composites, a stronger interface does not necessarily mean a stronger composite, since a too strong interface can result in a brittle and flaw-sensitive composite material. However, for most polyolefin thermoplastics, the interface should be as strong as possible if a strong composite is the aim, since the interaction between the polar natural fibre and the non-polar aliphatic polymer matrix is very small.
- *Fracture toughness:* In crack propagation in fibre composites, the energy dissipation is affected by pull-out of fibres in the wake of the crack. The interfacial properties may also affect to which degree the crack diverts from planar growth as it encounters fibres as obstacles at the matrix crack tip. Pull-out is where the fibre-matrix interface comes into play, especially for composites with fibres primarily ordered in the load direction. The interfacial shear strength will affect the cohesive tractions of bridging fibres, which in turn will affect the fracture toughness or critical energy release rate as shown by McCartney (1989). The two extreme cases of a vanishing interfacial strength and an infinitely strong interface can be envisaged, where the first case would lead to effortless pull-out of fibres whereas the second case would lead to brittle scission of fibres. The most energy dissipating mechanisms would be in an intermediate region, where a sufficiently strong interface would demand a high level of work to pull-out fibres in the crack wake without breaking the fibres in a brittle manner. Thus, an optimum in fracture toughness can be expected for intermediately strong interfaces. These issues have been investigated experimentally and discussed by Feih et al. (2005).
- *Stiffness:* Generally, the elastic properties are improved when the interface is stronger, i.e. the stress-transfer ability is improved. Bogren et al. (2006a) measured the complex viscoelastic properties during dynamic cyclic loading, and observed a difference between the measured values and the predicted moduli based on a model with a perfect interface. This difference may be attributable, at least partly, to an imperfect interface with reduced stress transfer. Most models to predict to predict elastic properties of composites based on the elastic properties of the constituents assume an ideal interface, cf. e.g. Neagu et al. (2006) for wood-fibre composites, although there are models with

imperfect interfaces (Hashin 1990) which can be applied if there is sufficient data for estimation of the parameter describing the interface imperfection. It should be borne in mind that for each envisaged unit cell or representative volume element, the crack opening displacement for a suitable load level should be large enough to contribute to a measurable difference in stiffness compared to the case of a closed crack (Varna et al. 2001). For dispersed, dilute and small interfacial cracks, there might not be any measurable difference in composite stiffness.

- *Impact toughness*: The damage process during notched impact testing is essentially similar to that in testing of fracture toughness. The main difference is that the process is several orders of magnitude faster during impact than under quasi-static conditions. Since both the polymer matrix and natural fibres are viscoelastic in nature, the behaviour will be more brittle in impact. The polymer matrix has generally a more viscous behaviour than natural fibres, and the transition from slow and ductile yielding to brittle fracture will be more apparent in the matrix than in the fibres, when the strain rate is increased. However, the rank in impact toughness of different composites can be assumed to be very similar to the corresponding rank in fracture toughness for the same set of composites. Park and Balatinecz (1996) found a correlation between impact toughness and the work of fracture defined by the area under the stress-strain curve for wood-fibre reinforced polypropylene. The interface has probably the same role in impact testing as for quasi-static fracture toughness or strength testing, i.e. as an energy absorbing mechanism that contributes positively to the toughness property for a suitably strong interface. The interface should not be too weak to be pulled out without effort, and not too strong to induce brittle failure by fibre breakage in the same plane as the matrix crack. An example of the former situation has been presented by Bengtsson et al. (2006) who showed an increase in impact toughness for interface modified wood-fibre reinforced polyethylene. This is an example where the initial interaction is very weak between the non-polar polyethylene matrix and the polar cellulosic fibres. By silane cross-linking, the interface is made stronger resulting in an increased impact toughness.
- *Moisture uptake*: Joseph et al. (2002) showed a reduction in water uptake for sisal fibre reinforced polypropylene with improved interfacial adhesion. This result indicates that capillary water sorption mechanisms at the interface may be subdued with improved fibre-matrix bonding. Marcovich et al. (2005) showed that interfacial modification in lignocellulosic fibre reinforced unsaturated polyester led to improved fibre wetting during processing, which in turn led to less moisture uptake since capillary absorption through narrow channels along the interfaces are suppressed. Ballie et al. (2000) discuss pathways of moisture absorption found in wood, while maintaining high strength and toughness. By studying solutions in nature, ideas can be conceived of how to improve engineered composites while simultaneously optimizing several properties.
- *Dimensional stability*: For hydrophilic materials, such as natural-fibre composites, hygroelastic swelling goes hand in hand with moisture uptake: The more moisture the material absorbs, the more it will swell. If thermal deformation is ignored, the dimensional stability is typically characterized by the hygroexpansion coefficient, which describes the strain induced by a change in moisture content or in surrounding relative humidity. Increased hydrophilicity thus generally means increased dimensional instability. Typically, the cellulosic natural fibres swell more than polymer matrix materials (except maybe for certain thermoplastic starches). Higher fibre content leads to a higher degree of hygroexpansion. Grigoriou (2003) found less moisture-induced swelling for wood and waste paper composites containing higher degrees of resin. As

for moisture uptake, the fibre-matrix bond will also affect the eventual hygroexpansion. Naik and Mishra (2005) showed decreased moisture-induced swelling in maleic-anhydride treated natural-fibre reinforced polystyrene, where the fibre-matrix adhesion has been improved.

- *Time-dependent properties:* Creep and fatigue usually involve the same set of underlying damage mechanisms as in quasi-static failure, although at a different rate and to different degrees. These damage mechanisms include fibre fracture, fibre pull-out, matrix yielding, interfacial debonding, crack coalescence etc. Sain et al. (2000) showed only a marginal improvement in creep properties by maleic and maleimide interfacial modification in wood fibre polypropylene composites. A stronger effect of the interface is expected in cyclic loading under fatigue conditions, where an imperfect interface can lead to repeated frictional sliding, which induces temperature increase and energy dissipation. Gassan and Bledzki (1997) measured a significant decrease in energy dissipation during cyclic loading for jute fibre reinforced polypropylene with improved interface from maleic anhydride grafted polypropylene.

If the first step to characterize the mechanical integrity of the interface is considered, and the role of the interface on the mechanical property is ignored, a number of candidate test methods for quantitative measurements can be advocated. Most of these have been developed for glass or carbon fibres, which are comparably well-defined and uniform. Some of them are single-fibre fragmentation, fibre-pull out, Micro-Raman spectroscopy and transverse cracking in cross-ply lay-ups. Their main principles and noteworthy drawbacks are briefly outlined in the following sections. They all quantify a mechanical interfacial property, typically interfacial strength, but may also be reformulated in terms of fracture toughness, if the interfacial crack is envisaged to propagate. Other techniques may quantify other measures that are more difficult to directly relate to stress transfer. Two such examples are contact angle measurements in wetting of wood samples with specific liquids using the Wilhelmy method (Wålinder and Ström 2001) and x-ray photoelectron spectroscopy of natural fibre surfaces compared with their adhesion to a polypropylene matrix (Park et al. 2004). Qualitative measures of physical and chemical interfacial interaction are however most useful in materials development when ranking different surface modifications, even though the values cannot be used directly to predict mechanical behaviour on a larger scale.

1.3 Single-fibre fragmentation. A single-fibre composite test consists of a fibre which is fully embedded in matrix block, and load is applied along the fibre direction. If the strain to failure of the matrix is substantially higher than that of the fibre, multiple fibre breakage will occur until saturation, when the interface cannot transfer sufficient load back to the fibres to cause further fibre breakage. The crack density at saturation can then be used to estimate the interfacial shear strength. A requisite is that matrix cracks perpendicular to the fibre and load direction do not form at the fibre breaks. Instead interfacial debonds should emanate from the fibre breaks. This puts further limitations to the types of matrix materials that can be used. Since natural fibres tend to have a high strain to failure, only very ductile matrix materials are suitable. In any case the single-fibre fragmentation test has been used for wood fibres embedded in vinyl ester to measure the distribution of strain to failure of wood fibres (Thuvander et al. 2001). Joffe et al. (2003) have shown that this method can also be used for interfacial characterization, where treated and untreated flax fibres were fragmented until saturation.

1.4 Fibre pull-out. A direct way to measure the interfacial shear strength is to pull out a fibre from a block of matrix material. The interfacial shear strength can be estimated from the maximum load divided by the circumferential area of the pulled-out fibre. Sanadi et al. (1993) loaded partially embedded wood fibre, and found that both the surface treatments and the type

of matrix affected the interfacial strength. One difficulty that arises in pull-out test is the influence of the shape of the meniscus at the location where the fibre protrudes from the matrix block. Depending on the local affinity of the polymer melt or viscous resin to the fibre surface, different contact angles will form and maintain as the melt or resin solidifies. The wetting angle can vary locally e.g. from contamination during handling and manufacture. Since the debond cracks starts from the surface, the shape of the meniscus will affect the local stress state and hence also the onset of debonding. The micro-bond test where a resin droplet is applied on the fibre is another alternative to a resin block. The shape of the droplet must be taken into consideration in the analysis to calculate the interfacial strength or fracture toughness (Scheer and Narin, 1995). The micro-bond test has been used for cellulosic fibres by e.g. Tze et al. (2007), and by Eichhorn and Young (2004). They complemented the pull-out test with Raman microscopy to gain further information of the debond process.

1.5. Micro-Raman spectroscopy. Embedded and visible fibres can be analysed with Raman spectroscopy. As the crystalline fibre is stretched, wave numbers of specific peaks shift. By calibration, the shift can be related to local axial strain in the fibre. By analyzing the change in strain profile along the fibre as an interfacial debond grows, the interfacial shear strength can be estimated from micromechanical models (e.g. Gamstedt et al. 2002). As mentioned previously, Eichhorn and Young (2004) and Tze et al. (2007) combined micro-Raman spectroscopy with the micro-droplet pull-out test to measure the interfacial load-transfer ability. The combination of mechanical testing of a model microcomposite and local strain analysis using micro-Raman spectroscopy is a particularly nice illustration of how micromechanics can be used to identify small-scale interfacial properties by direct measurements. Drawbacks are that these tests require a substantial measure of experience, the equipment is relatively expensive and that natural fibres show a lot of variability, implying that a lot of tests must be done in order obtain a sufficient amount of data to estimate the property with some degree of confidence.

1.6 Transverse cracking in cross-ply laminates. A simple macroscopic test, which has been used quite extensively for continuous-fibre composites (e.g. Sjögren and Berglund 2000 for glass-fibre composites), is measurement of transverse cracking in tensile loading of cross-ply laminates. In the middle layer, with transverse fibre orientation perpendicular to the load direction, cracks will accumulate and eventually saturate much like the process in the single-fibre fragmentation test. These transverse cracks typically emanate from coalescence of transverse fibre-matrix debonds into macroscopic and directly visible transverse cracks. The surrounding longitudinal plies are only used as supporting substrates. The onset of transverse cracking may be interpreted as an indicator of interfacial strength and can be related to measurements of the mechanical integrity of the interface by other techniques (Sjögren et al. 1999). Measurement of the onset of transverse cracking in cross-ply laminates is essentially identical to strength measurement of transversely oriented unidirectional composites. However, the subsequent cracking in cross-ply laminates, give further information on volume effects of transverse strength due e.g. to fibre bundle dispersion. Estimation of transverse strength can therefore be made with higher accuracy from a cross-ply test than for strength measurement of a transverse unidirectional composite. Van de Weyenberg (2006) observed higher transverse strength after alkaline treatment of flax fibres for improved interfacial adhesion in an epoxy matrix with unidirectional fibre orientation.

1.7 Novel characterization techniques. The aforementioned techniques have their advantages and drawbacks. Some techniques are suitable in some cases, depending on the constraints of the materials used, costs to carry out the tests and the intended application of the material. One particularity of natural fibres and other biological materials stemming from nature is a daunting variability in properties and morphology, depending on growth conditions, cambium age,

harvesting and fibre treatment. As has already been underscored, this inherent scatter for natural fibres implies that a considerable amount of tests have to be carried out to acquire a sufficient quantity of data to estimate the sought measure with a certain degree of confidence. If it is too costly to achieve this quantity of data, it can be wiser to adopt a macroscopic and indirect technique for interfacial characterization. There are two main ways to quantify the stress-transfer efficiency: (i) by measuring the loading limit of the interface, i.e. its strength, or (ii) by measuring the performance of the interface up to this limit, i.e. the stress-transfer ability of the interface without any further debonding or other irreversible inelastic deformation taking place. These quantities both describe the mechanical function of the interface. In daily functioning of natural fibre materials, load levels should be small enough not to render stress levels that lead to interfacial failure, and onset of damage accumulation that eventually leads to complete failure. In that case, the measure pertaining to interfacial performance up to, but not exceeding the limit, would be of interest. In this paper, two such candidate techniques are presented. They are both under development, and cannot yet be used completely quantitatively, although they show promise and can be used to rank different interfaces in terms of stress-transfer ability. The effect of moisture on interfacial stress-transfer has been investigated. They both rely on macroscopic dynamic tensile loading, which provides more information than quasi-static loading, since also the viscous part can be used in assessing the interfacial stress transfer. The first method is based on a comparison of the experimental values of the dynamic-mechanical properties of a composite with predicted values based on input of the dynamic-mechanical properties of the constituents, namely the fibres and the matrix. The second method is based on dynamic Fourier transform infrared (FT-IR) analysis during dynamic mechanical tensile loading. Different peaks in the FT-IR spectra are characteristic for the fibres and matrix, respectively. By investigating the behaviour of the peaks characteristic for the respective constituent, conclusions can be drawn on how effectively stress is transformed between them. Further information on the former method has been reported by Bogren et al. (2006a), and Bogren et al. (2006b) for the latter method. The two methods are presented in combination in the following sections, since they need the same experimental equipment, a dynamic mechanical analyzer (DMA). The only difference is that the FT-IR requires the DMA to be instrumented with an infrared detector. Both methods can not only be regarded as characterization methods, but also as measurements of effects of the interface (or interphase) in natural fibre composites.

Even though the two methods must still be regarded as qualitative, the aim is still to obtain a quantitative link from the stress transfer between fibres and matrix to a measured property of a natural-fibre composite material, where the natural fibres show a high degree of variability. This is possible by comparing the mechanical dissipation of the composite with a value predicted by a micromechanical model based on perfect interfacial stress transfer. The input parameters in the micromechanical model were experimentally characterized properties of the composite constituents. Damping of the material is due to viscoelasticity of the constituent materials and imperfections in the fibre-matrix bond. Imperfect adhesion allows the fibres to slide and the friction between fibres and matrix will then contribute to the damping of the material.

Effectively, these measurements are made macroscopically, but with the dynamic FT-IR spectroscopy technique it is possible to obtain information on stress transfer on the molecular level. The technique was introduced in the 1980s (Noda et al. 1983; Noda et al. 1987) for rheological characterization of polymers. The technique has also been applied to pulp fibres for structural and rheological studies (Hintertoisser and Salmén 1999; Åkerholm and Salmén 2001; Åkerholm and Salmén 2004). During the dynamic FT-IR measurement, thin samples are subjected to sinusoidal strain while irradiated with polarized IR radiation. Changes in intensity, or energy of molecular vibrations, occur when the applied load strains and reorients the polymers in the sample. A dynamic FT-IR spectrum differs from an ordinary/static FT-IR

spectrum in that only the molecular groups active in the stress transfer contributes to the spectrum, since the sample is unloaded in the static spectra. Consequently, qualitative studies on stress transfer down to the molecular level are possible to perform. Mechanical properties, such as Young's modulus and loss factor, can be measured simultaneously at the macroscopic level. Studies made by Wang et al. (2005), using a similar technique on synthetic materials, show correlation between the mechanical properties and the dynamic FT-IR response.

Raman microscopy has successfully been used to quantify stress transfer mechanisms in composite materials for quite some time, see e.g. Young (1996) and Galiotis et al. (1999). This method has more recently been adopted for cellulosic natural fibres by Eichhorn and Young (2004) and Tze et al. (2007). Interfacial efficiency has then been measured, and used as a tool in materials development. FT-IR microscopy has similar features to Raman microscopy, but has until now been used only scarcely to gain mechanical information on the microstructural level, even though the method should have potential use in experimental micromechanics. The present work is a feasibility study of dynamic FT-IR spectroscopy to gain further understanding of how stress is redistributed as a result of changed moisture content in a wood-fibre composite subjected to cyclic loading.

This study concerns wood fibres embedded in a polylactide (PLA) matrix. Wood fibres offer lower variability than many other cellulose-based fibres. The raw material is abundant and the pulp and paper industry is well established. The density of the fibres is low and their specific material properties are comparable to those of synthetic fibres (Nabi Saheb and Jog 1999). These qualities make it possible for wood fibres to replace synthetic fibres in some applications. PLA is a thermoplastic polymer produced from annual plants, typically maize, and can be totally degraded in aerobic or anaerobic environments (Auras et al. 2004). Modern technologies are reducing production costs which makes PLA suitable for many applications requiring disposable and biodegradable materials, recent research shows that natural fibre composites is one of them (Oksman and Selin 2004). Since both fibres and matrix in the composite material studied are produced from renewable natural resources and are biodegradable the resulting composite material meets the demands for an environmentally friendly material.

2. METHODS OF ANALYSIS

The results from a model that neglects the imperfections in adhesion, compared to measured values of damping in a material, offer a macroscopic measure of the microscopic fibre-matrix stress transfer. A microscopic interfacial parameter that describes the stress transfer efficiently would however be more desirable. Corrêa et al. (2005) measured dynamic-mechanical damping in wood flour filled polypropylene and calculated an interfacial efficiency factor based on a rule-of-mixtures method for rigid-particle composites (Kubát et al. 1990). A more accurate approach for elastic properties has been proposed by Hashin (1990) who introduced a set of interfacial spring constants that quantify the degree of interfacial imperfection. Nairn (2004) has illustrated how to identify such interface parameters from experimental data in static loading. For the viscoelastic case, a corresponding rheological spring-dashpot description of the interface could be devised (Hashin 1991). At this stage, however, we confine ourselves to compare predicted and measured damping of the composite. This approach provides an indirect quantitative measure of interfacial imperfection on the macroscopic scale during cyclic loading. The input to the model was viscoelastic material data for the constituent materials. Through micromechanical models and laminate theoretical predictions of the damping properties of a laminate were obtained.

2.1 Dynamic mechanical analysis. The Young's modulus and damping of a material can be

determined with a Dynamic Mechanical Analyzer (DMA). Both Young's modulus and damping of wood fibres and composites are dependent on the moisture content and therefore on the relative humidity (RH) in the surroundings. High moisture content generally increases the damping of the composite. A humidifier connected to the DMA was used to expose the composite sample to a relative humidity of relevance to wood-fibre composite applications. Due to swelling, the thickness of the sample will change. This is usually not accounted for in the DMA software and should be considered when using the material data as input in the model.

2.2 Dynamic vapour sorption. Moisture content at equilibrium conditions gives a better description of the state of the material than the ambient relative humidity. Therefore a Dynamic Vapour Sorption (DVS) unit was used to investigate the moisture content in the samples at the relative humidity used. This technique also makes it possible to investigate whether the water uptake of the fibres was constrained by the matrix in the composite.

2.3 Differential scanning calorimetry. DSC was used to determine the degree of crystallinity of the materials. The mechanical properties of PLA are dependent on the degree of crystallinity (Mezghani and Spruiell 1998; Kasuga et al. 2003; Weir et al. 2994) and it was therefore important to know whether or not the neat PLA used to generate input data to the model had a different degree of crystallinity compared with the PLA in the composite material. The DSC crystallinity can be determined according to:

$$X_c = \frac{\Delta H_m - \Delta H_c}{H_m^c} \quad (1)$$

where X_c is the degree of crystallinity, ΔH_m is the enthalpy of fusion, ΔH_c is the enthalpy of crystallization and $H_m^c = 93 \text{ J/g}$ is the enthalpy of fusion of a PLA crystal of infinite size (Garlotta 2001).

2.4 Dynamic Fourier transform infrared spectroscopy. Dynamic FT-IR was used to study stress transfer at molecular level. The method is relatively new in the wood-fibre composite field and was therefore not used as a quantitative method (Åkerholm et al. 2005). The obtained results can give a qualitative assessment of stress transfer at molecular level.

3. MODELLING APPROACH

The mechanical model is divided into a micromechanical model and a laminate analogy. Material parameters of the constituent materials, wood fibres and PLA, are used as input to the micromechanical model that provides the properties of unidirectional layers of wood fibres and matrix. The laminate analogy summarizes the contributions from the unidirectional layers to obtain the overall in-plane dynamic-mechanical properties of the composite. The fibres in the samples used are randomly oriented. In the model the samples are divided into infinitely many, infinitesimally thin, unidirectional and evenly oriented layers. The model is, however, readily generalized to an arbitrary fibre orientation distribution.

3.1 Loss factor. A summary of commonly used loss or damping measures is presented in this section. The stress, σ , and strain, ε , of a viscoelastic sample subjected to sinusoidal load with angular frequency ω can be expressed as $\sigma = \sigma_0 \sin \omega t$ and $\varepsilon = \varepsilon_0 \sin(\omega t - \delta)$. The loss angle, δ , may also be defined as the angle between the complex Young's modulus and its real component. The real part of the complex modulus, E' , i.e. the storage modulus, describes the elastic behaviour of the material and the imaginary part, E'' , i.e. the loss modulus, describes the viscous

behaviour,

$$E^* = E' + iE'' \quad (2)$$

In this text the superscript * is used to denote complex modulus. The loss angle is connected to the dissipated energy through the loss factor, η , according to

$$\eta = \frac{1}{2\pi} \frac{\Delta U}{U} \quad (3)$$

where ΔU is the energy dissipated during one load cycle and U is the maximum strain energy. The relations between the loss factor, loss angle and complex modulus are

$$\eta = \tan \delta \quad (4)$$

$$\tan \delta = \frac{E''}{E'} \quad (5)$$

3.2 Laminate theory. The laminate model presented in the following section is applied for laminates that consists of thin, unidirectional and orthotropic layers. The wood fibres are modelled as transversely isotropic and cylindrical. The longitudinal ‘f1’ direction of the fibres coincides with the longitudinal ‘1’ direction of the layers. Consequently the transverse ‘f2’ direction of the fibres coincides with the transverse ‘2’ direction of the layers. An angle, θ , describes the direction of fibres and layers relative to the global load direction.

A single unidirectional and orthotropic layer subjected to uniaxial load is considered. If the load is applied in the longitudinal direction the energy loss is (e.g. Melo and Radford 2003)

$$\Delta U = \pi \{\sigma\}^T [\eta] [S] \{\sigma\} \quad (6)$$

where $\{\sigma\}$ is the stress vector, $[S]$ is the compliance matrix and $[\eta]$ is a diagonal matrix containing the loss factors in the longitudinal, transverse, and in-plane shear directions of the layer, i.e. η_1 , η_2 and η_6 . In the case of a transversely isotropic material the non-zero components in the compliance matrix are given by $S_{11} = 1/E_1$, $S_{22} = 1/E_2$, $S_{12} = S_{21} = -\nu_{12}/E_1$ and $S_{66} = 1/G_{12}$, where E_1 , E_2 , G_{12} and ν_{12} are the longitudinal Young’s modulus, transverse Young’s modulus, shear modulus and Poisson’s ratio, respectively. These are the elastic material parameters of a single unidirectional composite layer.

The strain energy is given by

$$U = \frac{1}{2} \{\sigma\}^T [S] \{\sigma\} \quad (7)$$

If the load direction does not coincide with the fibre direction Eqs 6 and 7 are transformed according to

$$\Delta U = \pi \{\sigma\}^T [T]^T [\eta] [S] [T] \{\sigma\} \quad (8)$$

and

$$U = \frac{1}{2} \{\sigma\}^T [T]^T [S] [T] \{\sigma\} \quad (9)$$

where $[T]$ is the transformation matrix defined in Eq. 10

$$\begin{bmatrix} \sigma_1 \\ \sigma_2 \\ \sigma_{12} \end{bmatrix} = \begin{bmatrix} m^2 & n^2 & 2mn \\ n^2 & m^2 & -2mn \\ -mn & mn & m^2 - n^2 \end{bmatrix} \begin{bmatrix} \sigma_x \\ \sigma_y \\ \sigma_{xy} \end{bmatrix} \quad (10)$$

where $m = \cos\theta$ and $n = \sin\theta$. The stress vectors $[\sigma_1, \sigma_2, \sigma_{12}]^T$ and $[\sigma_x, \sigma_y, \sigma_{xy}]^T$ define the stresses in the local and global coordinate systems.

If σ is the only applied uniaxial stress the loss factor is given by Eq. 11 (Adams and Bacon 1973; Melo and Radford 2003)

$$\eta = \frac{1}{2\pi} \frac{\Delta U}{U} = \frac{\eta_1 S_{11} m^4 + (\eta_1 + \eta_2) S_{12} m^2 n^2 + \eta_2 S_{22} n^4 + \eta_6 S_{66} m^2 n^2}{S_{11} m^4 + (2S_{12} + S_{66}) m^2 n^2 + S_{22} n^4} \quad (11)$$

For a laminate consisting of several layers summation is performed over the contributions from the constituent layers. If the layers are infinitely many and infinitesimally thin the summation is expressed as an integral

$$\eta = \frac{\int_{-\pi/2}^{\pi/2} [\eta_1 S_{11} m^4 + (\eta_1 + \eta_2) S_{12} m^2 n^2 + \eta_2 S_{22} n^4 + \eta_6 S_{66} m^2 n^2] p(\theta) d\theta}{\int_{-\pi/2}^{\pi/2} [S_{11} m^4 + (2S_{12} + S_{66}) m^2 n^2 + S_{22} n^4] p(\theta) d\theta} \quad (12)$$

If the layers are evenly oriented in the interval the orientation distribution function $p(\theta)$ is constant and equals $1/\pi$. Integration of Eq. 12 gives the damping of the composite laminate

$$\eta = \frac{\eta_1 (3S_{11} + S_{12}) + \eta_2 (3S_{22} + S_{12}) + \eta_6 S_{66}}{3S_{11} + 2S_{12} + 3S_{22} + S_{66}} \quad (13)$$

3.3 Micromechanical model. The rule of mixtures was used to obtain Young's modulus in longitudinal direction and Poisson's ratio and the Halpin-Tsai model were used to obtain the transverse Young's modulus and in-plane shear modulus for the composite layers, respectively. Even though the analytical model of Hashin (Hashin and Rosen 1964; Hashin 1979) is known to be more accurate, the Halpin-Tsai model has shown to give similar results to finite element solutions of unidirectional short-fibre composites (Tucker and Liang 1999). Considering the experimental scatter for wood-fibre materials and the simplicity of the Halpin-Tsai model, this model was used in the present investigation. The correspondence principle was used to transfer the material models from the elastic to the viscoelastic case by a complex representation of the governing equations (Chandra et al. 2002).

Unless excessively beaten and refined, individual wood fibres have high aspect ratios and can be considered continuous from a mechanical point of view. The rule of mixture is hence applicable. The complex Young's modulus in the longitudinal direction and Poisson's ratio is given by the rule of mixtures

$$E_1^* = V_f E_{f1}^* + V_m E_m^* \quad (14)$$

$$\nu_{12} = V_f \nu_{f12} + V_m \nu_m \quad (15)$$

where the complex Young's modulus of fibre in the longitudinal direction is denoted E_{f1}^* and E_m^* is the complex Young's modulus of the matrix. Poisson's ratio, ν_{12} , is assumed to be purely elastic. The major Poisson's ratios of wood fibre and matrix are ν_{f12} and ν_m . The volume fractions of fibre and matrix in the lamina are denoted V_f and V_m , respectively. The volume fibre fraction is determined as

$$V_f = \frac{w_f / \rho_f}{w_f / \rho_f + w_m / \rho_m} \quad (16)$$

where w_f and w_m are the measured weight fractions and ρ_f and ρ_m are densities of fibres and matrix, respectively. The matrix volume fraction is simply found as $V_m = 1 - V_f$ for void-free composites.

The Halpin-Tsai equation and the correspondence principle give the complex moduli in transverse and in-plane shear directions (e.g. Chandra et al. 2002)

$$M^* = M_m^* \frac{1 + \zeta \lambda^* V_f}{1 - \lambda^* V_f} \quad (17)$$

where

$$\lambda^* = \frac{M_f^* / M_m^* - 1}{M_f^* / M_m^* + \zeta} \quad (18)$$

where M^* is the complex modulus (E_2^* or G_{12}^*), M_f^* is the complex fibre modulus (E_{f2}^* or G_{f12}^*) and M_m^* is the complex matrix modulus (E_m^* or G_m^*). The shape factor, ζ , depends on the cross-sectional geometry and packing of the fibres. It is assumed to be 2. The loss factors of the layer are given by η_1 , η_2 and η_6 in the longitudinal, transverse and shear directions of the layer, respectively. The imaginary component of the complex moduli are found through the loss factors according to Eq. 5.

3.4 Material parameters. The micromechanical models require elastic and viscous components of the material parameters, i.e. the longitudinal and transverse Young's modulus of the fibres, Young's modulus of the matrix and shear modulus and Poisson's ratio for both fibres and matrix, i.e. E_{f1}^* , E_{f2}^* , E_m^* , G_{f12}^* , ν_f , G_m^* and ν_m . These parameters should be determined from experiments.

3.5 Properties of wood fibres. The assumption that wood fibres are transversely isotropic is a simplification of the rather complex nature of the wood fibres. Due to the miniscule dimensions of wood fibres it is difficult to determine the elastic properties of single fibres. The properties vary from fibre to fibre which make the results uncertain. Measurements with special equipment must be done to determine the properties through direct methods. Therefore a more straightforward method was used. The elastic modulus in the longitudinal direction of the fibres was determined through tensile tests of a dense fibre mat and back-calculation.

The fibre mat is considered to be a laminate built up by infinitesimally thin unidirectional layers according to the laminate theory described above. Bonds between fibres are assumed to be perfect since wet-formed highly consolidated sheets were used in this study. Lu et al. (1995)

have shown that a laminate model is more suitable than a network or web model for well-bonded paper sheets. The fibre mat consists of wood fibres and air and the volume fraction of fibres in the fibre mat is given by

$$V_f = \frac{W_{\text{mat}}}{t\rho_f} \quad (19)$$

Where W_{mat} is the basis weight of the fibre mat and t is the thickness of the same. The density of the collapsed fibres is denoted ρ_f and equals 1.5 g/cm^3 (Kellog and Wangaard 1969).

The damping in the longitudinal direction of a unidirectional fibre mat layer, η_{f1} , is assumed to be small compared to other directions and is therefore neglected. The loss factors in transverse and shear directions are modelled as equally large based on experimental results for other kinds of unidirectional fibre composites (Lee et al. 1994). Simulations have also indicated that this is a plausible assumption (Hashin 1991). Eq. 13 was used to determine the damping in transverse and in-plane shear directions. With $\eta_{f1} = 0$ and $\eta_{f2} = \eta_{f6}$ Eq. 13 reduces to

$$\eta_{\text{DMA}} = \frac{\eta_{f2}(3S_{f22} + S_{f12} + S_{f66})}{3S_{f11} + 2S_{f12} + 3S_{f22} + S_{f66}} \quad (20)$$

Where S_{f11} , S_{f22} , S_{f12} and S_{f66} are compliance parameters for wood fibres and η_{DMA} is the experimentally determined damping of the fibre mat.

The transverse elastic modulus, shear modulus and Poisson's ratio are obtained through imposed realistic ratios $E_{f1}/E_{f2} = 2$, $G_{f12}/E_{f1} = 0.1$ and $\nu_{f12} = 0.3$ (Neagu et al. 2005). Young's modulus of the fibres can then be determined by finding the least square sum of the experimentally measured values

$$\min_{E_{f1}} [\{ E_{\text{mat}}^{\text{exp}} - E_{\text{mat}}(E_{f1}, E_{f2}, G_{f12}, \nu_{f12}) \}^2] \quad (21)$$

where $E_{\text{mat}}^{\text{exp}}$ is the experimentally determined Young's modulus of the wood-fibre mat and E_{mat} is the predicted value.

3.6 Properties of polylactide. The studied PLA films were isotropic and the Young's modulus and damping were hence the same in transverse and longitudinal directions. These values were obtained through DMA measurements of PLA film. The Poisson's ratio and density were estimated through literature values, $\nu_m = 0.35$ and $\rho_m = 1.27 \text{ g/cm}^3$ (e.g. Woodings 2000).

3.7 Moisture absorption and hygroexpansion. If one of the constituent materials absorbs more moisture than the other, the volume fractions of fibres and matrix change. This is accounted for by using the actual weight fractions at the chosen relative humidity in Eq. 16. The software of the DMA equipment does not take into account that the thickness of the sample is dependent on the relative humidity in the test chamber. Wood-fibre composites tend to swell and this must be accounted for when the Young's modulus is determined. The thickness change is assumed to be linear within the interval under investigation. For linear out-of-plane hygroexpansion the thickness change is

$$\Delta t = t\beta_z \Delta c \quad (22)$$

where β_z is the hygroexpansion coefficient and Δc is the change in moisture content at given

equilibrium conditions. The in-plane hygroexpansion was neglected.

4. EXPERIMENTAL PROCEDURES

4.1 Materials and manufacturing. Mechanical testing was performed on wood-fibre mats, PLA films and wood fibre/PLA composites. The wood fibres were delivered as fully bleached sulphite softwood pulp from Nordic Paper. The pulp was processed similarly to pulp used for greaseproof applications. The PLA, Terramac[®] PL01, was delivered as fibres, with length of 5.1 mm and width of 13 μm , from Unitika Fibers Ltd. The weight fraction of wood fibres in the composite material was 60%. The composites were manufactured by hot pressing sheets of wood and PLA fibres in a modified MTS 448. The samples were pressed at 180 °C and 150 bar for 5 minutes.

4.2 Dynamic mechanical testing. The dynamic mechanical tensile testing was performed in a Perkin Elmer DMA 7. Unidirectional load was applied to the sample at constant temperature (30 °C) and with constant frequency (1 Hz). The stress ratio, $R = \sigma_{\min} / \sigma_{\max}$, was 0.09 and the displacement amplitude was set to 4 μm , which typically corresponds to strain levels below 0.1%. Linear viscoelasticity of the constituent polymers was therefore assumed.

The composite material was tested to study the moisture induced softening of the material. The humidifier started the program with 90% RH for 30 minutes, followed by 30% RH for 30 minutes. This procedure was repeated once. After the conditioning the sample was dried at 0% RH for three hours, where 0% RH is an approximate value for the dry state since humidity can never entirely be avoided. Then the relative humidity was increased by 0.1% per minute until 90% RH was reached. The wood-fibre mat, PLA film and composite samples were tested to determine modulus and damping of the materials at 0% RH and 80% RH. Wood-fibre and composite samples were conditioned according to the program described above which was followed by 80% RH for 300 minutes and 0% RH for 300 minutes. The program for the PLA films was shorter; the program started at 0% RH for 60 minutes and thereafter the relative humidity was increased with 1% per minute until 80% was reached. This relative humidity was kept constant for 60 minutes. 0% and 80% RH will be referred to as dry and humid conditions, respectively.

The length of the samples tested with the DMA was approximately 15 mm and the width was approximately 5 mm. The thickness of the samples depends on the material, approximately 28 μm for wood-fibre mat, 50 μm for PLA film and 34 μm for composite material. At least five samples of each material were tested at dry and humid conditions.

4.3 Molecular stress transfer. When a polymer film is stretched, the load bearing polymers are strained, which results in an increase or decrease of IR radiation absorbed at a given energy. Stretching of covalent bonds also result in energy changes of the vibrations in the molecule. This leads to frequency shifts and changes in width of the absorption maxima. Unstrained molecules give no contribution to the dynamic IR spectra. This means that if a sinusoidal strain is applied, the IR absorption will vary sinusoidally. The possibility to time-resolve spectra gives the opportunity to obtain the elastic and viscous response of each individual molecular vibration. A more detailed description of the FT-IR technique is found in references (Noda et al. 1983; Åkerholm and Salmén 2004).

Samples of PLA film and composite material were studied. The spectra were recorded on a Digilab FTS 6000 FT-IR spectrometer using a Mercury Cadmium Telluride (MCT) detector. During the dynamic testing the samples were loaded in a Polymer Modulator (PM-100)

manufactured by Manning Applied Technologies Inc. For further description of the experimental procedures see Åkerholm and Salmén (2004).

Measurements of swelling, moisture absorption and DSC were done by standard techniques, and details of the experimental set-ups etc. can be found in Bogren et al. (2006a).

5. RESULTS AND DISCUSSION

5.1 Results of mechanical testing. The DMA was used to study the moisture induced softening of the composite material. Measurements were performed on samples of wood-fibre mat, PLA film and composite material at the above mentioned levels of relative humidity. The experimental values of the loss factor, η , are presented in Fig. 1. Although the batch-to-batch variability was large, at least four samples of each material were tested to show that the average values were estimated with some accuracy. The intra-batch variability was low, and a significant increase in the loss factor was found for a given specimen (fibre mat, polymer film, or composite material) in humid conditions compared with the loss factor at dry conditions.

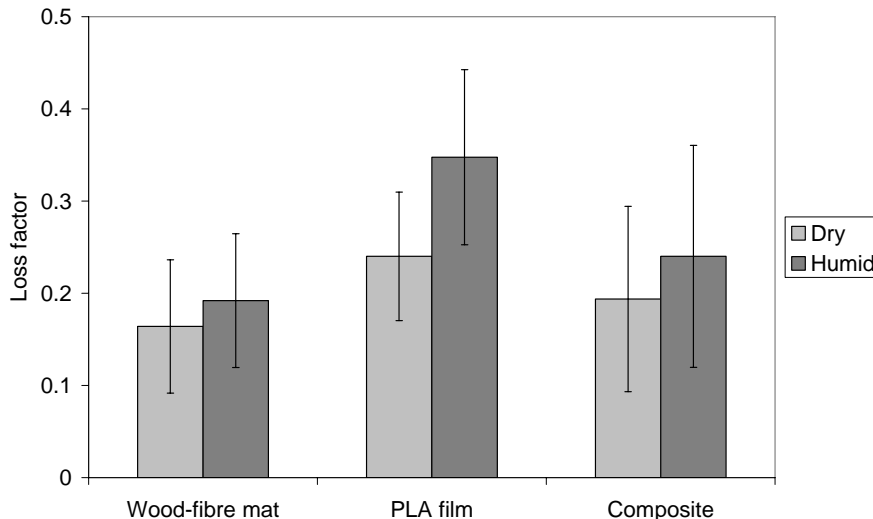


Fig. 1. Loss factor for the constituents and the composite at dry and humid conditions.

Swelling also affects the volume fractions of the constituent materials. The DVS was used to study the water content of the composite and constituent materials during equilibrium conditions for selected levels of relative humidity. Experimental data for the composite sample showed an increase of weight with 6.7% when relative humidity was increased from 0% to 80%. The predicted value of mass change, using a linear rule of mixture, where the experimentally determined absorption for wood fibres and PLA were used as input, was slightly higher, 7.4%. The difference is small and not necessarily due to a constrained hygroexpansion of the wood fibres. It is more likely to be caused by material heterogeneity. The mass increase of PLA when the relative humidity was increased from 0% to 80% was less than 1%, which also supports the assumption that the thickness change of PLA can be neglected. With the knowledge of the thickness change and moisture content, the out-of-plane coefficient of hygroexpansion, β_z , could be determined according to Eq. 22. The hygroexpansion coefficient for the fibre mat was as expected higher than for the composite material, i.e. 0.25 % strain/% moisture content and 0.16 % strain/% moisture content, respectively.

The Young's moduli for the three materials at the dry and humid state, when thickness change

and changes in volume fractions of the constituent materials in the composite are accounted for, are presented in Bogren et al. (2006a). The obtained values for Young's modulus of the fibre mat were used to predict the longitudinal Young's modulus of single wood fibres. Additionally, the Young's modulus for PLA and the loss factor for the two materials, were used as input data to the model to predict the composite loss factor, as outlined in the modelling section.

Information from DSC runs were inserted in Eq. 1 showed 22% crystalline material in the PLA film and 18% crystalline PLA in the composite material, respectively. The difference is small and should not have a significant effect on the result of the modelled or measured values. It can therefore be assumed that the viscoelastic behaviour of a neat PLA film can be used to model the matrix in the composite in the micromechanical models, in spite of the semicrystallinity of the thermoplastic PLA.

5.2 Comparison of experimentally determined and predicted values. The Young's modulus and the loss factor of the composite material were predicted using micromechanical models and laminate analogy where perfect bonds between fibres and matrix were assumed. The complex form of the rule of mixture and the Halpin-Tsai equation, i.e. Eqs 14, 17 and 18; were used to determine the mechanical properties of unidirectional orthotropic layers and their contributions to stiffness and damping were summarized through laminate analogy to predict the mechanical properties of a laminate with uniformly oriented fibres.

Dynamic mechanical properties of the constituent materials, wood-fibre mat and PLA, were determined experimentally and used as input data to the model. DMA was used to determine the Young's modulus of wood-fibre mat and PLA film at dry and humid conditions. The hygroexpansion coefficient was determined according to Eq. 22 and the thickness change of the wood-fibre mat was thereby accounted for in the stress analysis. The Young's modulus of the fibres in the longitudinal direction was determined through back calculation from the fibre-mat stiffness, see Eq. 21. The loss factor of the fibres in transverse direction was determined through laminate analogy according to Eq. 20.

The damping predicted by the model was, as expected, lower than the experimentally determined values. The values are presented in Table 1. The predicted value was 63% of the experimentally determined value at dry conditions. For humid conditions the value was 66%.

Table 1. Experimentally determined and predicted values of the loss factor of the composite at dry and humid conditions.

	Loss factor in dry state	Loss factor in humid state
Experimental	0.19	0.24
Modelled	0.12	0.16

The predicted values of Young's modulus were slightly lower than the experimentally determined values. The predicted values, 1.01 GPa and 0.88 GPa, respectively, were 92% of the experimentally determined values. This shows that the difference between measured and predicted values of loss factor really is a measure of energy losses in the material due to mechanisms that are unaccounted for in the model. Dissipation at the fibre-matrix interface, which was assumed to be perfectly bonded in the micromechanical model, contributes to the loss factor mismatch. Since the fibres were of finite length, increased dissipation can be assumed at the fibre ends. Stress concentration in the adjacent matrix is expected along the ineffective lengths at the fibre ends, and debonding is known to initiate primarily at fibre ends. Nevertheless, the wood fibres have aspect ratios in excess of ~ 50 , and the influence of the fibre

ends is considered to be negligible. The overall interfacial bond efficiency is believed to play a principal role in the measured dissipation difference.

5.3 Molecular stress transfer. The results of the dynamic FT-IR analysis give information about the local loss angle in molecular bonds. The purpose of the FT-IR measurements was to see if the same general trends apply on the molecular level as on the macroscopic scale measured with DMA. Dynamic FT-IR absorption spectrum for a composite material and PLA film at dry and humid conditions were studied. In Table 2 loss factors for some specific molecular bonds of the composite, the PLA and the cellulose of the fibres in the fibre mat, are listed.

Table 2. Molecular loss factors of selected wavenumbers from dynamic FT-IR spectra. Values are given for PLA films and composites materials at dry and humid conditions.

		Dry state		Humid state	
Molecular bond and material	Wavenumber	PLA	Composite	PLA	Composite
Asymmetric CH ₃ bend, PLA	1454 cm ⁻¹	1.30	0.14	3.50	1.20
COH bend, cellulose	1439 cm ⁻¹	-	0.07	-	0.45
Symmetric CH ₃ bend, PLA	1382 cm ⁻¹	0.47	0.05	0.49	0.51
CH ₂ bend, cellulose	1315 cm ⁻¹	-	0.11	-	0.75

The damping determined with FT-IR follows the same trend as the values obtained from the DMA: the damping of the PLA is higher than the damping of the cellulose in the fibres and the introduction of moisture makes the damping increase significantly. In some cases the damping is very high. This is considered to be a local phenomenon for specific bonds rather than representative for the entire polymer. If calibration is done to relate local loss factors from dynamic FT-IR to the macroscopic mechanical loss factors, this method have the potential of being used quantitatively and directly on composites without having to resort to DMA measurements of matrix films and fibre mats.

6. CONCLUSIONS

The implications of the fibre-matrix interface on mechanical properties in natural fibre composites have been discussed. Clearly, there is a great potential for further materials development in composites reinforced by lignocellulosic natural fibres with regard to the fibre-matrix interface. The chemistry and physics of natural fibres unlock possibilities of tailoring the interface. However, further knowledge on the influence of the interface on the mechanical properties is necessary. In particular, test methods should be developed to assess the stress-transfer ability in natural-fibre composites, to rank surface treatments etc. Methods based on model composites with single fibres developed for glass and carbon fibre composites are not always suitable for natural fibres which show a very large scatter in properties and geometry. Two alternative methods are presented in this paper. These are based on dynamic-mechanical loading of the composite and its constituents. The effect of humidity was investigated, since interfaces in natural-fibre composites are known to be very prone to moisture adsorption. A biocomposites composites of wood-fibres in a polylactide matrix was investigated.

The predicted values of damping in the composite were 63% and 66% of the experimentally determined values at dry and humid conditions, respectively. This was expected as the model does not cover all energy losses in the material and hence should deliver values that are lower

than the experimentally determined data. The imperfection in fibre-matrix bonds should certainly contribute to some of the energy loss that was not accounted for. Viscoelastic effects on the molecular level were observed by the use of dynamic FT-IR spectroscopy. These changes correlated well with the trends observed with dynamic-mechanical testing.

REFERENCES

- Åkerholm, M., and Salmén, L. (2001). Interactions between wood polymers studied by dynamic FT-IR spectroscopy. *Polymer* 42: 963-969.
- Åkerholm, M., and Salmén, L. (2004). Softening of wood polymers induced by moisture studied by dynamic FT-IR spectroscopy. *J. Appl. Polym. Sci.* 94: 2032-2040.
- Åkerholm, M., Berthold, F., Lindström, M., and Salmén, L. (2005). Dynamic FT-IR spectroscopy - A suitable tool for fibre-matrix interfacial characterisation of wood fibre composites? In: Pre-symposium on chemistry and performance of composites containing wood and natural plant fibres at the 59th Appita annual conference and exhibition. (Appita, Auckland) 95-100.
- Auras, R., Harte, B., and Selke, S. (2004). An overview of polylactides as packaging materials. *Macromol. Biosci.* 4: 835-864.
- Baillie, C., Tual, D., and Terrailon, J.C. (2000). Interfacial pathways in wood. *Adv. Compos. Lett.*, 9: 45-57.
- Bengtsson, M., Oksman, K., and Stark, N.M. (2006). Profile extrusion and mechanical properties of crosslinked wood-thermoplastic composites. *Polym. Compos.* 27: 184-194.
- Bogren, K.M., Gamstedt, E.K., Neagu, R.C., Åkerholm, M., and Lindström, M. (2006a). Dynamic-mechanical properties of wood-fiber reinforced polylactide: Experimental characterization and micromechanical modelling. *J. Thermopl. Compos. Mater.* 19, 613-637.
- Bogren, K., Gamstedt, E.K., Åkerholm, M., Salmén, L., and Lindström, M. (2006b). Effects of relative humidity on load redistribution in wood-fibre composites analyzed by dynamic Fourier transform infrared spectroscopy. In: Proceedings of the 5th Plant Biomechanics Conference. Ed. L. Salmén (STFI-Packforsk AB, Stockholm) 157-162.
- Chandra, R., Singh, S.P., and Gupta, K. (2002). Micromechanical damping models for fiber-reinforced composites: A comparative study. *Composites Part A* 33: 787-796
- Corrêa, C.A., Razzino, C.A., and Hage, J.E. (2005). DMTA analysis of interface adhesion in wood-plastic composites. In: The 8th international conference on woodfiber-plastic composites. Ed: N.M. Stark (Forest Products Society, Madison) 179-184.
- Eichhorn, S.J., and Young, R.J. (2004). Composite micromechanics of hemp fibres and epoxy resin microdroplets. *Compos. Sci. Technol.* 64, 767-772.
- Feih, S., Wei, J., Kingshott, P., and Sørensen, B.F. (2005). The influence of fibre sizing on the strength and fracture toughness of glass fibre composites. *Composites Part A* 36: 245-255.
- Galiotis, C., Paipetis, A., and Marston, C. (1999). Unification of fibre/matrix interfacial measurements with Raman microscopy. *J. Raman Spectr.* 30: 899-912.
- Gamstedt, E.K., Skrifvars, M., Jacobsen, T.K., and Pyrz, R. (2002). Synthesis of unsaturated polyesters for improved interfacial strength in carbon fibre composites. *Composites Part A*, 33: 1239-1252.
- Garlotta, D. (2001). A literature review of poly(lactic acid). *J. Polym. Environ.* 9: 63-84.
- Gassan, J., and Bledzki, A.K. The influence of fiber-surface treatment on the mechanical properties of jute-polypropylene composites. *Composites Part A* 28: 1001-1005.
- George, J., Sreekala, M.S., and Thomas, S. (2001). A review on interface modification and characterization of natural fiber reinforced plastic composites. *Polym. Eng. Sci.* 41: 1471-1485.
- Grigoriou, A.H. (2003). Waste paper-wood composites bonded with isocyanate. *Wood Sci. Technol.* 37: 79-89.

- Hashin, Z., and Rosen, B.W. (1964). The elastic moduli of fiber-reinforced materials. *J. Appl. Mech.* 31: 223-232.
- Hashin, Z. (1979). Analysis of properties of fiber composites with anisotropic constituents. *J. Appl. Mech.* 46: 543-550.
- Hashin, Z. (1990). Thermoelastic properties of fiber composites with imperfect interface. *Mech. Mater.* 8: 333-348.
- Hashin, Z. (1991). Composite materials with viscoelastic interphase: Creep and relaxation. *Mech. Mater.* 11: 135-148.
- Hinterstoisser, B., and Salmén, L. (1999). Two-dimensional step-scan FTIR: A tool to unravel the OH-valency-range of cellulose. *Cellulose* 6: 251-263
- Joffe, R., Andersons, J., and Wallström, L., (2003). Strength and adhesion characteristics of elementary flax fibres with different surface treatments. *Composites Part A.* 34, 603-612.
- Joseph, P.V., Rabello, M.S., Mattoso, L.H.C, Joseph, K., and Thomas, S. (2002). Environmental effects on the degradation behaviour of sisal fibre reinforced polypropylene composites. *Compos. Sci. Technol.* 62: 1357-1372.
- Kasuga, T., Maeda, H., Kato, K., Nogami, M., Hata, K., and Ueda, M. (2003). Preparation of poly(lactic acid) composites containing calcium carbonate (Vaterite). *Biomater.* 24: 3247-3253.
- Kellog, R.M., and Wangaard, F.F. (1969). Variation in the cell-wall density of wood. *Wood Fiber Sci.* 1: 180-204.
- Kubát, J., Rigdahl, M., and Welander, M. (1990). Characterization of interfacial interactions in high density polyethylene with glass spheres using dynamic-mechanical analysis. *J. Appl. Polym. Sci.* 39: 1527-1539.
- Lee, I., Kim, B.N., and Koo, K.N. (1994). Dynamic characteristics of thermoplastic composite laminates. *Composites* 25: 281-286.
- Lu, W., Carlsson, L.A., and Andersson, Y. (1995). Micro-model of paper. Part 1: Bounds on elastic properties. *Tappi* 78: 155-164.
- Marcovich, N.E., Reboredo, M.M., and Aranguren, M.I. (2005). Lignocellulosic materials and unsaturated polyester matrix composites: Interfacial modifications. *Compos. Interfaces.* 12: 3-24.
- McCartney, L.N. (1989). New theoretical model of stress transfer between fiber and matrix in a uniaxially fiber-reinforced composite. *Proc. Roy. Soc. Lond. A* 425: 215-244.
- Melo, J.D.D., and Radford, D.W. (2003). Viscoelastic characterization of transversely isotropic composite laminae. *J. Compos. Mater.*, 37: 129-145.
- Mezghani, K., and Spruiell, J.E. (1998). High speed melt spinning of poly(L-lactic acid) filaments. *J. Polym. Sci. Part B Polym. Phys.* 36: 1005-1012.
- Mohanty, A.K., Misra, M., and Drzal, L.T. (2001). Surface modifications of natural fibers and performance of the resulting biocomposites: An overview. *Compos. Interfaces* 8: 663-699.
- Nabi Saheb, D., and Jog, J.P. (1999). Natural fiber polymer composites: A review. *Adv. Polym. Technol.* 18: 351-363.
- Naik, J.B., and Mishra, S. (2006). The compatibilizing effect of maleic anhydride on swelling properties of plant-fiber-reinforced polystyrene composites. *Polym. Plast. Technol. Eng.* 45: 923-927.
- Nairn, J.A. (2004). Generalized shear-lag analysis including imperfect interfaces. *Adv. Compos. Lett.* 13: 263-274.
- Neagu, R.C., Gamstedt, E.K., and Lindström, M. (2005). Influence of wood-fibre hygroexpansion on the dimensional instability of fibre mats and composites. *Composites Part A* 36: 772-788.
- Neagu, R.C., Gamstedt, E.K., and Berthold, F. (2006). Stiffness contribution of various wood fibers to composite materials. *J. Compos. Mater.* 40: 663-699.
- Oksman, K. (1996). Improved interaction between wood and synthetic polymers in

- wood/polymer composites. *Wood Sci. Technol.* 30: 197-205.
- Oksman, K., and Selin, J.-F. (2004). Plastics and composites from polylactic acid. In: *Natural fibers, plastics and composites*. Eds: F.T. Wallenberger, and N. Weston (Kluwer, Boston) 150-165.
- Noda, I., Dowery, A.E., and Marcott, C. (1983). Dynamic infrared linear dichroism of polymer films under oscillatory deformation. *Polym. Sci. Polym. Lett. Ed.* 21: 99-103.
- Noda, I., Dowery, A.E., and Marcott, C. (1987). Characterization of polymers using polarization-modulation infrared techniques: Dynamic infrared linear dichroism (DIRLD) spectroscopy. In: *Characterization of polymers*. Ed: H. Ishida (Plenum, New York) 33-59.
- Park, B.D., and Balatinecz, J.J. (1996). Effects of impact modification on the mechanical properties of wood-fiber thermoplastic composites with high impact polypropylene (HIPP). *J. Thermopl. Compos. Mater.* 9: 342-364.
- Park, B.D., Wi, S.G., Lee, K.H., Singh, A.P., Yoon, T.H., and Kim, Y.S. (2004). X-ray photoelectron spectroscopy of rice husk surface modified with maleated polypropylene and silane. *Biomass Bioenergy* 27, 353-363.
- Sain, M.M., Balatinecz, J., and Law, S. (2000). Creep fatigue in engineered wood fiber and plastic compositions. *J. Appl. Polym. Sci.* 77: 260-268.
- Sanadi, A.R., Rowell, R.M., and Young, R.A., (1993). Evaluation of wood-thermoplastic-interphase shear strengths. *J. Mater. Sci.* 28, 6347-6352.
- Scheer, R.J., and Nairn, J.A., (1995). A comparison of several fracture mechanics methods for measuring interfacial toughness with microbond tests. *J. Adhesion* 53, 45-68.
- Sjögren, A., Joffe, R., Berglund, L., and Mäder, E. (1999). Effects of fibre coating (size) on properties of glass fibre vinyl ester composites. *Composites Part A* 30: 1009-1015.
- Sjögren, B.A., and Berglund, L.A. (2000). The effects of matrix and interface on damage in CRP cross-ply laminates. *Compos. Sci. Technol.* 60: 9-21.
- Thuvander, F., Gamstedt, E.K., and Ahlgren, P. (2001). Distribution of strain to failure of single wood pulp fibres. *Nord. Pulp Paper Res. J.* 16, 46-56.
- Tucker, C.L., and Liang, E. (1999). Stiffness predictions for unidirectional short-fiber composites: Review and evaluation. *Compos. Sci. Technol.* 59: 655-671.
- Tze W.T.Y., O'Neill, S.C., Tripp, C.P., Gardner, D.J., and Shaler, S.M. (2007). Evaluation of load transfer in the cellulosic-fiber/polymer interphase using a micro-Raman tensile test. *Wood Fiber Sci.* 39, 184-195.
- Van de Weyenberg, I., Truong, T.C., Vangrimde, B., and Verpoest, I. (2006). Improving the properties of UD flax fibre reinforced composites by applying an alkaline fibre treatment. *Composites Part A* 37: 1398-1376.
- Varna, J., Joffe, R., and Talreja, R. (2001). A synergistic damage-mechanics analysis of transverse cracking in $[\pm\theta/90_4]_s$ laminates. *Compos. Sci. Technol.* 61: 657-667.
- Wålinder, M.E.P., and Ström, G. (2001). Measurement of wood wettability by the Wilhelmy method. Part 2. Determination of apparent contact angles. *Holzforschung* 55, 33-41.
- Wang, Y., Aubuchon, S.R., Smith, M.E., Schoonover, J.R., and Palmer, R.A. (2005). Dynamic infrared linear dichroism study of the temperature-dependent viscoelastic behavior of a poly(ester urethane). *Appl. Spectr.* 59:305-315.
- Weir, N.A., Buchanan, F.J., Orr, J.F., Farrar, D.F., and Boyd, A. (2004). Processing, annealing and sterilisation of poly-L-lactide. *Biomater.* 25: 3939-3949.
- Woodings, C. (2000). New developments in biodegradable nonwovens. In: *Edana's 2000 Nonwovens Symposium* (Edana, Prague).
- Young, R.J. (1996). Evaluation of composite interfaces using Raman spectroscopy. *Key Eng. Mater.* 116:173-192.

THE CHEMICAL ASPECTS OF FIBRE SURFACES AND
COMPOSITE INTERFACES AND INTERPHASES, AND THEIR
INFLUENCE ON THE MECHANICAL BEHAVIOUR OF
INTERFACES

F. R. Jones

University of Sheffield, Department of Engineering Materials,
Sir Robert Hadfield Building, Mappin Street, Sheffield, S1 3JD, UK

ABSTRACT

This paper reviews aspects of interface and interphase formation in fibre composite materials. The majority of the study is concerned with carbon and glass fibres although advanced polymer fibres are also addressed for completion. It is demonstrated that the formation of a strong interfacial bond involves both chemical reactions and other physico chemical phenomena. It is also proposed that gas phase functional sizing through plasma polymerisation is a potential route to controlling the micromechanics of composite failure. Preliminary results on optimising composite strength are also included.

1. INTRODUCTION

The interface which forms between a reinforcing fibre and a polymer resin in the fabrication of a fibre matrix composite is an essential aspect of the material which needs to be designed. It plays an important role in the fracture of these materials. The interface controls the reintroduction of stress into either component at a damage site. For example, in the multiple fracture of single filaments the fibre still remains a reinforcing component providing there is a stress transfer from the resin back into the fibre. Similarly, in brittle matrix materials, there is stress transfer between the fibre and the matrix to reload it to fracture. The interface, therefore, controls the micromechanics of failure and is an essential design tool for these materials. However, it is now recognised that an interphase region forms at the interface between fibre and matrix. An interphase is a region of matrix of differing properties to the bulk matrix and arises through the interaction of the fibre and the resin. While it is recognised that there are different activities between resins and fibre surfaces, by far the most important aspect of the formation of interphases is the presence of a sizing coating on the reinforcing fibre. This is particularly relevant to glass fibre materials which include an adhesion promoter in the film former which is applied to the fibre prior to composite manufacture. With carbon fibres, it is believed to be

associated, not only with the polymeric film former, but also with the strength to the interaction of the sizing polymer and the surface of the fibre. The surface activity of a carbon fibre is strongly dependent on its modulus because of differing crystal structures. For PAN-based carbon fibres the fibre has a turbostratic graphite structure of small crystallites. This gives some integrity to the fibre in the transverse direction. The modulus is strongly determined by the orientation of the graphitic planes along the axis of the fibre. On the other hand, for pitch-based carbon fibres, the alignment of the crystallites is determined by the liquid crystal-spinning process. In this case the transverse strength of the fibres, which have a highly oriented crystal structure, is relatively low and, as a consequence, the nature of the transverse failure process of these composites made from pitch-based carbon fibres differs from those from high strength PAN-based carbon fibres.

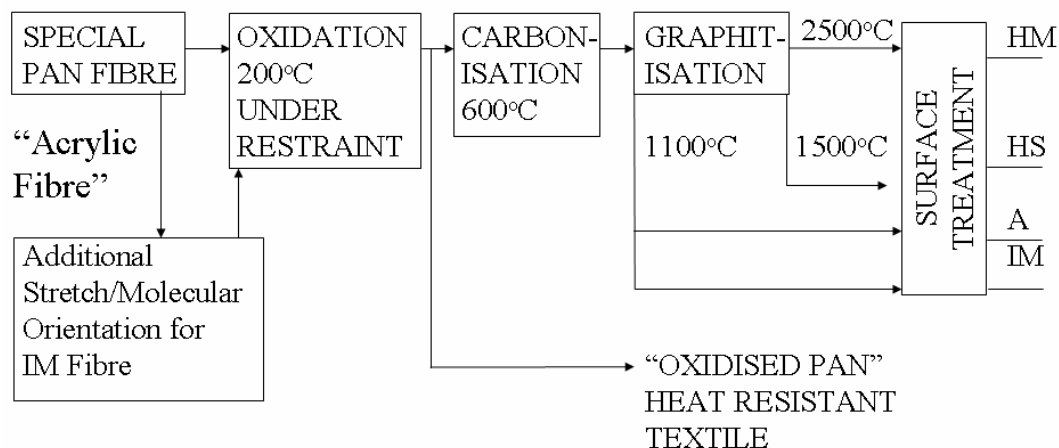
Other high performance fibres, such as the aramids and PBO are spun from liquid crystalline mesophase solutions which organises the crystallites axially along the fibre direction. As with pitch-based carbon fibre, this leads to a relatively weak transverse strength. In these cases, strong adhesion between the fibre and the matrix will lead to transverse failure of the fibre rather than failure of the matrix or the interface or interphase region.

In this paper we will review the mechanisms and formation of interfaces and interphases between fibres and resins in the manufacture of a high performance composite material. Since the interactions that occur between glass fibres, carbon fibres and high performance fibres differ, these will be considered separately.

2. CARBON FIBRE SURFACES

Carbon fibres (CF) manufactured from polyacrylonitrile copolymers are carbonised into turbostratic carbon fibres as illustrated in Fig. 1. The fibres are formed by orientating the molecular structure of the polyacrylonitrile copolymer along the axis of the fibre. Prior to oxidation and carbonation the degree of drawing of the fibre determines the modulus of the carbon fibre. The whole process for manufacturing carbon fibres has been discussed by Watt (1985) and Morgan (2005). The essence of the preparation of the precursor fibre is to provide a highly orientated polyacrylonitrile molecule which can form thermally a ladder polymer. The ladder polymer on oxidisation yields a graphitic planar ladder which acts as the precursor for the condensation of the aromatic rings in subsequent graphitisation. The modulus of the fibre is determined by the degree of orientation of the molecular chains and, hence, the length of the ladder polymer which forms in the heat treatment process. It is essential that the polymer molecule is not allowed to relax during the oxidation process which is designed to stabilise the chains in their axial orientation. Generally speaking, the special acrylic fibre precursor is spun from a filtered dope under clean room conditions so as to maximise strength at the lowest graphitisation temperature, to provide a carbon fibre of diameter 7 μm . Additional orientation is introduced into the precursor fibre for the manufacture of intermediate modulus carbon fibres. The graphitisation temperature also determines the modulus of the fibre. Temperatures up to 1100 $^{\circ}\text{C}$ can produce Type A fibres, at 1500 $^{\circ}\text{C}$ high strength fibres, and 2500 $^{\circ}\text{C}$ high modulus fibres. The fibres are then subjected to a surface treatment process prior to coating with an epoxy-type polymer in emulsion form to provide a protective coating for subsequent manufacturing routes. The surface treatment of carbon fibres is an electrolytic oxidation process, usually in an aqueous solution of ammonium bicarbonate, although ammonium bisulphate is also reported in the literature. By passing a current through the carbon fibres, the generation of active oxygen at the carbon fibre anode where the edges of the basal planes can be activated and provided with a range of oxygen containing functional groups, which range from carboxylic acid, hydroxyl and anhydride. In addition, the electrolyte will contain ammonium

ions and aqueous ammonia, which can react with the carboxylic acid groups to produce amides on the surface of the fibres. Alexander and Jones (1996) demonstrated the formation of amide groups in a surface analytical study of carbon fibre.



- HM - High Modulus (7 μm)
- HS - High strength (7 μm)
- A - Type A (7 μm)
- IM - Intermediate modulus (5 μm)

Figure 1: Schematic of the manufacture of High Strength Carbon Fibres from Polyacrylonitrile precursors.

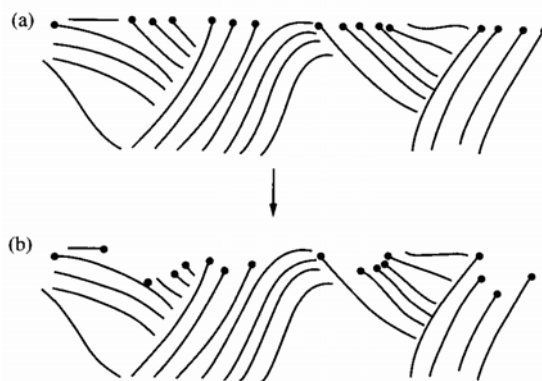


Fig. 2. Schematic of the mechanisms of the electrolytic oxidation of type A Carbon Fibres. This shows the activation of the edges of the graphite basal planes and the formation of micropores (Packham 2004).

Depending on the modulus of the fibre and, hence, the orientation of graphitic planes to the axis of the fibre, the degree of reactivity during the electrolytic oxidation varies. A Type A fibre, in which the graphitic planes are fairly random and emerge at the surface of the fibre, can be readily oxidised and functionalised in the electrolytic process (Fig. 2). However, for high modulus fibres, where the graphitic planes tend to be orientated at the surface, the oxidation process requires more vigorous conditions. Fig. 3 illustrates the oxidation process of a high modulus carbon fibre showing the generation of micropores and functionalised adsorbent sites.

The role of these sites will be discussed later. Generally, the degree of oxidation of carbon fibre is determined by the optimisation of the composite properties. The seminal work of Dunford et al is illustrated in Fig. 4, showing that a so-called 100% degree of fibre surface treatment has provided an optimal interlaminar shear strength, impact strength and notched tensile strength. It is clear that the formation of an interfacial bond between the resin and the oxidised fibre surface controls the micromechanics. In the early work of Dunford et al. (1981), it was generally assumed that the degree of debonding of a fibre from the resin at a micromechanical event such as fibre-break was the explanation for the optimisation of the performance. The micromechanics of a carbon fibre composite, which absorbs a large amount of energy, can be attributed to these types of mechanisms. This is why two brittle materials, such as carbon fibre and an epoxy resin can be made to absorb large amounts of fracture energy.

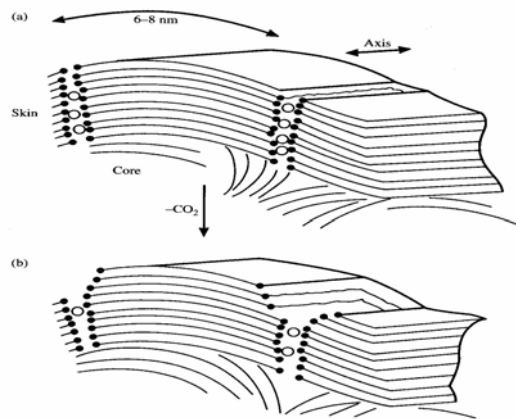


Fig. 3. Schematic of the electrolytic oxidation of HM carbon fibre showing the formation of micropores and adsorbent sites. O is an adsorbate molecule such as water, • is a site which may or may not be functionalized (Jones 1994).

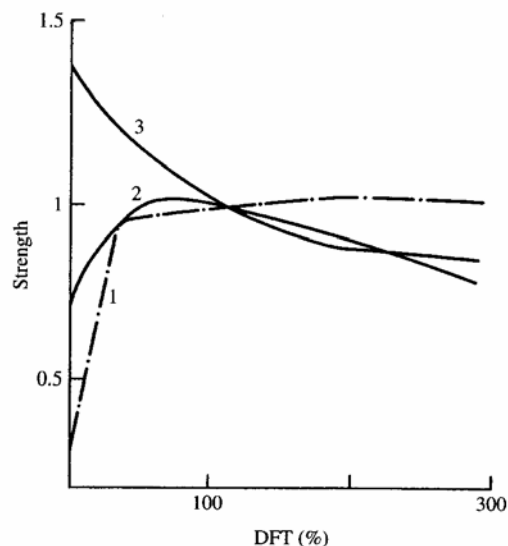


Fig. 4. Effect of surface treatment on the mechanical performance of Type II Carbon Fibre Composites. 1 – interlaminar shear strength of a unidirectional composite 2- impact strength, 3- notched tensile strength of a $(0^\circ/\pm 45/0^\circ)_s$ laminate. The degree of fibre surface treatment (DFT) has been optimised accordingly at 100% (Jones 1994; Dunford et al. 1981).

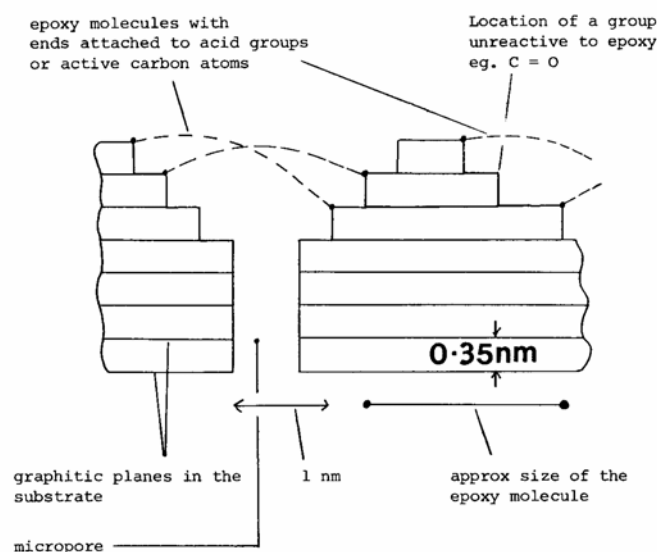


Fig. 5. Schematic structure of the Model Surface of HM Carbon Fibre showing chemisorption of epoxy resin molecules (Denison et al. 1988a).

2.1 The interaction of carbon fibre surfaces with epoxy resins. Denison et al. (1986) developed a barium labelling technique to quantify the acidity of carbon fibre surfaces. They applied this approach to fibres with pre-adsorbed epoxy resin. Table 1 shows that the acid groups had been blocked by the adsorption of the epoxy resin molecule. But the XPS analysis showed that not all of the acid had been ‘reacted’ and that only partial coverage of the surface had been achieved. The micropores which form need to be of similar dimensions to the epoxy group in the resin molecule for reactivity. The dimensions of the microposity was also quantified by adsorption of CHCl_3 as a function of DFT (Denison et al. 1988b). As a result it could be shown that functional groups located in the micropores are only accessible to appropriately sized epoxy molecules. Table 1 also shows the increase in acidity after electrolytic oxidation. The argument is developed further in section in 2.3. This aspect was also confirmed in the modelling studies of Attwood and Marshall (1996).

Table 1. The adsorption of epoxy resin (Epikote 828) by HM Carbon Fibre surfaces from 1% solution in using Barium labelling ($\text{BaCl}_2/\text{Ba}(\text{OH})_2$)

DFT (%)	TREATMENT	AS- Received				Epoxy Resin			
		C	O	N	Ba	C	O	N	Ba
0	Control	95	4.8	0	-	89.5	10.2	0	-
0	Ba labelled	92	6.9	1.2	0.09	90	9.4	0	0
49	Control	87	9.6	3.4	-	82	14.6	2.2	-
49	Ba labelled	80	13.3	2.7	0.59	83.5	13.2	2.75	0.16

This study has been extended to the adsorption of brominated epoxy resins used as sizings. Fig. 6 shows the retention of the brominated epoxy resins and polyether sulphone polymer on carbon fibre surfaces. Thus the sizing polymer cannot be completely removed from the surface in an extraction process showing that the carbon fibre surface is strongly adsorbent to polymeric molecules.

2.2. Assessment of adhesion. There are several techniques for assessing the adhesion of fibres

to resin. These include the micro debond pull-out test, the pull-out test, the fragmentation test, interlaminar shear strength measurements (Drzal and Madhukar 1993). We have used the fragmentation test extensively because it simulates the failure of a unidirectional composite in which the fibre failure strain is less than matrix. In this way, the stress transfer from the resin to the fibre is directly examined in the reloading of the fragmented fibre to further fracture. The key need for this test method is that the fracture failure strain of the resin is significantly higher than that of the fibre. It is, therefore, essential to fragment the fibre to saturation when it is assumed that the fibre is fully debonded and cannot be reloaded to its failure stress. The fragmentation test and the data analysis methodologies have been described in detail by Tripathi and Jones (1998).

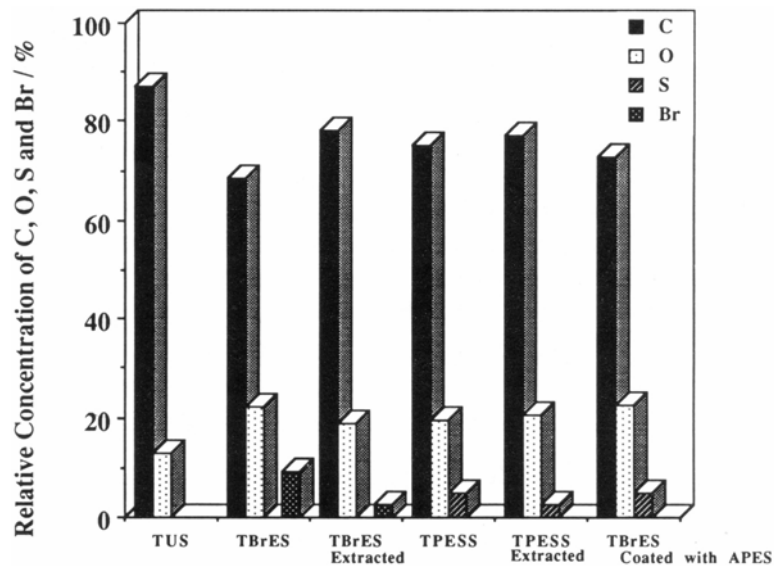


Fig. 6. Sorption of Sizing Resins onto treated Type A (Tenax J) CF Surfaces. Treated unsized (TUS) sized with Brominated epoxy (TBrES) sized with polyether sulphone copolymer (TPES); TBrES sized fibres coated with amino end group polyether sulphone (APES) (Yumitori et al. 1994).

2.2.1 The role of surface treatment and sizing on interfacial shear strength. Fig. 7 shows the fragmentation measured interfacial shear strengths of a series of Type A carbon fibres with different treatments and sizings. It is clear that on oxidative treatment the interfacial shear strength rises from 20 MPa to 35 MPa. However, in the presence of the brominated epoxy size, the interfacial shear strength is reduced 25 MPa. It appears, therefore, that an interphase forms in the presence of the sizing polymer and that this modifies the stress transfer mechanism. One concludes, therefore, that a brominated epoxy polymer used to coat the fibres is not readily dissolved into the epoxy resin matrix. With the same fibres in a thermoplastic matrix, such as polyethersulphone. Fig. 8 shows that you get a similar improvement in interfacial shear strength on surface treatment of the fibres from 20 to 30 MPa. However in the presence of the brominated epoxy resin size, a further improvement in interfacial shear strength to 40 MPa was observed. The implication of this is that the brominated epoxy coating on the fibre is more compatible with a thermoplastic polyether sulphone polymer than it is with an epoxy resin. On the other hand, with polyether sulphone type of sizing which was expected to be more compatible with the matrix, the interfacial shear strength is lower. To confirm that interphases form, we examined the fracture surfaces of high volume fraction composites containing the brominated epoxy-sized fibres in both the thermoset epoxy resin and the thermoplastic polyethersulphone. The fracture surfaces were analysed using time of flight secondary ion mass spectrometry. In Tof-SIMS we can use the sputtered ions from the surface to create a chemical

image. By choosing an ion which is typical of the sizing polymer and an ion which is typical of the matrix polymer, we can explore the compatibility of the two components at the interface. We deliberately chose to use matrices which contain a sulphur label and a sizing polymer with a bromine label. Therefore, if we overlay the sulphur and bromine ion image on the fracture surfaces of these composites, we can identify the formation of interphase regions in the composite. Fig. 9 shows the image for the epoxy resin composite. The 'bromine' ion image is coloured red and the 'sulphur' ion image is green. The image is dominated by the bromine ion indicating that the sizing polymer is well adhered to the fibre.

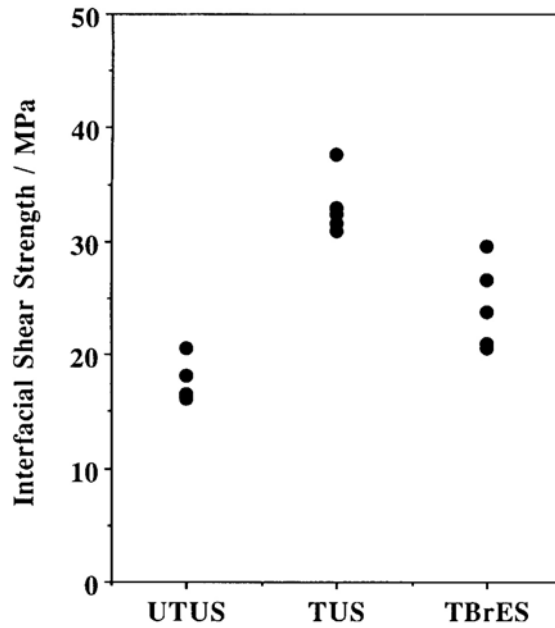


Fig. 7. Fragmentation Interfacial shear strengths of untreated/unsized (UTUS), treated unsized (TUS) brominated epoxy resin sized treated, unsized (TBrES) fibres in epoxy resin matrix (Yumitori et al. 1994).

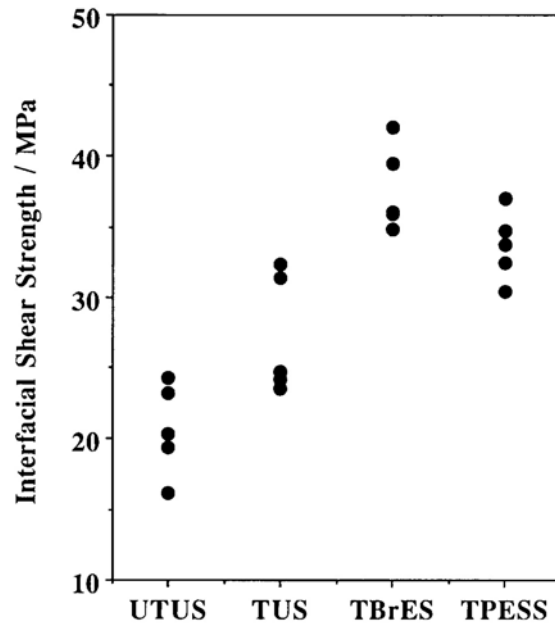


Fig. 8. Fragmentation Interfacial shear strengths of UTUS, TUS, TBrES and Polyethersulphone copolymer sized (TPES) fibres in a polyethersulphone (PES) matrix (Yumitori et al. 1994).

The equivalent ToF-SIMS image for the same fibres coated with a brominated epoxy resin size in the polyether sulphone matrix is given in Fig. 10. Here the image is clearly dominated by a mixture of the two ion labels indicating that the sizing resin and the polyether sulphone matrix have mixed together to form an interphase region. Therefore, we can rationalise the performance of this composite in Fig. 11, where we schematically represent the presence of an essentially graded interphase region for the thermoplastic PES composite material and an approximately distinct interphase region for the epoxy resin composite materials. In other words, the compatibility of the coating with the matrix shows up clearly in the stress transfer between fibre and interphase in these two composites. The performance of the interphase in this particular instance is critical to the development of high performance composites material. The compatibility of the sizing with the matrix is further illustrated by an examination of the molecular weight of the sizing polymer. In this experiment we have compared the compatibility of three emulsified epoxy resins which have been deposited onto treated carbon fibres and manufactured into composites using two epoxy resin systems. In Fig 12 the interfacial shear strength for the unsized fibres in a different epoxy resin is a function of the properties of the two epoxy resin matrices. This point will be discussed further in a later section. What is more important in this particular case is the observation that there is a gradual increase in the interfacial shear strength with the inverse of the molecular weight of the epoxy resin sizing polymer. Fig. 13 shows the fracture surface of a fragmentation specimen manufactured from the two extremes of molecular weight of the sizing polymer. In the presence of the low molecular weight epoxy size, an interphase region has formed which has plasticised the local matrix to create a relatively “soft” interphase region. The high molecular weight sizing polymer is not compatible with the matrix and debonding has occurred between the fibre and resin. These micrographs show that the role of the sizing resin and its compatibility with the matrix is a crucial issue in the optimising micromechanics of failure of a composite. Furthermore, yielding of an interphasal region as well as debonding at the interface must be considered in any model of the interface.

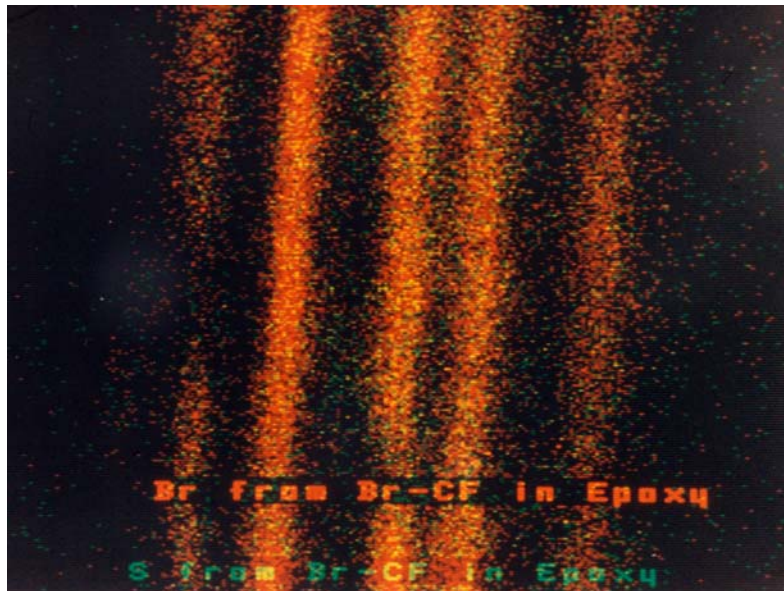


Fig. 9. Time of Flight SIMS image of the fracture surface of brominated epoxy resin sized fibre in a sulphur hardened epoxy resin matrix (Yumitori et al. 1994).

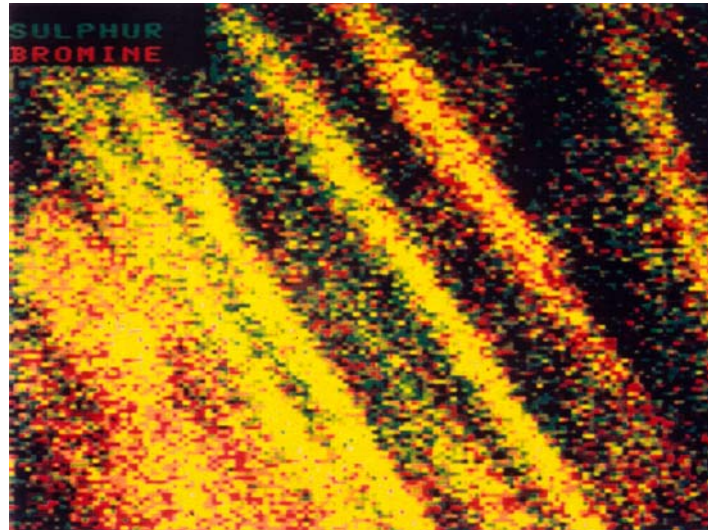


Fig. 10. Time of Flight SIMS image of brominated epoxy resin sized fiber in PES thermoplastic matrix. (Yumitori et al. 1994).

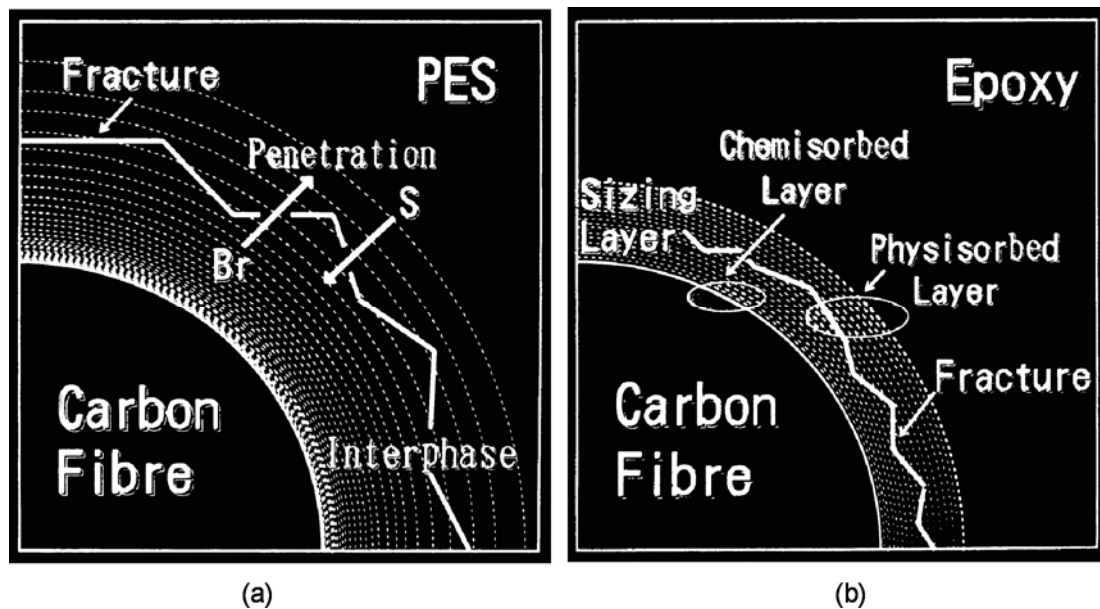


Fig. 11. The concept of the interphase structure in the preparation of carbon fibre composites. (a) Brominated Epoxy Resin sized fibre in thermoplastic PES matrix and (b) Brominated Epoxy Resin sized fibre in thermoset epoxy resin matrix (Yumitori et al. 1994).

2.3 Chemical bonding versus mechanical interlocking. The debate about the role of chemical bonding in the formation of adhesive bonds between fibres and resins has been continuing for many years. We showed, already, in Fig. 2 how the electrolytic oxidation process provides the carbon fibre surface with chemical functionality and microporosity. It has been argued that microporosity is the major contributing factor to the creation of a strong interfacial bond. Equally, it can be argued that the correct functional chemistry is responsible. The differentiation between mechanical interlocking and the formation of the chemical bond has been attempted by removing the functional groups present on the carbon fibre surfaces and examining its response to the adhesive bond. It was considered by Drzal (1990), Denison et al. (1989) and Denison et al. (1988c) that the functional chemistry can be removed from the carbon fibre surface by thermal heating in vacuum at 1100 - 1400 °C. It was assumed that the organic functional groups

would be lost by thermal desorption and any adhesive bond could be attributable to mechanical interlocking. However, Denison et al. (1989) and Denison et al. (1988c) considered that the desorption of functional groups would activate the carbon fibre surface. Furthermore the functional groups could reform in the presence of residual moisture in the resin matrix. It is therefore difficult to draw the conclusion that chemical bond formation has not also occurred when composites were manufactured from thermally detreated fibres. Table 2 shows that detreatment to 1000°C did not lead to a reduction in ILSS although the surface oxygen concentration is significantly reduced. The microposity determined by chloroform (CHCl₃) adsorption remained similar. Detreatment of the fibres to 1400 °C lead to a reduction in ILSS for the tetrafunctional epoxy (MY720) but not the difunctional epoxy (Epikote 828). Above 1100 °C, the carbon atoms become mobile, so that a reduction in microposity occurs. The difference between the interfacial bond for the two resins can be attributed to the relative molecular dimensions of a single epoxy group and the micropores where the active carbon atoms exist. Therefore, the arguments about mechanical interlocking, and chemical bond formation at the fibre matrix interface is a difficult one to resolve because of the nature of the ambiguity in the experimental evidence. Kettle et al. (1997) attempted to resolve this issue by providing a carbon fibre surface with known functionalities. They coated carbon fibres with plasma polymers, with appropriate retained functional chemistry; amine, hydroxyl and carboxyl groups. This was achieved with use of plasma copolymers of allylamine, allyl alcohol, acrylic acid with hexane. They demonstrated that carboxyl groups provided the highest interfacial bond strength. Surprisingly, the amino groups were less effective. Since the hydrocarbon plasma polymer deposit exhibited a very poor bond with epoxy resin, the authors argued that chemical bond formation was the most likely explanation for the formation of a strong interface. The use of plasma polymers as functional sizings will be discussed in section 5. However, the debate over chemical bond formation is, to some extent, irrelevant because of the common use of sizing polymers. A sizing polymer is used to coat the carbon fibre surfaces to protect them from damage and to provide handleability for composite manufacture. It is common to coat the fibres with an aqueous emulsion of an epoxy-like resin. It has been shown above that the sizing polymers strongly influence the micromechanics of composite failure.

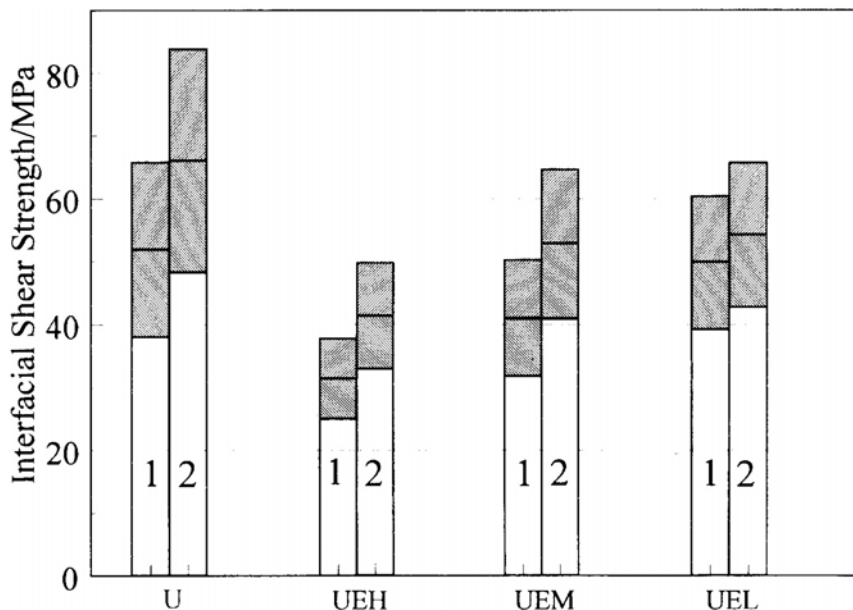


Fig. 12. Interfacial shear strength of carbon fibres in epoxy Matrix 1 and Matrix 2 after sizing with commercial aqueous emulsion based sizing agents of differing epoxy equivalent weight (EPW) (Tripathi and Jones 1998). L = low molecular weight, M = medium molecular weight, H = high molecular weight (Cheng et al. 1994).

Table 2. The effect of Fibre Detreatment for 2 h at high temperature (1000 or 1400 °C) on the microposity and acidity of HM fibres and properties of their epoxy resin composites (Denison et al. 1989); Kettle et al. 1997).

Fibre or T _D (°C)	XPS Surface Atomic Concentrations (%)											CHCl ₃ molecule (10 ² nm ²)	*ILSS (MPa)	
	CONTROLS			Ba Labelled				CHCl ₃ labelled					MY 720	E828
	C	O	N	C	O	N	Ba	C	O	N	Cl			
(HMU)	95	5.2	0	92	6.9	1.2	0.09	95	3.8	0	0.95	135	24.8	25.0
(HMT)	86.5	10.0	3.3	85	11.6	3.1	0.46	86	10.6	3.6	0.68	105	72.8	78.0
1000	97.5	2.8	0	85.5	13.5	0.85	0.49	95	5.0	0	0.95	135	70.3	-
1400	-	-	-	-	-	-	-	96	3.7	0	0.4	56	43.7	75.1

T_D = Detreatment temperature, HMU = untreated, HMT, = treated or oxidised

* ILSS = Interlaminar Shear Strength, MY720 four functional epoxy, E828 difunctional epoxy 80 phr NMA hardener, 1.5 phr BDMA acceleration

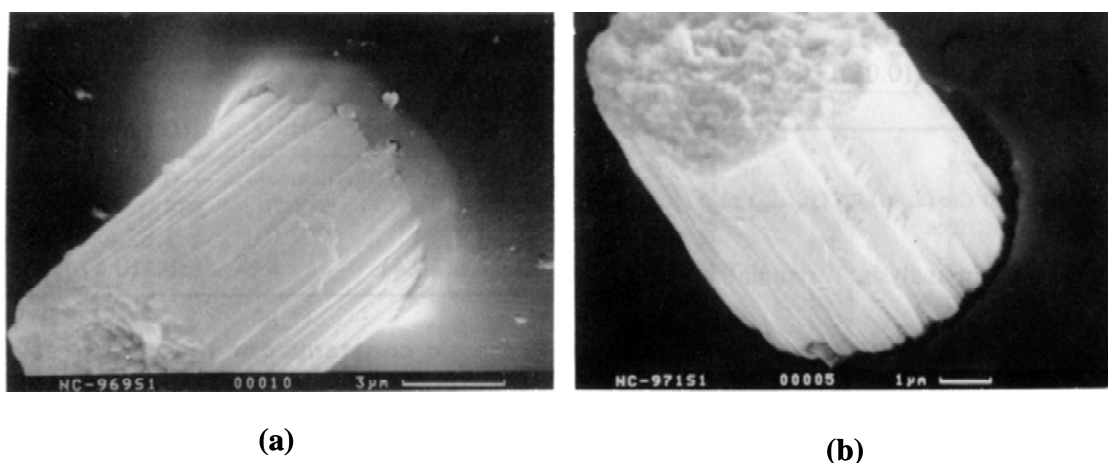


Fig. 13. SEM micrographs of the interfacial region of embedded single filament carbon fibres in Matrix 1 epoxy resin after fragmentation. The emulsion coated HS fibres: (a) low molecular wt (b) high molecular wt

3. GLASS FIBRE SURFACES

Glass fibre surfaces are wholly different from carbon fibre surfaces. The glass is an amorphous material without any crystalline order. It is generally assumed that the fibres are isotropic with uniform properties throughout the fibre. This contrasts with carbon fibres, which are crystalline with the graphite planes orientated parallel to the fibre axis. This provides the fibre with its high modulus in the axial direction. The formation of an interface between a glass fibre and a resin provides an interesting conundrum. There are several reports in the literature whereby a virgin fibre has a strong interfacial bond to an epoxy resin. However, the tradition within the glass fibre industry is to coat the fibres with a complex sizing using an aqueous emulsion technique. As shown in Fig. 14, the fibres are immediately cooled with water on leaving the bushing and coated with an aqueous emulsion to size the fibre with a protective coating. The sizing consists of a protective polymer which is chosen to be compatible with the matrix; an adhesion promoter which is normally a silane coupling agent, together with lubricating agents. The role of the emulsified polymers and aqueous coating media is principally to displace the water from the surface of the fibre and provide the surface with the appropriate hydrophobicity for compatibility with relatively non-polar polymers. Because of the variety of matrices into which these fibres are embedded, there is a huge variety of sizing coatings applied to glass fibres.

Individual manufacturers are highly secretive about the coating formulation because this is the main commercial advantage that they have over their competitors. Thomason and Adzima (2001) have discussed science of sizing of glass fibres in detail. The most important component of the sizing is considered to be the silane coupling agent. The unknown question is whether the silane dominates the glass fibre interface or whether an interphase is formed in which the silane is an integral component. We shall consider the silane coupling agents separately.

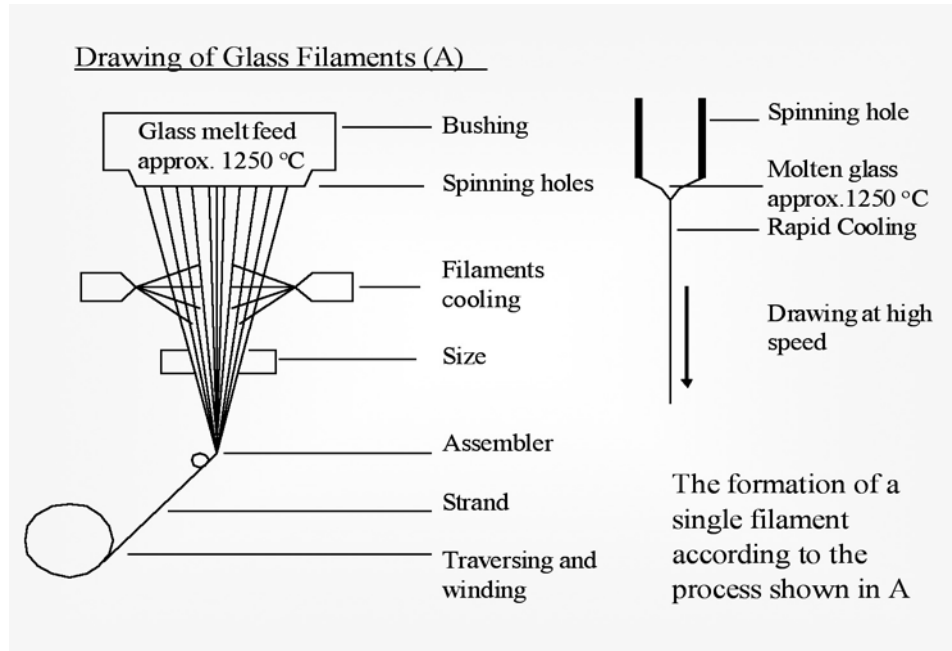


Fig. 14. Fibre Spinning size is applied at roller immediately after cooling.

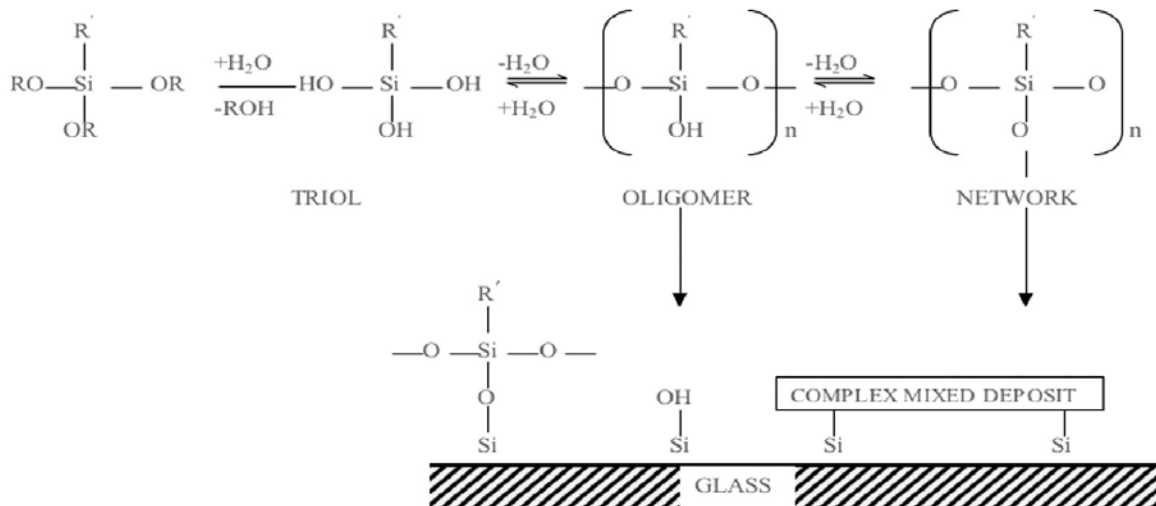


Fig. 15. The structure of hydrolysed silane deposit on glass surface. RO is an alkoxy group, usually ethoxy or methoxy. R' is a resin reactable or compatible group.

3.1. Silane coupling agents. Glass fibres are coated with an aqueous size containing the silane coupling agent which is invariably a functional trialkoxy silane. As shown in Fig. 15, the first stage is the hydrolysis of the alkoxy groups on the silane to silanols during the preparation of the sizing emulsion. The pH of the emulsion is adjusted to promote the hydrolysis of the alkoxy groups. These silanol groups can condense into oligomers and polymers. Depending on the concentration of the silane coupling agent and the nature of the functional alkyl group, the

degree of polymerisation will vary. There is also a competition between the silanol groups on the glass fibre surface and the silanol groups in the hydrolysed coupling agent for the condensation process. Silanol groups on the glass fibre can form a chemical bond through intermolecular reaction while intramolecular-reaction within the hydrolysed silane coupling agents will lead to polymer formation. The coating on the glass fibre, therefore, is one of a complex mixture of polymers and oligomers. Fig. 16 identifies typical silane coupling agents for use in different resin systems, for example, the amino silane (γ -APS) is chosen as a general coupling agent for use in a variety of polymers, although an epoxy resin would be an ideal matrix, because the amino group can react readily with the epoxy groups within the resin.

R ¹	Matrix	Example	
-NH ₂	Epoxy General	NH ₂ - (CH ₂) ₃ - Si (OC ₂ H ₅) ₃	(γ -APS)
$\begin{array}{c} \text{O} \\ \diagup \quad \diagdown \\ \text{CH}_2 - \text{CH} - \end{array}$	Epoxy	$\begin{array}{c} \text{O} \\ \diagup \quad \diagdown \\ \text{CH}_2 - \text{CH} - \text{CH}_2 - \text{O} - (\text{CH}_2)_3 - \text{Si} (\text{OCH}_3)_3 \end{array}$	(γ -GPS)
CH ₂ = CH -	Unsaturated Polyester and Related Resins	CH ₂ = CH - Si (OCH ₃) ₃	(VTS)
CH ₂ = C(CH ₃) -	Unsaturated Resins	$\begin{array}{c} \text{CH}_3 \\ \\ \text{CH}_2 = \text{C} - \text{COOCH}_2 \text{CH}_2 \text{CH}_2 \text{Si}(\text{OCH}_3)_3 \end{array}$	γ MPS

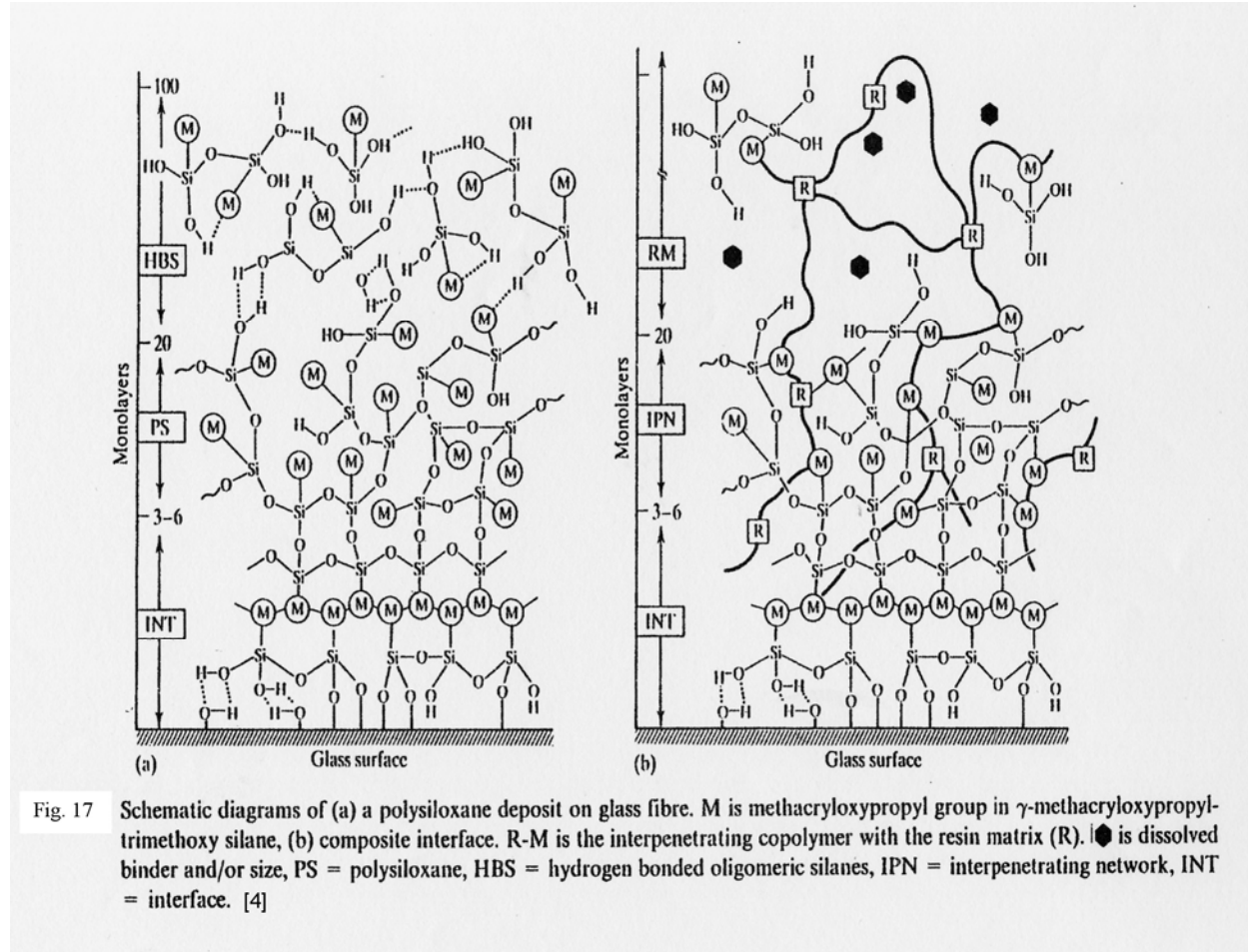
Fig. 16. Typical silanes showing the choice of R' for compatibility with different resin systems.

The nature of the R'-group determines the degree of polymerisation which occurs in the deposit on the fibre surface. It is generally recognised that the vinyl silane (VTS) forms a highly crosslinked deposit, which limits its use as a coupling agent, because the vinyl functional group is occluded in the densely crosslinked nature of the deposit (Ishida et al. 1982). Contrastingly, the amino silane (γ -APS) is known to deposit a mixture of oligomers and polymers. Studies on the extractability of the hydrolysed silane deposit have demonstrated that warm water washing at 50 °C removes the water soluble oligomeric component, or loosely adsorbed material, whereas hot water washing at 100 °C hydrolytically removes linear hydrolysable or strongly adsorbed component from the deposit. The water solubles can be considered to be the mobile component of the deposit which can migrate into the polymer matrix during composites manufacture. This means that the interphase region within a glass fibre composite is likely to be at a larger scale than with carbon fibres. The migration of the soluble oligomeric component into the matrix also leaves molecular pores in the silane deposit into which the resin can permeate. Therefore, the adhesion mechanisms for glass fibres in resins can be quite complex. These can be described as follows:

- (1) Chemical coupling of the glass fibre surface with the resin.
- (2) Mechanical interlocking on the molecular scale through formation of a semi-interpenetrating network between the preformed polymeric silane and the matrix polymer. This may explain the effectiveness of γ -APS with resins without an obvious reaction mechanism.
- (3) Reacted semi-interpenetrated network as described in (2) but with coupling reactions.

The interphase region, therefore, in a glass fibre composite is quite complex. It is reported by Ishida and Koenig (1979). that the number of silane monolayers deposited onto a glass surface

is typically of the order of 100 monolayers, of which 80 monolayers may migrate into the matrix resin. Furthermore the sizing polymer and added lubricating agents migrate into the matrix, therefore the interphase will also have a scale of the order of 20 – 200 nm. Jones and co-workers (1994) have illustrated this phenomena as shown in Fig. 17.



Wang et al. (1992) have also argued that the glass fibre surface is involved in the formation of the polymeric silane deposit. They demonstrated that the aluminium concentration on the silanised fibre surface remains after partial removal of the silane using warm water and hot water extraction techniques. They concluded after an exhaustive thermodynamic study that the aluminium ions within the surface of the glass fibre could be extracted and incorporated into the silane deposit. Other modifying ions from the glass were apparently present in the coating. The Ca^{2+} ion, however, was readily removable by warm water extraction. It was therefore not covalently bonded to the silane deposit, as in the case of the aluminium. Therefore, it could be considered that the tenacious deposit on the surface of the glass fibre might well be a result of the incorporation of the glass fibre surface in the silane deposit. Equally, the silane deposit may well penetrate, partially, into the surface of the glass fibre. This aspect also further complicates the structure of a silane deposit on a glass surface. Fig. 18 is a schematic of the structure γ -APS deposit on E-glass. A time of flight SIMS image of the silane deposit on glass fibres confirmed the incorporation of aluminium into the silane deposit. The technique was also applied to glass fibre composite fracture surfaces where it was demonstrated that the pulled out fibres had polymeric coatings attached to them. This illustrated that the failure of the composite had occurred principally by interphasal response within the material. Most studies involve the generic E-glass fibres but more advanced formulations are used for specific applications such as chemical resistant E glass (ECR), high strength (S) alkali resistant (AR). More recently, boron

free E-glass formulations have been introduced. There is only limited information on the effect of glass surface chemistry on the silane structure so that further research is needed.

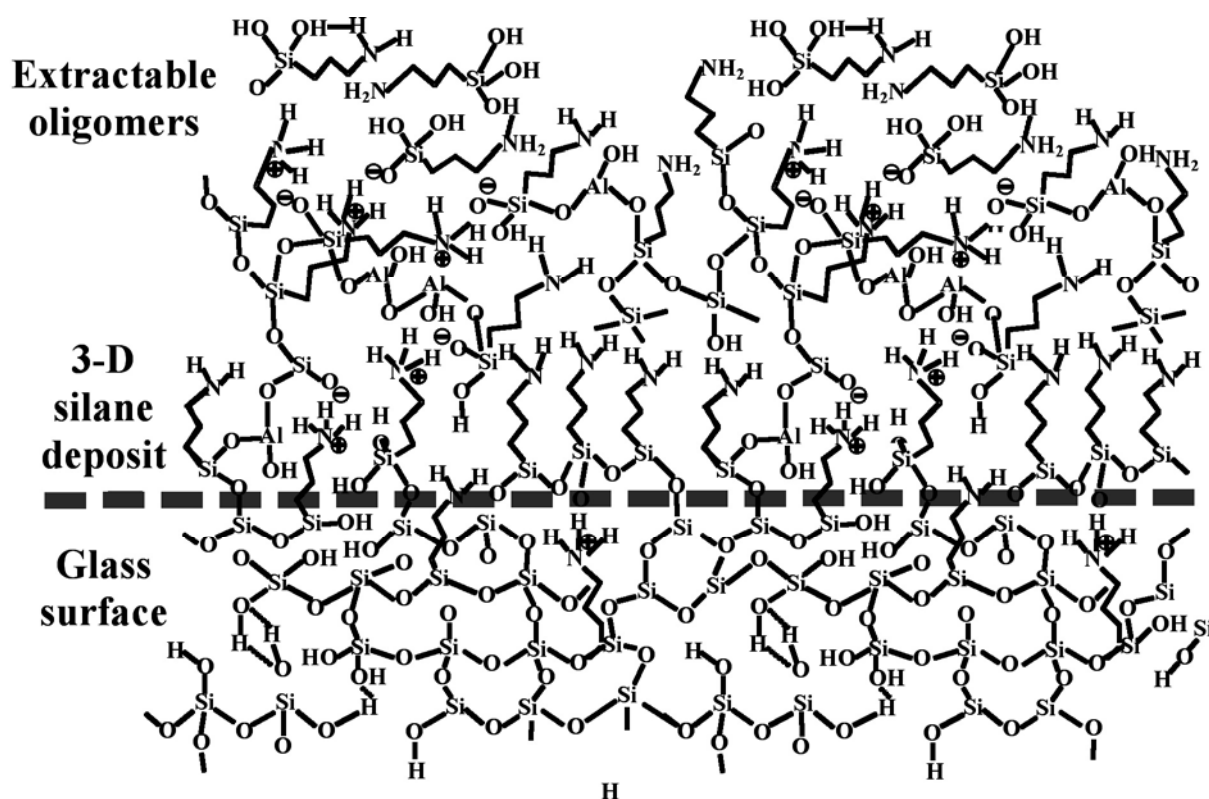


Fig. 18. Model of Hydrolysed γ -APS Deposit on Glass Surface (Redrawn from Choudhury and Jones 2000).

4. ADVANCED POLYMER FIBRES

Advanced high performance polymeric reinforcing fibres such as the aramids (poly (1-4 phenylene terephthalamide)) or PBO (poly(p-phenylene benzobisoxazole) fibres) are available commercially. Aramids are typified by Kevlar and Twaron, which have a modulus up to 180 MPa, PBO which is commercialised under the trade name Zylon, can have a axial modulus as high as 370 GPa (Kitagawa et al. 2000). In the case of the interface formation in these fibres, it has to be recognised that their transverse strength is relatively low because it is dominated by the weak interactive forces between the molecules within the crystal structure. Attempts have been made with the new “M5” fibre, in which hydroxyl groups are introduced into the chemical structure to provide added hydrogen bonding between the individual molecular layers within the crystalline polymer fibre. Since these high performance fibres have been manufactured by liquid crystal techniques, their properties are dominated by the orientation of the liquid crystallites during the spinning process. It is, therefore, essential to use a coating rather than surface treatment to improve the integrity of the fibre as well an adhesive surface. For aramid fibres, it also provides a barrier to moisture absorption and UV protection. These fibres are, therefore, normally coated with a crosslinked coating using an aqueous medium. De Lange et al. (2001) has reported the coating of Twaron fibres to make them compatible with resins in the formation of a composite material. These coatings consist of an epoxy-like crosslinked polymer which has residual reactivity to resins in composite manufacture. Other high performance polymer fibres such as high modulus polyethylene are normally surface treated with an oxygen

corona discharge which oxidises the fibre surface to provide adhesion to resins. Alternatively self-adhesion occurs in the formation of compacted composites, through melting of the fibre surface (Ward and Hine 2004). A similar approach has been used by Peijs for self reinforced polypropylene artefacts (Alcock et al. 2006). Sugihara and Jones (2005) and Sugihara and Jones (2007) have demonstrated how a functional plasma polymer can enhance the adhesion of Zylon fibres to epoxy resin.

5. DESIGNING INTERPHASES FOR OPTIMUM COMPOSITES

In the preceding sections we have demonstrated that interphase formation is always going to occur when a fibre is in contact with a polymer. Even unsized fibres are reported to induce differential properties in the matrix at the interface to form an interphase. To control the micromechanics of a composite we need to avoid interfacial debonding because it is a fracture phenomenon. Thus a sizing technique which provides an interphase with correct properties is required. For design purposes, the thickness and mechanical properties of the interphase should be optimised. Fig. 19 shows the results of a finite element study of the stress transfer from a fibre-break in a single type A carbon filament composite in the presence of an interphase of different properties to the matrix. The first observation is that the stress transfer profile, in particular the stress transfer length has increased on reducing the modulus of the resin. In the figure, 60:40 is a relatively high modulus epoxy resin and 50:50 is a low modulus or soft epoxy resin. It can be seen that the strain transfer profiles from the fibre-break, are all effectively coincidental even with a soft interphase of thickness $0.2 \mu\text{m}$. Thus, the interphase dimensions should be of nanometre dimensions, $>200 \text{ nm}$. From Fig. 19, we can infer that a low modulus interphase would increase the ineffective length of a broken fibre. Therefore the modulus of the interphase should be close to that of the matrix, but with a lower yield strength. The role of an elasto-plastic interphase on the strength of a unidirectional fibre composite, is illustrated in Fig. 20 and Table 3. Fig. 20 shows the strain concentrations in an adjacent fibre to a fibre-break in a square array within the composite. This finite element model has been interrogated by varying the properties of the matrix and the interphase.

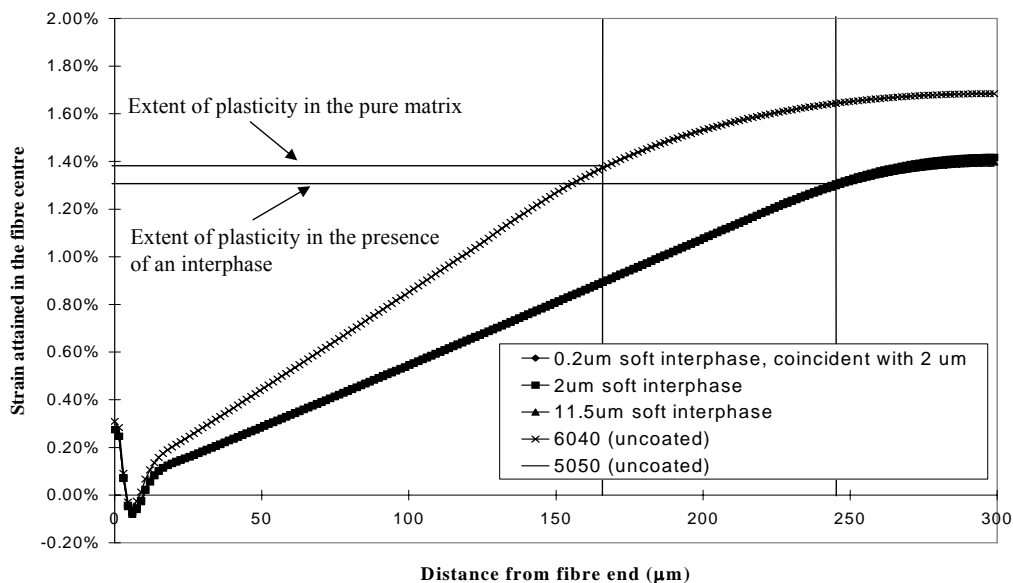


Fig. 19. Strain development within a CF fragment in the presence of soft interphases of differing thickness, at 2% applied strain (see Table 3 for resin details) (Hayes et al. 2001).

As shown in Fig. 20, there is a strain concentration in the neighbouring fibre which can be quantified. This will determine the probability that the adjacent fibres will fracture and create a critical flaw for composite fracture. However, as shown in Table 3, the presence of an elastoplastic interphase region reduces the strain concentration from 15% to 5%. It is therefore clear that interphase control is the key to improving the reliability of continuous fibre composite in the fibre direction.

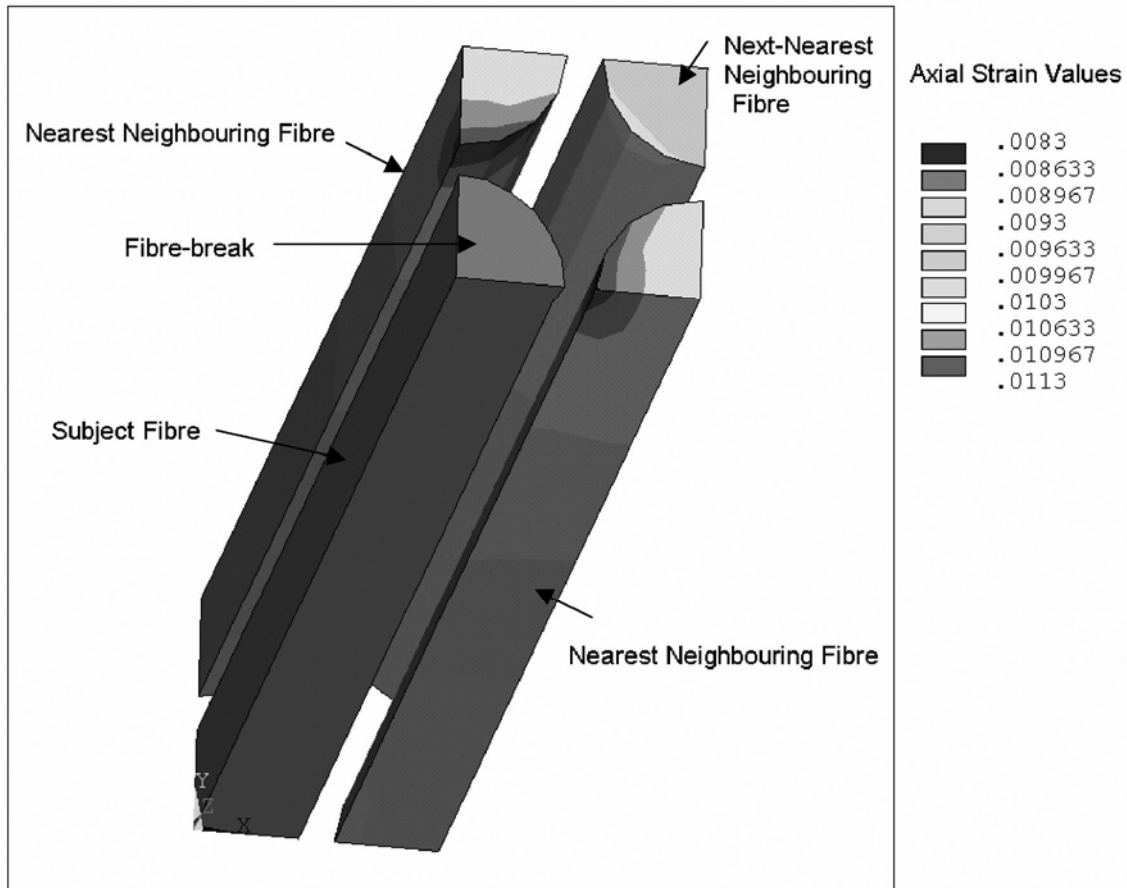


Fig. 20 Finite element study of the effect of matrix and interphase plasticity on the axial strain concentration in a neighbouring fibre to a fibre-break in a square-array (Lane et al. 2001).

Table 3. The effect of matrix and interphase plasticity on the strain concentration factor in a neighbouring fibre to a fibre-break in CFRP (Lane et al. 2001).

Deformation Process	Matrix/Interphase Properties			
	Stiff/Not Present	Stiff/Soft	Soft/Stiff	Soft/Not Present
Elastic	1.15	1.13	1.13	1.12
Plastic	1.07	1.05	1.05	1.05

Stiff = resin 6040 (E = 3.48 GPa, γ = 53.50 MPa); soft = resin 5050 (E = 1.76 GPa, γ = 35.16 MPa)

5.1 Modern sizing technologies Future modern sizing methodologies need to be developed in order to optimise the performance of a composite material. Table 4 lists the requirements of any future sizing technique. As described above, the current sizing of carbon fibres involves a two-stage process of surface treatment followed by polymer coating. In the glass fibre systems, the adhesion promoter is included in the size but that leads to a complex interphase region. Therefore the requirements for a future fibre sizing technique are as given in Table 4. The most important one is that the polymer coating is conformal, but has the chemistry to provide the functionality for adhesion. This can be achieved, as illustrated in Tables 4,5 using plasma polymerisation. Plasma polymerisation provides a functional conformal coating to the fibres. The coating is also tuneable in terms of chemical reactivity for incorporation into a variety of matrix resins. It also has the potential for designing the properties of the interphase, thereby creating micromechanical control over the failure process of a composite.

Table 4. Requirements for Future Fibre Sizing and Interphase Design

	Requirements	Function
1	On-line environmentally clean technology	Recyclable chemicals solvent free
2	Functionalised conformal coating	Chemistry tunable to application
3	Provide Adhesion	Interfacial and Interphasal Control
4	Resin Compatible	Processing Control
5	Fibre Protective	Fibre Strength retention
6	Uniform coating of all fibres in a tow	Reliable composites
	Potential Sizing Technique	Benefit
7	Gas Phase Technology	Readily adjustable
8	Plasma Polymerisation	Conformal functional coating from gas phase
9		Easy thickness control Interphase Micromechanical Control

5.2 Plasma polymerisation as a functional fibre size Table 5 gives the properties of a plasma polymer coating, showing why this gas phase environmentally friendly technique can be considered to be an ideal next step for fibre sizing. We have used this approach to study the chemistry of interface formation between a carbon fibre and a resin. In early studies we found that low power plasma copolymers of acrylic acid provided superior adhesion compared to allylamine and allyl alcohol plasma copolymers. In this study we concluded that the acrylic acid reactivity was responsible for the good interface formation. More recently, we have used a continuous fibre coating plasma reactor, as illustrated in Fig. 21, for the preparation of high volume fraction composites for interlaminar shear strength and tensile strength measurements. For convenience, we have used glass fibres for this study and composites with a fibre volume fraction of $57\% \pm 1$ have been prepared. The resin chosen for this study was an NMA-cured Epikote 828-type resin, which has a shear yield stress of 75 MPa and a modulus of 3.3 GPa. The fracture surface of the interlaminar shear strength specimens demonstrated clearly that, on increasing the chemical functionality of the coatings for both allylamine and acrylic acid plasma copolymers with 1,7- octadiene, had increasing resin adhered to the fibres. The full data set are not included here and will be reported elsewhere (Liu et al. 2007a). However, the other variable within the study is the thickness of the plasma copolymer film, which has been varied from 5 nm to 15 nm. Fig. 22 shows that the interlaminar shear strength is a function of retained functional chemistry when the thickness of the plasma polymer coating is 15 nm. However, at 5

nm the interlaminar shear strength of the composites from acrylic acid plasma polymer coating converged to one value which appears to be slightly above the shear yield strength of the matrix.

Table 5. Properties of Plasma Polymer Coatings

- | |
|---|
| <ol style="list-style-type: none"> 1. Ultra thin polymeric coatings (thickness 0-200 nm) 2. No regular repeat unit but can retain the monomer functionality when synthesised from low power radio frequency plasmas 3. Both conventional and non-conventional monomers 4. Crosslinked, pinhole free films 5. At low plasma powers, coating stability is reduced (lower degrees of monomer fragmentation and hence crosslinking) 6. Copolymerisation can be used to maintain mechanical properties while retaining functionality |
|---|

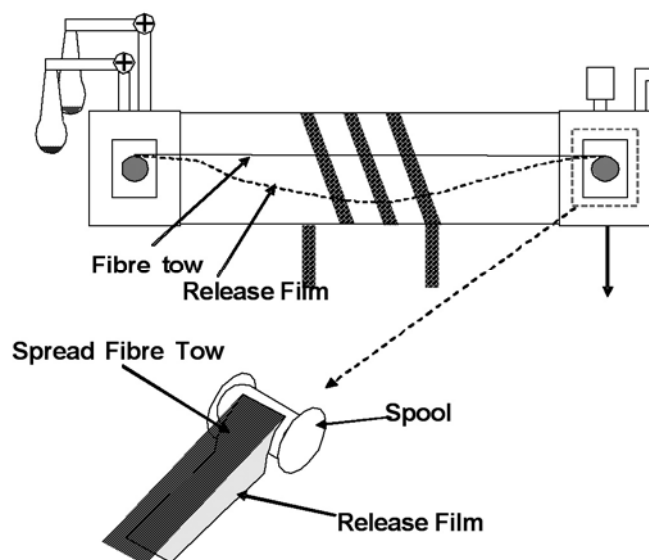


Fig. 21. Plasma reactor for continuous coating of fibres illustrating technique for maintaining fibre alignment for quality composites. (Sugihara and Jones 2005).

A similar set of data were obtained for plasma copolymers of allylamine and 1,7- octadiene (Fig. 23). Here, the effect of thickness is completely different and convergence using 5 nm plasma polymer films has not been achieved. On the other hand, if one considers the upward trend of the least functional coating, namely the one containing 36% allylamine, it would appear that the convergence might occur at a plasma polymer film thickness of approximately 2 nm. We have interpreted this data in terms of another variable which comes into play when we create an interfacial bond between the fibre, which is plasma coated, and the epoxy resin matrix. This is illustrated in Fig. 24, where we see that, if the penetration depth of the epoxy resin into the plasma polymer coating is less than the thickness of the plasma polymer coating, then there will be a plasma polymer interlayer at the fibre surface. In other words, we would not have a completely graded interphase, but a multi-layer interphase. The properties of the interlayer, therefore, will control the interlaminar shear strength. On the other hand, when the penetration depth of the resin is equal to that of the plasma polymer thickness, then the interpenetrating network which forms between the plasma polymer and the epoxy resin will dominate the interfacial failure stress.

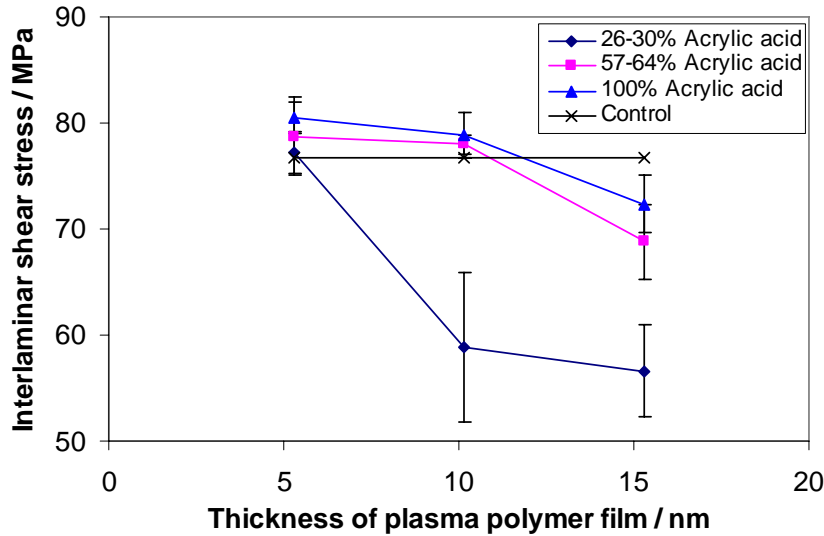


Fig. 22. Interlaminar shear strength of high fibre volume composite as a function of plasma polymer thickness for different monomer ratios of acrylic acid and 1, 7-octadiene (Liu et al. 2007a).

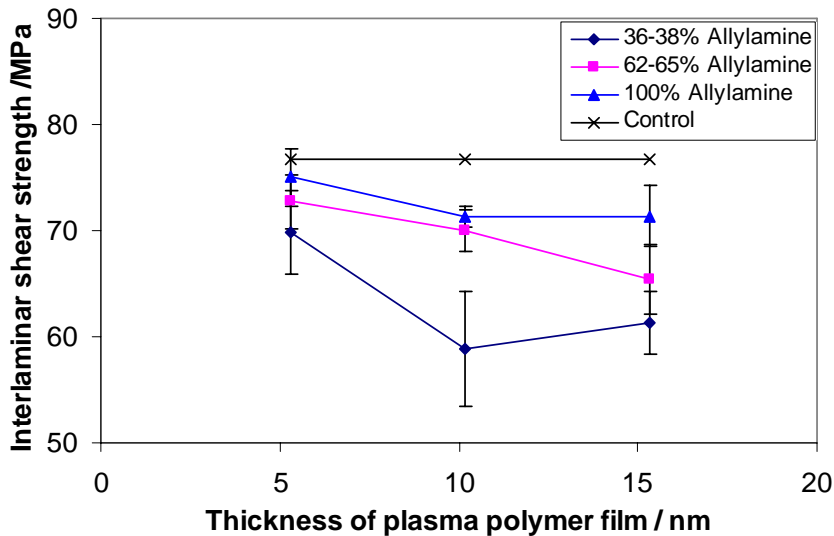


Fig. 23. Interlaminar shear strength of high fibre volume composite as a function of plasma polymer deposition time for different monomer ratios of allylamine and 1, 7-octadiene (Liu et al. 2007a).

We can understand this phenomena when we examine the mechanical properties of the plasma polymer layers. Nanoindentation experiments have been carried out to measure the reduced modulus of thin films of plasma polymer and of the matrix. Table 6 gives the reduced moduli of these plasma polymer films. We have also included the tensile and compressive moduli of the matrix epoxy resin for comparison. The nanoindentation technique for recording modulus has some uncertainty with regard to the cross sectional area of the indenter because of elastoplasticity within the polymer. However, the relative modulus of the allylamine system demonstrates that the cross linked density of this coating is higher than that of the acrylic acid coating, and that can explain the differing trends in interlaminar shear strengths in Figs 22 and 23 as the thickness of the plasma polymer sizing layer is reduced.

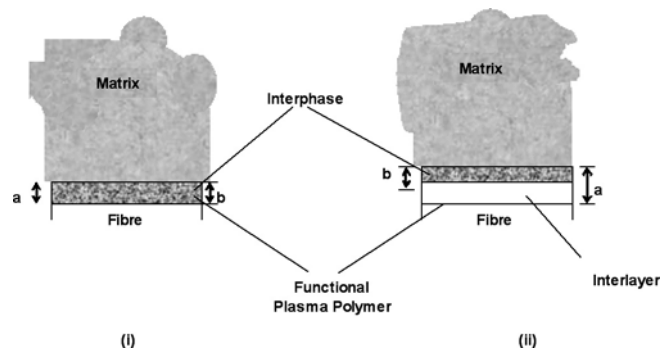


Fig. 24. Formation of an interphase between a plasma polymer conformal coating and a matrix epoxy resin. (i) Penetration depth exactly equal plasma polymer thickness. (ii) Penetration depth is less than plasma polymer thickness. Liu et al. (2007b).

We can now understand why there would appear to be differences in the measured interfacial shear strength of single filaments coated with these plasma polymers, as measured in a fragmentation test (Sugihara and Jones 2005). It is clear that the stress transfer profile of a single filament is determined also by not only the compatibility of the plasma polymer and its reactivity with the epoxy resin, but also on the mechanical properties of the interphase region which forms.

5.3. Tensile properties of plasma coated fibres in an epoxy resin. More recently (Swait et al. 2007) we have used the plasma polymer coated fibres to prepare tensile test specimens. While we cannot do the tensile test on specimens of standard dimensions, the dimensions of these smaller specimens have been calibrated with commercial laminated composites. Therefore, the data in Fig. 25 is very interesting because we demonstrate, clearly, that the tensile strength of the composite is now significantly influenced by the presence of the plasma polymer interphase region. The interphase region formed in these composites will invariably be a complex semi-interpenetrating network between the plasma polymer and the matrix resin. This study shows the benefits of controlling, not only the chemistry of adhesion between fibres and resins, but also the compatibility between any fibre sizing (or coating) and the matrix resin and the formation of an interphase region. It also demonstrates that control of the mechanical properties of a nanoscale interphase has a major impact on the reliability of a composite material.

Table 6. The mechanical properties of the matrix resin and plasma polymer

Modulus	Plasma Polymer		Matrix
	60% Acrylic Acid	60% Allylamine	
Reduced (GPa)*	5.3 ± 1.0	8.0 ± 0.4	4.6 ± 0.4
Compressive (GPa)	-	-	3.4 ± 0.1
Tensile (GPa)	-	-	3.34 ± 0.1

* Nanoindentation

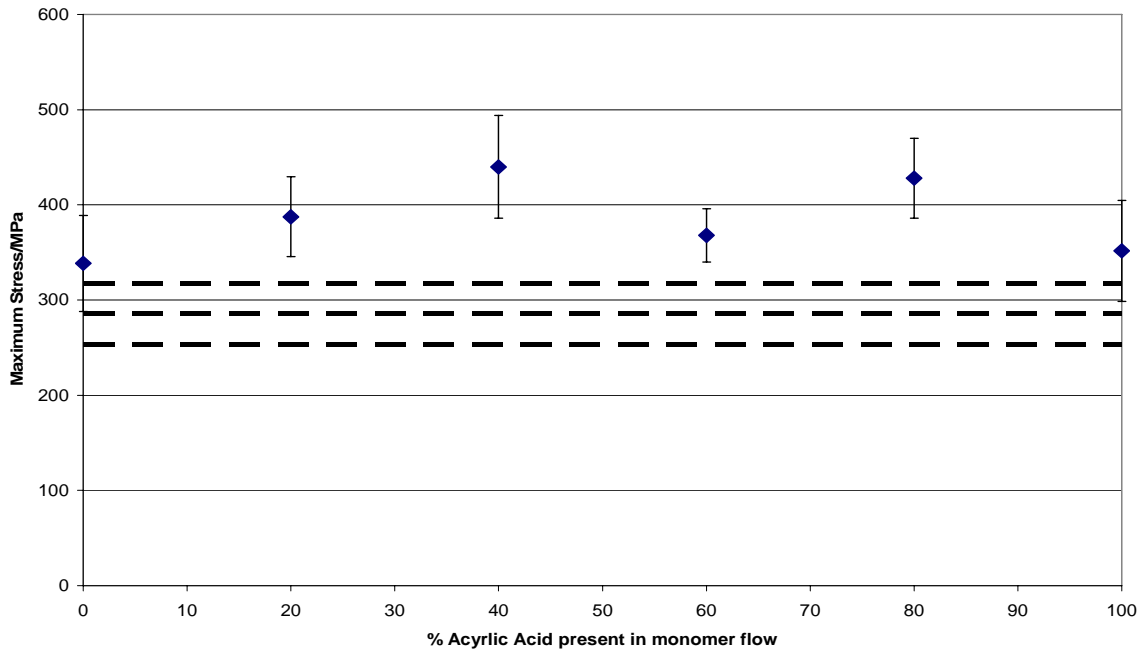


Fig. 25. Tensile Strength of Glass Fibre Composites prepared from fibres coated with plasma polymers of acrylic acid-co-1,7 octadiene (10 nm). The dotted lines are for the uncoated controls shows standard deviation (Swait et al. 2007).

6. CONCLUSIONS

The chemical aspects of interface formation in advanced fibre composites have been reviewed. Furthermore the role of the interphase, which forms between a fibre and matrix, is discussed with respect to its thickness and thermomechanical properties. Therefore we have demonstrated that the knowledge about interfaces and interphases in fibre composite materials has been extended significantly over recent times. Modern techniques are required to create interphase regions, with which the performance of unidirectional fibre composites can be improved. Plasma polymerisation is a potential new sizing approach. We have demonstrated that interlaminar shear strength properties can be controlled by careful control of interphase thickness and properties. Furthermore, we can use plasma polymer sizings to optimise the tensile strength of these materials. In future studies, we intend to examine the transverse properties of these composites using cross ply laminates and, eventually, examine the energy absorption capability of composites using plasma polymer interphases. Finally, techniques for controlling the chemistry at the interface and the mechanical properties of the interphase are important development areas for fibre composite materials.

ACKNOWLEDGMENTS

The author thanks EPSRC for funding through the Ceramics and Composites Laboratory. In this review, research carried out over >20 years has been described and full recognition of collaborators and sponsors is given in the original publications. A complete literature review has not been attempted because of limited space and I apologise too many colleagues for omitting their contributions. However the citations in the books and papers should also be consulted.

REFERENCES

- Alcock, B., Cabrera, N.O., Barkoula, N. M., Loos, J., and Peijs, T. (2006). The mechanical properties of unidirectional all-polypropylene composites. *Composites A* 37, 716-726
- Alexander, M.R., and Jones, F.R. (1996). Effect of electrolytic oxidation upon surface chemistry of type A carbon fibres Pt III, Chemical state, source and location of surface nitrogen. *Carbon* 34, 1093-1102.
- Attwood, D., and Marshall, P.I. (1996). Atomistic modelling of the adsorption of epoxy and amine molecules on the surface of carbon fibres. *Composites A* 27A, 775-779.
- Cheng, T.H., Zhang, J., Yumitori, S., Jones, F.R., Anderson, C.W. (1994). Sizing resin structure and interphase formation in carbon fibre composites. *Composites* 25, 661-670.
- Choudhury, T., and Jones, F.R. (2000). The interaction of Rescole and Novolak phenolic resins with γ -amino propyl triethoxysilane treated E-glass surface: A high resolution XPS and micromechanical study in Silane and Other Coupling Agents. Vol. 2. Ed. K. Mittal, 79-97.
- de Lange, P. J., Maeder, E., Mai, K., Young, R. J., Ahmad, I. (2001). Characterization and micromechanical testing of the interphase of aramid-reinforced epoxy composites. *Composites A* 32, 331-342.
- Denison, P., Jones, F.R. and Watts, J.F. (1988a). The chemistry and micro porosity of carbon fibre surfaces and its interaction with epoxy resin model compounds using labelling techniques for XPS analysis. In: *Interfaces in Polymer, Ceramic and Metal Matrix Composites*. Ed H. Ishida, Elsevier, 77-85 .
- Denison, P., Jones, F.R., and Watts, J.F. (1986). XPS Analysis of barium labelled carbon fibres and interfacial effects in fibre-epoxy composites. *Surface and Interface Analysis* 9, 431-435.
- Denison, P., Jones, F.R., and Watts, J.F. (1988b). A quantification and investigation of surface micro porosity in carbon fibres using labelling and XPS . *Surface and Interface Analysis*. 12, 455-460.
- Denison, P., Jones, F.R., Humphreys, P., and Watts, J.F. (1989). An investigation of debonding micro mechanics of CFRP. In *Interfacial Phenomena in Composite Materials* 89. Ed. F.R. Jones (Butterworths, London) 105-110
- Denison, P., Jones, F.R., Dorey, G., and Jones, L.F. (1988c). The use of XPS and labelling techniques to investigate the role of carbon fibre surface micro porosity in composite interfacial bond formation. In: *Carbon* 88. Eds McEnaney, B. and Mays, T. J. (IOP) 634-6.
- Drzal, L.T., Madhukar, M., J. (1993). Fiber Matrix adhesion and its relationship to composite - mechanical properties. *J. Mater. Sci.* 28, 569-610.
- Drzal, L.T. (1990). In: *Controlled Interphases in Composite Materials*. Ed. H. Ishida (Elsevier, Amsterdam) 309-320
- Dunford, D.V., Harvey, J., Hutchings, J., and Judge, C. H. (1981) RAE Tech Rep. TR81096.
- Hayes, S.A., Lane, R., Jones, F.R. (2001). Fibre/matrix stress transfer through a discrete interphase. Pt 1 Single- fibre model composites. *Composites A* 32, 379-389.
- Ishida, H., Naviroj, S., Tripathy, S.K., Fitzgerald, J.J., Koenig, J.L. (1982). The structure of an aminosilane coupling agent in aqueous-solutions and partially cured solids. *J. Polymer Sci. Polym. Phys.* 20, 701-718.
- Ishida, H., Koenig, J.L. (1979). Investigation of the coupling agent matrix interface of fiberglass reinforced-plastics by fourier-transform infrared spectroscopy. *J Polym Sci. Polym, Phys Ed* 17, 615-626.
- Jones, F.R. (Ed), (1994). *Handbook of Polymer- Fibre Composites*, Longman.
- Kettle, A.P., Beck, A.J., O'Toole, L., Jones, F.R., Short, R.D. (1997). Plasma polymerisation for molecular engineering of carbon fibre surfaces for optimised composites. *Comp. Sci.Tech.* 57, 1023-1032.
- Kitagawa, T., Ishitobi, M., Yabuki, K. (2000). An analysis of deformation process on poly-p-phenylenebenzobisoxazole fiber and a structural study of the new high-modulus type

- PBOHM plus fiber. *J. Polym. Sci B.: Polym, Phys.* 38, 1605-1611.
- Lane, R., Hayes, S.A., Jones, F.R. (2001). Fibre/matrix stress transfer through a discrete interphase Pt2. High volume fraction systems. *Comp. Sci. Tech.* 61, 565-578.
- Liu, Z., Zhao, F.M., Jones, F.R. (2007a). Optimising the interfacial response of high volume fraction composites using a functional plasma polymer. *Comp. Sci. Tech.* submitted.
- Liu, Z., Zhao, F. M., Jones, F.R. (2007b). Optimising the interfacial response of high V_f glass fibre composites using functional plasma polymer. *Proc. ICCM16 (CDROM) Kyoto (JSCM)*.
- Morgan, P. (2005). *Carbon Fibres and their Composites* (Taylor and Francis, Boca Raton).
- Packham, D. (Ed), (2004). *Handbook of Adhesion*, 2nd Edition (Wiley), 177-186.
- Sugihara, H., Jones, F.R. (2007). Promoting the adhesion of high performance fibres using functional plasma polymer coatings. *Polymer Composites* submitted
- Sugihara, H., Jones, F. R. (2005). In: *Polymer Surface Modification and Polymer Coating by Dry Process Technologies*. Ed. S. Iwamori (Research signpost) 127-156.
- Swait, T., Soutis, C., Jones, F.R. (2007). Optimisation of Interfacial Properties for Tensile Strength by Plasma Polymerisation. *Comp. Sci, Tech.* in press.
- Thomason, J.L. and Adzima, L.J. (2001). Sizing up the interphase: an insider's guide to the science of sizing. *Composites A* 32, 313-321.
- Tripathi, D., Jones, F.R. (1998). Single filament fragmentation test for assessing adhesion in fibre reinforced composites - A review. *J. Mater. Sci.* 33, 1-16.
- Wang, D., Jones, F.R., Denison, P.J. (1992). A ToF SIMS and XPS study of the interaction hydrolysed γ -aminopropyl-triethoxysilane with E-glass surfaces. *Adh. Sci. Tech.* 6, 79-98.
- Ward, I.M., Hine, P.J. (2004) .The science and technology of hot compaction. *Polymer* 45, 1413-1427.
- Watt, W. (1985). *Strong Fibres*. Eds Watt and Perov (Elsevier, Amsterdam) 327-388.
- Yumitori, S., Wang, D., and Jones, F.R. (1994). The role of sizing resins in carbon fibre reinforced polyether sulphone . *Composites* 25A, 698-705.

CONTROLLING FIBER/MATRIX ADHESION WITH BINARY SELF-ASSEMBLED MONOLAYERS

Kenneth M. Liechti and William D. Tandy, Jr.

Research Center for the Mechanics of Solids, Structures and Materials
Department of Aerospace Engineering and Engineering Mechanics
The University of Texas at Austin
Austin, TX 78712

ABSTRACT

A mixed self-assembled monolayer was applied to sapphire fibers using two alkyl silanes, dodecyltrichlorosilane (DTS), and bromoundecyltrichlorosilane, (BrUTS), in varying ratios. Fibers were cured in an epoxy matrix and pulled in tension to initiate interfacial cracking. The interfacial toughness was calculated from the data and compared across BrUTS to DTS ratios of 25%, 50%, 75% and 100% as well as uncoated or bare sapphire. After an initial drop in the interfacial toughness from the bare sapphire to the 25% BrUTS to DTS ratio, the remaining behavior was linear in the ratio of BrUTS. In addition, a finite element model was created to determine the mode-mix angle so that comparisons could be made with previous data on flat interfaces. The experiments demonstrated an ability to directly control the mechanical properties of the composite by modifying the interfacial region of the fiber and matrix.

1. INTRODUCTION

Polymeric self-assembled monolayers (SAMs) generally form covalent bonds with the surface on which they are deposited. Self-assembly is usually a consequence of dense packing (Ulman, 1996) of the molecules on the substrate. As a result, the tail group at the other end of the chain may have a range of interactions with the material deposited on top of the monolayer. Depending on the materials involved, the interactions may be strong (covalent, ionic bonding or polar) or weak (non polar) in nature. One form of adhesion control can be achieved by making use of mixed SAMs where the tail groups of each SAM have very different interactions with the material above (Zhuk et al. 1998; Kent et al. 2004).

Zhuk et al. (1998) used methyl (CH₃) and carboxy (COOH) terminal groups on 15-carbon alkanethiols to control adhesion between gold and epoxy. The thermodynamic work of adhesion of epoxy on the coated surface was linearly proportional to the COOH/CH₃ fraction in solution up to about 80%, and was constant thereafter. A series of superlayer fracture experiments

revealed that the interfacial fracture toughness increased strongly with the thermodynamic work of adhesion. The rate of toughening increased with the work of adhesion, suggesting that more and more plastic dissipation was excited in the epoxy layer. Kent et al. (2004) used mixed monolayers of dodecyltrichlorosilane (DTS) and bromoundecyltrichlorosilane (BrUTS) to control adhesion between silicon and epoxy. Both make strong covalent bonds with the silicon. The methyl terminal group on the DTS again makes weak, non-polar interactions with the epoxy. The authors indicate that the BrUTS forms an alkyl ammonium bromide compound with the amine crosslinker that was used to cure the EPON 828 epoxy. As a result, an ionic bond was achieved with the epoxy through $R-NH_2^+Br^-R'$ bonds. Between 10 and 20% bromine termination, there was a strong increase in the tensile and shear strengths of the silicon/epoxy interface as determined by cruciform and napkin ring shear experiments. Asymmetric double cantilever experiments were used to determine the toughness of the interface, which increased linearly with the bromine fraction. The linear relationship was ascribed to the linear increase in the thermodynamic work of adhesion with bromine fraction. In contrast to the gold/epoxy experiments, any plastic dissipation effects were apparently the same for all bromine fractions, even though the toughness of the silicon/BrUTS/DTS/epoxy was much higher than that of the gold/COOH/CH₃/epoxy interface in moist environments. The mode-mix in the asymmetric double cantilever beam experiments was -8° at a reference length of 10 μm , whereas it was about 50° in the superlayer experiments.

More recently Mello and Liechti (2006) explored the potential of mixing DTS and BrUTS in order to directly control the interphase region's mechanical properties under the controlled application of mixed SAMs on a flat sapphire substrate. The specimens were subjected to a wide range of fracture mode-mixes using a specially developed loading device. A 10% BrUTS to DTS ratio increased the interfacial toughness by a factor of about 4 over the bare sapphire. A 55% mixture raised the interfacial toughness slightly, but it was not possible to obtain interfacial crack growth at 75% BrUTS. Instead, voids nucleated and grew ahead of the starter crack. An examination of the epoxy fracture surfaces revealed very different crack growth mechanisms. In specimens made of bare sapphire, crack growth occurred via void nucleation and lateral tunneling, which resulted in discrete forward movement of the main crack. This left a series of very regular ridges on the epoxy fracture surface, something that had also been observed in fracture at glass/ epoxy interfaces (Swadener and Liechti 1998). The epoxy fracture surfaces associated with SAM coated interfaces consisted of many ligaments as though epoxy chains had been pulled out in a highly localized manner. This difference in the appearance of the fracture surfaces was reflected in the traction-separation laws associated with each case. For bare sapphire, the traction-separation law was independent of mode-mix. The maximum traction was about 120 MPa and full separation occurred at about 25 nm. Since the yield strength of the epoxy was 80 MPa, shear-induced toughness was attributed to increases in the plastic zone size around the crack front. For coated sapphire, the traction-separation law was highly dependent on the fracture mode-mix. In all cases, the maximum traction dropped below 80 MPa and the critical separation was as large as 250 nm. This appears to be consistent with the ionic bonding of the Br groups to the amine in the epoxy and the pulling out of epoxy chains or strands. All the toughening with increasing shear came from the intrinsic adhesion associated with the traction-separation law. There was no plastic dissipation around the crack tip.

The objective of the present work was to consider a wider range of areal densities of BrUTS to DTS and to consider the use of SAMs for modifying fiber surfaces rather than flat surfaces. The toughness of sapphire fiber/epoxy interfaces was determined from fiber pull out experiments and associated fracture analyses.

2. EXPERIMENTAL

This section describes the specimen design and fabrication, including surface preparation. This is followed by a description of the fiber pullout experiments themselves.

2.1 Specimen. The specimen geometry (Fig. 1) is shown below. The 125 μm diameter sapphire fiber was centrally placed in a mold. The epoxy was a Bisphenol A resin cured with amido amine (CIBA-GEIGY products Araldite GY502 and Aradur HY955-1, respectively). The two components were mixed with a weight ratio of 100:40 resin to hardener and placed in a vacuum chamber for about 30 minutes to remove bubbles and solvents. Following this, the epoxy was poured into the mold and allowed to cure at room temperature for a week, thereby minimizing residual stresses. The initial crack $a_0 = 6\text{mm}$ was produced by masking the sapphire fibers prior to surface treatment. The specimen was supported by paper backing following removal from the mold. This ensured that the fibers were not broken during mounting in the loading device. The gripping section on the left was shorter and did not require any radius. This allowed the amount of fiber used per specimen to be minimized.

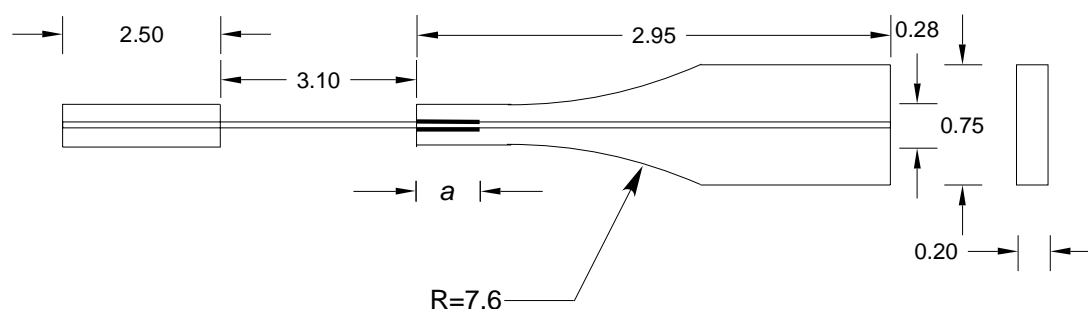


Fig. 1. Specimen geometry (dimensions in cm)

Any chemicals not necessary for the creation of the monolayer, and even excessive amounts (such as water) of required elements interfere with the bonding process. Previous work (Mello and Liechti 2006; Goodfellow 2004; Mitchon and White 2006) in this area showed the importance of pre-treating the sapphire surface with a “Piranha” chemical treatment consisting of one part sulfuric acid (H_2SO_4 , 95.8%) and 1 part hydrogen peroxide (H_2O_2 , 31.6%) by volume in order to both clean the surface and to help make the surface more hydrophilic. It was also shown that heating the sample in a vacuum oven to evaporate surface water just before applying the monolayer chemicals helped reduce the formation of islands and correspondingly provided a more even distribution of the SAM. In addition, the use of an anhydrous atmosphere in an argon or nitrogen dry box reduces the presence of atmospheric moisture in unwanted chemical reactions which would create island formations. The samples were prepared using the following process.

- Sonicate in Acetone for 15 minutes
- Sonicate in Isopropyl Alcohol for 15 minutes
- Sonicate in De-Ionized Water for 15 minutes
- Place in Piranha Solution at 49-66 $^{\circ}\text{C}$ for 30 minutes
- Rinse in De-Ionized Water
- Dry in N_2 Stream
- Heat to 49 $^{\circ}\text{C}$ for 5 Minutes in a Vacuum Oven
- Promptly Transfer to Argon filled Dry Box (< 100 ppm O_2)

- Submerge in BrUTS/DTS solution (below), let sit for 48 hours
- Remove from the Dry Box while submersed in CCl_4
- Sonicate in CCl_4 for 15 minutes
- Sonicate in Toluene for 15 minutes
- Sonicate in Ethyl Alcohol for 15 minutes
- Sonicate in De-Ionized Water for 15 minutes

Each sample was subjected to these steps, with the variation coming in the application of the BrUTS/DTS. Specifically, the formula for the solution was as follows:

- 10 parts hexane
- 1.7 parts CCl_4
- 1 part Chloroform
- 4 Drops of the DTS/BrUTS combination

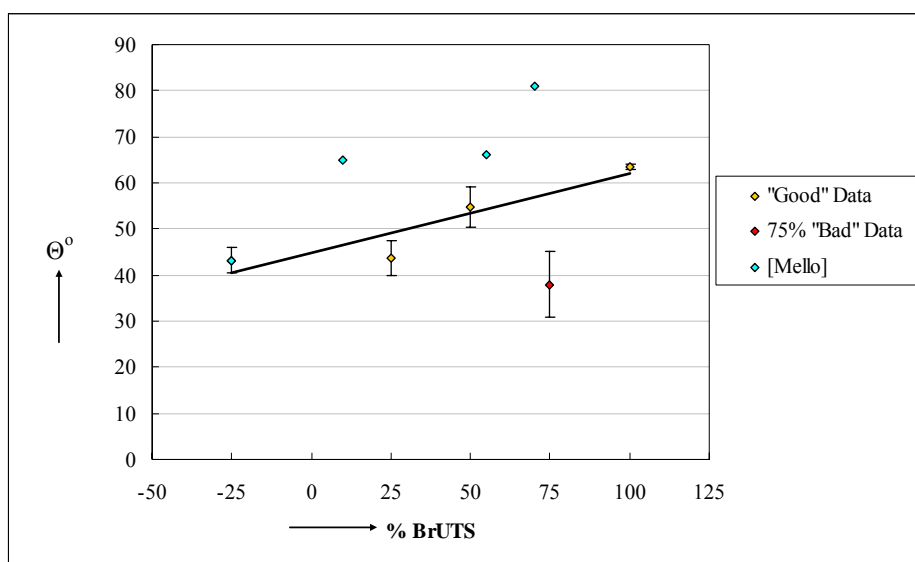


Fig. 2. Effect of BrUTS coverage on contact angle

A set of flat sapphire samples was exposed to the deposition process just outlined and subjected to X-ray Photoelectron Spectroscopy (XPS) in order to check its effectiveness.

Spectra taken before and after deposition indicated that the SAM coverage was extensive.

Ellipsometry was used to determine a layer thickness of 2.7 ± 1.3 nm. The chain length of the BrUTS and DTS molecules is 2.4 nm, which would be further shortened by a characteristic tilt from the surface normal. The results therefore confirmed the presence of a monolayer. Fig. 2 displays the measured contact angles between the water and the sapphire strands. As seen in the figure, higher ratios of the BrUTS to DTS SAM mixture corresponded with an increase in the surface energy of the wetted fiber.

Contact angle measurements were made by vertically dripping treated fibers into de ionized water. Although such a measurement does not necessarily detect monolayers, it is an indicator of surface modification. The same microscope that was used to detect cracks in the fiber pull out experiments was used to image the contact angle. The measured values are shown in Fig. 2,

along with values obtained by Mello and Liechti (2006) on flat sapphire surfaces. With the exception of the 75% case, increasing the BrUTS density increased the contact angle, indicating an increase in the surface energy. The 75% case appears to be an anomalous result, which was also reflected in the fracture data. The contact angle for bare sapphire fibers and flat sapphire surfaces was the same. For coated surfaces, the contact angles obtained from the fiber surfaces were uniformly lower than those obtained from flat surfaces. These results suggest that the curved surface of the fibers allows more interaction between the sapphire and the de ionized water.

2.2 Fiber Pullout Experiments. The specimen, were placed in a custom built loading device with a 100 lb load cell. The experiments were conducted in displacement control at a constant cross head speed. The load was recorded on a computer data acquisition system. A video microscope was used to track the crack front. The recording was synchronized with the load data.

3. ANALYSIS

Analytical and numerical stress and fracture analyses were used to extract the interfacial toughness values associated with the various amounts of BrUTS on the sapphire fiber surface. The analytical solutions were available from the literature. The finite element code ABAQUS was used to obtain the numerical solutions, which also yielded the fracture mode-mix

The initial cracks in the experiments were 50 times greater than the fiber diameter. This allowed the energy release rate to be determined from the simple analyses presented by Charalambides and Evans (1989) and Sigl and Evans (1989). Energy arguments were used to determine the energy release rate as

$$\frac{GE_f}{t^2 a} = \frac{1}{4} \frac{\Sigma}{\Sigma + \frac{f}{1-f}}, \quad (1)$$

where a is the fiber radius,
 t is the traction applied to the fiber,
 f is the volume fraction of fiber and
 Σ is the ratio of matrix tensile modulus E_m to fiber tensile modulus E_f .

The finite element analysis was conducted using the ABAQUS code. Values of energy release rate were determined from the J-integral extracted from solutions. Sufficient levels of mesh refinement were indicated by agreement with values obtained from the analytical solution. The fracture mode-mix ψ was obtained from the crack opening displacements through

$$\psi = \tan^{-1} \left(\frac{\Delta u_x}{\Delta u_y} \right) + \arctan(2\varepsilon) - \varepsilon \ln(r), \quad (2)$$

where r is the distance from the crack front,
 Δu_x and Δu_y are the crack opening displacements and
 ε is the bimaterial constant

$$\varepsilon = \frac{1}{2} \pi \ln \left[\frac{1-\beta}{1+\beta} \right], \quad (3)$$

$$\text{where } \beta = \frac{\mu_1(\kappa_2 - 1) - \mu_2(\kappa_1 - 1)}{\mu_1(\kappa_2 + 1) + \mu_2(\kappa_1 + 1)}. \quad (4)$$

For the sapphire and epoxy used in the study $\beta = 0.217$ and $\varepsilon = 0.07$.

The mode-mix was 53° for distances from the crack front of $9 \times 10^{-7} \leq r \leq 5 \times 10^{-6}$ m.

4. RESULTS

The load-time responses of all the specimens contained one or more regimes where the load was constant (Fig. 3). This suggested the propagation of a frictional slip front along the crack faces from the exterior to the interior of the specimen. All the specimens presented the initial plateau during the initial stages of the pullout. This was due to friction between the epoxy and the sapphire faces of the initial 6mm seed crack. Subsequently, further frictional pullout occurred at larger load levels after the crack had grown, due to the larger surface area that was presented.

In the 140-160 s time frame of Fig. 3 the plateau in load was due to frictional slip along the 6mm starter crack faces. Once slip had occurred over the full 6mm, the load increased. Then there were several crack growth and arrest events (160-190s) followed by another region of frictional slip (190-220s). Because the exposed fiber length was larger, the friction force was higher.

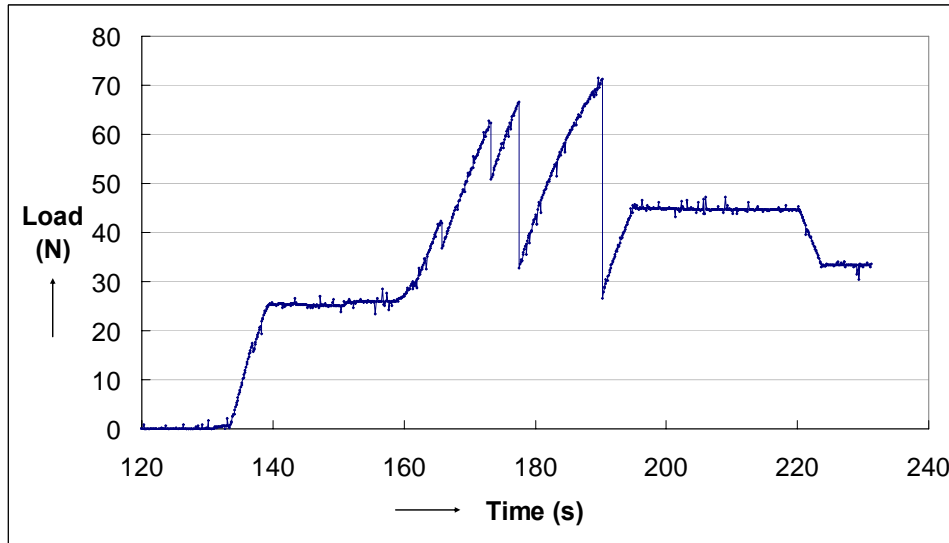


Fig. 3. A typical load response during fiber pullout

A differential Poisson effect causes the epoxy matrix, with a Poisson's ratio of 0.36, to contract onto the fiber, which has a Poisson's ratio of 0.20. Data taken during the initial plateau suggested the frictional shear strength $\tau_F = \frac{P_F}{A} = \frac{P_F}{2\pi al}$ was independent of the areal density of

BrUTS (Fig. 4). This suggests that bond breakage was occurring at some intermediate location on the molecular chain or in the epoxy, regardless of BrUTS content.

In some samples, where fiber failure occurred at some intermediate location between the initial crack front and the end of the specimen, fiber pull-out was again observed. In such cases, the load vs. time plot would display a plateau, as seen in the time from 200~220 seconds in Fig. 3 above. By measuring the length of the fiber that was pulled out, a relationship between the force

and the length of the fiber was observed (Fig. 5).

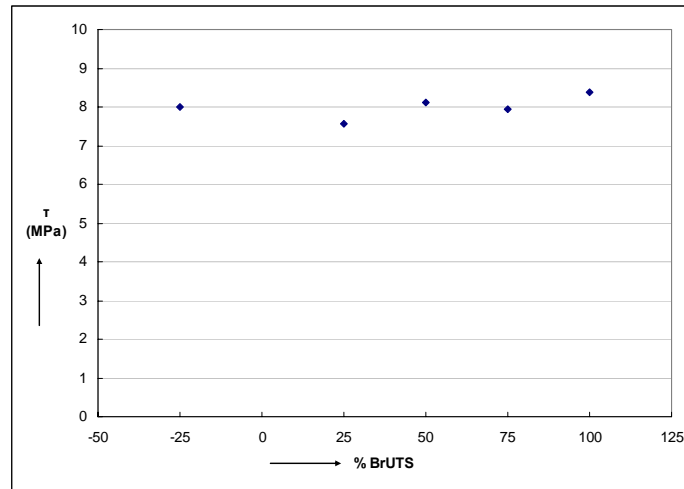


Fig. 4. Frictional shear strength of sapphire/epoxy fracture surfaces.

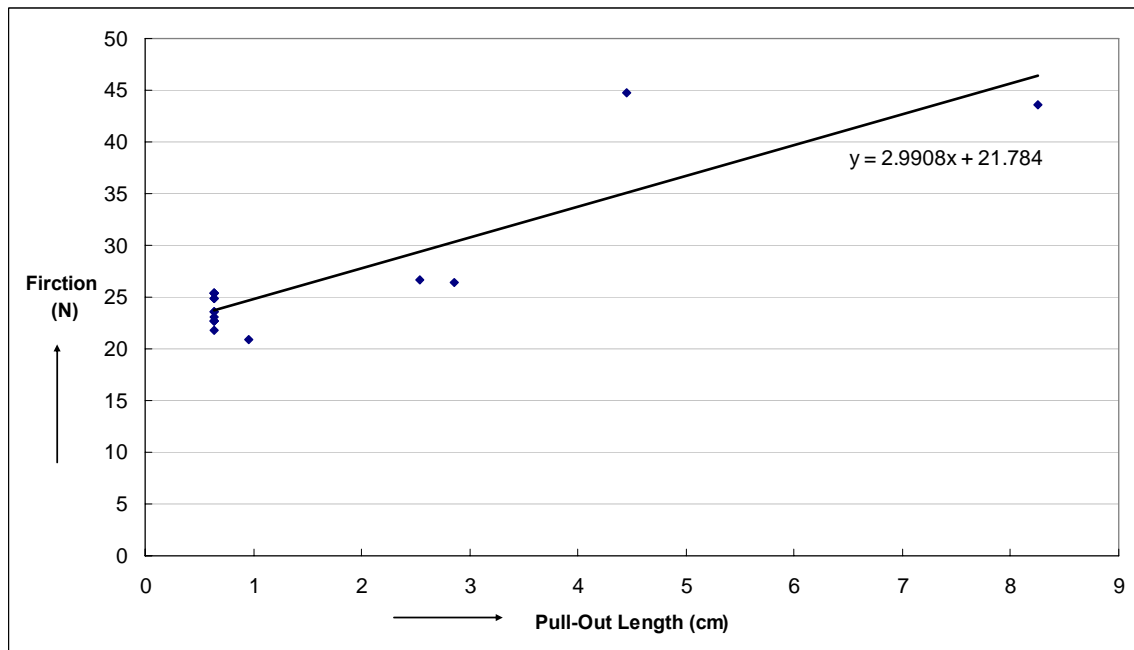


Fig. 5. Friction force vs. fiber pullout length.

As seen in the figure, and as expected, a longer fiber pullout length corresponded to a higher friction load. The values at the 6 mm mark are taken from the initial loading plateau. Although there were only a few data points, a linear fit was applied to the data to determine a frictional force of $2.99l + 21.8$ N where l is the fiber pullout length. We expect the load to increase linearly through $P_F = 2\pi a\tau_F l$. Using the value of $\tau_F = 8$ MPa from Fig. 4 makes the slope $2\pi a\tau_F = 3.14$. This agreement between the fit and the data suggested that friction was indeed playing a consistent role in the experiments.

Consequently, in determining the toughness of each interface presented by the different areal densities of BrUTS, the difference between the frictional load and the total load at crack initiation was substituted in equation (1). The resulting interfacial toughness values are plotted in Fig. 6 and compared with the values obtained by Mello and Liechti (2006) on flat sapphire.

There was a notable increase in toughness with BrUTS content, with full coverage yielding a ten fold increase. The results from the fiber pullout experiments were quite consistent with previous results for bare sapphire and 50% coverage. The previous values obtained at 10% coverage (Mello and Liechti 2006) appear to be high and the fiber pullout results at 75% coverage were low as was expected from the contact angle experiments. One additional point of interest is that it was possible to produce crack growth at large coverage in the fiber pullout experiments, whereas as void growth was observed in the sandwich specimens employed in Mello and Liechti (2006). This is presumably due to the lower degree of triaxiality that arises in fiber pullout.

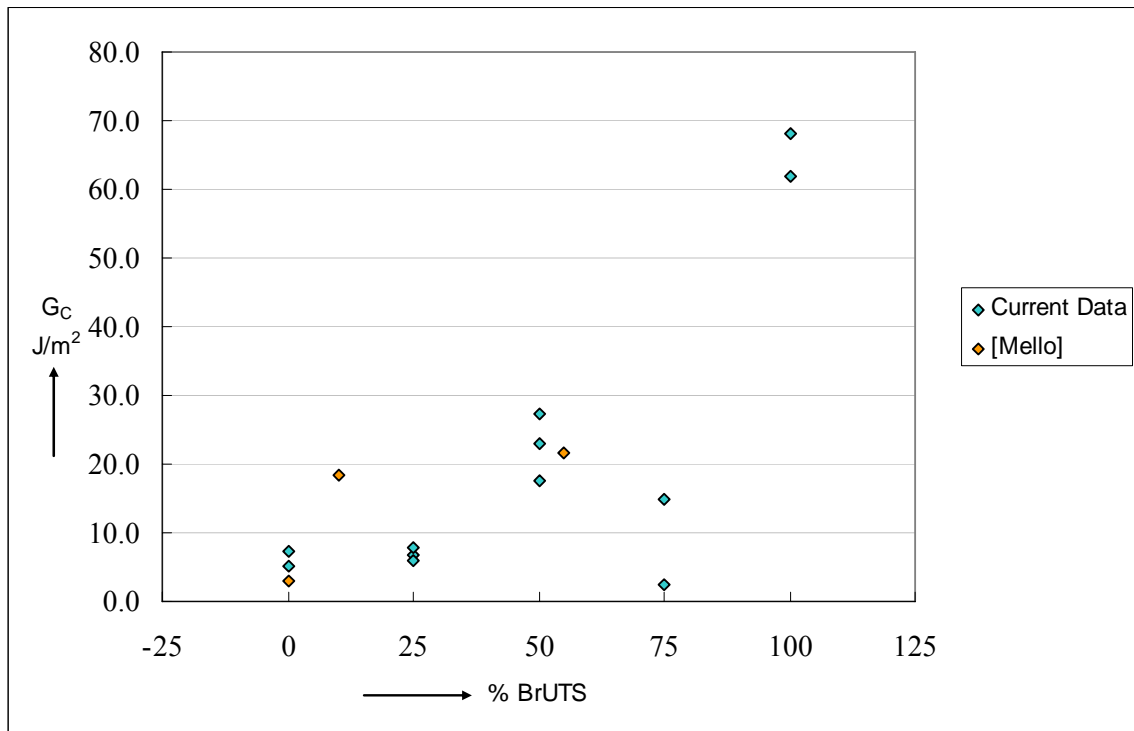


Fig. 6. Interfacial toughness values as a function of BrUTS content; comparison between current data and previous literature data.

5. CONCLUSIONS

The work presented here suggests that it is possible to coat sapphire fibers with mixed SAMs of BrUTS and DTS. Furthermore, increases in BrUTS coverage led to significant increases in interfacial toughness. The results suggest that SAMs provide a suitable degree of adhesion control.

REFERENCES

- Charalambides, P.G. and Evans, A.G. (1989). Debonding Properties of Residually Stressed Brittle-Matrix Composites. *J. Am. Ceram. Soc.* 72, 746-753.
- Goodfellow, B. (2004). Design and application of a fiber pullout test for examining controlled interfaces in fiber reinforced polymers. In: Center for Mechanics of Solids, Structures and Materials Reports, University of Texas at Austin.
- Kent, M.S., Reedy, E.D., Yim, H., Matheson, A., Sorenson, J., Hall, J., Schubert, K., Tallant, D., Garcia, M., Ohlhausen, T., and Assink, R. (2004). Using self-assembling monolayers to study crack initiation in epoxy/silicon joints. *Journal of Materials Research* 19, 1682-1695.
- Mello, A.V. and Liechti K.M. (2006). The effect of self-assembled monolayers on interfacial fracture. *Journal of Applied Mechanics* 73, 860-870.

- Mitchon, L.N. and White, J.M. (2006). Growth and analysis of octadecylsiloxane monolayers on Al₂O₃ (0001). *Langmuir* 22(15), 6549-6554.
- Sigl, L.S. and Evans, A.G. (1989). Effects of Residual Stress and Frictional Sliding on Cracking and Pull-Out in Brittle Matrix Composites. *Mechanics of Materials* 8, 1-12.
- Swadener, J.G., and Liechti, K.M. (1998). Asymmetric Shielding Mechanisms in the Mixed-Mode Fracture of a Glass/Epoxy Interface. *Journal of Applied Mechanics* 65, 25-29.
- Ulman, A. (1996). Formation and structure of self-assembled monolayers. *Chemical Reviews* 96, 1533-1554.
- Zhuk, A.V., Evans, A.G., Hutchinson, J.W., and Whitesides, G. M. (1998). The adhesion energy between polymer thin films and self-assembled monolayers. *Journal of Materials Research* 13, 3555-3564.

FROM INTERFACE LAWS TO COMPOSITE BEHAVIOUR

Bent F. Sørensen, Lars P. Mikkelsen, Rasmus C. Østergaard
and Stergios Goutianos

Materials Research Department, Risø National Laboratory,
Technical University of Denmark, Roskilde, Denmark

ABSTRACT

This paper summarizes efforts to characterize, model and link the mechanic response of polymer matrix composites from nanoscale, through microscale to macroscale. Particular attention is given to cracking parallel to the fibre direction. For this failure mode, large scale crack bridging occurs by cross-over bridging. Mechanical characterization is made in the form of interface cohesive laws, representing the fracture process zone of the fibre/matrix interface. Micromechanical models are use for prediction of composite cohesive laws, representing crack bridging for the cross-over bridging mechanism. Comparisons are made between model and experiments.

1. INTRODUCTION

Polymer matrix composites based on aligned, continuous fibres have gained widespread use in engineering applications, in particularly in load-carrying structures where weight savings are of high importance (Brøndsted et al. 2005). Furthermore, composite materials offer the possibility of tailor-making materials for specific purposes, since they can be designed at many scales. Typically, composites are considered from the nanometer scale, over the micrometer scale, lamina (or ply) level to laminate and macroscale. Although a number of models exist at the various scales, it is still fair to claim that a complete understanding of how macroscale properties of composite materials depend on micro- and nanometer scale parameters does not yet exist.

It is therefore a long term ambition in materials research is to create a comprehensive knowledge of the connection between the various scales, so that fibre composites can readily be designed at the nanometer scale for optimal macro scale properties, e.g. high tensile strength and high fracture toughness.

At the shorter term a goal is to focus at the effect of the fibre/matrix interface properties. Fig. 1 shows a schematic of how properties of the fibre/matrix interface at nanoscale can be connected

to the composite behavior at the microscale and macroscale. At the nanometer scale the interface can be described the fibre surface, which has characteristic roughness characteristics. The surface roughness and chemistry can be manipulated and it is anticipated that the roughness and chemistry at the fibre/matrix interface plays a key role in controlling the fracture behavior of the composite material.

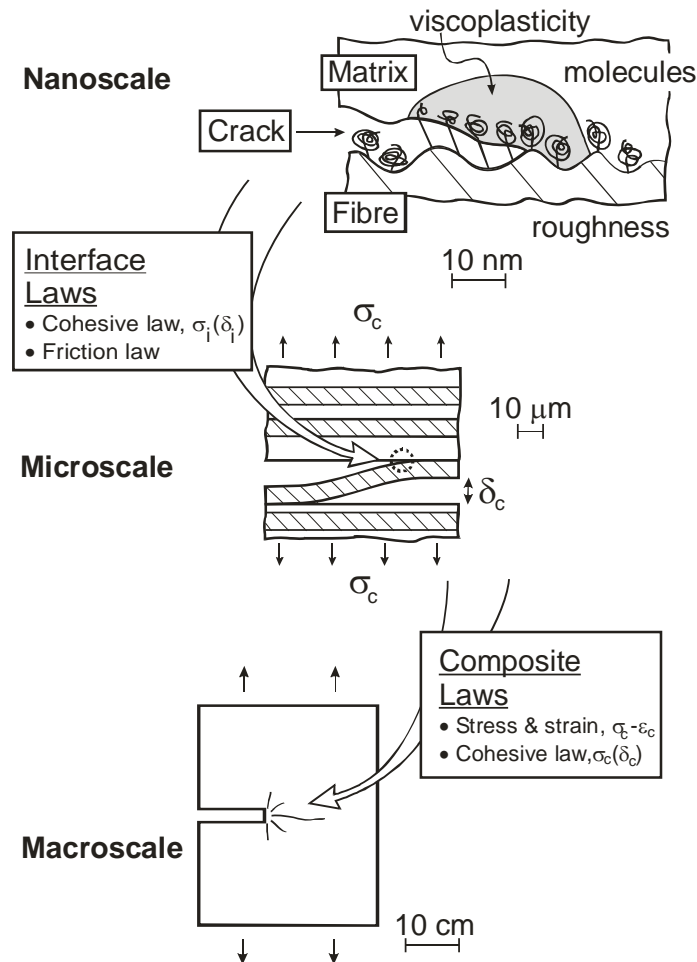


Fig. 1. The interface law represents the mechanical response of the interface (as controlled by chemistry and surface roughness) by connecting surfaces at the microscale. The composite law is used at macroscale to represent the interaction between the discrete fibre, matrix and crack in a continuum model where the composite is treated as a homogenized anisotropic continuum.

One of the ways to modify the fibre/matrix interface is to graft long molecule chains to the surface so that the molecules are pulled out during interface separation. If the forces from the molecules are sufficiently high, they may result in the formation of a (visco-)plastic zone at the crack tip. This is expected to cause the fracture toughness of the interface to increase (Tvergaard and Hutchinson, 1993). Thus, the nanoscale/microscale levels can only be understood by a combination of skills belonging to chemistry and to mechanics.

From the perspective of mechanics, one of the challenges is to characterize the interface behavior properly. Earlier, the mechanics of a fibre/matrix interface was characterized in terms of a maximum shear stress. Models and experiments such as the single fibre fragmentation test rely on determination of a critical shear strength for the interface. More recent models and test methods are based on fracture mechanics and incorporate interface fracture energy for fibre/matrix debonding. However, even this approach has its shortcomings. The most severe issue

concerns the interplay with plasticity in the matrix. The size of the crack tip fracture process zone and the surrounding plastic zone can be comparable or larger than the spacing between the fibres. Then fibre/matrix debonding becomes a so-called Large-Scale-Failure-Process problem, implying that it cannot be properly analyzed in terms of Linear Elastic Fracture Mechanics (LEFM).

We favor an approach where the interface separation is described in terms of a cohesive law. Cohesive laws have been used to represent failure from the microscale to the macroscale (Needleman 1987; Tvergaard and Hutchinson 1993; Mohammad and Liechti 2000; Yang and Thouless 2001; Yang and Cox 2005). We will denote the cohesive law of the fibre/matrix interface by *interface cohesive law*. The use of a representation based on interface cohesive laws allows the separation of fracture energy due to the decohesion process and the energy dissipation due to crack tip plasticity.

In the present paper, we focus at the development of methods that allow the determination of interface cohesive laws. Having obtained interface cohesive laws, they can be used for prediction cohesive laws at the macroscale. In the present paper we will call cohesive laws at the macroscale for *composite cohesive laws*. We illustrate interface cohesive laws and composite cohesive laws in Fig. 1. The principle of modeling a fracture process zone by a cohesive zone is shown schematically in Fig. 2.

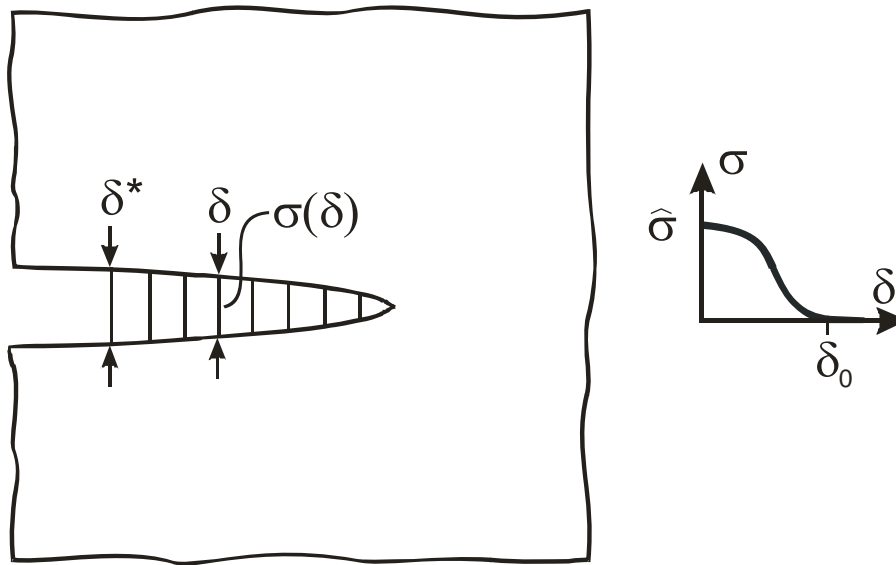


Fig. 2. A fracture process zone can be modeled by a cohesive zone. The cohesive law is the relationship between opening and the stress transmitted across the fracture process zone. The area under the curve represents the fracture energy.

The major macroscale problem that we address in the present paper is cracking along a weak plane parallel to the fibre direction, e.g. delamination (interlaminar cracking) and splitting (intralaminar cracking). This cracking mode can be accompanied by large scale fibre bridging, which from a safety point of view is beneficial since it leads to rising fracture resistance (R-curve behavior). Obviously, the fracture resistance increase depends on the fibre/matrix interface properties. It is therefore of interest to establish tools that can characterize and model fibre bridging in composite materials at various scales.

The paper is organized as follows. First, we describe some basic mechanics and test specimens for interface characterization. Examples of measured cohesive laws are given and their effect on

overall interface toughness is discussed. Next, interface cohesive laws are used to predict macroscopic composite cohesive laws, representing crack bridging by cross-over fibres. Effects of interface properties are exploited for both mode I and mixed mode cracking. Finally, composite cohesive laws are used in the prediction of the load -carrying capability of large composite structures.

2. INTERFACE COHESIVE LAWS

In this section experimental methods are described for characterising the mechanical interface properties (fracture energy, cohesive laws, friction laws and fracture resistance curves). Planar, well-defined geometries are used since they allow fundamental studies on surface properties using advanced chemical analysis techniques. Furthermore, the mechanical analysis, by a J integral approach elaborated below, is straightforward.

Interfaces with different properties (weak, intermediate and strong) are created through plasma polymerisation. A thin polymer film (20-150 nm) is deposited on planar substrates. The type and number of chemical functional groups are varied by using different monomers and parameters during plasma polymerisation.

2.1 Test principle. DCB (Double Beam Cantilever) sandwich specimens are loaded by pure bending moments for the measurement of the interface cohesive laws under nominal Mode I (normal opening) as shown in Fig. 3(a). The sandwich specimen consists of two planar substrates bonded together by an adhesive representing the matrix material of a composite, reinforced with steel beams. The J integral (Rice 1968) evaluated along the external boundaries of the specimen gives (Bao et al. 1992)

$$J_{ext} = \frac{1-\nu_2^2}{E_2} \frac{M^2}{B^2 H^3 \eta^3 I}, \quad (1)$$

where E_2 and ν_2 are Young's modulus and Poisson's ratio of the steel. M is the applied moment, H the thickness of the steel beams and B the specimen width. The parameters η and I depend on the geometry and elastic properties of the steel and the substrate (Bao et al. 1992). In (1) the contribution from the adhesive is neglected as its stiffness is much lower than the steel and the substrate. Note from (1) that the J integral is independent of the crack length, a ; then for this specimen crack growth is stable.

The J integral along a path just outside the failure process zone is (Rice 1968)

$$J_{ext} = \int_0^{\delta_n^*} \sigma_n^i(\delta_n, \delta_t) d\delta_n, \quad (2)$$

where δ_n^* is the normal end-opening of the cohesive zone (see Fig. 3(a)) and σ_n^i is the interface cohesive law normal stress. Due to the integration path independence of the J integral, $J_{ext} = J_{loc}$. Differentiation with respect to δ_n^* gives (Suo et al. 1992):

$$\sigma_n^i(\delta_n^*) = \frac{dJ}{d\delta_n^*}, \quad (3)$$

i.e., the cohesive stress as a function of the end-opening (the interface cohesive law under normal openings). Thus, by recording J (via the moment, M) and the end-opening δ_n^* simultaneously during loading until crack growth begins, the interface cohesive law can be obtained from (3).

A precise method is necessary to accurately measure the end-opening of the failure process zone as the deformations are of the order of a micron. Therefore, a Speckle pattern of particles is made on the specimen surface. By following the movement of individual particles across the interface using image analysis the displacements can be determined. A similar approach is to use Digital Image Correlation (Berfield et al. 2007), can also give information about the displacement field near the crack. These measuring techniques can be even used with a normal optical microscope providing sufficient magnification capabilities. In this case sub-pixel resolution techniques usually need to be employed to obtain a sufficient accuracy.

A similar principle can be used to derive the interface cohesive law under pure Mode II. A schematic illustration of a test specimen that could be used for this purpose is shown in Fig. 3(b). The J integral evaluated along the external boundaries can be obtained in closed analytical form. An equation similar to (2) is obtained when evaluating the J integral locally around the failure process zone, except that the interfacial shear appears instead of the normal stress and the tangential end-opening displacement replaces the normal crack opening displacement. This approach enables the determination of the Mode II cohesive law.

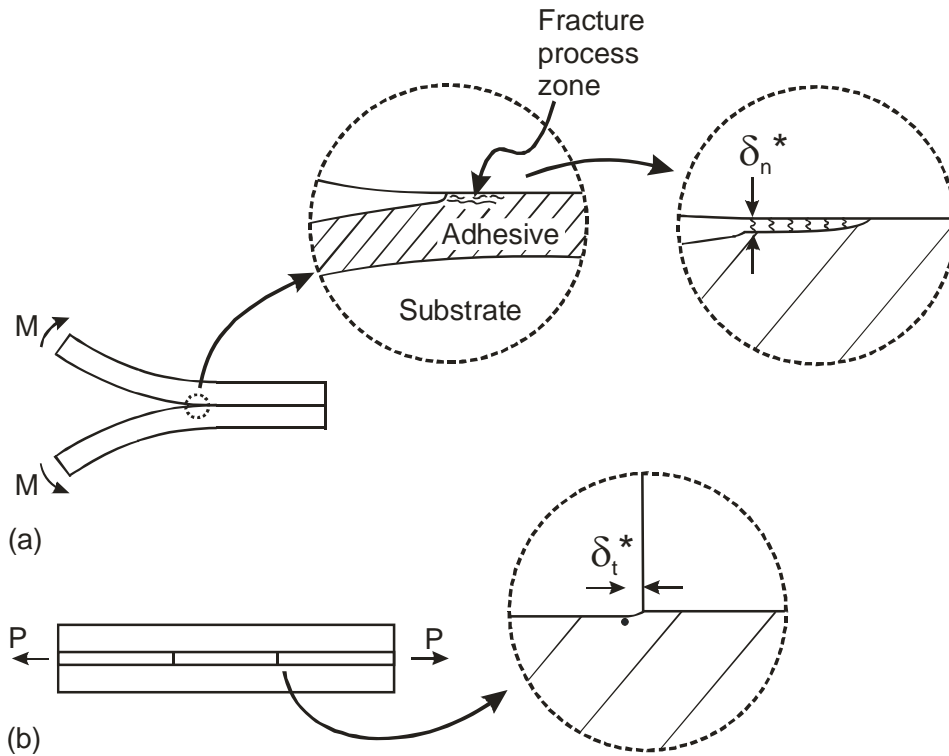


Fig. 3. (a) Schematic illustration of a DCB specimen loaded with pure bending moments for characterising interface properties under Mode I conditions. The adhesive is in between the two substrates. (b) Planar specimen geometry for Mode II interface testing. Two substrates are embedded in an adhesive.

2.2 Example of measurement of interface cohesive law. As an example, planar glassy carbon substrates (Sigradur G, HTW Hochttemperatur, Germany) were used as an experimental model of carbon fibres. Glassy carbon is a fully disordered material in contrast to carbon fibres and its mechanical properties are significantly lower than carbon fibres. However, its chemical properties resemble those of carbon fibres quite well (Launay et al 2007).

Specimens were made as follows. An epoxy resin was poured between two plasma treated glassy carbon substrates ($65 \times 1 \times 5 \text{ mm}^3$). Teflon films, 0.5 mm thick, were used to keep the glassy carbons apart. The cured samples were ground and polished to facilitate optical observations of crack growth. Subsequently the sandwich specimens were reinforced with 6 mm thick stainless steel beams.

During the loading, the end-opening was measured by following the movement of two particles across the interface. Images were recorded using a low magnification optical microscope with a resolution of approximately 650nm per pixel.

Fig. 4 shows a typical result. The J integral is shown as a function of the end-opening. There is realtive large scatter in the measurements of the end-openings. Since the critical crack opening is less than a micron, almost all the details of the cohesive law need to be calculated using sub-pixel calculation for the present the experimental set-up. Thus the interface cohesive law to be derived below should be regarded as an illustrative example of the approach.

Due to uncertainties especially at very low crack openings a linear approximations is used to fit the experimental data. For larger crack openings an exponential function is chosen. The associated interface cohesive law is given in Fig. 5. The ambiguity mainly concerns the shape of the cohesive law and the peak stress; the measured critical crack opening agrees well with openings measured in experiments performed inside the chamber of an ESEM (Environmental Scanning Electron Microscope). For more accurate results a higher magnification microscope or an ESEM should be used.

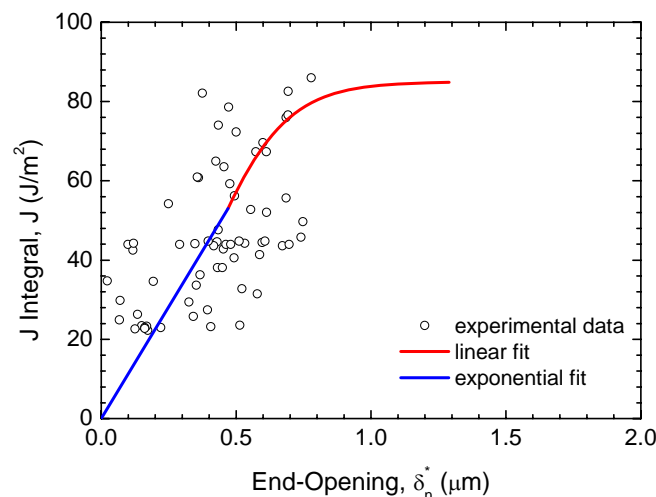


Fig. 4. J integral as a function of the end-opening of the failure process zone.

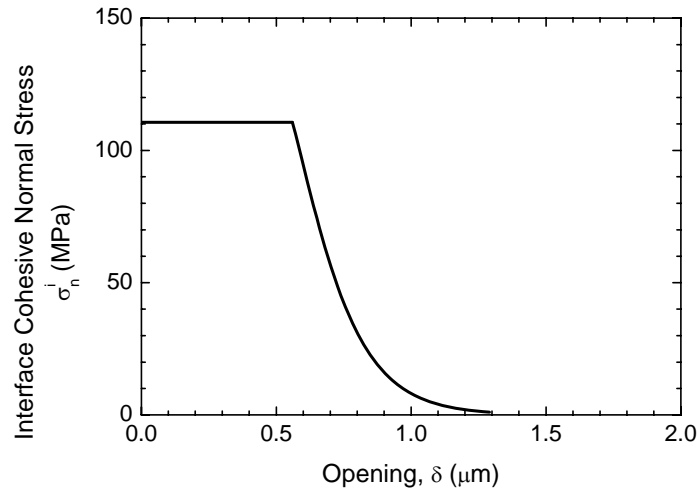


Fig. 5. Interface cohesive law obtained from the data presented in Fig. 4.

2.3 Fracture resistance curves. Once the crack begins to propagate, the fracture resistance, calculated by the J integral no longer represents just the interface cohesive law of fracture process zone; if a plastic zone develops near the crack tip, unloading will take place during crack propagation. As the plastic zone increases in size, the J integral value increases as the crack length increases (R-curve behavior).

Examples of fracture resistance curves are depicted in Fig. 6 for a weak, an intermediate and a strong interface. For the weak interface the fracture energy is almost constant as a function of crack extension. For the intermediate and strong interfaces a significant R-curve behaviour is observed. This extrinsic toughening is probably due to plasticity (Tvergaard and Hutchinson, 1992, 1993). Almost all experiments were terminated by the onset of unstable crack growth with specimens showing R-curve behaviour being more prone to unstable crack growth. In some cases the interface crack kinked into the glassy carbon. The instability characterized by a very high crack velocity and it is possible a visco-plastic effect of the epoxy resin.

3. PREDICTIONS OF COMPOSITE COHESIVE LAWS

3.1 Mechanism of crack bridging by cross-over bridging. Fig. 7 shows a micrograph of the crack bridging mechanism in a unidirectional fibre composite. Single fibres and ligaments consisting of several fibres are attached to the two crack faces and act as a bridge between the two crack faces. The bridging ligaments thus generate tractions that tend to restrain the crack opening. With increasing crack opening, the ligament debonds along an interface, increasing the length of the ligament. Following Bao and Suo (1992) we will call this bridging mechanism for *cross-over bridging*.

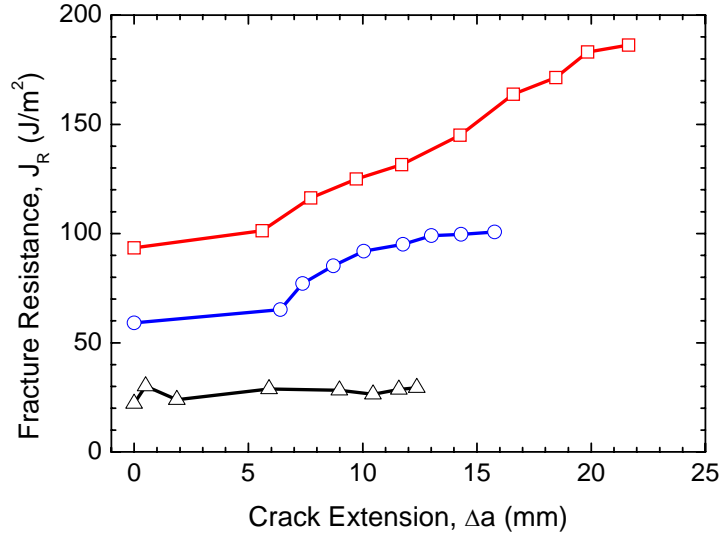


Fig. 6. Fracture resistance curves for a weak (black triangles), intermediate (blue circles) and strong (red squares) interfaces.

3.2 Analytical models for cross-over bridging. An analytical model for Mode I crack bridging by cross-over bridging was developed by Spearing and Evans (1992). They modelled cross-over bridging by a Timoshenko-type beam peeling off along an interface. Their model only describes the interface separation process in one parameter, the interfacial fracture energy, G_c^i . Thus, effects of other interface cohesive parameters cannot be uncovered by such a model. Never the less the model gives insightful results. When the shear deformation is neglected, the model predicts a relationship between the normal stress and normal opening at the composite level as (Sørensen and Jacobsen, 1998)

$$\sigma_n^c = \sigma_n^c(\delta_n) = \frac{1}{4} \left[\frac{2 G_c^i}{3 E h} \right]^{3/4} \sqrt{\frac{2h}{\delta_n}} \eta b h E, \quad (4)$$

where σ_n^c is the normal stress (superscript c is used for indicate that the equation concerns composite cohesive law), E is the Young's modulus, b and h denote the width and height of the bridging ligaments, η is the number of bridging ligaments per unit crack area and δ_n is the normal opening of the crack. This approximate solution is not expected to be accurate for very short ligaments. Consequently, the singular stress predicted for $\delta_n \rightarrow 0$ should not be taken literally.

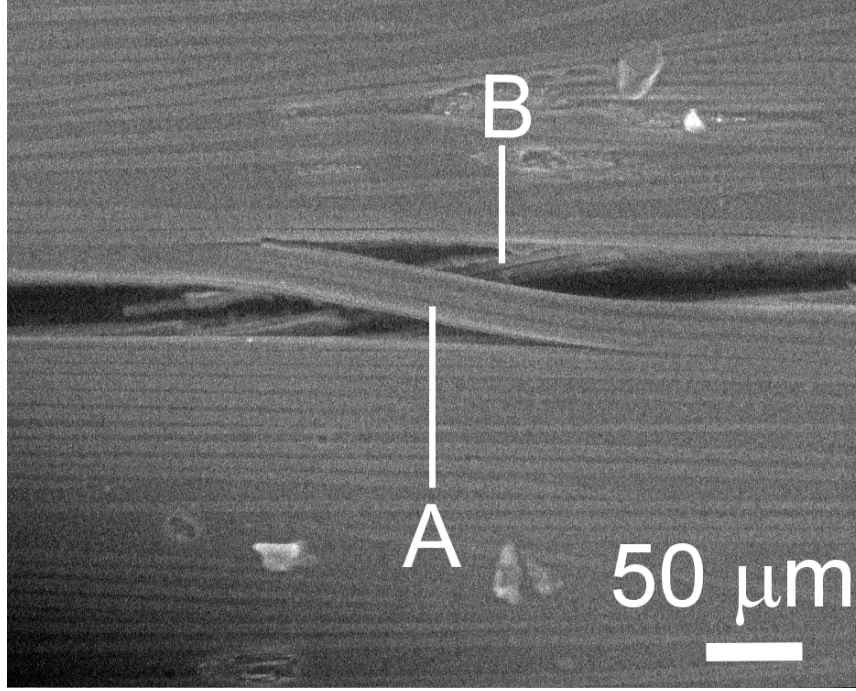


Fig. 7. Micrograph of a cross-over bridging in a unidirectional polymer matrix composite.

Recently, the model of Spearing and Evans was extended to mixed mode (Mode I-II) by Sørensen et al. (2007a). Assuming that only ligaments loaded in axial tension transmit stresses between the crack faces and neglecting shear deformation, the normal stress of the composite cohesive law is predicted to be

$$\frac{\sigma_n^c}{\eta b h E} = \frac{\frac{\delta_n}{h} \left[\frac{G_c^i}{E h} \right]^{3/2}}{\left[\left(\frac{\delta_t}{2h} \right)^2 + \sqrt{\left(\frac{\delta_t}{2h} \right)^4 + 6 \frac{G_c}{E h} \left(\frac{\delta_n}{2h} \right)^2} \right]^{3/2}} \quad (5)$$

where δ_t is the tangential crack opening. The composite cohesive shear stress σ_t^c is found as

$$\frac{\sigma_t^c}{\eta b h E} = \frac{\frac{\delta_t}{h} \left[\frac{G_c^i}{E h} \right]^{1/2}}{\left[\left(\frac{\delta_t}{2h} \right)^2 + \sqrt{\left(\frac{\delta_t}{2h} \right)^4 + 6 \frac{G_c}{E h} \left(\frac{\delta_n}{2h} \right)^2} \right]^{1/2}} \quad (6)$$

A plot of the mixed mode cohesive stresses is shown in Figs. 8 and 9. In the Figures, the cohesive stresses are shown as a function of magnitude of the opening and the phase angle of the end-openings, φ , defined such that $\varphi = 0^\circ$ corresponds to pure normal opening (Mode I) and $\varphi = 90^\circ$ corresponds to pure tangential opening (Mode II).

Fig. 10 shows the predicted fracture resistance curves (the J integral value, J_R , as a function of

the magnitude of the end-opening of the cohesive zone, δ^*) obtained by integration of the bridging stresses locally around the cohesive zone according to the J integral:

$$J_R = \int_0^{\delta_n^*} \sigma_n^c(\delta_n, \delta_t) d\delta_n + \int_0^{\delta_t^*} \sigma_t^c(\delta_n, \delta_t) d\delta_t \quad (7)$$

where δ_n^* and δ_t^* denote the opening in the normal and tangential directions at the end of the cohesive zone, respectively. It is seen from Fig. 10 that for $\varphi = 0^\circ$ (Mode I), the fracture resistance increases as $\sqrt{\delta^*}$ in agreement with earlier findings (Sørensen and Jacobsen, 1998). For higher values of φ , the fracture resistance increases almost linearly with δ^* . The model predicts, for the same end opening, a higher fracture resistance for a higher value of φ . Thus, under the assumption of constant η and constant h , the cross-over bridging mechanism is a more effective toughening mechanism under mixed mode and Mode II than under Mode I.

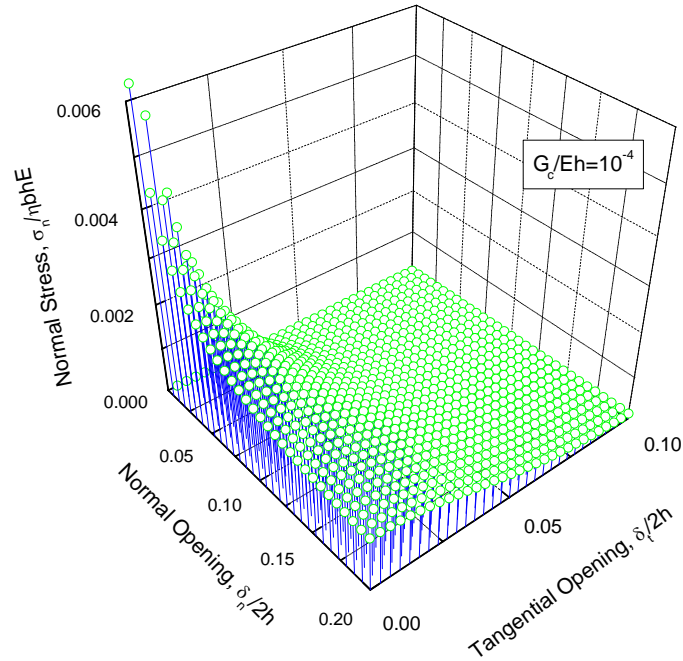


Fig. 8. Normal stress predicted as a function of normal and tangential crack opening displacements.

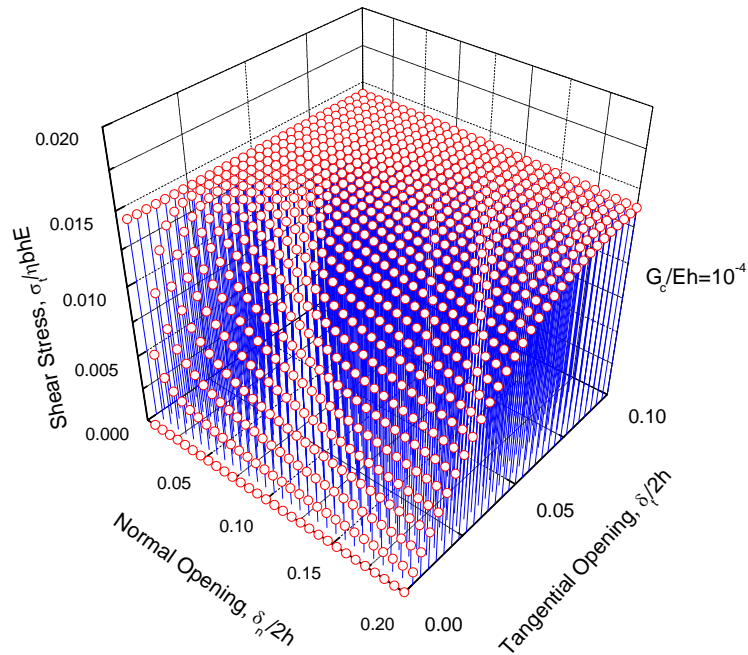


Fig. 9. Composite cohesive law shear stress predicted as a function of normal and tangential crack opening displacements.

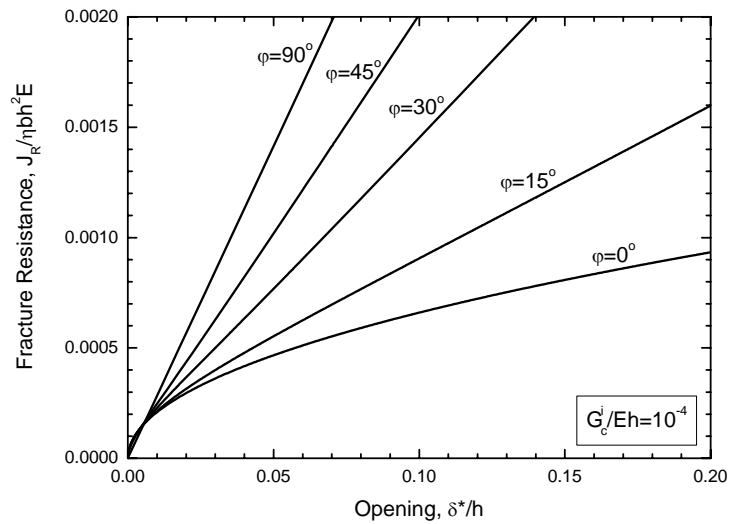


Fig. 10. Fracture resistance curves predicted from the micromechanics model.

3.3 Numerical model for cross-over bridging. Mode I crack bridging was modeled by Østergaard et al. (2007) using the finite element method that accounts for large displacements and finite strains. The detachment of a bridging ligament along the interface was modeled by the use of a cohesive zone. The interface cohesive law was taken to have the trapezoidal shape proposed by Tvergaard and Hutchinson (1992). Composite cohesive laws were obtained by

prescribing a monotonic opening of the crack faces. The solution was obtained in increments. A stable solution path was obtained by the use of a special Rayleigh-Ritz procedure.

A comparison of a predicted composite cohesive law obtained from the finite element/cohesive zone model and one predicted from the analytical Spearing-Evans model is found in Fig. 11. Here, ℓ is the distance between the bridging ligaments. It is seen from the Figure that the two cohesive laws are in agreement for small crack openings ($\delta_n/h < 2$). For large crack openings the model predictions deviate: The analytical model predicts that the composite cohesive stress decreases asymptotically to zero whereas the numerical results approach a constant value. This difference can be attributed to the fact that the numerical model accounts for finite displacements which the analytical model does not.

The effect of the interface fracture energy, G_c^i , on predicted composite cohesive laws is shown in Fig. 12. A higher interfacial fracture energy results in a higher composite cohesive stress, but the shape is not significantly altered.

Fig. 13 shows the effect of the critical opening for which the interface cohesive stresses vanishes, $\delta_{n,c}^i$ (for at fixed interfacial energy, this is the same as altering the peak interfacial cohesive stress; an increasing is equivalent to a decreasing peak stress). It is seen from the figure that the predicted composite cohesive laws deviate significantly for small openings ($\delta_n/h < 0.5$). A smaller critical opening of the interface cohesive law gives a higher peak stress for the composite cohesive laws. However, for larger openings, the curves converge; the results become insensitive to the critical opening when the ligament length is long.

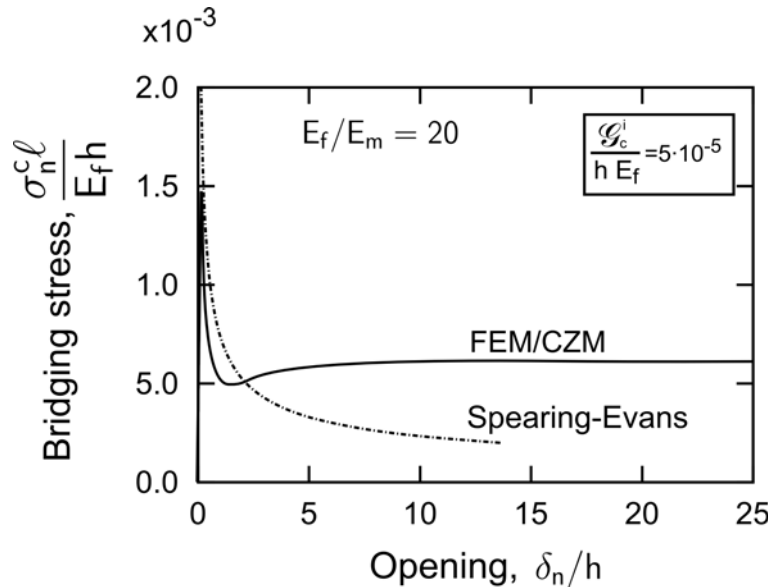


Fig. 11. Comparison of Mode I composite cohesive law predicted by the analytical Spearing-Evans model and predicted by the finite element/cohesive zone model.

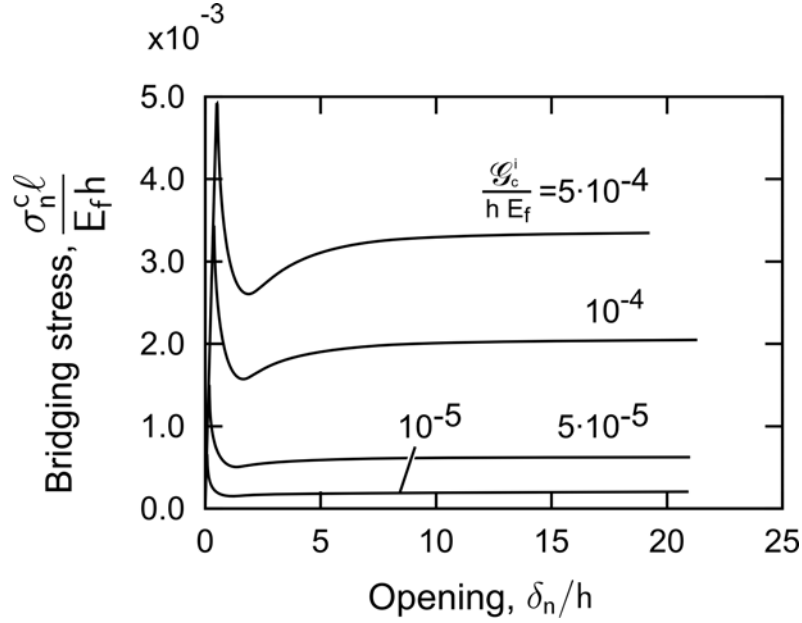


Fig. 12. Effect of interface fracture energy on the Mode I composite cohesive law.

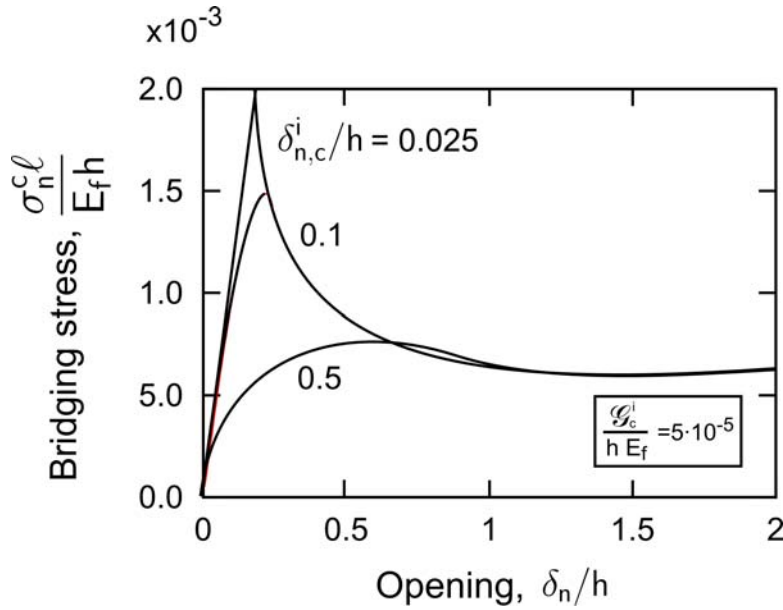


Fig. 13. Effect of the critical separation opening of the interface cohesive law on the Mode I composite cohesive law.

4. MEASUREMENT OF COMPOSITE COHESIVE LAWS

4.1 Approach for the determination of mixed mode cohesive laws. Having made predictions of composite cohesive laws, we proceed to experimental determination of composite cohesive laws. To do so, we utilize a J integral based approach (Sørensen and Kirkegaard 2006). Using the common assumption the composite cohesive law stresses are derived from a potential function, Φ ,

$$\sigma_n^c(\delta_n, \delta_t) = \frac{\partial \Phi(\delta_n, \delta_t)}{\partial \delta_n} \quad \sigma_t^c(\delta_n, \delta_t) = \frac{\partial \Phi(\delta_n, \delta_t)}{\partial \delta_t}, \quad (8)$$

the J integral result (7) becomes

$$J_R = \Phi(\delta_n^*, \delta_t^*). \quad (9)$$

Thus, the value of the fracture resistance equals the potential function evaluated at the end openings of the cohesive zone. Combining (8) and (9) gives

$$\sigma_n(\delta_n^*, \delta_t^*) = \frac{\partial J_R(\delta_n^*, \delta_t^*)}{\partial \delta_n^*} \quad \sigma_t(\delta_n^*, \delta_t^*) = \frac{\partial J_R(\delta_n^*, \delta_t^*)}{\partial \delta_t^*}. \quad (10)$$

It follows that mixed mode cohesive laws can be derived by simultaneous measurements of J_R , δ_n^* and δ_t^* .

In order to determine fracture resistance in a J integral consistent manner, specimens should be used for which a J integral solution exists also in the case of Large Scale Bridging (LSB). We have used the DCB-specimen loaded with uneven bending moments (DCB-UBM), see Fig. 14. When the distances from the beam ends to the failure process zone are longer than a few times the beam height, the J integral value evaluated along the exterior boundaries of the specimen can be obtained analytically. The result is (plane strain) (Sørensen et al. 2006).

$$J_{ext} = (1 - \nu^2) \frac{21(M_1^2 + M_2^2) - 6M_1M_2}{4B^2H^3E}, \quad (11)$$

where M_1 and M_2 are the applied bending moments (positive signs are shown in the figure), E and ν denotes the Young's modulus and the Poisson's ratio, B is the specimen width and H is the beam height. For plane stress, the factor $1 - \nu^2$ should be replaced by unity. J_{ext} equals the fracture resistance, J_R when cracking takes place. Thus, by recording J_R , δ_n^* and δ_t^* during experiments, we can determine the mixed mode cohesive laws from (10).

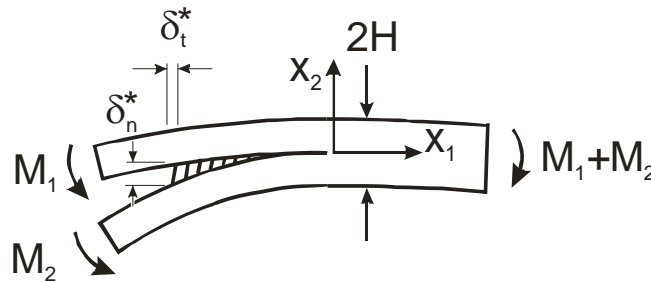


Fig. 14. A fracture mechanics test specimen: The Double Cantilever Beam specimen loaded with Uneven Bending Moments (DCB-UBM).

4.2 Example of measurement. DCB-UBM specimens were made from a plate of a unidirectional glass fibre polymer matrix composite. Fracture mechanics tests were conducted at a special test fixture that applies pure, uneven bending moments to the DCB specimen via two transverse arms, using a wire and roller arrangement (Sørensen et al. 2006). The applied moments as well as displacements at the initial crack tip (that becomes the end-opening of the cohesive zone) were recorded during the tests. After the tests, J_R was calculated using (11) and a fit (orthogonal

polynomials) was made to the $J_R - \delta_n^* - \delta_t^*$ data. The cohesive laws were then obtained by partial differentiation according to (10). Here, only the pertinent results will be reviewed; details about the specimen manufacture, testing approach and data analysis are given elsewhere (Sørensen and Jacobsen 2007).

Fracture resistance curves, J_R as a function of δ^* are shown in Fig. 15 for various ratios of the applied moments. Here, $M_1/M_2 = -1$ corresponds to Mode I and $M_1/M_2 = 1$ corresponds to Mode II. Fig. 16 shows the recorded $\delta_n^* - \delta_t^*$ data. It is seen from Fig. 16 that $M_1/M_2 < 0$ results in end-openings dominated by normal opening, δ_n^* . Only for M_1/M_2 approaching 1 the openings becomes dominated by δ_t^* . Observe from Fig. 15 that the fracture resistance curves of the δ_n^* -dominated experiments are smooth, indicating completely stable crack growth; the fracture resistance curves has a rough form due to rapid decrease in load with increasing amount of δ_t^* . Furthermore, and the curves do not flatten out to attain steady-state values with increasing amount of δ_t^* ; rather they take a nearly constant slope. Comparing the experimental fracture resistance data with the prediction of the mixed mode micromechanics model (Fig. 10) we observe that they are qualitatively similar in form.

Composite cohesive laws obtained from the fracture resistance data are shown in Fig. 17 and Fig. 18. Only data until the transition to steady-state are plotted. Fig. 17 shows the cohesive normal stress, σ_n^c , as a function of δ_n and δ_t . We find that σ_n^c has a peak value $\hat{\sigma}_n^c \approx 8$ MPa near $(\delta_n, \delta_t) = (0, 0)$, but decreases rapidly with increasing values of δ_n and δ_t . In the region near pure Mode II ($\delta_n^* \approx 0 - 0.5$ mm), σ_n^c comes out being negative (i.e., compressive) around $\delta_t \approx 0.3 - 0.7$ mm; the minimum value is about -1.7 MPa. For $\delta_t \approx 1 - 2$ mm, σ_n^c increases to a near-constant value around 1-2 MPa.

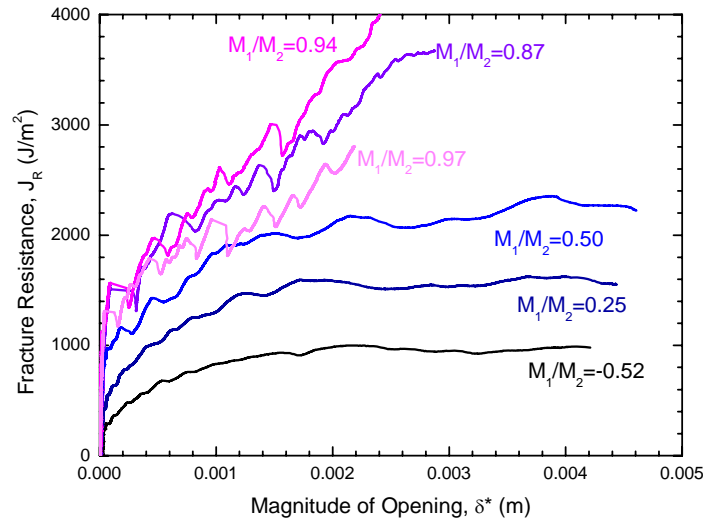


Fig. 15. Measured fracture resistance data for various M_1/M_2 ratios.

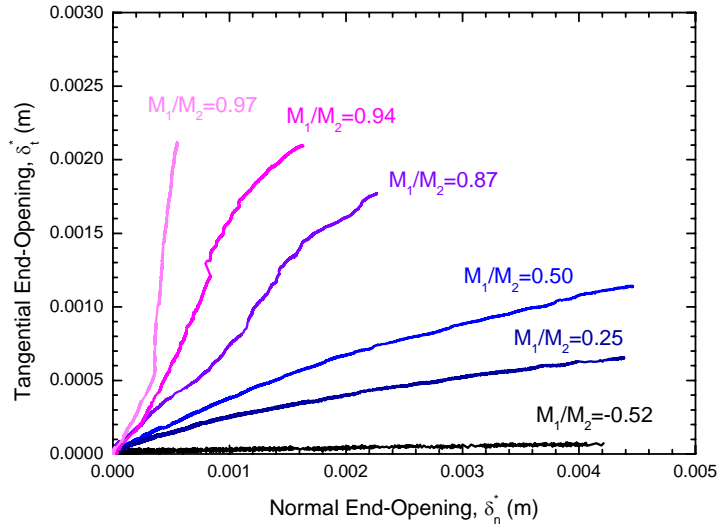


Fig. 16. Measured end-openings for various M_1/M_2 ratios.

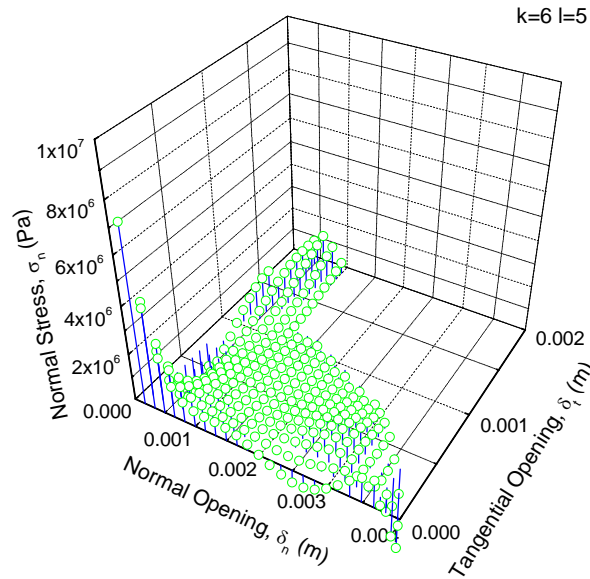


Fig. 17. Composite cohesive laws obtained from the mixed mode fracture mechanics data: The normal stress as a function of the normal and tangential crack opening displacements.

The cohesive shear stress, σ_t^c , is shown in Fig. 18. The peak value, $\hat{\sigma}_t^c$, around 15-22 MPa, is found to be located at $(\delta_n, \delta_t) = (0, 0)$. Away from the origin, σ_t^c decreases to a near constant value of 1-2 MPa. For $\delta_n \approx 0$, σ_t varies in a wavy fashion around zero, in particularly at $\delta_n \approx 4$ mm. This wavy behaviour is considered invalid, since σ_t is expected to vanish for $\delta_n = 0$.

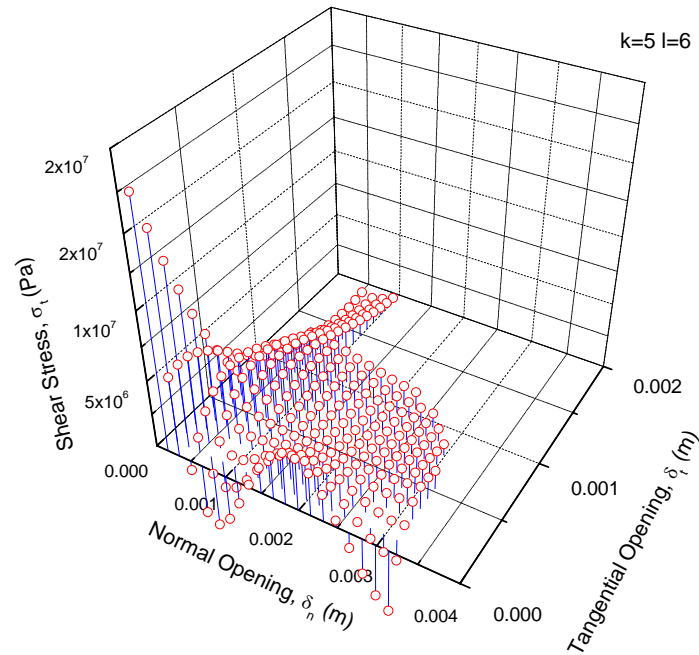


Fig. 18. Composite cohesive laws obtained from the mixed mode fracture mechanics data: The shear stress as a function of the normal and tangential crack opening displacements.

5. PREDICTION OF RESPONSE OF STRUCTURES FROM COMPOSITE COHESIVE LAWS

5.1 Outline for a case story: Medium scale adhesive joint specimens. We now proceed to use composite cohesive laws for the prediction of structural behavior of a large structure. The problem that we consider is crack growth along the interface of an adhesive joint joining two parts made of unidirectional polymer matrix composite consisting on nearly unidirectional glass fibres. The specimens are 2 meter in length; we will refer to them as "medium" size specimens, since they are significantly larger than standard laboratory specimens, but smaller than real structural parts like a wind turbine blade. The medium size specimen is loaded in four-point flexure, as shown schematically in Fig. 19. Three ratios of the thickness of the two parts (denoted h_1 and h_2 , respectively) were investigated. The cracking problem involves LSB due to cross-over bridging; this invalidates the use of LEFM. Instead, composite cohesive laws will be used in the strength prediction.

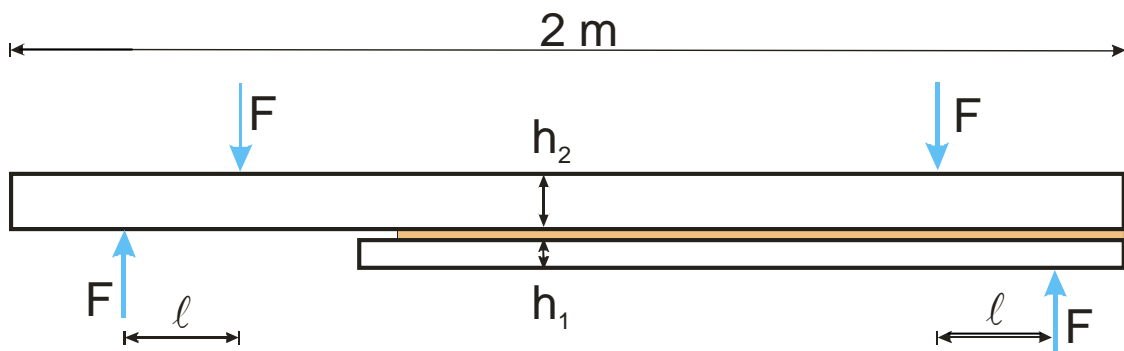


Fig. 19. Geometry and loading of medium scale specimens.

We continue as follows. First, fracture mechanics testing (using the DCB-UBM specimen shown in Fig. 14) was used for measurement of the fracture resistance of the adhesive joint under the full combination of loads, from $M_1/M_2 = -1$ to $M_1/M_2 = 1$. The steady-state fracture resistance was 2.0 kJ/m^2 for Mode I and 4.0 kJ/m^2 for Mode II. Furthermore, the normal and tangential crack opening displacement where the cohesive stresses vanish under pure Mode I and pure Mode II, denoted $\delta_{n,0}^c$ and $\delta_{t,0}^c$ respectively, were determined to be $\delta_{n,0}^c = 1.8 \text{ mm}$ and $\delta_{t,0}^c = 0.2 \text{ mm}$. Having established the fracture resistance data, parameters for composite cohesive laws were determined.

Independent linear softening composite cohesive laws were used for the normal and shear stresses

$$\sigma_n^c = \hat{\sigma}_n^c \left(1 - \frac{\delta_n}{\delta_{n,0}^c} \right) \quad \sigma_t^c = \hat{\sigma}_t^c \left(1 - \frac{\delta_t}{\delta_{t,0}^c} \right). \quad (12)$$

Noting from (7) that the area under the cohesive laws equals the steady-state fracture resistance, the following values were obtained for the peak stresses: $\hat{\sigma}_n^c = 2.2 \text{ MPa}$ and $\hat{\sigma}_t^c = 40 \text{ MPa}$.

Second, the problem was modeled with the aim of simulation the crack growth and thereby predicting the load-carrying capacity. The cracking was modeled by cohesive zone modeling using the commercial code Abaqus (version 6.6). The explicit version was used to solve the problem under quasi-static conditions (the kinetic energy of the model was a small fraction of the total energy). The increment in moment was prescribed by controlling the rotation of the beam in using a procedure developed by Jacobsen and Sørensen (2001). A quadratic traction-interaction failure criterion was used for damage initiation in the cohesive elements under mixed mode conditions

$$\left(\frac{\sigma_n^c}{\hat{\sigma}_n^c} \right)^2 + \left(\frac{\sigma_t^c}{\hat{\sigma}_t^c} \right)^2 = 1. \quad (13)$$

Third, 2 meter long medium size specimens were manufactured and tested under four-point flexure. The medium size specimens were tested under four-point flexure. Data for the applied moment and the crack length were recorded during the cracking of the specimens. More details about the experiments and modelling will be published elsewhere (Sørensen et al. 2007b).

5.2 Experimental and model results. Results, in the form of the applied moment at crack growth as a function of crack extension are shown in Fig. 20. Both experimental results and mode predictions are shown. It is seen that there is a good agreement with the overall trend of the experiments and predictions: the fracture resistance rises and attains a (steady-state) value. Both experiments and simulations show that the moment at steady-state cracking was highest for the specimens having the smallest h_1 .

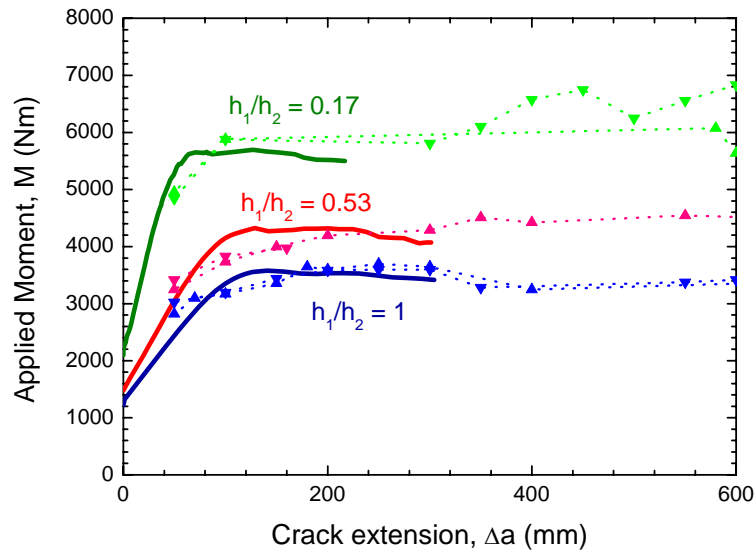


Fig. 20. Predicted and measured relationship between crack length and the applied moment. Dotted lines with symbols are experimental data; solid curves are mode predictions.

6. SUMMARY AND CONCLUSIONS

Experiments and modeling has been performed for the study of the connection between interface properties and overall macroscopic strength properties. Experimental methods for the determination of interface cohesive laws have been established. Models have been developed for predicting composite cohesive laws from interface cohesive laws. Strength prediction from composite cohesive laws was demonstrated.

ACKNOWLEDGEMENTS

This research was supported by the STVF Frame Work Programme "Interface Design of Composite Materials", Grant no. 26-03-0160.

REFERENCES

- Bao, G. and Suo, Z. (1992). Remarks on crack-bridging concepts", *Applied Mech. Rev.* 45, 355-61.
- Bao, G., Ho, S., Suo, Z., and Fan, B. (1992). The role of material orthopy in fracture specimens for composites", *Int. J. Solids Structures* 29, 1105-16.
- Berfield, T.A., Patel, J.K, Shimmin, R.G., Braun, P.V., Lambros, J. and Sottos, N.R. (2007). Micro- and nanoscale deformation measurement of surface and internal planes via digital image correlation. *Exp. Mech.* 47, 51-62.

- Brøndsted, P., Lilholt, H., and Lystrup, Aa. (2005). Composite materials for wind power turbine blades", *Annu. Rev. Mater. Res.* 35, 505-38.
- Jacobsen, T. K., and Sørensen, B. F. (2001). Mode I Intra-laminar crack growth in composites - modelling of R-curves from measured bridging laws. *Composites part A* 32, 1-11.
- Mohammad, I., and Liechti, K. M. (2000). Cohesive zone modelling of crack nucleation at bimaterial corner", *Journal of the Mechanics and Physics of Solids.* 48, 735-64.
- Launay, H., Hansen, C. M., and Almdal, K. (2007). Carbon, submitted.
- Needleman, A. (1987). A continuum model for void nucleation by inclusion debonding", *J. Appl. Mechn.* 54, 525-531.
- Rice, J. R. (1968). A path independent integral and the approximate analysis of strain concentrations by notches and cracks. *J. Appl. Mech.* 35, 379-86.
- Suo, Z., Bao, G., and Fan, B. (1992). Delamination R-curve phenomena due to damage. *J. Mech. Phys. Solids.* 40, 1-16.
- Spearing, S. M., and Evans, A. G. (1992). The role of fiber bridging in the delamination resistance of fiber-reinforced composites. *Acta Metall. Mater.* 40, 2191-9.
- Sørensen, B. F., Gamstedt, E. K., Østergaard, R. C., and Goutianos, S. (2007a). Micromechanical model of cross-over fibre bridging - prediction of mixed mode bridging laws. *Mechanics of Materials*, accepted.
- Sørensen, B. F., Goutianos, S., and Jacobsen, T. K. (2007b). Strength scaling mechanics of polymer composites. *Composites part A*, manuscript in progress.
- Sørensen, B. F. and Jacobsen, T. K. (1998). Large scale bridging in composites: R-curve and bridging laws. *Composites part A* 29, 1443-51.
- Sørensen, B. F., and Jacobsen, T. K. (2007). Characterizing delamination of fibre composites by mixed mode cohesive laws. *Journal of the Mechanics and Physics of Solids*, submitted.
- Sørensen, B. F., Jørgensen, K., Jacobsen, T. K., and Østergaard, R. C. (2006). DCB-specimen loaded with uneven bending moments. *International Journal of Fracture* 141, 159-172.
- Sørensen, B. F., and Kirkegaard, P. (2006). Determination of mixed mode cohesive laws. *Engineering Fracture Mechanics* 73, 2642-61.
- Tvergaard, V., and Hutchinson, J. W. (1992). The relation between crack growth resistance and fracture process parameters in elastic-plastic solids. *J. Mech. Phys. Solids* 40, 1377-97.
- Tvergaard, V., and Hutchinson, J. W. (1993). The influence of plasticity on mixed mode interface toughness. *Journal of the Mechanics and Physics of Solids* 41, 1119-35.
- Webb, T. E., and Aifantis, E. C. (1995). Oscillatory fracture in polymer materials. *Int. J. Solids Structures* 32, 2725-43.
- Yang, Q, and Cox, B. (2005). Cohesive models for damage evolution in laminated composites. *Int. J. Fract.* 133, 107-37.
- Yang, Q. D. and Thouless, M. D. (2001). Mixed-mode fracture analysis of plastically-deforming adhesive joints. *Int. J. Fracture.* 110, 175-87.
- Østergaard, R. C. and Sørensen B.F. (2007), Prediction of composite scale cohesive law for delamination with fiber bridging, to appear.

INTERFACES AND INTERFACIAL EFFECTS IN GLASS REINFORCED THERMOPLASTICS

J.L. Thomason

University of Strathclyde, Department of Mechanical Engineering,
75 Montrose Street, Glasgow G1 1XJ, Scotland, United Kingdom

ABSTRACT

Optimization of the fibre-matrix interphase region is critical to achieving the required performance level in thermoplastic matrix composites. Due to its initial location on the fibre surface, the sizing layer is an important component in the formation and properties of the composite interphase. Consequently, any attempt to understand the science of the composite interphase must encompass an understanding of the science of sizing. In this paper the role of sizings from fibre manufacture through to performance of composite parts is reviewed. In particular the role of organosilane coupling agents and how the formation of a polysiloxane interphase is influenced by the surface properties of the fibre is examined. The influence of the sizing film former in terms of its level of interaction with the silane coupling agent is also examined. The importance of residual stresses in thermoplastic composites in the values obtained for the apparent adhesion levels in these systems is highlighted. These residual stresses are shown to play a significant role in determining the level of interfacial strength in thermoplastic composites and in particular in polyolefin matrices. By applying some of the available models for this phenomenon this analysis is extended to explore the effect of the anisotropic fibre microstructure of carbon, aramid and natural fibres on the apparent interfacial strength in thermoplastic composites.

1. INTRODUCTION

There has been a rapid growth in the development and application of fibre-reinforced thermoplastic polymer composites in recent years. Parallel to this growth has been the increasing recognition of the need to better understand and measure the micro-mechanical parameters which control the structure-property relationships in such composites. The properties of thermoplastic composites result from a combination of the fibre and matrix properties and the ability to transfer stresses across the fibre-matrix interface. Variables such as the fibre content, aspect ratio, strength, orientation and the interfacial strength are of prime importance to the final balance of properties exhibited by injection moulded thermoplastic composites. Although the

field of composite materials is highly diverse in terms of the raw materials used as reinforcement, matrix and additives, it is well known that glass fibres represent more than 95% of the fibre reinforcement used today in the global composite materials market. In terms of the critical role of the interface region in these composite materials one must fully understand the role of fibre sizings. Sizing is a surface coating of mainly organic materials applied to nearly all types of man-made fibres during their manufacture. In the case of glass-fibres, sizing is probably the key component influencing the success or failure of most reinforcement products. This is due to the major role played by the sizing in the profitability, processibility, and performance of that product. Due to its physical location on the fibre surface, sizing is also a critical component in the formation and properties of the fibre-matrix interface region or the interphase (Thomason and Adzima 2001; Wu, Dwight and Huff 1997). Therefore, any attempt to understand the science of the composite interphase must encompass an understanding of the science of sizing. In this paper we will review the role of sizings from fibre manufacture through to performance of composite parts. In particular we will examine the role of organosilane coupling agents and how the formation of a silane interphase is influenced by the surface properties of the fibre. We will further examine the role of the sizing film former in terms of its level of interaction with the silane coupling agent.

The ability to transfer stress across the fibre-matrix interphase in thermoplastic composites is often reduced to a discussion of 'adhesion' which is a simple term to describe a combination of complex phenomena on which there is still significant debate as to what it means and how to measure it. Certainly, one of the generally accepted manifestations of 'adhesion' is in the mechanically measured value of interfacial shear strength (IFSS). However, many methods of determining IFSS exist and there is no overall consensus as to which method is 'best'. This situation is further complicated by the fact that sample preparation for many of these techniques is not optimised for use with thermoplastic matrices. Despite the elegance of the many techniques which have been developed for the quantification of composite micro-mechanical parameters, these techniques have found little enthusiastic support in the industrial product development environment. It is unfortunate that many of these techniques are indeed viewed as time consuming, complex, inefficient, labour intensive, and in many cases unproven or inapplicable in 'real' systems. Consequently their application in most industrial product development programmes is rare (Thomason 2002a). This leads to a classic situation where, because these methods have little support in an industrial environment, they rarely get the time and development to show their usefulness. This occurs despite the fact that the underlying science of even the most apparently mundane industrial development often necessitates solutions which require a deep understanding of structure-performance and micro-structural analysis. Most laboratories involved in the development of thermoplastic composites will routinely measure composite mechanical properties such as tensile strength, and determine residual fibre length. A series of papers by Bader and Bowyer (1972; 1973) in the early seventies presented a method for deriving values for the IFSS from a simple combination of the tensile stress-strain curve and the composite fibre length distribution. It is interesting to note that, despite the recent wealth of activity in the development of micro-mechanical test techniques (or perhaps because of it) there has been little follow-up to these papers. In this paper we present results on the IFSS in various thermoplastic composites obtained using an improved version of this method and compare those results with more traditional single fibre pullout data. We discuss these data in terms of the adhesion levels found in typical thermoplastic composites and illustrate the synergistic role of film formers and coupling agents in determining composite performance.

Finally we highlight the role of residual stresses in thermoplastic composites in the values obtained for the apparent IFSS in these systems. Our analysis indicates that residual stress may play a significant role in determining the level of IFSS in thermoplastic composites and in particular in polyolefin matrices. Although glass fibres are accepted as having a generally homogeneous structure many of the other fibres used for polymer composite applications are highly anisotropic in structure. By applying some of the available models for this phenomenon we extend our analysis to examine the role of fibre microstructure, such as found in carbon, aramid or natural fibres, on the apparent interfacial strength in thermoplastic composites.

2. RESULTS AND DISCUSSION

2.1 Introduction to Sizing. Continuous glass fibres were first manufactured in substantial quantities by Owens Corning in the 1930's. Today glass fibres account for 95% of fibre reinforcements used in the composites industry, primarily due to of their highly attractive performance/price ratio. The basic fibre forming process is shown in Figure 1. The molten glass flows to platinum/rhodium alloy bushings and then through individual bushing tips with orifices ranging from 0.75 to 2.0 mm. On exiting the bushing the glass is rapidly quenched and attenuated (to prevent crystallization) into fine fibres with diameters ranging from 3 to 24 μm . As a result of the high lineal speeds of the glass fibres (mechanical winders or choppers pull the fibres at velocities up to 60 m/s), the very high cooling rates and the immediate interaction of the fibres with a coolant water mist, unique compositions and structures are created in the top layer of the fibre surfaces (Thomason and Adzima 2001; Wu, Dwight and Huff 1997; Lowenstein 1993).

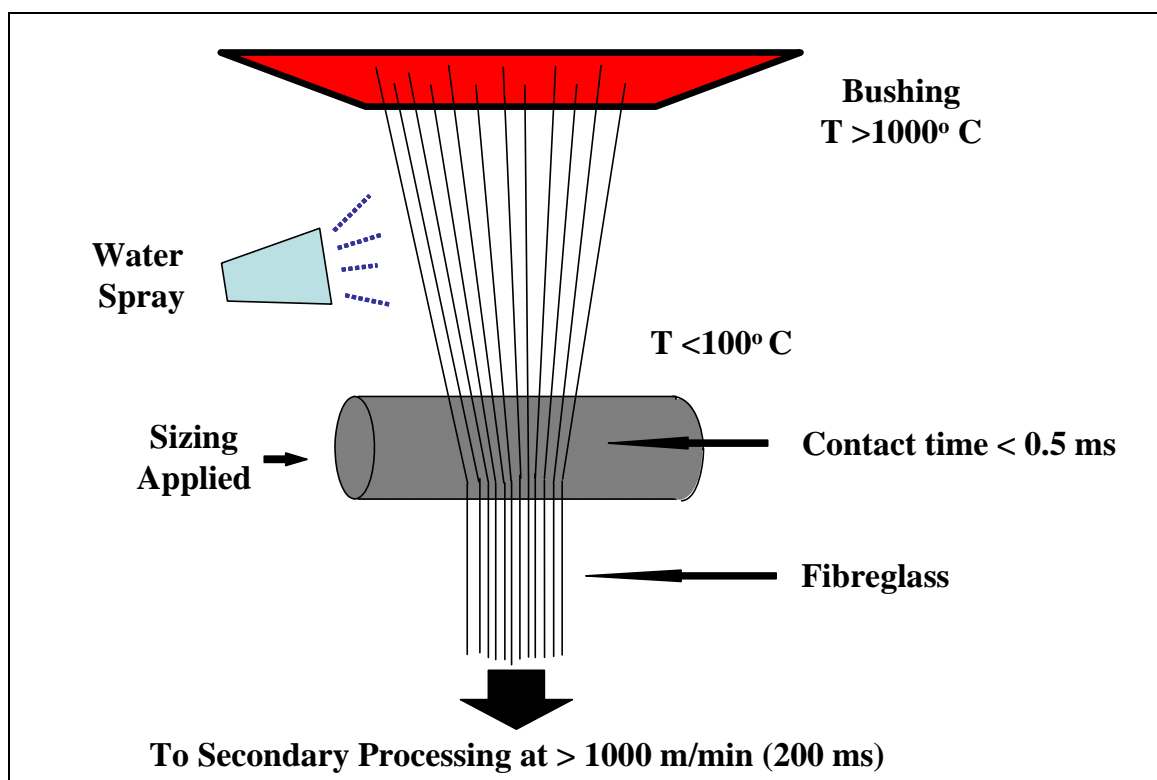


Fig. 1 Schematic of glass fibre forming and sizing operation

Within milliseconds of forming and cooling, this unique glass fibre surface is coated with a sizing - commonly by contacting an applicator roll carrying a layer of the aqueous mixture or emulsion. The sizing pickup occurs over a contact distance of less than 10 mm and therefore occurs in less than 0.5 ms. The fibres are then brought together in a strand and pass on to the secondary processing stage, which will be reached in approximately 0.2 s. In terms of processibility during chopping or winding, the sizing must therefore perform certain functions within a fraction of a second after it has been applied. After drying (2 minutes to 1 day, depending upon the type of product) the sizing must provide a new set of properties to optimize composite processing and performance. All this combines to make sizing formulation and application one of the major technological challenges of glass fibre production, and attaining the optimum composition and coverage one of the major challenges to the subsequent formation of the composite interphase.

Optimizing the sizing layer is a complex art involving a compromise of manufacturing, marketing, technical and economic factors. Such an optimised sizing requires the correct balance of (Thomason 1999; Thomason and Adzima 2001) profitability, processibility and performance. As with all balancing acts these three key properties are closely linked. The importance of sizing to the glass fibre composites industry cannot be understated since practical glass-fibre-reinforced composites cannot be made without it. Furthermore, sizing is one of the most important factors that differentiate one glass reinforcement product from another. To achieve this delicate balance, sizings have been developed which are aqueous chemical systems containing 0.05-10% "solids", the remainder is water. The composition of these "solids" generally consists of a number of multi-purpose components. There will be a film former which, when dried, holds the filaments together in a strand and protects the filaments from damage through fibre-fibre contact and fibre-process contacts. Film formers are chosen to be as closely compatible to the intended polymer matrix as possible and still fulfil all the other requirements of a sizing. Therefore the range of typical film former materials reflects the range of composite matrix materials. Commonly used film formers include polyurethanes for polyamide compatible products; maleic anhydride modified polyolefins (MAPP) for polypropylene reinforcement, and polyurethanes and/or modified epoxies for thermoplastic polyester applications (Lowenstein 1993, Thomason and Adzima 1999; Campbell 1999). Emulsion/dispersion technology allows many of these high molecular weight and water insoluble materials to be applied to glass fibre surfaces. Sizing will nearly always contain an organofunctional silane commonly referred to as a coupling agent. However, these multifunctional molecules perform many roles other than just the simple fibre-matrix link which is implied by this name. Indeed, the non-coupling aspects of silanes are one of the areas where a much more fundamental understanding is needed in order to develop improved sizings and composites. Sizings may also contain cationic or non-ionic lubricants to reduce fibre-fibre abrasion. There may also be a number of other additives, such as anti-static agents, emulsifiers and wetting agents. The amount of sizing on any particular glass reinforcement product is also a carefully controlled parameter which is usually expressed as the "loss on ignition" (LOI), which is the percentage weight loss obtained by burning off the sizing. Finally it is worth mentioning the importance of water in the glass manufacture process. Water is used in large volumes of relatively high purity in a number of roles. It is used to cool the fibres and it acts as a carrier for the sizing. Since small amounts of size are applied to a huge surface area, water is used as a diluent so that the correct amount of sizing is applied. Water wets glass easily and aids the distribution of the sizing on the glass surface. During the fibre forming process water also acts as a lubricant to some degree.

2.2 Silane in Thermoplastic Sizings. It is probably not an overstatement to say that organosilanes can be considered the most important class of chemicals used in the glass fibre, and consequently the composites, industry. Without these versatile molecules it is unlikely that

the glass fibre reinforcement of polymers would be anywhere near as successful as it has become. One of the best-known properties of these multifunctional silane molecules is their apparent ability to promote adhesion. They have been reported to give improvements in interfacial strength and hydrothermal resistance of the composite interface (Pluddemann 1982; Emadipour, Chiang and Koenig 1982). The silane coupling agents have the general structure $[R'-Si(OR)_3]$ where R is methyl or ethyl and R' contains a group which may interact with either or both the film-former and the composite resin. The nature of this interaction is intuitively accepted as being of a chemical nature when the matrix resin is thermosetting and consequently the R' group on the silane has the opportunity to react with the matrix components. It is not quite so clear that chemical reactions play a role when reinforcing high molecular weight thermoplastic polymer matrices. On the other side of the silane molecule, the hydrolysed silanol group may interact and react with the glass surface, primarily through condensation with surface hydroxyl groups.

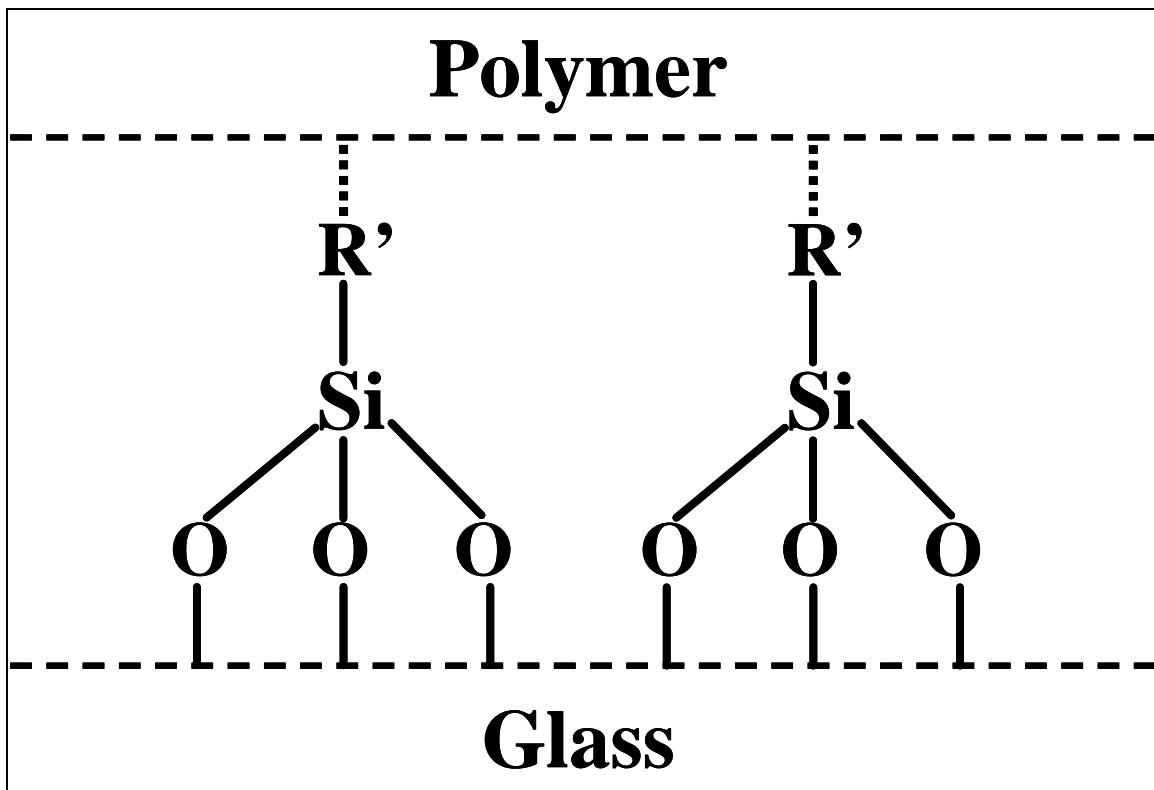


Fig. 2 Simple schematic of silanes at an interface

When the silane is used to treat the glass fibres in an aqueous sizing it is first hydrolysed to a (tri-)ol named silanol. This unstable silanol can be condensed onto the fibre glass by the elimination of a water molecule to produce a siloxane network. Si-OH groups on the glass surface may also participate in the process, with the result that the siloxane network becomes covalently bonded to the fibre glass surface. When glass fibre is then used in the polymer matrix it has to reinforce, the R' reactive groups of the silane may still be available to react with the reactive functions of the polymer which can lead to a strong network bridging the fibre-polymer interface. This situation is often depicted as shown in Figure 2 with three condensed silanol groups reacted with the glass surface and the R' group interacting with the polymer matrix.

Although there are very many different silane molecules available the glass fibre industry has

focused its sizing products mainly on the (Pluddemann 1982; Lowenstein 1993) four shown in Figure 3 where the R' group contains amino, epoxide, carbonyl and carbon - carbon double bonds. Once again the organic groups on these four silanes are typical of those which might be considered for co-reacting with the range of thermosetting resins used in the composites industry. However, it is the aminosilane versions which form the largest proportion of silanes employed. When we come to consider sizings for thermoplastic polymer reinforcement it is, once again, less clear that we are dealing primarily with chemical interactions. Furthermore, it is interesting to note that a review of the available literature and patents on sizings indicates that aminosilanes are used almost universally for thermoplastic compatible sizings. Consequently any progress in the interface region in thermoplastic composites will require an improved understanding of the role the ubiquitous aminosilane molecule.

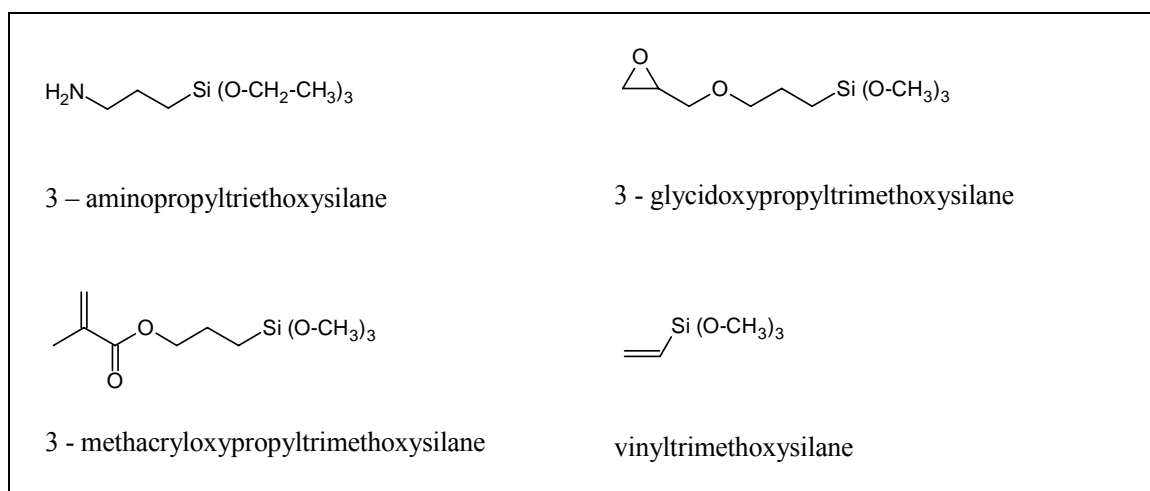


Fig. 3 Typical silanes used in glass fibre sizing

Examination of the simple cartoon in Figure 2 raises some other important points about the strength of the fibre-matrix interface. One could presume that the strength of this interface might be expected to be, in some way, proportional to the bond density across the interface. Consequently we might also expect that the interfacial strength may be proportional to the hydroxyl group density on the glass surface since this will play a role in determining the silane concentration in the first layer(s) of the interphase.

2.3 Quantification of hydroxyl group concentration on glass surface. Surface hydroxyl groups are the primary site on the surface of silica and glass for the adsorption and reaction of water and organic molecules. Zhuravlev (1993) has extensively reviewed work on the adsorption of water and the role of hydroxyl groups on the surface of silica. For a completely hydroxylated surface, the average number of silanol groups was found to be 4.9 OH/nm^2 , which includes the number of free, isolated silanol groups and the vicinal OH groups which are hydrogen bonded (Zhuravlev 1987; 1993). It has also been shown that the bonded hydroxyl groups can be removed from the silica surface by treatment in the temperature range from 200 to 400-500 °C. Thus, the concentration of silanol groups on a silica surface at 400 °C, 2.35 OH/nm^2 , corresponds to the concentration of isolated hydroxyl groups. The concentration of OH groups continues to drop with an increase in temperature from 400 to 1100 °C ($< 0.15 \text{ OH/nm}^2$) by silanol condensation to form siloxane bonds as the mobility of the network chains increases. In addition, Zhuravlev (1993) has also investigated the rehydroxylation of silica surface. It was found that the complete rehydroxylation of silica surface can be achieved easily for those samples of silica which were subjected to heat treatment at temperature below 400 °C. After the treatment at a higher temperature, only partial rehydroxylation takes place.

Since glass surfaces are also silica rich they have an analogously hydrated structure. Nishioka and Schramke (1983) compared the thermal desorption of water from E-glass fibres with powdered silica and observed more water per unit area adsorbed on E-glass fibres. However, the immediate surface was considered to be a multilayer of hydrogen bonded water molecules. They concluded that three molecular layers of adsorbed water were desorbed between 55°C to 200°C and silanol group condensation occurred at temperatures above 200°C. Sub-surface water desorbed at 300°C and at this temperature, silica skeletal bonds are reported to be hydrolysable, so that the surface composition of the fibres is highly variable. The quantity of water desorbed between 500°C and 800°C was suggested to result from the diffusion of bulk water from the inner structure. Pantano, Fry and Mueller (2003) employed solid state ¹⁹F nuclear magnetic resonance (NMR) to study (3,3,3-trifluoropropyl) dimethylchlorosilane (TFS) labelled silanol groups on glass fibre surfaces and determined the concentration of hydroxyl groups to be 0.50 to 1.44 OH/ nm² depending on the boron content of the glass. Carré, Lacarriere and Birch (2003) have estimated the density of silanol groups at the surface of microscope slide glass as 2.5 silanol groups per square nanometre. They showed how this value could be calculated from the contact angle of water under octane at the point of zero charge (pzc). The interaction between water and the non-charged glass surface at the pzc is non-dispersive and primarily generated by hydrogen bonding. Therefore, from the water contact angle at pzc, the non-dispersive hydrogen bonds energy of interactions expressed per unit of interface area and from the molar energy of hydrogen bonds, the number of hydrogen bonds per unit interface area could be obtained which also corresponds to the density of hydroxyl groups.

Liu, Thomason and Jones (2007) have used the same method to investigate the surface concentration of hydroxyl groups on the surface of an E-glass formulation used for glass fibre production. They studied the contact angle made by water droplets of different pH on the surface of polished E-glass slides under dry octane. Figure 4 show the results for E-glass slides in a fully hydrolysed state and after dehydroxylation for one hour at 600°C under dry nitrogen gas. In both cases a maximum in contact angle is clearly observed at a pH of 3. This value is in good agreement with other published values of the pzc of bare E-glass obtained by Electrokinetic Analysis (Mäder, Jacobasch, Grundke, and Gietzelt 1996; Wu et al. 1997). There is also a clear difference in the level of interaction between the water and the two surfaces as indicated by the large difference in the level of contact angle values with the dehydrolysed glass being much less hydrophilic. Table 1 summarizes these results and gives the values for hydroxyl group concentration. The value of 2.3 OH/ nm² is in good agreement with the value obtained by Carré et al. (2003) and, if we follow the model of silane condensation onto glass shown in Figure 2, translates into a silane surface density of 0.8 molecules/nm².

Table 1 Surface density of hydroxyl groups on E-glass

	Hydrolysed E-glass	Dehydrolysed E-glass
Max Contact Angle	39 ± 3	71 ± 2
pH of pzc	3	3
n _{OH} (nm ⁻²)	2.29 ± 0.04	1.71 ± 0.03

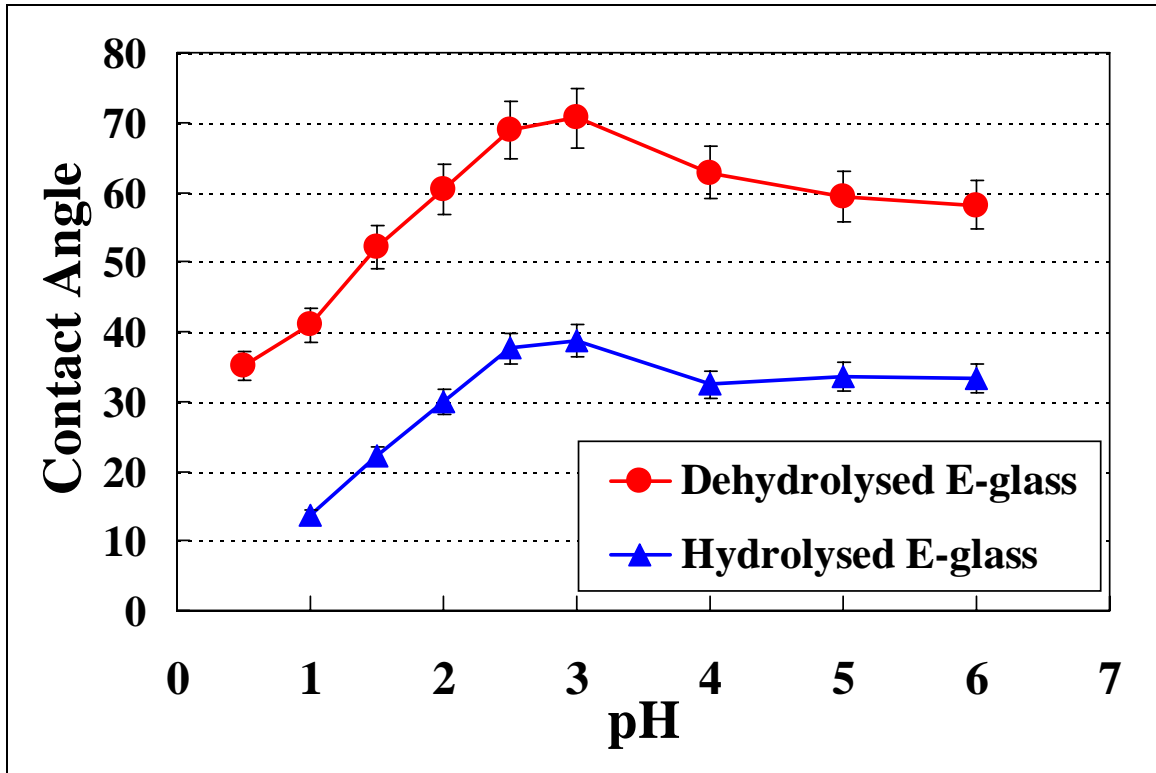


Fig. 4 Contact angle of water on glass under octane

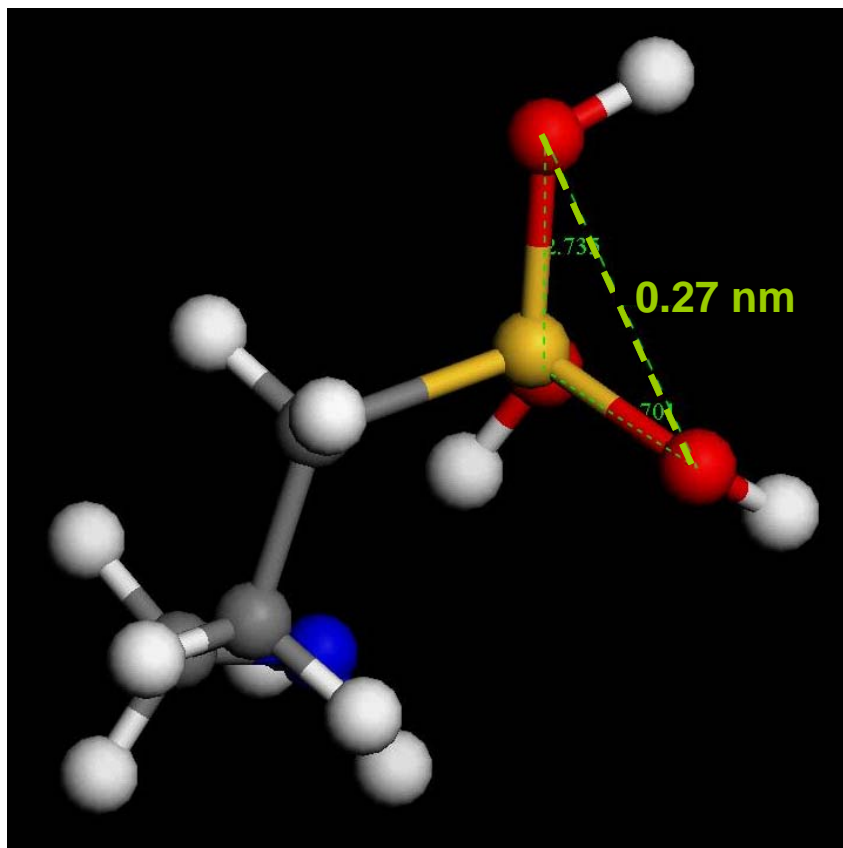


Fig. 5 Model of hydrolysed APS molecule

However, this value of hydroxyl group concentration actually has significant consequences for the veracity of the cartoon of silane-glass interaction shown in Figure 2. A value of 2.3 OH/nm^2 translates into an average hydroxyl group spacing of 0.7 nm for a uniform surface distribution. Figure 5 shows the result of a molecular dynamics simulation of one of the lowest energy states of a hydrolysed aminopropylsilane (APS) molecule. It can be seen that the average spacing of the oxygen atoms of the silanol groups is only 0.27 nm. This implies that it is extremely unlikely that any silane molecule will condense with more than one glass surface silanol. Moreover, it is also unlikely that silane molecules which have condensed with individual surface silanols will be close enough to react with each other. If we assume that each glass surface silanol reacts with an individual aminosilanes molecule then we obtain approximately 0.5 mg/m^2 of APS reacted with the glass surface. Combining typical sizing silane concentrations with typical LOI values for glass reinforcement indicates the presence of between $4\text{-}12 \text{ mg/m}^2$ of aminosilanes on the surface of dry thermoplastic compatible glass reinforcements. In contrast to Figure 2 this implies the presence of a more complex multi-layer interphase on the surface of these glass fibres and subsequently in their composites. If distributed uniformly on the fibre surface this would result in a polysiloxane interphase of up to 10nm on the surface of each fibre. Clearly the presence and properties of such an interphase could have significant influence on the performance of the macroscopic composite and requires further investigation.

2.4 Silane-Film Former Synergies. Following the example of many others in this area we have simplified the above discussion on the formation of a silane interphase by the lack of consideration of the other sizing components. However, in the real world the silane coupling agent forms approximately only 10% of the active material in a sizing formulation. Indeed the bulk of the sizing formulation is usually made up of the film former(s). It is interesting to observe that in the case of thermoplastic compatible sizings there is more intuitive expectation of reaction between any aminosilane coupling agent and the film former than with the polymer matrix of the composite. Consider the chemical nature of the typical film formers, blocked polyurethanes, epoxy resins, maleic anhydride modified polyolefins, which all offer the possibility of chemical reactions with amino groups. Consider also that the film former and the coupling agents are intimately mixed in the sizing and may be heated to temperatures in excess of 200°C during the drying process. It seems quite possible that, in many cases, the silane coupling agent may already be partially or completely reacted with film formers long before the sized glass fibres come in contact with the composite matrix polymers.

The potential synergies between APS coupling agent and thermoplastic film formers are further illustrated in Figures 6-8. Figure 6 shows some single fibre pullout results of Thomason and Schoolenberg (1994) on the influence of sizing on the IFSS of glass fibre with unmodified polypropylene homopolymer. Bare glass fibre gave an IFSS of 3.6 MPa which was increased to 4.5 MPa by the application of APS to the fibre. However when the fully sized fibres were investigated, values of 10.3 and 15.4 MPa were obtained for IFSS. In both these cases the sizing contained both APS coupling agent and a maleic anhydride modified polyolefin film former which may certainly react together. In a similar vein Figure 7 summarizes data from two papers by Thomason (2002b; 2007) on IFSS in glass reinforced polypropylene obtained by the improved Bader and Bowyer method. In this Figure we can see how the presence of MAPP in either the sizing or added to the PP homopolymer matrix affects the apparent IFSS in glass PP composites. Once again the system without any MAPP exhibits a very low IFSS in the region of 2 MPa. Addition of MAPP to either the sizing or the composite matrix raises the level of IFSS to approximately 8 MPa and when MAPP is present in both sizing and matrix an IFSS of 16 MPa

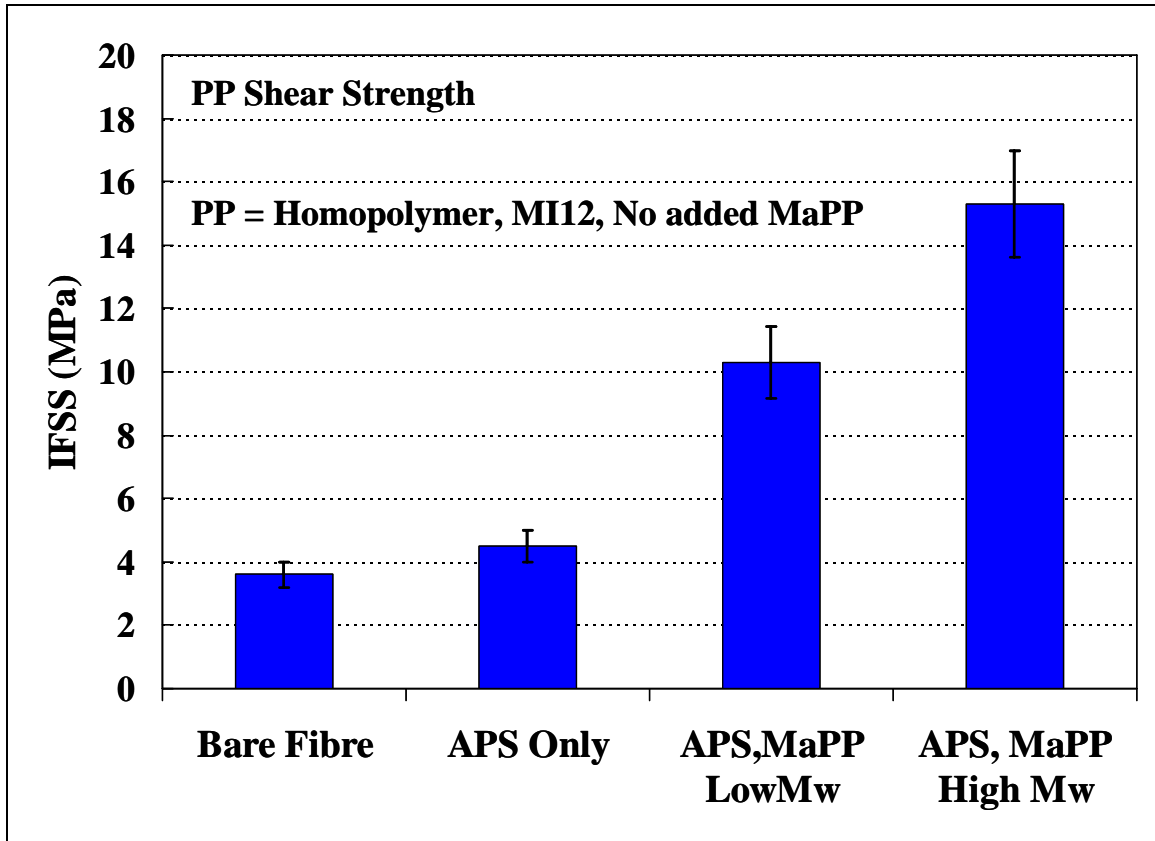


Fig. 6 IFSS in single glass fibre polypropylene samples

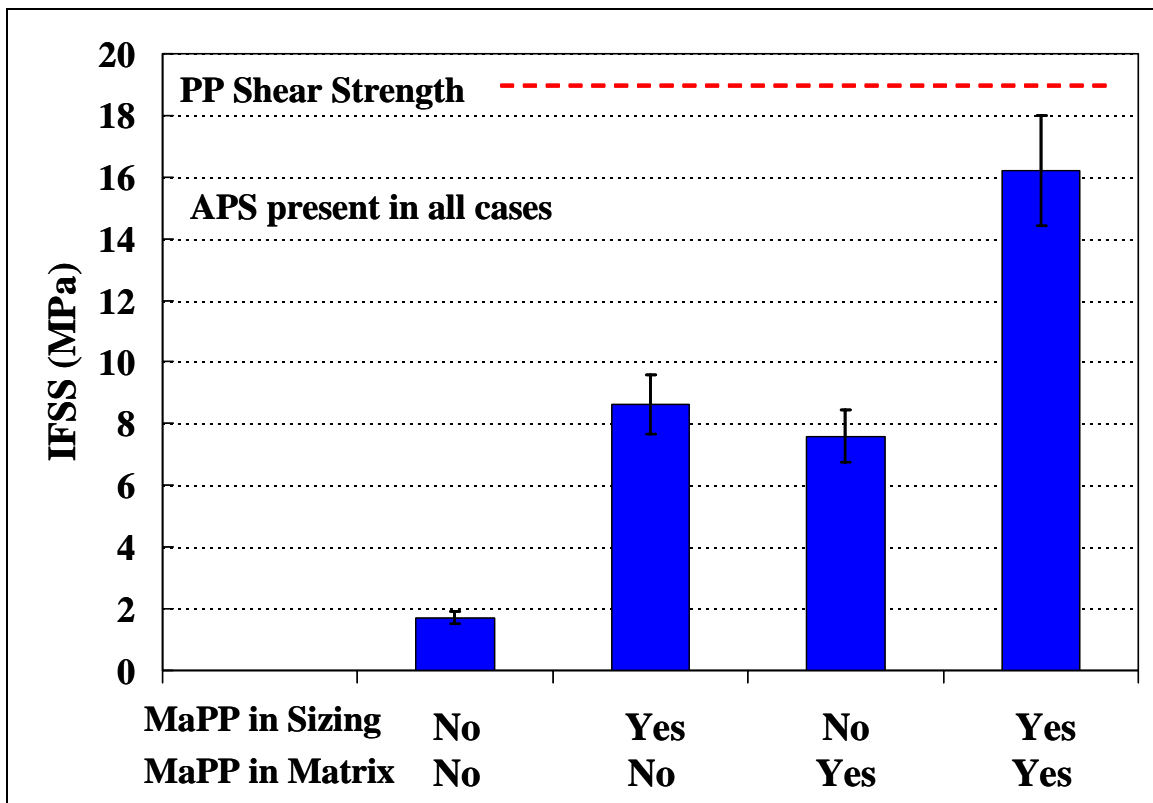


Fig. 7 IFSS in glass fibre polypropylene composites

is observed. It should be noted that this is close to the upper limit of measurable IFSS defined by the shear strength of polypropylene. Figure 8 shows data of Thomason and Adzima (2001) on the effects of sizing on the mechanical performance of injection moulded glass fibre reinforced Polyamide 6,6. They presented data on a simple sizing system containing only APS coupling agent and a PU emulsion. It can be seen that the performance of the combined sizing system is considerably better than when the glass fibres are only coated with either the silane or the film former alone. It seems quite likely from these results that there exists a significant synergy between the coupling agent and the film formers used in sizing for thermoplastic compatible glass fibres. As discussed above this is perhaps not so surprising given the chemical nature of these materials, their intimate proximity in the sizing systems, and the temperature history which glass fibre products experience. However, it does indicate once more that the simple model of fibre-matrix interface shown in Figure 2 is not particularly useful in understanding the performance of real thermoplastic composite systems. In this context it is interesting to note the comment of Thomason and Schoolenberg (1994) on their results of IFSS between PP and bare glass or silane only coated glass where no MAPP was present in the system. They observed that the levels of apparent IFSS observed in these cases could be explained by the residual stresses and resulting fibre-matrix friction in this system.

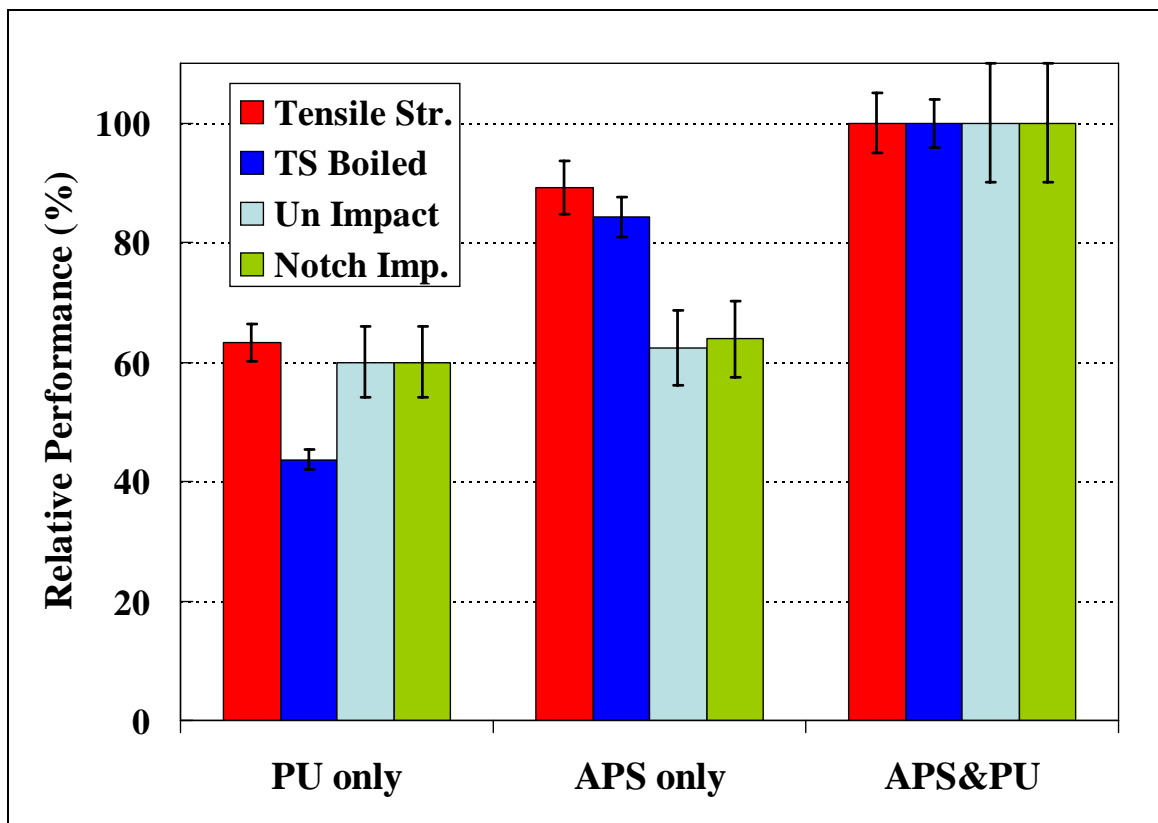


Fig. 8 APS-PU synergy in glass fibre polyamide composites

2.5 IFSS and Residual Stresses in Thermoplastic Composites. Thomason (2002a) has recently published data comparing the apparent IFSS in injection moulded glass fibre reinforced composites based on four different thermoplastic matrices. The polymer matrix materials studied were Polyamide 6,6 (PA66), Polybutyleneterephthalate (PBT), Polypropylene homopolymer (PPh) and Polypropylene containing 2% of maleated-PP coupling agent (PPm). These were compounded with 4 mm chopped strands containing 14 mm diameter E-glass fibres coated with the appropriate sizings for polymer matrix compatibility whose formulations followed the descriptions given in previous sections of this paper. The mechanical performance ranking of these composites (PA66 > PBT > PPm > PPh) was as expected and it was noted that the strength of the GF-PP mouldings were significantly increased by the addition of the MAPP polymer coupling agent. Figure 9 shows their results for the apparent IFSS in these systems based on Thomason's modified version of the Bader and Bowyer method of analysis of the composites tensile stress-strain performance. The values for IFSS are ranked in the order that one might expect from the fibre-matrix combinations and in all cases are realistically below the upper limit of apparent IFSS set by the shear strength of the polymer.

A number of authors have commented on the role of shrinkage stresses contributing to the stress transfer capability at the interface (Di Landro and Pegoraro 1996; Wagner and Nairn 1997; Nairn 1985; Piggott 1980). Most composite materials are shaped at elevated temperature and then cooled. Since in most cases the thermal expansion coefficients of thermoplastic polymers are much greater than reinforcement fibres this cooling process results in compressive radial stress σ_r at the interface. Assuming that the coefficient of friction (β) at the interface is non-zero these compressive stresses will contribute a frictional component $\tau_f = \beta \cdot \sigma_r$ to the apparent shear strength of the interface. In the case of thermoplastic polymer matrices where there may often be little or no chemical bonding across the interface these frictional stresses can make up a large fraction of the apparent IFSS. An exact calculation of the frictional fraction of the IFSS requires detailed knowledge of the interfacial friction and the temperature dependence of the stiffness and thermal expansion coefficient of the composite constituents which was beyond the scope of this study. However, they did estimate the magnitude of σ_r in their glass reinforced thermoplastics using a number of different models and fixed room temperature values of the required input parameters (Nairn 1985; Piggott 1980; Thomason and Vlug 1996). The relevant model input values are shown in Table 2. The results from all three models followed the same general trends, differing only in the absolute level of radial stress predicted. In Figure 9 we compare the results from Nairn's model for radial shrinkage stress with the measured IFSS values. It can be seen that results follow a similar trend. By an appropriate choice of coefficient of friction it is possible to obtain a good fit of any of the three models with the experimental data. Figure 9 also shows an example of the predictions of Nairn's model combined with $\beta = 0.67$ to give an estimate of the frictional component of the IFSS. It can be seen that there is excellent agreement with the experimental data. The excellent agreement in the observed trends does imply that shrinkage stress and interfacial friction may play an important role in the IFSS of these materials. Thomason (2001a; 2001b; 2002b; 2006; 2007) has expanded on this original work in a series of papers examining the apparent IFSS in various thermoplastic matrix composites varying the matrix type, the fibre content, the fibre length and the level of MAPP present in the GF-PP system. In all these cases the data for the apparent IFSS in these systems can be well fitted by the residual stress model of Nairn when an appropriate value for the static coefficient of friction is selected.

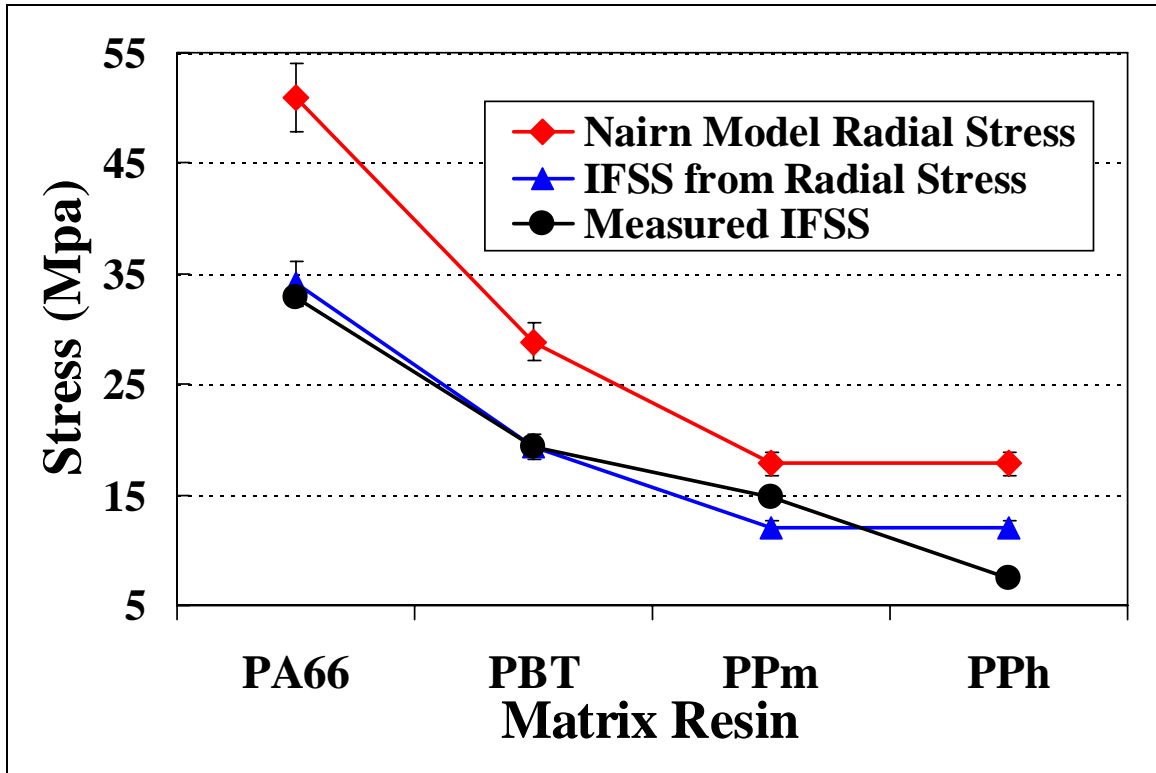


Fig. 9 IFSS in glass fibre thermoplastic composites

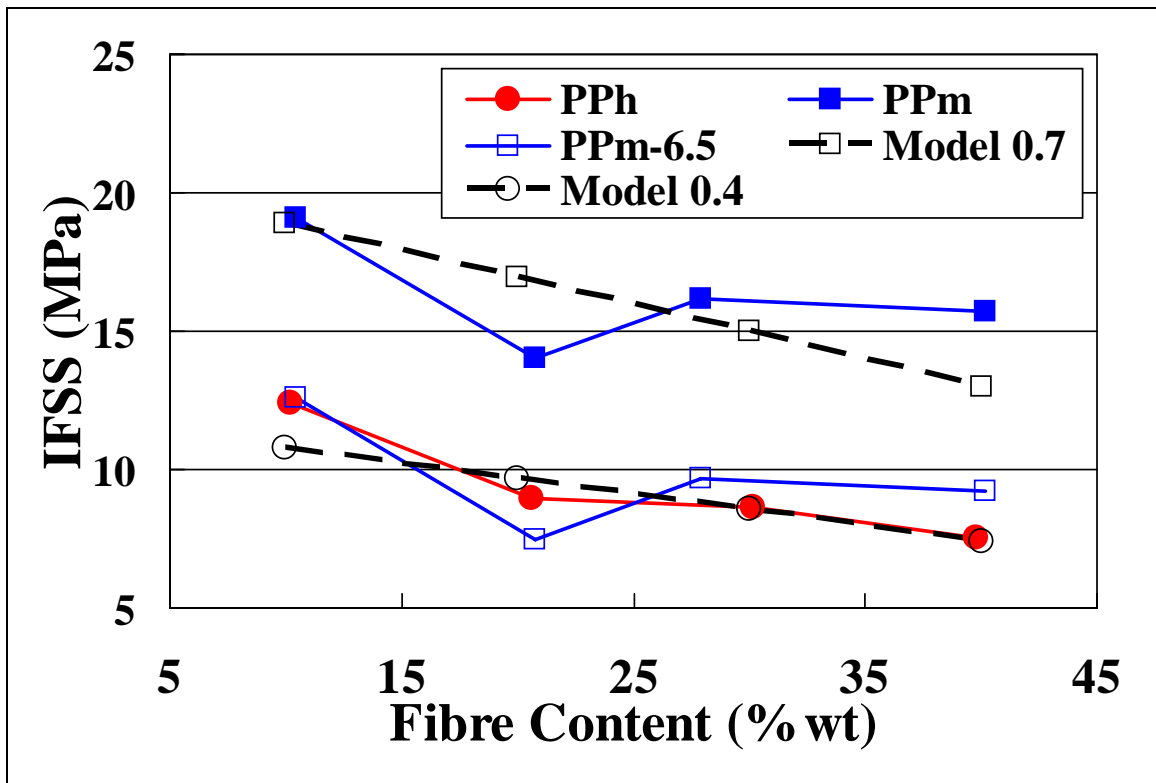


Fig. 10 MAPP effect on IFSS in glass fibre polypropylene composites

Figure 10 presents data from one of these papers showing the effect on apparent IFSS of adding MAPP to the matrix of GF-PP system at different glass fibre contents. The IFSS appears to be decreasing with increasing glass content and the trend appears to be approximately the same for both the PPh and the PPM series. The influence of the MAPP polymer coupling agent can be seen as giving an increase in the apparent IFSS of approximately 6.5 MPa. In this case the sizing system on the glass fibre also contained a maleic anhydride modified polyolefin (Campbell 1999). We have again estimated the magnitude and fibre content dependence of σ_r in glass reinforced PP using Nairns model and fixed room temperature values of the required input parameters. The results are shown in Figure 10 and it can clearly be seen that the values obtained for the apparent IFSS follow a similar trend to the model calculations of the radial compressive stresses at the interface due to fibre-matrix shrinkage mismatch. By an appropriate choice of coefficient of friction it is possible to obtain a good fit with the experimental data. Figure 10 shows an example of the predictions of the model combined with values of β of 0.4 and 0.7 to give an estimate of the frictional component of the interfacial shear stress. It can be seen that we get excellent agreement with the experimental data is obtained. At this point it is stressed that there should not be any strong relevance attached to the absolute value of β since the theoretical analysis requires a much greater level of detail (i.e. temperature dependence of many parameters) before it can be considered realistic. However the excellent agreement in terms of the observed trends does imply that shrinkage stress and interfacial friction may play an important role in the IFSS of these materials. Furthermore the reduction in IFSS with increasing fibre content is a factor which, in combination with the fibre length reduction, may explain the reduction of reinforcement effectiveness at high fibre loading (Thomason 2005; 2007).

The above results indicate that the apparent IFSS in glass reinforced PP can be matched by the calculated frictional contribution from the radial thermal stresses when an appropriate value (0.4-0.7) for the coefficient of static friction is selected. Although these might appear to be relatively large values, it should be noted that this refers to a coefficient of static friction which can be significantly higher than the more common dynamic value. Schoolenberg and Elmendorp (1995) have shown that the apparent IFSS in single fibre pullout testing of glass fibre and polypropylene can be explained fully by residual interfacial compressive stresses and a coefficient of static friction of 0.65. Although it is unlikely that the frictional contribution actually contributes 100% of the IFSS in all fibre-matrix combinations the fact that the trends can be explained by only residual frictional stresses is a strong indication that they do contribute significantly. In this context the result shown in Figure 10 merits further discussions. It is well known that the addition of the MAPP “coupling agents” can result in improved mechanical performance in glass fibre reinforced PP (Thomason 2007). This improvement in performance is often attributed to the possible formation of chemical bonds across the fibre-matrix interface between the polymeric coupling agent and the silane coupling agents in the fibre sizing which are assumed to be chemically reacted to the fibre surface. The increase of 6.5 MPa seen in Figure 10 could be taken as supporting evidence for this hypothesis. However, in this case the glass fibres used in these experiments were coated with a sizing which already contained maleated polymers which, as discussed above, had already had sufficient opportunity to react with the silane coupling agent in the sizing. This casts some doubt on the hypothesis that additional MAPP in the PP matrix would have the opportunity to form further covalent bonds across the interface region. One alternative explanation which could be pursued is that the wetting of the fibres by the PP matrix has been significantly improved at the molecular level and that this results in an increase in the coefficient of static friction and consequently the frictional component of the apparent IFSS. Clearly this is a hypothesis which merits further investigation.

2.6 Influence of fibre structure on interface strength. It would appear from the foregoing results and discussion that we can make a case for residual thermal stresses contributing a significant

amount to the apparent IFSS in thermoplastic composites. Moreover, the relative proportion of this contribution is higher in polyolefin basin composites where the levels of other fibre-matrix physical and chemical interaction are low. The magnitude of these residual stresses can be adequately estimated using models such as that of Nairn (1985). The main missing requirement in converting these residual stresses into IFSS is an accurate estimation of the coefficient of static friction for any particular system. A better understating of the role of wetting and interfacial interaction on this coefficient of friction is also required. It may be that many of the chemical modifications applied to thermoplastic composites which are assumed to improve adhesion through increased chemical bonding across the interface may actually be changing the level of matrix-fibre wetting and consequently the static coefficient of friction. Notwithstanding these points it is interesting to compare the relative levels of residual compressive stress in polypropylene composites where different reinforcements are used. Unlike glass, many of the other typical reinforcement fibres available are anisotropic in their mechanical and thermal properties and this may have significant influence on the residual stress state in any composite.

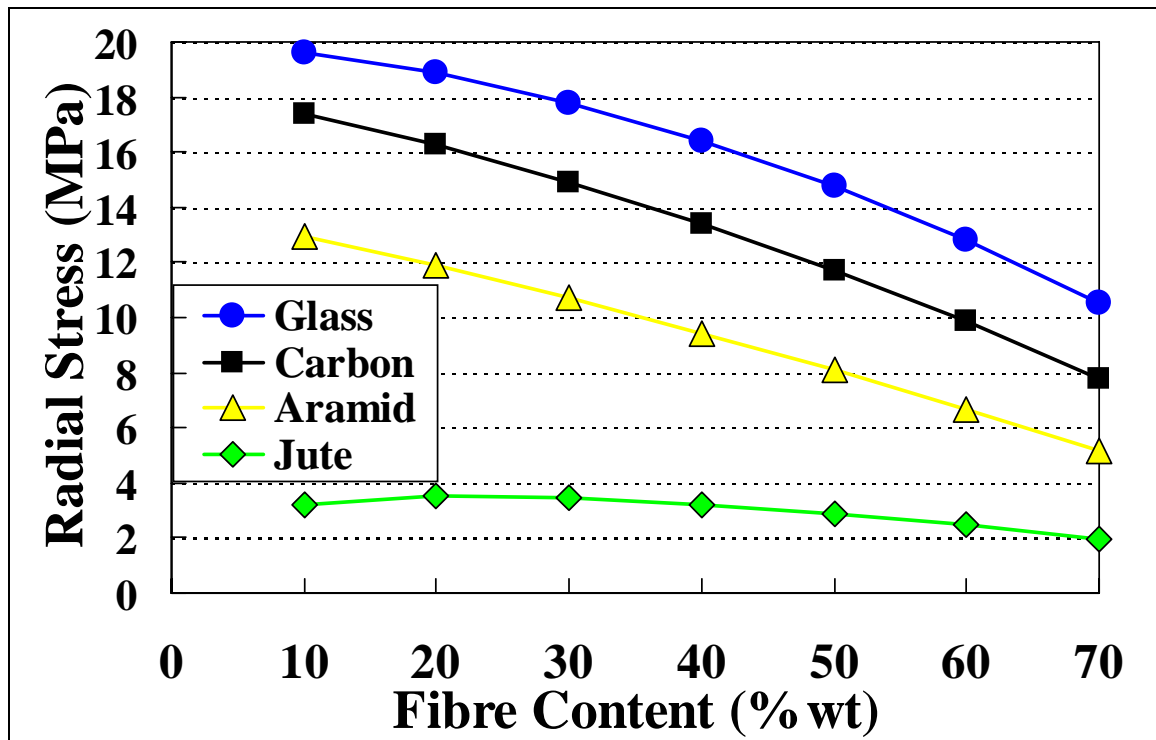


Fig. 11. Residual radial compressive stress at the interface in polypropylene composites.

To illustrate this point Figure 11 shows results of calculations of the residual radial compressive stress present at the fibre-matrix interface in polypropylene containing glass, carbon, aramid and natural (jute) reinforcing fibres. The relevant input parameters for the calculation are given in Table 2 (Nairn 1985; Wagner and Nairn 1997; Thomason 2002a; Cichocki and Thomason 2002). As indicated above it can be seen from Table 2 that carbon, aramid and jute are highly anisotropic in comparison with glass. These fibres all have small but negative LCTE's in the fibre direction and much larger positive LCTE's (approaching polymer matrix values) in the transverse direction. The effect of this anisotropy is clearly illustrated in Figure 11. All these systems exhibit compressive residual stress at the interface at room temperature and all show a mild dependence on the fibre content as previously discussed. However, the magnitude of these residual stresses is strongly dependent on the fibre properties. Glass fibres exhibit the highest

levels of residual stress with carbon fibres lower but at a similar level. Aramid fibres show significantly lower levels and the natural fibres have a very low level of residual radial compressive stress at all fibre contents. These results are well in line with the generally accepted view on interfacial adhesion in thermoplastic composites that glass and carbon are often well bonded, aramid fibres present some challenges to obtained good adhesion, and that there are serious problems with IFSS levels in natural fibre composites. Although the explanations and remedies for these issues are often sought in the chemistry of the system, these results suggest that, for improved reinforcement of polyolefins, we also need to better understand the role of fibre structure, the levels of residual stress, and the interfacial friction, on the apparent interfacial strength in thermoplastic composites.

Table 2. Input parameters for residual thermal stress calculations

	Glass	Carbon	Aramid	Jute	PP	PBT	PA66
Longitudinal Modulus (GPa)	72	220	130	39.4	1.5	2.8	1.5
Transverse Modulus (GPa)	72	14	10	5.5	1.5	2.8	1.5
Longitudinal Poisson Ratio	0.22	0.08	0.3	0.11	0.35	0.35	0.35
Transverse Poisson Ratio	0.22	0.01	0.1	0.01	0.35	0.35	0.35
Longitudinal LCTE ($\mu\text{m}/\text{m}\cdot^{\circ}\text{C}$)	5	-0.36	-3.6	-0.6	120	90	110
Transverse LCTE ($\mu\text{m}/\text{m}\cdot^{\circ}\text{C}$)	5	18	50	77.2	120	90	110
Temperature Range ($^{\circ}\text{C}$)					100	160	220

3. CONCLUSIONS

The optimization of the fibre-matrix interphase region is critical to the end-use performance of glass-fibre reinforced thermoplastic matrix composites. An essential requirement to improving that optimization process is acquiring a better understanding of the function of the various components of the fibre sizing in the formation of the interphase. In particular for thermoplastic composites an improved model for the role of aminosilanes in these systems is required. A combination of results from glass surface hydroxyl group concentration and molecular modelling of silane molecule dimensions indicates that the majority of silane molecules which react with the glass surface can only do so through formation of a single Si-O-Si bond. Furthermore, it appears that the majority of silane molecules in the first layer(s) of the interphase are not directly bonded with the glass surface. The likely interactions between the silane coupling agent and the typical film formers are shown to be important in the performance of the interphase and in determining composite performance. It is shown that for most glass fibre reinforced thermoplastics it is unlikely that the coupling agent interacts directly with the polymer matrix. More probable is the formation of a copolymerised aminosilane-film former interphase on the glass surface during the fibre manufacturing process with subsequent more complex interactions within the composite. It is clear that in many cases there is a need for an improved model of the interphase in the determination of the fibre-matrix adhesion performance in thermoplastic composites. It is suggested that an important component of this model should be a consideration of the role of residual radial compressive thermal stresses at the interface. In this context a much better understanding of the quantification of, and the factors that affect, the coefficient of static friction is needed in thermoplastic composites. The use of the thermal stress model also indicates the importance of fibre microstructure in determining the level of residual

stress contribution to the apparent interfacial strength and appears to be a possible explanation for the poor levels of adhesion exhibited by many natural fibre thermoplastic composites.

ACKNOWLEDGEMENTS

The authors wish to thank Dr X. Liu of the University of Sheffield for her assistance with the contact angle data and Dr N.T. Huff of Owens Corning for providing the molecular modelling Figure.

REFERENCES

- Bader, M.G., and Bowyer, W.H. (1973). An improved method of production of high strength fibre reinforced thermoplastics. *Composites* 4, 150-6
- Bowyer, W.H., and Bader, M.G. (1972). On the reinforcement of thermoplastics by perfectly aligned discontinuous fibres. *J. Mater. Sci.* 7, 1315-1321.
- Campbell, L.E. (1999). *Handbook of Polypropylene and Polypropylene Composites*. (Marcel Dekker, New York)
- Carré, A., Lacarriere, V., and Birch, W. (2003). Molecular interactions between DNA and an aminated glass substrate. *Journal of Colloid and Interface Science* 260, 49-55.
- Cichocki, F.R., and Thomason, J.L. (2002). Thermoelastic anisotropy of a natural fiber. *Compos.Sci.Technol.* 62, 669-678.
- Di Landro, L. and Pegoraro, M. (1996) Evaluation of residual stresses and adhesion in polymer composites. *Composites Part A* 27, 847-853.
- Emadipour, H., Chiang, P. and Koenig J.L. (1982). Interfacial strength studies of fibre-reinforced composites. *Res.Mech.* 5, 165-176.
- Loewenstein, K.L. (1993). *Glass science and technology 6, The manufacturing technology of continuous glass fibres*. (Elsevier, Amsterdam)
- Liu, X., Thomason, J.L., and Jones, F.R. (2007) The concentration of hydroxyl groups on glass surfaces and their effect on the structure of silane deposits. Manuscript in preparation
- Mäder, E., Jacobasch, H.J., Grundke, K. and Gietzelt, T. (1996) Influence of an optimized interphase on the properties of polypropylene/glass fibre composites, *Composites Part A* 27, 907-912.
- Nairn, J.A. (1985). Thermoelastic analysis of residual stresses in unidirectional, high-performance composites. *Polym. Compos.* 6, 123-30.
- Nishioka, G.M. and Schramke, J.A. (1983). Desorption of water from glass fibres, in *Molecular Characterisation of Composite Interfaces*. (Plenum, New York).
- Pantano, C.G., Fry, R.A., and Mueller, K.T. (2003). Effect of boron oxide on surface hydroxyl coverage of aluminoborosilicate glass fibres: a ¹⁹F solid state NMR study. *Phys. Chem. Glasses* 44, 64-68.
- Piggott, M.R. (1980). *Load-bearing fibre composites* (Pergamon Press, Oxford) p. 203-209.
- Pluddemann, E.P. (1982) *Silane Coupling Agents* (Plenum Press, New York)
- Schoolenberg, G.E. and Elmendorp, J.J. (1995). Some wetting and adhesion phenomena in polypropylene composites, Chapter 3.6 in *Polypropylene: Structure, blends and composites*. (Chapmann and Hall, London).
- Thomason, J.L. (1999). The influence of fibre properties of the performance of glass-fibre-reinforced polyamide 6,6. *Compos.Sci.Technol.* 59, 2315-28.
- Thomason, J.L., (2001a). Micromechanical Parameters from Macromechanical Measurements on Glass Reinforced Polyamide 6,6. *Compos.Sci.Technol.* 61, 2007-16.
- Thomason, J.L., (2001b). Micromechanical Parameters from Macromechanical Measurements on Glass Reinforced Polybutyleneterephthalate. *Composites Part A* 33, 331-39

- Thomason, J.L., (2002a). Interfacial Strength in Thermoplastic Composites – At Last an Industry Friendly Measurement Method ? *Composites Part A* 33, 1283-8.
- Thomason, J.L., (2002b). Micromechanical Parameters from Macromechanical Measurements on Glass Reinforced Polypropylene. *Compos.Sci.Technol.* 62, 1455-68.
- Thomason, J.L., (2005). The influence of fibre length and concentration on the properties of glass fibre reinforced polypropylene: 6) The properties of injection moulded long fibre PP at high fibre content. *Composites Part A* 36, 995-1003.
- Thomason, J.L. (2006) Structure-property relationships in glass reinforced polyamide: 1) The effects of fibre content. *Polymer Composites* 27, 552-562.
- Thomason, J.L., (2007). The influence of fibre length and concentration on the properties of glass fibre reinforced polypropylene: 7) Interface strength and fibre strain in injection moulded long fibre PP at high fibre content. *Composites Part A* 38, 210-216.
- Thomason, J.L. and Adzima, L.J. (2001). Sizing up the interface: an insider's guide to the science of science. *Composites Part A* 32, 313-321.
- Thomason, J.L., and Schoolenberg, G.E. (1994). An investigation of glass fibre/polypropylene interface strength and its effect on composite properties. *Composites* 25, 197-203
- Wagner, H.D., and Nairn, J.A. (1997) Residual thermal stresses in three concentric transversely isotropic cylinders: application to thermoplastic-matrix composites containing a transcrystalline interphase. *Compos.Sci.Tech.* 57, 1289-1302.
- Wu, H. F., Dwight, D. W. and Huff, N.T. (1997), Effects of silane coupling agents on the interphase and performance of glass-fiber-reinforced polymer composites, *Compos.Sci.Tech.* 57, 975 - 983.
- Zhuravlev, L.T. (1993). Surface characterization of amorphous silica : a review of work from the former USSR. *Colloids Surf. A Physicochem. Eng. Asp.* 74, 71-90.
- Zhuravlev, L.T. (1987). Concentration of Hydroxyl Groups on the Surface of Amorphous Silicas. *Langmuir* 3, 316-318.

MIXED-MODE COHESIVE-ZONE MODELS FOR DELAMINATION AND DEFLECTION IN COMPOSITES

M. D. Thouless* and J. P. Parmigiani**

* Department of Mechanical Engineering,
Department of Materials Science & Engineering,
University of Michigan, Ann Arbor, MI 48109, USA.

** Department of Mechanical Engineering
Oregon State University, Corvallis, OR 97331, USA.

ABSTRACT

Cohesive-zone models for interfaces incorporate both strength and energy parameters. Therefore, they provide a natural bridge between strength-based models and energy-based models for fracture, allowing delamination to be described by a single framework that covers a range of applications for which the strength or energy criteria alone might not be sufficient. In this paper, the relationships between cohesive-zone models and fracture models based on strength or energy are discussed. A mixed-mode formulation of cohesive-zone models has been used to investigate a number of issues related to the delamination of interfaces. It has been shown that linear-elastic fracture mechanics (LEFM) provides an excellent description of mixed-mode delamination, beyond the limits where LEFM would usually be thought to be appropriate. In particular, the concept of a nominal phase angle, calculated from stress-intensity factors is very robust. Compressive normal stresses on interfaces can be accommodated by the finite thickness of cohesive-zone models, resulting in increased levels of nominal toughness. The length scale naturally associated with cohesive zones allows them to describe mixed-mode fracture of interfaces with a modulus mismatch across them. Cohesive-zone models have also been used to explore the phenomenon of crack deflection at interfaces. The results of these calculations appear to be more consistent with strength-based models of deflection, rather than with energy-based models. They indicate that the strength ratio between the cohesive strengths of the interface and substrate play an important role in determining whether crack deflection or propagation occurs.

1. INTRODUCTION

Crack propagation along interfaces often controls the mechanical behaviour of composites (Fig. 1). The toughness of a fibre composite depends on delamination of the matrix-fibre interfaces, and frictional sliding along the interfaces. Failure of laminated composites can

occur by delamination of the plies. However, crack deflection along interfaces, and multiple delaminations between successive plies or bonded interfaces, can lead to enhanced tensile strengths and energy dissipation. Historically, two approaches have been used to analyze these aspects of composite mechanics: a strength-based approach to fracture (Inglis 1913), and an energy-based approach (Griffith 1920). While the energy-based approach of fracture mechanics is the most versatile of the two for linear-elastic systems, and is the dominant tool currently used for analysis, there are regimes for which the other approach may be more appropriate (particularly at small length scales). Furthermore, for many practical applications, such as when large-scale plasticity dominates the fracture process, neither approach is sufficient. The relatively recent development of numerical cohesive-zone analyses provides a much more general model of fracture and allows the limiting regimes, in which either energy or strength alone are the dominant failure criteria, to be bridged within a single framework.

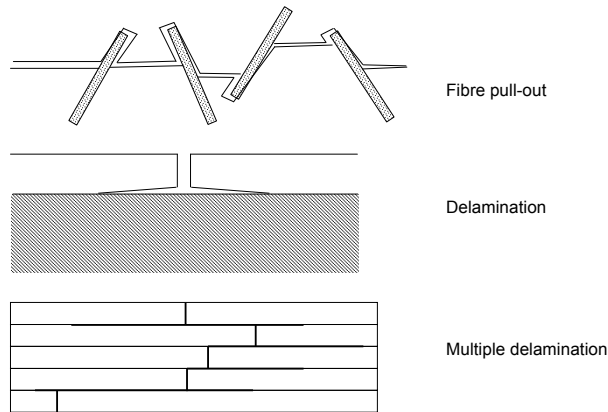


Fig. 1: Effects of interfacial failure and crack deflection in composites. Figure adapted from Parmigiani and Thouless (2006).

2. MODELS OF FRACTURE

2.1 Energy-based approach to fracture. The energy-based approach to fracture assumes that crack growth occurs when the energy-release rate \mathcal{G} reaches a critical value, Γ , the toughness. However, when delamination of an interface occurs, the crack is constrained by geometry to grow along a fixed path. Depending on the geometry and the nature of the applied loads, the crack may grow under mixed-mode conditions with both normal and shear components to the crack-tip deformation, and the toughness of an interface is a function of the relative amounts of normal and shear deformation. Experimental observations indicate that the toughness under pure mode-II conditions, Γ_{II} , is generally larger than the toughness under pure mode-I conditions, Γ_I . The relative proportions of shear to normal deformations contributing to crack growth is defined by interfacial fracture mechanics through use of a concept known as the phase angle. In a plane problem, and in the absence of a modulus mismatch across the interface, the nominal phase angle, ψ^∞ , is defined in terms of the nominal mode-II and mode-I stress intensity factors, K_I and K_{II} as calculated from the assumption

of sharp cracks and linear elasticity:

$$\psi^\infty = \tan^{-1}(K_{II}/K_I). \quad (1)$$

This can be re-expressed in terms of the mode-I and mode-II energy-release rate components, \mathcal{G}_I and \mathcal{G}_{II} as

$$\psi^\infty = \tan^{-1}(\sqrt{\mathcal{G}_{II}/\mathcal{G}_I}), \quad (2)$$

where the total energy-release rate is the sum of the two components:

$$\mathcal{G} = \mathcal{G}_I + \mathcal{G}_{II}. \quad (3)$$

A mixed-mode failure criterion is established by assuming that the toughness is a function of the nominal phase angle, so that it varies from Γ_I when $\psi^\infty = 0^\circ$ to Γ_{II} when $\psi^\infty = 90^\circ$. Many different functional dependences have been proposed in the literature; they are generally monotonic between the two limits and, beyond the observation that the effects of mode-II can often be neglected at phase angles below about 45° , experimental observations tend not to be sensitive enough to argue for one particular function over another. One functional dependence, that follows the general trend of experimental observations, results from an assumption that the values of the two components of the energy-release rate at fracture are given by the condition:

$$\frac{\mathcal{G}_I}{\Gamma_I} + \frac{\mathcal{G}_{II}}{\Gamma_{II}} = 1. \quad (4)$$

If these components are denoted by \mathcal{G}_I^* and \mathcal{G}_{II}^* , so that

$$\frac{\mathcal{G}_I^*}{\Gamma_I} + \frac{\mathcal{G}_{II}^*}{\Gamma_{II}} = 1, \quad (5)$$

then the mixed-mode toughness of the interface is given by

$$\Gamma = \mathcal{G}_I^* + \mathcal{G}_{II}^*, \quad (6)$$

at a phase angle of

$$\psi^\infty = \tan^{-1}\left(\sqrt{\mathcal{G}_{II}^*/\mathcal{G}_I^*}\right), \quad (7)$$

Combining Eqns. 5, 6 and 7, results in a mixed-mode failure criterion of

$$\Gamma = \Gamma_I \frac{\lambda(1 + \tan^2 \psi^\infty)}{\lambda + \tan^2 \psi^\infty}, \quad (8)$$

where $\lambda = \Gamma_{II}/\Gamma_I$. This relationship is plotted in Fig. 2. This functional form (or any other similar form) can be used in linear-elastic fracture mechanics (LEFM) analyses to

predict the strength of mixed-mode geometries. The concept of mixed-mode fracture can

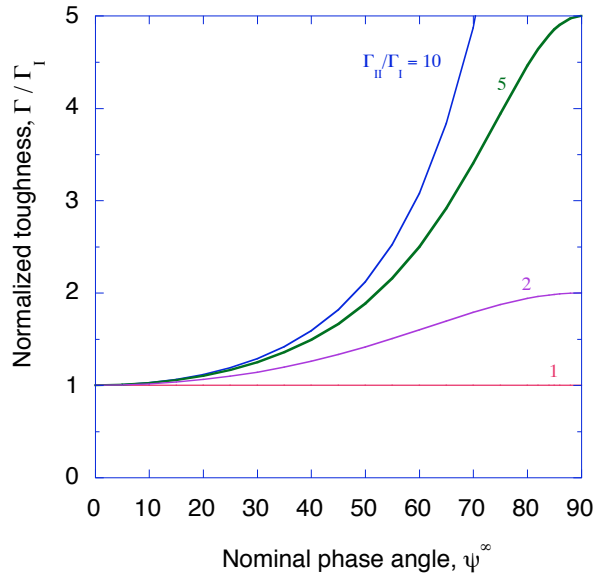


Fig. 2: Dependence of toughness on nominal phase angle following the mixed-mode failure criterion of Eqns. 4 and 8.

be slightly more involved when there is modulus mismatch across the interface. In a plane geometry containing an interface between two different isotropic materials with moduli E_1 and E_2 , and Poisson's ratios ν_1 and ν_2 , the mechanics depends on two non-dimensional groups of the elastic parameters. These two groups are given by (Dundurs 1969)

$$\alpha = \frac{\bar{E}_1 - \bar{E}_2}{\bar{E}_1 + \bar{E}_2}, \quad (9)$$

and

$$\beta = \frac{\bar{E}_1 f(\nu_2) - \bar{E}_2 f(\nu_1)}{\bar{E}_1 + \bar{E}_2}, \quad (10)$$

where $\bar{E} = E(1 - \nu^2)$ and $f(\nu) = (1 - 2\nu)/[2(1 - \nu)]$ in plane strain, and $\bar{E} = E$ and $f(\nu) = (1 - 2\nu)/2$ in plane stress. If $\beta = 0$, then the discussion of the previous paragraph about mixed-mode fracture still applies, since the shear and normal components of the crack-tip stress field are well-defined. However, if $\beta \neq 0$, the nominal phase angle has to be defined with respect to a characteristic length scale, such as the layer thickness, h_1 :

$$\psi^\infty = \tan^{-1} \left[\Re(Kh^{i\epsilon}) / \Im(Kh^{i\epsilon}) \right], \quad (11)$$

where K is the complex stress-intensity factor (Rice 1988), and

$$\epsilon = (1/2\pi) \ln [(1 - \beta)/(1 + \beta)]. \quad (12)$$

Now, the mixed-mode failure criterion depends on the choice of the characteristic length scale chosen to define the phase angle.

The condition for whether a crack impinging on an interface will continue into the underlying substrate, or whether it will deflect along the interface, is computed by comparing the energy-release rate and toughness for two separate problems (He and Hutchinson 1989): (i) for a small kink extending ahead of the crack across the interface, and (ii) for a small kink extending from the crack along the interface (Fig. 3). For a homogeneous composite that has the same modulus on both sides of the interface, crack deflection will occur if the toughness of the interface Γ is less than about 25% of the mode-I toughness of the substrate Γ_2 (He and Hutchinson, 1989; Thouless, Cao and Mataga 1989). However, since the interface is generally under mixed-mode conditions, the ratio of Γ_{II}/Γ_I for the interface also affects the conditions for crack deflection. In particular, the effect of Γ_{II} becomes increasingly important when the crack is trying to penetrate into a compliant material (He and Hutchinson, 1989; He, Evans and Hutchinson, 1994), and crack deflection tends to be suppressed if the interface has a high value of the mode-II toughness.

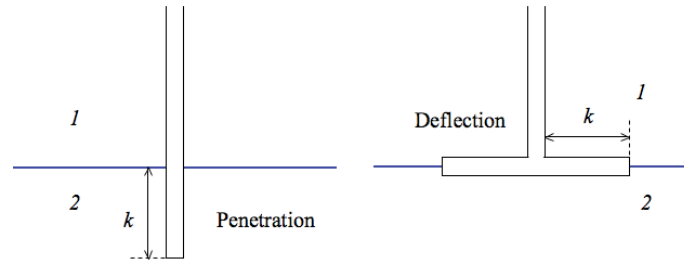


Fig. 3: Crack deflection and crack penetration across an interface are analyzed by considering two distinct geometries: (i) a kink extending across an interface, and (ii) a kink extending along an interface.

2.2 Strength-based approach to fracture. There are two types of strength-based analyses. One type involves elastic stress calculations, with an assumption that an interface fails when the stress reaches a critical value. For example, the normal stress distribution along the interface of a fiber or a laminate being subjected to an applied load (Fig. 4) can be calculated if the stresses are completely elastic along the interface (Muki and Sternberg, 1970). When the maximum stress on the interface reaches a critical value, corresponding to either the normal or shear cohesive strength of the interface, $\hat{\sigma}$ or $\hat{\tau}$, debonding is initiated (Hsueh 1990). While such an elastic calculation gives a value for the debond strength of a fiber or laminate, it is very sensitive to stress concentrations and elastic singularities.

An elastic stress analysis can also be used to compute the conditions for crack deflection at an interface in a composite. A classic example is the Cook-Gordon analysis (Cook and Gordon 1964) in which the normal stresses ahead of a matrix crack (modelled as an elliptical flaw) is compared to the normal stresses along an interface perpendicular to the crack (Fig. 5). By equating the ratio of the maximum values of the two stresses, it can be shown that the debond strength of the interface will be reached before the matrix crack grows if the cohesive strength of the interface is less than about 20% of the matrix strength. A similar result was also obtained by an elastic stress analysis for cracks approaching an interface with a modulus mismatch (Gupta, Argon and Suo 1992).

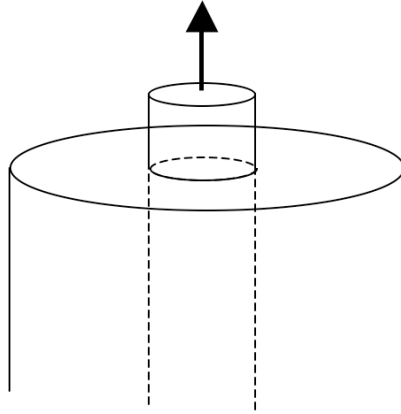


Fig. 4: Stress analysis for debonding of a fibre in a composite.

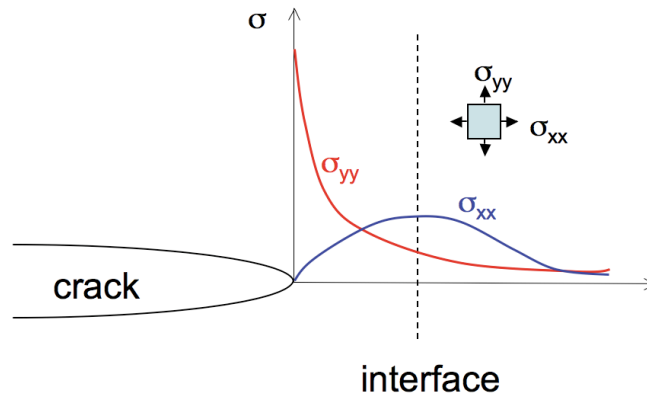


Fig. 5: The Cook-Gordon model for delamination at an interface in a composite.

An alternative type of stress analysis for debonding of an interface, that is less sensitive to the effects for stress concentrations, are shear-lag analyses. In these calculations, it is recognized that the maximum stress that can be supported by an interface is limited by the shear cohesive strength $\hat{\tau}$. But, it is assumed that when this stress level is reached, the interface maintains its stress-bearing capability, with relative slip occurring across the interface. A force equilibrium calculation then permits a calculation of the slip length over which the maximum shear strength is exhibited. For example, if a fibre of radius R is subjected to an applied load P (Fig. 6), then the slip length is $L_c = P/2\pi R\hat{\tau}$.

Embedded within this model is an implicit assumption that an infinite shear strain can be supported across the interface. As the applied load supported by the fibre is increased, it is assumed that the slip length can increase without limit until the fracture strength of the fibre is reached (or until the slip zone extends across the matrix and the fiber is pulled out of the matrix). If there is a limit to the relative displacement that could be accommodated across the interface while still maintaining the full strength of the interface, then the concept of an interfacial toughness would be introduced into such a model. The notion that the properties of an interface can be described by both a strength and a toughness leads naturally into the concept of a cohesive-zone model.

2.3 Cohesive-zone approach to fracture. The toughness of a material or interface is performance limiting for energy-based fracture criteria, but the strength is not. Conversely,

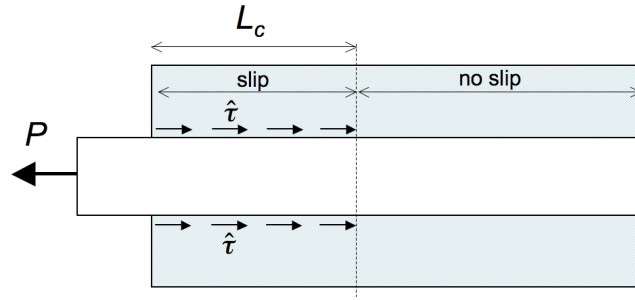


Fig. 6: Shear-lag analysis for a fibre embedded in a matrix.

strength, not toughness, is performance limiting for strength-based fracture criteria. By explicitly modelling the tractions across an interface, cohesive-zone models allow for a full description of fracture that incorporates both types of behaviour. These tractions may be associated with physical, chemical or mechanical bonding across a plane, or they can be associated with the deformation of an intermediate layer between two planes. There is a degree of arbitrariness as to the volume of material assigned to the cohesive-zone, which depends upon the scale at which the fracture process is being described. For example, various amounts of the plastic deformation that may be intimately coupled with crack growth can be incorporated into a cohesive zone. At the most fundamental level, the cohesive zone might incorporate only atom-to-atom bonding, with no plasticity. Less computationally intensive zones will generally include material in which plasticity might occur. The choice of how much plasticity to assign to the fracture process, and how much to assign to the bulk deformation of the material, will depend on what gives an adequate description of failure at the scale of interest within the set of parameters required to describe the problem. For adhesively-bonded joints or laminated composites, a natural size-scale for the cohesive-zone is the thickness of the adhesive layer (Yang, Thouless and Ward 1999; Yang and Thouless 2001) or the interlaminar region. In this case, the properties of the traction-separation law represent the entire deformation of the adhesive layer, and may depend on the details of the geometry. However, this is not an issue limited to cohesive-zone models; energy and strength-based approaches to adhesive fracture all incorporate the same assumption that the entire adhesive layer is associated with the fracture process, and have the same issues of geometry dependence.

In fibre-composite materials, cohesive-zone models can be used to represent the bridging tractions imposed by the pull-out of fibres; the size and properties of the cohesive-zone then have to capture fibre pull-out (Fig. 7). It is possible to use such a traction-separation law to explore the behavior of a tensile composite bar of width, W , with different sizes of initial crack, a_o , (Li, Thouless, Waas, Schröder and Zavattieri 2005b). A comparison between the predictions for the load-displacement curves and the actual experimental observations are shown in Fig. 8a. It will be observed from this plot that the energy dissipated by the specimen varies with initial crack size. This is related to the stability of the crack (Fig. 8b), and is a geometrical effect captured by the cohesive-zone model, rather than being associated with any change in the cohesive properties.

For complete fidelity in mimicking the fracture process, the traction-separation law of the cohesive should accurately represent the bonding across the interface or the deformation of the bonding layer. In linear-elastic systems this can be determined by a J -integral approach (Li, Maalej and Hashida 1994; Sørensen and Jacobson 2003). However, in general, much of the fracture behavior at a practical engineering scale of observation can be captured

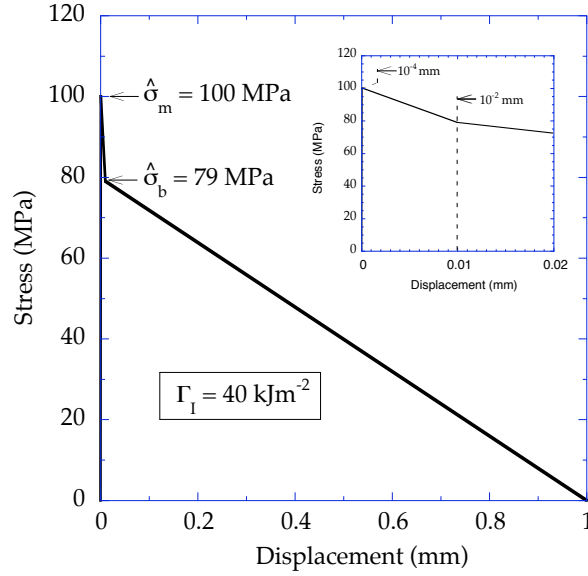


Fig. 7: Traction-separation law for a polymer-matrix composite, with a matrix cracking strength of $\hat{\sigma}_m = 100$ MPa, and a bridging strength of $\hat{\sigma}_b = 79$ MPa. The decreasing portion on the right of the traction-separation law corresponds to fibre pullout, after matrix cracking has occurred. Figure taken from Li, *et al.* (2005a).

by two parameters that describe the cohesive law: the area under the traction-separation curve (the toughness), and a characteristic strength (typically, the cohesive strength) or a characteristic displacement that represents the failure strain of the cohesive zone. Beyond these two parameters, the details of the cohesive law are often not significant for practical purposes.

Mixed-mode fracture can be accommodated within a cohesive-zone model if it is recognized that each mode of the energy-release rate can be defined as the area traversed under the appropriate traction-separation law, as shown in Fig. 9 (Yang and Thouless, 2001). The phase angle can be described at any point along the fracture plane, at all stages during the loading process, by comparing the appropriate ratio of the components of the energy-release rate:

$$\psi = \tan^{-1} \left[\frac{\mathcal{G}_{II}}{\mathcal{G}_I} \right]. \quad (13)$$

Of particular interest is the energy-release rate at the tip of the crack, just when the crack is about to advance. This is given by

$$\psi_o = \tan^{-1} \left[\frac{\mathcal{G}_{II}^*}{\mathcal{G}_I^*} \right], \quad (14)$$

where \mathcal{G}_{II}^* and \mathcal{G}_I^* are the values of the energy-release rate components at the crack tip that satisfy Eqn. 4. As discussed above (Eqn 6), the sum of these two components (or three components if a mode-III problem is being considered) is equal to the toughness at

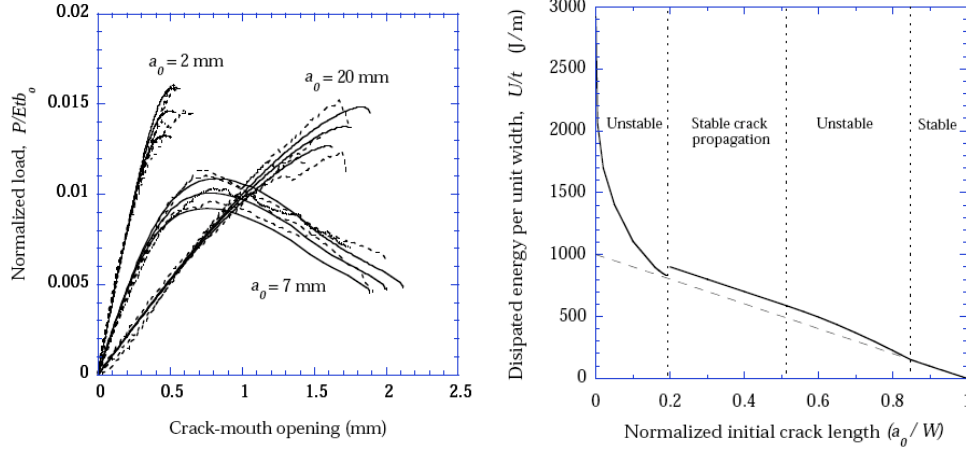


Fig. 8: (a) Comparison between load-displacement plot for a tensile specimen of width 25 mm, thickness 2.8 mm, and length 140 mm (gauge length of 25 mm), for different initial crack sizes. (b) Energy dissipation as a function of crack length, showing different regimes of stability predicted by the cohesive-zone model. Figures taken from Li, *et al.* (2005b).

the corresponding value of phase angle. In this formulation of mixed-mode fracture, no assumptions need to be made about the nature of the crack tip, and the definitions apply through any arbitrary range of cohesive laws. The same formulation would be applicable for different choices of mixed-mode failure criterion, or cohesive-laws.

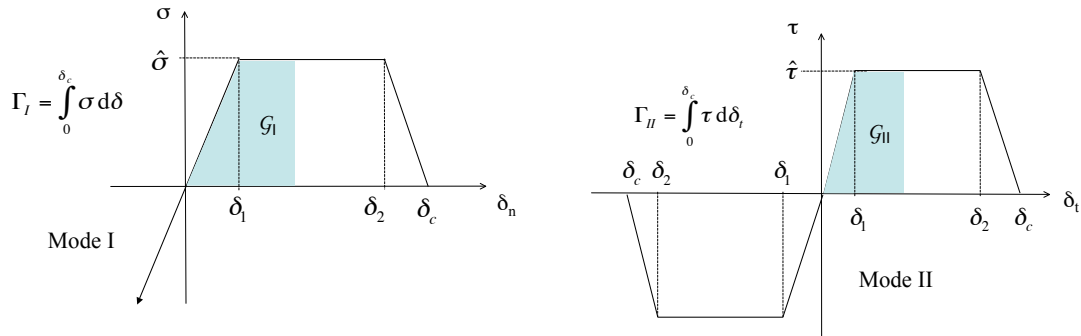


Fig. 9: Traction separation laws for mode-I and mode-II deformation, showing the definitions of the mode-I and mode-II components of the energy-release rate. Figures adapted from Yang and Thouless (2001).

A comparison between the predictions of the mixed-mode cohesive-zone model and the equivalent linear-elastic fracture-mechanics (LEFM) predictions were explored using a simple centrally-cracked bar of modulus \bar{E} with a normal and shear force, P and Q applied to the crack (Parmigiani and Thouless, 2007). Cohesive elements with a traction-separation law of the form shown in Fig. 9 were placed along the entire length of the interface. The elements were *not* embedded in any continuum elastic elements. The LEFM prediction for the failure load, P_{LEFM} , was computed using the form of the mixed-mode failure criterion given

by Eqn. 8. Figure 10a shows how the load for failure, P_f tends to P_{LEFM} at small values of the fracture-length scale (defined as $\bar{E}\Gamma_I/\hat{\sigma}^2$), when the toughness criterion dominates over the strength criterion. The corresponding normal stresses ahead of the crack is shown in Fig. 10b, where an approximation to the expected $1/\sqrt{r}$ stress field can be seen in the limits where LEFM conditions apply. For large values of the fracture-length scale, the stress is uniform across the uncracked ligaments, as would be expected when a strength-criterion for fracture is appropriate.

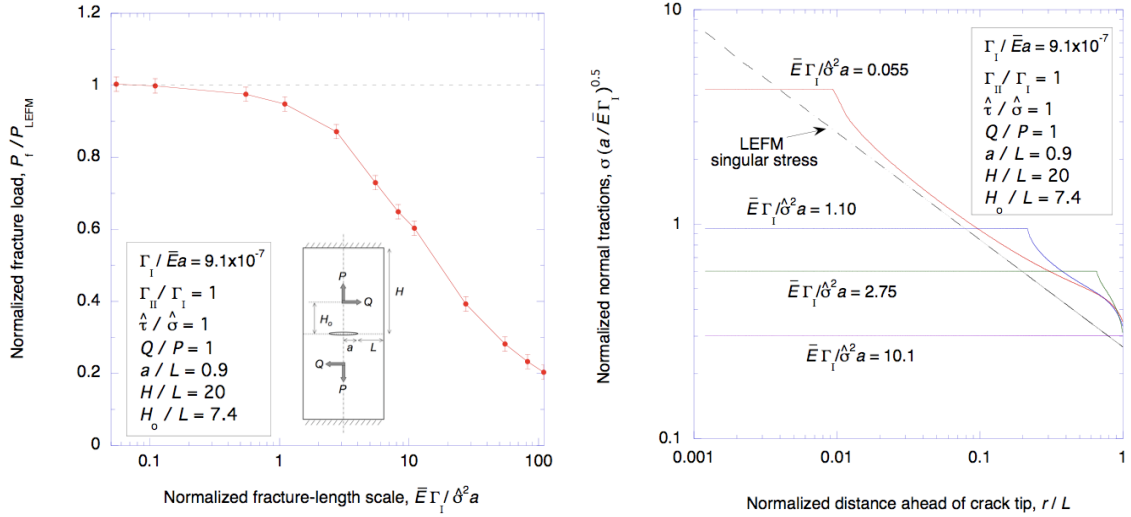


Fig. 10: **(a)** Failure load for a mixed-mode tensile test. **(b)** Normal stresses ahead of a crack in a mixed-mode tensile test. Figures taken from Parmigiani and Thouless (2007).

3. DELAMINATION OF INTERFACES

Any arbitrary loading on a laminated structure can be decomposed into four sets of load acting on an interface crack (Fig. 11): a set of axial forces, N ; a set of moments, M ; and two sets of shear forces, V_s and V_u . Results from linear-elastic fracture mechanics (LEFM) can be used to compute the combined energy-release rate and nominal phase angle from this complete set of four loads (Suo and Hutchinson, 1990; Li, Wang and Thouless 2004). When combined with a mixed-mode failure criterion such as Eqn. 8, the delamination strength can be computed. In principle, it would be expected that these LEFM results should be accurate in the limit when the stresses at the crack tip are controlled by a $1/\sqrt{r}$ stress field. In the recent work of Parmigiani and Thouless (2007), the LEFM predictions for the phase angle and delamination loads were compared to the results obtained using a cohesive-zone model, to explore the regimes in which the LEFM equations can be used to describe fracture.

3.1 Mixed-mode delamination. Figure 12a shows how the phase angle, as defined from a cohesive-zone calculation (Eqn. 13), varies with distance from the crack tip for a laminated geometry with equal moduli across the interface. As can be seen in that plot, the phase angle asymptotes to a constant value in the region near the crack tip. This constant value is equal to ψ^∞ , the value based on LEFM predictions. While it is the phase angle at the crack tip, ψ_o , that controls fracture, Fig. 12a shows there is nothing special about the crack tip. This would be consistent with a constant value of the phase angle expected in the

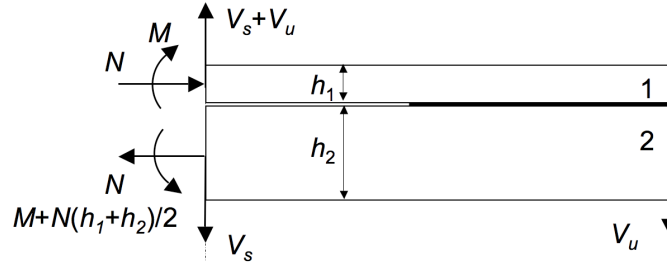


Fig. 11: Any arbitrary loading on a laminated structure can be decomposed into four sets of load acting on an interface crack: a set of axial forces, N ; a set of moments, M ; and two sets of shear forces, V_s and V_u .

immediate vicinity of a crack tip where the stresses are dominated by the singular stress field in an a linear-elastic geometry. However, a plot of the normal and shear stresses along the interface (Fig 12b) shows that there is nothing remotely resembling a $1/\sqrt{r}$ stress field for this particular set of cohesive properties. Furthermore, the phase angle matches ψ^∞ in the region where the stresses are limited by the cohesive strengths.* LEFM calculations provide accurate predictions of the phase angle and, hence, of the strength of elastic laminated geometries, even when the actual fracture-length scales of the interface are far in excess of what might have been expected to approximate LEFM conditions. An example of the range of fracture length scales over which LEFM calculations appear to provide reasonably accurate predictions for the strength are shown in Fig. 13a. In this context it should be noted that when the toughness does not depend on phase angle, the energy-release rate associated with the moment and axial components of the loading on the crack tip do not depend on the nature of the interface, only the shear component is affected (Li, *et al.* 2004). For this reason, the results for $\Gamma_{II}/\Gamma_I = 1$ tend to be particularly accurate even for very large fracture length scales. The accuracy of the phase angle for this particular mixed-mode geometry, which is more dominated by mode-II than the geometry shown in Fig 12, is illustrated in Fig 13b.

3.2 Effects of crack-tip compression. One issue into which a cohesive-zone model gives particular insight is fracture under conditions when the crack tip is subjected to a closing normal force. Experimentally, fracture is seen under these conditions (Thouless, Liniger and Hutchinson 1992; Thouless, Liniger and Jensen 1994), but the concept of a negative mode-I is generally rejected owing to the implication of crack-surface interpenetration. For LEFM analyses, it is assumed that crack-surface contact enforces conditions of pure mode-II on the crack tip, with the possibility of additional energy dissipation associated with friction (Stringfellow and Freund 1992). However, the effects of friction do not seem to be great enough to account for the rise in fracture resistance above the mode-II toughness that can be seen (Thouless *et al.* 1992).

A cohesive-zone approach to fracture introduces the concept that all fracture planes (especially, laminates and joints with a compliant adhesive layer) have a non-zero value of equilibrium thickness, and can accommodate some normal compression. This normal compression can store energy, beyond that associated with frictional effects, but will not contribute to failure, which is expected to occur when $\mathcal{G}_{II} = \Gamma_{II}$. If the interface is very thin, the contri-

*In this regard, it is noted that a definition of phase angle based on shear-to-normal stress ratios, as the phase angle is sometimes described in terms of, would fail in a cohesive-zone context, because it would just give the ratio of the two cohesive strengths.

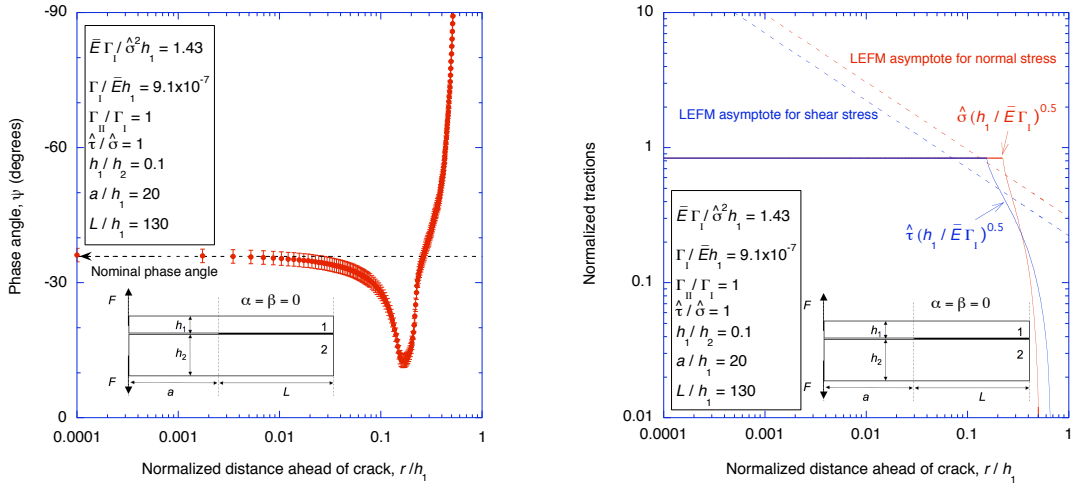


Fig. 12: (a) Variation of phase angle with distance from crack tip in a cohesive-zone model (b) Normal and shear stresses ahead of a crack. Figures adapted from Parmigiani and Thouless (2007).

tribution of the mode-I compression will be minimal. However, if the interface is thicker, the mode-I compression can be more significant. This is demonstrated in Fig. 14. The load to fracture a laminated geometry calculated from a cohesive-zone model was used to compute a nominal toughness using the equations of linear-elasticity. The nominal phase angle was changed by varying the ratio of the axial to transverse load, and the loading conditions were taken over a range for which LEFM would predict a compressive normal stress on the interface (corresponding to nominal phase angles with a magnitude greater than 90°). The resultant plots of nominal toughness against nominal phase angle (both calculated from the geometry and loads using LEFM calculations) are shown in Fig. 14 for three conditions: (i) a thin interface with a thickness given by $t = 0.00174h_1$, and no friction between the crack surfaces; (ii) the same interface, but with a coefficient of friction $\mu = 0.5$; (iii) an interface ten times as thick, but with no friction. When the cohesive layer is very thin, the toughness has a maximum value equal to Γ_{II} if there is no frictional dissipation. Friction increases the energy dissipated by fracture (and, hence, the nominal value of toughness). When the thickness of the cohesive zone is large enough, energy can be stored by mode-I compression, and the nominal toughness is enhanced, even in the absence of friction.

3.3 Effects of modulus mismatch. When there is a modulus mismatch across the interface, such that $\beta \neq 0$, the phase angle, as defined by linear-elasticity depends on the length scale chosen to describe it (Rice, 1988). In particular, if the nominal phase angle is described by the laminate thickness, h_1 , as indicated in Eqn. 11, then the phase angle can be shifted to a new reference scale, ξ , by

$$\psi = \psi^\infty + \epsilon \ln(\xi/h_1). \quad (15)$$

If $\Gamma_{II}/\Gamma_I = 1$, then the possible complications of a modulus mismatch are limited to frictional dissipation if the surfaces of the crack are forced into contact by the oscillatory displacement field. However, the general problem of mixed-mode fracture is complicated by a lack of knowledge about the appropriate length scale with which to define the phase

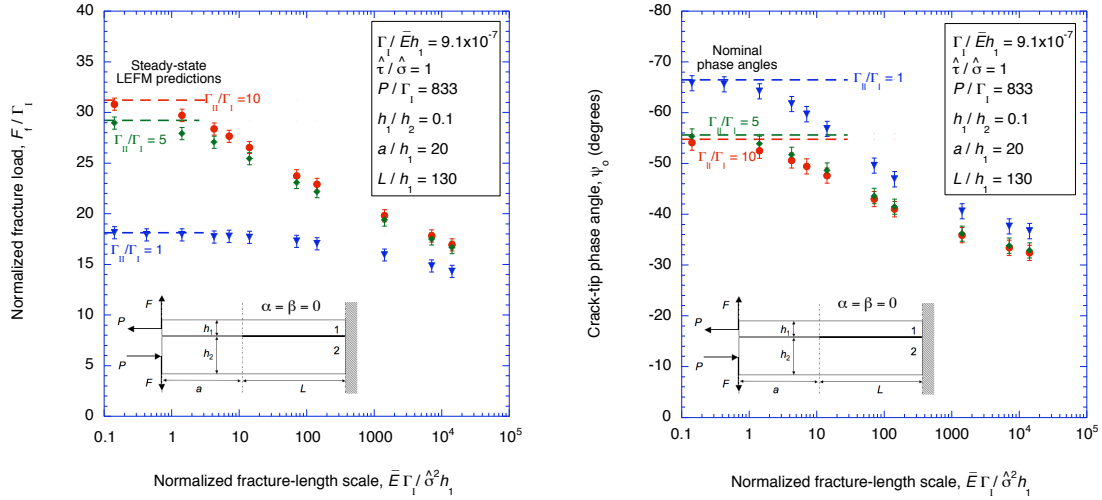


Fig. 13: (a) Variation of the strengths of a laminated geometry with the fracture length scale, and a comparison with the LEFM predictions for the strength. (b) Associated crack-tip phase angles. Figures adapted from Parmigiani and Thouless (2007).

angle. A cohesive-zone model incorporates a length scale naturally (Parmigiani and Thouless, 2007). As can be seen from Fig. 15a, the phase angle for a laminated geometry with a non-zero value of β plateaus at the crack tip, in the same way that the phase angle plateaus when $\beta = 0$. This crack tip value of ψ_o is the phase angle that controls fracture. It will be noted from Fig. 15a that the cohesive-zone parameters chosen for the plot are such that the fracture-length scale is sufficiently small for there to be a small region in which the phase angle has a logarithmic dependence on distance from the crack tip, as predicted by LEFM (Rice, 1988). Furthermore, a series of calculations using the same cohesive zone, but with different elastic mismatches indicates that the appropriate length scale to describe the phase angle in this particular case is $0.0018h_1$ (Fig. 15b). No obvious link has been found between this length scale and any features of the cohesive zone.

4. CRACK DEFLECTION INTO AN INTERFACE

As described in Section 2.1, an LEFM calculation of whether a crack will kink into an interface of a laminate (Fig. 16a) is done by comparing the energy-release rates for a small kink of length k extending across the interface with the energy-release rate for the separate problem of a small kink, also of length k , deflecting into the interface. If the modulus is the same on both sides of the interface, and $h_1 \ll h_2$, the condition for crack deflection is (He *et al.* 1994)

$$\Gamma_2/\Gamma \geq 3.83 + 5.77(k/h_1)^{1/2} + 2.18(k/h_1). \quad (16)$$

where Γ_2 is the mode-I toughness of the material beneath the interface, and Γ is the appropriate mode-dependent toughness of the interface (which depends on Γ_I and Γ_{II}). Cohesive-zone calculations for crack deflection introduce three additional parameters: the mode-I and mode-II cohesive strengths for the interface, $\hat{\sigma}$ and $\hat{\tau}$, and the mode-I cohesive strength for the substrate $\hat{\sigma}_2$. Cohesive-zone calculations for the two separate problems of deflection

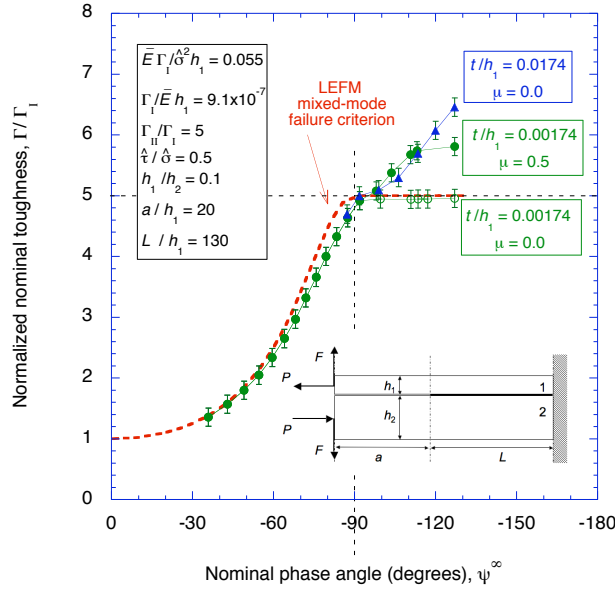


Fig. 14: Normalized nominal toughness as a function of nominal phase angle for a laminated geometry with different thicknesses of cohesive layer, and different coefficients of friction ($\mu = 0$ and $\mu = 0.5$). Modified figure from Parmigiani and Thouless (2007).

and propagation, with kink sizes much smaller than the relevant fracture-length scales of $\bar{E}\Gamma_I/\hat{\sigma}^2$ and $\bar{E}\Gamma_2/\hat{\sigma}_2^2$, result in excellent agreement with the expression given in Eqn. 16 (Parmigiani and Thouless, 2006).

However, significantly different results are obtained when cohesive elements are placed along the interface and through the substrate simultaneously (Fig. 16b). Under these conditions, the cohesive-zone calculations permit the crack to choose whether to propagate across the interface or to deflect along it, rather than being set *a priori*. The conditions for deflection or penetration in a homogeneous system with $\Gamma_{II}/\Gamma_I = 1$ are shown in Fig. 17a. This figure shows that crack deflection is promoted by high values of both $\hat{\sigma}_2/\hat{\sigma}$ and Γ_2/Γ_I . Conversely, crack penetration is promoted by low values of these two ratios. There appears to be a critical value of the strength ratio ($\hat{\sigma}_2/\hat{\sigma}$) below which crack penetration is guaranteed, irrespective of the toughness ratio. This limit was explored using fracture-length scales well into the regime where LEFM is expected to be valid, and was determined to be about 3.2 for elastically homogeneous laminates. This value is very consistent with the results of analyses based on strength criteria (Cook and Gordon 1964; Gupta, *et al.* 1992). In contrast to LEFM analyses, there does not appear to be a critical toughness ratio that ensures crack penetration.

Similar results were obtained from calculations with a modulus mismatch. While, in general, both the toughness and strength ratios determine whether crack deflection or penetration takes place, there appear to be lower bounds for $\hat{\sigma}_2/\hat{\sigma}$ below which crack penetration will always occur (Fig. 17b). Mode-II effects for the interfacial cohesive zone become particularly important when the crack resides in the stiffer material ($\bar{E}_1 > \bar{E}_2$). A relatively large value of mode-II interfacial toughness impedes delamination under these conditions, thus increasing the tendency for the crack to propagate through to the substrate. Conversely, when the substrate is stiff ($\bar{E}_1 < \bar{E}_2$), mixed-mode effects are less important, and the possibility of

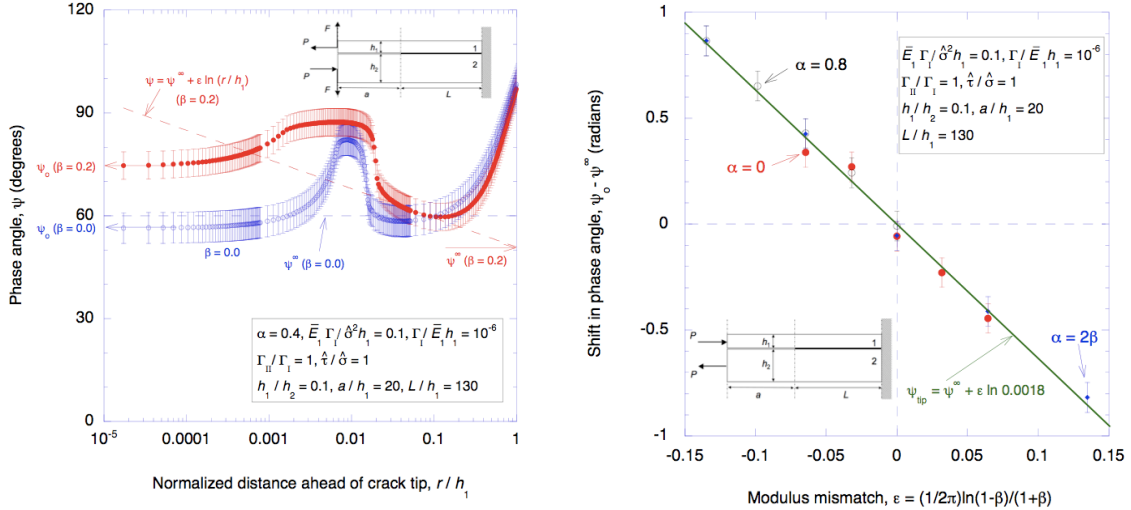


Fig. 15: (a) Phase angles for a mixed-mode geometry with a modulus mismatch. (b) Shift in phase angle between the crack tip phase angle and the nominal phase angle defined in terms of h_1 as a function of the mismatch parameter ϵ . This plot shows that the characteristic length scale describing fracture for this particular cohesive law is $0.0018h_1$. Figures taken from Parmigiani and Thouless (2007).

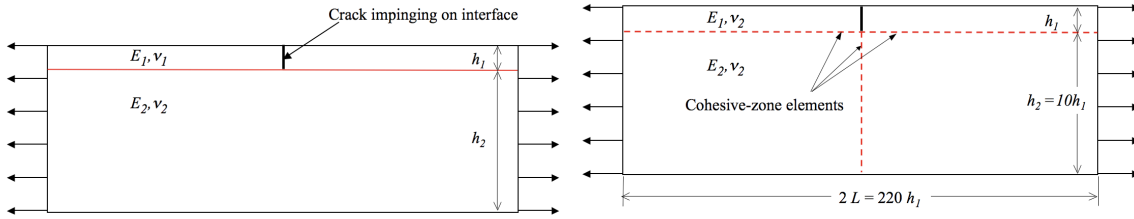


Fig. 16: (a) The geometry for crack deflection at an interface in a laminated geometry. (b) Geometry for a cohesive-zone model for crack deflection. Figures adapted from Parmigiani and Thouless (2006).

crack deflection is enhanced.

The apparent difference between the criteria for crack deflection from LEFM calculations and from cohesive-zone calculations can be rationalized examining the magnitude of the applied stress required to propagate the crack along the interface or into the substrate (Fig. 18). If $\Gamma_{II}/\Gamma_I = 1$, the applied stress required to propagate a kink across an interface of the elastically homogeneous laminate shown in Fig. 16a is

$$\sigma_a = 0.471\sqrt{\bar{E}_1\Gamma_2/h_1} \quad (17)$$

while the applied stress required to deflect the crack along the interface is

$$\sigma_a = 0.923\sqrt{\bar{E}_1\Gamma_I/h_1} \quad (18)$$

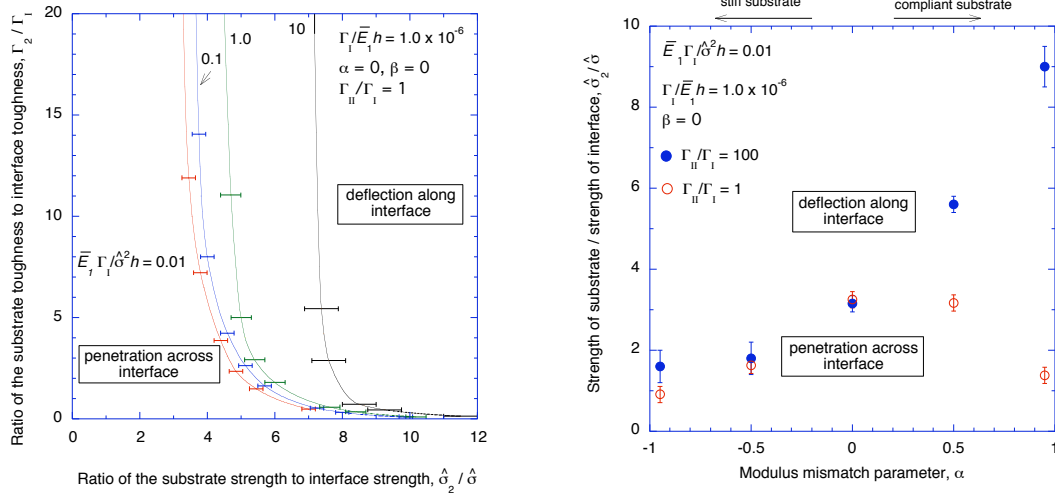


Fig. 17: **(a)** The conditions for a transition between crack deflection and propagation at an interface with no elastic mismatch. **(b)** The lower-bound for the strength ratio associated with the transition at an interface with elastic mismatch. Figures adapted from Parmigiani and Thouless (2006).

These equations have been plotted on Fig. 18, from which the LEFM result of $\Gamma_2 / \Gamma_I = 3.83$ for the transition between deflection and penetration can be seen graphically. In the limits of very high and very low values of the ratio Γ_2 / Γ_I , the cohesive-zone model agrees with the two LEFM results for the stresses required to deflect or propagate the crack. However, in general, the cohesive zones that develop in the substrate or along the interface shield each other, and raise the required stresses for both mechanisms. This interaction between the two cohesive zones is believed to be at the heart of the discrepancy between the LEFM results of He and Hutchinson (1989), and the cohesive-zone results presented above. When the fracture-length scales for the substrate and interface are comparable (or when the fracture-length scale of the substrate is larger than that of the interface), interfacial crack growth is shielded more strongly than crack penetration across the interface. This shifts the criterion for the transition to higher values of Γ_2 / Γ_I (or, equivalently, to lower values of $\hat{\sigma}_2 / \hat{\sigma}$). When the fracture-length scale for the substrate is significantly smaller than that for the interface, crack penetration across the interface is shielded more strongly than crack deflection. Under these conditions, the critical toughness ratio decreases, and the critical stress ratio increases.

An estimate of the amount of shielding provided by the cohesive zones, can be obtained by solving the LEFM problem for a crack impinging on an interface with *simultaneous* kinks extending across the interface and along the interface. This problem has been solved by finite-element methods. If the kinks are all of equal size ($k/h = 10^{-5}$), the applied stress required to propagate a kink across an interface in an elastically homogeneous laminate is

$$\sigma_a = 0.543 \sqrt{\bar{E}_1 \Gamma_2 / h_1}. \quad (19)$$

This is not significantly different from the result of Eqn. 17. However, the stress required to propagate a kink along the interface is raised substantially by the presence of a substrate

kink to

$$\sigma_a = 1.699\sqrt{\bar{E}_1\Gamma_I/h_1} \quad (20)$$

A comparison of these two equations indicates that a transition between the two modes of crack growth would occur at a toughness ratio of $\Gamma_2/\Gamma_I = 9.79$. It will be observed that this is very close to the critical ratio shown in Fig. 18a when the cohesive zones along the interface and in the substrate are comparable. Furthermore, it can be seen from Fig. 18 that the maximum stress, when the cohesive zone sizes are comparable, is almost identical to that given by Eqn. 20. It is expected that repeating similar LEFM calculations for different relative sizes of kinks would rationalize the range of deflection behavior observed in the cohesive-zone analyses for different fracture-length scales. The relative cohesive strengths affect the transitions between deflection and penetration behavior, even in the range of cohesive parameters where LEFM results are expected to be valid, because the relative strengths affect the relative lengths of the cohesive zones.

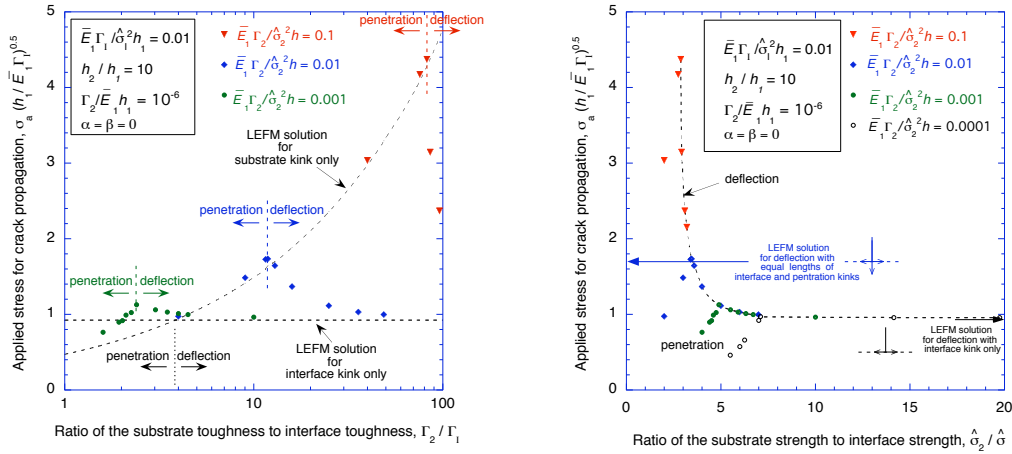


Fig. 18: The applied stress to propagate a crack, either along the interface or across it, for different fracture-length scales as a function of (a) toughness ratio, and (b) strength ratio.

5. CONCLUSIONS

Cohesive-zone models of fracture provide a natural bridge between conditions in which energy-based fracture criteria are appropriate and the conditions in which strength-based fracture criteria are appropriate. A mixed-mode cohesive-zone model has been used to explore the concepts of phase angle and mixed-mode failure criteria. It has been shown that linear-elastic fracture mechanics (LEFM) analyses of mixed-mode delamination are very robust, providing excellent predictions for the crack-tip phase angle and delamination strength, even under conditions which might not seem to be appropriate for using the equations of LEFM. In particular, the notion of a phase angle calculated from LEFM seems to be appropriate, even when the stress distribution along the interface has no relationship to what would be expected from a linear-elastic analysis. A finite thickness that can be associated with a cohesive zone, permits delamination to occur when the interface is subjected to a compressive stress. This provides an additional contribution to the energy

dissipation, beyond friction, that can raise the nominal toughness of an interface above the mode-II toughness. Since they involve a fracture-length scale, cohesive-zone models allow delamination in the presence of a modulus mismatch to be modelled naturally.

Crack deflection at interfaces can also be modelled by mixed-mode cohesive-zone models. It has been shown that the interaction between competing cohesive zones fundamentally changes the problem from existing LEFM models of crack deflection. In particular, the relative magnitudes of the cohesive strengths of the interface and substrate play an important role in determining the transition between crack deflection and penetration.

REFERENCES

- Cook, J., and Gordon, J.E. (1964). A mechanism for the control of crack propagation in all-brittle systems. *Proc. R. Soc. London, Ser. A* **282**, 508-520.
- Dundurs, J. (1969). Edge-bonded dissimilar orthogonal elastic wedges. *J. App. Mechs.* **36**, 650-652.
- Griffith, A.A., (1920). The phenomenon of rupture and flow in solids. *Philos. Trans. Roy. Soc. London A* **221**, 163-198.
- Gupta, V., Argon, A.S., and Suo, Z. (1992). Crack deflection at an interface between two orthotropic media. *J. Appl. Mechs.* **59**, S79-S87.
- He, M. Y. and Hutchinson, J. W. (1989). Crack deflection at an interface between dissimilar elastic materials. *Int. J. Solids Structures*, **25**, 1053-1067.
- He, M. Y., Evans, A. G. and Hutchinson, J. W. (1994). Crack deflection at an interface between dissimilar elastic materials: Role of residual stresses. *Int. J. Solids Structures* **31**, 3443-3455.
- Hsueh, C. H. (1990). Interfacial debonding and fiber pull-out stresses of fiber-reinforced composites. *Mat. Sci. Eng.* **A123**, 1-11.
- Inglis, C.E., (1913). Stresses in a plate due to the presence of cracks and sharp corners. In: *Proceedings of the Institute of Naval Architects*, vol. 55., pp. 219-230.
- Li, S., Thouless, M. D., Waas, A. M., Schroeder, J. A., and Zavattieri, P. D. (2005a). Use of mode-I cohesive-zone models to describe the fracture of an adhesively-bonded polymer-matrix composite. *J. Comp. Sci. Technol.* **65**, 281-293.
- Li, S., Thouless, M. D., Waas, A. M., Schroeder, J. A., and Zavattieri, P. D. (2005b). Use of a cohesive-zone model to analyze the fracture of a fiber-reinforced polymer-matrix composite. *J. Comp. Sci. Technol.* **65**, 537-549.
- Li, S., Wang, J., and Thouless, M. D. (2004). The effects of shear on delamination in layered materials. *J. Mech. Phys. Solids*, **52**, 193-214.
- Li, V. C., Maalej, M., and Hashida, T. (1994). Experimental determination of the stress-crack opening relation in fibre cementitious composites with a crack-tip singularity, *J. Mat. Sci.* **29**, 2719-2724.
- Marshall, D. B., Cox, B. N., and Evans, A. G. (1985). The mechanics of matrix cracking in brittle matrix composites, *Acta Metall.* **33**, 2013-2021.
- Muki, R. and Sternberg, E. (1970). Elastostatic load-transfer to a half-space from a partially embedded axially loaded rod. *Int. J. Solids Structures* **6**, 69-90.
- Parmigiani, J. P., and Thouless, M. D. (2006). Roles of toughness and cohesive strength on crack deflection. *J. Mech. Physics Solids* **54**, 266-287.
- Parmigiani, J. P., and Thouless, M. D. (2007). The effects of cohesive strength and toughness on mixed-mode delamination of beam-like geometries. *Eng. Frac. Mechs.* (in press).
- Rice, J. R. (1988). Elastic fracture-mechanics concepts for interfacial cracks. *J. App. Mechs.* **55**, 98-103.

- Sørensen B. F. and Jacobsen, T. K. (2003). Determination of cohesive laws by the J-integral approach. *Eng. Frac. Mechs.* 70, 1841-1858.
- Stringfellow, R. G., and Freund, L. B. (1993). The effect of interfacial friction on the buckle-driven spontaneous delamination of a compressed thin film. *Int. J. Solids Structures* 30, 1379-1395.
- Suo, Z., and Hutchinson, J. W. (1990). Interface crack between two elastic layers. *Int. J. Fract.* 43, 1-18.
- Thouless, M. D., Cao, H. C. and Mataga, P. A. (1989). Delamination from surface cracks in composite materials. *J. Mat. Sci.* 24, 1406-1412.
- Thouless, M. D., Hutchinson, J. W. and Liniger, E. G. (1992). Plane strain buckling-driven delamination of thin films: Model experiments and mode-II fracture. *Acta Metall. Mater.* 40, 2639-2649.
- Thouless, M. D., Jensen, H. M. and Liniger, E. G. (1994) Delamination from edge flaws. *Proc. Roy. Soc.* A447, 271-279.
- Yang, Q. D., Thouless, M. D., and Ward, S. M. (1999). Numerical simulations of adhesively-bonded beams failing with extensive plastic deformation. *J. Mech. Phys. Solids*, 47, 1337-1353.
- Yang, Q. D., and Thouless, M. D. (2001). Mixed-mode fracture analyses of plastically-deforming adhesive joints. *Int. J. Fract.* 110, 175-187.

COHESIVE MODELS FOR INTERFACE DEBONDING

Viggo Tvergaard

Department of Mechanical Engineering, Solid Mechanics
Technical University of Denmark
DK-2800 Kgs. Lyngby, Denmark

ABSTRACT

In modeling crack growth along an interface between a ductile material and an elastic material, or between two elastic-plastic materials, cohesive models have been a valuable tool for representing the evolution of failure in the process region just ahead of the crack tip. When ductile yielding occurs in the material surrounding the crack-tip this significantly increases the fracture toughness above the value corresponding to the work of separation per unit area in the crack plane. Here different cohesive models will be discussed. One follows the usual idea of a specified traction separation law on the interface, one modifies this approach by introducing a strain dependence, and the last approach uses special cohesive zone elements in which a damage model can be used to represent the fracture process zone. Due to mismatch of elastic properties across the interface the corresponding elastic solution has an oscillating stress singularity, that has to be accounted for if conditions of small scale yielding are used in analyzes.

1. INTRODUCTION

Crack growth in metals has been modeled in a number of studies by representing the local fracture process in terms of a traction-separation law along the crack plane with a specified work of separation per unit area, while the surrounding material is represented as elastic-plastic (Tvergaard and Hutchinson, 1992, 1993; Tvergaard, 2001a). The analyses have shown that plastic work in the material surrounding the crack-tip contributes significantly to the fracture toughness, such that the macroscopic work of fracture is much larger than that of the local fracture process. Mixed mode loading was considered and it was found that plastic flow near the crack-tip results in much increased resistance to crack growth when mode II conditions dominate, rather than mode I conditions. Recently, this type of analysis has also been used to

study crack growth along an interface between an anisotropic ductile material and an elastic material that does not yield plastically (Tvergaard and Legarth, 2006).

The standard cohesive zone model is only stress dependent, and it turns out for a ductile material that such traction-separation laws do not allow for crack growth if the peak stress is too large. Thus, if the crack growth occurs by a ductile mechanism that relies on voids, it has found in some cases that failure is highly strain dependent. As an alternative approach that involves a dependence on plastic strain Tvergaard (1992) and Tvergaard and Hutchinson (1996) have employed a modified traction-separation law that includes a strain dependence in a simplified manner. With this modification the peak stress is gradually reduced when the effective plastic strain along the crack path has exceeded a critical value.

For interface crack growth by a ductile failure mechanism special cohesive zone elements have been used to represent the fracture process zone Tvergaard (2001b; 2004). The modified Gurson model has been used in the cohesive zone elements to represent the nucleation and growth of voids to coalescence. The initial width of the interface is here taken to be zero, but the traction separation relations represented in terms of special cohesive zone elements are based on assuming an interface width of the order of the void spacing. The formulation has some relations to models in which a porous ductile material model has been applied in a single row of elements in front of the crack-tip (Xia and Shih, 1995; Xia et al., 1995), and to a cohesive zone formulation used by Siegmund and Brocks (1998). This description of the stress strain history in the special cohesive zone elements is not tied to the modified Gurson model, but can in principle be used with any damage model. This model has been applied for symmetric mode I loading as well as for interface crack growth under mixed mode loading (Tvergaard , 2001; 2004).

2. SMALL SCALE YIELDING FOR INTERFACE CRACK

The interface crack growth analyses to be considered here under mixed modes I and II loading are carried out for conditions of small-scale yielding. Both material No. 1 above the interface and the substrate (material No. 2) are elastic-plastic, with the elastic properties E_1 and ν_1 , the uniaxial yield stress σ_{Y1} and the strain hardening exponent N_1 above the interface (see Fig. 1), and the corresponding parameter values E_2 , ν_2 , σ_{Y2} and N_2 in the substrate. Both materials are described by a finite strain generalization of J_2 -flow theory (Hutchinson, 1973), with the uniaxial true stress-natural strain curve represented by a piecewise power law

$$\varepsilon = \begin{cases} \frac{\sigma}{E} & \sigma \leq \sigma_{Yi} \\ \frac{\sigma_{Yi}}{E} \left(\frac{\sigma}{\sigma_{Yi}} \right)^{1/N_i} & \sigma > \sigma_{Yi} \end{cases} \quad (1)$$

The elastic interface crack problem has been treated by many authors (e.g. England, 1965). Following the formulation of Rice (1988) (see also Hutchinson and Tvergaard, 1993), the crack has tractions acting on the interface which are given by

$$\sigma_{22} + i\sigma_{12} = (K_I + iK_{II})(2\pi r)^{-1/2} r^{i\varepsilon} \quad (2)$$

where K_I and K_{II} are the two stress intensity factor components. Here, r is the distance from the tip, $i = \sqrt{-1}$, ε is the oscillation index

Cohesive models for interface debonding

$$\varepsilon = \frac{1}{2\pi} \ln \left(\frac{1-\beta}{1+\beta} \right) \quad (3)$$

and β is the second Dundurs' parameter

$$\beta = \frac{1}{2} \frac{\mu_1(1-2\nu_2) - \mu_2(1-2\nu_1)}{\mu_1(1-\nu_2) + \mu_2(1-\nu_1)} \quad (4)$$

where the shear moduli are $\mu_1 = E_1 / (2(1+\nu_1))$ and $\mu_2 = E_2 / (2(1+\nu_2))$. The relation between the energy release rate G and the magnitude $|K|$ of stress intensity factors is

$$G = \frac{1}{2} (1-\beta^2) \left[\frac{1-\nu_1^2}{E_1} + \frac{1-\nu_2^2}{E_2} \right] |K|^2, \quad |K| = \sqrt{K_I^2 + K_{II}^2} \quad (5)$$

With a reference length L chosen to characterize the remote field, an L -dependent measure of mode mixity ψ is defined by

$$\tan \psi = \frac{\text{Im} \left[(K_I + iK_{II}) L^{i\varepsilon} \right]}{\text{Re} \left[(K_I + iK_{II}) L^{i\varepsilon} \right]} \quad (6)$$

which reduces to the more familiar measure, $\tan \psi = K_{II} / K_I$, when $\varepsilon = 0$. The displacement components associated with the singularity field, with amplitude $|K|$, are specified in (Tvergaard and Hutchinson, 1993).

The x_1 -axis is in the crack plane and the initial crack-tip is located at $x_1 = x_2 = 0$ (see Fig. 1). The traction-separation relation used to model the fracture process is specified everywhere on the boundary $x_1 > 0, x_2 = 0$ of the region analyzed, while zero tractions are specified for $x_1 \leq 0, x_2 = 0$.

If the work of separation per unit area of the interface is denoted by Γ_0 , a reference stress intensity factor is defined as

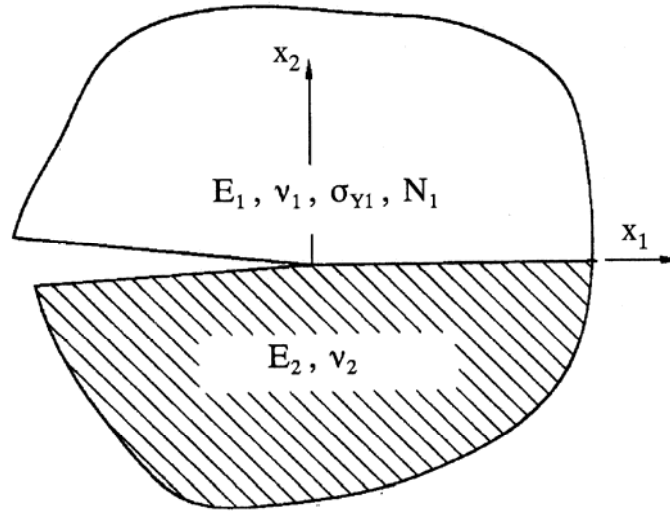


Fig. 1. Interface crack with elastic-plastic material properties above the interface and elastic properties below.

$$K_0 = \left[\frac{1-\nu_1^2}{E_1} + \frac{1-\nu_2^2}{E_2} \right]^{-1/2} \left(\frac{2\Gamma_0}{1-\beta^2} \right)^{1/2} \quad (7)$$

Here, K_0 represents the value of $|K|$ needed to advance the interface crack in the absence of any plasticity. This value is independent of ψ when a potential is used to generate the relation of tractions to crack face displacements of the interface. A length quantity R_0 , which scales with the size of the plastic zone in material No. 1 (when $|K| \cong K_0$), is defined by

$$R_0 = \frac{1}{3\pi} \left(\frac{K_0}{\sigma_{Y1}} \right)^2 = \frac{2}{3\pi} \left[\frac{1-\nu_1^2}{E_1} + \frac{1-\nu_2^2}{E_2} \right]^{-1} \frac{\Gamma_0}{(1-\beta^2)\sigma_{Y1}^2} \quad (8)$$

While the mode mixity measure ψ refers to the distance L from the tip, it is natural to define a reference measure of mixity, ψ_0 , based on the reference length R_0 . The relation between ψ_0 and ψ is

$$\psi_0 = \psi + \varepsilon \ln(R_0/L) \quad (9)$$

3. A TRACTION-SEPARATION LAW

The traction-separation law used by Tvergaard and Hutchinson (1993) to analyze interface crack growth under mixed mode loading is a special version of that proposed by Tvergaard (1990) as a generalization of the model of Needleman (1987). Here, δ_n

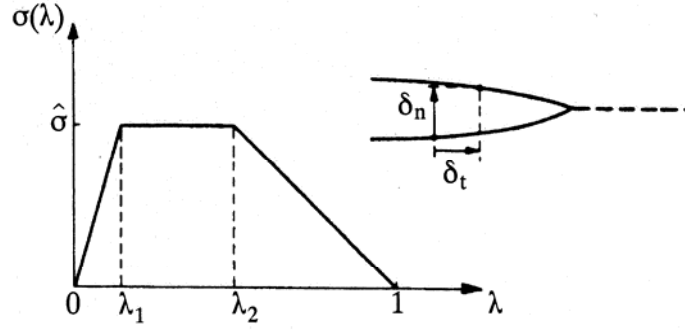


Fig. 2. Specification of traction-separation relation.

and δ_t denote the normal and tangential components of the relative displacement of the crack faces across the interface in the zone where the fracture processes are occurring (Fig. 2). When δ_n^c and δ_t^c are critical values of these displacement components and a single non-dimensional separation measure is defined as $\lambda = \left[(\delta_n / \delta_n^c)^2 + (\delta_t / \delta_t^c)^2 \right]^{1/2}$ the tractions drop to zero when $\lambda = 1$. With $\sigma(\lambda)$ displayed in Fig. 2, a potential from which the tractions are derived is defined as

$$\Phi^*(\delta_n, \delta_t) = \delta_n^c \int_0^\lambda \sigma(\lambda') d\lambda' \quad (10)$$

The normal and tangential components of the traction acting on the interface in the fracture process zone are given by

$$T_n = \frac{\partial \Phi^*}{\partial \delta_n} = \frac{\sigma(\lambda)}{\lambda} \frac{\delta_n}{\delta_n^c}, \quad T_t = \frac{\partial \Phi^*}{\partial \delta_t} = \frac{\sigma(\lambda)}{\lambda} \frac{\delta_t}{\delta_t^c} \frac{\delta_n^c}{\delta_t^c} \quad (11)$$

The peak normal traction under pure normal separation is $\hat{\sigma}$, and the peak shear traction is $(\delta_n^c / \delta_t^c) \hat{\sigma}$ in a pure tangential separation. The work of separation per unit area of interface is given by Eq. (10) with $\lambda = 1$, and for the separation function $\sigma(\lambda)$ in Fig. 2 the work is

$$\Gamma_0 = \frac{1}{2} \hat{\sigma} \delta_n^c (1 - \lambda_1 + \lambda_2) \quad (12)$$

It has been found in (Tvergaard and Hutchinson, 1992; 1993) that the two most important parameters characterizing the fracture process in this model are Γ_0 and $\hat{\sigma}$. Scheider and Brocks (2003) have found cases where also differences in the shape of the separation law have an important effect.

The traction-separation law given above is specified by the values of three parameters, i.e. $\hat{\sigma}$, δ_n^c and δ_t^c . But it is noted that Tvergaard (1990a) used an extra parameter α such that

$$T_t = \alpha \frac{\sigma(\lambda)}{\lambda} \frac{\delta_t}{\delta_t^c} \frac{\delta_n^c}{\delta_t^c} \quad (13)$$

Then the traction-separation law cannot be derived from a potential, as in Eqs. (10) and (11), but this model with four parameters is able to represent the situation often observed in adhesive bonding that the work of separation is larger in pure tangential separation than in a pure normal separation (Högberg, 2006). This observation of the average behaviour in adhesive fracture appears to be a result of plasticity inside the adhesive layer (Tvergaard and Hutchinson, 1996; Tvergaard, 1997). A toughness Γ_0 that varies with the mode-mix has also been found in a recent study of a sapphire-epoxy interface with the sapphire enhanced by coating (Mello and Liechti, 2006).

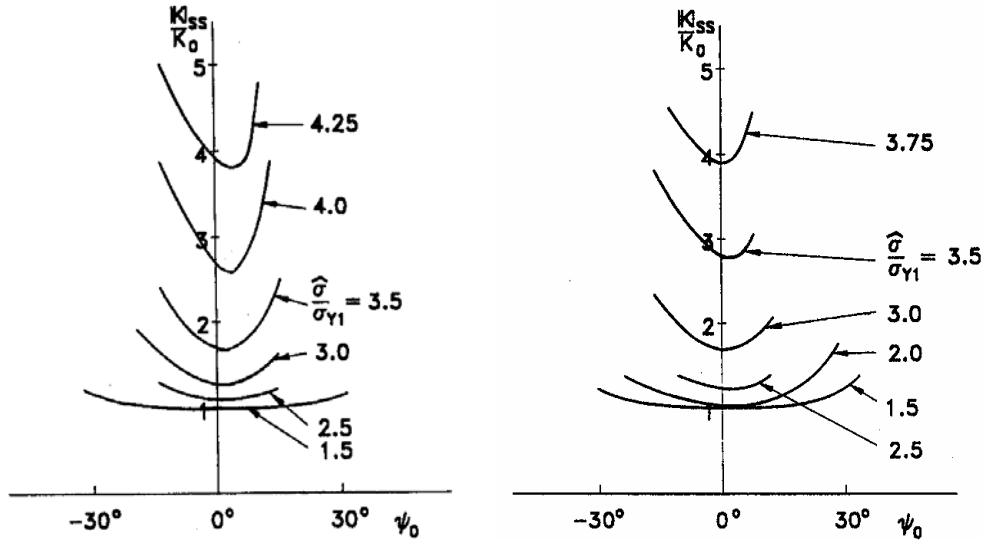


Fig. 3. Steady-state interface toughness as a function of the local mixity measure ψ_0 , for $\sigma_{y1}/E_1 = 0.003$ and $\sigma_{y2} = \infty$, considering different values of $\hat{\sigma}/\sigma_{y1}$. (a) $E_2/E_1 = 2$, (b) $E_2/E_1 = 6$. (From Tvergaard, 2001a).

Fig. 3 shows examples of the steady-state fracture toughness calculated for an elastic-plastic material on an elastic substrate. It is seen that the minimum fracture toughness is predicted for $\psi_0 \approx 0^\circ$, i.e. for cases where conditions near the crack-tip are close to pure mode I. Also, the fracture toughness is higher if the ratio of Young's moduli, E_2/E_1 , is increased.

4. STRAIN-DEPENDENT COHESIVE ZONE MODEL

It was found by Tvergaard and Hutchinson (1992) that the traction-separation law (10) to (12) does not allow for crack growth if the stress ratio $\hat{\sigma}/\sigma_y$ is too large. Thus, if the crack growth occurs by a ductile mechanism that relies on voids, it was found failure involving the simultaneous growth of several voids ahead of the crack-tip can be described by a traction-separation law as (10)-(12), but the often observed regime where only one void interacts with the crack-tip until they coalesce, then the next void, etc., cannot adequately be described. This void by void mechanism is highly strain dependent, whereas the traction-separation law described in Section 3 is entirely stress dependent.

Cohesive models for interface debonding

As an alternative approach that involves a dependence on plastic strain Tvergaard (1992) and Tvergaard and Hutchinson (1996) have employed a modification of the traction-separation law (10)-(12) that includes a strain dependence in a simplified manner. With this modification the peak stress $\hat{\sigma}$ in the expression for $\sigma(\lambda)$ (see Fig. 2) is gradually reduced when the effective plastic strain ε_e^P along the crack path has exceeded a critical value ε_c

$$\hat{\sigma} = \begin{cases} \hat{\sigma}_0, & \text{for } \varepsilon_e^P \leq \varepsilon_c \\ \hat{\sigma}_0 - \Delta\hat{\sigma}(\varepsilon_e^P - \varepsilon_c)/\Delta\varepsilon, & \text{for } \varepsilon_c < \varepsilon_e^P < \varepsilon_c + \Delta\varepsilon \\ \hat{\sigma} - \Delta\hat{\sigma}, & \text{for } \varepsilon_e^P \geq \varepsilon_c + \Delta\varepsilon \end{cases} \quad (14)$$

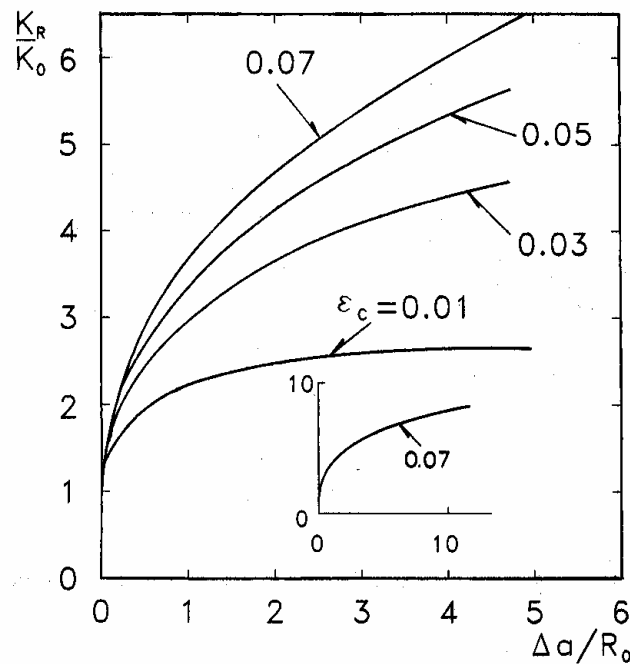


Fig. 4. Crack growth resistance curves for $\hat{\sigma}_0/\sigma_Y = 4.4$ and $T/\sigma_Y = 0$. (From Tvergaard and Hutchinson, 1996).

Fig. 4 shows computations for Mode I loading with a crack in a homogeneous material. Here the peak stress is so high, $\hat{\sigma}/\sigma_Y = 4.4$, that crack growth would not be predicted by (10)-(12), but the results in Fig. 4 for different values of ε_c show that the model functions as expected. For $\varepsilon_c = 0.01$ a steady-state is reached in the range analyzed. Also for the highest critical strain value considered, $\varepsilon_c = 0.07$, the crack grows with a high slope of the resistance curve, and the insert in Fig. 4 shows that the computation would have to be continued well beyond $\Delta a/R_0 = 12$ before a steady-state might be reached. A disadvantage of this model is that the values of ε_e^P to be used in (14) are taken from the elements closest to the crack plane, and the values obtained are sensitive to the mesh size used in the numerical analysis.

5. CRACK GROWTH BY VOID EXPANSION MECHANISM

For interface crack growth by a ductile failure mechanism special cohesive zone elements can be used to represent the fracture process zone. The modified Gurson model is then used in the cohesive zone elements to represent the nucleation and growth of voids to coalescence, as has been done for symmetric mode I loading by Tvergaard (2001b).

The initial width of the interface is here taken to be zero, but the traction separation relations represented in terms of the special cohesive zone elements are based on assuming an interface width of the order of the void spacing. The formulation has some relations to models in which a porous ductile material model has been applied in a single row of elements in front

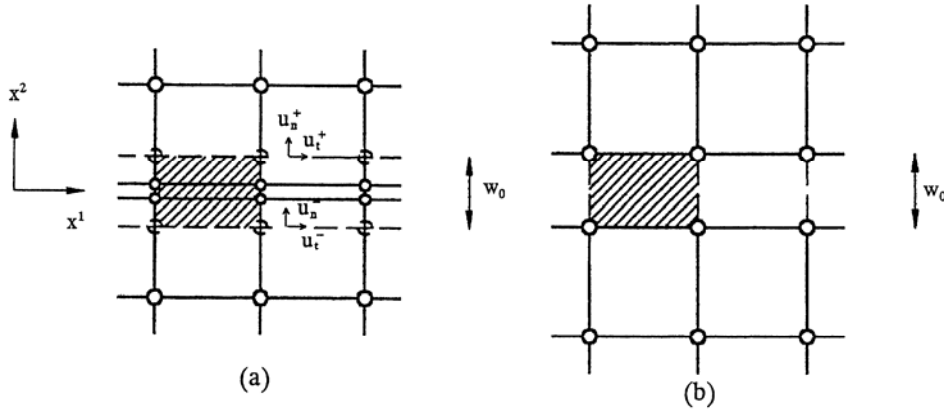


Fig. 5. Interface elements along the crack plane. (a) Shows the artificial overlap between interface elements and surrounding elements. (b) A corresponding configuration with no overlap.

The initial width of the special cohesive zone for ductile failure is taken to be zero, as in other cohesive zone calculations (Tvergaard and Hutchinson, 1992, 1993), but the traction-separation relations represented in terms of the special cohesive zone elements are based on assuming an interface width w_0 of the order of the void spacing. Fig. 5a illustrates the finite element mesh near the crack plane, with the background interface element sketched in, while Fig.5b indicates the configuration if this interface element is attached to the surrounding elements as a common element (see also Tvergaard, 2004). The displacement components on the top side of the element are denoted by u_n^+ and u_t^+ , respectively, while those on the bottom side of the element are denoted by u_n^- and u_t^- (see Fig. 5a). These displacements are required to be compatible with the displacements on the edge of the adjacent finite elements. Then, with the assumptions that the displacements inside the interface element vary linearly through the element width (in the x^2 -direction) and with the gradients replaced by their averages through the element width, the displacement gradients inside the elements are approximated as

$$\frac{\partial u_1}{\partial x^2} = \frac{u_t^+ - u_t^-}{w_0}, \quad \frac{\partial u_2}{\partial x^2} = \frac{u_n^+ - u_n^-}{w_0} \quad (15)$$

$$\frac{\partial u_1}{\partial x^1} = \frac{1}{2} \left(\frac{\partial u_t^+}{\partial x^1} + \frac{\partial u_t^-}{\partial x^1} \right), \quad \frac{\partial u_2}{\partial x^1} = \frac{1}{2} \left(\frac{\partial u_n^+}{\partial x^1} + \frac{\partial u_n^-}{\partial x^1} \right) \quad (16)$$

Cohesive models for interface debonding

In the analyses, all field equations are specified in the context of a convected coordinate, Lagrangian formulation, both inside and outside the interface elements. From the expressions (15) and (16) for the displacement gradients, and from their increments, it is possible to determine the current metric tensor G_{ij} , the Lagrangian strain tensor η_{ij} and its increment $\dot{\eta}_{ij}$

in any point on the middle surface, $x^2 = 0$, of the interface element, and thus a set of constitutive relations can be used to calculate the evolution of stresses and the evolution of damage inside the interface. These constitutive relations are based on the modified Gurson model (Gurson, 1977; Tvergaard, 1990b), which makes use of an approximate yield condition for the porous solid is of the form

$$\Phi = \frac{\sigma_e^2}{\sigma_M^2} + 2q_1 f^* \cosh \left[\frac{\sigma_k^k}{2\sigma_M} \right] - 1 - (q_1 f^*)^2 = 0 \quad (17)$$

Here, σ_M is an equivalent tensile flow stress representing the actual microscopic stress state in the matrix material, and $\sigma_e = (3s_{ij}s^{ij}/2)^{1/2}$ for $s^{ij} = \sigma^{ij} - G^{ij}\sigma_k^k/3$. The void volume fraction is f and $f^*(f)$ is a function that approximately describes final failure by void coalescence. Void nucleation is taken to be described as a normal distribution, with the volume fraction f_N of void nucleating particles, the mean strain ε_N for nucleation, and the standard deviation s_N . Outside the interface elements a finite strain Mises material is applied (see Hutchinson, 1973; Tvergaard, 2004).

As described in (Tvergaard, 2001b, 2004), an extra parameter r_0 is introduced, to be able to reduce the tangential components of the nodal forces calculated by the interface element procedure described above. The tensile or compressive stress components σ_{11} along the interface layer are already fully accounted for in the finite element mesh outside the interface, due to the somewhat artificial overlap of the background interface element with the neighbouring element mesh (Fig. 5a). The nodal forces on the top side of the interface element are denoted P_n^+ and P_t^+ , respectively, taken to be positive in the direction of u_n^+ and u_t^+ , and on the bottom side the force components P_n^- and P_t^- are positive in the directions of u_n^- and u_t^- . The nodal force components calculated by the standard element procedure are denoted by $(P_t)_{\text{elm}}$. For full mixed mode loading on the interface the reduction in the symmetric part of the tangential nodal forces obtained from the interface element is specified by taking the forces P_t^+ and P_t^- to be given by (Tvergaard, 2004)

$$P_t^+ = (P_t^+)_{\text{elm}} - \frac{1-r_0}{2} \left((P_t^+)_{\text{elm}} + (P_t^-)_{\text{elm}} \right) \quad (18)$$

$$P_t^- = (P_t^-)_{\text{elm}} - \frac{1-r_0}{2} \left((P_t^+)_{\text{elm}} + (P_t^-)_{\text{elm}} \right) \quad (19)$$

In the study of Tvergaard (2001b) for pure mode I loading both $r_0 = 1$ (no reduction) and $r_0 = 0$ (full reduction) were analysed and compared with other studies, and it was found that $r_0 = 0$ gave the best representation of an initially sharp crack. Therefore, $r_0 = 0$ will be used here. The value of the initial width w_0 of the strip (Fig. 5) is non-zero, representing about 0.7 times the initial void spacing.

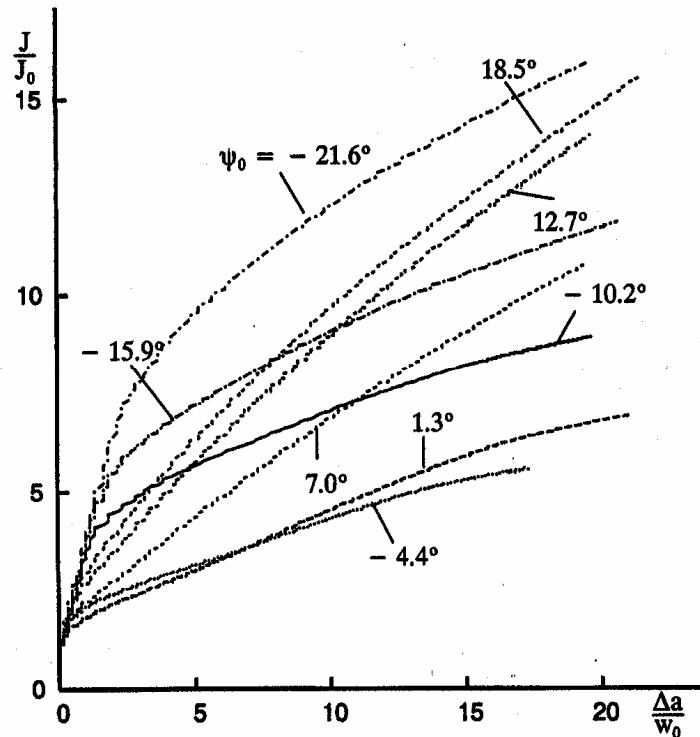


Fig. 6. Interface crack growth resistance curves for $\sigma_{Y1}/E_1 = 0.002$, $E_2/E_1 = 2$ and $\sigma_{Y2}/\sigma_{Y1} = 2$, when $f_I = 0$, $f_N = 0.02$, $\varepsilon_N = 0.2$ and $s_N = 0.1$. (From Tvergaard, 2004).

Fig. 6 shows examples of crack growth resistance curves computed by using these special cohesive zone elements for a case where there are no voids initially but where void nucleation takes place inside the special cohesive elements, leading to failure by void coalescence. The mode mixity applied for each curve is indicated by the value of ψ_0 and it is seen that the lowest fracture toughness is found for $\psi_0 \approx 0^\circ$, as in Fig. 3.

REFERENCES

- England, A.H. (1965). A crack between dissimilar media. *J. Appl. Mech.* 32, 400-402.
- Gurson, A.L. (1977). Continuum theory of ductile rupture by void nucleation and growth: Part I – yield criteria and flow rules for porous ductile media. *J. Engng. Mater. Tech.* 99, 2-15.
- Hill, R. (1950). *The Mathematical Theory of Plasticity*. (The Clarendon Press, Oxford).
- Hutchinson, J.W. (1973). Finite strain analysis of elastic-plastic solids and structures. In: *Numerical Solution of Nonlinear Structural Problems*. Ed. R.F. Hartung (American Society for Mechanical Engineers, New York) p. 17.
- Högberg, J.L. (2006). Mixed mode cohesive law. *Int. J. Fracture* 141, 549-559.

Cohesive models for interface debonding

- Mello, A.W. and Liechti, K.M. (2006). The effect of self-assembled monolayers on interfacial fracture. *J. Appl. Mech.* 73, 860-870.
- Needleman, A. (1987). A continuum model for void nucleation by inclusion debonding. *J. Appl. Mechanics* 54, 525-531.
- Rice, J.R. (1988). Elastic fracture mechanics concepts for interfacial cracks. *J. Appl. Mech.* 55, 98-103.
- Scheider, I. and Brocks, W. (2003). The effect of the traction separation law on the results for cohesive zone crack propagation analyses. *Key Engineering Materials* 251-252:313-318.
- Siegmund, T. and Brocks, W. (1998). Local fracture criteria: lengthscales and applications. *J. Phys.* IV 8, 349-356.
- Tvergaard, V. (1976). Effect of thickness inhomogeneities in internally pressurized elastic-plastic spherical shells. *J. Mech. Phys. Solids* 24, 291-304.
- Tvergaard, V. (1990a). Effect of fibre debonding in a whisker-reinforced metal. *Mater. Sci. Engng.* A125, 203-213.
- Tvergaard, V. (1990b). Material failure by void growth to coalescence. *Adv. App. Mech.* 27, 83-151.
- Tvergaard, V. (1992). Effect of ductile particle debonding during crack bridging in ceramics. *Int. J. Mech. Sci.* 34, 635-649.
- Tvergaard, V. (1997). Analyses of debonding in metal ceramic systems. In *Advances in Fracture Research, ICF9*, (eds. B.L. Karihaloo et al.), 2, 651-662, Pergamon 1997.
- Tvergaard, V. (2001a). Resistance curves for mixed mode interface crack growth between dissimilar elastic-plastic solids. *J. Mech. Phys. Solids* 49, 2689-2703.
- Tvergaard, V. (2001b). Crack growth predictions by cohesive zone model for ductile fracture. *J. Mech. Phys. Solids* 49, 2191-2207.
- Tvergaard, V. (2004). Predictions of mixed mode interface crack growth using a cohesive zone model for ductile fracture. *J. Mech. Phys. Solids* 52, 925-940.
- Tvergaard, V. and Hutchinson, J.W. (1992). The relation between crack growth resistance and fracture process parameters in elastic-plastic solids. *J. Mech. Phys. Solids* 40, 1377-1397.
- Tvergaard, V. and Hutchinson, J.W. (1993). The influence of plasticity on mixed mode interface toughness. *J. Mech. Phys. Solids* 41, 1119-1135.
- Tvergaard, V. and Hutchinson, J.W. (1996a). Effect of strain-dependent cohesive zone model on predictions of crack growth resistance. *Int. J. Solids Structures* 33, 3297-3308.
- Tvergaard, V. and Hutchinson, J.W. (1996b). On the toughness of ductile adhesive joints. *J. Mech. Phys. Solids* 44, 789-800.

Tvergaard

Tvergaard, V. and Legarth, B.N. (2004). Effect of plastic anisotropy on crack growth resistance under mode 1 loading. *Int. J. of Fracture* 130, 411-425.

Tvergaard, V. and Legarth, B.N. (2006). Effect of anisotropic plasticity on mixed mode interface crack growth. *Engineering Fracture Mechanics* (to appear).

Xia, L. and Shih, C.F. (1995). Ductile crack growth – I. A numerical study using computational cells with microstructurally-based length scales. *J. Mech. Phys. Solids* 43, 233-259.

Xia, L., Shih, C.F. and Hutchinson, J.W. (1995). A computational approach to ductile crack growth under large scale yielding conditions. *J. Mech. Phys. Solids* 43, 389-430.

THE IMPORTANCE OF INTERFACES IN THERMOPLASTIC MATRIX COMPOSITES AND THEIR TAILORING DURING MANUFACTURE

Richard P. Wool

Department of Chemical Engineering and Center for Composite Materials,
University of Delaware, Newark DE 19716-3144 USA.

ABSTRACT

The thermoplastic composite interfaces involve a variety of chemical and structural parameters: chemical composition, crystalline and amorphous content, compatibility and incompatibility, molecular weight distribution, additives and several others. The structure of the interfaces will be examined, and then related to the interface fracture strength. This relation is established on the basis of microscopic deformation mechanisms involving chain disentanglement and bond rupture. The relationship is developed in terms of the entanglement percolation model of Wool; the deformation mechanisms consume a known amount of energy, from which the strength of the interface can be determined. In this paper the focus is on the theory of model thermoplastic symmetric A/A interfaces with respect to understanding strength and fatigue issues for different polydispersive matrices. These are typically encountered during manufacture of thermoplastic composites using tow placement, lamination, co-extrusion, welding and sintering.

1. INTRODUCTION

The subject of thermoplastic composite interfaces is very rich when we consider the wide variety of possible pairs involving polymers and materials with different chemical composition, crystalline and amorphous content, compatibility, incompatibility, molecular weight distributions, additives, surface chemistry, etc. We first examine the structure of these interfaces and then relate the structure to fracture strength through microscopic deformation mechanisms involving chain disentanglement and bond rupture. The evolution of structure at diffuse interfaces is controlled by the dynamics of the chains and the thermodynamics of chemically interacting species. Once the structure is known, a “connectivity relation” is required to relate the structure to mechanical properties. The connectivity relation for amorphous polymers is developed in terms of an entanglement percolation model Wool, (1995, 2006, 2005). We can then understand what is required to break the connectivity at the interface by disentanglement and/or bond rupture. The latter microscopic deformation mechanisms consume a known amount of energy from which the strength of the interface can be determined. In this paper, we focus on the theory of model thermoplastic symmetric A/A interfaces with respect to understanding

strength and fatigue issues for different polydisperse matrices. These are typically encountered during the manufacture of thermoplastic composites using tow placement, lamination, co-extrusion, welding and sintering

2. FRACTURE OF POLYMER INTERFACES-FUNDAMENTAL THEORY

A useful approach to evaluating the fracture energy G_{1c} , of a polymer or interface of A/B polymers, is represented in Figure 1. (Wool 2005). Typically, a crack propagates through the interface region preceded by a deformation zone at the crack tip. For cohesive failure, the fracture energy can be determined by the J-Integral method, as described by Hutchinson (1997), Tvergaard et al. (1993), Tvergaard et al (1996), where G_{1c} is the integral of the traction stresses with crack opening displacements δ , in the cohesive zone, following yielding at a local yield or craze stress σ_Y . The cohesive zone at the crack tip breaks down by a percolation process Tvergaard et al (1996), Wool (2007), Kantor, Webman. (1984), Born. and Huang, (1954), Wool et al (2004), Wool., Bretzlaff, Li, Wang, Boyd (1986), as described herein, at a maximum stress value, $\sigma_m > \sigma_Y$. Typical ratios of σ_m / σ_Y are about 4-5 Hutchinson (1997). The yield stress dominates the fracture process for non-crazing matrices such as thermosets and this is determined by the Twinkling Fractal Theory (TFT) Wool (2007). Both σ_m and δ are rate dependent and in the simplest case, the fracture energy is determined by

$$G_{1c} = \sigma_m \delta_m, \tag{2.1}$$

where δ_m is the critical crack opening displacement. Both σ_m and δ_m depend on the zone structure and the microscopic deformation mechanisms controlling the percolation fracture process via disentanglement and bond rupture.

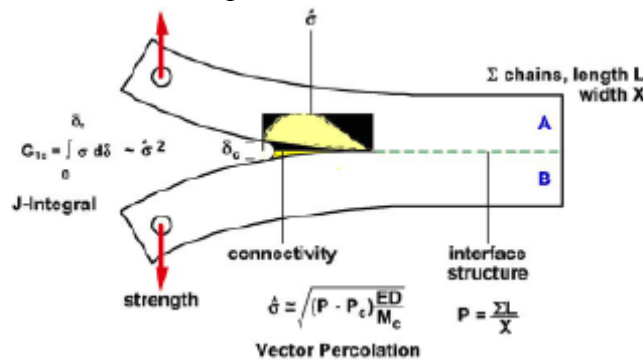


Fig. 1 The microscopic entanglement structure, e.g. at an interface or in the bulk, is related to the measured macroscopic fracture energy G_{1c} via the RP theory of breaking connectivity in the embedded plastic zone (EPZ) at the crack tip. The RP theory determines σ_{max} in the EPZ, which is related to G_{1c} via Hutchinson's J-Integral theory. The percolation parameter p is related to the interface molecular structure via $p \sim \Sigma L / X$, where Σ is the number of chains of length L in an interface of width X (Wool, 2006).

To convert these percolation concepts into quantitative fracture terms, consider a percolation experiment applied to any 3d lattice with initial tensile modulus E and subject to random bond fracture. The Hamiltonian for the stored elastic energy can be formulated using the Kantor and Webman approach for specific lattices Kantor, Webman (1984) the Born and Huang method (1954) or using the more simple engineering strain energy density approach as follows. The stored elastic strain energy density U , (energy per unit volume), in the lattice due to an applied uniaxial stress σ is determined by,

$$U = \sigma^2/2E \quad (2.2)$$

The stored strain energy dissipation per unit volume U_f , to fracture a network consisting of v bonds per unit volume is,

$$U_f = vD_o [p - p_c] \quad (2.3)$$

Where D_o is the bond fracture energy, and $[p - p_c]$ is the percolation fraction of bonds which must be broken to cause fracture in the network. In this approach, the strain energy U , is first stored in the net and we inquire if this energy is sufficient to break $v[p-p_c]$ bonds per unit volume when it releases at a critical strain energy density $U^* = \sigma^{*2} / 2E$, such that at the critical condition,

$$U^* \geq U_f \quad (2.4)$$

Substituting for U^* and U_f in Eq 2.4 and solving for the critical stress σ^* , we obtain the “Net solution” for the critical fracture stress as

$$\sigma^* = \{2E vD_o [p-p_c]\}^{1/2} \quad (2.5)$$

Applications of Eq (2.5) are shown in Table 1 where $v = \rho/M_c$.

Table 1. Comparison of RP theory and experimental fracture stress Wool (2005)

Polymer	M_c g/mol	σ (Theory) 10⁴MPa/M_c^{1/2}	σ (Expt) MPa	T °C	Ref
PE	4,000	158	160	-196	14
PP	7,000	119	98	-120	14
PVC	11,000	95	142	-180	14
PMMA	18,400	74	68	-60	14
PC	4,800	144	145	-140	14
			120	20	12
PS	31,000	57	56	20	14
PTFE	13,200	87	117	-196	14
PLA	12,000	65 (E = 1 GPa)	64	20	15
Starch	200,000	22	--	20	15

This equation predicts that the fracture stress increases with the square root of the bond density $v \sim 1/M_c$. The percolation parameter p , is in effect, the normalized bond density such that for a perfect net without defects, $p = 1$, and for a net that is damaged or contains missing bonds, then $p < 1$. Obviously, as p approaches p_c , the fracture stress decreases towards zero and we have a very fragile material. The fatigue lifetime is also calculated using this concept and is presented

in a later section. This fracture relation could therefore be used to evaluate durability, fatigue damage accumulation, healing processes, or retention strength of a material by tracking damage through a single parameter p . For thermosets, p is related to the extent of reaction of the crosslink groups and this could be critical in the fiber-matrix interface of composites Wool et al (2004).

3. THE TWINKLING FRACTAL THEORY OF THE GLASS TRANSITION AND YIELD STRESS

We examine the onset of the glass transition temperature T_g in Figure 2 by considering the anharmonic interaction potential of quasiharmonic diatomic oscillators (Fig 3) in the liquid state as a function of temperature. The anharmonicity controls the vibrational frequencies ω , with temperature T , pressure P and stress σ Wool et al (1986), and the extent of the anharmonicity controls the magnitude of the thermal expansion coefficient α (Fig 3). The vibrational frequencies, degree of freedom ($d=1, 2$ or 3) and their density of states $G(\omega)$ determines the thermal properties such as the specific heat capacity C_p and thermal conductivity K . As T_g is approached from above, the average bond distance X between the oscillators contracts, the volume V decreases and the bond expansion factor X approaches its critical value X_c , such that when $X > X_c$, the molecules are in the ergodic liquid state and when $X < X_c$, the molecules on average exist in the non-ergodic solid state. The latter idea parallels the Lindemann (1910) theory of melting which states that when the vibrational amplitudes exceed a critical value of the bond length ($X \approx 0.11$), then melting occurs. In our case we have a Boltzmann distribution of oscillators at various quantized energy levels in the anharmonic potential energy function of the atoms such that at any temperature T , there exists a fraction P_s of solid atoms ($X < X_c$) and a fraction P_L of liquid atoms.

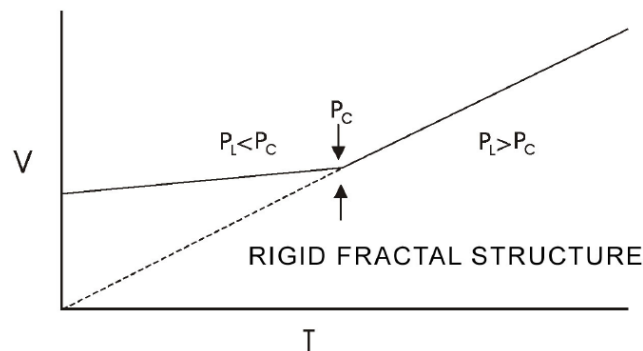


Fig. 2 Volume-Temperature curve for a glass former. T_g occurs at $P_s = P_c$ when the fractal structure form.

Interfaces and their tailoring

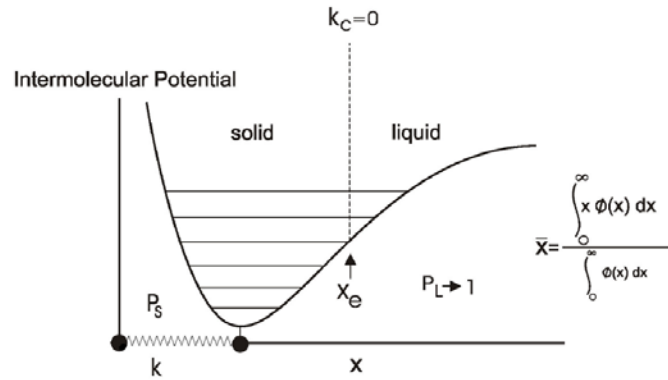


Fig.3 Diatomic anharmonic Morse oscillator $U(x) = D_0[1 - e^{-ax}]^2$ with Boltzmann energy levels and populations $\phi(x) \sim \exp[-U(x)/kT]$ shows the Liquid ($X > X_c$) and Solid ($X < X_c$) phase diagram.

The solid fraction P_s at any T is determined from the integral of the energy populations $\phi(x)$:

$$P_s(T) = \int_0^{X_c} \phi(x) dx \quad (3.1)$$

in which $\phi(x) \sim \exp[-U(x)/kT]$. As T_g is approached from above, as shown for example in Figure 4, the fraction of solid atoms P_s grows with a cluster size distribution function determined by percolation theory and eventually percolates at the critical percolation threshold P_c .

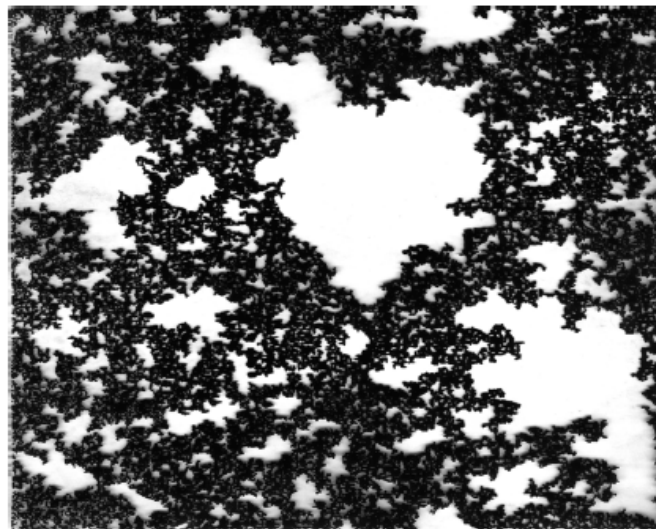


Fig.4 The Twinkling Fractal percolation cluster at T_g . The liquid white regions are in dynamic equilibrium with the solid black clusters. The Twinkling Fractal frequency spectrum mirrors the vibrational density of states $F(\omega) \sim \omega^{D_f-1} \exp[-|U(T) - U_c|/kT]$ such that at temperatures much greater or lower than T_g , the twinkling rate shuts off in the pure liquid or very cold solid.

The percolation cluster has a fractal dimension D_f and is not stationary but is quite dynamic since the solid and liquid atoms are in dynamic equilibrium. Thus at T_g , to the observer, there appears to exist a fractal structure which “twinkles” with a frequency spectrum $F(\omega)$ as liquid and solid atoms exchange. This “twinkling” fractal structure is invisible to the usual scattering

experiments since the liquid and solid are essentially indistinguishable to such scattering experiments.

The existence of the twinkling fractal near T_g has a profound effect on many properties, such as the mechanical loss peak. For example, it suggests that the onset of T_g is purely kinetic rather than thermodynamic such that at very slow rates, the fractal appears liquid and at very high rates approaching $1/\omega$, the fractal appears quite rigid. This effect dominates the physics of the rate dependence of yield in amorphous thermoplastic polymers and the physics of liquid armor. The change in heat capacity ΔC_p which appears as a pseudo second order phase transition near T_g should be determined predictably by the changes in the degree of freedom of the oscillators from $d=3$ to $d=D_f$ (fracton dimension) as well as the density of states $G(\omega) \sim \omega^{d_f}$. The T_g value of thin films will be affected by finite size percolation effects. The existence of the twinkling fractal will also allow welding of glassy polymers below their T_g via gradient percolation effects, where the fractal *dances* while twinkling.

When the temperature drops below T_g , then the fractal has its greatest manifestation on the evolution of the glassy structure. With decreasing temperature, the low frequency components of the twinkling fractal spectrum slow down or become negligible and the fractal becomes quite rigid such that the normal volumetric contraction experienced in the liquid state deviates from the extrapolated liquidus line V_∞ and a non equilibrium fractal cavitation process commences resulting in the usual ΔV noted between V_g and V_∞ . Thus, the thermal expansion coefficient in the glass α_g is less than in the liquid state α_L approximately as $\alpha_g \approx p_c \alpha_L$. For the Morse oscillator of equilibrium interatomic distance R_o , anharmonicity factor a , bond energy D_o , the critical distance $X_c = 1/3a$ and T_g is determined at p_c by:

$$T_g = D_o/9k \quad (3.2)$$

The (linear) thermal expansion coefficient in the liquid is

$$\alpha = 3k/[4 D_o R_o a] \quad (3.3)$$

which is related to T_g via Eq 3.2. For example, if $D_o = 7$ kcal/mol, Eq 3.2 gives $T_g = 391$ °K (118 °C); using $R_o = 3$ Å and $a = 2/\text{Å}$, then Eq 3.3 predicts that $\alpha = 35$ ppm/°K.

Physical aging occurs thru the relaxation of this ΔV and is complex. Even below T_g , there is a non-zero predictable fraction of liquid atoms remaining, which will cause the twinkling process to continue at an ever slowing pace but allow the non equilibrium structure to eventually approach a new equilibrium value near V_∞ .

When the fracture stress is dominated by yield, the TFT predicts that at $p = p_c$, the stored strain energy required to overcome a percolation number of interatomic oscillators of strength $U(X_c)$ and molar volume V_m is given for a Morse potential by:

$$\sigma_y = [0.16 E [p-p_c] D_o/V_m]^{1/2} \quad (3.4)$$

Note that the term D_o/V_m corresponds to the traditional Cohesive Energy Density. For example, if $E = 1$ GPa, $p = 1$ (high rate of deformation), $p_c = 1/2$, $D_o = 6$ kcal/mol, $V_m = 2 M_o/\rho$, $\rho = 1$ g/cc, the monomer molecular weight $M_o = 100$ g/mol, then Eq 3.4 predicts that $\sigma_y = 100$ MPa. The value of p is also rate and temperature dependent in a manner determined by the

Twinkling Fractal density of states. As T approaches T_g from below, p decreases towards p_c and σ_y decreases accordingly. At high rates of deformation, p increases towards $p = 1$ and σ_y increases. At low rates of deformation, p decreases towards p_c and this is the basis for designing liquid armor, which are liquid layers with particles at $p > p_c$ that turn into solids at high rates.

4. WELDING OF SYMMETRIC THERMOPLASTIC INTERFACES

Symmetric interfaces are the most common type encountered during manufacture by lamination, tow placement and welding of thermoplastic matrices. Figure 5 shows an interface formed by random walk chains diffusing by Reptation dynamics across a polymer-polymer weld line Wool,(1995, 1993). The molecular aspects of interdiffusion of linear entangled polymers ($M > M_c$) during welding of polymer interfaces are summarized in Table 2 (Wool 1995, 2006).

Table 2. Molecular Aspects of Interdiffusion at a Polymer-Polymer Interface

Molecular Aspect	Symbol	Dynamic Relation, $t < T_r$	Static Relation H $t = T_r$	r, s
General Property	$H(t)$	$t^{r/4} M^{-s/4}$	$M^{(3r-s)/4}$	r,s
Average Contour Length	$l(t)$	$t^{1/2} M^{-1/2}$	M	2,2
Number of Chains	$\Sigma(t)$	$t^{1/4} M^{-5/4}$	$M^{-1/2}$	1,5
Number of Bridges	$P(t)$	$t^{1/2} M^{-3/2}$	M^0	2,6
Average Monomer Diffusion Depth	$X(t)$	$t^{1/4} M^{-1/4}$	$M^{1/2}$	1,1
Total Number of Monomers Diffused	$N(t)$	$t^{3/4} M^{-7/4}$	$M^{1/2}$	3,7
Center of Mass Diffusion	X_{cm}	$t^{1/2} M^{-1}$	$M^{1/2}$	2,4

The Reptation dynamics and the interface structure relations have been demonstrated experimentally by a series of interdiffusion experiments with selectively deuterated polymers using Dynamic Secondary Ion Mass Spectroscopy (DSIMS) and Neutron Reflectivity Welp (1998), Agrawal, Wool, Dozier, Felcher, Zhou, Mays, Russel (1996); Russel, Deline, Dozier, Felcher, Agrawal, Wool, Mays (1993), Agrawal et al(1994); Whitloe, Wool, (1989). The scaling laws and the complete concentration profiles have been calculated by Kim et al (1983) and Zhang et al (1983). The important result for the contour length $L \sim (t/M)^{1/2}$, was also supported by welding computer simulations of Anderson et al (2004). Initially, as the symmetric (A=B) interface wets by local Rouse segmental dynamics, we find that rapid interdiffusion occurs to distances of the order of the radius of gyration of the entanglement molecular weight, ca 30 Å. This can also occur below T_g when the top surface layer becomes more mobile than the bulk and can be explained by finite size rigidity percolation theory Wool et al (2006). However, at this point, the interface is very weak and fracture can be described by the Nail solution Wool, Bailey, Friend (1996). At the wetting stage, the frictional pullout of intermeshed chain segments, which have “elbowed” their way across the interface, determines the fracture energy. As welding proceeds, Σ minor chains of length L diffuse into an interface of width X and

considerable strength develops. The diffusing chains are fractal random walks and interpenetrate with chains, which are fully entangled (ignoring surface reflection configuration effects on entanglement density).

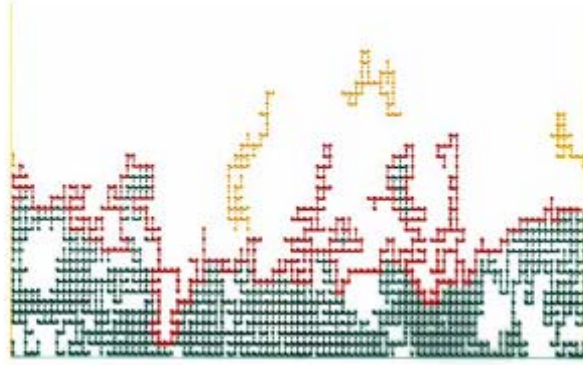


Fig.5 Fractal interface formed by interdiffusing polymer chains. Only one side is shown: Green region. Chains connected with other side at bottom; Yellow chains—those chains which have reached their equilibrium diffused distance and continue to diffuse away but are no longer connected top the other side. Red region. The fractal diffusion line separating the non-connected from the connected chains which provide strength at the interface.

The structure of the diffuse weld interface in Figure 5 resembles a green box of average width X , with fractal edges containing a gradient of interdiffused chains, as shown by Wool and Long Wool, Long (1993). Gradient percolation theory Sapoval, Rosso, Gouyet (1985) requires that chains, which contribute to the interface strength (green), straddle the interface plane during welding, such that chains in the concentration gradient which have diffused further than their radius of gyration (yellow) cease to be involved in the load bearing process at the interface. We have shown that this amounts to a very small number and for narrow molecular weight distributions, can be ignored Wool (1983); Wool et al (1993). However, for broad molecular weight distributions, as we show in a later section of this paper, the fraction of non-connected chains expressed through gradient percolation, can be significant. When the local stress exceeds the yield stress, the deformation zone forms and the oriented craze fibrils consist of mixtures of fully entangled matrix chains and partially interpenetrated minor chains. Fracture of the weld occurs by disentanglement of the minor chains, or bond rupture. It is interesting to note that if the stress rises to the point where random bond rupture in the network begins to dominate the deformation mechanism, instead of disentanglement, then the weld will appear to be fully healed, regardless of the extent of interdiffusion. This can occur at high rates of testing when the minor chains cannot disentangle and bond rupture pervades the interface, breaking both the minor chains and the matrix chains.

The percolation term $[p-p_c]$ determines the number of bonds to be broken, or disentangled such that when Σ chains, each with L/L_c entanglements per chain, interdiffuse in an interface of width X , we obtain Wool (1995); Wool et al (2006):

$$[p-p_c] \sim \{\Sigma L/X - [\Sigma L/X]_c\} \quad (4.1)$$

where $p_c \sim [\Sigma L/X]_c$. Since $\Sigma/X \sim 1/M$ (Table 2), it follows that $p_c \sim L_c/M$. Thus, when the interdiffused minor chain length $L \approx M_c$, we have no strength (above that of the Nail solution),

and when $M \gg M_c$, $p_c \approx 0$, which we will assume henceforth for the welding analysis. In terms of a time argument, the time at which p_c is reached is controlled largely by Rouse segmental dynamics, which is much shorter than the long interdiffusion time determined by Reptation dynamics de Gennes (1971). Thus, the slower interdiffusion process will dominate strength evolution vs. time.

The interface of width X is composed of a fraction L/M of diffusing chains and the matrix chain fraction $(1-L/M)$, into which the chains are diffusing. The total stored strain energy in the interface $U \sim X$, is consumed in disentangling only the Σ minor chains of length L , from the matrix chains, the latter being stretched also but cannot disentangle at the same rate as the minor chains, and we obtain, $G_{1c} \sim p$ as:

$$G_{1c} \sim \Sigma L / X \quad (4.2)$$

When the matrix chains disentangle or break along with the interdiffused chains, then $p = 1$ and the virgin strength is reached. The number of diffusing chains Σ , contributing to the strength at the interface is governed by gradient percolation, such that chains, which do not straddle the interface, are not counted. Also, the length L implies the number of entanglements per minor chain L/L_c , which can decrease significantly, for example, if brush-like ordering occurs at the interface, or the entanglement topology changes such that L_c becomes very large as in a solvent where $M_c \sim$ polymer concentration.

Since $\Sigma \sim X/M$ (Table 4.1) and $L \sim t/\tau^{1/2}$, we obtain the time dependence of welding as:

$$G_{1c}(t) = G_{1c}^* (t/\tau^*)^{1/2} \quad (4.3)$$

where G_{1c}^* is the maximum strength obtained at $M^* \approx 8M_c$ and is independent of molecular weight. The average contour length $\langle L \rangle$ controls the disentanglement process via $\lambda_c \approx [\langle L \rangle / L_c]^{1/2}$. The welding time τ , to achieve complete strength, according to the Reptation modeled de Gennes (1971); Edward (1967), behaves as $\tau \sim M^3$, in which $M < M^*$.

When $M > M^*$, the welding time is determined by the time required to diffuse a distance of order of the radius of gyration of M^* , such that $\tau^* \sim M^{*2}M$. Even though the welding time $\tau^* \sim M$ is shorter than $T_r \sim M^3$, the molecular weight dependence of the welding rate remains unaffected and we have for all molecular weights:

$$G_{1c}(t) \sim t^{1/2} M^{1/2} \quad (4.4)$$

which is consistent with the early Wool-O'Connor welding theory $G \sim L$. Experimental support for Eq 4.4 was reported by O'Connor Wool et al (1981); (1982) and Wool, Yuan, McGarel (1989) and reviewed by Wool (1995).

In the case of chain-end segregation to the surfaces, as can occur in crack healing and some latex particle coalescence during film formation, the number of chains Σ is constant and the percolation term becomes $p \sim L/X$, or $p \sim X$, since $X \sim L^{1/2}$. Thus, from Table 4.1, the strength development would be $G_{1c} \sim (t/M)^{1/4}$, rather than the usual $t^{1/2}$ dependence. This $t^{1/4}$ result was also predicted by Prager and Tirrell, using a crossing density analysis Prager, Tirrell (1981), but with a different molecular weight dependence for both the welding and virgin state.

The full interpenetration of chains (X approaches R_g) is not necessary to achieve complete strength, when $M > M^*$ and $\tau^* < T_r$. However, a cautionary note: while complete strength may

be obtained in terms of critical fracture measures, such as G_{1c} and K_{1c} , the durability, measured in sub-critical fracture terms, such as the fatigue crack propagation rate da/dN , may be very far from its fully healed state at τ^* . We have shown that while the weld toughness K_{1c} increases linearly with interdiffusion depth X as $K_{1c} \sim X$, the fatigue crack propagation behavior of partially healed welds behaves as Wool (1995); Wool et al (1981):

$$da/dN \sim X^5 \quad (4.5)$$

This fatigue behavior is a very strong function of interdiffusion and underscores the penalty to pay for partial welding. Thus, the weld strength may be close to the virgin strength but the fatigue strength may be dramatically reduced below its maximum value. Thus, one should always design a welding time with respect to T_r to achieve maximum durability of welds and interfaces. The time to achieve complete strength is related to the Reptation time by:

$$\tau^* = 64 (M_c/M)^2 T_r \quad (4.6)$$

such that when $M = 8M_c$, $\tau^* = T_r$. The Reptation time T_r is determined from the self-diffusion coefficient D and the end-to-end vector R , by:

$$T_r = R^2/(3\pi^2 D) \quad (4.7)$$

For example, when welding polystyrene at 125 C, $D \approx 4 \times 10^{-6}/M^2$ (cm²/s) [21], $R^2 = 0.45 \times 10^{-16}$ M (cm²) such that $T_r = 4 \times 10^{-13}$ M³ (s) and $\tau^* = 0.0234$ M (s). For the case where $M = 400,000$ and $M_c = 30,000$, we have $\tau^*/T_r = 0.36$, where $T_r = 435$ min and $\tau^* = 156$ min. In this example, if the maximum weld strength is obtained at an allowed welding time of 156 min, the durability as measured by da/dN , would only be about 1/5 of its virgin value compared to complete welding at $T_r = 435$ min. When plastic parts are being injection molded, laminated, sintered or co-extruded, many internal weld lines are encountered and this aspect of welding needs to be considered in designing materials with optimal durability Wool(1995).

In summary, the strength development during welding of polymers is well described by the relation,

$$G_{1c} = G_{1c}^* (t/\tau)^{1/2} \quad (4.8)$$

where G_{1c}^* is the virgin strength determined by the percolation theory, and τ is the welding time, such that $\tau \sim M$ when $M > M^*$, and $\tau \sim M^3$ when $M < M^*$. Eq 4.8 reflects the scaling law for welding processes which are dominated by the diffusion stage of healing. However, as discussed in detail elsewhere Wool (1995); Wool, O'Conner (1981), the other stages of welding, such as surface approach, surface rearrangement, wetting and randomization can play a major role in the time dependence of the overall strength development.

5. IMPORTANT ISSUES ON FATIGUE OF WELDED THERMOPLASTIC INTERFACES

The total interpenetration of chains (X approaches R_g) is not necessary to achieve complete strength when $M > M^*$ and $\tau^* < T_r$. However, a word of caution: while complete strength may

be obtained in terms of critical fracture measures such as G_{1c} and K_{1c} , the durability, measured in sub-critical fracture terms, such as the fatigue crack propagation rate da/dN , may be very far from its fully healed state at τ^* . We have shown that while the weld toughness K_{1c} increases linearly with interdiffusion depth X , as $K_{1c} \sim X$, the fatigue crack propagation behavior of partially healed welds behaves as Wool (1995):

$$da/dN \sim X^5 \quad (5.1)$$

which is a very strong function of interdiffusion and underscores the penalty to pay for partial welding. Thus, the weld strength may be near, or at the virgin strength, but the fatigue strength may be dramatically reduced below its maximum value. Thus, one should always design a welding time with respect to T_r to achieve maximum durability of welds and interfaces. This is a rather subtle processing point, which is often not appreciated by the manufacturing industry.

In fatigue of polymers with applied stress $\sigma_{app} < \sigma_c$, the percolation theory suggests a new approach as follows: the lifetime τ occurs when the initial fraction of bonds p_i is reduced to p_f , such that fracture occurs at the applied stress in accord with Eq (2.5) as Wool(2006):

$$\sigma_{app} = \{2ED_o\nu [p_f - p_c]\}^{1/2} \quad (5.2)$$

This gives p_f for the applied stress as

$$p_f = p_c + \sigma_{app}^2 / \{2ED_o\nu\} \quad (5.3)$$

The time dependence of p can be deduced from a steady state bond fracture concept via

$$P_f = p_i - \tau dp/dt \quad (5.4)$$

such that the failure time τ is the time required to reduce p_i to p_f at the prevailing breakage rate dp/dt . The rate of bond rupture dp/dt can be given by a thermally activated state theory (ala Zhurkov discussed in ref Kausch (1984) as:

$$dp/dt = (1/\tau_o) \exp -D_o[1 - \sigma_{app}/\sigma_c]/kT \quad (5.5)$$

in which the energy for fracture D_o is linearly reduced by the applied stress. Substituting for dp/dt and p_f in Eq 5.4 and solving for τ , we obtain the lifetime of the material as:

$$\tau = \tau_o \{ [p_i - p_c] - \sigma_{app}^2 / (2ED_o\nu) \} \exp D_o[1 - \sigma_{app}/\sigma_c]/kT \quad (5.6)$$

where $D_o/kT \approx 133$ at room temperature and $\tau_o \approx 10^{-12}$ sec is the vibrational period for the bonds being broken. For a material without defects, $p_i = 1$ and σ_c is determined from Eq (5.2) using $p_f = 1$. Note that the applied stress enters in both the front factor and exponential factor for τ . When the applied stresses are small, the exponential factors dominate and the ratio of two lifetimes at applied stresses σ_1 and σ_2 would be:

$$\tau_1/\tau_2 = \exp [(\sigma_2 - \sigma_1)/\sigma_c] D_o/kT \quad (5.7)$$

Representative S-N fatigue data is shown above and compared with Eq 5.7 in which $D_o/kT = 17.27$ and $\sigma_c \approx 300$ MPa

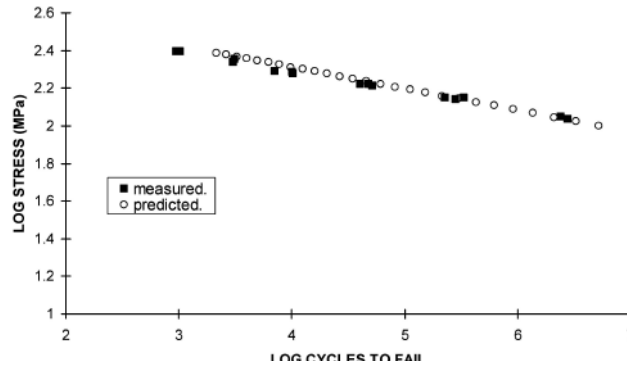


Fig.6 Stress Failure Cycle data for Nylon 66 Polyamide (33% wt% glass filled) subjected to cyclic flex fatigue. Wyzgoski and Novak (2005).

6. POLYDISPERSITY EFFECTS ON WELDING AND FATIGUE

A method to analyze the interdiffusion of polydisperse interfaces with a molecular weight distribution function $\phi(M)$ was developed by for both isothermal any non-isothermal welding conditions. The number average molecular weight M_n and weight average molecular weight M_w is related to the weight fraction w_i of M_i by:

$$M_n = 1 / [\sum w_i / M_i] \quad (6.1)$$

$$M_w = \sum w_i M_i \quad (6.2)$$

Fig.7 Shows a molecular weight distribution used in thermoplastic matrices which has about 12 different M_i species. $\phi(M)$ has a Polydispersity $PD = M_w/M_n = 8.6$ with $M_n = 50,000$. The resulting interdiffused contour length L is determined at ant time during welding from the summation of the individual fractions of $\phi(M)$ which are dynamic $L(t)$ and those which have interdiffused to their equilibrium contour lengths L_∞ . At any welding time t , the molecular weight distribution $\phi(M)$ can be separated into its dynamic components $L_i(t)$ and those that have fully interdiffused $L_{i\infty}$, by the “scanning” molecular weight M^{++} (red line in Fig 7), such that when $M_i < M^{++}$, those values of M_i which have reached their equilibrium or fully interdiffused state and those M_i values with $M_i > M^{++}$ are partially interdiffused. The average interdiffused contour length is given by the summation:

$$L(t, M^{++}) = \sum^{++} w_i M_i + \sum^{++} w_i M^{++3/2} / M_i^{1/2} \quad (6.3)$$

in which M^{++} is related to the diffusion time by

$$M^{++} \sim t^{1/3} \quad (6.4)$$

Interfaces and their tailoring

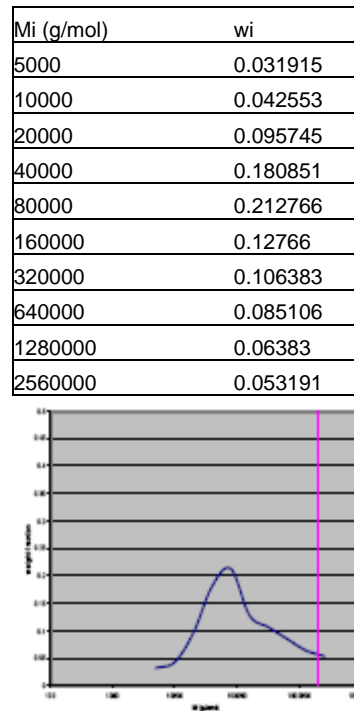


Fig.7 Molecular weight distribution $\phi(M)$ for a typical Thermoplastic Matrix. The weight fractions w_i and molecular weights M_i are listed above

The resulting interdiffusion contour length for a typical A/A weld is shown in Figure 6.2, where $L(t)$ is plotted vs. $t^{1/2}$. We have shown in detailed studies that the fracture energy G is related to the average interdiffused contour length via:

$$G \sim L \quad (6.5)$$

Figure 8 shows that the initial slope of L vs. $t^{1/2}$ increases linearly as expected since all molecular weight species are interdiffusing according to

$$L_i \sim (t/M_i)^{1/2} \quad (6.6)$$

However, at longer times we see that the diffusion slope continues to decrease as the higher molecular weight species continue to diffuse more slowly and the low molecular weight species (which give high initial slopes) have reached their equilibrium state and no longer contribute additional strength in accord with gradient percolation theory. The latter theory basically states that molecules only contribute to strength which straddle the interface or are in contact with both sides, thus providing connectivity. Such polydisperse plots shown in Figure 8 are non-linear on a $t^{1/2}$ scale and when plotted as $\text{Log } G$ vs $\text{Log } t$ will provide a slope typically closer to $1/4$, but definitely less than $1/2$. This slope has no particular dynamics or structural meaning and has often been misinterpreted. It is a simple consequence of the Polydispersity effect allowing chains of different lengths to interdiffuse at different rates.

Wool

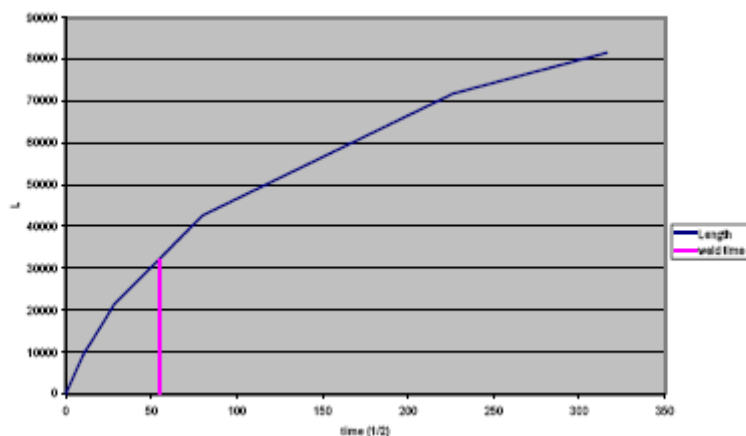


Fig.8 Average contour length $L(t)$ vs. weld time $t^{1/2}$ for a polydisperse interface with $PD = 8.4$ containing 10 monodisperse fractions of different weight fractions. The weld time for fracture stress is shown by the red line at $L = 32,000$ corresponding to $L^* = 8 M_c$. The weld time for maximum fatigue resistance corresponds to $L = 80,000$.

7. BI-DISPERSE MODEL THERMOPLASTIC INTERFACES

We examined the weld strength of bi-disperse samples of polystyrene, where the $\phi(M)$ was derived by mixing two monodisperse fractions of varying weight fractions and molecular weights. Bi-disperse interfaces were prepared from two polystyrene batches with different molecular weights; 184 kDa and 1044 kDa. Equal weight samples from both batches were mixed in 5 mL of toluene for about 30 minutes. The mixture was then pasted onto two trays and left overnight to let the toluene evaporate completely. The two interfaces were brought together to allow wetting at the temperature of 70°C for about 24 hours. The samples were then welded for different lengths of time: varying between 10 minutes to 25 hours in a vacuum chamber. The fracture strength of each sample was tested using the Double Cantilever Beam (DCB) method Wool (1995). Figure 9 shows predicted simulation results for $M_1 = 187$ kDa and $M_2 = 1044$ kDa with $w_1 = w_2 = 0.5$ [34]. The “knee” break in the data is quite explicit and should occur at a precise time.

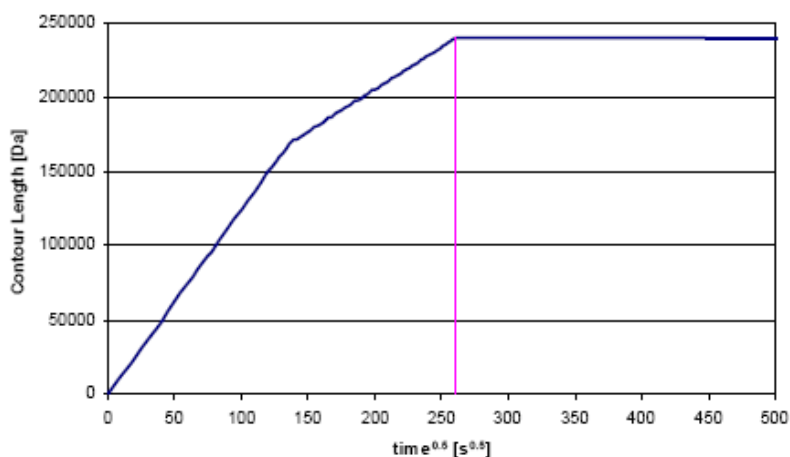


Fig.9 Contour length versus welding time for bi-disperse symmetrical interface: 184 kDa and 1044 kDa, $PDI=1.9$

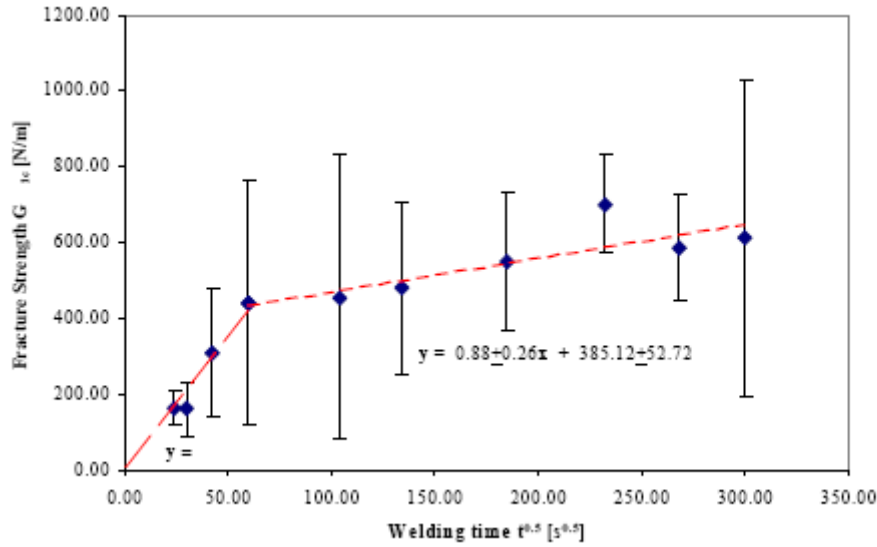


Fig. 10 Fracture energy G_{IC} versus welding time $t^{1/2}$ for a bi-disperse symmetrical interface: $M_1 = 184$ kDa and $M_2 = 1044$ kDa, PDI=1.9

Figure 10 shows the experimental results for the bi-disperse PS welding experiments Adnan, Wool (2006). It is observed that before the slope break, the fracture strength, G_{IC} is proportional to $t^{0.5}$ with the prefactor 7.04 ± 0.37 . After the slope break, G_{IC} has a proportionality constant of 0.88 ± 0.26 to $t^{0.5}$. The initial slope $M^{-1/2}$ is dominated by the lower molecular weight fraction. After it reaches its equilibrium state near the bend in the curve, the higher molecular weight fraction dominates with a proportionately lower slope. The welding time τ_w to optimize fracture strength for a bi-disperse interface is given by:

$$\tau_w = [(L^* - w_1 L_1)/w_2]^2 L_2 \quad (7.1)$$

where $L_1 \sim M_1$, $L_2 \sim M_2$ and $L^* \sim M^* = 8 M_c$. Note that $L_1 < L^*$ and $L_2 > L^*$. As w_2 goes to 1, $\tau_w = L_2 L^{*2} \sim M_2$, which is correct. As w_2 goes to zero τ_w goes to infinity since L^* is never reached. The fastest welding time occurs when $L_1 = L^*$ and $w_1 = 1$. The slowest welding time occurs when $w_2 = 1$.

8. SUB-TG WELDING

Welding below T_g , as demonstrated by Boiko et al (2003), (2004) can occur due to softening of the surface layer as shown in Figure 8.1. We have treated the surface layer softening as a gradient rigidity percolation issue Wool et al (2006). The surface rubbery layer concept in thick films is interesting and this percolation theory suggests that for free surfaces there is a gradient of $p(x)$ near the surface, where $x < \xi$ (cluster size correlation length) and hence a gradient in both T_g and modulus E . If the gradient of p is given by $p(x) = (1 - x/\xi)$ then the value of X_c for which the gradient percolation threshold p_c occurs, and which defines the thickness of the surface mobile layer, is given by the percolation theory as Wool et al (2006)

$$X_c = b (1-p_c) / \{p_c^v [1-T/T_g]^v\} \quad (8.1)$$

Wool

Here b is the bond length and ν is the critical exponent for the cluster correlation length $\xi \sim [p - p_c]^\nu$. For example with polystyrene, when $T = T_g - 10$ °K, $T_g = 373$ °K and using $b = 0.154$ nm, $p_c = 0.4$, $\nu = 0.82$, then the thickness of the surface mobile layer $X^* = 3.8$ nm. This could allow for healing to occur below T_g assuming that the dynamics are fast enough, since the mobile layers on both surfaces effectively disappear when the interface is formed.

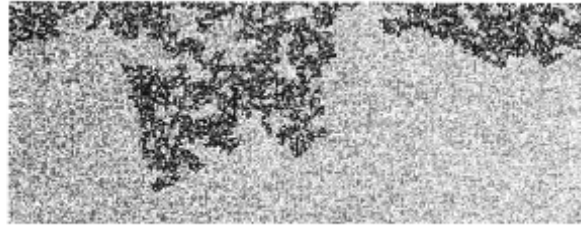


Fig. 11 Simulation of Finite clusters of liquid atoms (black) are shown in a film of thickness h at $T < T_g$. The fraction $p = 0.58$. The accessed (dark) fraction $f = 17\%$ Wool et al (2006)

Since $G_{1c} \sim X^2$ for entangled polymers, then we could deduce for sub T_g healing at $\Delta T = T_g - T$, that G_{1c} should behave as:

$$G_{1c} \sim [1/\Delta T]^{2\nu} \quad (8.2)$$

This appears to be in qualitative agreement with Boiko's data et al (2004) who examined the fracture energy of polystyrene interfaces during welding at temperatures up to 40 °K below T_g .

ACKNOWLEDGEMENTS

The author is grateful to the Army Materials Research Laboratory, Aberdeen MD, for financial support of this work through the CMR-ARL program at the Center for Composite Materials, University of Delaware

REFERENCES

- Adnan N. and Wool R.P (2006), summer research at the University of Delaware
- Agrawal, G, Wool, R. P., Dozier, W.D., Felcher, G. Z. P., Zhou, J., Mays, J.W., and Russell T P (1996). *J. Polym. Sci., Part B*, 34, 2919
- Agrawal, G., Wool, R. P., Dozier, W. D., Felcher, G. P., Russell, T. P., and Mays, J. W (1994). *Macromolecules*, 27, 4407.
- Anderson K. L., Wescott J. T., Carver T. J. and Windle A. H. (2004). "Mesoscale modeling of polymer welding", *Materials Science and Engineering A*, Vol 365, Issue 1-2, Page 14,
- Barnette, A., McAninch, I., Wool R.P (2006). *Bull Amer. Phys Soc.*
- Boiko Y.M. (2003). *Mechanics of Composite Materials*, 31(1) 89.

Interfaces and their tailoring

- Boiko, Y. M.; Bach, A.; Lyngaa-Jørgensen, J. (2004). *J. Polym Sci., Part B, Polym Phys*, 42 1861.
- Born M. and Huang K (1971), *Dynamical Theory of Crystal Lattices*, Oxford University Press.
- De Gennes, P.-G. (1971). *J. Chem. Phys.*, 55, 572.
- Edwards, S. F, (1967). *J. Chem. Soc, London*, 92, 9.
- Hutchinson J .W (1997), “Linking Scales in Fracture Mechanics” Plenary Address, Proceedings of the Ninth International Conference on Fracture, Sydney Australia.
- Kantor, Y. and Webman, (1984), *Phys. Rev Lett.*, 52, 1891, New York, 1954.
- Kausch, H. H. (1984), *Polymer Fracture*, 2nd ed., Springer-Verlag, Berlin,
- Kim, Y. H. and Wool, R. P. (1983), *Macromolecules*, 16, 11.
- McCormick, H.W., Brower F.M. and Kin, L, (1959), *J. Polym. Sci*, 39, 87.
- Pitman, G.L. and Ward, I.M. (1970), *Polymer*, 20, 897.
- Prager, S. and Tirrell, M. (1981), *J. Chem. Phys.*, 75, 5194.
- Russell, T. P., Deline, V. R., Dozier, W. D., Felcher, G. P., Agrawal, G., Wool, R. P., and Mays, J. W (1993), *Nature*, 365, 235.
- Sapoval, B; Rosso, M.; Gouyet, J. F. J. (1985). *Physique Lett.*, 46, L149.
- Tvergaard. V, and Hutchinson, J.W. (1996). *J de Physique IV*, 6(C6), 165.
- Tvergaard V and Hutchinson J.W. (1993). *J. Mechanics and Physics of Solids*, 41: (6) 1119
- Vincent, P.I., (1972). *Polymer*, 13, 557.
- Welp, K. A., Wool, R. P., Mays J., Pispas, A and Satija S., (1998). *Macromolecules*, 31(15) 49
- Whitlow, S. J. and Wool R. P. (1989). *Macromolecules*, , 22, 2648: 1991, 24, 5926
- Wool, R. P (1995), *Polymer Interfaces: Structure and Strength*, Hanser Press, NewYork
- Wool, R. P., (2006). *C. R Chimie*, Vol 9, 25-44
- Wool R. P (2005), *J. Polym Sci, Part B., Polym Phys Ed.*, 43, 168
- Wool R. P. (2007), “Twinkling Fractal Theory of The Glass Transition and Yield”, *Polymer Preprints, Amer. Chem. Soc., Proceedings, Boston*

Wool

- Wool R. P. et al (2004) "Bio-Based Composites", Proceedings of the European Congress of Composites Materials, ECCM-11, Rhodes, Greece.
- Wool R. P., Bretzlaff, R. S., Li, B. Y., Wang C. H. and Boyd, R. H (1986), *J. Polym. Sci., Polym. Phys. Ed*, 24, 1039.
- Wool, R. P and Sun X.S (2005), *Bio-based Polymers and Composites*, Elsevier
- Wool, R.P. and Long, J.M (1993) *Macromolecules*, 26, 5227.
- Wool R. P., Bailey D., Friend, A, J (1996). *Adhesion Sci. and Technol.*, 10, 305
- Wool, R. P. and O'Connor K. M. (1981), *J. Appl. Phys.*, 52, 5953.
- Wool, R. P. and O'Connor K. M. (1982), *J. Polym. Sci., Polym. Lett. Ed.*, 20, 7.
- Wool, R. P, Yuan B.-L and McGarel O. J (1989), *Polym. Eng. and Sci.*, 29, 1340.
- Wool, R.P (2006), Proceedings of the 13 th International Conference on Deformation, Yield and Fracture of Polymers, Kerkrade, NL, 27-31
- Zhang, H. and Wool R. P. (1989), *Macromolecules*, 22, 3018

INFLUENCE OF TEMPERATURE ON COHESIVE PARAMETERS FOR ADHESIVES

Anders Biel¹ and Thomas Carlberger²

¹University of Skövde, PO Box 408, SE-541 28 Skövde, SWEDEN
anders.biel@his.se, telephone: +46 500-44 85 27

²SAAB Automobile AB, SE-461 80 Trollhättan, SWEDEN
thomas.carlberger@se.saab.com, telephone: +46 520-84 119

ABSTRACT

Experiments are performed to evaluate the temperature dependence of the stress-elongation relation for an engineering epoxy adhesive. Seven temperatures from -40°C to 80°C are considered. At each temperature, about seven experiments are performed with a double cantilever beam specimen. The experiments are evaluated using an inverse solution. The results show that the peak stress decreases monotonically with temperature, from about 55 MPa at -40°C to about 11 MPa at 80°C. Thus, the shape of the stress-elongation relation varies with the temperature. At higher temperatures, the fracture energy decreases slightly.

1. INTRODUCTION

Polymers are known to be strongly temperature dependent. Adhesives, which consist mainly of polymers, are therefore believed to be temperature dependent. In an automotive car body, the material temperature may span a significant temperature range. Excluding the engine compartment, measurements show temperatures in the range -40°C to 125°C. Thermo-set adhesives typically show a glass transition temperature, T_G , between 85°C and 120°C. Thus, the temperature effect is expected to be significant in the present temperature range.

An automotive structure subjected to impact is supposed to fulfil the crash requirements throughout its specified temperature range. In the open literature, only limited information is available concerning temperature dependencies of the stress-elongation relation. Some temperature studies have been performed cf. e.g. Ashcroft et al. (2001) which show a transition in fracture mode from brittle at -50°C, stick-slip at 22°C to ductile at 90°C. To this end, it is noticeable that recent developments of crashworthy adhesives are focusing on increasing fracture energy rather than ultimate strength. This new behaviour is created through alteration of the chemical mixture e.g. by adding minerals or thermoplastics. Such chemical modifications are likely to influence the temperature dependency of the adhesive, inducing the need for

renewed temperature studies.

It is well known that adhesives in the form of a thin layer between stiffer adherends behave differently from the adhesive as a bulk material. This is due to the constrained state of deformation. An effect of the influence of the constraint is the variation of the fracture energy with the thickness of the adhesive layer; cf. e.g. Kinloch (1987).

A convenient method to determine the adhesive properties is the use of simple test geometries and inverse formulas as described in e.g. Andersson and Biel (2006) and Leffler et al. (2007). Olsson and Stigh (1989) develop an inverse method for pure peel using the double cantilever beam (DCB) specimen, cf. Fig. 1.

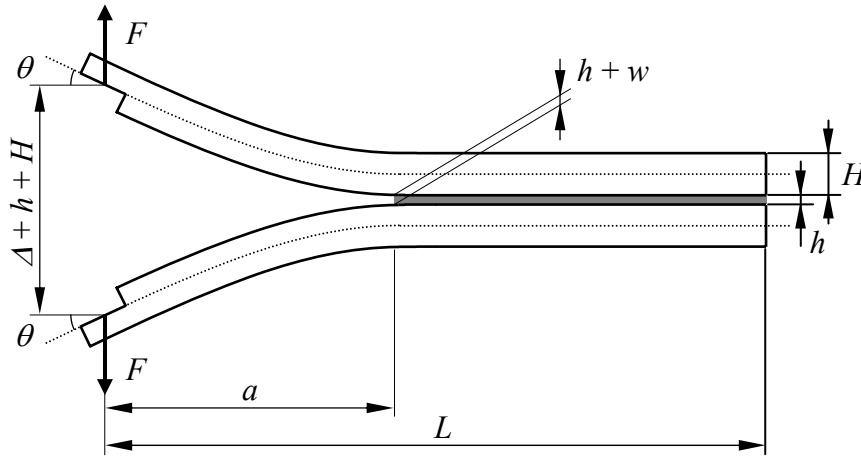


Fig. 1. Double cantilever beam specimen. Unbonded part of the specimen can be considered as a crack, i.e. a is the crack length.

During an experiment, the applied force, F , and the rotation of the loading point, θ , are measured as functions of the elongation w of the adhesive at the start of the adhesive layer. The inverse formula reads

$$\sigma = \frac{dJ}{dw} = \frac{d}{dw} \left(\frac{2F\theta}{b} \right), \quad (1)$$

where b is the width of the specimen. The result is the stress-elongation relation for the adhesive layer. This relation is closely related to the fracture energy of the adhesive. An application of the path independent J -integral shows that the area under the stress-elongation relation equals the fracture energy, cf. e.g. Andersson and Stigh (2004). The present adhesive, DOW-Betamate XW 1044-3, has been extensively studied at room temperature, cf. Andersson and Stigh (2004); Andersson and Biel (2006).

In the present study we study the influence of temperature on the stress-elongation relation. The temperature range is -40°C to 80°C in intervals of 20°C . Special consideration is given the variation of fracture energy and peak stress with temperature.

2. EXPERIMENTS

2.1 Experimental setup and procedure

The test machine is specially designed for testing of DCB-specimens, cf. Fig. 2. The specimen is oriented vertically. Both crossheads are moving symmetrically around the centre of the machine. Two horizontally working ball screws powered by an electric motor control the motion. A load cell measures the force F . The angle, θ , at the loading point is measured with an incremental shaft encoder. The position of the crossheads is measured with a linear potentiometer. Two Linear Voltage Differential Transformers (LVDT) are applied at the outside of the adherends to measure the elongation of the adhesive layer at the start of the layer (not shown in Fig. 2).

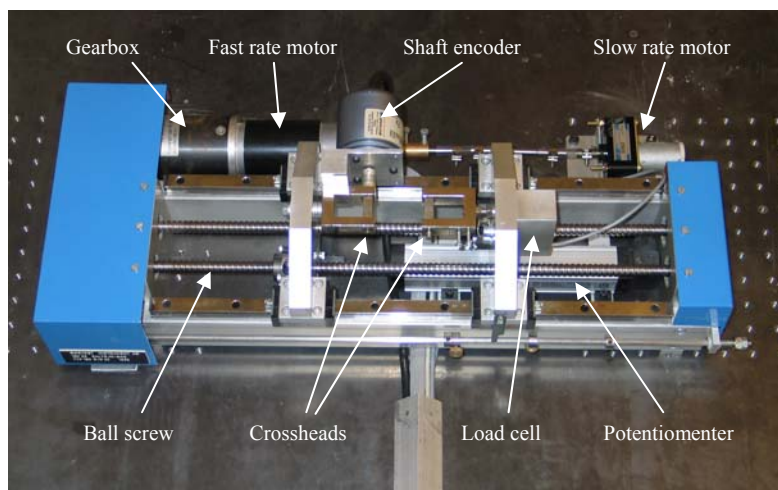


Fig. 2. Test machine without LVDT:s and specimen

The specimens and the entire tensile test machine, except the control box and the computer for data acquisition, are placed in a climate chamber. When the desired temperature is stabilised the test equipment is calibrated. Subsequently a specimen is mounted. After an additional temperature check the experiment is performed. The temperature is measured individually for each experiment using a thermocouple attached to a dummy specimen in the climate chamber. A temperature variation of $\pm 2^\circ\text{C}$ is allowed.

2.2 Specimens

The adhesive is an engineering epoxy, DOW-Betamate XW 1044-3. The curing condition is 180°C for 30 minutes. At room temperature the adhesive has a viscosity of 4 kPas (similar to toffee) and it is preheated to about 50°C before application. After curing, $T_G \approx 90^\circ\text{C}$.

The dimensions of the specimens are $L = 165$ mm, $a = 80$ mm, $b = 5$ mm, $H = 6.6$ mm, and $h = 0.2$ mm, cf. Fig. 1. The adherends are made of tool steel, Rigor Uddeholm, with a yield-strength larger than 500 MPa securing elastic behaviour of the adherends during the experiments. Two plates are joined with the adhesive. The initial crack length is created by a 0.2 mm thick PTFE-film that also works as a distance giving the correct layer thickness. Before applying the adhesive, the plates are cleaned with heptane and acetone. The adhesive is cured for 30 minutes at 180°C . Slow cooling is allowed in order to minimise the influence of residual stresses. After curing, the plates are cut into specimens by use of band saw. Subsequently, the specimens are machined to final dimensions.

2.3 Experiments

The experiments are performed with a nominally constant crosshead velocity, $d\Delta/dt = 10$ $\mu\text{m/s}$. Due to friction in the machinery, the crosshead velocity varies with the temperature. This is

indicated in Fig. 3 where the strain rate at the peak stress is shown at the different temperatures considered. It may be noted that a constant crosshead velocity results in an increasing strain rate during an experiment. A total of 53 experiments are performed with about seven experiments at each temperature. The mean strain rate at peak stress is shown in Fig. 3 for each temperature.

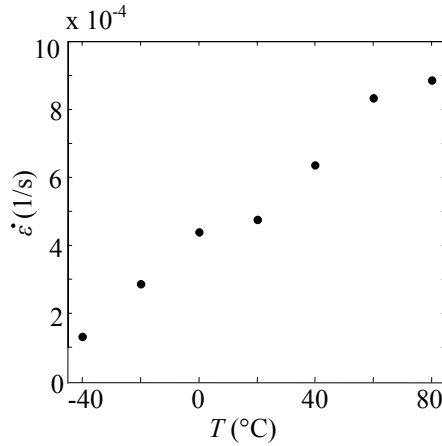


Fig. 3. Strain rate, $\dot{\epsilon}$, at the moment of peak stress in the adhesive vs. temperature, T .

2.4 Experimental results

Figure 4 shows J and σ as functions of w for all temperatures. At each temperature, an average curve is calculated. Evaluation of J is performed by fitting a Prony-series to the J - w curve of each specimen cf. Andersson and Biel (2006). Differentiation of the Prony-series gives the constitutive relation, σ - w , of the adhesive according to Eq. (1).

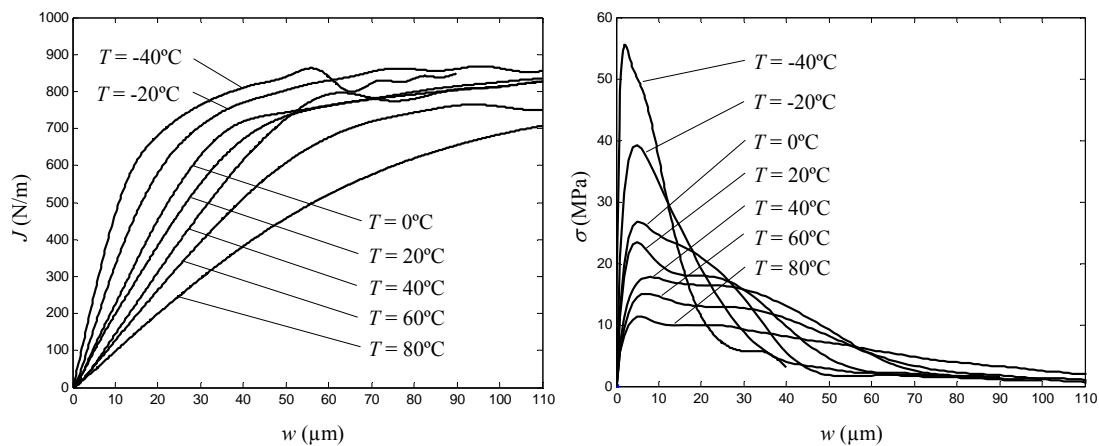


Fig. 4. *Left*: J as a function of w ; *Right*: σ as a function of w .

As shown in Fig. 4, the peak stress and the critical elongation are strongly dependent on the temperature. The elongation at the peak stress occurs at about 2-6 μm for all experiments.

Four of the experiments, three at -40°C and one at 0°C , show an abrupt cusp in the J - w -curve. These four experiments are considered as failures. Initial studies show no signs of initial flaws in the adhesive that might explain this behaviour. Further investigations are required. The result is interpreted as due to a zone of weakness at the start of the adhesive layer. These four experiments are neither included in Fig. 4 nor in the further evaluation of the experiments. The number of evaluated experiments is given in Table 1.

Temperature influence on cohesive parameters for adhesives

Table 1. Number of evaluated test specimens at each temperature.

T	-40°C	-20°C	0°C	20°C	40°C	60°C	80°C
Number of specimens	5	6	7	7	8	8	8

Figure 5 shows the fracture energy for all evaluated experiments; both the average value at each temperature and the standard deviation, s , are shown. At lower temperatures, the fracture energy seems independent of the temperature. For the experiments performed at 60°C and 80°C the fracture energy is slightly lower indicating the vicinity to the glass transition temperature. The maximum temperature for automotive applications is around 120°C. The present test equipment is not specified for this temperature, but future research should include at least this temperature.

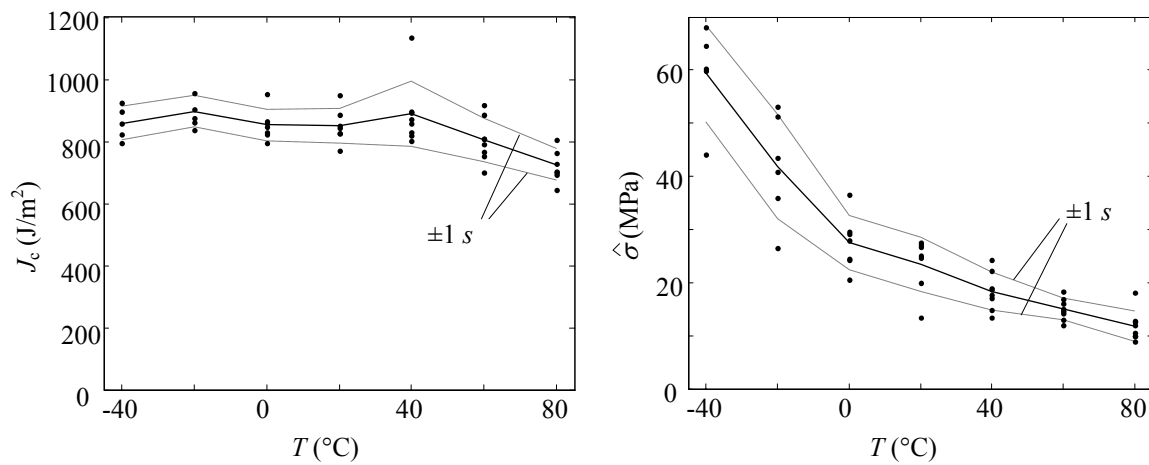


Fig. 5. *Left:* J_c vs. temperature; *Right:* $\hat{\sigma}$ vs. temperature.

Figure 5 shows the peak stress, $\hat{\sigma}$, of the adhesive. The peak stress decreases monotonically with increasing temperature. Thus, there is a substantial difference in the temperature dependence of the fracture energy and the peak stress. An explanation might be that the fracture energy is associated with the covalent bonds in the molecular structure while the peak stress is dependent on both the van der Waals and covalent bonds. The number and stiffness of the van der Waals bonds are expected to decrease with temperature and disappear at T_G . This can be the reason for the monotonic decrease in peak stress. Experiments at temperatures above T_G would then result in a temperature independent peak stress.

Figure 6 shows two fracture surfaces put together and photographed. The fracture surface at 80°C shows more stress-whitening than the fracture surface at -40°C. With the interpretation of the effects of the van der Waals bonds given above, the increase in stress whitening would be associated with increased molecular mobility due to a gradual decrease of van der Waals bonds.

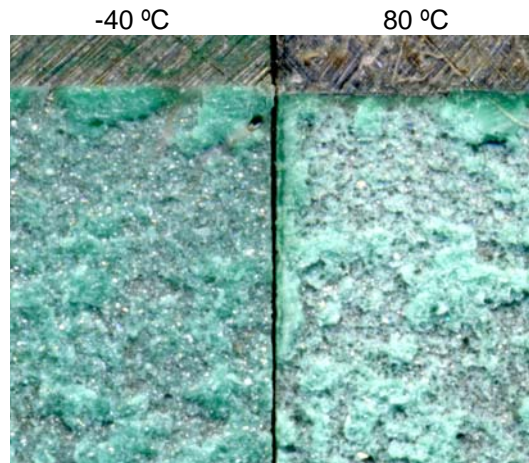


Fig. 6. Fracture surfaces at -40°C and 80°C.

3. CONCLUSIONS

Experiments have been performed to evaluate the temperature dependence of the stress-elongation relation for an engineering epoxy adhesive. The area under the stress-deformation relation, i.e. the fracture energy is virtually independent of the temperature at the lower temperatures considered. At higher temperatures, J_c decreases slightly with T . At the highest temperature, 80°C, J_c has decreased 20 %. The peak stress decreases monotonically for all temperatures considered.

ACKNOWLEDGEMENTS

The authors wish to thank Stefan Zomborcsevics for helping with manufacturing of the specimens and the Swedish Consortium for Crashworthiness for funding this project. Special thanks are also directed to Professor Ulf Stigh for fruitful discussions and help during the work presented in this paper.

REFERENCES

- Andersson T. Biel A. (2006), On the effective constitutive properties of a thin adhesive layer loaded in peel. *Int. J. Fracture*; 141: 227-246.
- Andersson T. Stigh U. (2004). The stress-elongation relation for an adhesive layer loaded in modulus I using equilibrium of energetic forces. *Int. J. Solids Struct.*; 41: 413-434.
- Ashcroft I. A. (2001). Mode I fracture of epoxy bonded composites joints: 1. Quasi-static loading. *Int. J. Adhesion and Adhesives*; 21: 87-99.
- Kinloch, A. J. (1987). *Adhesion and Adhesives – Science and Technology*. Chapman and Hall, London..
- Leffler K. Alfredsson, K. S. and Stigh U. (2007). Shear behaviour of adhesive layers. *Int. J. Solids Struct.*; 44: 530-545.
- Olsson P. and Stigh U (1989),. On the determination of the constitutive properties of the interphase layers – an exact solution. *Int. J. Fracture*; 41: 71-76.

INFLUENCE OF POLYMER GRADE AND COMPATIBILIZER
CONCENTRATION ON THE INTERFACIAL SHEAR STRENGTH
IN SISAL FIBRE POLYPROPYLENE COMPOSITES

C. Burgstaller, W. Stadlbauer

Transfercenter für Kunststofftechnik - UAR
4600 Wels, Austria

ABSTRACT

In this work we investigated the interfacial shear strength for the system sisal polypropylene, regarding the presence of a compatibilizer (maleic anhydride grafted polypropylene) as well as the grade of polypropylene, namely two homopolymers with different flow behaviour. Composites containing different concentrations of sisal fibre and compatibilizer were produced using a co-rotating twin screw extruder and subsequently injection moulded to retrieve test specimens. These specimens were investigated for tensile and notched impact properties, as well as the final fibre length in the composites was determined. With this data, a simple rule of mixtures model was applied to evaluate the tensile strength and notched impact strength for the interfacial shear strength. Further, single fibre pull out tests have been carried out with sisal fibres from polypropylene.

Data for interfacial shear strength, acquired by the single fibre pull out tests fit the data acquired by the evaluation of the mechanical testing very well. Furthermore the presence of a compatibilizer improves the interfacial shear strength, as well as the polypropylene grade shows an influence, which is also found from the single fibre pull out tests. In conclusion this shows good applicability of single fibre pull out tests for estimating composite properties. However, one has to keep in mind several influences, due fibre orientation and processing method, when comparing the results from macromechanical measurements with single fibre pull out tests.

1. INTRODUCTION

Natural fibres in common are known as reinforcements in polymers for a long time. While the first intention to use materials like hemp, flax or wood in thermoplastic polymers was mainly related to their relatively low price, further developments due to their good mechanical performance in combination with their low density and renewability took place. Scientific and industrial interest in these materials increased steadily over the last years. Especially the role of the interface between fibre and matrix, which is known to be a dominant factor in glass fibre

reinforced composites (Thomason 2002, Thomason and Schoolenberg 1994), was investigated several times in literature. A method of characterization, which is often used, is the preparation of fibres with a certain surface treatment and the subsequent processing to yield a composite, which is tested for its properties. This method has the advantage that it shows the final properties in correlation to fibre treatment or additive dosage, but information about the interface, especially about the interfacial shear strength, is hard to acquire most times.

On the other hand, acquisition of the interfacial shear strength is possible via different micromechanical tests, like single fibre pull out or microfragmentation tests (Kim and Mai 1998). Such methods characterize the interface very well, (although there can be some serious problems in sample preparation, especially with thermoplastic matrices) but suffer from the problem that the estimation of composite properties from this key figure is very limited.

The aim of this work was to compare the interfacial shear strength acquired from single fibre pull out tests with the one calculated from the mechanical properties of the composite, especially regarding the influence of the presence of a compatibilizer in two different polypropylene grades.

2. MATERIALS AND METHODS

For this study, 10 – 50 wt% of sisal fibres (with cut length 6 mm) and 0 – 4 wt% compatibilizer (Exxelor PO1020, Exxon Mobile Chemicals) were compounded into the polypropylene matrix (Daplen HD120MO, MFR 8 g/10 min, and HC205TF, MFR 4 g/10 min, Borealis) by means of a co rotating parallel twin screw extruder Thermo Prism TSE24HC with a processing length of 28 D. The compounder was equipped with a gravimetric dosing system. Throughput was 8 kg h⁻¹ and the barrel temperature was set to 200°C. All process parameters were held constant throughout the whole processing. The melt strands were cooled via a water bath and cut to granules. These granules were dried for at least 4 h in a circulating air oven at 80°C prior to injection moulding.

Injection moulding of universal test specimens was carried out on an Engel ES80 injection moulding machine in compliance with ISO 3167. Barrel temperature was set to 210°C. The specimens were stored at least for 88 h at 23°C and 50% relative humidity prior to mechanical testing. Specimens for impact testing were produced from the universal test specimen using a pneumatic punch.

Tensile strength and modulus were measured using a Zwick-Roell Z020 universal testing machine complying with ISO 527. Crosshead speed was set to 1 mm min⁻¹ for the acquisition of the elastic modulus, after that the speed was set to 2 mm min⁻¹ until the break of the samples. The impact specimens were notched with a Coesfeld moulding cutter and were tested on a Zwick/Roell 5113.300 impact testing machine according to ISO 179eA.

To regain the fibres from the polymer, 1 g of the sample, taken from the parallel part of the universal test specimen, was extracted in boiling xylene under reflux for 3 h (Takase and Shiraishi 1989). After that the hot solution was vacuum filtered to yield the fibres, which were dried afterwards. Fibre distribution scans were carried out on an Olympus BX61 light microscope with a CCD camera and a motorized, fully automated stage. The sisal fibres were illuminated by transmitted light. Image analysis was carried out with analySIS Five from Soft Imaging Systems to yield the length of the different fibres. To get reliable values, at least 500 fibres were detected with the image analysis. This was accomplished by multiple image alignment, a method where the microscope is taking multiple pictures by altering stage position

along a grid and these are assembled to get a bigger display window. The length weighted lengths were calculated from these results to get reliable key values for fibre length.

Samples for single fibre pull out tests were prepared from the raw sisal fibres with a cut length of 60 mm. The fibres were pushed into a molten polypropylene film with a thickness of about 1 mm. This embedding was done between two microscopic slides at a hot press. The polypropylene grades used were the same as for composite production. After the embedding, the samples were cooled down to room temperature. These samples were tested in the single fibre pull out test apparatus, which was built up from a Physikinstrumente stage, type M-403.DG, a Tensiometric load cell, type Stak 1390, with a range from 0 – 30 N, and a self assembled frame of aluminium profiles. This setup was designed to fit under the light microscope mentioned above, to measure the embedded length and the fibre diameter, as well as to get the possibility to monitor the whole pull out procedure. Furthermore this setup provides the possibility to inspect the quality of the interface, e.g. if voids or cracks are present between fibre and matrix, prior to measurement, to discard samples with poor quality. The measurements have been carried out at a crosshead speed of 1 mm min⁻¹.

3. RESULTS AND DISCUSSION

The tensile strength of the different produced composites was evaluated using equation (1), a modified version of the Kelly-Tyson model (Kelly and Tyson 1964), valid only for subcritical fibres.

$$\sigma_c = \eta_o \tau_c \frac{l}{d} V_f + \sigma_m (1 - V_f), \quad (1)$$

where σ_c and σ_m are the composite and matrix strength, η_o is an orientation factor, τ_c is the interfacial shear strength, V_f is the fibre volume fraction and l and d are fibre length and diameter. The orientation factor η_o was determined to be around 0.77 for injection moulded sisal fibre composites, as shown in a previous work (Burgstaller 2007). With this model, the results from mechanical testing and the fibre scans, it was possible to calculate the interfacial shear strength. Looking at the results from this calculation (Table 1), one can see that the interfacial shear strength for the composites containing some compatibilizer is increasing with increasing fibre content. Therefore we calculated the concentration of the compatibilizer in the matrix (C_m), because we found good correlations between this concentration and the improvement in mechanical properties for wood plastic composites in a previous work (Burgstaller and Stadlbauer 2006).

The evaluation of the notched impact strength was done with the model shown in equation (2). This approach is based on the Cottrell model (Thomason and Vlug 1997), but again only accounts for subcritical fibres and the failure mode of fibre pull out.

$$a_{cNe,c} = \eta_o \tau_c \frac{l^2}{d} V_f + a_{cNe,m} (1 - V_f), \quad (2)$$

where $a_{cNe,c}$ and $a_{cNe,m}$ are the notched impact strength of the composite and the matrix, respectively, τ_c is the interfacial shear strength, V_f the fibre volume fraction and l and d are fibre length and diameter. Applying this model to the results of the mechanical testing, we again find the interfacial shear strength (Table 1), which is in the same range as in the according calculation for tensile strength in this case.

An exemplary plot for a single fibre pull out of sisal from polypropylene HD120MO is shown in Figure 1. In this plot, the maximum force is 2.61 N, and with a fibre diameter of 0.239 and an embedded length of 1.036 one yields an interfacial shear strength of 3.36 MPa using $\tau_c = F_{Max}/(\pi ld)$.

To get reliable values, 20 samples have been subjected to this testing. These were inspected for voids and imperfections under the microscope prior to testing, and samples with such failures were discarded. The arithmetic mean for τ_c from this set of samples is 6.21 MPa, with a standard deviation of 2.3 MPa.

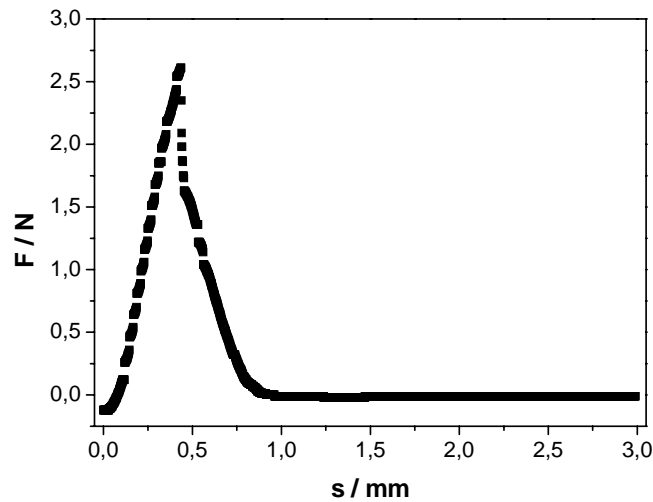


Fig. 1. Force – displacement curve for a pull out experiment with a single sisal fibre from polypropylene HD120MO

Table 1. Data from mechanical testing and interfacial shear strength calculated thereof

matrix	type	C_c^{***}	C_m^{***}	C_{fibre}	V_f	l/d	σ_c	τ_c^*	$a_{CNe.c}$	τ_c^{**}
[wt%]		[wt%]	[wt%]	[wt%]			[MPa]	[MPa]	[kJm ⁻²]	[MPa]
100				0	0	--	32.3	--	2.04	--
90				10	0.070	10.4	32.3	2.69	4.18	2.54
80		0	0	20	0.145	10.5	31.6	4.48	6.18	3.04
70				30	0.266	11.1	32.9	5.38	8.59	3.57
60				40	0.325	11.2	36.0	5.21	8.06	5.12
50	HD120MO			50	0.445	11.0	36.5	5.18	7.35	4.51
88			2.04	10	0.062	8.7	33.7	7.86	2.73	8.64
78			2.27	20	0.130	10.8	35.1	6.30	3.87	6.94
68		2	2.56	30	0.246	12.1	36.9	5.40	5.39	5.93
58			2.94	40	0.373	9.9	44.4	8.47	5.98	9.32
48			3.45	50	0.423	10.8	48.4	8.48	5.34	9.32
86		4	4.17	10	0.078	10.3	32.2	6.27	3.01	6.90
76			4.65	20	0.174	10.1	37.7	9.12	4.27	10.04

Influence of polymer and compatibilizer on interfacial shear strength

66		5.26	30	0.266	10.3	45.4	10.83	5.10	11.91
56		6.06	40	0.349	10.2	50.3	11.06	5.40	12.16
46		7.14	50	0.443	10.0	54.8	11.07	5.31	12.17
100			0	0	--	37.3	--	1.80	--
90			10	0.078	8.3	36.1	3.5	3.79	3.83
80	0	0	20	0.162	10.3	36.5	4.1	5.55	4.49
70			30	0.268	10.4	36.4	4.2	6.94	4.64
60			40	0.367	10.1	36.5	4.5	7.55	4.97
50			50	0.489	9.6	33.8	4.1	6.47	4.51
88		2.04	10	0.082	10.1	38.3	6.5	13.54	7.16
78		2.27	20	0.135	10.8	42.6	9.3	12.89	10.26
68	2	2.56	30	0.295	9.8	47.8	9.7	10.13	10.65
58		2.94	40	0.391	10.3	50.6	9.0	11.18	9.92
48		3.45	50	0.496	10.3	62.2	11.1	5.41	12.16

* calculated from tensile strength, ** calculated from impact strength, *** C_c is the concentration of the compatibilizer in the whole formulation, C_m is the concentration in the matrix

As can be seen in Table 2, the two different polymers yield different interfacial shear strengths. The polypropylene HD120MO, which is the less viscous grade of the two, shows higher average interfacial shear strength than the more viscous grade. This should occur due to better wetting of the fibres with the less viscous grade. Interesting to note is that this trend is also observed from the evaluation of the tensile and impact strength, where the more viscous grade yields 4.08 ± 0.36 MPa interfacial shear strength versus 5.06 ± 0.39 MPa for the less viscous, especially when taking the production of the samples into account, which was done via injection moulding. Throughout this process pressure is applied, which should increase the wetting, but the viscosity of the matrix plays still a role. Another thing to note is the reduction of the scattering, expressed in terms of standard deviation here, which is considerably smaller for the interfacial shear strengths calculated from the mechanical properties. This is obvious, thinking of the structure of the composites, which were subjected to the mechanical testing. In these composites, many fibres and interfaces are strained, which results in a type of mean anyway. Furthermore, the production is done with injection moulding, where the applied pressure increases the wetting of the fibres again. In single fibre pull out, where just one fibre is strained at a time, the influence of the fibre surface is much bigger, and because we are using natural fibres there has to be some influence thereof.

Table 2. Data from single fibre pull out tests for sisal fibres from different matrices

matrix	C compatibilizer	τ_c	s
	[wt%]	[MPa]	[MPa]
	0	6,21	2,3
	3	9,12	2,78
HD120MO	5	10,13	3,59
	8	10,9	6,36
	25	12,76	5,45
	50	13,51	5,2
	100	12,58	3,36
HC205TF	0	4,58	1,11

The compatibilizer, which was added to the polymer for improving the interfacial shear strength, shows great effectiveness. The improvement is, depending on the concentration, up to 100% increase, which could be found from the data from mechanical testing for both polypropylene types.

For comparing the interfacial shear strength from the composites containing compatibilizer, the first step to do was to recalculate the compatibilizer concentration C_c , which is the concentration in 100% formulation, to a compatibilizer concentration in the matrix itself, C_m . Using this concentration, and comparing the interfacial shear strengths with the one from the single fibre pull out tests, one can see a good accordance, as shown in Figure 2. The only data point from mechanical testing, which shows considerably lower interfacial shear strength, is the one acquired from the sample containing 10wt% of sisal fibre in polypropylene HD120MO without compatibilizer. In this case, the low interfacial shear strength in combination with the low fibre content results more in distortion than in reinforcement of the composite, which explains the low value for tensile strength and successive interfacial shear strength.

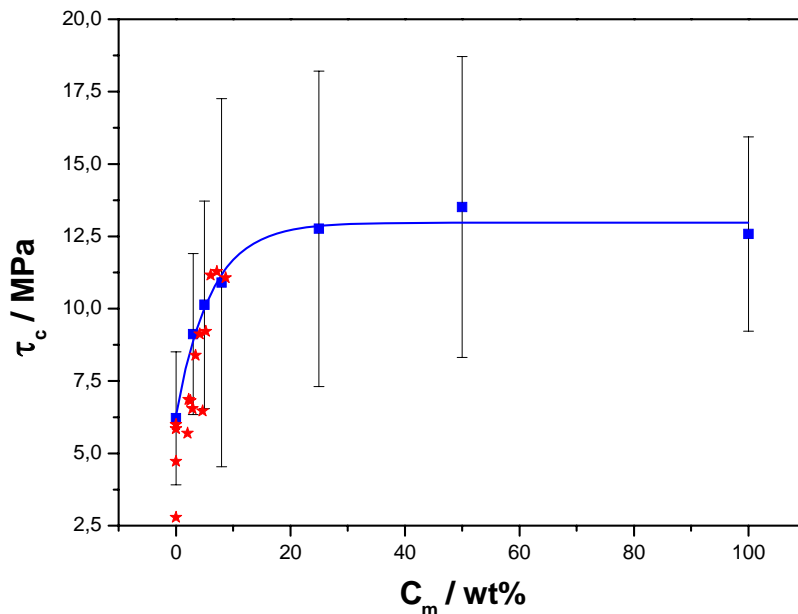


Fig. 2. Interfacial shear strength τ_c versus compatibilizer concentration in the matrix C_m for sisal in polypropylene HD120MO, acquired from single fibre pull out tests (blue) and from the evaluation of tensile strength (red)

4. CONCLUSIONS

As we showed in this work, the interfacial shear strength of sisal fibre reinforced polypropylene composites can be accessed through different pathways. On the one hand, evaluation of the mechanical properties can give reliable data, but suffer from the high effort of extracting the fibres from the composite and the fibre geometry determination. On the other hand, the single fibre pull out test can access the information about the interface, but the influence of sample preparation as well as the influences due to the origin and the surface of the fibres themselves must be considered when interpreting the data.

The polypropylene grade also shows a significant influence on the interfacial shear strength. The less viscous grade wets the fibre better, which results in increased shear strength, as can be seen from the single fibre pull out as well as from the mechanical tests. The addition of a compatibilizer improves the adhesion in a great manner, up to around 100%, depending on the concentration. Further, the results from mechanical testing and the single fibre pull out show very good accordance throughout the whole work.

ACKNOWLEDGEMENTS

The authors wish to thank Ms. Magdalena Mayer for production and testing of some of the composites as well as Mr. Michael Csombai for doing some work in the single fibre pull out tests.

REFERENCES

- Burgstaller C, (2007) "Comparison of Interfacial Shear Strength from Fibre Pull out and Mechanical Testing in Polypropylene Sisal Composites", in Proc: International Conference on Innovative Natural Fibre Composites for Industrial Applications, Rome,
- Burgstaller C, Stadlbauer W, (2006) "Investigations on the effects of coupling agents in wood plastic composites" in Proc: Progress in Wood & Bio-fibre Plastic Composites, Toronto,
- Kelly A and Tyson WR, (1964) Chapter 13: Fiber strengthened materials, ed. Zackay VF. High-Strength Materials, Berkeley, CA: John Wiley & Sons;
- Kim JK and Mai YW, (1998). Engineered Interfaces in fiber reinforced composites. 1st ed. ed. Netherlands: Elsevier;
- Takase S and Shiraishi N, (1989) Studies on Composites from wood and polypropylenes II. Journal of Applied Polymer Science., 37 645-659.
- Thomason JL (2002), Micromechanical parameters from macromechanical measurements on glass-reinforced polybutyleneterephthalate. Composites Part A: Applied Science and Manufacturing., 33(3) 331-339.
- Thomason JL and Schoolenberg GE, (1994) An investigation of glass fibre/polypropylene interface strength and its effect on composite properties. Composites, 25(3) 197-203.
- Thomason JL and Vlug MA, (1997) Influence of fibre length and concentration on the properties of glass fibre-reinforced polypropylene: 4. Impact properties. Composites Part A: Applied Science and Manufacturing, 28(3) 277-288.

THE EFFECT OF CURE CYCLE HEATING RATE ON THE FIBRE/MATRIX INTERFACE.

Victoria Coenen*, Andrew Walker*, Richard Day*, Alan Nesbitt*
Jin Zhang**, Bronwyn L. Fox**

*University of Manchester, North West Composites Centre,
Manchester, M60 1QD, UK

**Deakin University, Centre for Material and Fibre Innovation,
Geelong, VIC, 3217, Australia

ABSTRACT

Development of civil aerospace composites is key to future “greener” aircraft. Aircraft manufacturers must improve efficiency of their product and manufacturing processes to remain viable. The aerospace industry is undergoing a materials revolution in the design and manufacture of composite airframes. The Airbus A350 and Boeing 787 (both due to enter service in the latter part of this decade) will push utilisation levels of composite materials beyond 50% of the total airframe by weight. This change requires massive investment in materials technology, manufacturing capability and skills development. The Quickstep process provides the ability to rapidly cure aerospace standard composite materials whilst providing enhanced mechanical properties. Utilising fluid to transfer heat to the composite component during the curing process allows far higher heat rates than with conventional cure techniques. The rapid heat-up rates reduce the viscosity of the resin system greatly to provide a longer processing window introducing greater flexibility and removing the need for high pressure during cure. Interlaminar fracture toughness (Mode I) and Interfacial Shear Strength of aerospace standard materials cured using Quickstep have been compared to autoclave cured laminates. Results suggest an improvement in fibre-matrix adhesion.

1. INTRODUCTION

Advanced fibre reinforced polymer composite materials have not been as widely used within manufacturing industry applications as would be predicted from their structural performance characteristics. The main reasons for this are the complexity of their processing techniques and the associated high costs. The use of advanced composites has therefore, largely been restricted to industries with high product costs and low volume production. Currently, most high performance composite components are produced by hand or machine lay-up of prepreg

laminates followed by curing in an autoclave at elevated temperature and pressure in order to obtain the required structural properties.

Demand for increase in manufacturing speed is driven by the need to increase the rate of production of aircraft such as the Airbus A350 and Boeing 787 due to increasing orders. Autoclaves not capable of meeting these demands. Out-of-autoclave composite curing is of great interest to industry in this climate.

1.1 Out-of-autoclave composite cure. There has been an increase in the development of alternative composite manufacturing technologies, with the aim of producing materials of similar quality to aerospace grade composites, but in a shorter processing time and at a lower cost. The aim of these techniques is to utilize a more efficient method of applying heat to the composite component than in an autoclave. Traditionally, high-performance composites have been processed at relatively low heat-up-rates (1-2°/min) for two main reasons; to ensure uniform heating across the different parts in an autoclave and to reduce the risk of runaway exotherm of the epoxy based materials.

Microwave and radio Frequency heating offer alternatives to autoclave technology and provide the potential for higher heating rates. Such radiation techniques generate heating within the material, as opposed to the surrounding matter, thus resulting into rapid, volumetric and more efficient heating compared to conventional thermal heating. Cure cycle times and energy requirements are drastically reduced, as a result lower operational costs are achieved. However there are problems associated with such technologies, for instance non-uniform heating of the material mainly due to non-uniform distribution of the electromagnetic field leading and poor process control. To-date though promising alternatives to autoclave curing Microwave and RF techniques are not sufficiently advanced to be considered in a production environment.

1.2 The Quickstep Process. An alternative to the above heating techniques is to utilise liquid to transfer heat to and from the part, as fluids have a much greater volumetric heat energy capacity than gases, the heat transfer rate between the fluid and laminate is much higher than that achievable in an autoclave. This is the central idea behind the Quickstep process developed by an Australian company (Quickstep Technologies Pty Ltd). It is a balanced pressure, heated mould process that can be utilised for the out-of-autoclave curing of advanced composite material (Stanford et al. 2003; Stanford et al. 1996). Tight temperature control is maintained by circulating the fluid through the pressure chamber. This provides rapid and precise heating/cooling of the laminate and allows excellent consolidation to be obtained at low applied pressures.

The heat transfer fluid can also act as a thermal sink, removing any excess heat generated in an exothermic reaction, so that a constant cure temperature may more easily be maintained, even for thick laminates. The process benefits from versatile production facilities, fast cure cycles and reduced capital, tooling and operational costs (Bader 2002; Griffiths and Noble 2004; Bader and Noble 2004).

The high heat-up-rates allow rapid cure of parts and a consequential highly flexible manufacturing route through high-rate production principles. This would allow composite manufacturers to move away from a batch manufacturing philosophy, where a large number of uncured parts are installed in the processing plant and cured together, to a more flexible, one piece flow where individual parts are prepared and cured in an assembly line process.



Fig. 1. Quickstep QS5 Machine housed at The North West Composites Centre, University of Manchester

2. EXPERIMENTAL DETAILS

The composite laminates were cured by the Quickstep QS5 at Deakin University and the American Autoclave ‘mini-bonder’ MB-2036-415-315-800 at the Australian National University. The HexPly914 composites cured by the autoclave are represented by HexPly914-AC and those cured by the Quickstep are represented by HexPly914-QS. Similarly, the T800H/3900-2 composites cured by the autoclave are represented by T3900-2A and those cured by the Quickstep are represented by T3900-2Q. The HexPly914-AC was cured at 175°C for 1 hour under a nitrogen pressure of 690KPa and vacuum of -4KPa before a postcure at 190°C for 4 hours inside the autoclave chamber. The HexPly914-QS cure featured an initial dwell at 110°C for 30 minutes and then a 170°C cure for 1 hour inside of the Quickstep chamber under a vacuum of -97KPa ~ -98KPa. The panels were then postcured in an oven for 4 hours at 190°C. Both the heating rate and the cooling rate for the HexPly914-QS cure were 10°C/min. 1.5°C/min was applied to heat up and cool down the HexPly914-AC laminates. The Quickstep cure cycle for the HexPly914 system was reduced by 300 minutes when compared to the autoclave cure cycle due to the faster heating rate possible with this low pressure process.

The autoclave cure for the T800H/3900-2 utilized ramp rates of 3°C/min for heating and 2°C/min for cooling. The T3900-2A was cured at 180°C for 2 hours under 640KPa nitrogen pressure and a vacuum of -4KPa. The T3900-2Q was heated at rate of 9°C/min, prior to a dwell for 30 minutes at 150°C, the cure was then continued at 180°C for 2 hours before finally being cooled at a rate of 10°C/min to 60°C. A vacuum of -98KPa was maintained during the Quickstep cure. By comparison with the autoclave cure, the Quickstep cure reduced the cycle time by 40 minutes.

The interlaminar fracture toughness tests (mode I and mode II) were performed on a LLOYD 30K universal tester in accordance with the protocol of the European Structural Integrity Society (Davis 1993). Five specimens were tested for each type of test. Aluminum foil with thickness of 15µm was treated with SRC 722 semi permanent release agent before careful placement into the mid-plane of the DCB specimens. The mode I critical energy release rate GIC and the mode II critical energy release rate GIIC were calculated by the modified beam theory derived by

Hashemi et al. (1990). The fracture surfaces were examined using a LEO 1530 scanning electron microscope (SEM).

Indentation-debond tests were performed on the Ultra-Micro indentation system (UMIS) and the Dual Scope™ DS 45-40 atomic force microscope. Specimens were finely polished before indentation. A three-sided pyramidal Berkovich tip was employed to indent on fibres within composite specimens. To measure the interfacial shear strength from indentation-debond tests, the fibres were loaded to a specific value, unloaded to inspect for debonding, and then reloaded to a higher value. This process was repeated until debonding was observed. Loading was started from 30mN and increase in increments of 10mN.

3. RESULTS AND DISCUSSION

3.1 Mode I Interlaminar fracture toughness. HexPly914 and T800H/3900-2 are both commercial thermoplastic toughened carbon epoxy prepregs; however, the toughening mechanisms differ in each. The HexPly914 utilizes a semi-interpenetrating network (IPN) approach to toughening, in which the thermoplastic phase is dispersed into the epoxy resin; the T800H/3900-2 makes use of an interlayer toughening mechanism in which the thermoplastic particles are dispersed onto the surface of the carbon/epoxy lamina to achieve high fracture toughness.

Results from mode I delamination tests are presented in Fig. 2. The average value for G_{IC-PROP} was 160J/m² for the HexPly914-AC and 297J/m² for the HexPly914-QS. This represents an 86% increase in the average value. The T3900-2A had an average G_{IC-PROP} of 300J/m², however, the average G_{IC-PROP} was 783J/m² for the T3900-2Q which was substantially higher. The resistance curves for the autoclave-cured HexPly914 and T800H/3900-2 specimens were relatively stable, however the Quickstep-cured specimens exhibited a rising resistance curve along with increased fibre bridging. Since the G_{IC-PROP} is generally associated with fibre/matrix adhesion, interlaminar bonding strength and fibre bridging (Hashemi et al. 1990), these factors may all have influenced the resistance to crack propagation in these specimens. The fracture surfaces of selected specimens were examined using Scanning Electron Microscopy and these results will be discussed in the presentation. The fibre/matrix adhesion was characterized by performing the indentation-debond tests which will be illustrated in a later section.

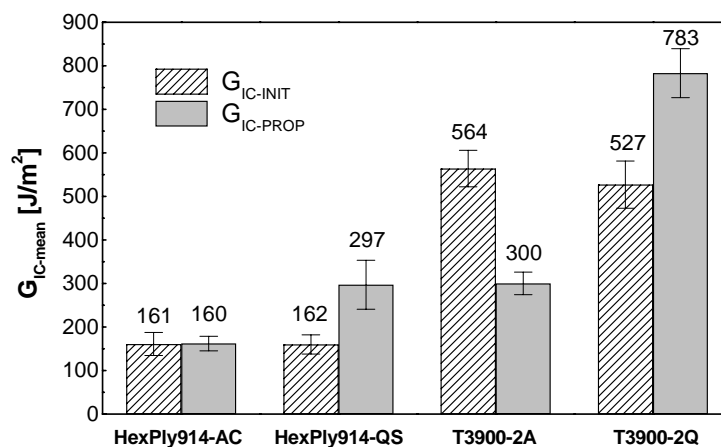


Fig. 2. Mode I fracture toughness of HexPly914 and T800H/3900-2 composites cured by Autoclave and Quickstep processes.

3.2 Interfacial Shear Strength. Plateaus in the indentation load vs. depth curves were used as an indication of the occurrence of the debonding of the fibre to the matrix. These plateaus can be clearly observed in seen in Fig. 3. The fibres in Fig 3a. and Fig 3b. debonded when indented to the maximum load of 60mN. The debonding load was defined from the intersection point of the tangents drawn along the initial elastic part of the loading curve and the plateau. Atomic Force Microscope (AFM) images in Fig. 4 clearly show the debonded fibre in both composite systems. The ‘resin ring’ around the fibres due to debonding is evident in these AFM images (Fig. 4).

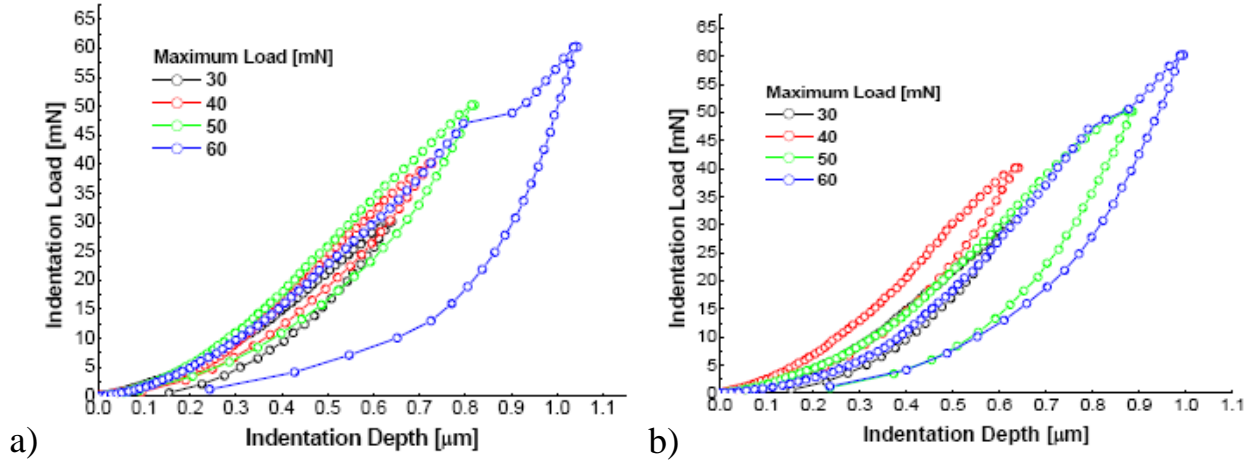


Fig. 3. Indentation-debond loading history for the HexPly914 composites cured using a) autoclave and b) Quickstep processes, showing a plateau indicating debonding.

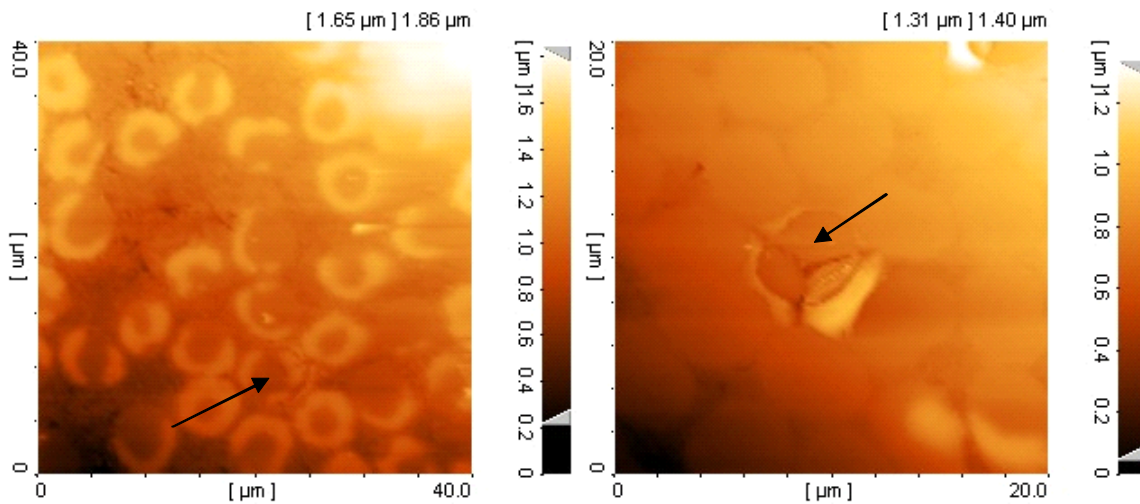


Fig. 4. AFM images on the debonded fibres within the HexPly914 (left) and the T3900-2 (right) composites. The “resin ring”, indicating debonding can be observed in both images.

Desaegar and Verpoest’s (1993) shear lag analytical approach was used to calculate the interfacial shear strength (IFSS).

$$\tau_{debond} = \frac{nF_{debond}}{2\pi r^2}, \quad (1)$$

$$\text{where } n = \frac{2E_m}{E_f(1+\nu_m)\ln\left(\frac{2\pi}{\sqrt{3}}V_f\right)}, \quad (2)$$

where τ_{debond} is the interfacial shear strength, F_{debond} is the measured debonding load, r is the fibre radius, E_m is the matrix modulus, E_f is the fibre modulus, ν_m is the matrix Poisson's ratio and V_f is the local fibre volume fraction. The results are summarized in Table 1. The thermoplastic toughened composites cured by the Quickstep process exhibited higher IFSS than those cured by the autoclave. This suggests an improvement in the fibre/matrix adhesion in these samples. A parallel study of the Hexply 6376 system (Davies et al. 2007) investigated the effect of heating rates on the viscosity of the matrix. The authors compared heating rates of 10C/min (to model the Quickstep process) and 2C/min (to model an autoclave cure) and found that the viscosity of the resin was significantly lower when heated at 10C/min. The lowered viscosity in the initial stages of the Quickstep cure cycle may possibly contribute to the increase in fibre/matrix adhesion via an improvement in fibre wetting during this stage of the cure. In addition to this, the microwave process, which also employs rapid heating rates during cure, was also found to improve the fibre/matrix adhesion in E-glass fibre/epoxy composites as evidenced by transverse tensile and four-point bending flexure tests (Bai and Djafari 1995).

Table 1. IFSS calculation on the HexPly914 and the T800H/3900-2 composite systems cured by the autoclave and the Quickstep processes. *Reported by Desaegeer and Verpoest (1993).

Material	E_m (GPa)*	E_f (GPa)*	ν_m *	V_f (%)	IFSS (MPa)	Standard Deviation (MPa)
HexPly914-AC	3.7	234	0.41	54.86	38.85	2.94
HexPly914-QS	3.7	234	0.41	52.17	40.10	6.36
T3900-2A	3.7	234	0.41	54.00	36.33	4.92
T3900-2Q	3.7	234	0.41	49.66	55.04	5.91

3.3 Manufacture of demonstration components. Work at the North West Composites Centre based at the University of Manchester aims to prove the validity of the Quickstep process for industrial applications, specifically its applicability for Aerospace materials and components.

The Quickstep process has been evaluated for a number of aerospace standard pre-preg material systems. Cure cycle quality is assessed in terms of laminate properties; Interlaminar Shear Strength, Flexural Strength (3 Point Bend), Glass Transition Temperature and Void Content. Results are typically compared to data for autoclave or oven cured laminates dependant on material systems and supplier. Results have shown equivalent material properties and reductions in cure cycle duration of between 50–70% (Bond et al. 2005; Coenen et al. 2005).

A number of product demonstrators have been manufactured for Aerospace customers, examples of these can be seen in Figure 5.

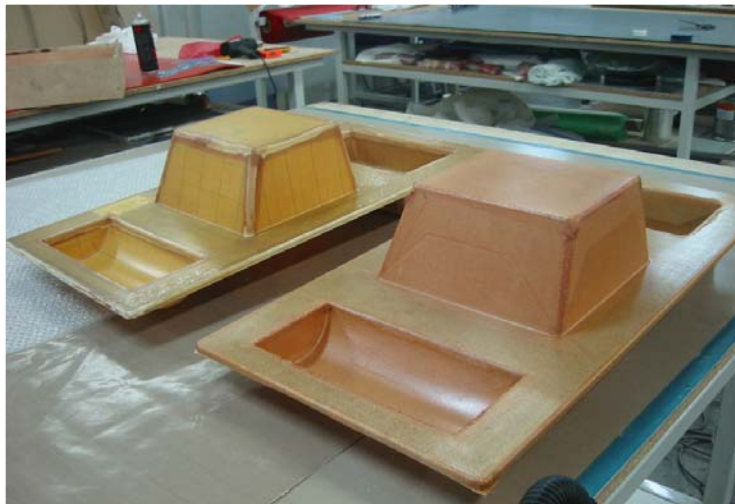
The effect of cure cycle heating rate on the fibre/matrix interface



a)



b)



c)

Fig. 5. Demonstrator Parts manufacture on the QS5 Quickstep Machine at The NWCC, Manchester. a) Aircraft Ducting. b) Wing Access Panel. c) Overhead baggage compartment.

4. CONCLUSION

The Quickstep process is a viable out-of-autoclave process with composite mechanical properties being equivalent to or slightly better than autoclave properties. The process can be applied to a range of component geometries typical of aerospace components.

Interlaminar fracture toughness found to be increased in QS specimens, increased fibre bridging observed.

Interfacial shear strength also observed to increase in QS cured sample – evidence of improved fibre/matrix adhesion.

ACKNOWLEDGEMENTS

The authors wish to thank the Victorian Centre for Advanced Materials Manufacturing (VCAMM) and the North West Composite Centre (NWCC) for support.

REFERENCES

- Bader, M.G. (2002). Selection of composite materials and manufacturing routes for cost-effective performance, *Composites Part A*, 33, 913-934.
- Bader, M.G. and Noble, N. (2004). A comparison of the costs of manufacture of a laminated composite component by conventional autoclave and a non-autoclave process. Proceedings of SAMPE-EUROPE, Paris.
- Bai, S.L. and Djafari, V. (1995). Interfacial properties of microwave cured composites. *Composites* 26 645-651.
- Bond, D.A., Nesbitt, A., Coenen, V. and Brosius, D. (2005). The evaluation and development of the Quickstep out-of-autoclave composites processing method. *Proceedings of the UK Composites Processing Association*, Stoke, UK.
- Coenen, V., Hatrick, M., Law, H., Brosius, D., Nesbitt, A. and Bond, D.A. (2005). A Feasibility Study of Quickstep Processing of an Aerospace Composite Material, Proceedings of SAMPE-EUROPE, Paris
- Davis, P. (1993). Protocols for interlaminar fracture testing of composites. Delft, the Netherlands: European Structural Integrity Society (ESIS).
- Davies, L.W., Day, R.J., Bond, D., Nesbitt, A., Ellis, J., and Gardon, E. (2007). Effect of cure cycle heat transfer rates on the physical and mechanical properties of an epoxy matrix composite. *Composites Science and Technology* 67 (9), 1892-1899.
- Desaeger, M. and Verpoest, I. (1993). On the use of the micro-indentation test technique to measure the interfacial shear strength of fibre-reinforced polymer composites. *Compos Sci Technol* 48, 215-226.
- Griffiths, B. and Noble, N. (2004). Process and tooling for low cost, rapid curing of composite structures, *SAMPE Journal*, 40(1), 41-46.
- Hashemi, S., Kinloch, A.J., and Williams, J.S. (1990). The analysis of interlaminar fracture in uniaxial fibre-polymer composites. In: Proceedings of the Royal Society of London Series A, 427, 173-199.
- Stanford, J.L., Still, R.H. and Wilkinson, A.N. (2003). Effects of soft-segment prepolymer functionality on structure-property relations in RIM copolyurethanes, *Polymer*, 44(14), 3985-3994.
- Stanford, J.L., Still, R.H. and Wilkinson, A.N. (1996). Effects of soft-segment prepolymer functionality on the thermal and mechanical properties of RIM copolymers, *Polymer International*, 41(3), 283-292.

PULSED PLASMA DEPOSITED MALEIC ANHYDRIDE THIN
FILMS AS FUNCTIONALISED SURFACES IN COMPOSITE
MATERIALS

Joanna Drews^a, Stergios Goutianos^d, Keld West^c, Søren Hvilsted^b,
Kristoffer Almdal^a

^a Polymer Department, Risø National Laboratory, Technical
University of Denmark, Frederiksborgvej 399, DK-4000 Roskilde

^b Danish Polymer Centre, Technical University of Denmark,
Produktionstorvet 423, DK-2800 Kgs. Lyngby

^c Nano-Science Center, University of Copenhagen, Universitetsparken
5, DK-2100 Copenhagen

^d Materials Research Department, Risø National Laboratory, Technical
University of Denmark, Frederiksborgvej 399, DK-4000 Roskilde

ABSTRACT

A low power AC 2-phase plasma setup was used for surface deposition of thin films of maleic anhydride (ppMAH) on glassy carbon or on polyethylene. The planar glassy carbon substrate models carbon fibres in composite materials. The substrates are treated with different plasma power levels. The present study focuses on the effect of plasma power on the surface chemistry, the properties of the modified layers and the adhesion between the substrates and an epoxy resin (interface properties). The discussion of the surface characteristics is based on surface chemistry analyses (XPS and toluidine blue staining method) and the interfacial fracture energy (measured by the double cantilever beam test method). To explain the observed differences in interfacial fracture energy, some of the samples were hydrolysed in alkaline solution. The hydrolysis ratio of preserved anhydride groups on the surface was monitored with the toluidine blue staining method.

1. INTRODUCTION

It is well known that the macroscopic properties of composite materials are strongly dependent on the integrity of the fibre-matrix interface. The optimisation of the fibre-matrix interface is essential for improved physical and in particular mechanical properties of fibre reinforced polymer composites. The adhesion between the fibres and the matrix is realised through bonds

which play an essential role for the interface strength, especially in the case of polymeric materials, which often consist of cross-linked constituents (Hansen (1999), Doi (1996), Launay et al, (2007)). The cross-links can be either covalent bonds or physical interactions, e.g. hydrogen bonds or dispersion and electrostatic forces. The Hansen solubility parameters can help in quantifying the physical affinities between the constituents.

Wet/solution chemistry is usually used to surface modify the fibres, whereas plasma treatment is mostly being used for cleaning (Keller et al (2005)). In this study the authors used the plasma polymerisation technique as a method of fibre surface modification by thin polymeric film deposition. The advantage of plasma polymerisation is that it is a solvent-free technique, which is rather easy and inexpensive to use. Post-treatment e.g. cleaning and purifying of the samples is not necessary unless further modifications are desired. The structure of plasma polymerised layers is usually very complex and thus difficult to understand and analyse. Properly understood and controlled, the complex structure can, however, be used in designing new high strength composite materials by tailoring the fibre/matrix interface or interphase.

The complex nature of layers modified with pulsed plasma comes from two processes taking place simultaneously, one is the polymerisation (time *off* – time for inactive plasma where addition of monomer molecules progress) and the other is creating radicals (mostly on the surface; time *on* – time for active plasma). The time *on* and *off* influences the chemistry and properties of polymerised layers (Schiller et al (2002)). Using the SoftPlasma™ technique the ratio between times *on* and *off* were controlled by the plasma power level – a higher plasma power level thus results in a more active (more radicals) polymerisation. The output of this process could be observed as an increase of the polymerisation rate (with constant flow of monomer and Ar). The plasma polymers created with low power are expected to have a high content of low molecular weight polymers. This could mean that the modified layer actually contained oligomers instead of polymers and was only weakly cross-linked. This material could often be easily dissolved. Hence, to obtain a stable layer of polymer, it is necessary that the power input to the system exceeds a minimum energy (Hegemann et al (2005)).

For the surface modification in the present study we used maleic anhydride (MAH). The layers of pulsed (rf) and continuous (CW) plasma polymerised maleic anhydride (ppMAH) had previously been investigated and characterised using surface characterisation techniques (Ryan et al (1996)). It was concluded from their work that with manipulation of plasma power it is possible to preserve anhydride groups during the plasma polymerisation. The system of SoftPlasma™ used power less than 1 W/l. The distinct advantage of this plasma polymerisation method is that the required energy supplied into the system is low enough to run the polymerisation in a way very close to the conventional way (polymerisation in the solution).

In this paper we focus on the characterisation of the surface coatings made by soft plasma polymerisation of maleic anhydride. We also showed that the complex nature of the polymeric coating can be advantageous. The surface chemistry is analysed with X-ray photoelectron spectroscopy (XPS) and the toluidine blue staining method (Sano et al (1996)). The rate of hydrolysis of preserved anhydride groups, in the ppMAH films, during plasma surface modification as a function of plasma power levels was investigated. The hydrolysis ratio was monitored by toluidine blue staining. The fracture energy of the planar glassy carbon/epoxy interface was measured under nominal Mode I using the double cantilever beam method test method.

2. EXPERIMENTAL SECTION

Materials. Planar glassy carbon substrates (SIGRADUR G) were purchased from HTW Hochtemperatur, Germany in sizes of 20x20x1 mm³ and 65x5x1 mm³. Polyethylene (PE) foil (thickness 1 mm) was extruded in-house from BOREALIS FA 3220 granules. Toluidine Blue O was obtained from Sigma Aldrich and stored at room temperature in the dark. Maleic anhydride (MAH) was obtained from Sigma Aldrich as briquettes, which were ground into fine powder in a hood and placed in a metal container under vacuum. Ultra-pure water was obtained using a MilliQ system from Millipore.

Substrate preparation. The PE substrates were cleaned in an ultrasonic bath for 5 minutes in different solvents, including acetone, methanol and miliQ water. The glassy carbon substrates were cleaned in an ultrasonic bath in different solvents, using chloroform (5 minutes), acetone (twice – 2x5 minutes) and methanol (5 minutes). Finally, all substrates were dried with a jet of argon. The cleaned substrates were stored in polystyrene Petri dishes until use. The substrates were stored no longer than a few hours before the surface modification, after which they were kept under vacuum in the plasma chamber until further use.

Plasma polymerisation. The plasma chamber set-up is described in detail by Winther-Jensen et al. (2003; 2004) and Ademovic et al. (2005). This plasma coating technique, called SoftPlasma™. The process of plasma polymerisation is described in detail by Drews et al. (2007). The plasma polymerisation information is given in units of power per litre (W/L) and plasma polymerisation time (min). The power of the plasma may be calculated from the formula $P = \frac{U * I}{Vol}$, where U is the voltage across the chamber, I is the current during plasma polymerisation, and Vol is the plasma volume equal to 11.5 l. In order to obtain a uniform coating on both sides, the PE substrates were suspended freely close to the centre of the plasma chamber and a 10 mm wide border around the edges was discarded. The glassy carbons for the mechanical tests were mounted on double sticky tape on a glass tube.

Surface analysis. X-ray photoelectron spectroscopy (XPS) was performed using a SPECS Sage 100 instrument with a non-monochromatic MgK_α X-ray source at a power of 275 Watts (11 keV and 25 mA). The pressure in the chamber was always below 1 x 10⁻⁷ mbar. Two kinds of spectra were obtained: survey and high resolution. Atomic concentration of the surface composition was calculated from the intensity of the peaks of survey spectra (0-1100 eV, 100 eV pass energy). The high resolution spectra (23 eV pass energy) of surface components was used to fit 4 peaks with full-width at half-maximum (FWHM) of 2.0 eV. The positions of the peaks was as follow: 285.0 eV for C-C/C-H (referencing peak), 286.5 eV for C-O, 288.0 eV for C=O, 289.4 eV for C(O)O.

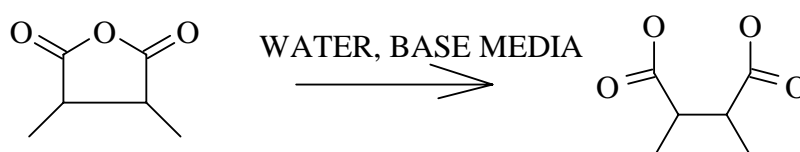
Fracture mechanics test. Double Cantilever Beam (DCB) sandwich specimens were prepared using the plasma treated glassy carbon wafers (65x5x1 mm³). The resin used was an epoxy system (Prime-20, SP Systems, UK). The resin and the hardener were mixed at a weight ratio of 4:1, degassed for 2x5 min under full vacuum, and then casted into silicon rubber moulds between two glassy carbon wafers. Teflon films (0.5 mm in thickness) were used to keep the wafers apart and to create a notch of 20 mm in length necessary to initiate a crack along the glassy carbon-epoxy interface. The DCB specimens were cured for 24 hours at room temperature and subsequently post-cured at 50°C for 16 hours. The cured samples were ground and polished to facilitate optical observations of the interface crack growth. Subsequently, the sandwich specimens were glued on specially made stainless steel beams (6 mm in thickness) that could be mounted on the test fixture. An epoxy adhesive (Scotch Weld) was used to glue

the DCB specimens to the steel beams. The curing time for the adhesive was 24 hours at room temperature. More detailed description of the DCB method can be found in the following references: Bao et al (1992) and Sørensen et al. (1996)

Surface derivatisation. The toluidine blue surface derivatisation method of Sano et al (1993) was used to determine the number of carboxylic acid groups in the volume of the coatings. In brief, a polyethylene plate with size 20x20x1 mm³ modified on both sides (the reactive area of the surface is approximately 8 cm²) was incubated with 5 ml of fresh toluidine blue solution (2×10^{-4} M) in 0.1 mM NaOH for 1 hour at 40°C in a water bath. Each carboxylic acid group was assumed to bind one molecule of toluidine blue. Afterwards, the solution was removed and the surface rinsed 3 times with fresh 0.1 mM NaOH. The samples were placed in clean, dry HDPE flasks with 5 ml of 50% (v/v) acetic acid for 30 minutes at 40°C to release the bound toluidine blue into the solution. The absorbance of the solutions was measured with a UV-1700 Shimadzu spectrophotometer at a wavelength of 630 nm. The number of reactive carboxylic acid groups in the films was determined from a standard curve of toluidine blue.

3. RESULTS AND DISCUSSION

Surfaces were modified with pulsed plasma maleic anhydride (ppMAH) with different power levels (0.3, 0.7, 1.2 W/l) in such a way that the thickness of the films remained the same (approx. 80 nm). The freshly deposited layer of ppMAH on PE was placed into 0.1 mM NaOH for hydrolysis of the preserved anhydride groups on the surface. After hydrolysis of an anhydride group two carboxylic acid groups are obtained:



From XPS analysis we had previously shown that the surface chemistry was not influenced by plasma power level (Drews et al. (2007)). The XPS technique is a surface sensitive method, where about 70% of the signal comes from the first monolayer (approx. 1 nm). Only the last 30% comes from deeper layers (max. 10 nm). In other words, this analysis is equivalent to seeing the plasma modified layer (ppMAH) as a strictly 2-D structure, regardless of thickness. The average surface chemistry from XPS measurements for all plasma treatments yielded an oxygen content of $31 \pm 2\%$ (O 1s) and a carbon content of $69 \pm 2\%$ (C 1s).

Consistent results were found from the toluidine blue staining method, where the maximum number of carboxylic acid groups after full hydrolysis in the plasma layers was found to be the same within uncertainty, approx. 36 nmol/cm² (see Figure 1), i.e. it did not seem to be influenced by the plasma power level. We thus concluded that the changes of surface chemistry as a function of plasma power were negligible.

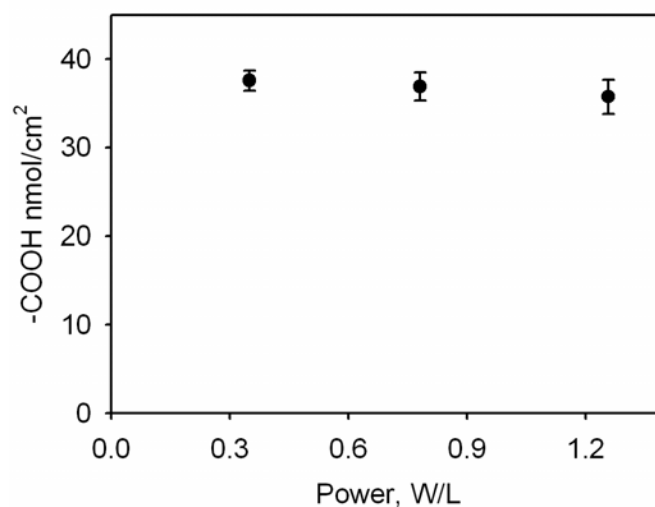


Fig. 1. Maximum number of carboxylic acid groups from toluidine blue staining method in the 80 nm thick films created with different power levels.

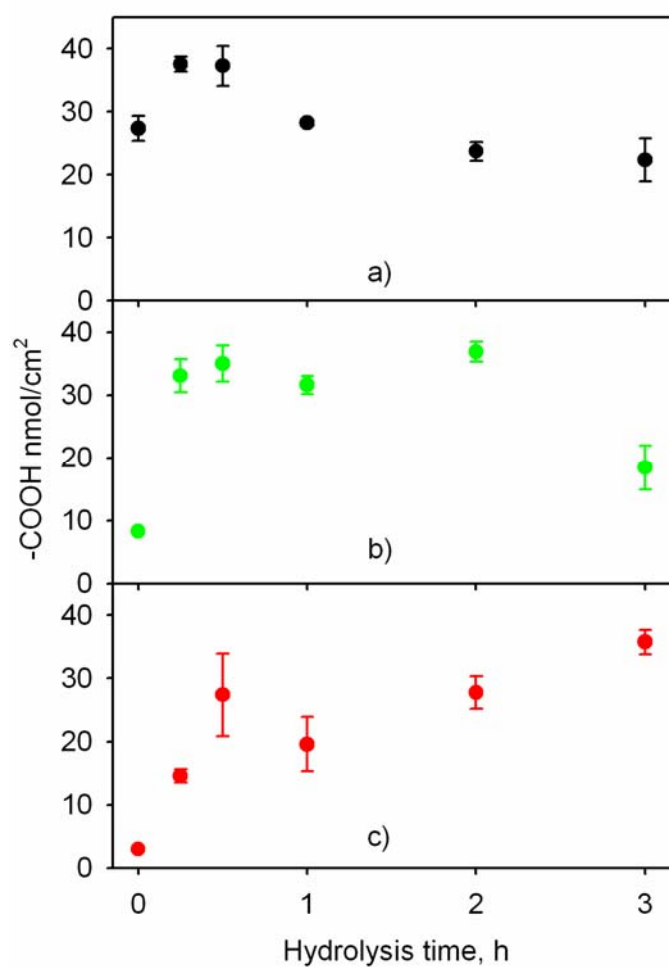


Fig. 2. Hydrolysis of preserved anhydride groups in a 80 nm plasma film created with different power levels as function of hydrolysis time in 0.1 mM NaOH: a) 0.3 W/l, b) 0.7 W/l 10 min, and c) 1.2 W/l, 8 min.

As mentioned above, in order to investigate the hydrolysis, films were placed into a 0.1 mM NaOH hydrolysing medium. As shown in Figure 2, the time evolution of the hydrolysis of the plasma polymerised layers of maleic anhydride is found to be strongly dependent on the plasma power used. The hydrolysis of ppMAH prepared with low power (Figure 2(a)) shows a tendency of fast hydrolysis and slow constant dissolution, i.e. a fast initial increase of the number of carboxylic acid groups, followed by a gradual decrease after a short time in sodium hydroxide. A similar trend was observed for the ppMAH prepared with medium power (Figure 2(b)). The hydrolysis of ppMAH made with high power (Figure 2(c)) progressed slower with a gradual increase in the number of carboxylic acid groups on the surface over time.

The observed slow increase in the number of carboxylic acid groups could be attributed to the cross-linking of the layers. The bonds prevent the swelling of the ppMAH layers (Chu et al (2006)), making it more difficult to hydrolyse the anhydride groups to carboxylic acid groups (Drews et al. (2007)). Similarly, the observed dissolution of the film could be an insufficient amount of cross-linking in the film and a high content of oligomers. An alternative explanation could be that the bonds are not between C-C (covalent bonds), as we would expect, but between C-O which during NaOH treatment can be hydrolysed.

The effect of plasma power can also be seen in the mechanical tests of the planar glassy carbon/epoxy specimens where ppMAH layers had been prior deposited on the glassy carbon surfaces. The substrates were plasma prepared with different plasma power levels from 0.3 W/l to 1.2 W/l. Figure 3 shows the dependence of interface fracture energy on the plasma power. The results show that there is an optimum plasma power value, 0.7 W/l, at which a very strong interface is obtained.

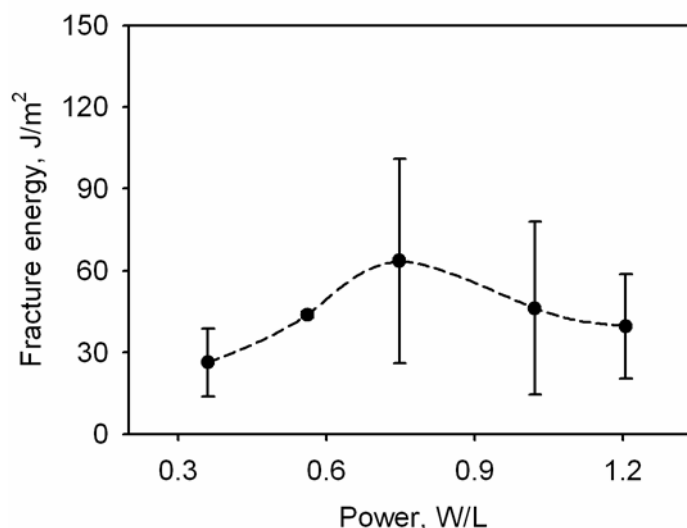


Fig 3. Fracture energy for crack initiation as a function of power level during ppMAH polymerisation (the polymerisation time is the same for all cases and equal to 10 min).

In Figure 4 the fracture resistance curves are shown for three different plasma treatments. For plasma power of 0.7 W/l the behaviour is significantly different from the other two treatments. Specimens prepared with a plasma power of 0.7 W/l exhibit a strong R-curve behaviour (increase of fracture energy with crack extension) and at some point unstable crack growth occurs. For the specimen shown in Figure 4 unstable fracture occurs after the crack has grown approximately 5 mm. On the other hand, specimens prepared with a plasma power of 0.3 W/l and 1.2 W/l show similar and stable crack growth up to approximately 10 and 15 mm,

respectively. The former could be evidence an extrinsic toughening mechanism (i.e. plasticity), whereas the latter would be a sign of low cohesion.

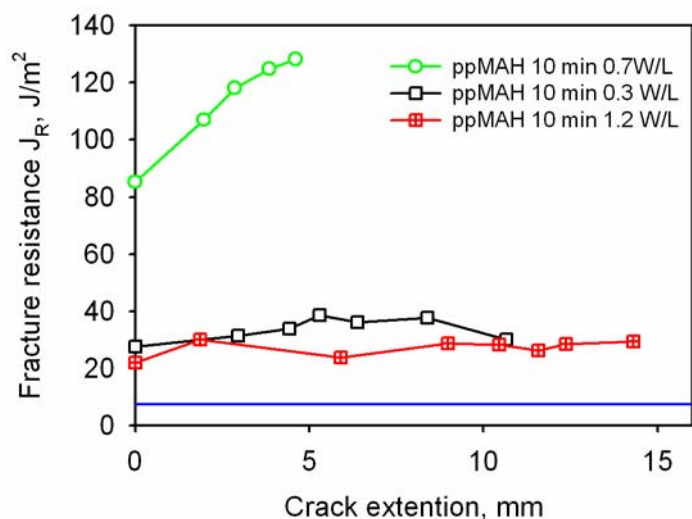


Fig. 4. Examples of fracture resistance curves of glassy carbon specimens prepared with different powers levels of ppMAH. The blue curve represents the value of untreated glassy carbon specimens (5-7 J/m²).

Arguably the reason for the different behavior of glassy carbon treated at different plasma levels could be the different amounts of cross-links in the plasma layers. If the plasma layers contain many oligomers, i.e. if they are weakly cross-linked – Figure 5(c), the material would be expected to show low cohesion. On the other hand, materials which exhibit a high amount of cross-links (Figure 5(a)) would also be expected to show low cohesion, since the linear polymers between cross-links are short. According to the theory of elasticity of rubber based on thermal motions of ideal chains, cross-linked material can be only fully stretched up to \sqrt{N} times, where N is the number of monomers (Doi, (1996)).

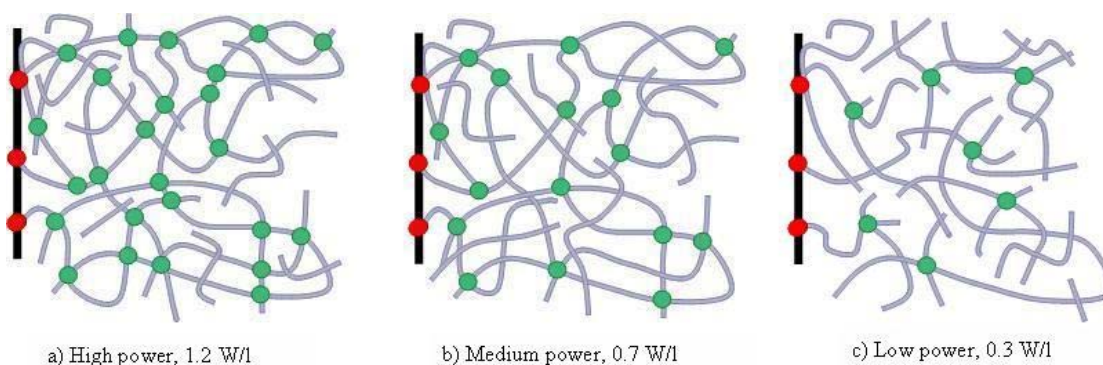


Fig. 5. Schematic illustration of the plasma deposited ppMAH layers. a) highly cross-linked layer, b) intermediate cross-linked layer and c) weakly cross-linked layer.

4. CONCLUSIONS

Using AC 2-phase plasma polymerisation technique it is possible to create a thin layer of maleic anhydride on glassy carbon and polyethylene substrates. If one considers these thin films only as

surfaces, the surface chemistry is not influenced by the plasma power. This is confirmed by the toluidine blue staining method and XPS results. If we consider, however, these films as bulk materials we can see that there is a significant dependence on plasma level. This was shown in the case of hydrolysis of the layer with the toluidine blue staining method and through the mechanical tests (interface fracture under nominal Mode I). The experiments show that it is important to carefully optimise the conditions of creating the plasma layers. On one side, we can obtain a layer with strong adhesion between substrate and coating and a strong R-curve behaviour. On the other side, we can obtain a highly cross-linked layer. In this case the adhesion is weak and quite probably problems of self cracking due to internal stresses are introduced (Yu and Yasuda, (1999)). Finally it was shown (Figure 3) that it is possible, through the plasma polymerisation technique used, to obtain interfaces with unique properties. Weak, intermediate or strong interfaces could be easily manufactured giving the ability to design composite materials for specific applications.

ACKNOWLEDGEMENTS

The Graduate School of Polymer Science and the Technical University of Denmark are gratefully acknowledged for financial support to the first author. This work was made as a part of the Framework Program “Interface Design of Composites Materials” which received its funding from the Danish Technical Research Council (STVF fund no. 26-03-0160). Lene Hubert is gratefully acknowledged for helping with the XPS measurements.

REFERENCES

- Ademovic Z, Wei J., Winther-Jensen B, Hou X, Kingshott P. (2005), *Plasma Process. Polym.*, 2, 53
- Bao G, Ho S, Suo Z, Fan B. (1992), *Int. J. Solids Structures*, 29, 1105
- Chu L-Q, Forch R, Knoll W, (2006) *Langmuir* 22, 2822
- Drews J, Goutianos S, Kingshott P, Hvilsted S, Rozlosnik N, Almdal K, Soerensen B.F, Accepted in *J. Vacuum Sci. Techn. A*
- Drews J, Launay H, Hansen C.M, West K, Hvilsted S, Kingshott P, Almdal K, (2007) Submitted to *Plasma Process. Polym.*
- Doi M, (1996) “Introduction to Polymer Physics”, Oxford Press.
- Hegemann D, Hossain M.-M, (2005), *Plasma Process. Polym.* 2, 554
- Hansen C. M, (1999) “Hansen solubility parameters – A user’s handbook” CRC Press LLC,
- Keller M, Ritter A, Reimann P, Thommen V, Fischer A, Hegemann D, (2005) *Surf. Coat. Technol.* 200, 1045
- Launay H, Hansen C.M, Almdal K, (2007) submitted to *Carbon*.
- Ryan M.E, Hynes A.M, Badyal J.P.S, (1996), *Chem. Mater.*, 8, 37
- Sano S., Kato K, Ikada Y, (1993), *Biomaterials* 14, 817
- Schiller S, Hu J, Jenkins A.T.A, Timmons R.B, Sanchez-Estrada F.S, Knoll W, Forch R, (2002) *Chem. Mater.*, 14, 235
- Sørensen B. F, Horsewell A., Jørgensen O, Kumar A. N, Engbæk P, (1998) *J. Am. Ceram. Soc.*, 81, 661
- Winther-Jensen B, Glejboel K. (2003) US 6628084 B1
- Winther-Jensen B, Christensen S.F, Petersen S.G (2004) US 0086660 A1
- Winther-Jensen B, Norrman K, Kingshott P, West K, (2005) *Plasma Process. Polym.*, 2, 319
- Yu Q.S, Yasuda H.K, (1999) *J. Polym. Sci. A*, 37, 1577

MICROFRACTOGRAPHIC ASPECTS OF INTERFACES IN CFRP UNDER FATIGUE LOADING

Wolfgang Förtsch *Horst E. Franz *Klaus Friedrich **

* EADS Innovation Works, IW-MS Structural Behaviour and Failure
Analysis

** Institut für Verbundwerkstoffe, University of Kaiserslautern

ABSTRACT

The properties of thermoset CFRP materials correlate with microstructure and failure behaviour. Microfractography is the only method of verifying fatigue failure and it permits insights into fracture behaviour under the influence of microstructures. A multitude of research programmes have shown that the interface plays a key role in the failure process and hence for mechanical properties. Special attention has to be paid to the processes of crack initiation and fatigue crack propagation under different loading conditions. Crack initiation occurs in different ways depending on pre-existing damage. A very common failure mechanism of fatigue growth was identified as occurring in the form of adhesive fatigue with a characteristic path for the crack front.

1. INTRODUCTION AND BACKGROUND

Carbon-fibre-reinforced plastics (CFRP) with a thermoset matrix are commonly used for structural components critical to safety in the aerospace industry. In recent years, the focus has been on manufacturing fibre composite components using preform/RTM techniques. These advanced materials should make it possible to achieve high cost savings through the potential for automating the process. It would also be possible to manufacture components with specific reinforcements suited to local loading conditions.

However, before the potential of RTM materials can be fully harnessed as advanced materials, a model for assessing the properties and the long-term behaviour of the material must be developed. In order to originate such a model, a great deal of analysis has been carried out to identify the basic failure mechanisms under mechanical load. However, this work has primarily focused on mechanical fracture approaches, some of which are based on simple failure models at the structural level (Talreja, 1987, Glaessgen et. al., 1998). Other authors (Schulte, 1992) established structure-property correlations based on damage processes identified by means of x-ray methods and SEM investigations.

The properties of a material correlate with the microstructure and failure behaviour. The cause and the path of a failure are therefore mirrored by the related fracture surface. Microfractography is the only method of verifying fatigue failure and this method permits insights into fracture behaviour influenced by the microstructures of the materials at the submicroscopic level. The typical morphologies occurring on the fracture surfaces allow conclusions to be drawn about the load conditions determining failure and the formation and development of the fracture as a whole. Over recent decades a great deal of work has been carried out to correlate the fracture morphologies observed with the loading status during failure. The authors referred to here include GARTEUR, 1994 and various publications by Purslow and Franz. Although a lot of questions remain to be answered, the principle failure mechanisms at a microstructural level are well known today.

Generally speaking, it was found that the interface is a major factor in the failure process. The interface acts through four principal mechanisms: 1) as a crack initiation point due to local steps in the stiffness, 2) as the weakest point with preferred crack growth, 3) as a potential point for crack bifurcation and bridging, 4) as a potential point for energy dissipation (Förtsch 2005). Nevertheless, the interacting mechanisms and the complex load state means that the role of the interface was often not given due consideration in the failure process. This aspect will become increasingly important especially with the introduction of the RTM/preform process.

This paper will look at the microfractographic perspective and attempt to describe the main aspects of the role played by the interface during failure of thermoset CFRP under fatigue loading.

2. BASIC MICROSCOPIC FAILURE MECHANISMS

Mode I (tension) and mode II (shear) are the key players in the failure process from the microfractographic perspective. It can be shown for brittle thermoset materials that the microstructural fatigue failure (and the static failure) only occurs under local mode I (tension) stresses. The characteristic morphology of local fatigue under mode I conditions are fatigue striations (Fig. 1).

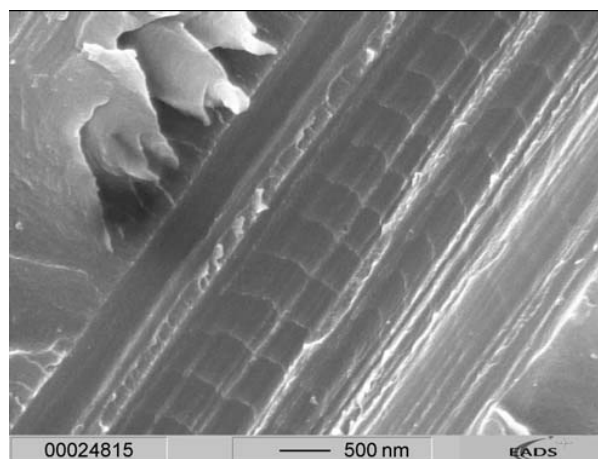


Fig. 1. Fatigue striations in a fibre imprint demonstrate the characteristic morphology of mode I loading

The fatigue striations can be found in fibre imprints and in the resin matrix. The appearance and the mechanism of formation for fatigue striations are defined in Franz 1980 and Förtsch 2005.

The well-known hackle structure as a characteristic sign of mode II failure and the rollers as morphology of mode II failure under fatigue are secondary structures based on local mode I failures at a deeper level (Heutling et. al. 1998 → Fig. 2). The first phase of the formation of the rollers reveals that microcracks grow from the fibre matrix interface into the shear region. The locally acting mode I means that fatigue striations can be found on the surface and these striations disappear as the fatigue process continues.

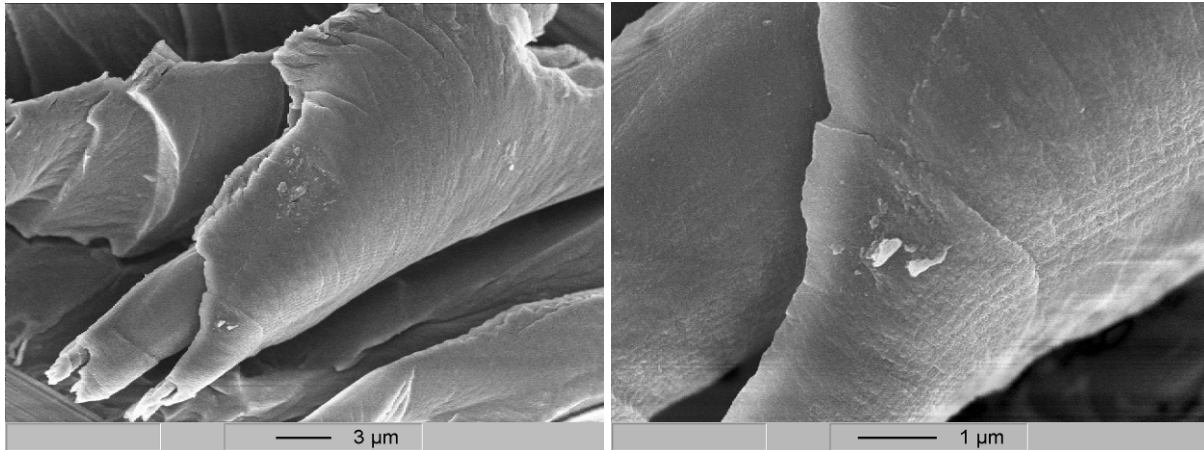


Fig. 2. First phase in the formation of rollers under mode II - fatigue load (left). Fatigue striations (right) on the surface demonstrate mode I acting locally.

Although a large number of research programs have carried out work on different reinforcement structures and under different loading conditions, it was possible to identify a principle failure mechanism under fatigue load (Förtsch et. al 2002): When an external alternating load is applied, an inhomogeneous stress field forms in the composite material. Fatigue growth occurs in areas stressed within the growth stress as secondary fractures within the matrix. The primary crack front runs along these damaged points in the material until global failure occurs. Failure therefore occurs between a homogenous crack growth and a discontinuous damage process as a gradual failure with secondary crack growth. This is dependent on the level of 3 dimensionality provided by the reinforcement.

3. THE ROLE OF THE INTERFACE

The basic microscopic failure mechanisms referred to above have varying consequences on the site of the interface in the failure process.

3.1 Crack initiation process

It is important to focus on crack initiation. This process is still not very well understood. Based on attempts at statistical crack formation, it is possible to verify initial growth by X-ray refraction (Hentschel et. al. 1994). However, this method only determines the relative increase of microcracks. The location of crack initiation cannot be seen. Nevertheless, it has been assumed, that the interface plays also a major role in this initial process.

Preparing cross-sections of specimens after being subject to compression fatigue loading for different periods enabled formation of the microcracks to be determined on model materials. Fig. 3 shows SEM pictures perpendicular to the 90°-plane of the material not subject to load compared to the material after compression fatigue loading. A multitude of microcracks appears in the material. On the one hand, this confirms the statistical crack formation. On the other hand, it can be seen that the crack initiation process for this material under fatigue load is independent

of the fibre/matrix interface. In this case, the ongoing damage process may take the form of a sudden global failure of the material as an extreme case of the principal failure mechanism under fatigue load referred to above.

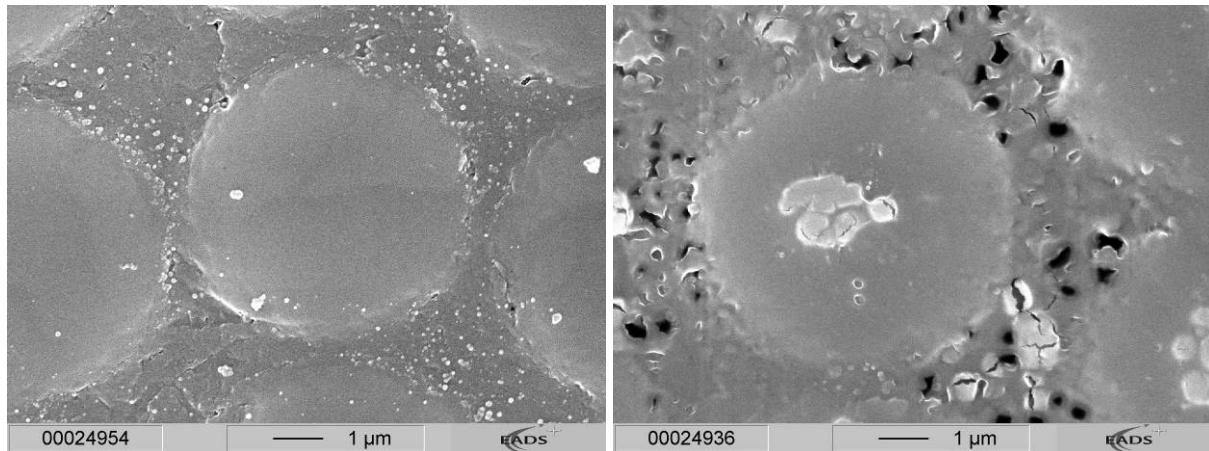


Fig. 3. Initiation of microcracks. Left: material not subject to load. Right: Microcracks after compression fatigue loading.

Notched and impacted specimens show more or less pronounced growth for a primary fatigue crack front depending on their reinforcement structure. Characteristic fracture morphologies appear on the fracture surface depending of the locally acting loading mode.

Mode I fatigue fractures exhibiting growth of a primary crack front are thereby initiated at the given impact cracks or notches. Secondary fractures are initiated at singularities inside the stress field of the primary crack front. The singularities are typically stages of stiffness in resin pockets or interacting fibres with different orientations. In both cases, the interface acts as the crack initiation point. To date, it has not been possible to identify crack initiation as a laminar adhesive failure between fibre and matrix. The fatigue fracture growth of the primary crack front and the secondary cracks under mode I is aligned on the next fibre/matrix interface.

Rollers are a characteristic morphology of fatigue failure under shear loading. They develop due to mode I stresses acting locally inside the shear band within the matrix (Fig. 4). The microcracks propagating formation in the first phase are initiated at the fibre/matrix interface and grow inside the matrix (arrows in Fig.4).

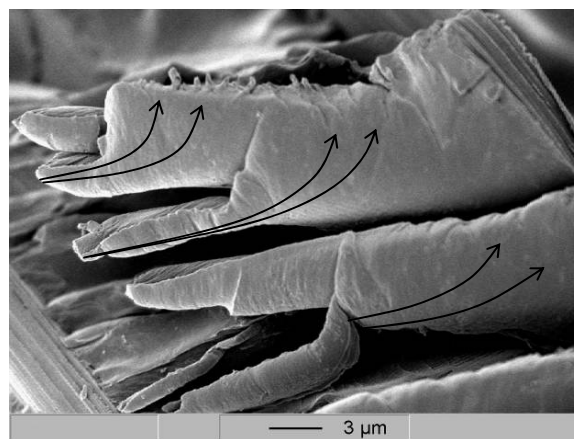


Fig. 4. Initiation and fatigue crack growth of the microcracks for the formation of rollers at the fibres (Heutling 1998).

3.2 Fatigue crack growth

It is necessary to distinguish between mode I and mode II loading in order to consider ongoing fracture growth of the primary crack front after the crack initiation process.

As mentioned before, the fracture becomes aligned on the next interface in the case of local mode I loading. The interface seems to be the weakest point in terms of adhesion. Since load transfer occurs through the fibres, fracture growth occurs afterwards primarily along the fibre/matrix interface.

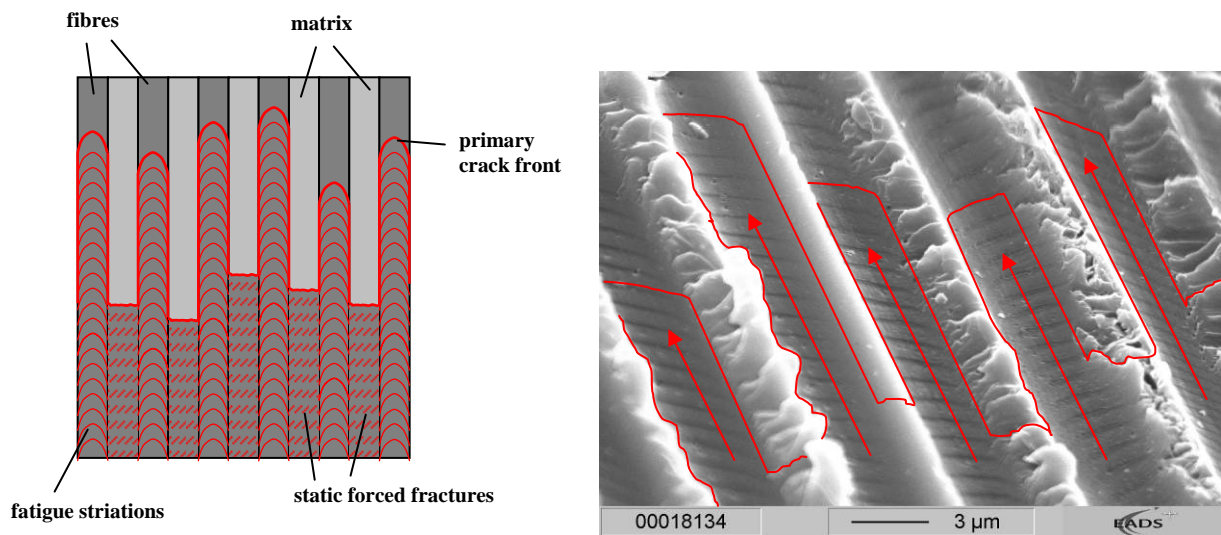


Fig. 5. Diagrams showing the finger growth (“adhesive fatigue”) under predominant mode I load (left), and schematic path of the primary crack front on a real fracture surface (right)

A type of “adhesive fatigue” occurs in the form of finger growth (Fig. 5): firstly, the fibres become detached from the matrix resin in stages as fatigue striations form in the fibre imprints. After fracture growth proceeds over a specific path length in the fibre imprint, the matrix between the fibres is stressed to the point of fracture elongation. A forced fracture occurs exhibiting a pure static fracture morphology between the fibres. Depending on the load conditions, sporadic fatigue failures can be found between the fibre imprints. However, the failure between the fibres is not connected with the fibre/matrix interface in every case (Franz 1991, Förtsch 2005).

In the case of pure mode II load, the interface plays a minor role. Although the local crack is caused by local mode I, the fracture direction is influenced by the shear band due to the given shear load. The actual fracture therefore occurs and dissipates its energy due to the shear stresses occurring primarily inside the matrix.

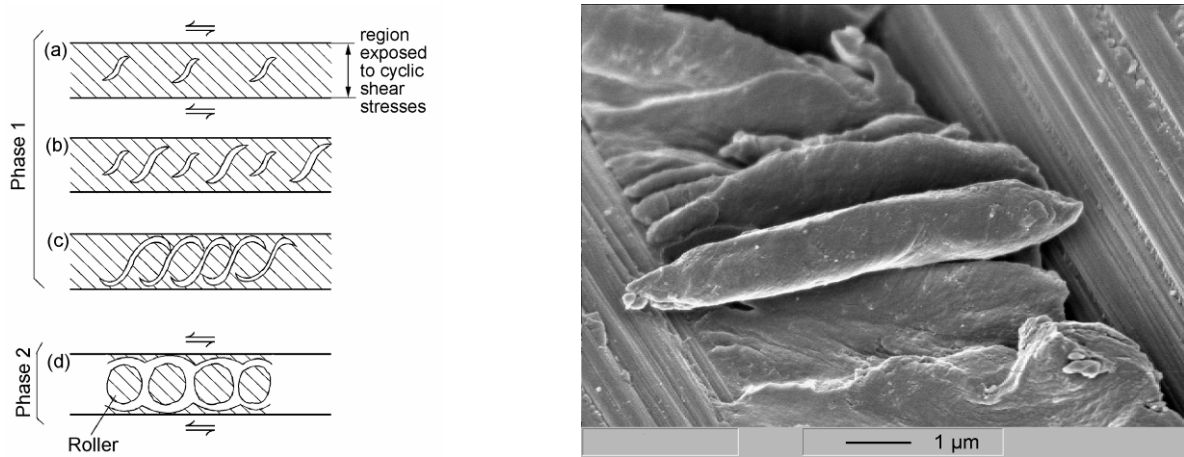


Fig. 6. Schematic diagram showing formation of the rollers (Heutling 1998).

Pure mode I or mode II loads represent extreme cases of loading conditions. In reality, the majority of failures occur under mixed-mode conditions. The investigations showed that mixed-mode loading leads to preferred growth at the interface with distinct formations of fatigue striations as “adhesive fatigue” with finger growth referred above. This is due to the mode I share. For example, Fig. 7 shows a fracture surface exhibiting typical fatigue striations inside the fibre imprints and static forced fractures in the matrix between the fibres. The static fractures between the imprints show the characteristic morphology of hackles as a sign of local shear loading. Due to the fact that pure mode II (shear) load occurs infrequently in practice, “adhesive fatigue” with finger growth is the most common failure mechanism.

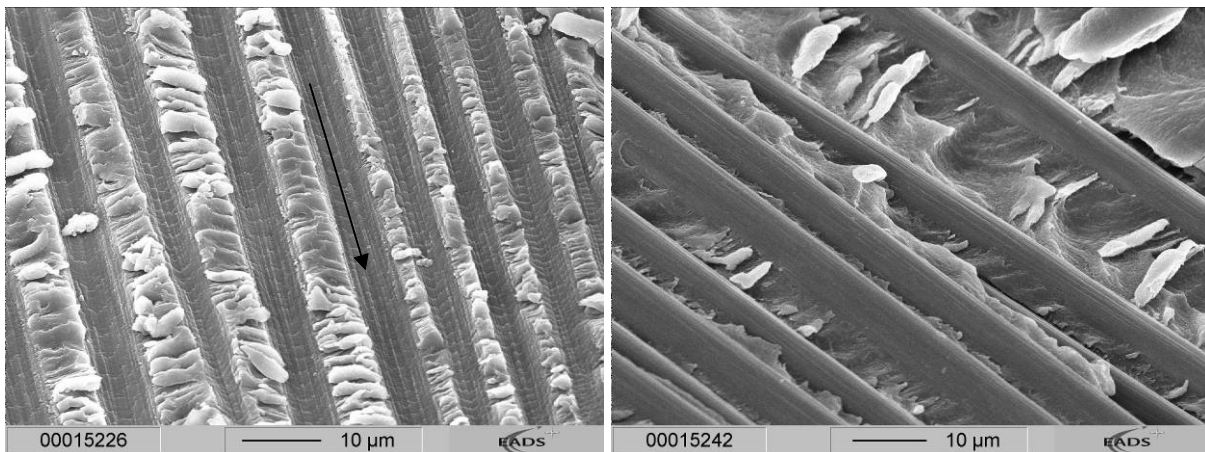


Fig. 7. Fracture surface and matching fracture surface of a mixed-mode fatigue area

4. CONCLUSION

The paper presents the principle microfractographic aspects of the interface under fatigue load. The investigations show that the interface plays a key role in the failure process and hence for the mechanical properties of thermoset CFRP materials:

- The crack initiation process in materials without pre-existing damage seems to be statistical and independent of the fibre/matrix interface.
- Crack initiation occurs in the stress field of a given crack primarily at single points of the interface due to stages in the stiffness in resin pockets or at interacting fibres with

different orientations. No evidence was found for crack initiation as a laminar adhesive failure between fibre and matrix.

- Under mode II loading, the microcracks for the formation of the characteristic rollers in the first phase are initiated at the fibre/matrix interface and grow inside the matrix
- The fibre/matrix interfaces are the preferred path of growth under mode I conditions as this appears to be the weakest point in terms of adhesion.
- The “adhesive fatigue” occurring with the growth of the primary crack front in the form of fingers along the fibre/matrix interface is the most common failure mechanism. The failure of the matrix between the fibres is not connected with the interface.

From the microfractographic perspective, it is difficult to distinguish overall between interface and fibre induced effects which may act at the interface. A tailored design would facilitate exploitation of the positive effects of energy dissipation and targeted failure processes. Nevertheless, there remain a large number of questions to be answered. In particular, modification of the interface for optimum performance has not yet been adequately investigated.

ACKNOWLEDGEMENTS

The authors would like to thank Mr. D. Paulisch, Wehrwissenschaftliches Institut für Werk-, Explosiv- und Betriebsstoffe (WIWEB) and Mr. G. Loriot, Centre d’Essais Aéronautique de Toulouse (CEAT), for their support and excellent cooperation.

REFERENCES

- Förtsch, W (2005): Mikrofraktographische Untersuchungen zum Ermüdungsversagen vorgeschädigter Preform-CFK-Werkstoffe mit EP-Matrizes. Institut für Verbundwerkstoffe GmbH
- Förtsch, W.; Franz, H.E, Friedrich. K June 3-7 (2002) . Investigation into damage mechanisms in advanced composite materials for the purpose of material improvement and damage prediction. 10th European Conference on Composite Materials, Bruges - Belgium,
- Franz, H.E. (1991) Mikrofraktographie an faserverstärkten Verbundwerkstoffen. Prakt. Met., 26, pp. 404 - 419
- Franz, H.E (1980) Schwingbruchstrukturen an faserverstärkten Kunststoffen. Z. Werkstofftech, 11, 343 - 360
- GARTEUR(1994), Group for Aeronautical Research and Technology in Europe, AG 14: Fractography of composites, Final Report. GARTEUR Report No. TP083,
- Glaessgen, E.H.; Raju I. S.; Poe Jr., C. C (1998) Debond Analysis for Stitched Composite Structures. International Conference on Computational Engineering Sciences. Atlanta, Georgia: October 6-9,
- Hentschel, M.P.; Harbich, K.W.; Lange, A (1994) Nondestructive evaluation of single fibre debonding by X-ray refraction. NDT and E International – Non Destructive Testing and Evaluation, 27, 5, , pp. 275 - 280
- Heutling, F., Franz, H.E., Friedrich, K. (1998) Mikrofraktographische Analyse des Delaminationswachstums in zyklisch belasteten Kohlenstoff/ Duroplastharz – Verbundwerkstoffen. Mat.-wiss. u. Werkstofftech. 29 , pp. 239-253
- Purslow, D (1983) Fractographic analysis of failures in CFRP. In: AGARD Conference Proceedings No. 355. 56th Meeting of the Structures and Materials Panel. London, United Kingdom 12 – 14 April

- Purslow, D (1989): Matrix fractography of fibre reinforced epoxy composites. *J. of Materials Science* 24, pp. 167 - 172
- Schulte, K., (1992) Faserverbundwerkstoffe mit Polymermatrix-Aufbau und mechanische Eigenschaften. Forschungsbericht DLR 92-28, Cologne
- Talreja, R (1987) *Fatigue of Composite Materials*. Lancaster, Technomic Publishing Company Inc., ISBN 87762-516-6,

ESTIMATION OF INTERFACE COHESIVE LAWS BY DIGITAL IMAGE CORRELATION

S. Goutianos^{*}, J. Drews^{**}

^{*}Materials Research Department, Risø National Laboratory, Technical
University of Denmark, Frederiksborgvej 399, DK-4000 Roskilde

^{**}Polymer Department, Risø National Laboratory, Technical
University of Denmark, Frederiksborgvej 399, DK-4000 Roskilde

ABSTRACT

A digital image correlation technique is used to estimate the interface cohesive laws between glassy carbon and an epoxy matrix. Glassy carbon is selected as model material to mimic carbon fibres. This choice enables the use of planar specimen for which the application the J-integral approach is straightforward. Digital image correlation enables measurements of deformation fields with a sufficient precision over large areas. The limitations of the technique are discussed and suggestions for improvements are given.

1. INTRODUCTION

Composite mechanical properties such as strength and maximum strain that are governed by the matrix and interface properties are strongly dependent on the level of adhesion, interfacial bond strength, between the reinforcing fibres and the polymeric matrix in which the fibres are embedded (Madhukar and Drzal 1991). An example is given in Fig. 1.(a) which shows schematically a notched unidirectional composite structure under general loading such that mixed mode crack growth takes place. The fracture resistance can be significantly enhanced by fibre bridging shown in Fig. 1(b). Fibre bridging is controlled to a great extent by the interface properties as interface failure (shown by the arrows in Fig. 1.(b)) occurs at a certain point under monotonic loading. To design a composite material with specific properties a relationship between the interface adhesion and fracture behaviour of the composite and a method to control the level of adhesion are required. The interfacial bond can be optimised through fibre surface chemical modification (Drews et al. 2007), whereas the former can involve both experiments and modeling. In both cases a method to measure the interface fracture behaviour is needed. Usually the fibre/matrix interface debonding is characterised in terms of fracture energy (linear fracture mechanics) under the assumptions of small-scale non-linear interface crack tip zone. If this assumption is not met, then cohesive laws (stress-separation relations) need to be used. The cohesive laws (see Fig. 1(c)) are particular favourite for simulating fracture. In the present work

we present an experimental method to directly measure interface cohesive laws under nominal Mode I (normal crack opening) using digital image correlation. The limitations of the method are discussed and suggestions for improvements are proposed.

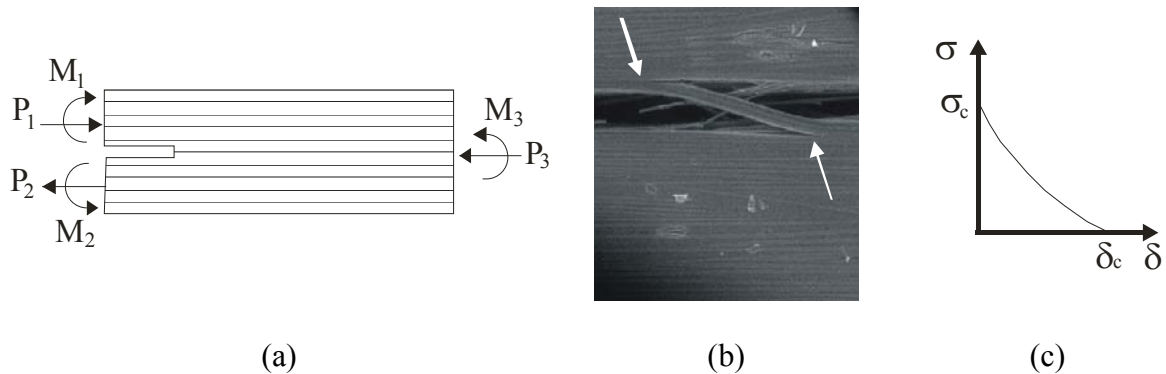


Fig. 1. (a) Schematic illustration of a notched unidirectional composite under general loading, (b) fibre bridging under mixed mode conditions, (c) Interface cohesive law.

2. MATERIALS AND SPECIMEN GEOMETRY

Planar glassy carbon (SIGRADUR G, HTW Hochttemperatur, Germany) substrates ($65 \times 1 \times 5 \text{ mm}^3$) were chosen to simulate carbon fibres. Planar specimens offer several advantages over circular fibres. Chemical treatment/modification and surface analyses are easier performed on flat surfaces. It is also possible to investigate their adhesion to an epoxy resin using DCB (Double Cantilever Beam) specimens (see Fig. 2) by the J-Integral approach which is explained in the subsequent section. However, the use of glassy carbons presents also some disadvantages as their much Young's modulus ($E = 35 \text{ GPa}$) is significantly lower than typical carbon fibres due to their disordered structure and there are quite brittle.

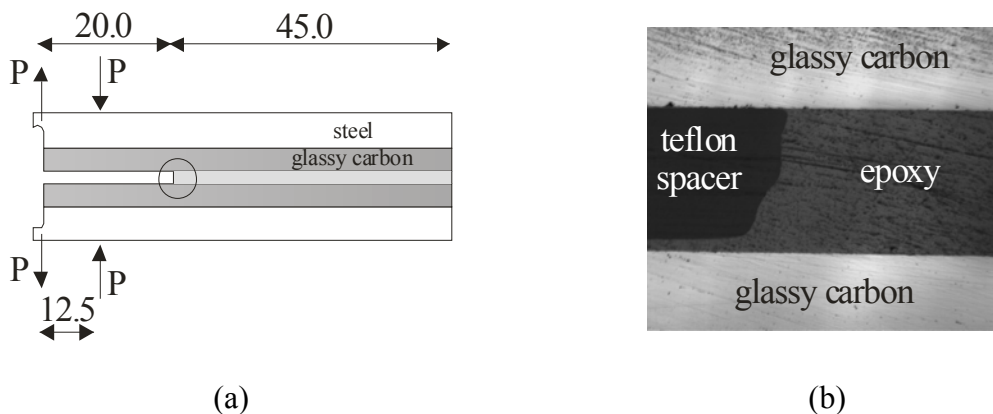


Fig. 2. (a) Sketch of the DCB sandwich specimens (all units in mm), (b) close view of the DCB specimens near the notch.

The glassy carbon substrates presented in the current work were pulsed plasma treated with 1,2-methylenedioxybenzene (ppMDOB). The plasma power was 0.7 W/L and the treatment time equal to 10 min. Under these conditions the thickness of the deposited polymer film is approximately 100 nm (Drews et al. 2007). This type of monomer was chosen because of its special abilities under soft plasma. During plasma the dioxy-ring opens and creates carboxylic acid groups or ester linkage while the ring structure is preserved (Winther-Jensen et al 2005). A schematic illustration of the possible ppMDOB film is given in Fig. 3.

The plasma treated glassy carbon substrates were placed in a rubber silicon mould and as epoxy resin (Prime-20, SP systems, UK) was cast in between the glassy carbons after it has been degassed to remove trapped air. Teflon spacers (0.5 mm thick) were used to keep the glassy carbon substrates apart during casting. The teflon spacer also acts as a crack starter as can be seen in Fig. 2(b). The DCB specimens were then cured for 24 hrs at room temperature and subsequently post-cured at 50°C for 16 hrs. After curing the specimens were ground and fine polished with a diamond paste to create a fine flat surface necessary for the digital image correlation technique. Then two steel beams (6 mm thick), which could be mount on the test fixture briefly described in the subsequent section, are glued in the sandwich specimens as can be seen in Fig. 2(a). An epoxy adhesive (Scotch Weld) was used to glue the DCB specimens to the steel beams. The curing time was 24 hrs at room temperature.

The specimens were placed into an aqueous environment. The plasma coating reacted with the water. A lost of adhesion was observed between the modified glassy carbon and the epoxy resin. This behaviour could be attributed to hydrolysis of the ester linkages e.g. breaking the polymer into smaller pieces. Such a low adhesion interface was selected as a test case to assess the capabilities of the digital image correlation technique to measure small deformation fields at low loads.

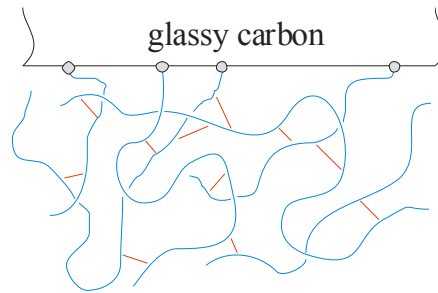


Fig. 3. Schematic illustration of the deposited MDOB film on the glassy carbon surface. The blue lines represent the entangled polymer chains, the red lines indicate cross-linking of the polymer chains and the grey circles bonds between the glassy carbon and MDOB

3. BASIC MECHANICS

3.1 J-integral measurement. A special fixture (Sørensen et al. 1998) was used to load the DCB sandwich specimens with force couples (Fig. 5). This creates pure bending moments as shown in Fig. 4. The plane strain energy release rate can be determined by taking the J-integral (Rice 1968) along the external boundaries of the specimen:

$$J = \frac{1-\nu_2^2}{E_2} \frac{M^2}{B^2 H^3 n^3 I} \quad (1)$$

where E_2 and ν_2 are Young's modulus and Poisson's ratio of the steel. M is the applied moment, H the steel thickness and B the width. The parameters η and I depend on the geometry and elastic properties of the steel beams and glassy carbon substrates. In Eq.1 the contribution from the epoxy is neglected as its stiffness is much lower than the steel and the glassy carbon. For this specimen crack growth is stable (Bao et al. 1992; Sørensen 2002) and the J-integral is independent of the crack length.

3.2 Derivation of cohesive law. The J-integral along a path just outside the failure process zone

is (Rice 1968):

$$J = \int_0^{\delta^*} \sigma(\delta) d\delta \quad (2)$$

where δ^* is the end-opening of the cohesive zone and σ are the cohesive stresses. Due to its path independence, the J-integral in Eq. 2 has the same value as in Eq. 1. Differentiation with respect to δ^* gives (Suo et al. 1992):

$$\sigma(\delta^*) = \partial J / \partial \delta^* \quad (3)$$

Thus, by recording J (function of the moment, M , from Eq. 1) and the end-opening, δ^* , simultaneously the cohesive law can be obtained from Eq. 3. In the next section a method to measure the end-opening via the digital image correlation technique is presented.

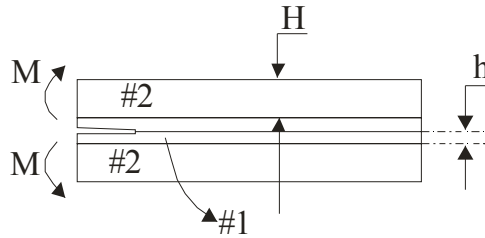


Fig. 4. Schematic illustration of a DCB specimen loaded with pure bending moments. #1: glassy carbon and #2: steel.

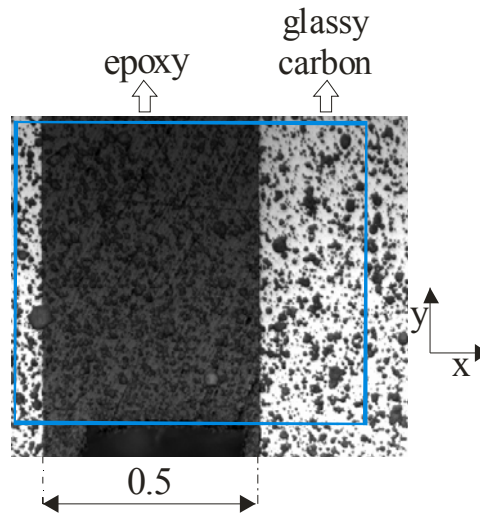


Fig. 5. Random speckle pattern (TiO_2) on the surface of the DCB sandwich specimens. The size of the image in pixels is 1280x1024. The blue frame indicates the area used in the digital image correlation technique (all dimensions in mm).

4. DIGITAL IMAGE CORRELATION

Digital image correlation is a robust experimental method to measure real-time deformation fields, usually on the surface of a body, by recording the motion of a speckle pattern before and after deformation. The accuracy of the correlation between recorded images depends upon the

quality of the speckle pattern and the resolution of the imaging equipment. The quality of the speckle pattern is described by the refinement, distribution and randomness of the speckle with respect to pixel size (Berfield et al. 2007). An optical microscope equipped with a CCD camera with 1280x1024 pixel resolution was used. The imaging set-up produced a resolution of 0.78 $\mu\text{m}/\text{pixel}$ limited by the magnification capabilities of the microscope. Given the image resolution, TiO₂ micro-particles were chosen for the speckle pattern. TiO₂ micro-particles were added in ethanol. The suspension was put into an ultra-sonic bath for 10 min to evenly distribute the titanium dioxide particles. The suspension was then left for 4 hrs to allow the larger particles to move to the ground. The suspension was then filled into a fine airbrush system - air was provided by a constant 3 bar pressure regulated compressed air system. The distance between the airbrush nozzle and the specimen was approximately 15 cm. During spraying the ethanol evaporates and afterwards it was make sure that particles that do not rest on the specimen were fall in the ground. A typical speckle pattern is shown in Fig. 5 where the blue rectangle is the boundary of the area analysed via digital image correlation. Although there are not well-define guidelines to assess the quality of a speckle pattern the image intensity profiles, where the number of pixels at a given grey-scale intensity value from 0 to 255 are plotted against the intensity value, can be used to qualitatively describe the quality of a pattern. Such a profile for the pattern given in Fig. 5 is shown in Fig. 6. The pattern appears to have a bimodal distribution and a sharp peak and at the end of gray scale. This is directly associated with the presence of two materials (glassy carbon and epoxy) with quite different reflectivity as can be seen in Fig. 6 where the image intensity profile is decomposed to two profiles: one from the region occupied from the epoxy and one from the glassy carbon area. The light was adjusted in such a manner to have a bell-shape distribution in the epoxy region while keeping the brightness in the glassy carbon to a low values. In this way the peaks in the glassy carbon are quite lower than in the epoxy resin as can be seen in Fig. 6.

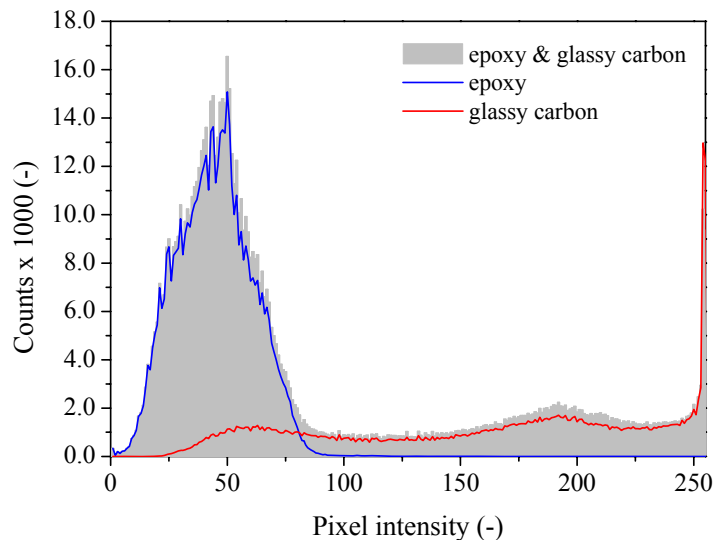


Fig. 6. Pixel intensity histograms for the pattern presented in Fig. 5.

The analysed area (see Fig. 5) via the digital image correlation (using the Aramis software) was divided in subsets (or facets) of 15x15 pixels. The overlapping of the facets was 2 pixels. Higher size of the subsets would lead to smoother results but at the same time it would be not possible to capture accurately local deformations. On the other hand smaller subset sizes could not be used due to the size of the TiO₂ particles which in turn were chosen based on the limited

magnification capabilities of the optical microscope that was available.

5. RESULTS & DISCUSSION

In Fig. 7(a) contours of displacement in x direction are given for four different loadings. Fig. 7(a) corresponds to the initial configuration – zero displacement. In Figs. 7(b) to 7(d) the applied moment is 0.19, 0.55 and 0.65 Nm respectively. The white elements indicate failure of the image correlation algorithm in these areas.

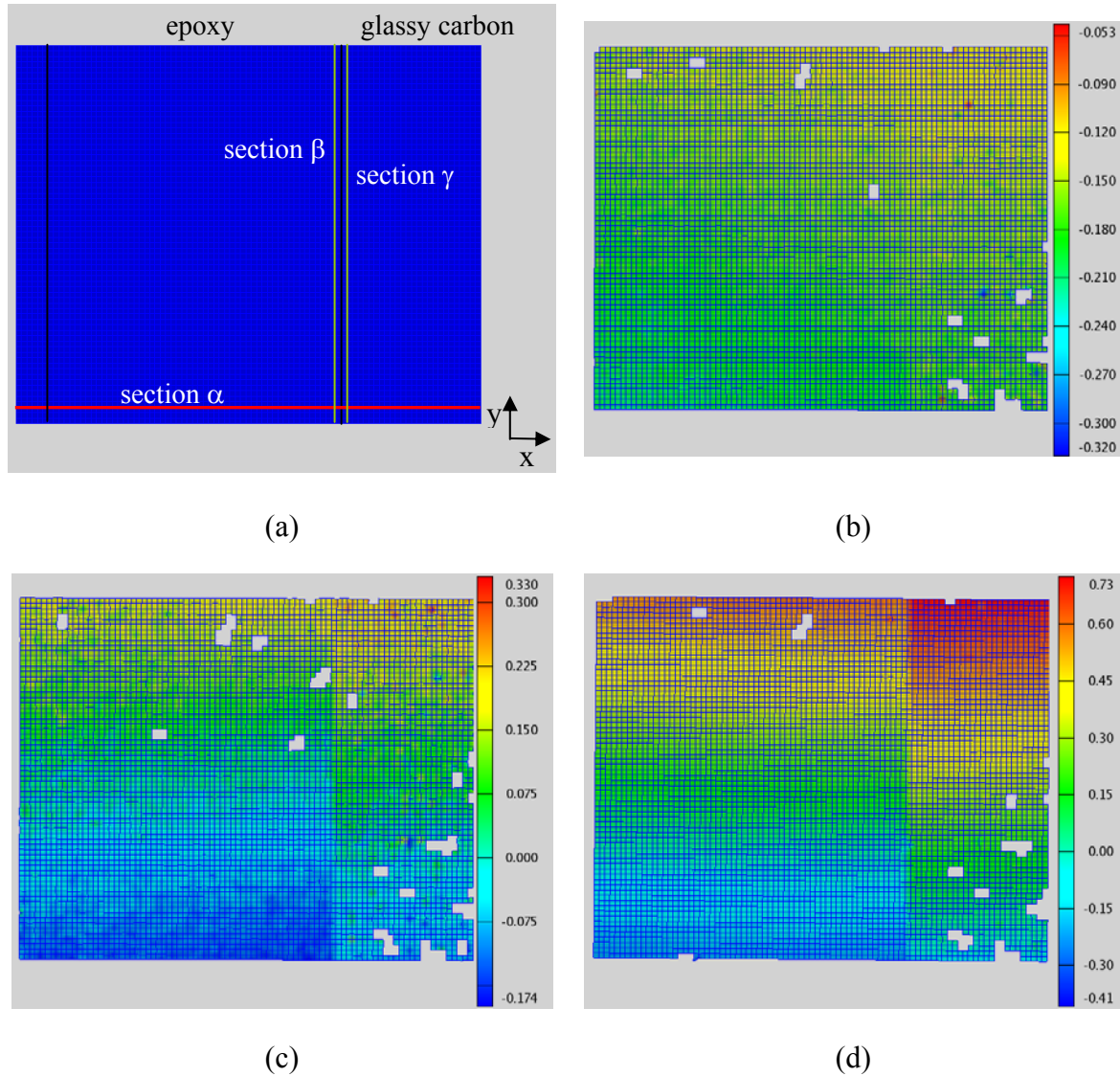


Fig. 7. Contours of displacement in x direction at different loadings: (a) undeformed configuration, (b) applied moment $M = 0.19$ Nm, (c) $M = 0.55$ Nm, and (d) $M = 0.65$ Nm.

In Fig. 7(b) the deformation field is uniform along the x direction indicating uniform straining of both the epoxy and the glassy carbon. In Fig. 7(c) a discontinuity in the displacements can be seen in the right interface, the interface starts to debond from the glassy carbon. The other interface (on the left side) is intact as the deformation field is still uniform. Finally, in Fig. 7(d) the interface is completely broken. To measure the end-opening, δ^* , the displacement in the x direction along section α (Fig. 7(a)) is used at different load steps. The profiles corresponding to Figs 7(b) to 7(d) are plotted in Fig. 8. The displacement discontinuity at the right interface can

be clearly captured by the digital image correlation technique. The end-opening, δ^* , can be calculated as the difference in displacements across the interface.

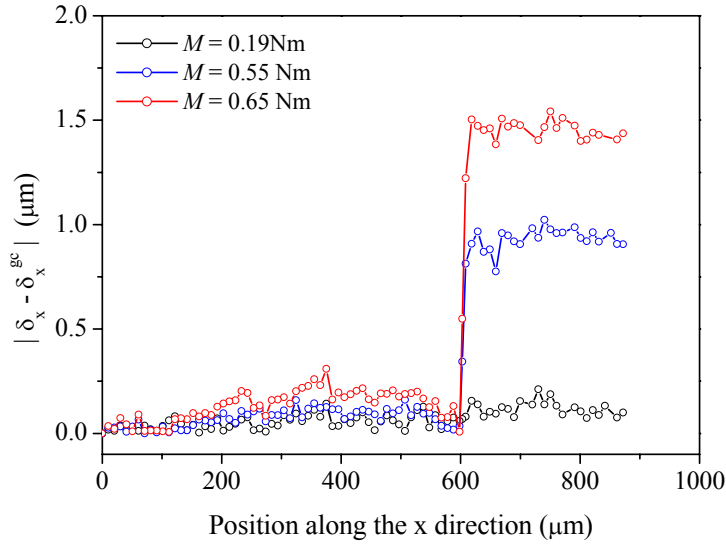


Fig. 8. Displacement x profiles along section α at different applied moments. δ_x^{gc} is the displacement of the point in the glassy carbon at the far right point of section α (see Fig. 7(a)).

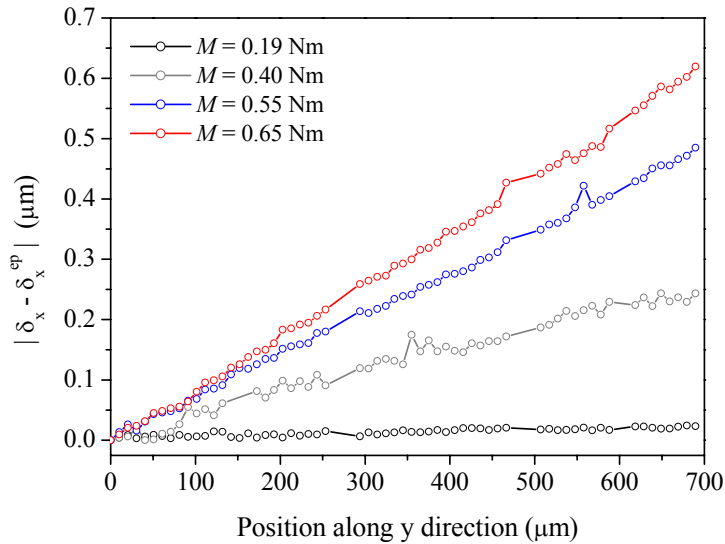


Fig. 9. Displacement x profiles along section β at different applied moments. δ_x^{ep} is the displacement of the point in the epoxy at the upper point of section β (see Fig. 7(a)).

The capabilities of the digital image correlation technique in measuring small deformation field can also be seen in Fig. 9 where the displacements in x direction along section β are plotted for different applied moments. If the displacement profile for $M=0.65$ Nm is considered then it can be seen that the difference in displacement between the upper and lower point of section β is

0.7 μm less than the image resolution which is 0.78 $\mu\text{m}/\text{pixel}$. All the intermediate points are calculated with sub-pixel resolution. Next in Fig. 10 the displacement in x direction are plot along sections β and γ for two different applied moments. The difference in displacement between the two sections gives the crack opening along the interface. For an applied moment the crack is fully open in the window analysed.

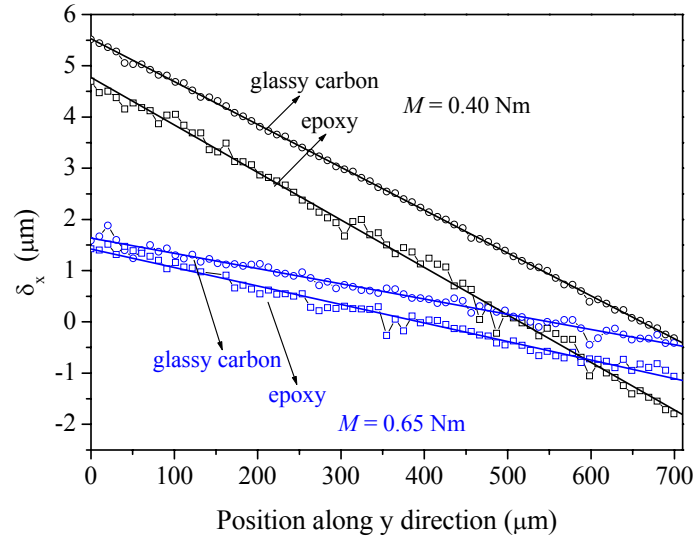


Fig. 10. Displacement x profiles along sections β (epoxy) and γ (glassy carbon) at two different applied moments.

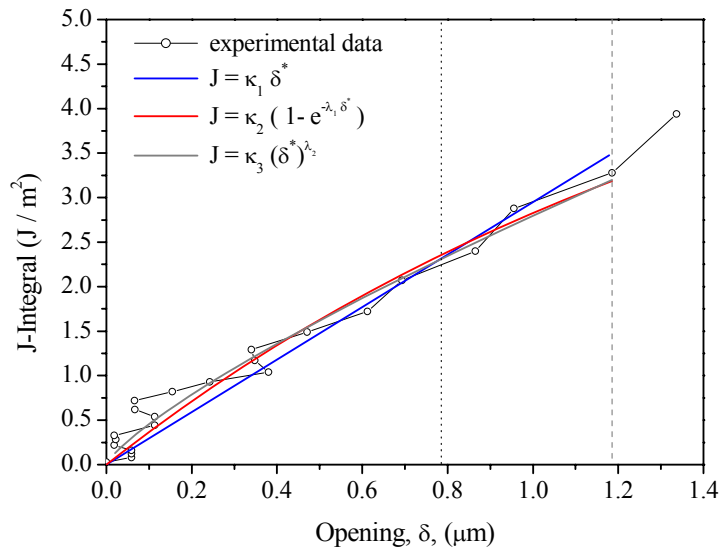


Fig. 11. J-integral as a function of the crack end-opening δ^* . The solid lines represent different fitting curves.

The J-integral calculated from Eq. 1 are plotted as a function of the crack opening measurements

obtained from the method described (see Fig. 8) in Fig. 11. The dashed lined indicates the critical crack opening. The experimental up to the critical crack opening are fitted with a number of different curves to obtain the interface cohesive laws through Eq. 3. All the experimental data below the dotted line in Fig. 11 are calculated with sub-pixel resolution. As it is realised that with the given magnification there are uncertainties in the measurements, simple functions were chosen to fit the experimental data. The estimated interface cohesive laws are shown in Fig. 12 with the cohesive stress set to zero at the point of the critical crack opening. The obtained interface cohesive laws should be considered only estimations of the actual interface cohesive laws. Although the method described here proved to be quite powerful more accurate analyses are required to allow measurement of interface cohesive law shape and accurate peak stress and critical interface crack opening. The required accuracy could be obtained by using a microscope with higher magnification capabilities or by performing the experiments inside the chamber of a scanning electron microscope. In this case nano-particles should be used instead of micron size TiO₂ particles used in the present work. Such experiments would also give detailed information about the deformation (i.e. plasticity) in the resin close to crack tip.

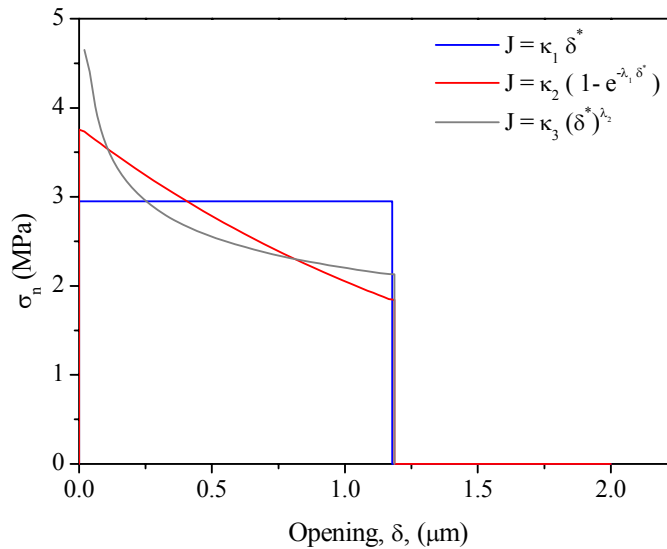


Fig. 12. Estimated interface cohesive laws.

5. CONCLUDING REMARKS

The feasibility of the digital image correlation technique in measuring interface cohesive laws at the micron scale was demonstrated. The micro-scale pattern was produced using TiO₂ particles and it was possible to measure deformations (displacements) less than a micron. The same technique can be equally used to different length scales, i.e. nano-scale, to measure both the interface cohesive laws more accurately and the strain filed in the matrix material near the failure process zone.

ACKNOWLEDGEMENTS

This work is supported by the Danish Technical Research Council under grand # STVF fund no. 26-03-0160 “Interface Design of Composites Materials”. C.H. Madsen and E. Vogeley are

acknowledged for technical assistance and Dr C. Berggreen from the Mechanical Engineering Department-Technical University of Denmark for providing access to the Aramis (GOM mbH) software.

REFERENCES

- Bao, G., Ho, S., and Suo, Z. (1992). The role of material orthotropy in fracture specimens for composites". *Int. J. Solids and Structures*, 29. 1105-1116.
- Berfield, T.A., Patel, J.K, Shimmin, R.G., Braun, P.V., Lambros, J. and Sottos, N.R. (2007). Micro- and nanoscale deformation measurement of surface and internal planes via digital image correlation. *Exp. Mech.* 47. 51-62.
- Drews, J., Goutianos, S., Kingshott, P., Hvilsted, S., Rozlosnik, N., Almdal, K. and Sørensen, B.F. (2007). Plasma polymerized thin films of maleic anhydride and 1,2-methylenedioxybenzene for improving adhesion to carbon surfaces. *J. Vacuum Sci. Techn. A.* 25. 1108-1117.
- Madhukar, M.S. and Drzal, L.T. (1991). Fiber-matrix adhesion and its effect on composite mechanical properties – Properties 2. Longitudinal (0-degrees) and transverse (90-degrees) tensile and flexural behavior of graphite epoxy composites. *J. Comp. Mat.* 8. 958-991.
- Rice, J. R. (1968). A path independent integral and the approximate analysis of strain concentrations by notches and cracks. *J. Applied Mech.* 35. 379-386.
- Suo, Z., Bao, G., and Fan B. (1992). Delamination R-curve phenomena due to damage. *Mech Phys Solids.* 40. 1-16.
- Sørensen B.F. (2002). Cohesive law and notch sensitivity of adhesive joints", *Acta Materialia.* 50. 1053-1061.
- Sørensen, B.F., Horsewell, A. Jorgensen, O., Kumar, A. (1998). Fracture resistance Measurement Method for in situ Observation of Crack Mechanisms. *J. Am. Ceram. Soc.* 81. 661-669.
- Winther-Jensen, B., Norrman, K., Kingshott, P., West K., (2005). Characterisation of plasma-polymerised fused polycyclic compounds for binding conducting polymers. *Plasma Processes and Polymers.* 2, 319-327.

SURFACE CHARACTERIZATION USING HANSEN SOLUBILITY (COHESION) PARAMETERS

Charles M. Hansen

Jens Bornøs Vej 16, 2970 Hørsholm, Denmark

ABSTRACT

Surfaces can be reliably characterized by the cohesion energy parameters, of the type commonly called Hansen Solubility parameters (HSP). Data for many fillers fibers, pigments and other surfaces are available. The implication for composites is that the physical affinity or cohesion between fibers and polymer matrix will be a maximum when the energy parameters match. The HSP parameters assigned to many liquids and polymers have recently been confirmed by statistical thermodynamic treatments.

1. INTRODUCTION

The purpose of this paper is to confirm that surfaces can be reliably characterized by the cohesion energy parameters of the type commonly called Hansen solubility parameters (HSP) (Hansen 1967a; 1967b; 1967c; 1967d; 1999; 2007). Comparing the HSP of a surface with the HSP of a given solvent or polymer allows prediction of their interaction. The HSP of many pigments, fillers, fibres, and other surfaces have been found by their interaction with a series of well-defined test solvents (Hansen, 1967b; 1967d; 1999; 2007). The HSP of the usual test solvents are derived from their energies of vaporization and are supported by thousands of data points. When a liquid is evaporated, all the bonds holding it together are broken. The total cohesive energy of the liquid is the sum of the different types of interactions holding the liquid together. These are the atomic dispersion interactions (D) that clearly are also present in all molecules, the molecular dipolar interactions (P), and molecular hydrogen bonding (H), which should be more properly called an electron interchange interaction. The sum of the cohesion energy deriving from these three types of interaction is equal to the total cohesion energy as measured by the energy of vaporization.

Solution, swelling, chemical resistance, permeation rate, or other effect based on solubility can be used to assign HSP to non-volatile, bulk materials, such as polymers. Surfaces have been characterized by two different techniques. Pigments, fillers, and fibres are usually studied by measuring sedimentation rates in many well-defined solvents. The absolute sedimentation rates are normalized by the solvent viscosities and the density difference between the solvents and sample to arrive at relative sedimentation rates for all the solvents. Those solvents with the longest relative sedimentation times are used to assign the cohesion energy parameters to the

surface by similarity of cohesion energy properties of the “good” test solvents. Plane surfaces can be characterized by well-defined test solvents in terms of whether or not an applied droplet spontaneously spreads and whether or not an applied film spontaneously retracts.

There has been great interest in characterizing surfaces because of the importance that this has for wetting, adhesion, lubrication, adsorption, dispersion of pigments and dyes, surface contamination and cleaning, etc. (Barton 1991). There are far too many references to discuss here, but the general conclusion is that the physical affinities of two materials are at a maximum when their energies match. These energies can be measured using the surface or interfacial free energy or different cohesion parameters, such as those of Hildebrand and Hansen. There is improved predictability when the energy of interest is divided into dispersion and “polar” parameters. The implication for the performance of composites is that the physical affinities or physical bonding between the matrix polymer and fibres will be a maximum when the energy properties match. It has been recognized in the coatings industry, however, that given segments or groups (alcohol, acid, amine) of the matrix polymer may prefer to adsorb on surfaces with energies (much) higher than that assigned to the polymer. These local segments or groups have energies that are more similar to the surface of the pigment, filler, or fibre, than they have for the rest of the matrix polymer. They will therefore seek the higher energy surface, thus matching energies, and this provides a stable anchor because there is no driving force for desorption. Water can have some influence on this type of bonding, however, since it also has high energy. It should also be recognized that chemical bonding between fibres and matrix polymer can be employed for still stronger bonds. Use of a sizing is a means to alter surface properties. Judicious choice of sizing can improve both processing and bonding, but the question of adhesion of the sizing to the fibres can also be raised.

2. HANSEN SOLUBILITY (COHESION) PARAMETERS

The cohesion energy parameters most widely used for the above characterizations are those developed by Hansen (1967a; 1967b; 1967c; 1967d; 1999; 2007). These are now called Hansen solubility (cohesion) parameters. They are based on an extension of the Hildebrand solubility parameter (Hildebrand and Scott 1950; 1962). The HSP assigned to many liquids and polymers many years ago by Hansen have recently been confirmed with amazing agreement using a statistical thermodynamics treatment by Panayiotou (2007). See Table 1. Panayiotou started by calculating the hydrogen bonding parameter discussed below, while Hansen found the hydrogen bonding parameter as a residual after having calculated the other parameters in equation (4). Both Panayiotou and Hansen end with essentially the same values for all three HSP for a large number of liquids and polymers.

The total cohesion energy of a liquid, E , can be divided into at least 3 separate parts by experiment or calculation (Hansen 1967a; 1967d; 1999; 2007; Panayiotou 2007). In the Hansen approach these parts quantitatively describe the nonpolar, atomic (dispersion) interactions, E_D , permanent dipole-permanent dipole molecular interactions, E_P , and the hydrogen bonding (electron interchange) molecular interactions, E_H .

$$E = E_D + E_P + E_H \quad (1)$$

E can be experimentally measured by determining the energy required to evaporate the liquid, thus breaking all of its cohesion bonds in the process.

$$E = \Delta H - RT \quad (2)$$

Surface characterization using HSP

where ΔH is the measured (or predicted) latent heat of vaporization, R is the universal gas constant, and T is the absolute temperature.

Dividing Equation 1 by the molar volume, V , gives the respective Hansen cohesion energy (solubility) parameters according to equation (4).

$$E/V = (E_D/V) + (E_P/V) + (E_H/V) \quad (3)$$

$$\delta^2 = (\delta_D)^2 + (\delta_P)^2 + (\delta_H)^2 \quad (4)$$

The cohesion energy divided by the molar volume is the total cohesion energy density. The square root of this is the Hildebrand total solubility parameter, δ . (Hildebrand and Scott 1950; 1962). The SI units for all of these are $\text{MPa}^{1/2}$. These units are 2.0455 times larger than the units $(\text{cal/cc})^{1/2}$.

HSP characterizations can be conveniently visualized using a spherical representation. The HSP are at the center of the sphere, and the radius of the sphere, R_o , indicates the maximum difference in affinity tolerable for a “good” interaction to take place. Good solvents are within the sphere, and bad ones are outside. A simple composite affinity parameter, RED, standing for Relative Energy, Difference, has been defined as the distance according to equation (5), R_a , divided R_o .

$$Ra^2 = 4(\delta_{D1} - \delta_{D2})^2 + (\delta_{P1} - \delta_{P2})^2 + (\delta_{H1} - \delta_{H2})^2 \quad (5)$$

$$RED = Ra/R_o \quad (6)$$

The subscripts are for the sample, 1, and test chemical, 2, respectively. Good solvents will have RED less than 1.0. Progressively poorer solvents will have increasingly higher RED. The "4" in equation (5) has been found correct experimentally for all practical purposes in over 1000 correlations using HSP, and agrees with predictions of the Prigogine theory as discussed in (Hansen 1999; 2007). It differentiates the atomic from the molecular interactions, the latter sometimes being referred to as specific interactions.

Table 1. Comparison of the δ_H parameter in $\text{MPa}^{1/2}$ between Hansen (1967) and Panayiotou (2007)

	HANSEN	PANAYIOTOU
Toluene	2.00	2.00
Tetralin	2.90	2.90
Acetone	6.95	7.00
Methyl Methacrylate	5.40	5.40
Ethanol	19.43	19.98
1-Butanol	15.80	15.80
Dimethyl sulfoxide	10.20	10.28
Water	42.32	42.17

3. SURFACE CHARACTERIZATION WITH HSP

Beerbower (1971) found a correlation for liquid surface tension (free energy), γ , and HSP (Hansen and Beerbower 1971). Here again the atomic dispersion interactions are differentiated by a constant from the dipolar and hydrogen bonding interactions.

$$\gamma = 0.0715V^{1/3}[\delta_D^2 + 0.632(\delta_P^2 + \delta_H^2)] \quad (7)$$

The constant was actually found to be 0.7147 in the empirical correlation. The units for the cohesion parameters are $(\text{cal}/\text{cm}^3)^{1/2}$ and those of the surface tension are dyn/cm , which, however, are numerically equal to those in mN/m . The constant was separately derived as being equal to 0.7152 by a mathematical analysis in which the number of nearest neighbors lost in surface formation was considered, assuming that the molecules tend to occupy the corners of regular octahedra. This simple relation alone suggests that correlations of surface phenomena can be made with the HSP.

3.1 Pigments, Fillers, and Fibres. The cohesion parameter (HSP) approach to characterizing surfaces gained impetus by experiments where the suspension of fine particles in pigment powders was used to characterize 25 organic and inorganic pigment surfaces (Hansen 1967b; 1967d). Small amounts of the pigments are shaken in test tubes with a given volume of liquid (10 ml) of each of the test solvents, and one then observes sedimentation or lack of the same. When the solid has a lower density than the test liquid, it will float. Rates of floating have also been noted, but the term sedimentation is retained for both sedimentation and floating. The amounts of solid sample added to the liquids can vary depending on the sample in question, and some initial experimentation is usually advisable. If the pigment or filler particle size is large, say, over $5 \mu\text{m}$, the surface effects are clearly less significant compared with a sample where the particle size is only $0.01 \mu\text{m}$. The larger particle size samples may sediment very rapidly, making characterizations for glass fibres, for example, very difficult.

Observations can be made visually. Some pigments have portions which suspend for years in spite of large density differences and relatively low solvent viscosity. Satisfactory results from this type of measurement require some experience regarding what to look for. This can vary from sample to sample. A characterization is less certain if there are only 4 or 5 “good” liquids out of the perhaps 40 to 45 tested, although this depends somewhat on which liquids are involved. “Good” here means suspension of particulates is prolonged significantly compared with the other test solvents after compensating for differences in density and viscosity. A relative sedimentation time, RST, can be found by modifying the sedimentation time, t_s .

$$RST = t_s(\rho_p - \rho_s)/\eta \quad (8)$$

ρ_p and ρ_s are densities of particle and test liquid, respectively, and η is the liquid viscosity.

A prolonged RST implies greater adsorption of the given solvent onto the surface in question. Characterizations based on these techniques tend to place emphasis on the nature of the surfaces for the smaller particle size fractions. Reference is made to the presentation by Hélène Launay (2007) at this symposium for more detail on this type of characterization and the conclusions that can be drawn relative to composite materials.

3.2 Plane Surfaces. One can determine the cohesion parameters for surfaces by observing whether or not spontaneous spreading is found for a series of widely different liquids. The liquids used in standard solubility parameter determinations are suggested for this type of surface characterization (Hansen 1999; 2007). It is strongly suggested that none of the liquids be

Surface characterization using HSP

a mixture, as this introduces an additional factor into the evaluations. Droplets of each of the liquids are applied to the surface and one simply observes what happens. If a droplet remains as a droplet, there is an advancing contact angle and the cohesion energy/surface energy of the liquid is (significantly) higher than that of the surface. The contact angle need not necessarily be measured in this simplified procedure, however. Contact angles have generally been found to increase for greater differences in cohesion parameters between the surface and liquid. If spontaneous spreading is found, there is presumed to be some “similarity” in the energy properties of the liquid and the surface. The apparent similarity may be misleading. As discussed in greater detail elsewhere (Hansen 1999; 2007) the fact of spontaneous spreading for a given liquid does not mean that its HSP are identical with those of the surface being tested. If a given liquid does not spontaneously spread, it can be spread mechanically as a film and observed to see whether it retracts. This can be done according to ASTM D 2578-84 or ISO 8296:1987 (E). This test determines whether or not there is a receding contact angle.

Fig.1 shows a complete energy description for an epoxy polymer surface (Hansen and Wallström, 1983; Hansen 1999; 2007) based on the testing procedure described previously. The Hansen polar and hydrogen bonding parameters, δ_P and δ_H , are used to report the data. The circular lines can be considered as portraying portions of HSP spheres, but the third Hansen parameter, δ_D , has not been specifically accounted for in the two-dimensional figure.

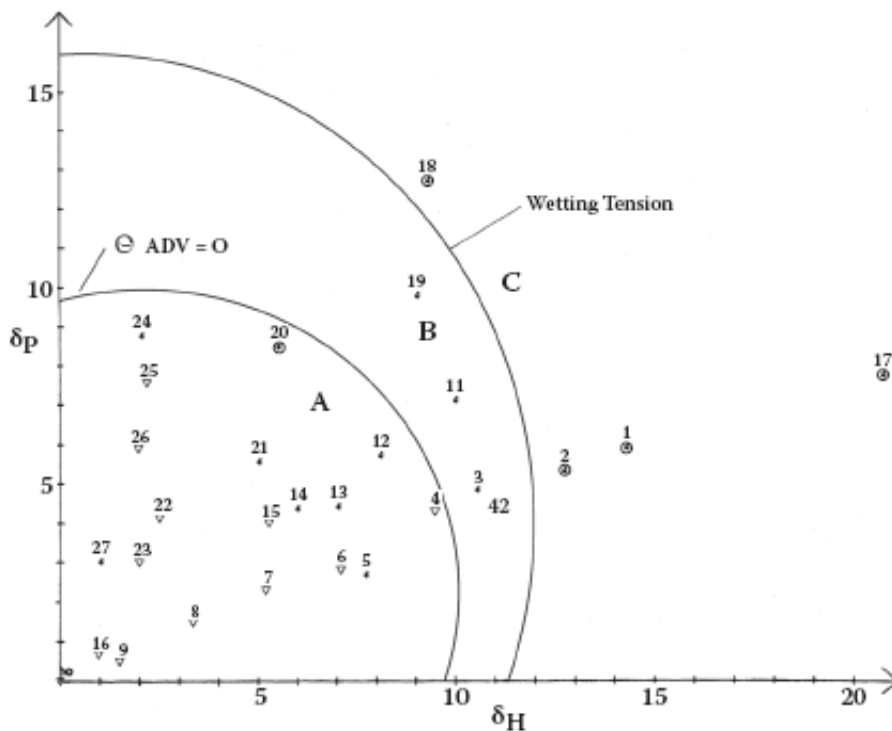


Fig.1. HSP surface characterization of an epoxy surface showing regions of spontaneous spreading of applied droplets (A), lack of dewetting of applied films (B), and dewetting of applied films (C). This characterization may not be valid for all epoxy surfaces. Units are $\text{MPa}^{1/2}$.

Fig. 1 shows two curves that are concave toward the origin. The lower of these divides the test liquids into two groups based on spontaneous spreading or not. Below the line one finds that liquids applied as droplets will spontaneously spread. Liquids that are found in the region above the upper curve will retract when applied as films. A test method to determine this is found in

the ASTM and ISO standards given previously, for example, except that one uses a large number of pure liquids instead of the liquid mixtures suggested in the standards. Receding contact angles will generally increase for liquids with still higher HSP. Intermediate between the two curves in Fig. 1 is a region where liquids applied as droplets will remain as droplets, while liquids applied as films will remain as films. The energy properties of these liquids are not as close to those of the surface as are the energy properties of the liquids that spontaneously spread. Spontaneous spreading is more related to adhesion since such liquids want to cover the surface spontaneously. The wetting tension test uses an external force to spread the liquids, after which they may continue to remain as a film. The mobility of the surface layer(s) will play a role in the wetting tension test. Hydrophilic segments can (perhaps) rotate toward a water droplet at some rate, for example, and increase the hydrophilic nature of the surface accordingly.

ACKNOWLEDGEMENT

This paper was supported by the Framework Programme "Interface Design of Composite Materials" (STVF fund no. 26-03-0160).

REFERENCES

- Barton, A. F. M. (1991). Handbook of solubility parameters and other cohesion parameters, 2nd Ed. (CRC Press, Boca Raton, FL)595-616.
- Beerbower, A. (1971). Surface free energy: a new relationship to bulk energies, *J. Colloid Interface Sci.*, 35, 126–132.
- Hansen, C. M. (1967a). The three dimensional solubility parameter - key to paint component affinities I. - solvents, plasticizers, polymers, and resins, *J. Paint Techn.*, 39, No. 505, 104-117.
- Hansen, C. M. (1967b). The three dimensional solubility parameter - key to paint component affinities II. - dyes, emulsifiers, mutual solubility and compatibility, and pigments, *J. Paint Techn.* 39, No 511, 505-510.
- Hansen, C. M., and Skaarup, K. (1967c). The three dimensional solubility parameter - key to paint component affinities III. - independent calculation of the parameter components, *J. Paint Techn.* 39, No. 511, 511-514.
- Hansen, C. M. (1967d). Doctoral Dissertation: The three dimensional solubility parameter and solvent diffusion coefficient, their importance in surface coating formulation, Danish Technical Press, Copenhagen.
- Hansen, C. M., and Wallström, E. (1983). On the use of cohesion parameters to characterize surfaces, *J. Adhesion*, 15, 275-286.
- Hansen, C. M. (1999). Hansen solubility parameters: a user's handbook, (CRC Press, Boca Raton, FL).
- Hansen, C. M. (2007). Hansen solubility parameters: a user's handbook, 2nd Ed., (CRC Press, Boca Raton, FL).
- Hansen, C. M. and Beerbower, A. (1971). Solubility parameters, in Kirk-Othmer Encyclopedia of Chemical Technology, Suppl. Vol., 2nd Ed., Ed. A. Standen, (Interscience, New York) 889–910.
- Hildebrand, J. and Scott, R. L. (1950). The solubility of nonelectrolytes, 3rd Ed., (Reinhold, New York).
- Hildebrand, J. and Scott, R. L. (1962). Regular solutions, (Prentice-Hall Inc., Englewood Cliffs, NJ).
- Launay, H. (2007). Hansen solubility parameters for a carbon fiber/epoxy composite, Paper

Surface characterization using HSP

presented at the Risø International Symposium, Sept. 3-5, 2007.

Panayiotou, C. (2007). Statistical thermodynamics calculations of the hydrogen bonding, dipolar, and dispersion solubility parameters. In: Hansen Solubility Parameters; A User's Handbook, 2nd Ed., Ed. C. M. Hansen (CRC Press, Boca Raton, FL)45-73.

INTERFACIAL PROPERTIES OF CARBON FIBRE – EPOXY COMPOSITES UNDER FATIGUE LOADING

Lars R. Jensen, Jens Chr. Rauhe & Ryszard Pyrz

Department of Mechanical Engineering
Aalborg University, DK-9220 Aalborg East, Denmark

ABSTRACT

The influence of cyclic loading on the interface between carbon fibers and an epoxy matrix has been examined using high cycle fatigue testing equipment and Raman spectroscopy. From the strain of the embedded fiber and the interfacial shear stress it was shown that the interface was unaffected by low cyclic loading up to $1,3 \times 10^7$ cycles. For a further amount of cycles initiation of interface damage was observed.

1. INTRODUCTION

Today, the wind turbine blade industry is looking for an alternative for glass fiber reinforced composites due to the increased size and performance requirements of the turbines. One such alternative is the carbon fiber reinforced composites. Changing to carbon fiber requires a thorough investigation of the fatigue properties of the carbon fiber reinforced composites since the rotor blades are subjected to a unique loading spectrum. Over a 20 – 30 year lifetime the wind turbine blades are expected to experience $10^8 - 10^9$ significant load cycles (Mandell et.al.2003, Brøndsted et.al. 2005). Furthermore, the different parts of the wing will be loaded differently bringing the material into both tension – tension, compression – tension and compression – compression cyclic loading.

Several studies have examined the fatigue behavior and mechanisms of the carbon fiber reinforced composites (Gamstedt and Talreja 1999, Harris et.al. 1990, Jen and Lee 1998, Tai et.al. 1995). The studies showed that carbon fiber reinforced composites generally are fatigue resistant provided the fibers carry the major part of the load and provided they are relatively stiff and do not permit elastic and/or viscoelastic deformations of the matrix. However, most of the studies have focused on the cycle regime up to $10^6 - 5 \times 10^6$ cycles and only a few studies have examined the fatigue behavior of composites subjected to load cycles beyond 5×10^6 (Michel et.al. 2006).

One of the many parameters affecting the fatigue behavior of the carbon fiber reinforced

composites is the interface between the fiber and the matrix. Only a few studies have been performed on this subject and the results of these studies are not very consistent. Koimtzoglou et.al. (1995, 2001) applied fragmentation tests and Raman spectroscopy in their study and showed that the interface was not affected by the cyclic loading. Afaghi-Khatibi and Mai (2002) used dynamic mechanical analysis on composites containing either sized or unsized fibers. The properties of the composites with the sized fibers did not change much during the testing while the properties of the composites containing the unsized fibers changed considerably. This indicates that the interface has influence on the degradation of the properties of the composite during cyclic loading.

In this study the effect of cyclic loading on the interface between a carbon fiber and an epoxy matrix has been examined using Raman spectroscopy. The development of the fiber strains and the interfacial shear stresses with respect to the number of cycles has been investigated for cyclic loading extending beyond 10^6 cycles.

2. EXPERIMENTAL

2.1 Materials and processing. The samples used in the fatigue experiments each consisted of a single fiber embedded in an epoxy matrix. The carbon fiber was a PAN based fiber of the type HM35 Tenax-J from TohoTenax and the epoxy resin and hardener was of the type LM-E20 and LM-H20, respectively, supplied by LM Glasfiber. The samples were dog-bone shaped having a thickness of 0,8 mm and the dimensions shown in Fig. 1.

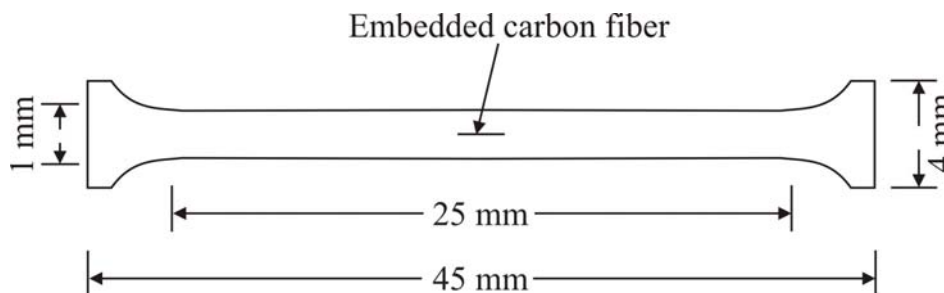


Fig. 1. Schematic illustration of the dog-bone samples

Approximately at the middle of the sample a single piece of carbon fiber is fully embedded in the epoxy matrix. The length of the carbon fiber piece was approximately 1 cm.

The small cross sectional area of the samples insures that the heat generated during testing can dissipate easily and hence not affect the results through e.g. resin hardening. The sample temperature was measured during the testing and no increase was detected.

The dog-bone samples were produced in silicone molds where the cavities were filled with epoxy and the fiber piece were embedded using a pair of tweezers. The molds were placed in a furnace and cured for 4 hours at 90°C .

2.2 Test methods. Performing high-cycle fatigue testing using a conventional servo-hydraulic fatigue testing machine is not feasible due to the enormous time consumption. A fatigue testing machine operating at 50 Hz will take more than 7 months to complete 10^7 cycles. Hence another approach has been employed through the use of the in-house built high-cycle fatigue testing machine, shown in Fig. 2.

Interfacial properties of carbon fibre – epoxy under fatigue loading

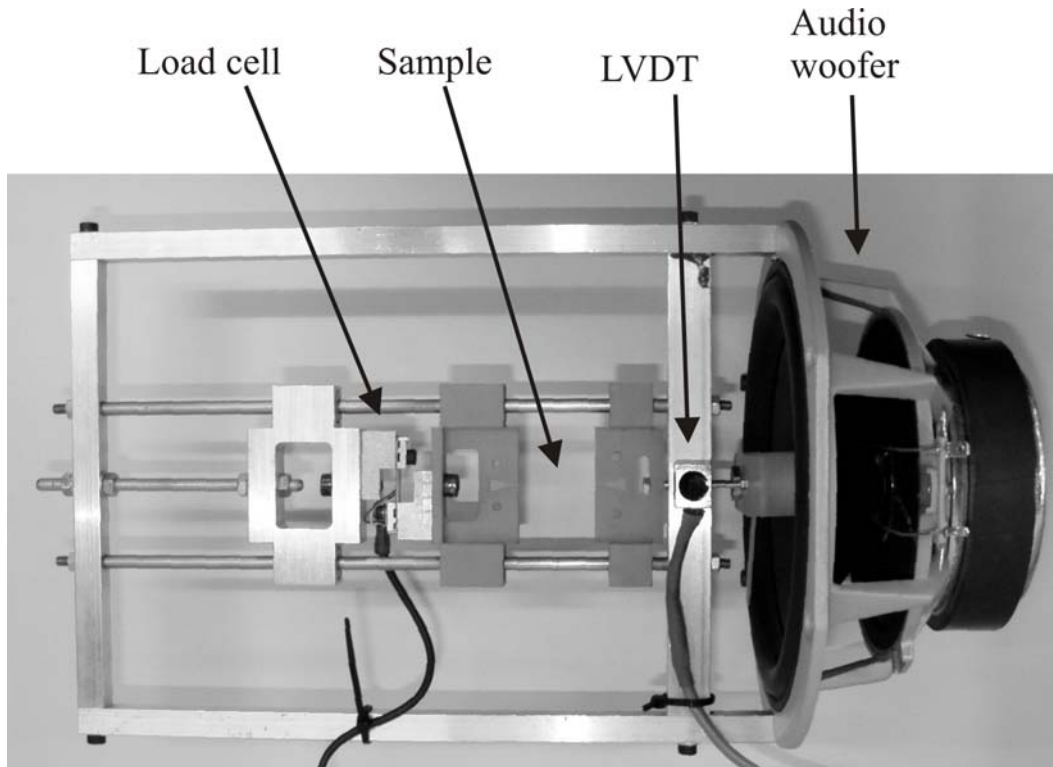


Fig 2. In-house built high-cycle fatigue testing equipment

The equipment is based on an audio woofer which creates the cyclic loading of the samples, a LVDT measuring the displacement of the clamps and a double bending beam type load cell measuring the applied load. The audio woofer is capable of delivering a long term maximum power of 150 W yielding a maximum force of around 40 N. The linear excursion of the woofer is $\pm 5,5$ mm and the maximum frequency of the equipment is 300 Hz. The woofer was connected to an audio amplifier and a signal generator which produced a sinusoidal wave function through an AC signal. This AC signal generated the cyclic loading of the samples. Furthermore, the signal generator produced a DC signal which was overlaid the AC signal. The DC signal was used to generate a pre-loading of the samples so that the samples were tested in the tension – tension fatigue regime

Data was collected from the signal generator, the LVDT and the load cell. Hence, the frequency, the maximum and mean values of the displacement and the applied force for a specified number of cycles was collected during the testing.

The equipment is constructed in such a way that it is possible to place the loading frame of the machine under a microscope. Thereby, it is possible to apply Raman spectroscopy to examine the interfacial properties of the carbon fiber – epoxy composite.

The Raman spectroscopy used for these studies was a Renishaw Invia spectroscopy with a He-Ne laser having a laser line at 633 nm. The spectroscopy is connected to an Olympus microscope with a $\times 50$ lens yielding a spot size of $\sim 2 - 10$ microns.

2.3 Testing procedure. The fatigue testing was carried out using constant amplitude load control and hence the maximum load on the sample was kept constant throughout the test. The test was started by applying the DC-signal followed by the AC-signal whereby the sample was subjected to both the pre-load and the cyclic loading. The maximum loading of the samples was around 13 N equivalent to a maximum stress of approximately 15 MPa for the 0,8 mm cross sectional area

of the samples. The cyclic loading was applied at a frequency equal to 100 Hz.

After a specified number of cycles the test was stopped and the sample was loaded up to the maximum level of the cyclic load using a lead screw. Under this static loading the sample was put under the Raman spectroscope and series of Raman spectra were obtained along the embedded fiber starting from the fiber end. Following the Raman spectroscopy the fatigue testing was continued by applying the DC and AC-signal to the woofer.

The interfacial properties of the carbon fiber – epoxy composite were examined by determining the strain of the embedded fiber through Raman spectroscopy. A Raman spectrum of the HM35 carbon fiber is presented in Fig. 3.

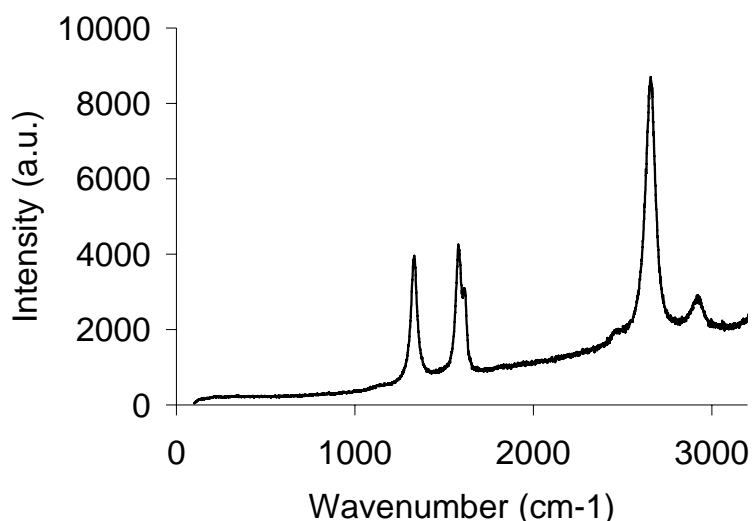


Fig. 3. Raman spectrum of the HM35 carbon fiber

By determining the position of the second order band located at $\sim 2660 \text{ cm}^{-1}$ and knowing the strain sensitivity of this peak it is possible to determine the strain of the carbon fiber. The strain, ϵ , can be found through $\epsilon = \Delta\nu / K$, where $\Delta\nu$ is the change in frequency (wavenumber) and K is the strain sensitivity. The strain sensitivity of the HM35 carbon fiber has previously been determined to $-20 \text{ cm}^{-1}/\%$ (Rauhe et.al. 2007).

Both the fatigue testing and the Raman spectroscopic measurements were performed at room temperature and hence temperature effects have been neglected in this study.

3. RESULTS AND DISCUSSION

From the measured shift in frequency the strain of the fiber has been determined for unloaded, static loaded and cyclic loaded samples. These strain profiles are presented in Fig. 4.

Interfacial properties of carbon fibre – epoxy under fatigue loading

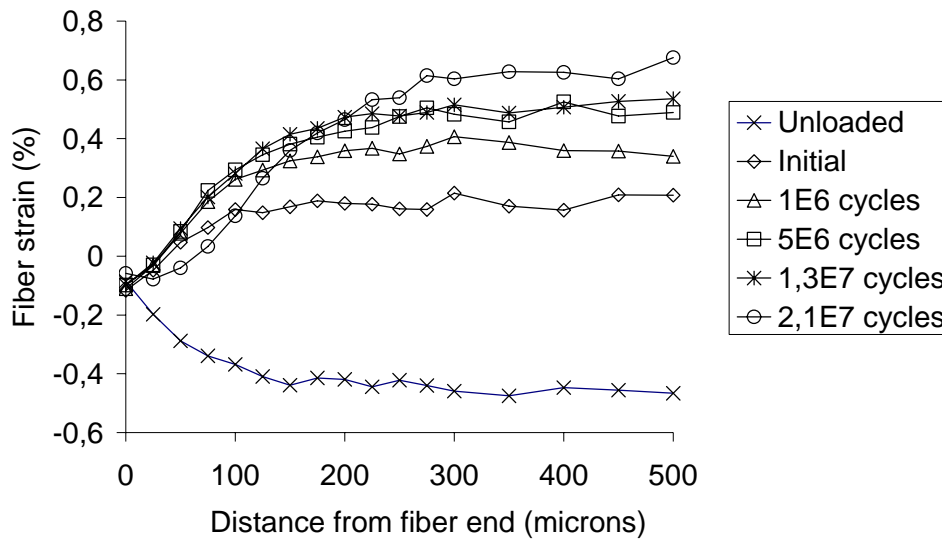


Fig. 4. Strain in fibers subjected to no loading, static loading and cyclic loading conditions

The strain profile of the unloaded fiber shows that the embedded fiber is subjected to compression up to a strain around -0,45 %. This is due to the mismatch between thermal expansion coefficients of the fiber and the matrix material and due to shrinkage of the epoxy matrix during curing. The curing induced compression affects the fatigue loading of the fiber since the sample is subjected to tension – tension loading but due to the compression the embedded fiber will experience a compression – tension cyclic loading. The compression – tension loading is known as a more severe loading condition than the tension – tension case and hence damage will be initiated earlier (Gamstedt and Sjögren 1999).

The strain profiles of the loaded cases shows that the maximum amount of strain induced in the fiber increases with increasing number of load cycles. This is understandable since amplitude load control was applied during the experiment. Hence the controlling factor was the load and not the elongation of the sample. The epoxy material behaves viscoelastically and for the same load the material will experience an increase in strain as time progresses.

The strain profile of the 2,1E7 cycles load case deviates from the other cases since the curve is flat in the region between 0 and 75 microns and then starts to increase. The flat part is probably due to failure of the interface beginning at the fiber end and/or matrix yielding.

From the strain profiles the interfacial shear stress can be calculated by considering the balance of forces acting on an infinitesimal small fiber element. This yield the following expression for the interfacial shear stress along the fiber.

$$\tau(z) = \frac{E_z R}{2} \frac{d\varepsilon(z)}{dz} \quad (1)$$

Where E_z is the Young's modulus in the axial direction, R is the fiber radius and $\varepsilon(z)$ is the strain distribution along the fiber. To obtain the strain distribution in a continuous and functional form the strain profiles in Fig. 4 are fitted using an exponential decay function. In Fig. 5 the development of the interfacial shear stress along the fiber has been plotted for the different loading conditions.

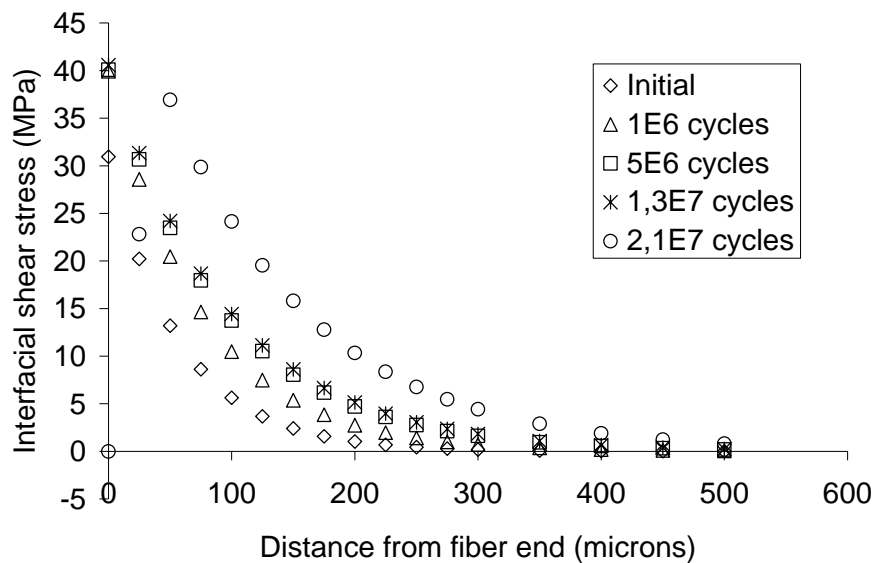


Fig. 5. Interfacial shear stress between fiber and matrix for static and cyclic loading conditions

All the interfacial shear stress profiles in Fig. 5 have a maximum value at the fiber end except for the 2,1E7 cycles case. The maximum stress varies between 31 to 40 MPa depending on the number of cycles and these values correlates well with other studies using the same material systems. For the 2,1E7 cycles case, the maximum value of the interfacial shear stress shifts inwards and the profile reaches its maximum value at around 75 microns. Again, this is due interfacial damage progressing towards the middle of the fiber.

In a previous study using the same material systems the interface has been examined under static loading (Kalashnyk and Ferri 2005). Using Raman spectroscopy it was shown that the interface between the carbon fiber and the epoxy matrix was intact for a fiber strain up to at least 1,4 %. When the interface fails under cyclic loading at a much lower fiber strain this has to be attributed the cyclic loading. Hence for cyclic loading at a relatively low loading level the interface is affected by the loading when the number of load cycles approaches 2×10^7 .

To quantify the degree of interface failure further the cyclic loading should have been extended further, maybe up to 10^8 cycles. However, this was not done in this study.

4. CONCLUSION

The influence of cyclic loading on the interface between a single carbon fiber and the epoxy matrix has been examined using an in-house built high cycle fatigue testing equipment based on an audio woofer. Through Raman spectroscopy the interfacial properties of the composite was examined and the fiber strain and interfacial shear stress were determined. It was shown that the interface was unaffected by the cyclic loading up to $1,3 \times 10^7$ cycles. For a larger number of cycles the fiber strain and interfacial shear stress profiles indicated that interface damage was occurring. Hence, the interface is affected by the cyclic loading when number of cycles reaches a sufficient large value.

ACKNOWLEDGEMENTS

This work is partially supported by the Framework Program “Interface Design of Composite Materials” (STVF fund no. 26-03-0106).

REFERENCES

- Afaghi-Khatibi, A. and Mai, Y.W. (2002). Characterisation of fibre/matrix interfacial degradation under cyclic fatigue loading using dynamic mechanical analysis. *Compos. Part A*. 33, 1585-1592
- Brøndsted, P., Lilholt, H. and Lystrup, A. (2005). Composite materials for wind power turbine blades. *Annu. Rev. Mater. Res.* 35, 505-538
- Gamstedt, E.K. and Talreja, R. (1999). Fatigue damage mechanisms in unidirectional carbon-fibre-reinforced plastics. *J. Mater. Sci.* 34, 2535-2546
- Gamstedt, E.K. and Sjögren, B.A. (1999). Micromechanics in tension-compression fatigue of composite laminates containing transverse plies. *Compos. Sci. Technol.* 59, 167-178
- Harris, B., Reiter, H., Adam, T., Dickson, R.F. and Fernando, G. (1990) Fatigue behavior of carbon fibre reinforced plastics, *Composites*. 21, 232-242
- Jen, M.H.R. and Lee, C.H. (1998). Strength and life in thermoplastic composite laminates under static and fatigue loads. *Int. J. Fatigue*. 20, 605-615
- Kalashnyk, N. and Ferri, O.M. (2005). Influence of fibre sizing on interface properties of carbon/epoxy composites. Project report, Aalborg University.
- Koimtzoglou, C., Kostopoulos, V., Melanitis, N.E. and Paipetis, S.A. (1995). The effect of cyclic loading on the micromechanics of the interface. *Adv. Comp. Lett.* 4, 151-155
- Koimtzoglou, C., Kostopoulos, V. and Galiotis, C. (2001) Micromechanics of reinforcement and damage initiation in carbon fibre/epoxy composites under fatigue loading. *Compos. part A*. 32, 457-471
- Mandell, J.F., Samborsky, D.D., Wang, L. and Wahl, N.K. (2003). New fatigue data for wind turbine blade materials. *J. Sol. Energ.* 125, 506-514
- Michel, S.A., Kieselbach, R. and Martens, H.J. (2006) Fatigue strength of carbon fibre composites up to the gigacycle regime. *Int. J. Fatigue*. 28, 261-270
- Rauhe, J.C., Jensen, L.R. and Pyrz, R. (2007) Electromechanical testing of carbon fibers. In: *Proceedings of The Sixteenth International Conference on Composite Materials*. Eds. K. Kageyama, T. Ishikawa, N. Takeda, M. Hojo, S. Sugimoto and T. Ogasawara, Po-24
- Tai, N.H., Ma, C.C. and Wu, S.H. (1995). Fatigue behavior of carbon fibre/PEEK laminate composites. *Composites*. 26, 551-559

ADHESION IMPROVEMENT OF CARBON FIBRES BY PLASMA SURFACE MODIFICATION

Y. Kusano^{a*}, T.L. Andersen^b, B. F. Sørensen^b, P.K. Michelsen^a

^aOptics and Plasma Research Department, ^bMaterials Research
Department, Risø National Laboratory, Technical University of
Denmark, P.O. Box 49, DK-4000 Roskilde, Denmark

ABSTRACT

Plasma surface modifications are attractive for the application of adhesion improvement because they avoid the use of toxic chemicals, only the surface is treated while the bulk properties remain unchanged, oxygen and/or nitrogen containing functional groups are easily introduced into the surfaces, surface cleaning and weak-layer elimination can be performed simultaneously with the surface modification, and physical and chemical micro-etching is expected, improving the mechanical interlocking with adhesives. Plasma surface modification of carbon fibres has been studied for adhesion improvement with polymer matrices for enhancing longitudinal tensile strength of carbon fibre reinforced polymer (CFRP) composites.

In the present work, atmospheric pressure dielectric barrier discharge is used to treat unsized electrochemically-treated carbon fibres in various gas conditions. An x-ray photoelectron spectroscopic analysis indicated that oxygen-containing polar functional groups are effectively introduced onto the carbon fibre surfaces by He, He/O₂ and Ar plasma treatments. CFRP composite plates were prepared using both untreated and He plasma-treated carbon fibres with an epoxy resin for the adhesion test. Improved wetting to the uncured epoxy resin was observed for the plasma treated ECFs. The plasma treated specimens showed a higher fracture resistance, indicating that adhesion between the fibres and the epoxy was improved by the plasma treatment.

1. INTRODUCTION

Carbon fibres have been extensively used for improving mechanical properties of polymer composite materials due to their high strength, high toughness and light weight. An epoxy resin is often preferred for the host matrix due to excellent electrical properties, high mechanical strength, high resistance against aging/hydrolysis, and high bond strength to many other polymer materials (Jones 1991).

In order to achieve high mechanical strength of the composites, fibre distribution, alignment,

fibre damage, and interface between fibre surfaces and a polymer matrix need to be considered. In particular strong adhesion between the fibre surfaces and the polymer matrix is one of the key issues for improving the longitudinal tensile strength of carbon fibre reinforced polymers (CFRP) (Dilsiz 2000). However, due to the non-polar nature of carbon fibres they are difficult to wet and almost impossible to chemically bond to general polymer matrices. It is noted that for adhesion improvement the chemical effect of oxygen containing polar functional groups such as -OH, =O, and -COOH at the carbon fibre surfaces is known to be more important than the mechanical effect of rough surfaces (Fukunaga 2000). Proper surface modification thus should be chosen so that carbon fibre surfaces can be wettable by the polymer matrix and bond to it tightly. Adhesion can be improved by surface treatment of the fibres, mainly by oxidation of the surfaces, introducing reactive groups onto the fibre surfaces so that they can react with matrices as well as increase the surface energy for improved wetting.

Extensive research has been devoted to the surface modification of carbon fibres in order to improve their bonding to the resin matrix, including dry or wet oxidation, electrochemical methods, polymer coatings, plasma treatment, plasma polymerization, and plasma enhanced chemical vapour deposition (PECVD) (Dilsiz 2000, Fitzer 1981, Hughes 1990). The wet oxidation and electrochemical methods use nitric acid, KMnO_4 , H_2SO_4 , sodium hypochlorite, chromic acid, and electrolytic NaOH, while the dry methods use oxygen, ozone, and catalysis. However, these kinds of chemical methods may be least preferable. For example, when the carbon fibres are oxidised in concentrated nitric acid, the equipment used must have good corrosion resistance and the acid absorbed on the fibre surfaces must be properly removed by subsequent washing, which is time-consuming and inevitably damages and tangles the carbon fibres (Dilsiz 2000, Hughes 1990). These methods can also produce environmental pollution. On the other hand, plasma surface modification techniques are attractive for this application, because they can be operated at room temperature, they do not require any use of solvents and toxic chemicals (environmentally friendly process), the bulk properties are retained, oxygen and/or nitrogen containing functional groups are easily introduced into the surfaces, which is often required for the application of adhesion improvement, a surface can be cleaned and weak-layers can be eliminated simultaneously with the surface modification, and physical and chemical micro-etching is expected, improving the mechanical interlocking with adhesives.

Plasma surface modification can usually be divided into two categories with opposite effects, depending mainly on the process gas(es) used. The first one mainly ablates the surfaces, and is usually called "plasma treatment", "plasma surface modification", "plasma ablation", or "non-polymer-forming plasma". The second one is usually called "plasma polymerization", "polymer-forming plasma" or "PECVD". In the following "plasma surface modification" is meant to cover both types while "plasma treatment" is used for the first one. If the used gas(es) has high proportions of carbon and hydrogen atoms, double- or triple- bonds in its composition such as methane, ethylene, acetylene and ethanol, or if they are precursors such as metal-organic (organometallic) gas(es), the plasma often results in plasma polymerization or PECVD. Here, metal-organic gases are those which contain a metal, particularly compounds in which the metal atom has a direct bond with a carbon atom. Otherwise, the plasma will have a tendency of ablation (plasma treatment). These techniques have been studied for adhesion improvement of carbon fibres (Dilsiz 2002).

It is argued, however, that to date none has changed the performance of the finished CFRP composite significantly enough to warrant large-scale development (Mason 2004). This kind of plasma is generally obtained at low pressure. These plasma surface modifications at low pressures, however, suffer from the drawbacks that they require expensive vacuum systems, and methods are only well-developed for batch or semi-batch treatments. To overcome these

drawbacks, plasma surface modification at atmospheric pressure has been developed, avoiding expensive vacuum equipment, it permits the treatment of large objects and continuous treatment on production lines can readily be designed. Atmospheric pressure plasma has already been used to treat glassy carbon plates, which are thought to be ideal model specimens for fundamental studies of adhesive properties of carbon fibres due to the structural similarity and easier handling than carbon fibres (Mortensen 2006, Kusano 2006, 2007a).

In the present work, carbon fibres are treated by atmospheric pressure dielectric barrier discharge (DBD) plasma for adhesion improvement with an epoxy resin.

2. EXPERIMENTAL METHODS

An atmospheric pressure DBD has been used to treat the unsized electrochemically-treated carbon fibres (TENAX HTA5001, 800tex). It was generated between parallel plate water cooled metal electrodes (50 mm × 50 mm) covered with alumina plates (100 mm × 100 mm × 3 mm) by an AC (ca. 40 kHz, $V_{pp} \sim 13$ kV) power supply (Generator 6030. SOFTAL Electronic GmbH, Germany). The average power input was 80-100 W corresponding to a power density of 6.5-8 W cm⁻², obtained by measuring voltage and current with a high voltage probe and a 50 Ω current viewing resistor.

He, Ar, a mixture of He with O₂, N₂ or NH₃, or a mixture of Ar with NH₃ was fed into the DBD. O₂ gas was used for enhanced surface oxidation, while NH₃ were attempted for introducing amino groups onto the carbon fibre surfaces. The gas conditions are summarized in Table 1. The carbon fibres were also treated with the DBD in an ambient air without feeding gas (air plasma).

Table 1 Condition of plasma treatments.

	Gas flow rate [sccm]					Treatment time [s]
	He	Ar	O ₂	N ₂	NH ₃	
Untreated	-	-	-	-	-	-
He plasma	1000	-	-	-	-	1
						2
						100
He/O ₂ plasma	1000	-	100	-	-	100
He/N ₂ plasma	1000	-	-	100	-	100
He/NH ₃ plasma	1000	-	-	-	1	100
Ar plasma	-	1000	-	-	-	100
Ar/NH ₃ plasma	-	1000	-	-	1	100
Air plasma	-	-	-	-	-	100

X-ray photoelectron spectroscopic (XPS) analysis were employed to study the changes of the functional groups on the carbon fibre surfaces using a Sage 100 (SPECS, Berlin, Germany) instrument operated at a pressure of 10^{-5} Pa. All the samples were analyzed using an unmonochromated Mg K α X-ray source operated at a power of 300 W at a take-off angle of 90°, resulting in a maximum probe depth of ≈ 10 nm. The number of scans was minimized in order to prevent X-ray induced sample damage, and kept constant for all the samples. Atomic concentrations of each element were calculated by determining the relevant integral peak intensities using a linear background. The systematic error is estimated in the order of 5 – 10 %.

A regional analysis was performed on the carbon 1s (C1s; pass energy 23 eV). The C1s binding energies at 284.8 and 286.2 eV correspond to C-C, hydrocarbons and C-N, C=N, C-O, respectively.

Plates for double cantilever beam (DCB) specimens were prepared for the adhesion test. At the end of the plate, a slip foil was inserted in the mid-plane to act as crack starter. Composite plates were prepared using both untreated, 1- and 2-s He plasma-treated carbon fibres with an epoxy resin (epoxy resin [Prime 20. SP Systems] mixed with diethylenetriamine / polyoxypropylamine). Steel beams were glued to the outside of each composite plate with an epoxy adhesive (Scotch Weld) which was cured for 24 h at room temperature. The fracture mechanics test was performed by applying pure bending moments to the DCB specimens using a dedicated test machine (Sørensen 2006).

3. RESULTS AND DISCUSSION

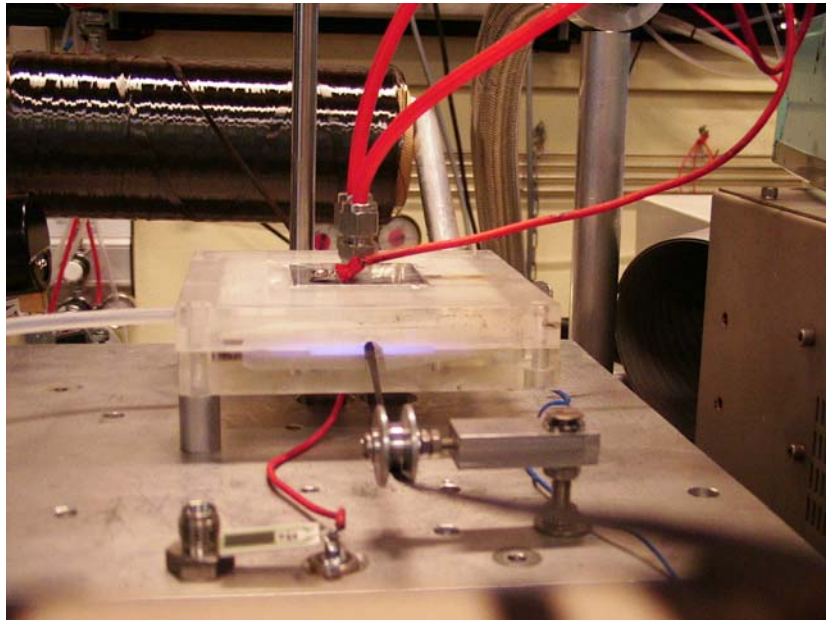


Fig. 1. Plasma treatment of carbon fibre surfaces using atmospheric pressure DBD.

Carbon fibre surfaces were continuously treated using the atmospheric pressure DBD as shown in Fig. 1.

XPS was used to analyse the elemental composition of the carbon fibre surfaces before and after the plasma treatments. The surfaces are dominated by carbon, oxygen and nitrogen. Fig. 2 shows ratios of O/C and N/C for each specimen. It is found that oxygen can be effectively introduced by He, He/O₂, and Ar plasmas. Additionally the He plasma treatment for 1 s resulted in significant oxidation, while the longer treatments did not improve oxidation drastically. However, further investigation is necessary for understanding the effect of treatment time. Regional analysis on carbon 1s spectra shows decrease in the binding energy peak at 284.8 eV and increase in that at 286.2 eV after each plasma treatment, indicating that a surface density of the C-O single bond increases after the plasma treatments.

CFRP plates were prepared using untreated, 1-s and 2-s He plasma treated carbon fibres for the adhesion test. Improved wetting to uncured epoxy resin was observed for the plasma treated carbon fibres.

Adhesion improvement of carbon fibres by plasma surface modification

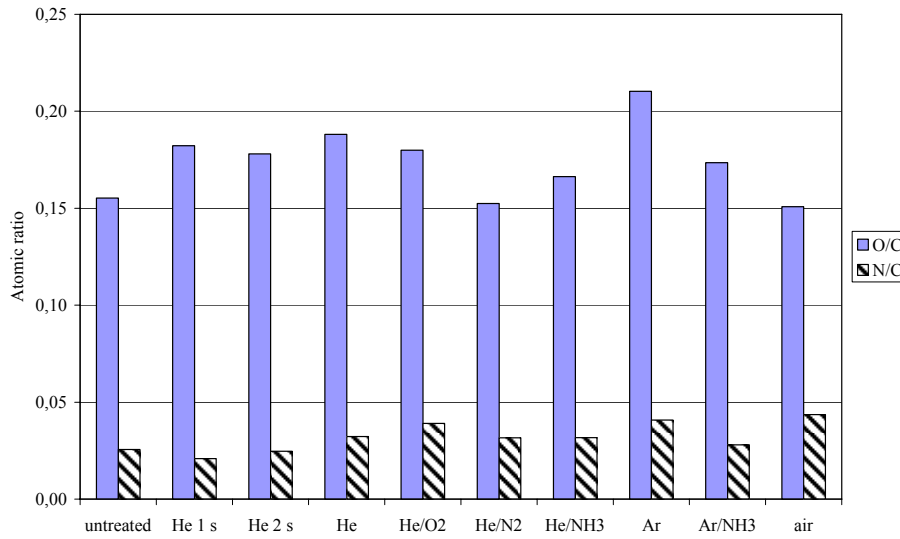


Fig. 2. O/C and N/C ratios of the carbon fibre surfaces.

Adhesive property was evaluated using fracture resistance values at the crack growth initiation and at the steady state. Data are taken when the stable crack growth is seen in the mid plane of the CFRP plates so that the adhesive property between the carbon fibre surfaces and the epoxy matrix can be properly evaluated. The results are summarized in Table 2.

Table 2

Treatment time [s]	Fracture energy [J m^{-2}]	
	Crack initiation	Steady state
0	160 – 260	1400 – 1800
1	160 – 280	1700 – 2200
2	230 – 310	1700 – 2400 (*)

* The fracture energy at the end-opening of about 5 mm.

The mechanical property of the CFRP composite plates improved after the He plasma treatment, indicating that adhesion of the carbon fibres to the matrix is improved with the treatment. In the case of untreated and 1-s treated specimens, the fracture energies reached steady state values at the end-opening of about 3.5 mm. On the other hand, as the crack growth proceeds, the fracture energies of 2-s treated specimens steadily increased without approaching to a steady state due to their better adhesion than the others. Since the oxygen content of 1- and 2-s treated carbon fibre surfaces are almost the same, a possible explanation of this adhesion improvement is enhanced surface roughness after longer plasma treatment (Kusano 2007b).

4. CONCLUSIONS

Carbon fibres were treated by atmospheric pressure DBD plasma for adhesion improvement with epoxy resin. He, He/O₂ and Ar plasma treatments increased oxygen containing polar functional groups on to the carbon fibre surfaces. He plasma treatment improved the wettability by the uncured epoxy resin, and increased the adhesion energy. It is suggested that longer He plasma treatment might increase the surface roughness

ACKNOWLEDGEMENT

This work is supported by a grant from the Danish Technical Research Council (Statens Teknisk-Videnskabelige Forskningsråd (STVF). Grant number 26-04-0251). Lene Hubert is gratefully acknowledged for the XPS analysis.

REFERENCES

- Dilsiz, N. (2000). Plasma surface modification of carbon fibers: a review. *J. Adhesion Sci. Technol.* 14(7), 975-987.
- Fitzer, E., and Weiß, R. (1981). Processing and uses of carbon fibre reinforced plastics (VDI-Verlag GmbH, Düsseldorf) p. 45.
- Fukunaga, A., and Ueda, S. (2000). Anodic surface oxidation for pitch-based carbon fibers and the interfacial bond strengths in epoxy matrices. *Comp. Sci. Technol.* 60(2), 249-254.
- Hughes, J.D.H. (1991). The carbon fibre/epoxy interface – a review. *Comp. Sci. Technol.* 41(1), 13-45.
- Jones, C. (1991). The chemistry of carbon fibre surfaces and its effect in interfacial phenomena in fibre/epoxy composites. *Comp. Sci. Technol.* 42(1-3), 275-298.
- Kusano, Y., Mortensen, H., Stenum, B., Rozlosnik, N., Strange, Kingshott, P., M., Goutianos, S., Sørensen, B.F., and Bindselev, H. (2006). Adhesion improvement of glassy carbon plates by atmospheric pressure plasma. *Proc. 27th Risø Int. Symp. Mater. Sci.* Eds. H. Lilholt et al. (Risø National Laboratory, Roskilde, Denmark) 191-196.
- Kusano, Y., Mortensen, H., Stenum, B., Goutianos, S., Mitra, B., Ghanbari-Siahkali, A., Kingshott, P., Sørensen, B.F., and Bindselev, H. (2007a). Atmospheric pressure plasma treatment of glassy carbon for adhesion improvement. *Int. J. Adhesion and Adhesives* 27(5), 402-408.
- Kusano, Y., Mortensen, H., Stenum, B., Kingshott, P., Andersen, T.L., Brøndsted, P., Bilde-Sørensen, J.B., Sørensen, B.F., and Bindselev, H. 2007b, Atmospheric pressure plasma treatment of glass fibre composite for adhesion improvement. *Plasm. Proc. Polym.* in press.
- Mason, K.F. (2004). Sizing and surface treatment: the keys to carbon fiber's future? *High-Performance Comp.* 12(2), 38-43.
- Mortensen, H., Kusano, Y., Leipold, F., Rozlosnik, N., Kingshott, P., Sørensen, B.F., Stenum, B., and Bindselev, H. (2006). Modification of glassy carbon surfaces by an atmospheric pressure cold plasma torch. *Jpn. J. Appl. Phys.* 45(10B), 8506-8511.
- Sørensen, B. F., Jørgensen, K., Jacobsen, T. K., and Østergaard, R. C. (2006). DCB-specimen loaded with uneven bending moments. *Int. J. Fract.* 141, 159-172.

APPLICATIONS OF SOLID STATE NUCLEAR MAGNETIC
RESONANCE TO PROBE THE INTERPHASE IN NATURAL
FIBER REINFORCED COMPOSITES

Marie-Pierre G. Laborie

Department of Civil and Environmental Engineering, Washington
State University, Wood Materials and Engineering Laboratory, 1445
Terre View Dr., Pullman, WA 99164, US,

ABSTRACT

Information on the interphase morphology of natural fiber reinforced composites can be gained by probing molecular relaxations on different time scales. In particular, solid state nuclear magnetic resonance utilizing cross polarization and magic angle spinning (^{13}C CP/MAS NMR) can be used to understand the interphase chemistry but also to monitor molecular motions in composites. In this presentation, the utility of ^{13}C CP/MAS NMR in combination with specific ^{13}C isotope labeling of the polymer matrix will be illustrated in various natural fiber reinforced composites. In particular NMR studies on wood/phenolic resins and on wood/polyolefin composites will be presented. It will be shown that characteristic relaxation times such as the spin lattice relaxation time in the rotating frame and cross-polarization times provide insight on homogeneity on the nanometer scale and on molecular rigidity. Such information is useful to understand the interphase morphology which likely plays a critical role in the composite performance.

1. INTRODUCTION

The development of Cross-Polarization and Magic Angle Spinning Nuclear Magnetic Resonance, CP/MAS NMR, has permitted high-resolution NMR in condensed matter (Mehring 1983). With this resolution, NMR affords a probe of molecular dynamics in solid polymers. In addition, because NMR measurements can be performed at particular chemical sites, molecular dynamics can be probed locally. This is especially true in that isotopic labeling may be used to enhance site specificity. Among the CP/MAS NMR methods for probing local molecular dynamics in polymers, relaxation time measurements constitute an ideal tool for examining molecular scale interactions in polymer blends (Schmidt-Rohr and Spiess 1994). That is, when polymers interact on a molecular scale their bulk dynamics and consequently relaxation times are altered. As a result, researchers in natural fibers composites have long taken advantage of

solid state NMR, clearly establishing its potential for wood science (Gil and Neto 1999). For instance, solid state NMR has been decisive for better understanding the morphology of wood, a natural composite, but also for probing the chemistry and morphology of the wood/adhesive bondline (Gil and Neto 1999).

In the solid state, the relaxation of nuclei may occur via spin-spin interactions at a characteristic time T_2 (transverse relaxation) or via spin-lattice interactions at a characteristic time T_1 or $T_{1\rho}$ (longitudinal relaxation) depending upon the reference frame considered (laboratory or rotating frame respectively). Such relaxation mechanisms portray molecular scale dynamics. For instance, megahertz frequency motions influence T_1 while $T_{1\rho}$ is affected by mid-kilohertz frequency motions (Schmidt-Rohr and Spiess 1994). In some cases, the individual polymers have distinct ^{13}C chemical shifts. As a result, the $^{\text{H}}T_{1\rho}$ for each polymer may be monitored in the blend or in the composite. Simply then, blend morphology can be determined from changes in the bulk polymer relaxation rates. If polymers interact on the time scale (and domain size) characteristic of a relaxation rate then this relaxation rate shall be altered as a result of blending. For instance changes $^{\text{H}}T_{1\rho}$ upon blending reflect nanometer scale interactions between polymers.

Another approach hinges upon the spatial requirements of relaxations. In organic solids, owing to the abundance and spatial proximity of protons spin diffusion also contributes to the T_1 and $T_{1\rho}$ relaxations. Spin diffusion refers to a static magnetization transfer between abundant and adjacent protons. Thus on top of the motional contribution to T_1 and $^{\text{H}}T_{1\rho}$, spin diffusion can average molecular motions of the so-called coupled-spins (Schmidt-Rohr and Spiess 1994). It follows that distinct nuclei (with distinct molecular motions) may have their T_1 and $T_{1\rho}$ converge to a common value by virtue of spin diffusion. However, spatial proximity is required for effective spin diffusion. Namely, spin diffusion occurs on nanometer scale domains. Conversely, spin diffusion is ineffective across phase boundaries (Schmidt-Rohr and Spiess 1994). As a result, polymer blends that are homogeneous on a nanoscale (2-30 nanometers) have their nuclei spin-coupled as reflected by a common $^{\text{H}}T_{1\rho}$. Phase separated polymer blends on the other hand exhibit distinct $^{\text{H}}T_{1\rho}$ for nuclei in separate domains. In the case of natural fiber reinforced composites, the measurements of relaxation times may therefore be useful not only to probe the molecular dynamics and interfacial interactions but also to reveal the phase morphology at the interphase.

2. OBJECTIVES

The objective of this work was to examine the potential of solid state NMR and relaxation time measurements to investigate the chemistry and morphology of the interphase in natural fiber reinforced composites. In particular this work evaluates the use of CP/MAS NMR in combination with specific ^{13}C labelling to investigate the coupling chemistry between wood and maleic anhydride functionalized polypropylene. Furthermore, the utility of relaxation time measurements for shedding light on the nanometer scale morphology at the wood / phenol-formaldehyde interphase is also investigated.

3. EXPERIMENTAL

3.1 Materials. Two composite systems were prepared and characterized by solid state NMR. For the first composite system a maleic anhydride polypropylene (MAPP) was synthesized with 100% ^{13}C enrichment at the C1 and C4 carbons and patterned after the A-C® 950 from Honeywell. Blends of MAPP and sugar maple (*Acer saccharum*) were prepared in 50/50 w/w ratio using a laboratory mixing molder (Dynisco) preheated at 180°C and operating at 50rpm for 2 minutes. After mixing the blends were allowed to cool down to room temperature after which they were pulverized with a pestle and mortar, vacuumed to remove any moisture and stored in a vacuumed dessiccator with calcium sulfate until analysis.

For the second composite system, a low molecular weight phenol-formaldehyde (PF-low) resin was synthesized with phenol, formaldehyde and sodium hydroxide in molar ratios 1:2:0.2. The resin displayed a low molecular weight distribution ($M_n=270$ g/mol, $M_w/M_n=1.22$) as detected from gel permeation chromatography (Laborie et al. 2006). Yellow-poplar (*Liriodendron tulipifera*) flakes with dimensions 3.5 mm in the radial direction, 0.85 mm in the tangential direction and 50 mm in the longitudinal direction were impregnated with the resin for 30 minutes by soaking under 90 kPa vacuum. The composite was then oven-cured at 110°C until vitrification and then post-cured at 150°C for 20 minutes.

3.2. Solid State NMR. The wood/MAPP composite powder was loaded in a zirconium oxide rotor, sealed with a Kel-f cap and examined on a Bruker Avance 400 MHz spectrometer equipped with a chemagnetics 7.5mm double resonance probe. The spectrometer frequency was set at 100.63 MHz for ^{13}C nuclei and the proton decoupling field was 70 kHz. Adamantane was utilized for establishing the Hartmann-Hahn match. The samples were spun at ca 5 kHz. A CP experiment was performed using a contact time of 1 ms, a recycle delay of 4 seconds and an acquisition time of 22 ms. A total of 512 scans were accumulated.

For the wood/PF composites disks were retrieved from the flakes with a paper hole puncher and loaded in a zirconium oxide rotor, sealed with a Kel-f cap and spun at 5 kHz \pm 20 Hz. The solids NMR spectrometer was a Bruker MSL-300 MHz using a 7 mm Probenkopf MAS.07.D8 probe. The spectrometer frequency was set at 75.47 MHz for ^{13}C nuclei and the spin locking frequency for the proton channel was approximately 56 kHz. A standard CP pulse with variable contact time was performed using 12 contact times within the 0.1-15 ms range. For each contact time, 1000 scans were accumulated. The recycle delay was 3.75 s and the signal acquisition time was 50 ms. Carbon T_{CH} and proton $T_{1\rho}$ relaxation rates were determined by fitting the carbon intensity vs. contact time curve to equation (1) (Mehring 1983):

$$I(T) = I^* \left(\frac{{}^H T_{1\rho}}{{}^H T_{1\rho} - T_{CH}} \right) \left(\exp^{-t/{}^H T_{1\rho}} - \exp^{-t/T_{CH}} \right) \quad (1)$$

where $I(t)$ represents the signal intensity at a contact time t and I^* is the corrected signal intensity. For each sample treatment, three specimens were analyzed for CP/MAS NMR relaxation measurements.

4. RESULTS AND DISCUSSION

4.1 CP/MAS NMR of the wood/[1,4- $^{13}\text{C}_2$]MAPP composite. The ^{13}C CP/MAS NMR spectrum for the neat MAPP, neat maple and the maple/MAPP blend are shown in Fig. 1. The NMR spectrum of [1,4- $^{13}\text{C}_2$]MAPP shows two distinct peaks in the carbonyl region at 180.1ppm and 173.5ppm that arise from the ^{13}C enriched C1 and C4 of the maleic anhydride (MA) grafts (Fig.

1.a). The chemical shift at 180.1ppm was assigned to both carbons in the carboxylic diacid form, whereas the 173.5ppm peak was ascribed to the same carbons in the MA anhydride.

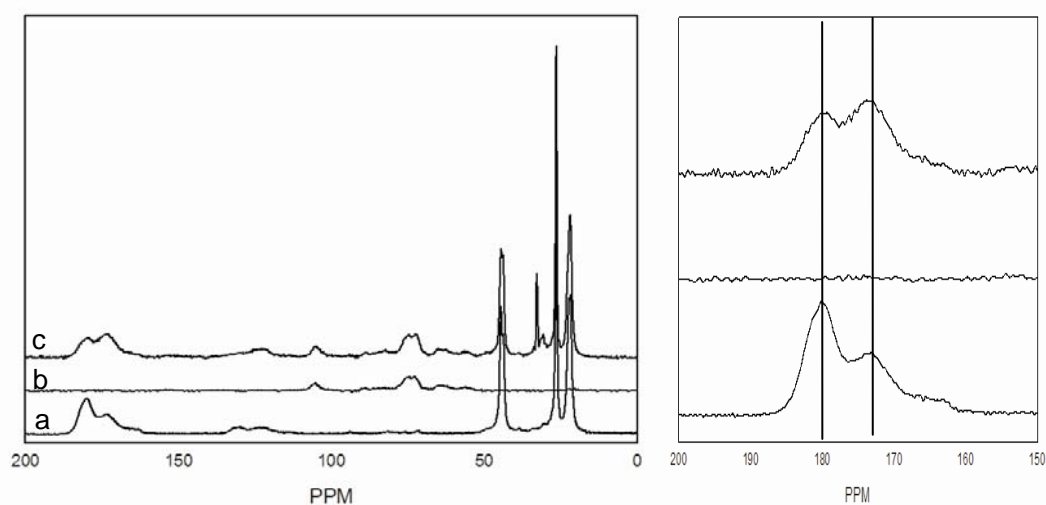


Fig. 1. ^{13}C NMR spectra of (a) MAPP, (b) maple and (c) MAPP/maple blend and close up of carbonyl region (right).

In the maple/MAPP blend the MAPP resonances are clearly detected and there are no overlapping wood signals in the carbonyl region (Fig. 1b-c). Therefore changes in the spectral features in the carbonyl region can be ascribed to the MAPP and its interactions with wood polymers. Interestingly, the relative intensity of the acid and anhydride MA resonances is significantly changed in the blend (Fig. 1c) compared to that of the neat MAPP. While in the control MAPP the carboxylic acid (180 ppm) was more intense than the anhydride peak (173.9 ppm), they are equally intense in the blend. Intensity variation may be due to 1) changes in relaxation times, 2) a shift in the anhydride/ diacid equilibrium due to the presence of the hygroscopic and acidic wood or 3) to the reaction of the MA with cellulose to form a monoester/monoacid or diester. However relaxation times for these resonances did no change in the blend. Moreover the weakly acidic character of wood would be expected to shift the equilibrium to the carboxylic diacid in the equilibrium which is not consistent with the observed spectral changes (Fig. 1c). Therefore, neither a shift in equilibrium nor a change in relaxation times could explain the observed change in intensity ratio of the 173.9 ppm and 180.1 ppm resonances. On the other hand, the chemical shift for an ester bond between MAPP and the hydroxyl groups of wood polymers, cellulose hemicellulose and lignin, is predicted at ca 174.5-177.0ppm. It is therefore likely that the 173.9ppm signal increase in the wood/MAPP blend is due to monoester and diester formation between MA and wood hydroxyls (Fig. 2). Hydrogen-bonding may also participate in the broadening of the carbonyl resonances observed in the blend (Fig. 1c).

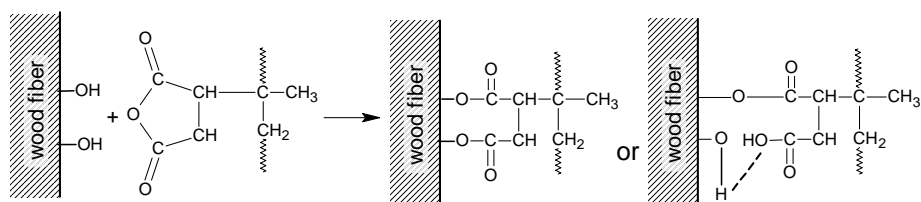


Fig. 2. Proposed reaction scheme between MAPP and wood polymers (reproduced from Takase and Shiraishi 1989)

Chemical bonding between MAPP and the wood fiber is likely at the root of MAPP effect on the performance of wood plastic composites. Indeed in wood/polypropylene composites the addition of ca 1% MAPP to the formulation gives rise to a two fold increase in the modulus of rupture (Takase and Shiraishi 1989). Primary bonding between wood and MAPP likely provides for a better stress transfer between the fiber and the polyolefin matrix thereby enhancing the composite performance. In this system, in spite of the scarcity of the maleic anhydride moieties on the MAPP polymer, the chemistry of the functional groups has been effectively deciphered with solid state NMR thanks to the targeted labelling of MAPP.

4.2 CP/MAS NMR of the wood/PF composite. Fig. 3 represents the superposed CP/MAS NMR spectra of wood, control treatment and the composite. In the control treatment and in the composite the lignin methoxyl carbon, the cellulose C₄ (amorphous and crystalline) and the C₁ of carbohydrates can be monitored at 56, 85, 90 and 105 ppm respectively. The PF resin also exhibits a distinct aromatic signal at 130 ppm in the composite spectrum.

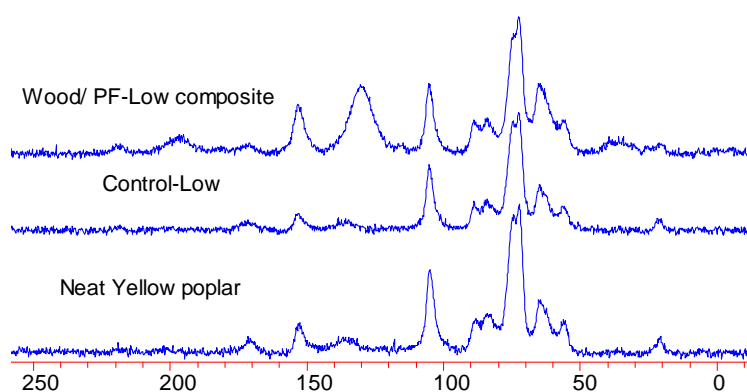


Fig. 3. ¹³C CP/MAS NMR spectrum of yellow-poplar, control sample and wood/PF composite.

Signal intensities for wood resonances and for the PF resin were monitored as a function of contact time so as to extract T_{CH} and T_{1ρ} relaxation times by fitting the carbon intensity to Equation 1. A good fit to the magnetization equation was generally found for the above-mentioned wood resonances (Fig. 4).

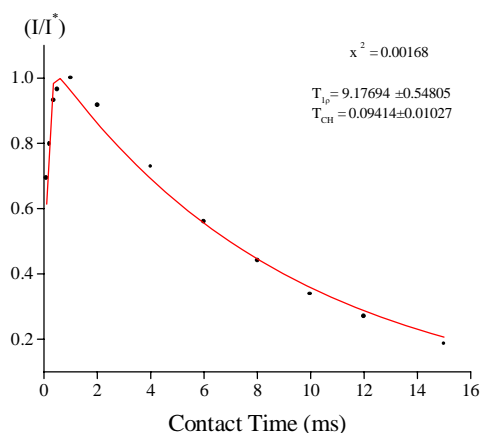


Fig. 4. Typical fit of signal magnetization versus contact time to equation 1.

In table 1 the relaxation times for the detectable resonances in the control and wood/phenolic composite are presented. When comparing the relaxations in the composite to those in the control wood, it is apparent that the PF resin cure treatment has systematically increased the

relaxation times for all wood signals. This is consistent with the expectations; the low molecular weight resin penetrates into the amorphous wood polymers prior to cure. It is also interesting to note that the PF-low treatment seems to have altered the spin coupling among polysaccharides. Typically, the intimate associations among wood polysaccharides are indicated by the similarity in $^H T_{1\rho}$ that is measured from distinct carbon signals (Newman 1996). For example, notice that the carbohydrate signals (85, 90 and 105 ppm) in the control yellow-poplar all exhibit numerically similar $^H T_{1\rho}$ values. This suggests that spin diffusion is providing an efficient magnetization transfer among all polysaccharides. This is not true for the wood/PF-low composite. To help demonstrate the point, ANOVA was conducted among the polysaccharide signals (85, 90 and 105 ppm) within each sample; the significance level (p-value) for each ANOVA is also presented in Table 1. The polysaccharide relaxations are non-uniform within the PF-low composite samples (p=0.03), whereas they are uniform in the control wood (p>0.20). Finally, the PF $^H T_{1\rho}$ is 10.8 ms in the composite, which also happens to be quite similar to the wood polymer relaxations. This suggests that the PF resin may be spin coupled with wood polymers (Laborie et al. 2006).

Table 1. Proton rotating frame spin lattice relaxations, $T_{1\rho}^H$ (ms), for wood and PF polymer in control yellow-poplar and composite samples (standard deviation from trireplicates in parenthesis)

	Control wood	Wood/PF Composite
Lignin methoxyl (57 ppm)	10.3 (0.6)	12.00 (0.6)
Amorphous Cellulose C ₄ (85 ppm)	8.9 (0.3)	10.0 (0.1)
Crystalline Cellulose C ₄ (90 ppm)	9.0 (0.2)	11.3 (0.7)
C ₁ carbohydrates (105 ppm)	9.1 (0.4)	11.1 (0.4)
p-value*	0.28	0.03
PF aromatic carbon (130 ppm)		10.8 (0.5)

* from ANOVA of 85, 90 and 105 ppm signals.

The CP/MAS NMR analysis of the PF-low is therefore consistent with a nanometer-scale morphology, which perturbed wood nuclear magnetic relaxations. Based on these observations, one can conceptualize the mechanism of interphase formation in the PF-Low composite. When the liquid adhesive is applied to wood, the low molecular weight species penetrate into wood amorphous domains. Upon cure of the resin, an in-situ network is generated, a nanoscale resin structure which constrains the wood polymers as suggested by the increase in wood polymers relaxation times. As a result an homogeneous phase morphology is generated in the composite explaining the similarity in $^H T_{1\rho}$ relaxations between the wood polymers and the PF resin. In other words an interpenetrating network is formed at the wood/PF interphase when a low molecular weight resin is used. This is in contrast to results on a high molecular weight PF resin which show that the resin is largely excluded from the wood polymer networks resulting in phase separated interphase morphology at least on the nanometer scale (Laborie et al. 2006). This example illustrates that in the case of polymeric composites in which the individual polymer resonances can be monitored relaxation time measurements are useful to shed light on the nanometer scale morphology of the wood adhesive interphase.

5. CONCLUSIONS

In this paper the utility of solid state NMR for probing the interphase chemistry and nanometer scale morphology in natural fiber reinforced composites has been illustrated in two composite systems involving natural fibers and both a thermoplastic polymer matrix and a thermosetting adhesive. It was shown that specific isotope labeling of a polymer can be used to enhance the detection of the chemistry at the interphase in the case of wood/ polyolefin composites. In other systems where both polymers are distinctively detected in the composite, simple relaxation time measurements suffice to shed light on the interphase morphology.

ACKNOWLEDGEMENTS

The work was partially sponsored by the Office of Naval Research, under the direction of Mr. Ignacio Perez, under Grant N00014-03-1-0949 and by the center for adhesive and sealant science at Virginia Tech. The authors thank Dr. Scott Hacker at Honeywell for synthesizing [1,4-¹³C₂]MAPP.

REFERENCES

- Gil, A.M. and Pascoal Neto, C. (1999). Solid state nuclear magnetic resonance studies of wood and other lignocellulosic materials, *Annual Reports on NMR Spectroscopy* 37, 76-117.
- Laborie, M.-P., Salmén L., and Frazier, C.E. (2006). A morphological study of the wood/phenol-formaldehyde resin interphase. *J. Adhes. Sci. Technol.* 20, 8, 729-741.
- Mehring, M. (1983). *Principles of high resolution NMR in solids*, (Springer-Verlag, Berlin). p. 342.
- Newman, R.H. (1996). Nuclear magnetic resonance study of spatial relationships between chemical components in wood cell walls, *Holzforschung* 46, 205-210.
- Schmidt-Rohr, K. and Spiess, H.W. (1994). *Multidimensional solid-state NMR and polymers* (Academic Press, New-York). p. 478.
- Takase, S. and Shiraishi, N. (1989). Studies on composites from wood and polypropylenes, II. *J. Appl. Polym. Sci.* 37, 645-659.

HANSEN SOLUBILITY PARAMETERS FOR A CARBON FIBER/EPOXY COMPOSITE

Hélène Launay^{*}, Charles Medom Hansen^{**}, Kristoffer Almdal^{*}

^{*} Danish Polymer Centre, Risø National Laboratory - Technical
University of Denmark, Frederiksborgvej 399, P.O. Box 49, 4000
Roskilde, Denmark.

^{**} Consultant, Jens Bornøs Vej 16, 2970 Hørsholm, Denmark.

ABSTRACT

The focus of this work is the evaluation of the physical compatibility between an epoxy resin used as a matrix and an oxidized, unsized carbon fiber, and between this same epoxy resin and glassy carbon. For this purpose, carbon fibers, glassy carbon and epoxy resin have been assigned Hansen solubility (cohesion) parameters (HSP) by analysis of their interactions with a set of well-defined liquids. A strong physical affinity between the epoxy matrix and the carbon fibers has been shown, since their respective HSP are close. The use of a glassy carbon substrate as a model for unsized carbon fiber has been demonstrated as appropriate for the study of interactions between the materials in composite carbon fiber-epoxy systems, since the HSP of glassy carbon are similar to the ones of the studied carbon fibers.

1. INTRODUCTION

Fiber-reinforced composites are used in a wide range of applications where high stiffness and strength-to-weight ratios are required. The mechanical performance of composite materials depends not only on the matrix and the reinforcing fiber properties, but also to a great extent on the fiber/matrix adhesion. The physical compatibility between the fibers and the matrix can have a profound effect on the interface properties.

The experimental investigation of the fiber/matrix adhesion often involves the use of glassy carbon as a planar model surface for carbon fibers. Glassy carbon is an amorphous-like, dense material consisting of disordered phases of sp^2 -hybridized carbon atoms randomly interspersed with regions of amorphous carbon (McCulloch, Praver, Hoffman 1994). Due to its structural similarities with carbon fiber (Jenkins, Kawamura 1976), extremely high hardness and modulus, chemical inertness, high temperature resistance, electrical conductivity, low cost and availability, glassy carbon is often considered as an ideal model for carbon fiber. Glassy carbon plates are moreover easier to handle and to surface characterize, thus allowing straightforward

analysis of the mechanical tests.

Hansen solubility (cohesion) parameters (HSP) are widely used for predicting compatibility between two materials (Hansen 1999). The concept described by Hansen is based on the fact that the cohesive energy of a liquid, which can be directly measured by its energy of vaporization, arises from the contribution of three kinds of interactions: (i) nonpolar, atomic (dispersion) interactions (D), (ii) molecular, dipolar interactions (P) and (iii) molecular, hydrogen bonding interactions (H) (Hansen 1999). These three major types of interaction are quantitatively described by the three Hansen parameters δ_D , δ_P , and δ_H , respectively. Materials with similar HSP will show physical affinities.

The experimental method for the determination of HSP is based on the observation of the interaction or absence of interaction between the studied material and well-known solvents (Hansen 1999). This difference of interaction is used to divide the solvents into two groups, one which is considered “good” and the other which is considered “bad”. “Good” solvents interacting strongly with the material have HSP closer to those of the material than “bad” solvents giving little interaction, and are used to assign HSP to the studied material.

In this study Hansen solubility (cohesion) parameters of an epoxy resin, oxidized, unsized carbon fibers and glassy carbon have been calculated by analysis of their interactions with a set of well-defined liquids. The degree of swelling is the type of interaction chosen for the characterization of the cross-linked epoxy resin studied here. Cohesion parameters of carbon fibers and glassy carbon, in powder form, were evaluated by observing the sedimentation behavior of the particles in different solvents (Hansen 1999). Particles with a strong affinity for a solvent give a lowered sedimentation rate and the solvent is then considered as “good”. On the other hand a relatively faster sedimentation in a given solvent happens in case of low affinity, and the solvent is considered as “bad”. The physical affinity between the fibers and the matrix is estimated, and a comparison of carbon fibers and glassy carbon HSP allows a discussion on the relevancy of using glassy carbon as a model for carbon fiber for the study of adhesive properties of carbon fibers.

2. EXPERIMENTAL

2.1. Materials. The epoxy resin (bisphenol F-epichlorhydrin epoxy/bisphenol A-diglycidylether) and the hardener (polyoxyalkyleneamine/3-aminomethyl-3,5,5-trimethylcyclohexylamine) were mixed at a ratio of 10/3 by weight at room temperature. The curing time was 48 hours at room temperature.

Planar glassy carbon (SIGRADUR G) was purchased from HTW Hochtemperatur. XPS analysis of the glassy carbon plate surface showed that the surface was slightly oxidized (about 5% O). Oxidized, unsized carbon fibers (TENAX J HTA-5001) were obtained from TOHO TENAXCO LTD.

Analytical grade test solvents with a wide range of known solubility parameters (Hansen 1999) were selected and used as received.

2.2. Measurements. The cured epoxy was cut into thin pieces of 25 mg. Each piece was placed into a standard test tube containing a test solvent (7.5 mL). The tube was sealed with a cap and allowed to stand at room temperature for two days. The behaviour of the epoxy sample was observed visually. Solvents in which a swelling of the resin was observed after two days of exposure were considered as being good. Solvents were labeled as bad in case of no interaction

at all between solvents and resin.

Glassy carbon plates were milled and sieved to obtain fine particles having diameters below 10 μm . A larger particle size should be avoided to enhance surface effects (Hansen 1999). Glassy carbon particles (0.5 mg) were placed into a standard test tube containing a test solvent (7.5 mL). The concentration of particles was 0.067 mg/mL. The tube was sealed with a cap and sonicated for 60 min. After sonication, the tube was allowed to stand. The dispersion stability was observed visually. Solvents in which particles were completely deposited on the tube bottom after 60 min sonication were considered as bad. Solvents were good when complete sedimentation required more than one hour after the sonication step.

For carbon fibers, a visual observation of the speed of sedimentation was not sufficient to discriminate between good and bad solvents unlike for glassy carbon. A relative sedimentation time (RST) was calculated using equation (1). This allowed a normalization of the observed sedimentation time t_s (min) with the solvent viscosity, η (Pa.s), and density difference between particles and solvent, $(\rho_p - \rho_s)$ ($\text{g}\cdot\text{mL}^{-1}$). Good and bad solvents were identified by choosing a cut-off value for RST.

$$RST = t_s (\rho_p - \rho_s) / \eta \quad (1)$$

Carbon fibers were cut to 3 mm length. Fiber length and concentration were optimized in a previous study, where the best conditions were 3 mm length with a fiber concentration of 0.033 mg/mL. These conditions allowed a sufficient visualization which did not require the help of a small laser. Another study on carbon nanotubes used a concentration of 0.067 mg/mL, which was diluted enough to prevent aggregation (Ham, Choi, Chung 2005). The same concentration of 0.067 mg/mL was chosen for studying the carbon fibers in the test solvents. The test tube with the fibers was shaken well and sedimentation time was measured. The sedimentation time measurements started when the test tube was allowed to stand and stopped with the complete sedimentation of the fibers.

Once good and bad solvents are identified, these data are processed by a computer program developed by Hansen (Hansen 1999) to obtain the three HSP and the radius value, R_o , of the sphere of interaction for the materials studied. R_o gives the maximum difference in affinity allowed for a “good” interaction between solvent and material. The level of interaction allowing the distinction between good and bad solvents is chosen arbitrarily, like for example the cut-off value for RST. Several attempts might be necessary for a good correlation (a correlation coefficient close to one).

3. RESULTS

The HSP for epoxy resin and glassy carbon were, by coincidence, identical with an excellent correlation coefficient of 1.0 (Table 1). The high data fit may be partly due to the low number of tested solvents. This helped to allow a perfect separation of the good and bad solvents by the HSP correlation. Fig. 1 shows a 3-dimensional plot of the HSP found with the glassy carbon correlation. The sphere, whose center is the HSP for glassy carbon and radius is R_o (Table 1), encompasses the region of the higher surface affinities of glassy carbon. The tested solvents are marked with dots. All the good solvents are inside the HSP sphere and all the bad ones are outside. 2-dimensional projections on the δ_D versus δ_H , and δ_H versus δ_P planes on Fig. 1 are shown to help for better visualization of the situation.

Table 1: HSP, radius of interaction R_o and correlation coefficients (data fit) of epoxy resin, glassy carbon and carbon fibers correlations.

Material	δ_D (MPa ^{1/2})	δ_P (MPa ^{1/2})	δ_H (MPa ^{1/2})	R_o (MPa ^{1/2})	Data fit	No.*
Epoxy resin	20.0	10.0	8.0	9.0	1.000	7/18
Glassy carbon	20.0	10.0	8.0	9.0	1.000	6/13
Carbon fibers	21.3	8.7	11.5	9.3	0.861	8/36

*No.: number of good solvents interacting with the studied material over the total number of solvents.

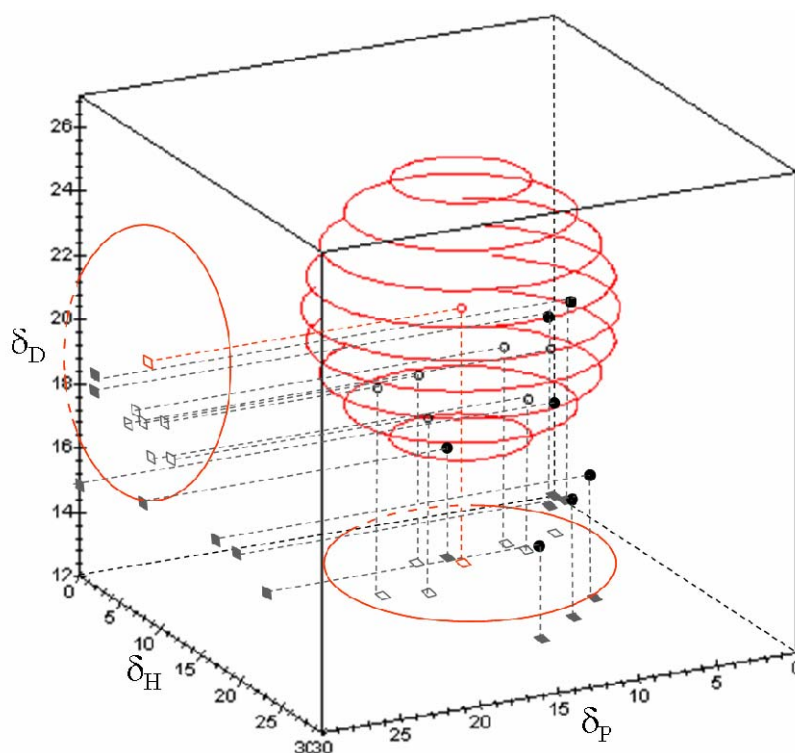


Fig. 1. 3- dimensional plot and projections of the glassy carbon sphere of surface affinity and of the tested solvents used for the correlation (○: inside the sphere, ●: outside the sphere).

HSP for carbon fibers were evaluated using 36 test solvents (Table 1). The more solvents tested, the better the sphere boundary is defined. This is important for a good correlation since it is the boundary which is used to define the center point of the sphere (Hansen, 2007). A preliminary study with 18 test solvents gave a sphere of interaction with a large radius (16.5 MPa^{1/2}) and several outlier solvents which were not considered in the correlation. Additional solvents with HSP in the boundary region were then selectively chosen and tested until the lowest radius R_o was reached with the maximum correlation coefficient (Table 1). A cut-off RST of $5.9 \cdot 10^3$ min.g.mL⁻¹.Pa⁻¹.s⁻¹ was chosen to separate good solvents from bad solvents, allowing a reasonably good correlation. The correlation coefficient was 0.861.

4. DISCUSSION

Table 1 shows that epoxy resin and glassy carbon have the same HSP and radius of interaction. Their regions of affinity/solubility are exactly superposed when the criteria of “good” and “bad”

were chosen as reported in the above. This indicates a very high physical attraction between them. In our study, epoxy resin was cured at room temperature. Specimen preparation for mechanical studies usually uses a curing procedure at high temperature for a faster process. At higher curing temperatures, no change of the center of the sphere of solubility should be expected, but the sphere radius might decrease, as observed by Storm, Gwisdalski, Lindvang and Rann (2005). A higher curing temperature leads to smaller radius value because of increased cross-linking and thus greater resistance to solvent uptake.

Mechanical tests for the glassy carbon-resin interface characterization involve the use of planar substrates. However the present investigation of the glassy carbon HSP was done on particles. The same kind of study could indeed have been carried out on glassy carbon plates comparing contact angles of the test solvents. But this method is less precise than sedimentation tests as only liquids with a higher surface tension than the surface allow measurement of a contact angle (Hansen 2007). Moreover glassy carbon particles were directly obtained from plates by grinding, thus ensuring the same surface properties to the extent that this is possible.

The sphere A in Fig. 2 represents the region of interaction of both epoxy resin and glassy carbon, these two materials having the same parameters. Comparing with the sphere of surface affinity of carbon fibers (sphere B, Fig. 2), it can be clearly seen that the two spheres are almost superposed. The carbon fibers of this study should have good physical affinities for epoxy materials, since their HSP regions of affinity/solubility are very similar. Moreover carbon fibers and glassy carbon have very close HSP regions. Their physical affinities towards another material should then be comparable. It appears that it is justifiable and relevant to use glassy carbon as a model for carbon fiber for the studies of interactions between the materials in composite carbon fiber-epoxy systems.

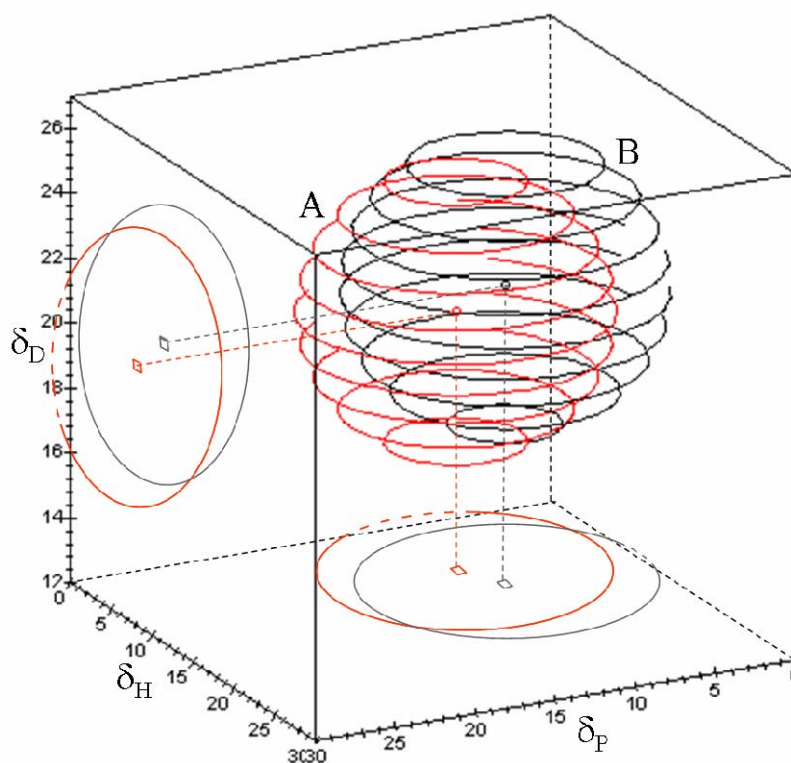


Fig. 2. 3- dimensional plot and projections of the cured epoxy/glassy carbon (A) and carbon fiber (B) spheres of interaction.

5. CONCLUSIONS

Hansen solubility parameters have been assigned to a cured epoxy resin, unsized and oxidized carbon fibers, and glassy carbon.

This study has shown that glassy carbon and unsized, oxidized carbon fibers have close HSP. Both materials have comparable and excellent physical affinities towards the epoxy matrix that was also studied. Glassy carbon appears then to be a good model for the carbon fibers studied here.

This investigation has focused on physical affinities only, at the interface between the carbon materials and the epoxy polymer. Chemical treatments which could provide covalent bonding between fibers and matrix, are clearly possible, but have not been considered here.

ACKNOWLEDGEMENTS

This work was done as a part of the Framework Program “Interface Design of Composite Materials” with the support of the Danish Technical Research Council (STVF fund no. 26-03-0160).

REFERENCES

- Ham, H.T., Choi, Y.S., Chung, I.J (2005). An explanation of dispersion states of single-walled carbon nanotubes in solvents and aqueous surfactant solutions using solubility parameters. *Journal of Colloid and Interface Science* 286, 216-223.
- Hansen, C.M. (1999). *Hansen Solubility Parameters – A User’s Handbook*. Boca Raton, FL: CRC Press.
- Hansen, C.M. (2004). Aspects of solubility, surfaces and diffusion in polymers. *Progress in Organic Coatings* 51, 55-66.
- Hansen, C.M. (2007). Surface characterization using Hansen Solubility (Cohesion) Parameters. 28th Risø International Symposium on Materials Science: "Interface design of polymer matrix composites - mechanics, chemistry, modelling and manufacturing".
- Jenkins, G.M., Kawamura, K. (1976). *Polymeric Carbons*. Cambridge University Press, Cambridge.
- McCulloch, D.G., Prawer, S., Hoffman, A. (1994). Structural investigation of xenon-ion-beam-irradiated glassy carbon. *Physical Review B* 50, 5905-5917.
- Storm, B.K., Gwisdalski, M., Lindvang, D., Rann, M. (2005). Investigation of degradation of structural adhesives under influence of chemicals. *Macromolecular Symposia* 225, 205-219.

WEAK SOLUTIONS IN ELASTICITY OF DIPOLAR MATERIALS WITH STRETCH

M. Marin

Faculty of Mathematics, University of Brasov, Romania

ABSTRACT

In the present paper we generalize the results obtained by Iesan and Quintanilla for microstretch elastic bodies in order to cover the dipolar elastic materials with stretch. For the boundary value problem considered in this context, we use some results from the theory of semigroups of the linear operators in order to prove the existence and uniqueness of a weak solution.

1. INTRODUCTION

First time, the micromorphic elastic material was introduced by Eringen and his co-workers (see, Eringen and Kafadar (1976), Eringen and Suhubi (1964)). Then Eringen, has generalized this theory in order to cover the theory of thermo-microstretch elastic materials (see Eringen (1990)). As it is already known, in this theory the material points can stretch and contract independently of their translations and rotations. Few applications of such materials are described in Eringen (1990). This theory is an extension of the theory of micropolar bodies and of the micromorphic theory. In our paper, first of all, we consider the basic equations and conditions for dipolar elastic materials with stretch in the context of linear theory. More exactly, we consider basic boundary value problems of Elastostatics and we use some results from the theory of semigroups of the linear operators in order to prove the existence and uniqueness of a weak solution.

2. NOTATIONS AND BASIC EQUATIONS

Consider that our elastic dipolar solid with stretch occupies at time $t = 0$ a properly regular region B of three-dimensional Euclidean space R^3 . We assume that the boundary of the domain B , denoted by ∂B , is a closed and bounded surface and it is sufficiently smooth to admit the application of the divergence theorem. In the following we designate by n_i the components of the outward unit normal to the surface ∂B . The closure of the domain B , denoted by \bar{B} , means $\bar{B} = B \cup \partial B$. Throughout this paper we refer the evolution

of the continuum to a fixed system of rectangular Cartesian axes Ox_i ($i = 1, 2, 3$) and adopt the Cartesian tensor notation. Points in B are denoted by x_i and $t \in [0, \infty)$ is temporal variable. The Italic indices will always assume the values 1, 2, 3 whereas the Greek indices will range over the values 1, 2. A superpose dot stands for the material derivate while a comma followed by a subsript denotes partial differentiation with respect to the respective Cartesian coordinate. Einstein convention regarding the summation over repeated indices is also used. Also, the spatial argument and the time argument of a function will be ommited when there is no likelihood of confusion. For convenience, the notations and terminology chosen are similar to those of paper Iesan and Quitanilla (1994). Our following considerations are dedicated to an isotropic and homogeneous dipolar elastic solid with stretch. The independent variables which describe the motion for the material are:

- $u_i = u_i(x, t)$, $\varphi_{jk} = \varphi_{jk}(x, t)$ – the components of displacement and dipolar displacement fields from reference configuration;
- $\varphi = \varphi(x, t)$ – the scalar function that characterize the stretch.

With the aid of a procedure similar to that used by Eringen in Eringen (1990), we obtain the following equations and conditions for the time independent behavior of linear elastic material (see, also, Marin (1995) and Marin (1997)):

- the equations of equilibrium:

$$\begin{aligned} (\tau_{ij} + \eta_{ij})_{,j} + F_i &= 0, \\ \mu_{ijk,i} + \eta_{jk} + G_{jk} &= 0; \\ \lambda_{k,k} - s + H &= 0; \end{aligned} \tag{1}$$

- the constitutive equations:

$$\begin{aligned} \tau_{ij} &= C_{ijmn}\varepsilon_{mn} + G_{mnij}\kappa_{mn} + F_{mnrij}\chi_{mnr} + D_{ijm}\gamma_m + a_{ij}\varphi, \\ \eta_{ij} &= G_{ijmn}\varepsilon_{mn} + B_{ijmn}\kappa_{mn} + D_{ijmnr}\chi_{mnr} + E_{ijm}\gamma_m + b_{ij}\varphi, \\ \mu_{ijk} &= F_{ijkmn}\varepsilon_{mn} + D_{mniijk}\kappa_{mn} + A_{ijkmnr}\chi_{mnr} + F_{ijkm}\gamma_m + c_{ijk}\varphi, \\ 3\lambda_i &= D_{mni}\varepsilon_{mn} + D_{mni}\kappa_{mn} + F_{mnri}\chi_{mnr} + g_{im}\gamma_m + d_i\varphi, \\ 3s &= a_{mn}\varepsilon_{mn} + b_{mn}\kappa_{mn} + c_{mnr}\chi_{mnr} + d_m\gamma_m + m\varphi; \end{aligned} \tag{2}$$

- the geometric equations:

$$\begin{aligned} 2\varepsilon_{ij} &= u_{j,i} + u_{i,j}, \quad \kappa_{ij} = u_{j,i} - \varphi_{ij}, \\ \chi_{ijk} &= \varphi_{ij,k}, \quad \gamma_i = \varphi_{,i}. \end{aligned} \tag{3}$$

The above equations are considered on the domain B and we have used the following notations:

- τ_{ij} , η_{ij} , μ_{ij} - the components of the stress tensors;
- λ_i - the components of microstress vector;
- F_i - the components of body force per unit mass;
- G_{jk} - the components of dipolar body force per unit mass;
- H - the scalar body load;
- s - the scalar microstress function;
- ε_{ij} , κ_{ij} , χ_{ijk} - the components of the kinematic characteristics of the strain tensors.

Finally, the tensors C_{ijmn} , B_{ijmn} , ..., D_{ijm} , E_{ijm} , ..., a_{ij} , b_{ij} , c_{ijk} , the vector of the components d_i and the scalar coefficient m represent the characteristic functions of the material

(the constitutive coefficients) and they obey to the following symmetry relations

$$\begin{aligned}
 C_{ijmn} &= C_{mnij} = C_{ijnm}, & B_{ijmn} &= B_{mnij}, \\
 G_{ijmn} &= G_{ijnm}, & F_{ijkmn} &= F_{ijknm}, & A_{ijkmnr} &= A_{mnrijk}, \\
 E_{ijm} &= E_{jim}, & D_{mni} &= D_{nmi}, & g_{ij} &= g_{ji}.
 \end{aligned} \tag{4}$$

For clarity and simplification in presentation, we consider the following regularity hypotheses on the considered functions:

- all the constitutive coefficients are functions of class C^2 on B ;
- the body loads F_i , G_{jk} and H are continuous functions on B .

We say that the ordered array $(u_i, \varphi_{jk}, \varphi)$ is an admissible process on $\bar{B} = B \cup \partial B$ provided $u_i, \varphi_{jk}, \varphi \in C^1(\bar{B}) \cap C^2(B)$. Also, the ordered array of functions $(\tau_{ij}, \eta_{ij}, \mu_{ijk}, \lambda_i)$ is an admissible system of stress on \bar{B} if $\tau_{ij}, \eta_{ij}, \mu_{ijk}, \lambda_i \in C^1(B) \cap C^0(\bar{B})$ and $\tau_{ij,i}, \eta_{ij,i}, \mu_{ijk,k}, \lambda_{k,k}, \lambda \in C^0(\bar{B})$. Finally, we assume that the components of the strain $\varepsilon_{ij}, \kappa_{ij}, \chi_{ijk}, \gamma_i \in C^1(B) \cap C^0(\bar{B})$. Let $\partial B_1, \partial B_2$ and ∂B_3 with respective complements $\partial B_1^c, \partial B_2^c$ and ∂B_3^c be subsets of the boundary ∂B such that

$$\begin{aligned}
 \partial B_1 \cup \partial B_1^c &= \partial B_2 \cup \partial B_2^c = \partial B_3 \cup \partial B_3^c = \partial B \\
 \partial B_1 \cap \partial B_1^c &= \partial B_2 \cap \partial B_2^c = \partial B_3 \cap \partial B_3^c = \emptyset.
 \end{aligned}$$

To the system of field equations (1) - (4) we adjoin the following boundary conditions

$$\begin{aligned}
 u_i &= \tilde{u}_i \text{ on } \partial B_1, & \varphi_{jk} &= \tilde{\varphi}_{jk} \text{ on } \partial B_2, & \varphi &= \tilde{\varphi} \text{ on } \partial B_3, \\
 (\tau_{ij} + \eta_{ij}) n_j &= \tilde{t}_i \text{ on } \partial B_1^c, & \mu_{ijk} n_i &= \tilde{\mu}_{jk} \text{ on } \partial B_2^c, & \lambda_i n_i &= \tilde{h} \text{ on } \partial B_3^c,
 \end{aligned} \tag{5}$$

where the functions $\tilde{u}_i, \tilde{\varphi}_{jk}, \tilde{\varphi}, \tilde{t}_i, \tilde{\mu}_{jk}$ and \tilde{h} are prescribed. By an external data system on \bar{B} we mean an ordered array

$$\mathcal{L} = (F_i, G_{jk}, H, \tilde{u}_i, \tilde{\varphi}_{jk}, \tilde{\varphi}, \tilde{t}_i, \tilde{\mu}_{jk}, \tilde{h})$$

with the properties:

- the functions $F_i, G_{jk}, H, \tilde{u}_i, \tilde{\varphi}_{jk}$ and $\tilde{\varphi}$ are continuous in their domains;
- the functions $\tilde{t}_i, \tilde{\mu}_{jk}$ and \tilde{h} are piecewise regular on their domains

The boundary value problem of the equilibrium theory for elastic dipolar bodies with stretch consists in finding the functions $(u_i, \varphi_{jk}, \varphi)$ that satisfy the equations (1) - (4) and the boundary conditions (5). Of course, the solution $(u_i, \varphi_{jk}, \varphi)$ corresponds to the loads (F_i, G_{jk}, H) .

3. WEAK SOLUTIONS

In the following we restricte our attentions to the Elastostatics of dipolar bodies with stretch. Firstly, we introduce the mathematical tools which help us to prove the existence of weak solutions. Let us consider that B is a Lipschitz region of the Euclidian three- dimensional space R^3 and introduce the notations

$$\mathbf{W} = \prod_{k=1}^m W^{k,2}(B), \quad \mathbf{W}_0 = \prod_{k=1}^m W_0^{k,2}(B),$$

where $W^{k,2}(B)$ and $W_0^{k,2}(B)$ are usually Sobolev spaces and m is a natural number. We denote by $A(\mathbf{v}, \mathbf{u})$ the following bilinear form, defined on $\mathbf{W} \times \mathbf{W}$ by:

$$A(\mathbf{v}, \mathbf{u}) = \int_B \sum_{r,s=1}^m \sum_{|i| \leq r, |j| \leq s} a_{ij}^{rs} D^i v_r D^j u_s dv,$$

where a_{ij}^{rs} are real bounded and measurable functions on B and D^α is the notation for the multiindex derivative, that is:

$$D^\alpha = \frac{\partial^{|\alpha|}}{\partial x_1^{\alpha_1} \partial x_2^{\alpha_2} \partial x_3^{\alpha_3}}.$$

Denote by \mathbf{V} a closed subspace of the space \mathbf{W} such that

$$\mathbf{W}_0 \subset \mathbf{V} \subset \mathbf{W}$$

and by $f(\mathbf{v})$ and $g(\mathbf{v})$ the following functionals

$$\begin{aligned} f(\mathbf{v}) &= \int_B \sum_{i=1}^m f_i v_i dv, \quad f_i \in L_2(B), \quad \mathbf{v} \in \mathbf{W} \\ g(\mathbf{v}) &= \int_S \sum_{j=1}^m g_j v_j da, \quad g_j \in L_2(S), \quad \mathbf{v} \in \mathbf{W} \end{aligned} \tag{6}$$

In the above relations we used the spaces $L_2(B)$ and $L_2(S)$ which represent, as it is well known, the space of real functions which are square-integrable on B , respectively, on $S \subset \partial B$. For a fixed $\bar{\mathbf{u}} \in \mathbf{W}$, we say that $\mathbf{u} \in \mathbf{W}$ is a weak solution of our boundary-value problem if $\mathbf{u} - \bar{\mathbf{u}} \in \mathbf{V}$ and for each $\mathbf{u} \in \mathbf{V}$ we have

$$A(\mathbf{v}, \mathbf{u}) = f(\mathbf{v}) + g(\mathbf{v}). \tag{7}$$

By $N_k \mathbf{v}$ we denote the following operators, which maping \mathbf{W} into $L_2(B)$,

$$N_k \mathbf{v} = \sum_{r=1}^m \sum_{|\alpha| \leq k_r} n_{k_r \alpha} D^\alpha v_r, \tag{8}$$

where $n_{k_r \alpha}$ are bounded and measurable functions on B . By definition, the operators $N_k \mathbf{v}$, ($k = 1, 2, \dots, h$) form a coercive system of operators on \mathbf{W} if for each $\mathbf{v} \in \mathbf{W}$ the following inequality

$$\sum_{k=1}^m |N_k \mathbf{v}|_{L_2}^2 + \sum_{r=1}^m |v_r|_{L_2}^2 \geq c_1 |\mathbf{v}|_{\mathbf{W}}^2, \quad c_1 > 0, \tag{9}$$

holds. In this inequality, c_1 does not depends on \mathbf{v} and the norms $|\cdot|_{L_2}$ and $|\cdot|_{\mathbf{W}}$ represent the usual norms in the spaces $L_2(B)$ and \mathbf{W} , respectively. In the following theorem we indicate a necessary and sufficient condition for that a system of operators is coercive.

Theorem 1. *Let $n_{p_s \alpha}$ be constant for $|\alpha| = k_s$. Then the system of operators $N_p \mathbf{v}$ is*

coercive on \mathbf{W} if and only if the rank of the matrix

$$(N_{ps}\xi) = \left(\sum_{|\alpha|=k_s} n_{ps\alpha} \xi_\alpha \right), \quad (10)$$

is equal to m for each $\xi \in \mathbf{C}_3$, $\xi \neq 0$, where \mathbf{C}_3 is the notation for the complex three-dimensional space, and

$$\xi_\alpha = \xi_1^{\alpha_1} \xi_2^{\alpha_2} \xi_3^{\alpha_3}.$$

The demonstration of this result can be find in the book Necas (1967). In the following we assume that for each $\mathbf{v} \in \mathbf{W}$, we have

$$A(\mathbf{v}, \mathbf{v}) \geq c_2 \sum_{k=1}^n |N_k \mathbf{v}|_{L_2}^2, \quad c_2 > 0, \quad (11)$$

where c_2 does not depends on \mathbf{v} . We denote by \mathcal{P} the following set

$$\mathcal{P} = \left\{ \mathbf{v} \in \mathbf{V} : \sum_{k=1}^h |N_k \mathbf{v}|_{L_2}^2 = 0 \right\}, \quad (12)$$

and by \mathbf{V}/\mathcal{P} the factor-space of classes $\tilde{\mathbf{v}}$, where

$$\tilde{\mathbf{v}} = \{ \mathbf{v} + \mathbf{p}, \mathbf{v} \in \mathbf{V}, \mathbf{p} \in \mathcal{P} \},$$

having the norm

$$|\tilde{\mathbf{v}}|_{\mathbf{V}/\mathcal{P}} = \inf_{\mathbf{p} \in \mathcal{P}} |\mathbf{v} + \mathbf{p}|_{\mathbf{W}}$$

In the following theorem it is indicated a necessary and sufficient condition for the existence of a weak solution of the boundary-value problem.

Theorem 2. *Let $A(\mathbf{v}, \mathbf{u}) = [\tilde{\mathbf{v}}, \tilde{\mathbf{u}}]$ define a bilinear form for each $\tilde{\mathbf{v}}, \tilde{\mathbf{u}} \in \mathbf{W}/\mathcal{P}$, where $\mathbf{u} \in \tilde{\mathbf{u}}$ and $\mathbf{v} \in \tilde{\mathbf{v}}$. If we suppose that the inequalities (9) and (11) hold, then a necessary and sufficient condition for the existence of a weak solution of the boundary value problem is*

$$\mathbf{p} \in \mathcal{P} \Rightarrow f(\mathbf{p}) + g(\mathbf{p}) = 0. \quad (13)$$

Moreover, the weak solution, $\mathbf{u} \in \mathbf{W}$ satisfies the following inequality

$$|\mathbf{u}|_{\mathbf{W}/\mathcal{P}} \leq c_3 \left[|\tilde{\mathbf{u}}|_{\mathbf{W}} + \left(\sum_{i=1}^m |f_i|_{L_2(B)} \right)^{1/2} + \left(\sum_{i=1}^m |g_i|_{L_2(S)} \right)^{1/2} \right] \quad (14)$$

where c_3 is a real positive constant.

Further, we have

$$A(\tilde{\mathbf{v}}, \tilde{\mathbf{v}}) \geq c_4 |\tilde{\mathbf{v}}|_{\mathbf{W}/\mathcal{P}}, \quad c_4 > 0, \quad (15)$$

for each $\tilde{\mathbf{v}} \in \mathbf{W}/\mathcal{P}$.

For the prove of this result, see the paper [4]. In the following, we intend to apply the above two results in order to obtain the existence of a weak solution for the boundary value problem formulated in the context of theory of dipolar elastic solids with stretch. Let us assume that our continuum occupies a bounded region B with Lipschitz boundary ∂B . Let $\partial B = S \cup S^* \cup C$ be a disjoint decomposition of the boundary ∂B , where C is a curve (that is, a set of surface measure zero) and S and S^* are either empty or open surfaces in ∂B . Let assume that the following boundary conditions hold:

$$\begin{aligned} u_i &= \tilde{u}_i, \varphi_{jk} = \tilde{\varphi}_{jk}, \varphi = \tilde{\varphi} \text{ on } \bar{S} \\ (\tau_{ji} + \eta_{ji}) n_j &= \tilde{t}_i, \mu_{ijk} n_i = \tilde{\mu}_{jk}, \lambda_i n_i = \tilde{h}, \text{ on } S^*, \end{aligned} \quad (16)$$

where $\tilde{u}_i, \tilde{\varphi}_{jk}, \tilde{\varphi} \in W^{1,2}(\bar{S})$ and $\tilde{t}_i, \tilde{\mu}_{jk}, \tilde{h} \in L_2(S^*)$. In this case we have $m = 12, k_s = 1, s = 1, 2, \dots, 12$. The set \mathbf{W} is defined as the space of all $\mathbf{u} = (u_i, \varphi_{ij}, \varphi)$, such that $u_i, \varphi_{ij}, \varphi \in W^{1,2}(B)$ with the norm

$$|\mathbf{u}|_{\mathbf{W}}^2 = \sum_{i=1}^3 \left(|u_i|_{W^{1,2}(B)}^2 + \sum_{j=1}^3 |\varphi_{ij}|_{W^{1,2}(B)}^2 + |\varphi|_{W^{1,2}(B)}^2 \right). \quad (17)$$

As a subspace \mathbf{V} we have that subspace of \mathbf{W} consists of all $\mathbf{u} = (u_i, \varphi_{jk}, \varphi)$ which satisfy the conditions

$$u_i = 0, \varphi_{jk} = 0, \varphi = 0, \text{ on } S.$$

Also, the bilinear form $A(\mathbf{v}, \mathbf{u})$ is defined on $\mathbf{W} \times \mathbf{W}$ by

$$A(v, u) = 2E(v, u) \quad (18)$$

where $E(v, u)$ is defined by

$$\begin{aligned} E(v, u) &= \frac{1}{2} \int_B \{ C_{ijmn} \varepsilon_{ij}(u) \varepsilon_{mn}(v) + G_{mnij} [\varepsilon_{mn}(u) \kappa_{ij}(v) + \varepsilon_{mn}(v) \kappa_{ij}(u)] + \\ &\quad + B_{ijmn} \kappa_{ij}(u) \kappa_{mn}(v) + F_{mnrj} [\chi_{mnr}(u) \varepsilon_{ij}(v) + \chi_{mnr}(v) \varepsilon_{ij}(u)] + \\ &\quad + D_{mnijk} [\chi_{ijk}(u) \kappa_{mn}(v) + \chi_{ijk}(v) \kappa_{mn}(u)] + A_{ijkmnr} \chi_{ijk}(u) \chi_{mnr}(v) + \\ &\quad + D_{ijm} [\varepsilon_{ij}(u) \gamma_m(v) + \varepsilon_{ij}(v) \gamma_m(u)] + E_{ijm} [\chi_{ijk}(u) \kappa_{mn}(v) + \chi_{ijk}(v) \kappa_{mn}(u)] + \\ &\quad + F_{ijkm} [\chi_{ijk}(u) \gamma_m(v) + \chi_{ijk}(v) \gamma_m(u)] + a_{ij} [\varepsilon_{ij}(u) \psi + \varepsilon_{ij}(v) \varphi] + \\ &\quad + b_{ij} [\kappa_{ij}(u) \psi + \kappa_{ij}(v) \varphi] + c_{ijk} [\chi_{ijk}(u) \psi + \chi_{ijk}(v) \varphi] + \\ &\quad + g_{im} \gamma_i(u) \gamma_m(v) + d_i [\gamma_i(u) \psi + \gamma_i(v) \varphi] + m \varphi^2 \} dv. \end{aligned}$$

By assuming that the constitutive coefficients satisfy the symmetry relations (4) and are bounded measurable functions in \bar{B} , we obtain:

$$A(v, u) = A(u, v), \quad A(u, u) = 2E(u),$$

where the functional $E(\cdot)$ is defined by

$$E(u) = \int_B \sigma(u) dv,$$

and the internal energy density σ has the expression:

$$\begin{aligned} \sigma(u) = & \frac{1}{2}C_{ijmn}\varepsilon_{ij}(u)\varepsilon_{mn}(u) + G_{mnij}\varepsilon_{mn}(u)\kappa_{ij}(u) + \\ & + \frac{1}{2}B_{ijmn}\kappa_{ij}(u)\kappa_{mn}(u) + F_{mnrj}\varepsilon_{ij}(u)\chi_{mnr}(u) + D_{mnijk}\kappa_{mn}(u)\chi_{ijk}(u) + \\ & + \frac{1}{2}A_{ijkmnr}\chi_{ijk}(u)\chi_{mnr}(u) + D_{ijm}\varepsilon_{ij}(u)\gamma_m(u) + E_{ijm}\kappa_{ij}(u)\gamma_m(u) + \\ & + F_{ijkm}\chi_{ijk}(u)\gamma_m(u) + \frac{1}{2}g_{im}\gamma_i(u)\gamma_m(u) + a_{ij}\varepsilon_{ij}(u)\varphi + \\ & + b_{ij}\kappa_{ij}(u)\varphi + c_{ijk}\chi_{ijk}(u)\varphi + d_i\gamma_i(u)\varphi + \frac{1}{2}m\varphi^2. \end{aligned}$$

Let assume that $F_i, G_{jk}, H \in L_2(B)$ and introduce the functionals $f(u)$ and $g(u)$ by

$$\begin{aligned} f(u) &= \int_B (F_i v_i + G_{jk} \psi_{jk} + 3H\psi) dv, \\ g(u) &= \int_{S^*} (\tilde{t}_i v_i + \tilde{\mu}_{jk} \psi_{jk} + 3\tilde{h}\psi) da, \end{aligned} \quad (19)$$

where $v = (v_i, \psi_{jk}, \psi) \in \mathbf{W}$.

Now, we consider $\mathbf{u} = (\tilde{u}_i, \tilde{\varphi}_{jk}, \varphi) \in \mathbf{W}$ such that the functions $\tilde{u}_i, \tilde{\varphi}_{jk}, \varphi$ may be obtained, on the surface S , by means of the embedding of the space $W^{1,2}(B)$ into the space $L_2(S)$. The function $\mathbf{u} \in \mathbf{W}$ is called **weak solution** of the boundary value problem if it satisfies the following two conditions:

i) $\mathbf{u} - \tilde{\mathbf{u}} \in \mathbf{V}$;

ii) $A(\mathbf{v}, \mathbf{u}) = f(\mathbf{v}) + g(\mathbf{v})$, for each $\mathbf{v} \in \mathbf{V}$.

We assume that the internal energy density is a positive definite quadratic form. That means there exists a positive constant c such that

$$\begin{aligned} A(v, v) \geq 2c \int_B [\varepsilon_{ij}(v)\varepsilon_{ij}(v) + \kappa_{ij}(v)\kappa_{ij}(v) + \\ + \chi_{ijk}(v)\chi_{ijk}(v) + \gamma_i(v)\gamma_i(v) + \psi^2] dv, \end{aligned} \quad (20)$$

for any $v = (v_i, \psi_{jk}, \psi) \in \mathbf{W}$. If we chose the operators $N_s v, (s = 1, 2, \dots, 49)$ in the form:

$$\begin{aligned} N_i v &= \varepsilon_{1i}(v), \quad N_{3+i} v = \varepsilon_{2i}(v), \quad N_{6+i} v = \varepsilon_{3i}(v), \\ N_{9+i} v &= \kappa_{1i}(v), \quad N_{12+i} v = \kappa_{2i}(v), \quad N_{15+i} v = \kappa_{3i}(v), \\ N_{18+i+j+k} v &= \chi_{ijk}(v), \quad N_{45+i} v = \gamma_i(v), \quad N_{49} v = \psi. \end{aligned}$$

Then it is easy to obtain the inequality:

$$A(v, v) \geq 2c \sum_{k=1}^{49} N_k v, \quad c > 0.$$

Based on Theorem 1 we deduce that the system of operators N_k is coercive on the space \mathbf{W} . According to the definition of \mathcal{P} we have that $\varepsilon_{ij}(v) = 0, \kappa_{ij}(v) = 0, \chi_{ijk}(v) = 0, \gamma_i(v) = 0,$

$\psi = 0$ for each $v \in \mathcal{P}$, $v = (v_i, \psi_{jk}, \psi)$. So, we deduce that \mathcal{P} reduces to

$$\mathcal{P} = \{v = (v_i, \psi_{jk}, \psi) \in \mathbf{V} : v_i = a_i + b_{ij}x_j, \psi_{jk} = b_{jk}, \psi = 0\},$$

where a_i and b_{jk} are arbitrary constants.

We shall consider two distinct cases. First, we suppose that the set S is non-empty. Then the set \mathcal{P} reduces to $\mathcal{P} = \{0\}$, and, by using the result of Theorem 2, we immediately obtain the following result

Theorem 3. *Let $\mathcal{P} = \{0\}$. Then there exists one and only one weak solution of our boundary-value problem.*

In the second case, we assume that S is an empty set. Then it is easy to prove the following theorem:

Theorem 4. *The necessary and sufficient conditions for the existence of a weak solution $\mathbf{u} \in \mathbf{W}$ of the boundary-value problem for elastic dipolar bodies with stretch, are given by:*

$$\int_B F_i f v + \int_{\partial B} \tilde{t}_i da = 0,$$

$$\int_B (F_i u_i + G_{jk} \varphi_{jk} + 3H\varphi) dv + \int_{\partial B} (\tilde{t}_i u_i + \tilde{\mu}_{jk} \varphi_{jk} + 3h\tilde{\varphi}) da = 0.$$

4. REFERENCES

- Eringen, A. C., Kafadar, C. B.(1976), *Continuum Physics*, Vol. 4, Academic Press,
 Eringen, A. C., Suhubi, E. S.(1964), *Int. J. Engng. Sci.*, **2**, 389
 Eringen, A. C.(1990), *Int. J. Engng. Sci.*, **28**, 1291
 Hlavacek, I., Necas, I.(1970), *Arch. Rational Mech. Anal.*, **36**, 305
 Iesan, D., Quintanilla, R.(1994), *Int. J. Engng. Sci.*, **6**, 991
 Marin, M.(1995), *C. R. Acad. Sci. Paris*, **t.321**, **Serie II b**, 475
 Marin, M.(1997), *J. Comp. Appl. Math.*, **82**, 291
 Necas, I.(1967), *Les Methodes Directes en Equations Elliptiques*, Academic, Prague

LENGTH-SCALE DEPENDENT CRACK-GROWTH

Lars Pilgaard Mikkelsen

Material Research Department, Risø National Laboratory
Technical University of Denmark, DK-4000 Roskilde, Denmark

ABSTRACT

The Fleck-Hutchinson strain gradient theory from 2001 are used in the presented work to predict the length-scale dependency of crack growth in the case of small scale yielding at a crack tip loaded in pure mode I. The gradient-dependent plasticity model has been implemented using the user element interface in the commercial finite element code ABAQUS. The crack-tip fields are found to be strongly influenced by the occurrence of an internal material length scale. Compared with a conventional plasticity theory, a large incorporated length scale relatively to the size of the current yield zone is found to give a significant higher stress level at the crack-tip. As a consequence, crack-growth is predicted to be more pronounced under the influence of a large incorporated length scale.

1. INTRODUCTION

A finite element model based on a conventional plasticity theory lack the information of the underlying microstructure of the material. Therefore, finite element predictions will be size independent in spite of the fact that deformations gradients at small scale is known in a number of material to give a scale effects. Such a scale effect has been reported for a number of cases in metals; see e.g. Fleck and Hutchinson (1997) but also other materials show scale dependency. For epoxy, Lam and Chong (2000) has measured a scale dependency using micro indentation test.

The stress field in crack-tip and crack growth simulation is strongly localized. Therefore, if a material length scale is present a large influence on the local stress field is expected. In addition, for strong interfaces (4-5 times the yield stress of the material), conventional plasticity theories can not simulate crack growth, Tvergaard and Hutchinson (1992). This in spite of the fact that crack-growth from an experimental point of view can occurs for such cases.

In fiber reinforced composites, extensive plastic deformation can occurs at the fiber/matrix interface, Wang and van der Giessen (2004) due to the relatively large interface strength compared with the yield stress of the matrix material, Goutianos, Drews, Nielsen, Kingshott,

Hvilsted and Sørensen (2006). Therefore, in order to predict crack-growth in such cases, a length scale dependent model can be important.

In the present work, crack-tip and crack growth is modeled for an elastic-plastic material loading in pure mode I. In addition, the strain gradient dependent material behavior is demonstrated in a simple essential one-dimensional shear problem.

2. GRADIENT DEPENDENT J₂-FLOW PLASTICITY MODEL

In the present work, only the one length scale version of the Fleck and Hutchinson (2001) gradient dependent model is used. More detailed on the theory can be found in Fleck and Hutchinson (2001) and only a short summary is given here. In the model, a gradient dependent effective plastic strain is proposed,

$$\dot{E}^{P^2} = \dot{\varepsilon}^{P^2} + \ell_* \dot{\varepsilon}_i^P \dot{\varepsilon}_i^P, \quad (1)$$

which depends not only on the local effective plastic strain, $\dot{\varepsilon}^P$, but also the spatial gradient thereof, $\dot{\varepsilon}_{,j}^P$. In addition to the higher order plastic strains, $\dot{\varepsilon}_{,j}^P$, the model introduce higher order stresses, $\dot{\tau}_i$, (work conjugated to $\dot{\varepsilon}_{,j}^P$) and higher order boundary condition

$$\dot{\tau}_i n_i = 0 \text{ or } \dot{\varepsilon}^P = 0 \quad (2)$$

E.g, corresponds the he boundary condition $\dot{\varepsilon}^P = 0$ to a case where to plastic deformation is “frozen” at an elastic-plastic/elastic interface where the elastic material prevent plastic deformation at the interface. The hardening of the material is chosen to be given by a standard power-law hardening such that the materials hardening modulus is given by

$$h[E^P] = \left(\frac{EE_T[E^P]}{E - E_T[E^P]} \right) \text{ where } E_T[E^P] = \frac{E}{n} \left(\frac{EE^P}{\sigma_y} + 1 \right)^{\frac{1}{n}-1} \quad (3)$$

where E denote Young’s modulus, σ_y the initial yield stress and n the hardening exponent. Note that in equation (3), the hardening modulus depends on the gradient dependent effective plastic strain E^P from equation (1) and not the conventional effective plastic strain ε_e^P .

3. NUMERICAL IMPLEMENTATION

The implementation of the strain gradient dependent plasticity model is inspired by Niordson and Hutchinson (2003) and many details regarding the implementation can be found there. Contrary to Niordson and Hutchinson (2003), the presented work implement the model in the user element subroutine interface in the commercial finite element code ABAQUS. In the finite element implementation, both the nodal displacement increments \dot{U}_i^n and the nodal increment of the effective plastic strain $\dot{\varepsilon}_n^P$ are taken as fundamental unknowns.

$$\dot{u}_i = \sum_{n=1}^{2k} N_i^n \dot{U}^n \quad \text{and} \quad \dot{\varepsilon}^P = \sum_{n=1}^l M^n \dot{\varepsilon}_n^P \quad (4)$$

where $N_i^n(x_j)$ and $M_i^n(x_j)$ are shape functions defined such that equation (4) gives their respective values in the point x_j inside the element. In the presented implementation, both the increment of the displacement and the increment of the effective plastic strain have been modeled using standard isoparametric shape functions. Nevertheless, the isoparametric element used to discretize the displacements increments and the effective plastic strain do not necessary include the same number of nodes. Later the best performance is found for an element with $k = 8$ and $l = 4$. Substitute (4) into the virtual work on incremental form, see Niordson and Hutchinson (2003) results in the system of linear equation shown in (5)

$$\begin{bmatrix} K_e & K_{ep} \\ K_{ep}^T & K_p \end{bmatrix} \begin{bmatrix} \dot{U} \\ \dot{\varepsilon}^P \end{bmatrix} = \begin{bmatrix} \dot{F}_1 \\ \dot{F}_2 \end{bmatrix} + \begin{bmatrix} C_1 \\ 0 \end{bmatrix} \quad (5)$$

where \dot{U} and $\dot{\varepsilon}^P$ are the fundamental unknowns in the finite element model. The term C_1 is the equilibrium term from where the unbalanced nodal forces can be extracted and from where ABAQUS found equilibrium when other element from ABAQUS is included in the model. The model is implemented in a plane strain version.

3. NUMERICAL RESULTS

Simple gradient dependent case. A simple case showing strain gradient dependent behavior is a thin slab loaded in shear. If the transverse displacement for all nodes is prescribed to vanish, it is essentially a one-dimensional problem; an infinity wide thin layer of material mounted between two rigid boundaries. Fig 1a show the predictions based on a conventional plasticity theory.

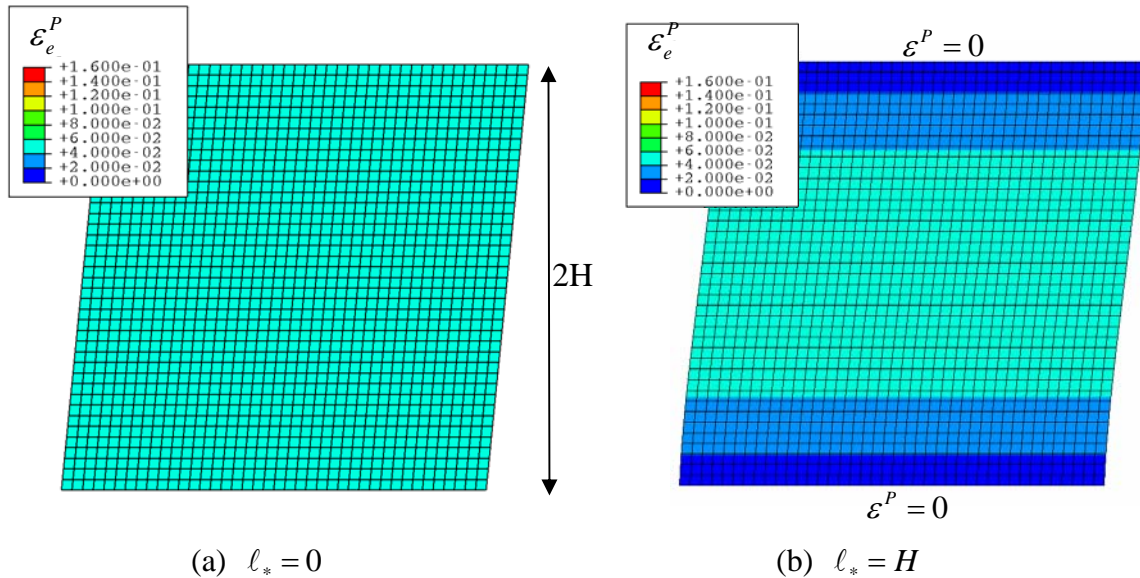
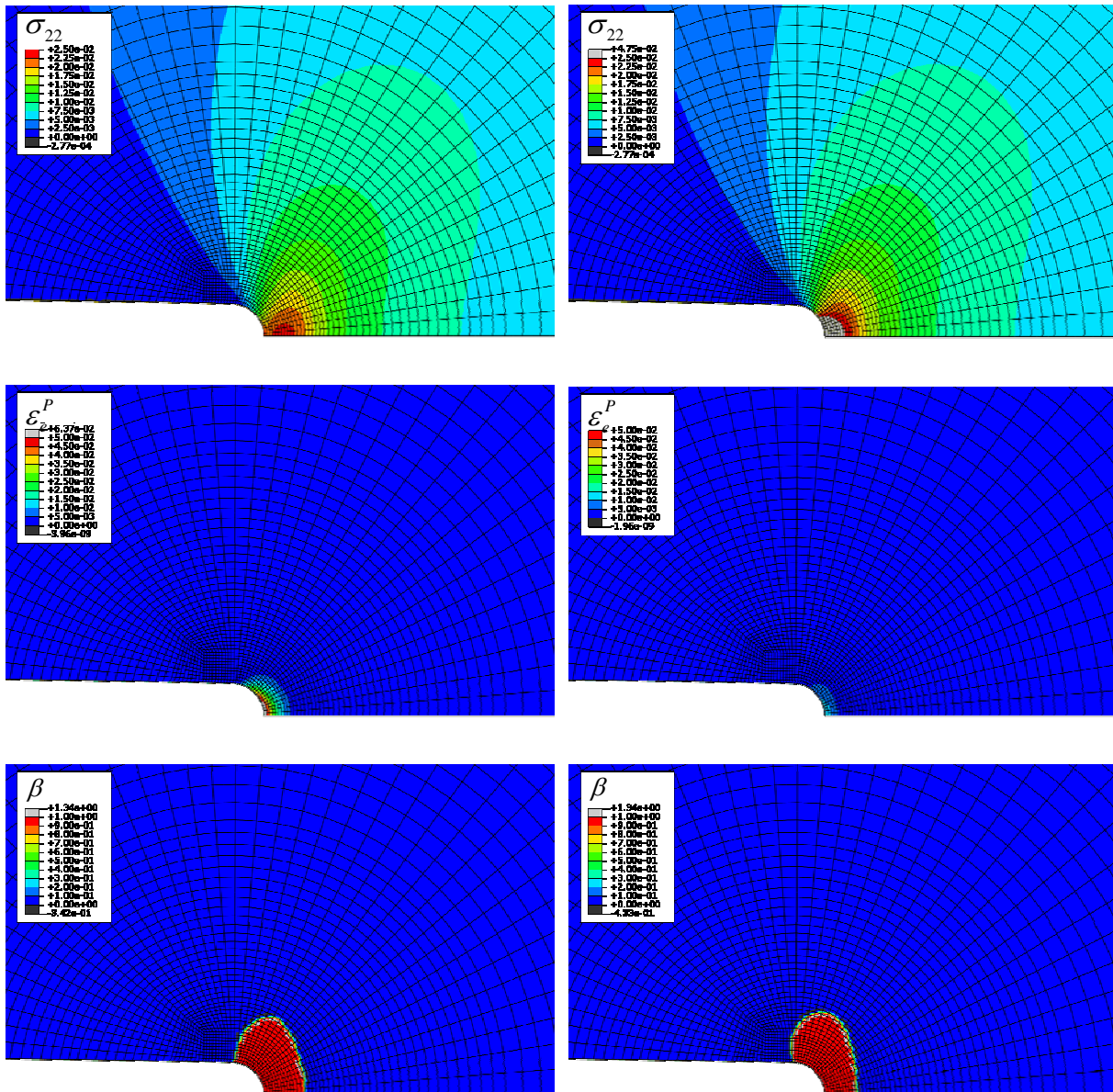


Fig. 1. The variation of the local effective plastic strain of an infinity wide thin slab mounted between two rigid boundaries loaded in pure shear.

The material is given by the parameters $\sigma_y / E = 0.01$, $\nu = 0.3$ and $n = 5$. Shearing the thin layer to a given shear deformation, $U = 10\sigma_y H / E$, results for the conventional case in a uniform shear deformation stage. On the other hand, including an internal length scale as shown in Fig. 1b together with an additional boundary condition $\varepsilon^P = 0$, will result in the same strain state in the middle of the specimen, but with a boundary layer with a vanishing plastic strain at the boundary fulfilling the prescribed boundary condition. The overall shear traction required to give this deformation is approximately 50% higher corresponding to the corresponding overall shear traction for the conventional case, see Niordson and Hutchinson (2003) and Mikkelsen (2007).

Crack-tip simulation.



(a) $l_* / R_p = 0.05$; $l_* / R_{tip} = 0.1$

(b) $l_* / R_p = 0.5$; $l_* / R_{tip} = 1.0$

Fig. 2. Crack-tip field at a blunted crack-tip loaded in pure mode I at level, K_I , corresponding to $R_p / R_{tip} = 2.1$.

Fig. 2 shows a crack tip simulation based on the enhanced strain gradient dependent plasticity model incorporating an internal length scale. The model represents a blunted crack-tip in an elastic-plastic material. The material is given by the parameters, $\sigma_y / E = 0.01$, $\nu = 0.3$ and $n = 5$. Fig. 2 shows a zoom-in on the crack tip. The distance to the boundary where the prescribed displacement field corresponding to a pure mode I crack opening K_I -field is applied, see Tvergaard and Hutchinson (1992) is $L_\infty = 500R_{tip}$ which was found to be sufficiently to represent a small scale yielding case. The crack tip is loaded to a level such that

$$R_p = \frac{1}{3\pi} \left(\frac{K_I}{\sigma_y} \right)^2 = 2.1R_{tip} \quad (6)$$

which represent a measurement of the size of the current yielding zone at the crack-tip. Compared with the contours for the β -value (which is 0 for elastic and 1 for plastic deformation) the size of the yielding zone is found to be of this order. Despite, the yielding zone is quite similar for the two length scale modeled, the contours of the effective plastic strain and the stress state is found to be quite difference. Increasing the incorporated length scale from 5% to 50% of the reference size of the plastic zone, R_p , is found to result in a responds going from a conventional (local) plasticity solution to a solution found for a pure elastic case, see Mikkelsen (2006). The maximum stress level is found to be increased with nearly a factor of 2 indicating the possibility for crack growth at a lower applied K-field.

Crack-growth simulation. Fig. 3 shows the crack resistant curve for such a crack growth simulation using cohesive elements in combination with the enhanced plasticity theory. It can be seen from Fig. 3 that a large incorporated length scale results in crack-growth at a lower steady state level.

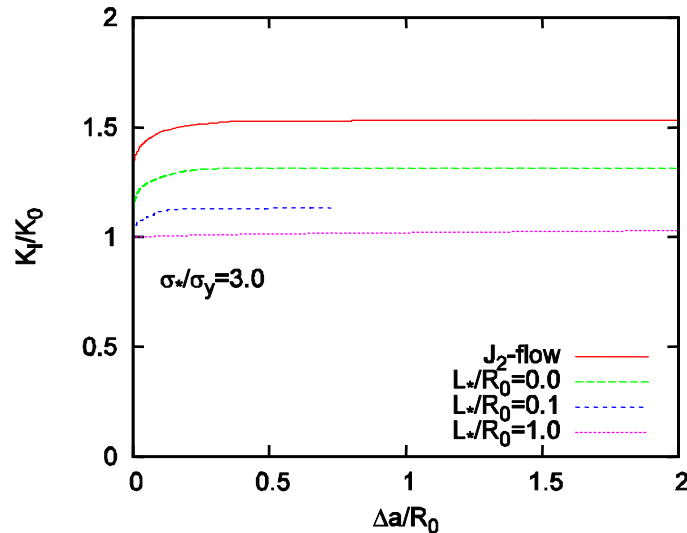


Fig. 3. Crack resistance curve for a the material $\sigma_y / E = 0.003$, $n = 10$, $\nu = 0.3$ and with a interface strength given by $\hat{\sigma} / \sigma_y = 3.0$ (from Mikkelsen, 2006).

ACKNOWLEDGEMENTS

The work has been financial supported by the Danish Technical Research Council through the project 'Interface Design of Composite Materials'.

REFERENCES

- Fleck, N.A. and Hutchinson, J.W. (1997). Strain gradient plasticity. In: Hutchinson, J.W., Wu, T.Y. (Eds.), *Advances in Applied Mechanics* 33, Academic Press, New York, 295-361.
- Fleck, N.A. and Hutchinson, J.W. (2001). A reformulation of strain gradient plasticity theory," *Journal of Mechanics and Physics of Solids*, Vol. 49, pp. 2245-2271.
- Goutianos, S., Drews, J., Nielsen, S.F., Kingshott, P., Hvilsted, S. and Sørensen, B.F. (2006). Controlling interface adhesion and fracture properties in composite materials by plasma polymerisation. *Polymer Composite Materials for Wind Power Turbines – Proceedings of the 27th Risø International Symposium on Materials Science*, Risø National Laboratory, Roskilde Denmark, 173-180.
- Lam, D.C.C. and Chong, ACM. (2000). Effect of cross-link density on strain gradient plasticity in epoxy. *Materials Science and Engineering A281*, 156-161.
- Mikkelsen, L.P. (2007). Implementing a gradient dependent plasticity model in ABAQUS. In: *Proc. of the 2007 ABAQUS Users' Conference*, Paris, France, 482-492.
- Mikkelsen, L.P. (2006). Crack-growth in a strain gradient dependent plasticity model. In: *Proc. of the 19th Nordic Seminar on Computational Mechanics* (eds O.Dahlblom, L.Fuchs, K.Persson, M.Ristinmaa, G.Sandberg and I.Svensson), Faculty of Engineering, Lund University, Sweden, 210-213.
- Niordson, C.F. and Hutchinson J.W. (2003), Non-uniform plastic deformation of micron scale objects. *International Journal Numerical Methods in Engineering*, Vol. 56, 961-975.
- Tvergaard, V. and Hutchinson, J.W. (1992). The relation between crack growth resistance and fracture process parameters in elastic-plastic solids. *J. Mech. Phys. Solids* 40, 1377-1397.
- Wang, G.F. and van der Giessen, E. (2004). Fields and fracture of the interface between a glassy polymer and a rigid substrate, *European Journal of Mechanics A/Solids* 23, 395-409.

SOFTWARE FOR AUTOMATIC GENERATION OF 3D
MICROSTRUCTURAL MODELS OF FIBER REINFORCED
COMPOSITES WITH DAMAGEABLE ELEMENTS

Leon Mishnaevsky Jr. and Povl Brøndsted

Risø National Laboratory, Technical University of Denmark

ABSTRACT

Computational tools for 3D numerical analysis of the microstructure-strength and microstructure-damage resistance relationships of fiber reinforced composites are presented. The program code "Meso3DFiber", which allows to automate the generation of 3D micromechanical finite element models of composites, was developed. The program, written in Compaq Visual Fortran, generates a command file for the commercial software MSC/PATRAN. The parameters of the model (volume content and amount of fibers, probabilistic/constant distributions of fiber radii, availability of interphase, etc.) are introduced interactively. In order to model interface damage and fiber cracking, damageable layers are introduced into the finite element model. Examples of the simulation of the fiber cracking and interface damage in polymer fiber reinforced composites are presented.

1. AUTOMATIC GENERATION OF 3D MICROMECHANICAL MODELS OF
COMPOSITES

One of the ways to determine the optimal microstructures of materials is to carry out the "virtual testing" of different microstructures, using the micro- and mesomechanical models of the materials behaviour. The concept of optimal design of materials on the basis of the numerical testing of microstructures can be realized if large series of numerical experiments for different materials and microstructures can be carried out quickly, in a systematic way, automatically. This can be done, if labor costs of the numerical experiments, a significant part of which are the efforts of the generation of micromechanical models, are kept very low. To solve this problem, a series of programs was developed, which should automate the step of the generation of 3D microstructural models of materials. After a 3D microstructural model of a material with a complex microstructure is generated, the numerical testing of the microstructure is carried out with the use of commercial finite element software.

The microstructure-strength and microstructure-damage resistance relationships of composites can be analyzed numerically with the use of the unit cell approach. In particular, multiparticle unit cells make possible to analyze the overall response, nonlinear behavior and damage evolution in composites, taking into account both the interaction between phases, between elements of each phase (e.g., particles) as well as with evolving microcracks and cracks. Often, the following methods are used to incorporate complex microstructures of materials into discretized (finite element) models of materials:

- microgeometry based generation of finite element models of materials,
- pixel- or voxel-based model generation,
- multiphase finite elements (see Mishnaevsky Jr and Schmauder, 2001, Mishnaevsky Jr et al, 2003, 2004).

In the framework of the geometry-based approach, the (micro)geometrical model is first created, and then meshed with finite elements using the free meshing technique (Thompson et al, 1999) (cf. schema in Figure 1). After that, the mesh can be automatically improved (e.g., made finer at the interfaces). In order to simplify and automate the generation of 3D multiparticle unit cell models of composite materials, a program "Meso3D" was developed (see Mishnaevsky Jr., 2004). The program defines the geometry, mesh parameters and boundary conditions of different multiparticle unit cell models of materials, and then a multiparticle unit cell model of a representative volume of a composite material is created automatically. Both 2D and 3D versions of the program are available. The FE models of both artificial and simplified real microstructures (with particles approximated e.g. by the ellipsoids) can be generated with this method.

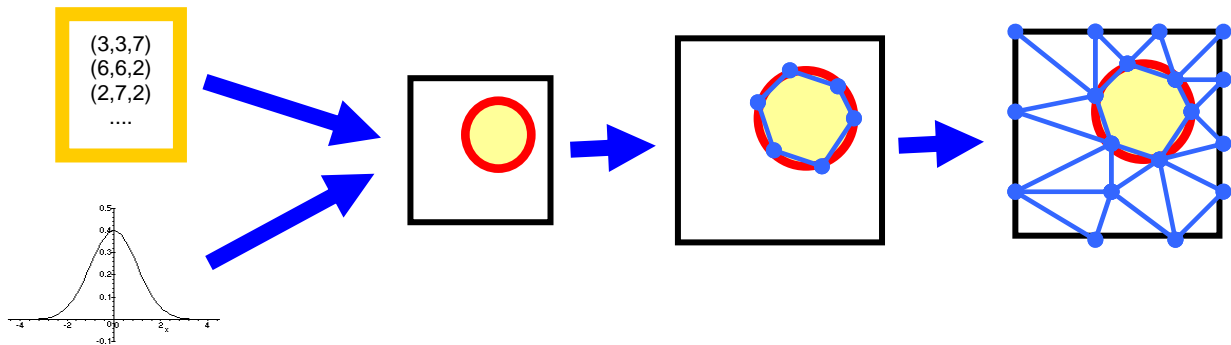


Figure 1. Schema of the generation of different artificial microstructures on the basis of pre-defined probability distribution of particle parameters.

However, the geometry-based approach, used in this program, is applicable only for relatively simple geometrical forms of microstructural elements in composites. In order to carry out the numerical analysis of arbitrarily complex 3D microstructures, an approaches based on the voxel array description of material microstructures, was realized in the framework of a new program "Voxel2FEM" (see Mishnaevsky Jr., 2005, 2007). The representative volume is presented as an $N_x \times N_y \times N_z$ array of points (voxels), each of them can be either black (particle) or white (matrix) (for a two-phase material). (This approach can be generalized on multiphase materials

simply as well.) The designed cells are meshed with brick elements, which are assigned to the phases automatically according to the voxel array data. Mishnaevsky Jr. (2007) compared the results of finite element simulations of mechanical behaviour of metal/ceramics composites carried out with the use of the geometry based and voxel array based models, and demonstrated that the differences are of the order of 5...6%. A disadvantage of the simple versions of the pixel or voxel based approaches to the model generation is that the smooth interfaces, available in real microstructures, are transformed into ragged interfaces in the pixel- and voxel-based models. However, this problem can be reduced to an acceptable level e.g. by adaptive remeshing.

The main idea of the multiphase element method is that the phase properties are assigned to individual integration points in the element independently on the phase properties assigned to other points in the element. Interfaces in the material can run through the finite elements in the mesh. Contrary to the microgeometry-based finite element mesh design, a FE-mesh in this case is independent of the phase structure of material, and one can use relatively simple FE-meshes in order to simulate the deformation in a complex microstructure. The disadvantage of the multiphase element method is that it does not allow taking into account fine interface effects. The multiphase finite elements, as well as some other methods (Voronoi finite element method, etc.) are discussed in more details in the review by Mishnaevsky Jr. and Schmauder (2001)..

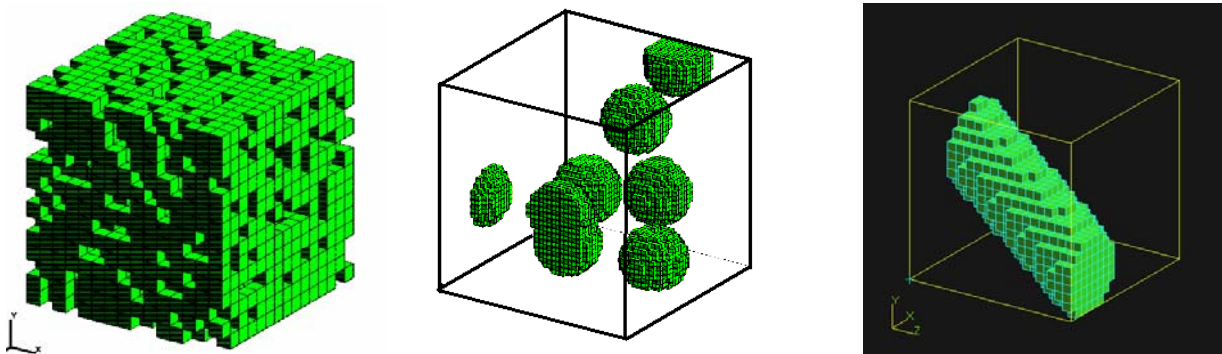


Figure 2. Examples of different generated microstructures: random 3D chessboard microstructure, a multiparticle unit cell, inclined fiber

2 COMPUTATIONAL TOOLS FOR THE MODELLING OF DAMAGE IN FIBER REINFORCED COMPOSITES

In order to simulate the strength and damage in fiber reinforced composites, a serie of special programs and subroutines were developed. A program code “Meso3DFiber“, which allows to automate the generation of 3D micromechanical finite element models of composites, was written in Compaq Visual Fortran. The program generates a command file for the commercial software MSC/PATRAN. The parameters of the model (volume content and amount of fibers, probabilistic/constant distributions of fiber radii, availability of interphase, etc.) are introduced interactively. The command file is played with PATRAN, and a 3D microstructural (unit cell) model of the composite with pre-defined parameters is generated. The finite element meshes are generated by sweeping the corresponding 2D meshes on the surface of the unit cell. The code allows to generate multifiber unit cells with random fiber arrangement, varied, random or constant fiber radii, as well as with some features allowing the damage modelling. Figure 3a shows an example of multifiber unit cells with 20 fibers generated with the use of the program “Meso3DFiber2.

Several damage modes are incorporated in the finite element model: fiber cracking, interface damage, matrix damage.

In order to model the *fiber cracking*, we used the idea of introducing potential fracture planes (in form of damageable cohesive elements) in random sections of fibers, suggested by González and LLorca (2006). Following this idea, we introduced damageable layers in several sections of fibers. These layers have the same mechanical properties as the fibers (except that they are damageable). The locations of the damageable layers in the fibers were determined using random number generator with the uniform distribution. The random arrangement of the potential failure planes in this case reflects the statistical variability of the fiber properties. Figure 3b shows a multifiber unit cells with 20 fibers, with removed damageable layers.

A similar concept was used to simulate the *interface damage*. Given that surfaces of fibers are usually rather rough, and the interface regions in many composites contain interphases (Huang and Petermann, 1996, Downing et al., 2000), the interface debonding was considered not as a two-dimensional opening of two contacting plane surfaces, but rather as a three-dimensional process in a thin layer. The interface was represented as a “third (interphase) material layer” between the homogeneous fiber and matrix materials. This idea was also employed by Tursun et al. (2006), who utilized the layer model to analyze damage processes in interfaces of Al/SiC particle reinforced composites. The thickness of the interface layer was taken 0.2 mm, but can be varied in further simulations. Figure 3 shows an example of a multifiber unit cell with 30 fibers of randomly varied radii, with and without the damageable layers. Figure 4 shows an example of a multifiber unit cell with 3 fibers with interphase layer (yellow).

In order to model the damage growth in the damageable layers (in fibers and in the interphase layers), the finite element weakening approach was employed (s. Mishnaevsky Jr, 2006, 2007). The idea of this approach is that the stiffness of finite elements is reduced if a stress or a damage parameter in the element or a nodal point exceeds some critical level. This approach has been realised in the ABAQUS subroutine User Defined Field. In this subroutine, the phase to which a given finite element in the model is assigned, is defined through the field variable of the element. Depending on the field variable, the subroutine checks whether the element failed or not, according to the properties of the matrix, interphase and fibers. Another field variable characterizes the state of the element (“intact” versus “damaged”). If the value of the damage parameter or the principal stress in the element exceeds the corresponding critical level, the second field variable of the element is changed, and the stiffness of the elements is reduced. The Young modulus of this element is set to a very low value (50 Pa, i.e., about 0.00001% of the initial value). The critical level of the maximum principal stress can be either a constant value, or a random value with a pre-defined probability distribution. The numbers of failed elements are printed out in a file, which can be used to visualize the calculated damage distribution.

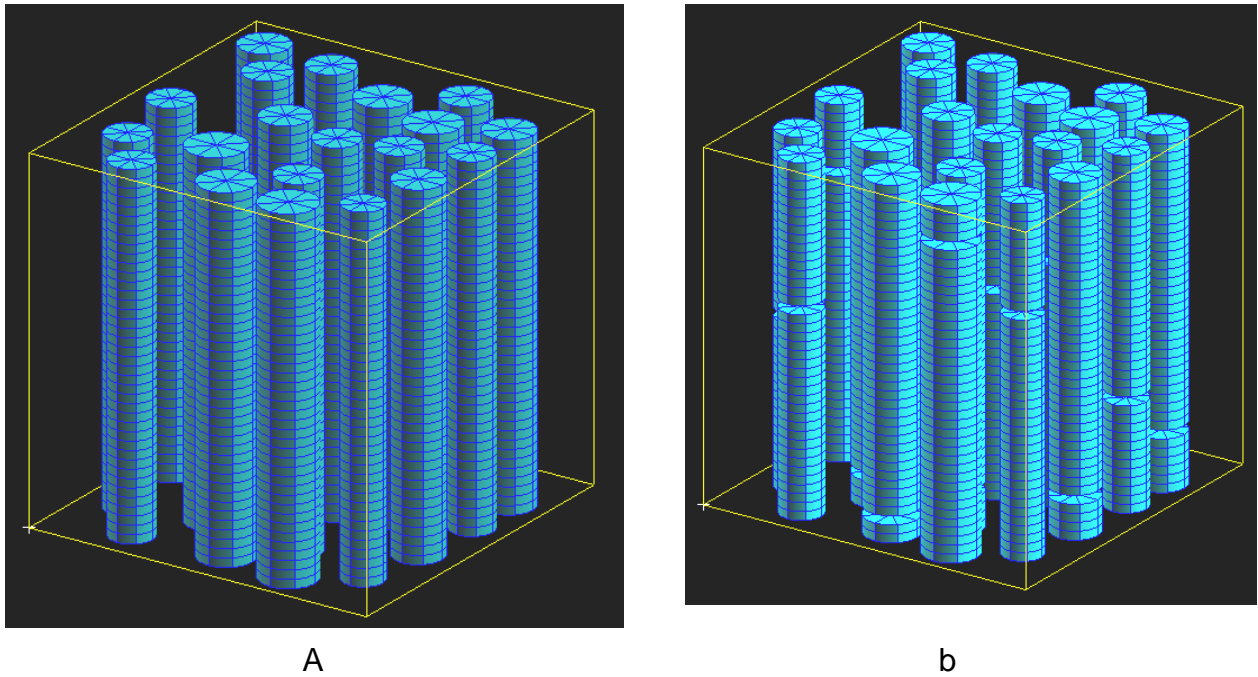


Figure 3. Examples of the 3D unit cell models: a unit cell with 30 fibers with randomly varied radii (a) and the cell with removed damageable layers (b).

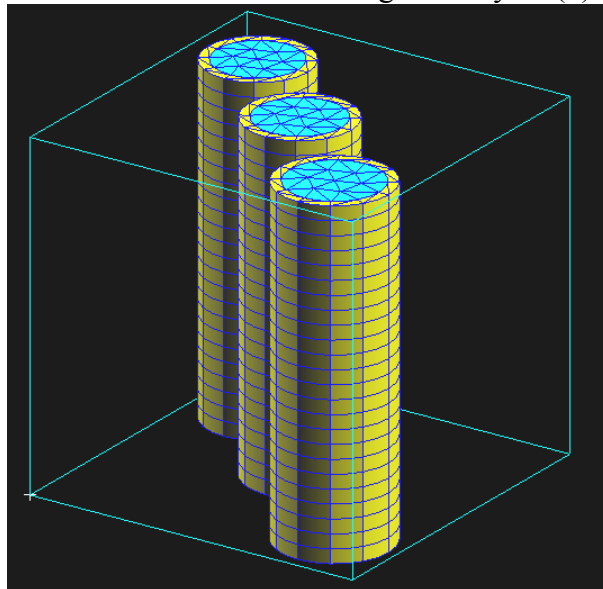


Figure 4. Example: a unit cell with 3 fibers and interphase (yellow) layers

3. EXAMPLES OF SIMULATION

The developed computational tools were employed to model the damage evolution in glass fiber reinforced fiber polymer (epoxy) reinforced composites. In so doing, the following properties of the composites were used. The glass fibers behaved as elastic isotropic solids, with Young

modulus $E_P=72$ GPa, and Poisson's ratio 0.26 (Agarwal and Broutman, 1990). The failure strength of glass fibers was assumed to be constant and equal to 3700 MPa (in our later simulations, the Weibull probability law distribution of fiber strengths with parameters $\sigma_0=1649$ MPa and $m=3.09$ was assumed, see Feih, et al, 2005). The elastic properties of the epoxy matrix were as follows: Young modulus 3790 MPa, Poisson's ratio 0.37, bulk modulus 5 GPa, instantaneous shear modulus 1.38 GPa. The viscoelastic properties were described by a single term Prony series, with the relaxation time 0.25 sec, and the modulus ratio $g=0.125$ (Gibson, 1976, Tevet-Deree, 2003, DeBotton and Tevet-Deree, 2004). The failure condition of epoxy matrix was the maximum principal stress, 67 MPa.

First, the damage evolution in fiber was considered. A number of three-dimensional multifiber unit cells with 20 fibers and volume content of fibers 25 % have been generated automatically with the use of the program "Meso3DFiber" and the commercial code MSC/PATRAN. The fibers in the unit cells were placed randomly in X and Y directions. The dimensions of the unit cells were 10 x 10 x 10 mm. The cells were subject to a uniaxial tensile displacement loading, 1 mm, along the axis of fibers (Z axis). Figure 5 shows the Von Mises stress distribution in fibers before and after the fiber cracking.

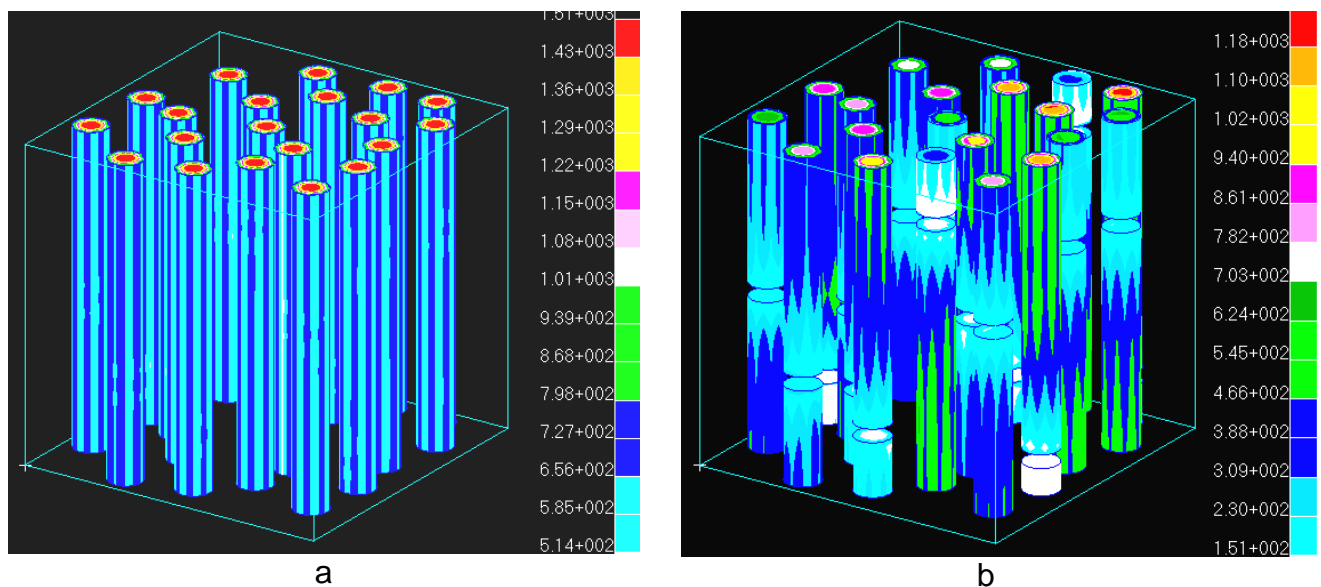


Figure 5. Von Mises stress distribution in fibers before and after the fiber cracking

Further, we sought to model the interface damage, caused by the fiber cracking. The interface layer was assumed to be a homogeneous isotropic material, with Young modulus 37.9 GPa (i.e., an averaged Young modulus of the fibers and matrix materials) and Poisson's ratio of the matrix. The thickness of the layer was taken 0.2 mm. As a first approximation, we chose the maximum principal stress criterion for the interface damage (therefore, assuming rather brittle interface), and the critical stress 770 MPa (i.e., again, the mean value of the average strengths of fibers and the matrix). Figure 6 shows the evolution of von Mises stress distribution under loading: a) intact fiber and nondamaged interface ($u=0.13$ mm), b) cracked fiber and stressed interface ($u=0.15$ mm), c) cracked fiber and damaged interface ($u=0.16$ mm)

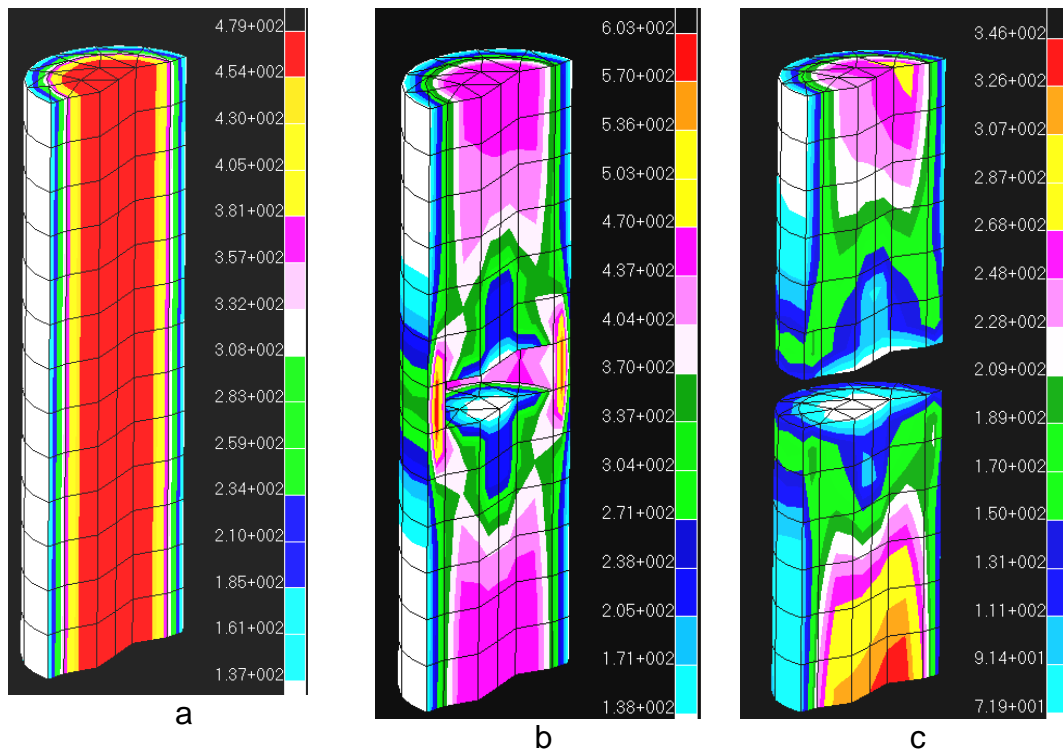


Figure 6. Evolution of Von Mises stress distribution: a) intact fiber and undamaged interface ($u=0.13\text{mm}$), b) cracked fiber and stressed interface ($u=0.15\text{ mm}$), c) cracked fiber and damaged interface ($u=0.16\text{ mm}$)

4. CONCLUSIONS

Computational tools for the micromechanical modelling of strength and damage in fiber reinforced composites are presented. A program code for the automatic generation of 3D multifiber unit cell models of composites with damageable fibers and interfaces has been developed. Examples of the 3D simulation of the fiber cracking and interface damage in polymer fiber reinforced composites, based on the developed programs, are presented.

ACKNOWLEDGEMENTS

The authors gratefully acknowledge the financial support of the European Community via “UpWind” project, and the Danida Project “Development of Wind Energy Technologies in Nepal on the Basis of Natural Materials” (Danida Ref. No. 104. DAN.8-913). We are further acknowledge the support of the STVF foundation via Framework Programme "Interface Design of Composite Materials" (STVF fund no. 26-03-0160).

REFERENCES

- Agarwal B. D. and Broutman L. J., (1990), *Analysis and performance of fiber composites*, Second Ed., Wiley, New York, 449 pp.
- Debotton G., Tevet-Deree L., (2004) The Response of a Fiber-Reinforced Composite with a Viscoelastic Matrix Phase, *Journal of Composite Materials*, Vol. 38, No. 14, 1255-1277
- Downing T. D. , Kumar R. , Cross W. M. , Kjerengtroen L. and Kellar J. J. (2000) Determining the interphase thickness and properties in polymer matrix composites using phase imaging atomic force microscopy and nanoindentation, *J. Adhesion Science and Technology*, Vol. 14, 14, pp. 1801-1812
- Feih S, Thraner A, and Lillholt H. (2005) Tensile strength and fracture surface characterisation of sized and unsized glass fibers, *Journal of Materials Science*, 40(7), 1615-1623,
- Gibson, R.F. (1976). Dynamic Mechanical Behavior of Fiber-reinforced Composites: Measurement and Analysis, *Journal of Composite Materials*, 10: 325-341.
- Gonzalez, C. and LLorca, J. (2006) Multiscale modeling of fracture in fiber-reinforced composites *Acta Materialia*, 54, pp. 4171–4181
- Huang Y, Petermann J (1996) Interface layers of fiber-reinforced composites with transcrystalline morphology. *Polymer Bulletin*, 36(4), pp.517-524
- Mishnaevsky Jr., L. (1998) *Damage and Fracture of Heterogeneous Materials*, Balkema, Rotterdam, 230 pp.
- Mishnaevsky Jr., L. and Schmauder, S. (2001) Continuum mesomechanical finite element modeling in materials development: A state-of-the-art review, *Applied Mechanics Reviews*, 54 (1), pp. 49-69
- Mishnaevsky Jr., L., Lippmann, N. and Schmauder, S. (2003) Computational modeling of crack propagation in real microstructures of steels and virtual testing of artificially designed materials, *International Journal of Fracture*, 120 (4), pp. 581-600
- Mishnaevsky Jr., L. (2004) Three-dimensional numerical testing of microstructures of particle reinforced composites, *Acta Materialia*, 52 (14), pp. 4177-4188
- Mishnaevsky Jr., L., Weber, U. and Schmauder, S. (2004a) Numerical analysis of the effect of microstructures of particle-reinforced metallic materials on the crack growth and fracture resistance, *International Journal of Fracture*, 125, pp. 33-50
- Mishnaevsky Jr., L. (2005) Automatic voxel based generation of 3D micro-structural FE models, *Materials Science & Engineering A*, 407, (1-2), pp.11-23
- Mishnaevsky Jr., L. (2006), L. Functionally gradient metal matrix composites: numerical analysis of the microstructure-strength relationships, *Composites Science and Technology*, 66/11-12, pp 1873-1887
- Mishnaevsky Jr., L. (2007) *Computational Mesomechanics of Composites*, John Wiley and Sons, 290 pp.
- Tevet-Deree, L. (2003) The Dynamic Response of Composite Materials with Viscoelastic Constituents, Msc Thesis, BGU Negev
- Thompson, J., Soni, B. and Weatherhill, N. (1999) *Handbook of grid generation*. CRC Press.
- Tursun, G., Weber, U., Soppa, E. and Schmauder, S. (2006) The influence of transition phases on the damage behaviour of an Al/10vol.%SiC composite, *Computational Materials Science*, 37 (1-2), pp. 119-133

THE INFLUENCE OF FIBER WAVINESS ON
THE CRITICAL BUCKLING LOAD OF
MULTILAYERED COMPOSITES

H.G. Rai, E.V. Honein, R.A. Dibo, and P.N. Ayoub

Faculty of Engineering, University of Balamand
Koura, Lebanon

ABSTRACT

The present research involves the development of theoretical model to investigate the effect of the in-plane fiber waviness on the critical shear buckling load of multilayered composite plates. This paper analyzes the in-plane shear buckling behavior of a clamped composite laminate in which fibers are considered as in-plane sinusoidal curves. The sinusoidal fiber orientation induces a change in the lamina elastic properties, which influence the laminate extensional, coupling and bending stiffness as well as buckling strength. Stability of the plate is investigated and reduction of critical buckling load versus fiber waviness is obtained. It was found that reduction of stiffness, and buckling loads are substantial.

1. INTRODUCTION

Fiber waviness in fabrication induced defects in unidirectional composite materials. It results from local buckling of prepreg, or from cure induced residual stresses in composite materials. Fiber waviness defects have been observed to occur in, or through the thickness of, the plane of lamination as continuous fibers with sinusoidal waviness in the matrix. Inspections of composite parts often reveal the presence of fiber waviness. Several investigators have introduced theoretical and experimental techniques to investigate the linear and nonlinear elastic behavior of unidirectional composites with fiber waviness. Bogetti, Gillespie, and Lamontia (1991) developed an analytical model for evaluating the stiffness and strength reduction of a laminate having out-of-plane ply waviness. Rai, Rogers, and Crane (1992) developed an incremental scheme to predict the general stress-strain response for a curved fiber composite lamina. (Chan and Wang 1994) evaluated the influence of in-plane fiber waviness on structural response and its sensitivity on a composite beam. (Hsiao and Daniel 1996) investigated

theoretically and experimentally the effect of fiber waviness on the elastic properties of composite materials. (Garnich and Karami 2004) developed a finite element micromechanical model for stiffness and strength of wavy fiber composite.

The main objective of this paper is to evaluate the influence of fiber waviness on the critical buckling load of multilayered composite laminate under shear loading.

2. ANALYSIS

2.1 Elastic Properties. Consider a lamina of unidirectional composite, whose fibers are initially as shown in Fig.1. The fiber shape is characterized by a sinusoidal wave function

$$y = A \sin\left(\frac{2\pi x}{L}\right) \tag{1}$$

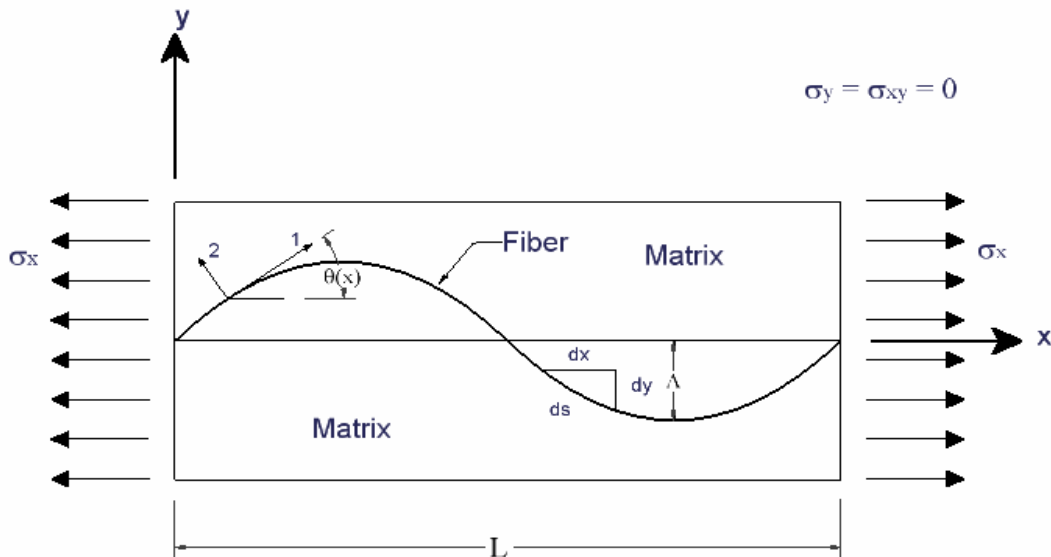


Fig.1. Wavy fiber under unidirectional state of stress

Here, A is the amplitude and L is the wave length of the sine shape. The scalar quantity A/L is defined as fiber waviness. The angle between local and structural coordinate system is:

$$\theta = \tan^{-1}\left[\left(\frac{2\pi A}{L}\right) \cos\left(\frac{2\pi x}{L}\right)\right] \tag{2}$$

We consider three cases of simple loading. First, when the lamina is subjected to a unidirectional state of stress (σ_x) in the x-direction ($\sigma_y = \tau_{xy} = 0$) as shown in Fig. 1, the gross strain over the wavelength in the x-direction becomes:

$$\bar{\epsilon}_x = \left(\frac{1}{L}\right) \int_0^L \bar{S}_{11} \sigma_x dx \tag{3}$$

and the extensional modulus in the x-direction is then

$$E_x = \frac{L}{\int_0^L \bar{S}_{11} dx} \quad (4)$$

Second, when the laminate is subjected to a state of pure transverse stress σ_y , and $\sigma_x = \sigma_{xy} = 0$, then the extensional modulus in the y-direction is given by

$$E_y = \frac{L}{\int_0^L \bar{S}_{22} dx} \quad (5)$$

Finally, when the laminate is subjected to a state of pure shear stress σ_{xy} , then the shear modulus is

$$G_{xy} = \frac{L}{\int_0^L \bar{S}_{66} dx} \quad (6)$$

The quantities $\bar{S}_{11}, \bar{S}_{22}, \bar{S}_{66}$, are the components of the transformed lamina compliance, they are function of the angle θ given in Eq. 2. Thus the moduli depend on A/L . Therefore, Eqs. 4, 5, and 6 represent an explicit relationship between lamina elastic properties and A/L . These elastic properties are used to compute the laminate bending, coupling, and extensional stiffness:

Laminate Bending stiffness:

$$D_{ij} = \int_{-t/2}^{t/2} (\bar{Q}_{ij})_k z^2 dz = \frac{1}{3} \sum_{k=1}^N (\bar{Q}_{ij})_k (z_k^3 - z_{k-1}^3) \quad i, j = 1, 2, 6, \quad (7)$$

Laminate coupling stiffness:

$$B_{ij} = \int_{-t/2}^{t/2} (\bar{Q}_{ij})_k z dz = \frac{1}{2} \sum_{k=1}^N (\bar{Q}_{ij})_k (z_k^2 - z_{k-1}^2) \quad i, j = 1, 2, 6, \quad (8)$$

Laminate extensional stiffness;

$$A_{ij} = \int_{-t/2}^{t/2} (\bar{Q}_{ij})_k z dz = \sum_{k=1}^N (\bar{Q}_{ij})_k (z_k - z_{k-1}) \quad i, j = 1, 2, 6, \quad (9)$$

where \bar{Q}_{ij} is the transformed lamina stiffness that depends also on A/L .

2.2 Buckling Analysis. The potential energy for clamped rectangular plate under in-plane shear load N_{xy}^o is

$$\begin{aligned} \pi = \frac{1}{2} \int_0^a \int_0^b [D_{11}(w_{,xx})^2 + 2D_{12}w_{,xx}w_{,yy} + 4D_{66}(w_{,xy})^2 \\ + D_{22}(w_{,yy})^2 - 2N_{xy}^o(w_{,x}w_{,y})] dx dy \end{aligned} \quad (10)$$

Where w is an out-of-plane displacement, a and b are the in-plane dimensions of the plate respectively, and D_{11}, D_{12}, D_{66} and D_{22} are components of laminate stiffness depending on fiber waviness. Assuming Ritz approximation of the form:

$$w(x, y) \approx \sum_i^m \sum_j^n c_{ij} \varphi_{ij}(x, y) \quad (11)$$

where

$$\varphi_{ij} = X_i(x)X_j(y) \quad (12)$$

and

$$X_i(x) = \sin \lambda_i x - \sinh \lambda_i x + \alpha_i (\cosh \lambda_i x - \cos \lambda_i x) \quad i = 1, 2, \dots, m \quad (13)$$

$$Y_j(y) = \sin \lambda_j y - \sinh \lambda_j y + \alpha_j (\cosh \lambda_j y - \cos \lambda_j y) \quad j = 1, 2, \dots, n \quad (14)$$

where λ_i and α_i are given by Reddy (2004a). Upon applying the minimum of total potential energy principal, we obtain the following equations, Reddy (2004b).

$$\left[\frac{537.181}{a^3} b D_{11} + \frac{324.829}{a b} (D_{12} + 2D_{66}) + \frac{537.181}{b^3} a D_{22} \right] C_{11} - 23.107 N_{xy}^o C_{22} = 0 \quad (15)$$

$$\left[\frac{3791.532b}{a^3} D_{11} + \frac{4227.255}{a b} (D_{12} + 2D_{66}) + \frac{3791.532}{b^3} a D_{22} \right] C_{11} - 23.107 N_{xy}^o C_{22} = 0 \quad (16)$$

In matrix form

$$\begin{bmatrix} a_{11} & N_{xy}^o a_{12} \\ N_{xy}^o a_{12} & a_{22} \end{bmatrix} \begin{Bmatrix} C_{11} \\ C_{22} \end{Bmatrix} = - \begin{Bmatrix} 0 \\ 0 \end{Bmatrix} \quad (17)$$

where

$$a_{11} = \frac{537.181}{a^4} D_{11} + \frac{324.829}{a^2 b^2} (D_{12} + 2D_{66}) + \frac{537.181}{b^4} a D_{22} \quad (18)$$

$$a_{22} = \frac{3791.532}{a^4} D_{11} + \frac{4227.255}{a^2 b^2} (D_{12} + 2D_{66}) + \frac{3791.532}{b^4} a D_{22} \quad (19)$$

$$a_{12} = \frac{23.107}{ab} \quad (20)$$

For nontrivial solution, the determinant of the coefficient matrix must vanish. Thus,

$$a_{11}a_{22} - a_{12}a_{12}(N_{xy}^o)^2 = 0 \quad (21)$$

Solving for the buckling load N_{xy}^o we obtain

$$N_{xy}^o = \pm \frac{1}{a_{12}} \sqrt{a_{11}} \sqrt{a_{22}} \quad (22)$$

The \pm sign represents that the shear buckling load may be either positive or negative. The coefficients a_{11} , a_{12} and a_{22} depend on bending stiffness as described in Eqs.18, 19, and 20. They are function of fiber waviness. Thus, the critical shear load is influenced by fiber waviness.

3. NUMRICAL EXAMPLE

Consider a square, graphite/epoxy AS4/3501-6 laminate $[0_2/90_2]_s$. The lamina material properties are: $E_1 = 148$ GPa, $E_2 = 10.5$ GPa, $G_{12} = 5.61$ GPa, and $\nu_{12} = 0.3$, and the lamina ply thickness is 0.127 mm. We assume that all plies contain the same amount of fiber waviness. Fig. 2 and Fig. 3 show respectively, the variation of the lamina extensional modulus and lamina shear modulus as function of fiber waviness A/L . Fig. 4 shows the variation of laminate bending stiffness with respect to A/L . The percent reduction in critical load versus fiber waviness is presented in Fig. 5.

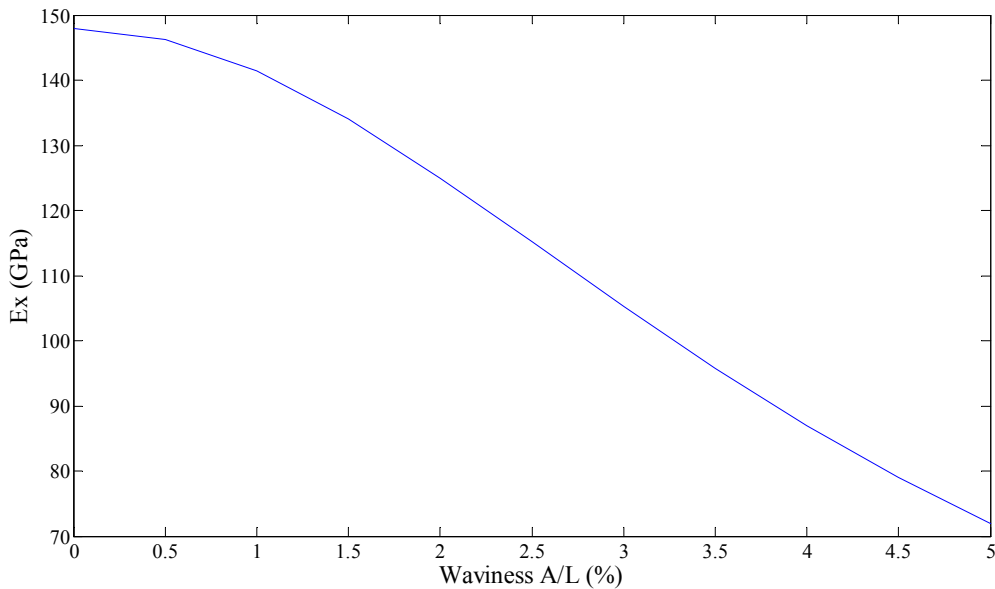


Fig.2. Variation of lamina extensional modulus with respect to fiber waviness

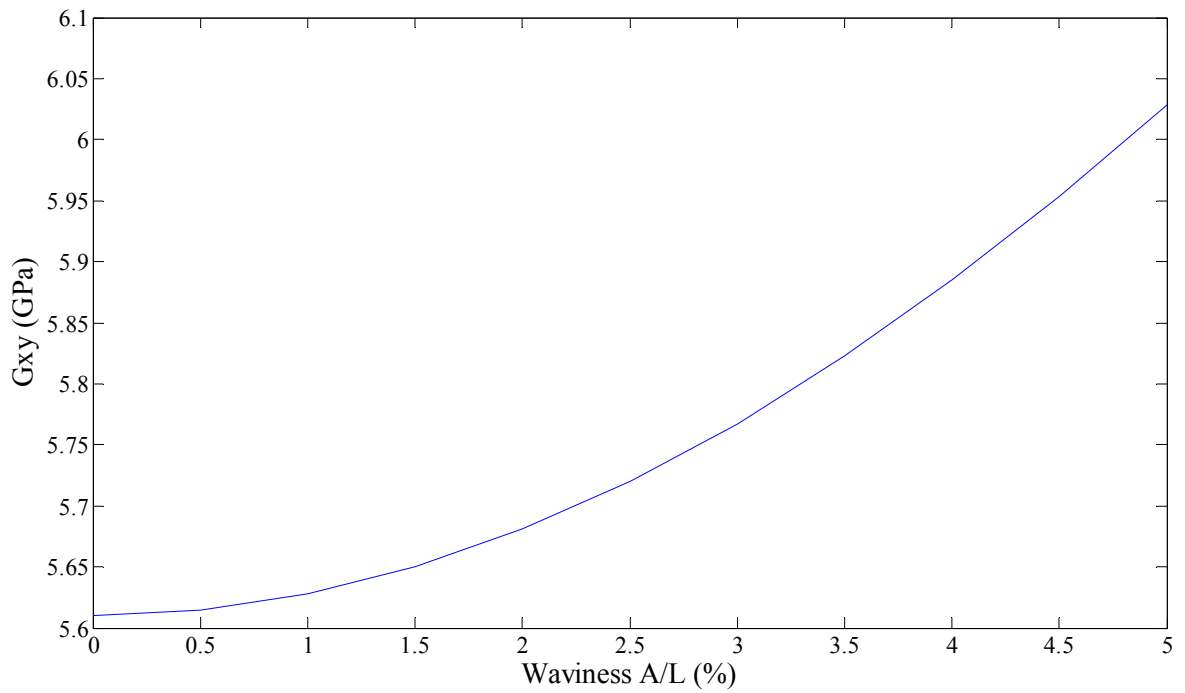


Fig.3. Variation of lamina shear modulus with respect to fiber waviness

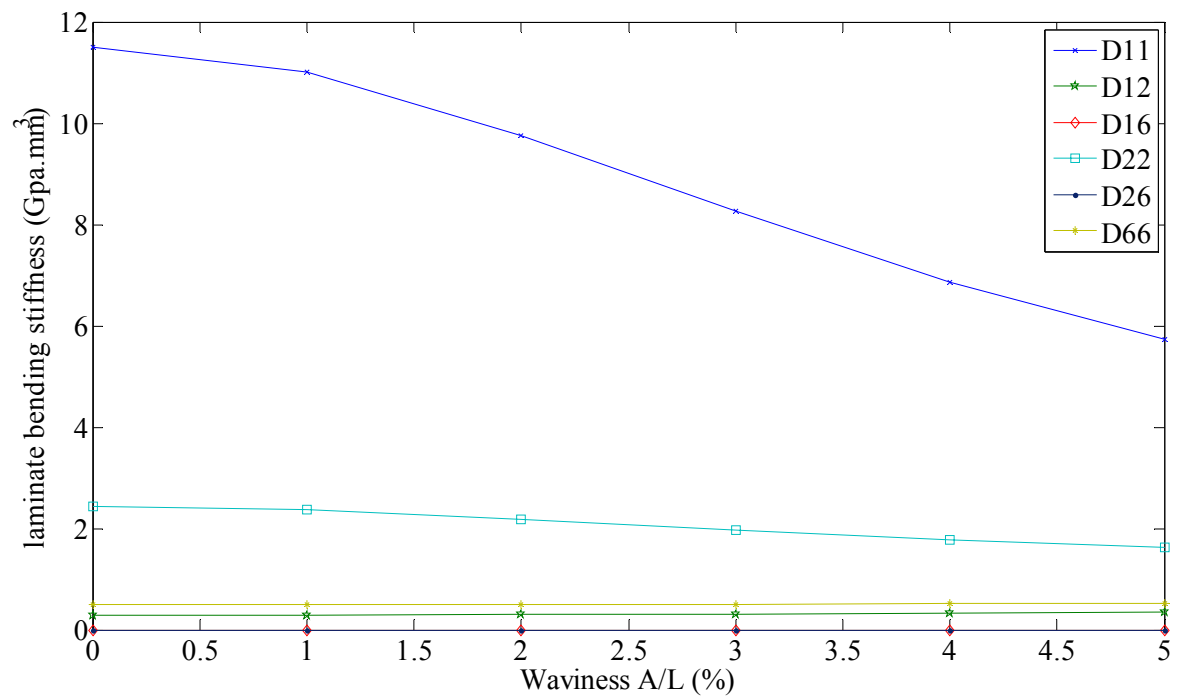


Fig.4. Variation of laminate bending stiffness with respect to A/L

Fibre waviness and buckling load of composites

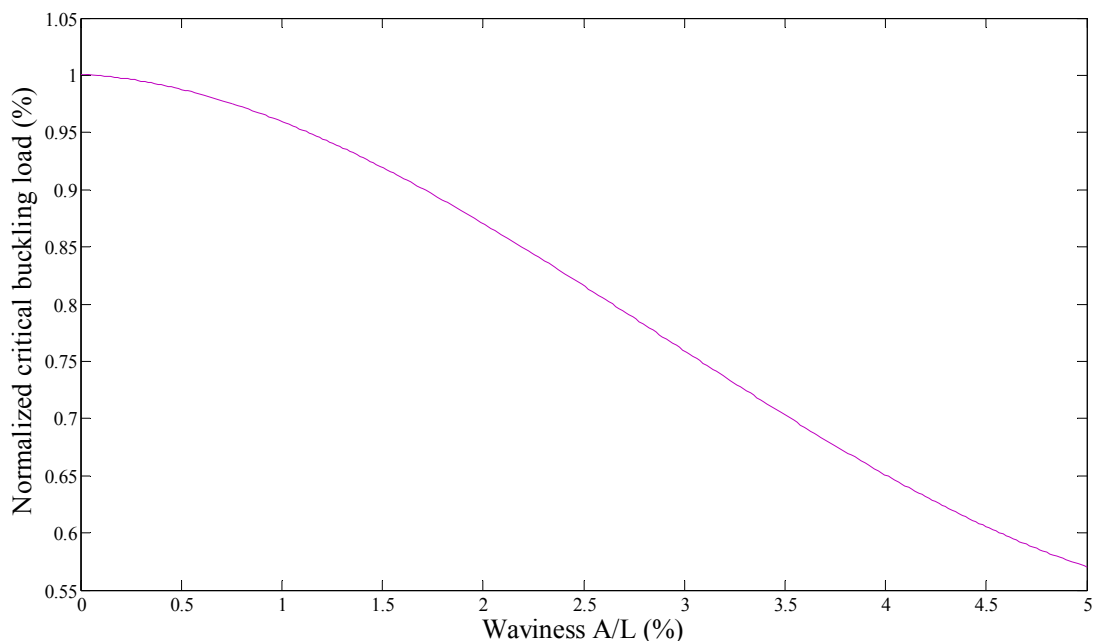


Fig.5. Normalized critical buckling load with respect to fiber waviness A/L

4. CONCLUSION

This work reveals the importance of the effect of fiber waviness on elastic properties of composites. The reduction of the lamina stiffness E_x is 28.91 % for 3% fiber waviness, the shear modulus G_{xy} increases by 2.8 % for 3% fiber waviness. Also, the laminate bending stiffness shows a reduction due to fiber waviness. A waviness of 3% reduces the bending stiffness D_{11} by 28.24 % and D_{22} by 18.78% other bending stiffness elements show a minor sensitivity against fiber waviness. Similarly, buckling load versus A/L for a square, symmetric and especially orthotropic laminate under shear loading reveals a 24.3% reduction in critical buckling load for about 3% fiber waviness. It is evident that fiber waviness is a quality variable that must be controlled in composite primary structural applications. Additional effort should be directed to develop manufacturing processes that insure fiber straightness in composite structural component.

REFERENCES

- Bogetti T. A., Gillespie W., and Lamontia M. A. (1991). Influence of ply waviness on the stiffness and strength and strength reduction on composite laminates. *J. Thermoplast. Compos. Mater.* 5,344-369
- Chan W.S., and Wang J.S. (1994). Influence of fiber waviness on the structural response of composite laminates. *J. Thermoplast. Compos. Mater.* 7, 243-260
- Garnich Mark R., and Karami Ghodrat. (2004). Finite element micromechanics for stiffness and strength of wavy fiber composites. *J. Compos. Mater.* 38,273-292
- Hsiao H.M., and Daniel I.M. (1996). Elastic properties of composites with fiber waviness. *Composites Part A*, 27A, 931-941
- Rai, H.G., Rogers, C.W., and Crane, D.A.(1992). Mechanics of curved fiber composites. *J. Reinf. Plast. Compos.*, 11, 552-566
- Reddy J.N. (2004). *Mechanics of laminated composite plates and shells theory and analysis* (CRC Press LLC Boca Raton)p.281-282.

STRAIN SENSING IN CARBON FIBER REINFORCED MATERIALS USING ELECTROMECHANICAL MEASUREMENTS

J. C. Rauhe, L. R. Jensen and R. Pyrz

Department of Mechanical Engineering, Aalborg University
Pontoppidanstraede 101, DK-9220 Aalborg East, Denmark

ABSTRACT

The strains in non-embedded carbon fibers are determined using an electromechanical method that has been developed. The method is subsequently used for determining the fiber strain in polymer based carbon fiber composites. The determined strains are verified through Raman spectroscopic measurements. A correlation between the change in resistance and the strain in the fiber is determined through tensile test of single non-embedded fibers and used to determine the strain in embedded fibers. From the determined fiber strains the quality of the interface between the carbon fiber and the matrix material can be estimated. From a number of experiments it has been found that the developed method is reliable, cheap and easy to use. A good correlation between the results obtained from the electromechanical measurements and obtained from Raman measurements is found.

1. INTRODUCTION

The most widely used fiber material in the production of wind turbine rotor blades is E-glass fiber, which is mainly due to the low cost of these fibers. With the increased requirements for size and performance of the wind turbines the use of carbon fiber reinforced composites for the wind turbine blades have gained increased interest, because of their high specific strength and modulus. However, when changing from E-glass fibers to carbon fibers different problems have to be considered. Determination of the quality of the interface between the reinforcing fibers and the matrix material to obtain the best possible utilization of the carbon fibers is one of the problems.

The interfacial properties of carbon fiber composites are precisely determined by determining the strain in the fiber using Raman spectroscopy. The method has been widely used to investigate the interfacial behavior and the effect of fiber sizing in carbon fiber composites (Young 1995; Schadler and Galiotis 1995). However, for companies which may have to test a large number of material systems to find an appropriate material system for their products

Raman spectroscopy may not be a feasible method. In order to perform the large number of tests it is necessary to have a method where the tests can be performed in a limited amount of time. Furthermore, the method has to be cheap and easy to use.

Utilizing that the electrical resistance of carbon fibers changes during loading the strain in the fibers can still be determined in a non-destructive way. However, examinations of the electromechanical properties of single carbon fibers have only been performed in relatively few studies. The main reason is that an appropriate method to connect the single fibers to the electrical measurement setup is required. It has been shown that the electrical properties of carbon fibers depend on their macroscopic properties such as the elastic modulus and their microstructure. Furthermore, it has been shown that the change in electrical resistance of the carbon fibers is mainly due to dimensional changes rather than changes in the resistivity, (Coner and Ownston 1969; Ownston 1970; Berg, Cumpston and Rinsky 1972; DeTeresa 1991; Wang and Chung 1997).

The electrical resistance measurements has focused on multiple fibers to monitor load transfer, damage and failure properties which is mainly due to the difficulties involved in handling single fibers. This includes non-embedded fiber bundles, (Li, Zhou and Ou 2004; Cho and Choi 2000), laminated composites consisting of both carbon fibers and a mixture of carbon and glass fibers, (Angelidis, Wei and Irving 2004; Todoroki and Yoshida 2004; Park, Okabe and Takeda 2003; Park, Okabe, Takeda and Curtin 2002; Xu, Liu, Gao, Fang and Yao 1996; Cho, Choi and Yoon 2002).

A limited amount of work has been performed on electromechanical studies of single fibers embedded in an epoxy matrix to study the load transfer and damage properties of the individual carbon fibers, (Wang, Lee, Chung and Park 2001; Wang and Chung 1997; Chung 2000; Park, Lee, Kim and Yoon 2001).

In the present work the main idea is to use the carbon fibers as stress/strain sensors and to compare the strain of embedded fibers obtained from the electromechanical measurements to fiber strains determined by use of Raman spectroscopic measurements. A method based on electromechanical measurements would be a useful method to investigate the interfacial properties between fiber and matrix as well as the damage of the embedded fibers. Furthermore, a cheap method to determine the interfacial properties in a non-destructive way could be provided by electromechanical measurements and would therefore be an industrial feasible method.

2. TEST SAMPLES AND EXPERIMENTAL PROCEDURE

The carbon fiber used in the present work was a PAN based TohoTenax HM 35 fiber and only a single fiber was used for each specimen. The fiber has been heat treated at 600 °C with an isotherm of 4 hours in an inert gas atmosphere. The matrix material used for the samples was the epoxy resin LM E20 with hardener LM H20 supplied by LM Glasfiber. The epoxy is mixed in the ration 100:30 and the recommended curing temperature is 90 °C for 4 hours.

Two different types of test specimen were used for the electromechanical measurements. The first type of sample was used to determine the relation between the straining of the fiber and change in resistance and consisted of a single non-embedded carbon fiber. The test specimen is based on a rectangular cardboard frame containing a rectangular hole as shown in Fig. 1.

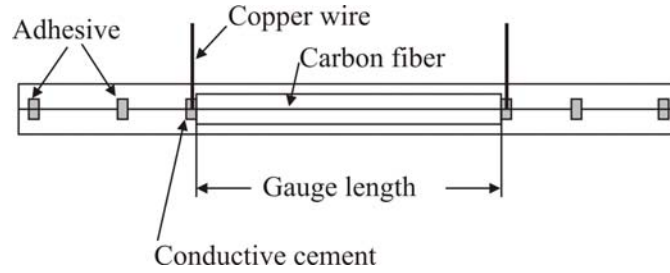


Fig. 1. Schematic illustration of non-embedded test specimen

The single fiber is mounted in such a way that it extends along the long axis of the cardboard frame crossing the rectangular hole as shown in Fig. 1. The fiber was attached to the cardboard with adhesive at four points and two copper wires were connected to the fiber using conductive carbon cement. With the cardboard frame it is possible to position the non-embedded fiber in the tensile test rig. The two ends of the frame are fixed in the rig and the two legs of the frame are cut. Thereby it is possible to apply the load to the non-embedded fiber in the testing rig.

The second type of specimen used in the electromechanical measurements was a single carbon fiber embedded in an epoxy matrix. The specimen has a thickness of 2 mm and is dog-bone shaped. The test specimen is shown in Fig. 2 and the gauge length of these samples is 60mm.

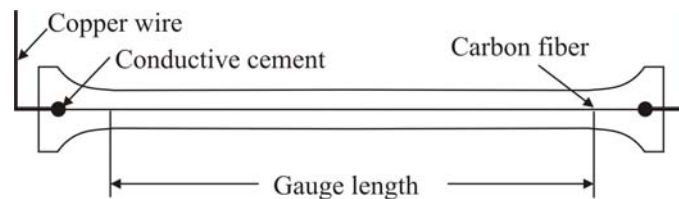


Fig. 2. Schematic illustration of dog bone shaped specimen

A silicon mold was used for the manufacturing of the dog-bone shaped specimens with a gauge length of 75 mm. A single carbon fiber was carefully aligned and fixed in the silicon mold to ensure it was positioned in the middle of the dog-bone specimen. Furthermore, a pair of copper wires was fixed in the silicon mold and electrical contact between the fiber and the copper wire was established using conductive carbon cement as used for the non-embedded fibers. After fixation of the fiber and copper wire the epoxy was poured in the silicon mold using a syringe. Afterwards the silicon mold was placed in a furnace and cured at 90 °C for 4 hours as described previously.

A Wheatstone bridge is used to determine the change in resistance of the carbon fiber and the test samples are coupled in a balanced half bridge. With the use of a Wheatstone bridge the relatively small changes in resistance can be measured with large accuracy. The bridge excitation voltage used in the current setup is 10 V. With the used bridge voltage no notable heat increase of the specimen was observed. The electromechanical testing of the carbon fiber specimens were performed by recording the bridge output voltage.

The output voltage from the Wheatstone bridge is directly related to the resistance during straining through the relation given in Eq. 1.

$$\Delta R = \frac{4V_0 R_0}{V_s} \quad (1)$$

Where V_0 is the bridge output voltage, R_0 is the resistance of the test specimen before straining

and V_s is the bridge excitation voltage.

For the Raman spectroscopic measurements a Renishaw inVia Raman microscope equipped with a Renishaw RL633 HeNe laser providing an excitation wavelength of 632.8 nm is used. A modified Olympus microscope with a $\times 50$ objective lens giving a spot size of the laser of approximately 2-10 μm was used. The Raman peak positioned at approximately 2661 cm^{-1} was used to determine the fiber strain. The tensile strain sensitivity of this peak was found to be $20\text{ cm}^{-1}/\%$ which is consistent with values reported by Rauhe, Jensen and Pyrz (2007). A purpose build straining rig fitting under the Raman microscope is used for the tensile tests and it is constructed as a conventional tensile testing rig.

A constant cross head speed of 0.001 mm/min was used for the tensile tests of the non-embedded fibers and the fiber strain was determined from the total cross head displacement. The low cross head speed was used to ensure that the fiber did not fail instantly and the cross head displacement and the bridge output voltage was recorded once per second. The applied load is not measured for the non-embedded fibers since the applied load is too small to sample with the load cells at hand.

For the dog-bone shaped specimens a constant cross head speed of 0.025 mm/min was used and a 2 kN load cell was used to measure the load applied to the sample. The applied load, the bridge output voltage and the cross head displacement was recorded once per second. At applied loads of 0, 50, 75, 100, 125, 150, 175 and 200 N Raman measurements were performed on the dog-bone shaped samples. At these loads the tensile test was paused and the Raman measurements were performed on the embedded fiber. The measurements were performed over a length of 140 μm in steps of 20 μm giving a total of eight measuring points for each load step.

The relation between the change in resistance determined from the output bridge voltage and the straining of the fiber is determined by performing tensile tests were performed on the non-embedded fiber as described above. To examine whether or not the determined strain sensitivity factor is influenced by the gauge length, tensile tests have been performed using different gauge lengths. From these tests it was found that the strain sensitivity factor not is influenced by the gauge length used. However, the noise in the system became more and more pronounced when shortening the gauge length and on the other hand the samples became more difficult to handle when increasing the gauge length. The results presented in the following for the non-embedded fiber are all obtained with a gauge length of 60 mm. The experimentally determined relation between the change in relative resistance determined from the bridge output voltage and the applied strain for the HM 35 fiber is shown in Fig. 3.

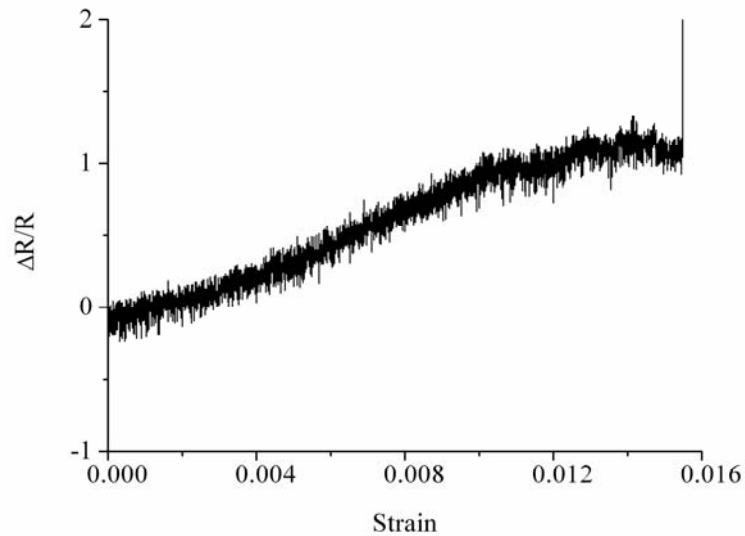


Fig. 3 Graph showing the change in resistance versus the applied strain

In many of the non-embedded fiber samples no change in resistance is observed in the beginning of the test due to the fact that the fiber is not fully stretched when the test is initiated. At the end of the test the slope of the curve also changes probably due to slippage of the fiber in the carbon cement contact points. This change does not influence the applicability of the electromechanical testing method since the strains measured in carbon fibers in carbon fiber/epoxy composites typically are below 0.012.

The average relative strain sensitivity factor is determined as the slope of the linear part of the strain/relative resistance curve shown in Fig. 3. The average of the strain sensitivity factor is calculated for a series of tests and is found to be 108.6 with a standard deviation of 11. TohoTenax reported the ultimate failure strain for the HM 35 fiber not to exceed 0.009. From the electromechanical tests it was generally observed that the fiber failed at an applied strain of approximately 0.005 which is significantly less than the value given by TohoTenax. The fiber did in all test fail at the point where the fiber is connected to the copper wire. Therefore, the reason for the large discrepancy in ultimate fiber strain is most probably due to introduction of stress concentrations at the connection points.

The determined strain sensitivity factor is only valid for the examined HM 35 fiber. The reason is that both the microstructural composition and the diameter of the fiber influence the strain sensitivity factor. Fibers of different grade and diameter may therefore result in different strain sensitivity factors. The same observations may be done if testing fibers of low quality where large variations in the microstructural composition may be observed. From the determined strain sensitivity factor the strain in the fibers of a carbon fiber composite can be calculated.

A typical stress/strain curve for the dog-bone measurements is shown in Fig. 4.

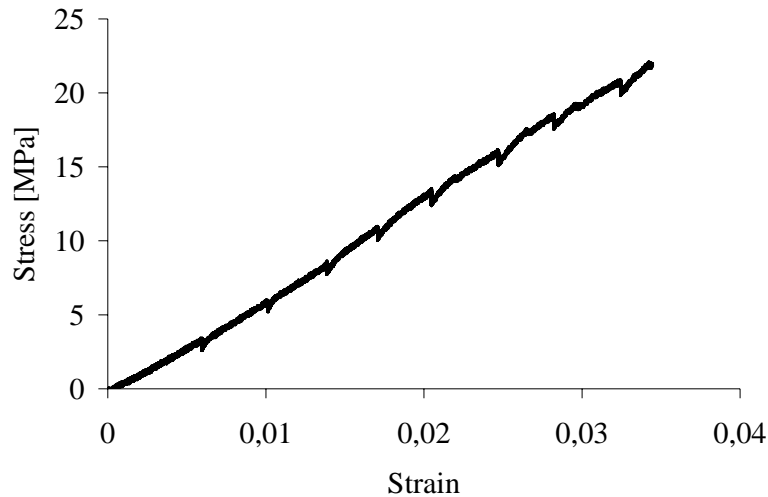


Fig. 4 Stress/strain curve for carbon fiber embedded in epoxy

Eight small drops are observed in the stress/strain curve shown in Fig. 4 and each of these drops corresponds to an applied strain at which the tensile test is paused and Raman measurements are performed. Each decrease in the stress is due to relaxation of the matrix material but the size of the decreases is minimal and therefore not estimated to influence the obtained results.

From the resistance and Raman measurements the fiber strain is determined and in Fig. 5 the calculated strains are plotted versus the applied strain for two different samples.

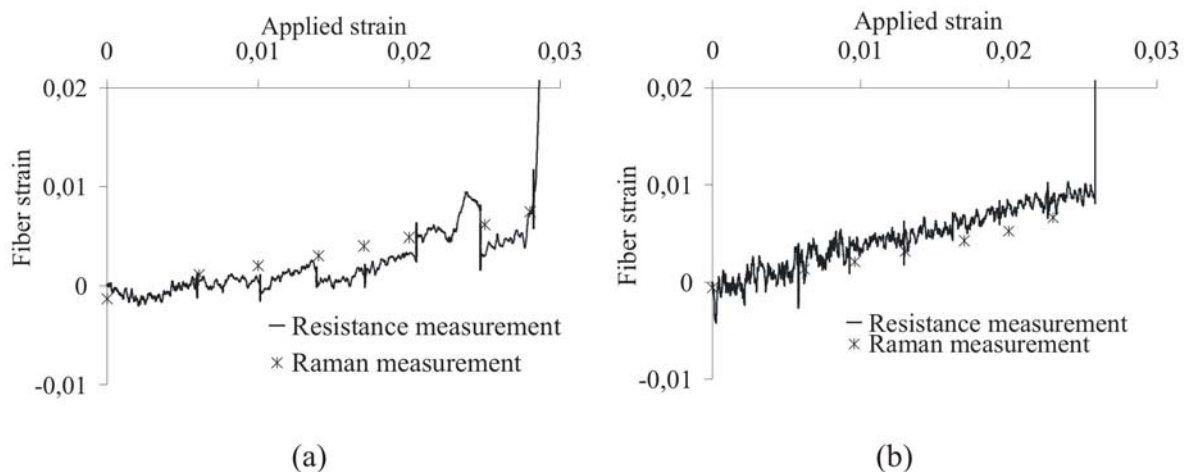


Fig. 5. Strain in the fibers obtained through resistance measurements and Raman measurements as a function of the applied strain.

A sudden increase and decrease is observed in the resistance measurement curve in Fig 5(a) for an applied strain between 0.02 and 0.025. This increase and decrease is most probably due to slippage in the contact points between the carbon fiber and the copper wire. This behavior is not observed in any of the other samples. In Fig. 5(a) and 5(b) singularities are observed at applied strains of 0.029 and 0.026, respectively, which correspond to fiber failure. The applied strain equals the strain applied to the dog-bone sample and not necessarily the strain level in the embedded fiber. A difference in strain levels could be a result of an interface between the carbon fiber and the matrix material of a poor quality and thereby a poor load transfer. Each of the Raman measurement points in Fig. 5(a) and (b) is determined as the average value of eight Raman measurements performed at different positions of the fiber as described previously.

A good correlation between the fiber strains determined through the two different methods are found for all the tested samples. A proportionality factor between the applied strain and the fiber strain is determined through a least square fit and it is determined to 0.36 and 0.30 for the electromechanical measurements and the Raman measurements, respectively. These values also show a very good correlation between the two different methods. Considering the strain levels in Fig. (5) it is seen that the strain level in the fiber is much smaller than the strain applied to dog-bone sample. As mentioned previously this is probably due to a poor quality interface between the two material constituents.

3. CONCLUSIONS

A method based on electromechanical measurements has been developed for determining the strain in non-embedded fibers. The electromechanical method is extended to carbon fibers embedded in a polymer matrix through a determined correlation between the strain and change in resistance in the carbon fiber. This correlation is determined through tensile tests on single non-embedded carbon fibers. A number of carbon fiber/epoxy dog-bone samples has been examined and the fiber strain determined from the electromechanical measurements have been verified through Raman spectroscopic measurements. From this verification good correlation is found between the fibers strains determined using the electromechanical method and those determined using Raman spectroscopy. Through a number of experiments it was shown that the developed method is reliable, cheap and easy to use.

ACKNOWLEDGEMENTS

This work is partially supported by the Framework Programme "Interface Design of Composite Materials" (STVF fund no. 26-03-0160)

REFERENCES

- Angelidis N., Wei C.Y. and Irving P.E (2004) "The electrical resistance response of continuous carbon fibre composite laminates to mechanical strain". *Composites*, A35, 1135-1147,
- Berg C.A., Cumpston H. and Rinsky A. (1972) "Piezoresistance of graphite fibres", *Textile Research Journal*, 42, 486-489
- Cho J.W. and Choi J.S (2000) "Relationship between Electrical Resistance and Strain of Carbon Fibers upon Loading". *J. Appl. Polym. Sci.* 77, 2082–2087,
- Cho J.W., Choi J.S. and Yoon Y.S. (2002) "Electromechanical behavior of hybrid carbon/glass fibre composites with tension and bending". *J. Appl. Polym. Sci.*, 83, 2447-2453,.
- Chung D.D.L (2000) "Fibrous Composite Interfaces Studied by Electrical Resistance Measurement". *Adv. Eng. Mater.*, 2. 788-796,
- Coner, P.C. and Ownston, C. N (1969) "Electrical resistance of single carbon fibres", *Nature*, 223, 1146-1147,.

- DeTeresa S.J (1991) "Piezoresistivity and failure of carbon filaments in axial compression", *Carbon*, 29, 397-409,
- Li H., Zhou W. and Ou J (2004) "Study on Electromechanical Behavior of Unidirectional Carbon fibre Sheet without Epoxy Resin Matrix". *Adv. Struct. Engineer.*, 7, 437-45,
- Ownston, C.N (1970) "Electrical properties of single carbon fibres", *J. Phys.*, D3, 1615-1626
- Park J.B., Okabe T. and Takeda N (2003) "New concept for modeling the electromechanical behavior of unidirectional carbon-fibre-reinforced plastic under tensile loading". *Smart Mater. Struct.*, 12, 105-114,
- Park J.B., Okabe T., Takeda N. and Curtin W.A (2002) "Electromechanical modeling of unidirectional CFRP composites under tensile loading condition". *Composites*, A33, 267-275,
- Park J.M., Lee S.I., Kim K.W. and Yoon D.J (2001) "Interfacial Aspect of Electrodeposited Conductive Fibers/Epoxy Composites Using Electro-Micromechanical Technique and Nondestructive Evaluation". *J. Colloid Interface Sci.*, 237, 80-90,
- Rauhe, J.C, Jensen, L.R. and Pyrz, R. (2007) Electromechanical testing of carbon fibers. In: *Proceedings of The Sixteenth International Conference on Composite Materials*. Eds. K. Kageyama, T. Ishikawa, N. Takeda, M. Hojo, S. Sugimoto and T. Ogasawara, Po-24.
- Schadler, L.S. and Galiotis, C (1995) "Fundamentals and applications of micro Raman measurements in fibre reinforced composites". *International Materials Review*, 40, 116-134,
- Todoroki A. and Yoshida J (2004) "Electrical resistance change of unidirectional CFRP due to applied load". *JSME International Journal A*, 47, 357-364
- Wang X.J. and Chung D.D.L, (1997). "Electromechanical behavior of carbon fiber", *Carbon*, 35, 706-709
- Wang S., Lee S.I., Chung D.D.L. and Park J.M (2001) "Load transfer from fiber to polymer matrix, studied by measuring the apparent elastic modulus of carbon fiber embedded in epoxy". *Composites Interfaces*, 8, 435-441,
- Wang X.J. and Chung D.D.L (1997) "Piezoresistive Behavior of Carbon Fiber in Epoxy". *Carbon*, 35, 1649-1651,.
- Xu M.X., Liu W.G., Gao Z.X., Fang L.P. and Yao K.D (1996) "Correlation of Change in Electrical Resistance with Strain of Carbon Fibre-Reinforced Plastic in Tension". *J. Appl. Polym. Sci.*, 60, 1595-1599,
- Young, R.J (1995) "Monitoring deformation processes in high-performance fibres using Raman spectroscopy". *J. Text. Inst.*, 86, 360-381,.

ON THE APPARENT INFLUENCE OF THE ADHERENDS ON THE FRACTURE TOUGHNESS OF ADHESIVE LAYERS

Kent Salomonsson and Ulf Stigh

University of Skövde
PO Box 408, SE-541 28 Skövde, Sweden

ABSTRACT

A detailed model of experiments with the double cantilever beam specimen is set up. Analysis of the model shows that an experimentally deduced apparent increase of fracture energy with severely deforming adherends is due to contributions of in-plane straining of the adhesive layer to the fracture energy. An analysis with the J -integral confirms the result.

1. INTRODUCTION

It has long been recognized that the fracture toughness of adhesive layers appears to be influenced by the behaviour of the adherends. For example, in carefully performed experiments with an engineering epoxy adhesive using adherends of varying properties a substantial increase of the fracture toughness is observed in modulus I; from about 700 J/m^2 with stiffer adherends to about 1000 J/m^2 with plastically deforming adherends (Andersson and Biel, 2006). This difference is larger than the expected experimental scatter and cannot be ignored.

In the present paper, experiments with the Double Cantilever Beam specimen (DCB) are simulated using a detailed mesomechanical model of the adhesive layer. The adhesive, DOW BETAMATE XW-1044-3, can be described as a composite with the continuous phase consisting of epoxy blended with a thermoplastic. Clusters of needle shaped mineral form the particles. The mesomechanical model is built-up by Representative Volume Elements (RVE's) developed by Salomonsson and Andersson (2007). In the RVE, the structure of the adhesive is mimicked using image analysis of SEM images, cf. Fig. 1. The FE-model is based on an idea developed by Xu and Needleman (1994) where all continuum elements are coupled by interface elements. Thus, decohesion is allowed along all element boundaries. Decohesion is governed by a modified version of the cohesive law introduced by Tvergaard and Hutchinson (1992). In this model, a relation between σ and λ is first assumed, cf. Fig. 2.

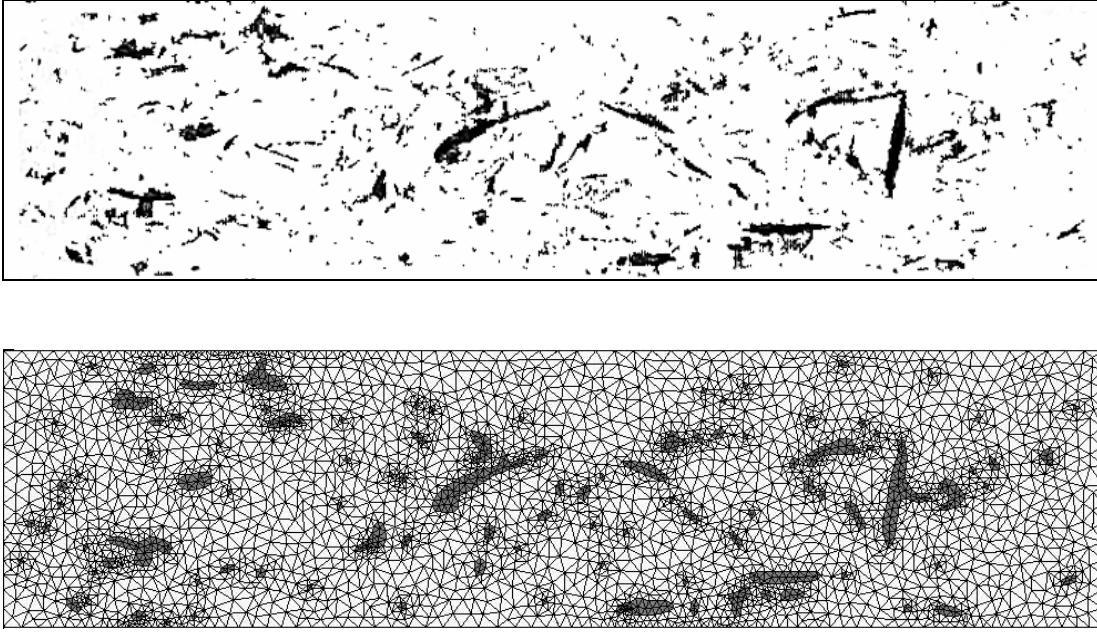


Fig. 1. Identification of material regions from a SEM-image. The upper figure shows a SEM-image with enhanced contrast. Mineral regions are identified as dark areas; the white areas correspond to a blend of epoxy and a thermoplastic. An unstructured FE-mesh with 7276 elements is created and the elements falling into the dark areas shown in the lower figure are given the properties of the mineral.

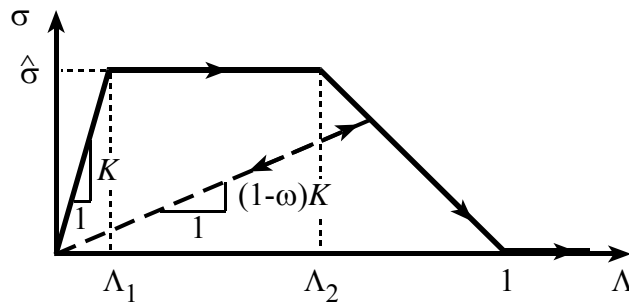


Fig. 2. Generalised cohesive relation. During monotonically increasing Λ , σ follows the filled curve; unloading follows the dashed curve.

Thus, during loading σ first increases to plateau $\hat{\sigma}$ at $\Lambda = \Lambda_1$. After Λ_2 , σ decreases linearly to zero at $\Lambda = 1$. After this point, σ remains equal to zero and the interface has failed. Unloading from a deformed state is assumed to take place according to the dashed curve in Fig. 2. This is accomplished in the cohesive model by introducing a damage variable ω that is only allowed to increase if Λ increases beyond any previously attained value on the original curve; ω is not allowed to decrease. The cohesive traction is split in a normal (T_n) and a shear (T_t) component with orientation according to the mid-plane formed by the separating cohesive surfaces. These tractions are given by

$$T_n = \frac{\sigma(\Lambda)}{\Lambda} \frac{\Delta_n}{\Delta_{nc}} \quad T_t = \frac{\sigma(\Lambda)}{\Lambda} \frac{\Delta_{nc} \Delta_t}{\Delta_{tc}^2} \quad (1a,b)$$

where Δ_n and Δ_t are the normal and shear separations, respectively and

$$A \equiv \sqrt{\left(\frac{\langle \Delta_n \rangle}{\Delta_{nc}}\right)^2 + \left(\frac{\Delta_t}{\Delta_{tc}}\right)^2} \quad (2)$$

Subscript c indicates the critical separation corresponding to zero traction and $\langle \dots \rangle$ the McCauley bracket. In compression, i.e. $\Delta_n < 0$, a penalty procedure is used to limit interpenetration of the cohesive surfaces, cf. Salomonsson and Andersson (2007). Thus, the cohesive law is governed by five parameters $\hat{\sigma}$, Λ_1 , Λ_2 , Δ_{nc} , and Δ_{tc} . In the RVE's, different sets of parameters are used to model decohesion in the mineral and the polymer parts of the adhesive. Moreover, a special set of parameters is used for the interfaces of the mineral and the polymer. The continuum phase of the polymer blend is modelled with conventional von Mises plasticity with isotropic hardening; the continuum phase of the mineral is assumed to be elastic. Thus, in the model, the well-known difference in yield strength in compression and tension for polymers is captured by the introduction of cohesive models.

A plane deformation FE-model of the RVE is developed, cf. Fig. 1. The model consists of 7276 three node triangular elements and 10792 four node interface elements. The constitutive parameters are optimized to experimental results in peel and shear loading, cf. Salomonsson and Andersson (2007). The data are given in Table 1. The RVE has the size 0.8 x 0.2 mm. A number of convergence studies have been performed to secure that the size and number elements of the RVE are large enough. Abaqus v. 6.5-1 is used with the interface elements implemented as user elements (UEL).

Table 1. Constitutive parameters of polymer, mineral and interface between the RVE's and the adherends. Poisson's ratio $\nu = 0.4$ for polymer and mineral.

Phase	E [GPa]	σ_Y [MPa]	$\hat{\sigma}$ [MPa]	Δ_{nc} [μm]	Δ_{tc} [μm]	Λ_1 [-]	Λ_2 [-]
Polymer	2	50	23	53	38	0.002	0.31
Mineral	55	∞	10	21	49	0.006	0.39
Interface	N/A	N/A	46	40	30	0.001	0.02

2. MESOMECHANICAL MODEL

Figure 3 shows the model of the DCB-specimen. The RVE's are used to model the adhesive layer. Due to the lack of symmetry of the RVE's, both the upper and lower parts of the DCB-specimen are modelled. This leads to a very large FE-model. However, in a DCB-specimen, only the first part of the adhesive layer is severely loaded. This is exploited here by replacing the RVE's far from the crack tip by cohesive elements COH2D4, cf. Fig. 3. With the relatively stiff adherends of the elastically deforming adherends, the length of the fully developed process zone is about 7-8 mm. Thus, only this part of the adhesive layer needs to be modelled with RVE's since the rest of the layer is loaded in the elastic regime. In this model, nine RVE's are used to model the first 7.2 mm of the adhesive layer. In the model with plastically deforming adherends, the length of the process zone is approximately 3-4 mm and only six RVE's are used. These occupy 4.8 mm of the layer. The length of the cohesive elements used to model the rest of the

adhesive layer is 0.25 mm in both models. The cohesive properties are adapted to the behaviour of a single RVE with a stress-deformation relation according to Fig. 4 with the fracture energy 740 J/m^2 .

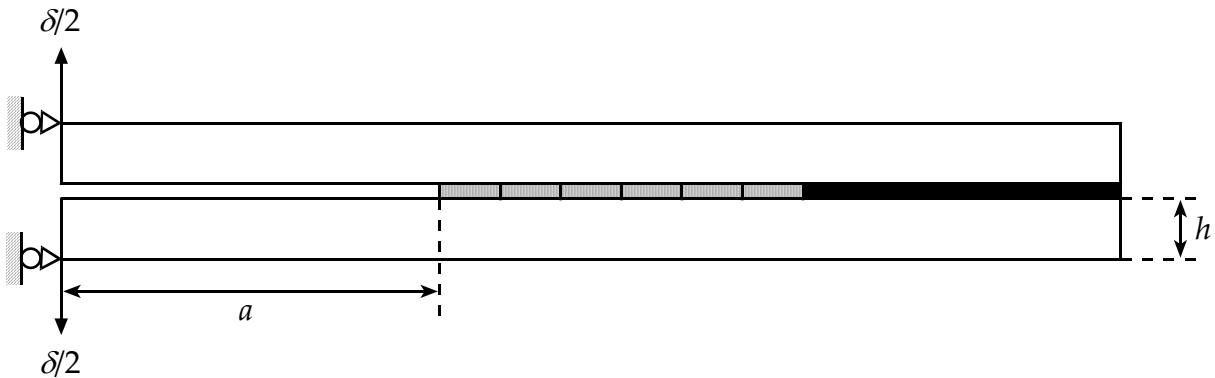


Fig. 3. DCB-specimen geometry with crack length a and adherend height h . Gray zones indicate the RVE's and the black region indicates the cohesive elements.

The adherends are modelled using plane stress 4-node continuum elements (CPS4R) except in the layer of elements at the interface to the RVE's and the cohesive elements. Here, 3-node plane stress continuum elements (CPS3) are used. The boundary conditions are indicated in Fig. 3. The loading points are separated at a prescribed rate. No time dependent properties are present in the model. Thus, the rate of separation is without significance.

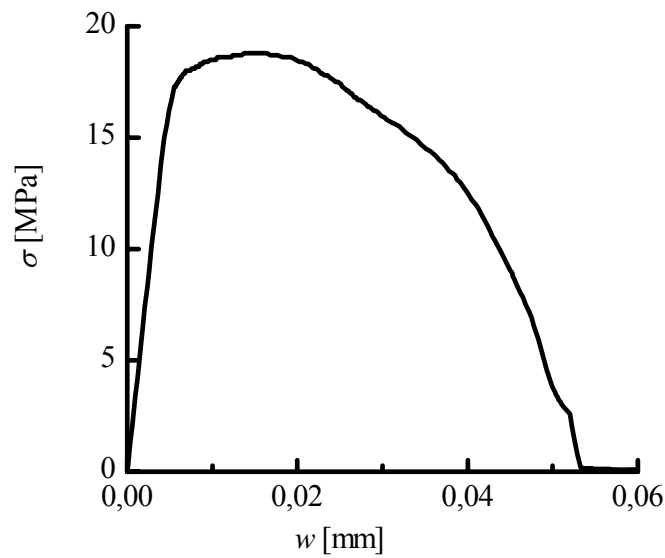


Fig. 4. The stress-elongation relation for a single RVE.

The adherends have Young's modulus $E = 200 \text{ GPa}$ and Poisson's ratio $\nu = 0.3$. In the model of the experiments with elastically deforming adherends the beam height is $h = 4.5 \text{ mm}$, width $b = 5 \text{ mm}$, initial crack length $a = 50 \text{ mm}$, and total length 150 mm , cf. Fig. 3. The yield strength of the adherends is larger than 500 MPa and the stress is always within the elastic regime during the experiments. For the plastically deforming adherends $h = 2 \text{ mm}$, $b = 8 \text{ mm}$, $a = 70 \text{ mm}$, and total length 170 mm . Independent tensile tests give the yield strength 130 MPa ; the hardening is well described up to at least 5% strain by a piecewise linear hardening model using only two

linear segments.

As indicated by the geometry of the specimen with plastically deforming adherends, the adherends are not expected to deform in plane stress nor is plane deformation a good approximation. Moreover, the deformation is substantial before the crack starts to propagate at about 30 mm deflection of the loading points. In the analysis by Andersson and Biel (2006), a shell element analysis in large deformation indicates substantial anticlastic deformation of the adherends. In effect, this deformation leads to a virtual increase in stiffness and hardening which can be interpreted as an effect of the increase of “height” of the adherends due to the anticlastic deformation. The same effect can be achieved artificially by increasing the stiffness, yield strength and hardening of a 2D-model of the adherends. Since the present paper is focused on the behaviour of the adhesive, we will exploit this possibility in order to save computer resources for a more accurate model of the adhesive. In order to achieve good agreement with the experiments, the properties of the adherends are altered by increasing the yield strength to 152 MPa; Young’s modulus remains unchanged. The parameters are chosen to give the correct behaviour up till the moment the crack starts to propagate. All analyses are done considering large deformations.

3. RESULTS

The analysis of the DCB-specimen with elastically deforming adherends shows that micro cracks initiate some distance from the crack tip, typically 0.3-0.6 mm from the start of the layer. That is, about 1.5 to 3 times the layer thickness, $t = 0.2$ mm. This corresponds to a reasonable estimate of the size of influence of the free edge of the adhesive layer, cf. Fig. 5.

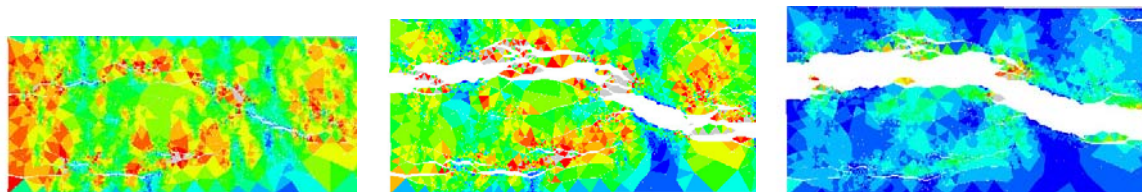


Fig. 5. Simulated crack tip regions. Peel separation increases from the left to the right image. White regions correspond to micro cracks. The crack tip is located at the left hand side of each image.

Due to the constraints of the adherends, the layer is essentially loaded in a state of uni-axial strain except in a region close to the free edge. The loading experienced by the layer is thus expected to be somewhat larger when moving away from the free surface and into the layer. This explains why cracks initiate some distance into the layer. Later on in the process, some of the micro cracks coalesce to form a larger crack. At about the same time a crack opens at the start of the layer. The two cracks coalesce and form a relatively flat major crack; thus, a process similar to a typical pop-in sequence observed in ductile metals.

The fracture process appears similar with plastically deforming adherends. However, in this case the first micro cracks initiate closer to the free edge, about 0.1-0.3 mm from the start of the layer. This is due to the large rotation experienced by the plastically deforming adherends in this area; the loading of the layer decreases more rapidly when moving into the layer than in the elastic case with stiffer adherends.

Figure 6 shows the force-displacement relation from the simulations and from the experiments with plastically deforming adherends. The curves consist of three parts. In the first part, the

adherends and the adhesive are in an elastic state and we get a linear relation starting at the origin. At about 17 N, the adherends start to deform plastically and a plastic hinge is formed at the start of the adhesive layer. Due to the hardening of the adherends, the load increases almost linearly until, at about 20 N in the experiments, the adhesive starts to fracture. After this point, the crack propagates and the load decreases.

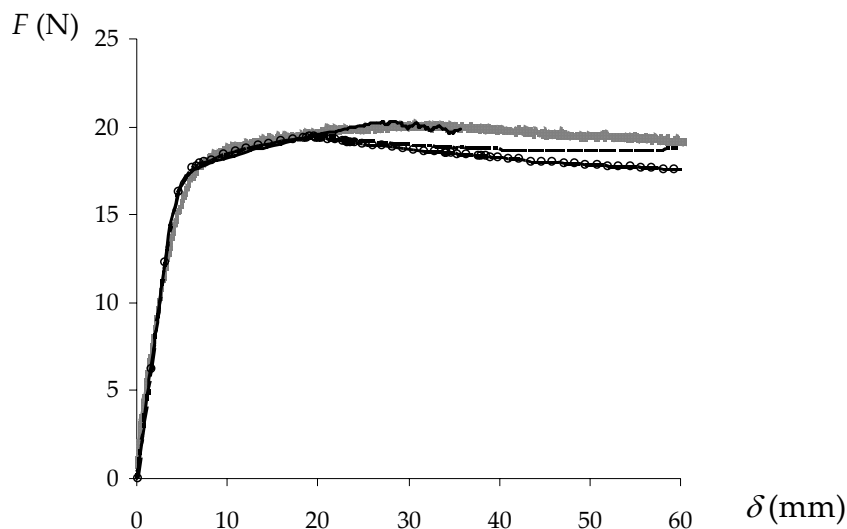


Fig. 6. Force-displacement curves for DCB-specimens with plastically deforming adherends. Solid grey curve: experiments; Solid black curve: simulation. For comparison, the dashed curve and the curve marked with circles correspond to simulation models with more conventional methods to represent the adhesive. Circles: adhesive layer represented by non-linear springs and adherends by beam elements; Dashed curve: adhesive layer represented by cohesive elements and adherends by the same elements as in the mesomechanical model.

The simulation corresponds well with the experiment. It is noted that the first two parts of the curve are used to calibrate the model of the adherends and the good correspondence at these stages should not be taken as a proof the success of the model. However, the load and load-point displacement for the initiation of crack growth and softening agrees with the experiment. This is critically dependent on the modelling of the adhesive layer. With more conventional methods to represent the adhesive layer, the crack initiation point is moved to the left in Fig. 6, cf. Salomonsson and Stigh (2007). As shown by Andersson and Biel (2006), a more conventional model of the adhesive layer can be brought in to agreement with the experiments if the cohesive law is given an increased fracture energy of 1000 J/m^2 . That is an increase of about 35 %.

The effect of the more severe deformation of the plastically deforming adherends on the apparent fracture toughness of the adhesive layer can be explained by an application of the J -integral (Rice, 1968). With index-notation, the integral is given by

$$J \equiv \int_S (W n_x - \sigma_{ik} u_{i,x} n_k) dS \quad (3)$$

where W , σ , \mathbf{u} and \mathbf{n} are the strain energy density, the stress tensor, the displacement vector and the unit outward normal to the counter-clockwise paths S encircling the start of the adhesive layer; repeated indexes indicate summation. By utilizing the path independent property of J , the path A to B in Fig. 7 is chosen and J is reduced to

$$J = \int_t W dy \approx \sum_{\forall S_c} \int_0^{\mathbf{u}} T_i(\tilde{\mathbf{u}}) d\tilde{u}_i + \frac{1}{8} \bar{E} h^2 t \kappa^2 \quad (4)$$

where κ is the curvature of the adherends at the crack tip and \bar{E} is the elastic in-plane stiffness of the adhesive. Thus, J equals the strain energy per unit adhesive area, captured in the adhesive layer at the start of the layer. This energy is build-up from two sources as indicated in the last expression: the first is the energy to create cohesive surfaces S_c and the second is the strain energy of the stretched continuum. In the last part of Eq. (4), this energy is approximated by the corresponding elastic strain energy in the adhesive.

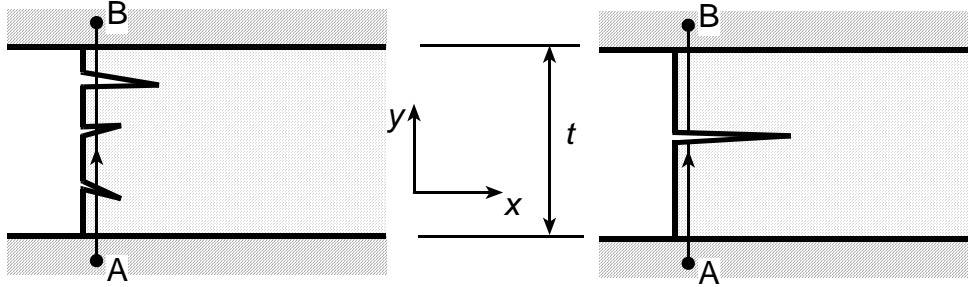


Fig. 7. Detail of start of adhesive layer with integration path A to B used for the evaluation of the J -integral. *Left*: In the earlier stages of the fracture process many cohesive surfaces opens and contribute to J . *Right*: At a later stage, at the moment a major crack is about to propagate, all except one of the cohesive surfaces have been un-loaded and one major cohesive surface remains. This is the moment J achieves its largest value, i.e. the fracture energy J_c .

The last expression in Eq. (4) is derived by assuming that cohesive surfaces open in the layer and the layer is stretched to follow the deformation of the adherends. At the late stage of cracking, i.e. at the moment a macro crack is about to form and J attends its maximum value J_c , one major cohesive surface remains and J_c is written

$$J_c = \Gamma_{\text{coh}} + \Delta J_c \quad (5)$$

where

$$\Gamma_{\text{coh}} \equiv \int_0^{u_c} \sigma_{\text{coh}}(\tilde{u}) d\tilde{u}, \quad \Delta J_c \approx \frac{1}{8} \bar{E} h^2 t \kappa^2 \quad (6a,b)$$

Here, Γ_{coh} is the cohesive energy of the adhesive given by the cohesive stress-separation relation, $\sigma_{\text{coh}}(u)$, assuming that all minor cohesive surfaces formed during the earlier stage above and below the remaining surface close in an elastic manner.

An evaluation of the simulation shows $\kappa_c \approx 0.035 \text{ mm}^{-1}$ at the moment of crack propagation. With $\bar{E} = 2 \text{ GPa}$, Eq. (6b) gives $\Delta J_c = 260 \text{ J/m}^2$. This corresponds well to the difference in fracture energies of the experiments with elastically and plastically deforming adherends.

4. CONCLUSIONS

Experiments show a variation of the fracture energy with the behaviour of the adherends in DCB-experiments, cf. e.g. Andersson and Biel (2006). Simulations with conventional cohesive models are incapable to reproduce the experiments. However, a mesomechanical model giving a detailed description of the fracture process captures the difference in fracture energy.

An analysis based on the J -integral provides a simple explanation to the variation of the fracture energy with the properties of the adherends. With a finite thickness of the adhesive layer and the substantial deformation of the adherends that occur with plastically deforming adherends, the in-plane straining of the adhesive layer gives a substantial contribution to the fracture energy.

REFERENCES

- Andersson, T. and Biel, A. (2006). On the effective constitutive properties of a thin adhesive layer loaded in peel. *Int. J. Frac.* **141**, pp. 227–246.
- Rice, J. R. (1968). A Path Independent Integral and the Approximate Analysis of Strain Concentration by Notches and Cracks. *ASME J. of Appl. Mech.*, **35**, pp. 379-386.
- Salomonsson, K. and Andersson, T. (2006). Simulation of crack initiation and propagation in an adhesive layer using a meso-mechanical model. *Proc. of 27th Risø International Symposium on Materials Science, Polymer Composite Materials for Wind Power Turbines.*
- Salomonsson, K. and Stigh, U. (2007). Influences of the root curvature on the fracture energy in adhesive layers. Submitted.
- Tvergaard, V., Hutchinson, J. W. (1992). The relation between crack growth resistance and fracture process parameters in elastic-plastic solids. *J. Mech. Phys. Sol.*, **40**, pp. 1377-1397.
- Xu, X.P., Needleman, A. (1994). Numerical simulations of fast crack growth in brittle solids. *J. Mech. Phys. Sol.*, **42**, pp. 1397–1434.

A STRONG TOUGHENING MECHANISM IN AN ELASTIC PLASTIC LAMINATE

P. Ståhle*, C. Bjerken*, J. Tryding† and S. Kao-Walter‡,

* Materials Science, Malmö University, SE 20506 Malmö, Sweden,

† Tetra Pak Packaging Solutions AB, Lund, Sweden,

‡ Engineering, Blekinge Inst. of Technology, Karlskrona, Sweden.

ABSTRACT

The fracture process of a laminate is analysed. The laminate is a material used for packaging. It consists of a thin aluminium foil with a polymer coating. In both materials, the fracture processes are supposed to be dominantly localized plastic deformation. A Barenblatt region is supposed to spread ahead of the crack tip. This region is analysed in its cross plane invoking plane deformation conditions. The fracture process is assumed to be continuous reduction of the cross sectional area in the crack plane until the load carrying capacity vanishes with the vanishing cross sectional area. One case where the interface between the two materials is perfectly bonded and one case with delamination of the interface are examined. The results are compared with the properties of the individual layers. At fracture mechanical testing of the laminate, it is observed that the load carrying capacity increases dramatically as compared with that of the individual layers. When peak load is reached for the laminate, strains are fairly small and only the aluminium is expected to carry any substantial load because of the low stiffness of the polymer. It is therefore surprising that the strength of the laminate is almost twice the strength of the aluminium foil. The reason seems to be that the constraint introduced across the interface, forces the polymer to absorb large quantities of energy at small nominal strain. The toughness compares well with the accumulated toughness of all involved layers. Based on the results, a method is suggested for designing ultra tough laminates based on careful selection of material combinations and interface properties. The method gives a laminate that produces multiple necking.

1. INTRODUCTION

A laminate consisting of a polymer film bonded to a thin aluminium foil is examined with respect to its fracture mechanical properties. The laminate is a packaging material used in food containers. An important functionality for the aluminum foil, in the food container, is be an oxygen barrier. The magnitude of damage in the aluminum foil have a negative impact its oxygen barrier functionality.

This material was the subject of earlier studies by Kao-Walter *et al.* (2002). In the experimental studies a centre cracked panel geometry was used. Four specimens were compared. These were a single aluminium foil, a single polymer layer and a laminate constructed of these two. The polymer material was a so called LDPE (low density polyethylene). The resulting strength of the laminate was compared with the fracture strength of the individual layers. A remarkable increase of the toughness of the laminate as compared with that of the individual layers, was observed, see Fig. 1.

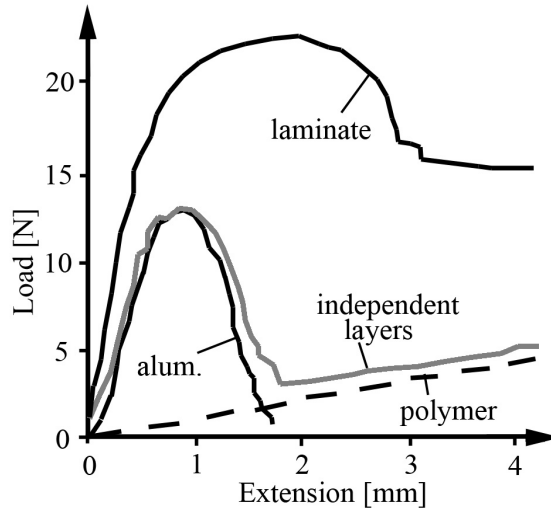


Fig. 1: Load displacement curves for the laminate, including the result for sheets of aluminium and polymer put together with no interconnection marked "independent layers". Included is also the test result for single aluminium foil and a single polymer film.

The stiffness of the polymer layer is only a fraction of that of aluminium at the straining when peak load is reached. Therefore the load carrying capacity obviously has increased dramatically as compared with that of the individual layers. When peak load is reached for the laminate, nominal strains are fairly small and only aluminium is expected to carry any substantial load because of the low stiffness of the polymer. It was somewhat of a surprise that the strength of the laminate was almost twice the strength of the aluminium foil. Improved mechanical properties has been observed and analysed before, e.g. by Macioncyk and Bruckner (1999) and Li *et al.* (2005). These studies focus on the integrity of the metal film and on structures without initial cracks.

In the present paper, the fracture mechanisms are simulated. The experimental study Kao-Walter *et al.* (2002) reports that necking seems to precede fracture. In the present analysis a Barenblatt region (cf. Barenblatt, 1962) is simulated in the sense that the local approximately plane deformation ahead of the crack tip is considered. This fracture mechanism was observed and analysed by Dugdale (1959). The fracture processes are assumed to be elastic-plastic and localized straining is assumed to continue until the cross section simply vanishes. Therefore, fracture criteria becomes obsolete. The analysis focus on the influence of the adhesion between the layers. Load capacity is computed for the process region of a two-layer laminate specimen as well as for the individual layers of the laminate. The results suggest a possibility for multiple necking that would increase the toughness several magnitudes.

2. THE MODEL

The necking region ahead of a crack tip is considered, see Fig. 2a. A coordinate system, attached to the crack tip, defines the initial position of the necking region as $0 \leq x \leq d$, $|y| \leq t/2$ and $|z| \leq t/2$. The considered geometry for this analysis is a cross section initially ahead of $x = d$. As the crack is growing, the complete development of the cross section is reflected along the x -axis, where time increases in the negative x -direction. The changes along the x -direction is assumed to be small over distances of the order of d . Therefore, the cross section is in an approximate plane strain in the y - z plane. Here plane strain is assumed for the geometry in Fig. 2b. Load is applied in the y -direction. The material is assumed to be elastic-perfectly plastic with the modulus of elasticity E , Poisson's ratio $\nu=0.3$ and the yield stress σ_o . The plastic deformation is associated to von Mises' flow surface.

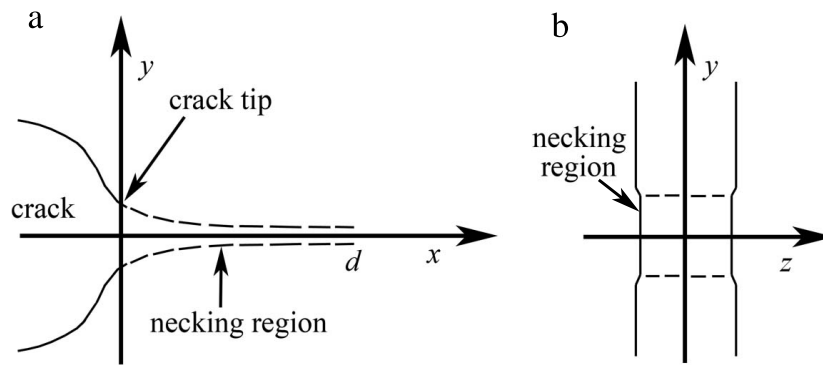


Fig. 2: Necking region a) the crack tip and the necking region, b) a cut through the necking region along the y - z plane.

3. ANALYSIS OF THE HOMOGENEOUS CASE

The problem may be solved analytically for a homogeneous material. Fig. 3 shows two snapshots of the states passed through by a cross section through the necking region. The flow rule does not allow for any volumetric plastic strains, *i.e.* the volume is preserved if elastic straining is assumed to be negligible. The slip occurs along planes forming 45° to the y -axis which leads to slopes of the surface adjacent to the necking region along $z = \pm y/2$ (cf. Hill 1952). The load carried per unit of original thickness, t , of the segment becomes

$$F = \sigma_o(t - v_p), \quad (1)$$

where v_p is the plastic part of the displacement across the necking region. If the strip is long compared with its thickness the elastic deformation has to be considered. As a function of the total elongation v of the strip the load becomes

$$F = \begin{cases} tvE/h & \text{for } v < \sigma_o h/E \\ \sigma_o(t - v)/[1 - \sigma_o h/(Et)] & \text{for } \sigma_o h/E \leq v \leq t \end{cases}, \quad (2)$$

where h is the original length of the strip. As the elongation of the strip increases, finally the thickness of the cross section vanishes, as also the load. This defines the crack tip.

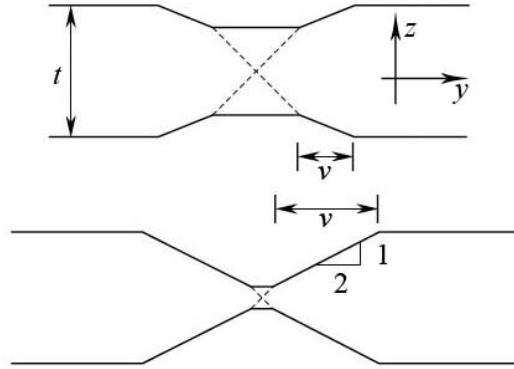


Fig. 3: Two states of a developing necking region. Loading is in the y -direction. The total plastic elongation is v_p .

Slip line solutions may also be constructed for laminated materials but, as far as the present authors understand, without large difficulties only for the initial slipping.

4. NUMERICAL ANALYSIS

For the laminated cases the problem is solved numerically using a commercial finite element code (ABAQUS, 2006). A regular mesh with 850 eight node isoparametric plane strain elements is used to cover a part with height t and length $h = 3t$. The meshed part was subjected to prescribed displacement at the edges $y = \pm h$. The position of the neck is controlled by a few surface nodes, that are displaced to make the width of the strip locally slightly smaller. To secure the desired position of the neck the width was made $0.999t$ at the centre of the segment. Some care also had to be taken to avoid necking near the edges where the prescribed displacement is applied.

Figures 4a and b shows the numerical result for aluminium respectively polymer. Included in the figure are also the corresponding analytical results. As observed both results are pretty accurate except for large displacements when the cross sectional area is reduced to and less than around 10 - 20%, or equally when the prescribed displacements are larger than $0.8t$ to $0.9t$. The slightly different results displayed by the two materials has to be contributed to the different ratios of modulus of elasticity versus yield stress. Plastic deformation localize in an initially t times t , quadratic region at the centre of the strip. In the most strained part the elements become very distorted. When the elongation reaches t , the aspect ratio of the most distorted element has exceeded 10, which makes the results less accurate.

Two cases are analysed for the laminate, *i.e.*, in the first case an aluminium foil and an polymer film with a perfectly bonded interface and in the second case the same materials bonded together but with rather brittle interface. The thickness of the aluminium foil is $9 \mu\text{m}$ and the thickness of the polymer film is $25 \mu\text{m}$. To extend the applicability of the results, the thicknesses are normalized with the total thickness t of the laminate. Thus, the thickness $0.265t$ is used for the aluminium foil and $0.735t$ is used for the polymer film. For aluminium, the modulus of elasticity is E , Poisson's ratio $\nu=0.3$ and the yield stress is σ_o . The modulus of elasticity of the polymer is $0.1E$, Poisson's ratio $\nu=0.3$ and the yield stress is $0.3\sigma_o$. For the case with a brittle bond the interface is unbonded along a segment with the length equal to the thickness of the aluminium layer, *i.e.* $0.265t$. The aluminium layer is made slightly thinner in the middle of that segment to achieve proper necking.

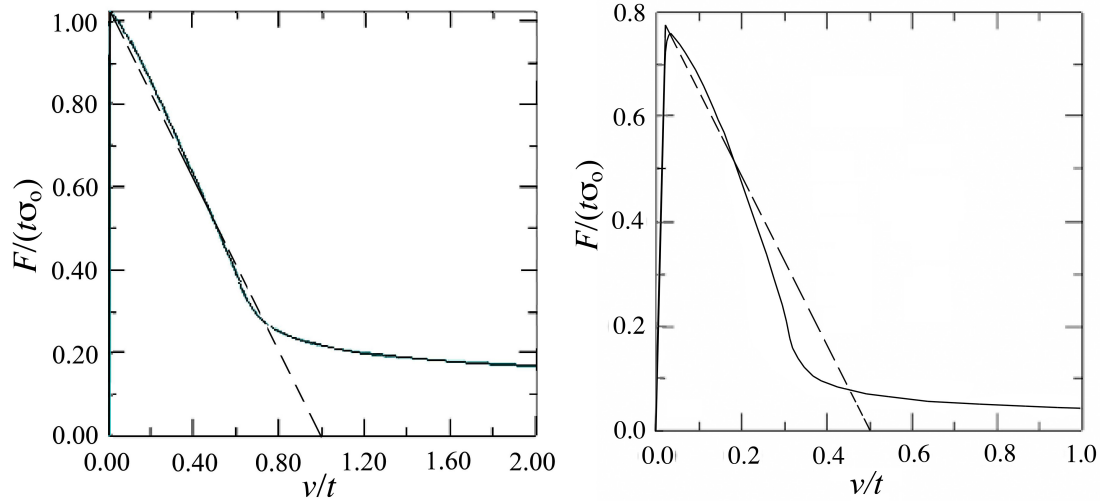


Fig. 4: Simulations of homogeneous sheets of aluminium (right) and polymer (left). Analytic solutions (dashed lines) are included for comparison. Note that the scaling of the tensile force is with respect to the yield stress σ_o for respective material.

In Figs. 5a and b the profile of the plastically deformed geometries obviously depends on the properties of the interface. The elongation of half of the specimen, $v=0.5t$. Comparison of the two cases shows that the plastic deformation of the polymer is to a large extent controlled by the plasticity of the aluminium layer. In Fig. 5a one observes how the polymer layer is sucked into the void area that is the result of the plastic deformation of the aluminium layer. The aluminium seems less affected by the presence of the polymer layer. As observed also in Fig. 5b the deformation becomes asymmetric in the polymer film and plastic deformation obviously becomes constrained by the contact with the aluminium foil.

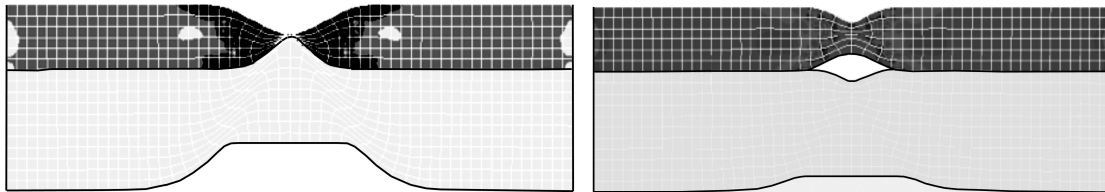


Fig. 5: Deformed geometries of (a) specimen with a perfectly bonded interface and (b) with an interface in which a crack has been introduced over a $0.265t$ long segment. The upper layer is aluminium.

The observed interaction between the two layers also affect the load carrying capacity of the laminate. This is shown in Fig. 6, where the cases for perfectly bonded and brittle interfaces are compared with two totally independent layers. In the latter case the results from single aluminium respectively single LPDE layers have been superimposed at the post-analysis. The analytical result is obtained from (2) applied to parameters for the two layers of the laminate.

The largest force is obtained for the perfectly bonded laminate and is $1.8F_o$ where F_o is the maximum force carried by the aluminium layer. The force decrease to $1.6F_o$ for the partly delaminated case and just above F_o for the unbonded layers.

The area under the curves represents the energy consumed during the necking. One may

note that no energy is attributed to the delamination process in the present analysis. The brittleness is revealed in Fig. 6 as the area under the curve for perfectly bonded laminate is found to be smaller than the area under the curve for the perfect bond case in the same figure. The area is close to 70% larger for the partly delaminated. The unbonded material requires slightly less energy for fracture than the perfectly bonded laminate.

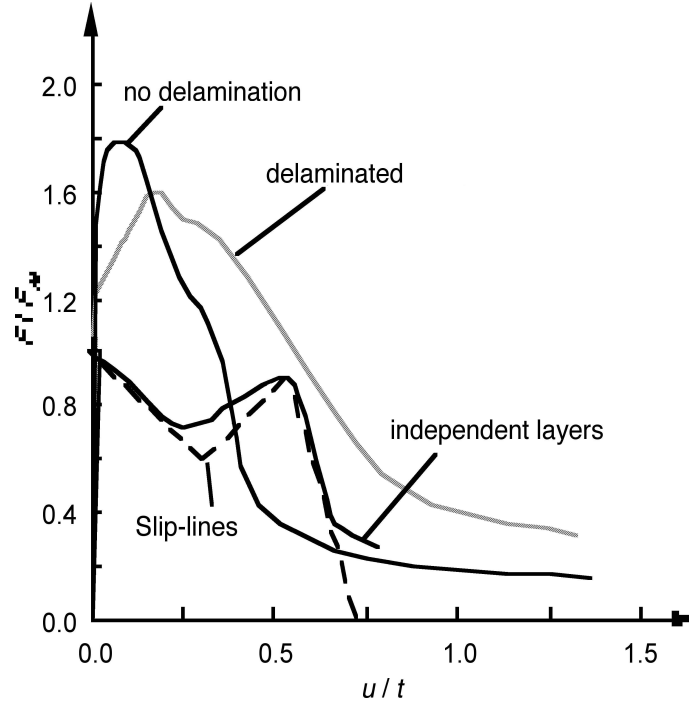


Fig. 6: Force versus displacement for the perfectly bonded and the partly delaminated materials are compared with to independent layers. The slip-line solution (2) for totally unbonded layers moving without any interaction, is included.

5. DISCUSSION AND CONCLUSIONS

The result presented in Fig. 6 provide a guide for selection and design of desired interface properties. If high strength is sought for a structure without cracks a large peak stress is desired because this is the stress at which cracks can be initiated. Thus, the interface should be made as strong as possible since the perfect bonded interface gives the largest peak force. The peak force is a slightly more than 10% above that for the partly delaminated structure.

The reason for the larger peak stress seems to be that the material is forced to large plastic strains in both materials because of the constraint introduced by the undamaged interface. The elastic strain limit is much lower in the aluminium than in the polymer. Therefore, plastic deformation is expected to occur first in the aluminium layer. This introduces large strains also in the polymer layer. Thus, the load carried by the polymer layer increase until its strength limit is reached. This hypothesis is supported by the observation in Fig. 6, that the maximum force is $1.8F_0$ when this is compared with the force $1.83F_0$, obtained by adding the maximum force that may be carried aluminium and the same carried by the polymer.

If the material contains a crack or if a crack is initiated at a notch it is a draw back is that the laminate with the perfectly bonded interface is more brittle than the laminate

that delaminates partly. The, around 70% larger energy needed to fracture the partly delaminated material as compared with the partly bonded laminate implies that the fracture toughness is around 30% larger for the delaminating structure.

The implication for the fracture process region, *i.e.* the necking region ahead of the crack, is that the linear extent of the region is approximately 70% larger for the delaminating material. This limits the applicability of linear fracture mechanics to 70% larger minimum crack length as compared with required minimum crack lengths for perfectly bonded laminates.

The result for independent layers has the most remarkable implication in the present analysis. The focus is set on the observation of two peaks for the force. The particular combination of materials studied here will obtain a single necking region. Once necking is initiated the force never exceeds the value needed for necking again. The process is described as follows: The force increases rapidly as long as both materials are elastic. Once the aluminium becomes plastic the load will decrease until the aluminium layer is broken. The polymer layer is still elastic. Because of that load continues to increase until also this layer become plastic. After this the load decreases under increasing displacements until both layers are broken. The observed behaviour lead us to the heuristic conclusion that a laminate with a slightly higher yield stress or larger thickness of the weaker layer, here the polymer layer, must behave quite different. As the load is increasing towards the second local peak force further loading is interrupted because other parts of the structure now reach loads exceeding the first peak force. Two possibilities are foreseen: multiple necking or a widening necking region. The load will not reach the second, presumably larger peak stress in any part of the structure until the entire laminate structure is plastic. This leads to an almost unlimited increase of the energy absorbed during loading. The two possibilities needs to be evaluated against the impact they have on the aluminium foils oxygen barrier functionality.

ACKNOWLEDGEMENT

Financial support from The Knowledge Foundation under grant no. 2004/0274 is acknowledged.

REFERENCES

- Barenblatt, G. I. (1962). *Advances in Applied Mechanics*. 7, 55.
- Dugdale, D. S. (1959). Yielding of Steel Sheets Containing Slits. *J. Mech. Phys. Solids* 8, 100.
- Hill R. (1952). On Discontinuous Plastic States, with Special Reference to Localized Necking in Thin Sheets. *J. Mech. Phys. Solids* 1, 19.
- Kao-Walter, S. Stähle, P and , Hägglund, R (2002). Fracture Toughness of a Laminated Composite, in: *Fracture of Polymers, Composites and Adhesives II*, Elsevier, Oxford, UK, ISBN: 0-08-044195-5, 355.
- Macionczyk, F. and Bruckner, W. (1999). Tensile Testing of AlCu Thin Films on polyimide foils. *J. Appl. Phys.* 86 4922.
- Li, T., Huang, Z. Y., Xi, Z. C., Lacour, S. P., Wagner, S., Suo Z. (2005). Delocalizing Strain in a Thin Metal Film on a Polymer Substrate. *Mech. Mater* 37, 261.
- Teng Li and Z. Suo (2007). Ductility of thin metal films on polymer substrates modulated by interfacial adhesion. *Int. J. of Solids and Structures* 44, 1696.

ON THE SIMULATION OF KINK BANDS IN FIBER REINFORCED COMPOSITES

Kim D. Sørensen*, Lars P. Mikkelsen**
and Henrik M. Jensen*

* Department of Civil Engineering, Aalborg University,
9000 Aalborg, Denmark

** Materials Research Department, Risø,
4000 Roskilde, Denmark

ABSTRACT

Simulations of kink band formation in fiber reinforced composites are carried out using the commercial finite element program ABAQUS. A smeared-out, plane constitutive model for fiber reinforced materials is implemented as a user subroutine, and effects of fiber misalignment on elastic and plastic deformation are studied under plane strain conditions.

Keywords: Kink band, constitutive model, ABAQUS, fiber misalignment

1. INTRODUCTION

Failure by kinking in fiber reinforced composites has been the subject of a number of recent investigations. It has been found that the compressive failure strength is considerably lower than the tensile strength, typically in the order of 50 to 60 percent for carbon fiber composites (Kyriakides et al., 1995). It has also been found that the compressive strength is governed by plastic yielding in the matrix (Budiansky, 1983), and furthermore, that small misalignments of the fibers have a large influence on the compressive strength, see Kyriakides et al. (1995). Several investigations of compression of a fiber reinforced material under the assumption of perfectly aligned fibers have predicted bifurcations stresses much higher than results obtained from experiments. Liu, Fleck and Sutcliffe (2004) include the effect of random waviness of the fibers using a Cosserat smeared-out finite element model.

In Kyriakides et al. (1995) the problem of predicting compressive strength for fiber reinforced materials is approached through an idealized model composite, with individual discretization of fiber and matrix material, and this two-dimensional micromechanical model was later (Kyriakides et al., 1998) extended to a three dimensional model. In these investigations the post-buckling response is also studied, and it is shown that deformation localizes into well-defined bands of bent fibers.

Kink band formation in fiber reinforced materials was investigated in Christoffersen and Jensen (1996) and in Jensen and Christoffersen (1997), where a plane constitutive model for perfectly bonded layered materials was introduced. It was found that this model contains essentially the same information in one point of the material as a complete finite element discretization of a representative volume element, like the model introduced in Kyriakides et al. (1995), and furthermore, that the critical stress is highly influenced by fiber volume fraction and the constitutive behavior of the constituents. Another conclusion is that the kink stress is reduced by taking non-linearity of the fibers into account compared to the predicted critical stress assuming linear-elastic fibers.

In the present study, a smeared-out plane constitutive model, as formulated by Christoffersen and Jensen (1996), is implemented as a user subroutine in the finite element program ABAQUS. Effects of fiber misalignment for elastic and plastic response are studied, and qualitatively compared to earlier results.

2. IMPLEMENTATION OF THE CONSTITUTIVE MODEL

For a detailed description of the constitutive model used in these kinkband simulations, see Jensen and Christoffersen (1997) and Christoffersen and Jensen (1996).

2.1 The constitutive model.

The general relations between rates of Cauchy stress and the strain rates in three dimensions are given by

$$\dot{\sigma}_{ij} = L_{ijkl}\epsilon_{kl} \quad (1)$$

where L_{ijkl} are the elastic-plastic tangent moduli. The strain rates are given by

$$\epsilon_{ij} = \frac{1}{2}(v_{i,j} + v_{j,i}) \quad (2)$$

with $v_{i,j}$ denoting the components of the gradient of velocity components v_i .

The two-dimensional constitutive equations implemented in ABAQUS are given in the form

$$\dot{s}_{ij} = C_{ijkl}v_{l,k}, \quad i, j, k, l \in \{1, 2\} \quad (3)$$

where \dot{s}_{ij} are components of the nominal stress rate, $v_{i,j}$ are components of the gradient of velocity components v_i , and C_{ijkl} are components of the tensor of nominal moduli, and from this formulation L_{ijkl} is found by the relation

$$L_{ijkl} = C_{ijkl} + \frac{1}{2}\delta_{il}\sigma_{kj} + \frac{1}{2}\delta_{ik}\sigma_{lj} + \frac{1}{2}\sigma_{il}\delta_{kj} - \frac{1}{2}\sigma_{ik}\delta_{lj}, \quad i, j, k, l \in \{1, 2\} \quad (4)$$

by furthermore using the assumption $\tau_{ij} \approx \sigma_{ij}$, with τ_{ij} being components of Kirchoff stress.

The components of the tensor of nominal moduli C_{ijkl} are found from a mixture of fiber and matrix properties.

The constitutive model is based on three assumptions:

- Material lines parallel with the fibers are subject to a common stretching and rotation

- Planes parallel with the fibers transmit identical tractions
- The material of the constituents is elastic or elastic-plastic

The first of these assumptions correspond to a Voigt estimate for effective material properties whereas the second corresponds to a Reuss estimate. The third assumption is a standard specification of time independent materials.

The expressions for C_{ijkl} , the components of the tensor of nominal moduli, can be found in Christoffersen and Jensen (1996).

2.2 The behavior of the constituents.

For both constituents we have the relations

$$\dot{s}_{ij}^c = C_{ijkl}^c v_{l,k}^c, \quad (5)$$

similar to equation 3. Furthermore, both materials are assumed to be characterized by a power-law hardening with isotropical hardening. The power-law is given by

$$\epsilon = \begin{cases} \frac{\sigma}{E} & , \sigma \leq \sigma_y \\ \frac{\sigma_y}{E} \left[\frac{1}{n} \left(\frac{\sigma}{\sigma_y} \right)^n - \frac{1}{n} + 1 \right] & , \sigma > \sigma_y \end{cases} \quad (6)$$

where σ_y is the yield stress of the material and n the hardening parameter. From this relation the tangentmodulus E_t is found, and subsequently the values of L_{ijkl}^c .

In the kink-band simulations in the present paper, yielding only occurs in the matrix material, and thus the fibers are treated as linear elastic.

2.3 ABAQUS implementation.

The user subroutine UMAT in ABAQUS is used to implement the material behavior of the composite. In this routine, stresses in fibers and matrix are updated within each increment, and the elastic-plastic moduli are calculated by mixture of the properties of the constituents. The moduli L_{ijkl} are determined from equation 4 and this value is returned to ABAQUS from UMAT. ABAQUS uses an updated Lagrangian formulation.

The model is implemented as a plane strain model, but can also be formulated for plane stress situations. In the present study, the fiber volume fraction is assumed to remain constant throughout the deformation.

Further details regarding the implementation of a constitutive model in ABAQUS can be found in Dunne and Petrinic (2005).

3. RESULTS

In this section, results for simulation of kink-band formation, and the response of compression of a single element, are presented. In the simulations, a rectangular block of fiber reinforced material, as shown in Fig. 1, is analyzed. The block is loaded under plane strain conditions, and has the dimensions $L = 10$ and $H = 3$ with the fiber direction outside the

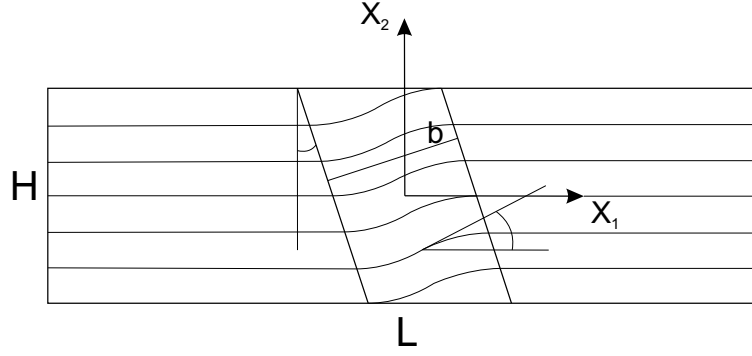


Fig. 1: Kink band geometry

kink band coinciding with the x_1 -axis. Furthermore, the displacements u_1 and u_2 satisfy the boundary conditions

$$u_1 = 0 \text{ on } x_1 = -\frac{L}{2} \quad (7)$$

$$u_2 = 0 \text{ on } (x_1, x_2) = \left(-\frac{L}{2}, -\frac{H}{2}\right) \quad (8)$$

The width of the imperfection is b and β is the angle of the kink band. Inside the kink band the fibers are assumed to be at an angle ϕ , and this imperfection is given by the expression:

$$\phi(x_1, x_2) = \frac{1}{2}\phi_m \left[\cos \left(\frac{2\pi \cos \beta}{b} (x_1 + x_2 \tan \beta) \right) + 1 \right] \quad (9)$$

where ϕ_m is the value of the angle in the middle of the kink-band. In all simulations, the values $b = 2$ and $\beta = 5^\circ$ are used.

The material parameters used in these simulations are found in Kyriakides et al. (1995), with superscripts f and m denoting fiber and matrix respectively:

$$\nu^f = 0.263, \nu^m = 0.356, \frac{\sigma_y^f}{E^f} = 0.019, \frac{\sigma_y^m}{E^m} = 0.013 \quad (10)$$

In all simulations, a fiber volume fraction of $c^f = 0.6$ is being used. The hardening parameters are chosen to be $n^m = 4.5$ and $n^f = 2.5$, so the power-law curve closely resembles the Ramberg-Osgood curve used in Jensen and Christoffersen (1997), and results are obtained for $E^f/E^m = 35$ and $E^f/E^m = 100$.

The dotted green curve in Fig. 2 shows the material response under compression of an element of the fiber reinforced material. In Fig. 2, the plastic deformation of the matrix material is suppressed. The material response is modeled using one 4-node element with 2×2 Gauss integration points. The fibers are given a small initial homogenous inclination of 1° . During the compressive deformation the fiber inclination will increase, resulting in a lower overall stiffness of the composite material. Nevertheless, for a stiffness ratio of the fiber/matrix system given by $E^f/E^m = 35$ the behavior is rather linear, whereas a stiffness ratio of $E^f/E^m = 100$ will result in a much more pronounced non-linear material response. However, even for this stiffness ratio the material will not experience a material softening behavior. Therefore, a localized deformation state in the rectangular block (Fig. 1) is not expected and is not found. Instead of a localized deformation state, an imperfection insensitive overall Euler buckling mode is developed as shown in Fig. 3. The red curve in Fig. 2

Simulation of kink bands

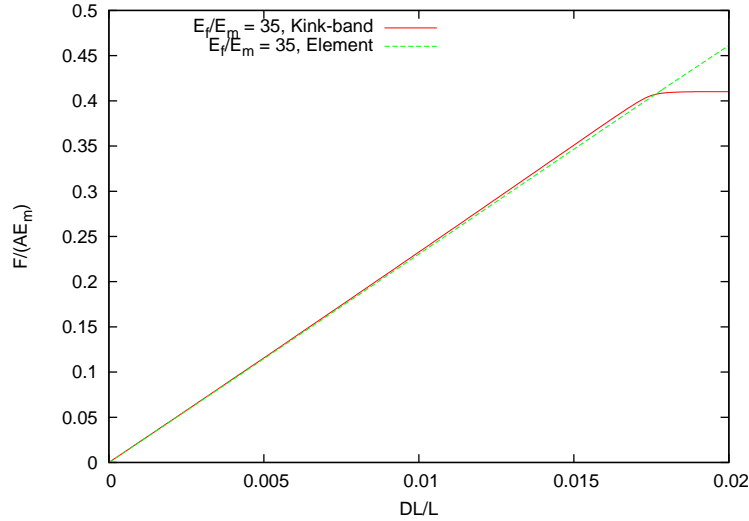


Fig. 2: Elastic deformation

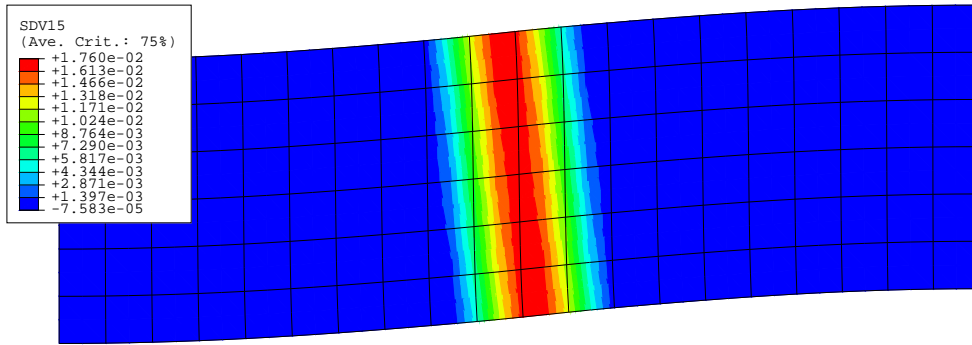


Fig. 3: Contourplot of imperfection

shows the corresponding load versus shortening curve for a rectangular block, indicating a maximum load carrying capacity of approximately $F/(AE^m) = 0.42$. In addition to the deformed mesh, Fig. 3 shows a contourplot of the initial prescribed misalignment of the fibers, with a maximum value of $\phi_m = 0.0176 \text{ rad}$ at the center of the kink band, corresponding to an imperfection of $\phi_m = 1^\circ$.

In Fig. 4, the load-displacement curves for one single element, Fig. 4a, and for a block of material, Fig. 4b, are given for the stiffness ratio of the fiber/matrix system $E^f/E^m = 35$. In contrast to Fig. 2, plastic yielding occurs in the following simulation in the matrix material. During compressive loading it can be seen from Fig. 4a, that the smeared out model show extensive material softening and actually also snap-back behavior. Consequently the deformation state in the rectangular block localizes into a kink-band as shown in Fig. 5. The load-displacement curves are linear until a kink stress is reached and for sufficiently small angles of fiber misalignment, the phenomenon of snap-back occurs. From Fig. 4 it can be seen that the critical stress is very sensitive to the initial fiber-misalignment. For instance, for the kink-band formation in the block of material the critical stress almost doubles when the maximum angle of fiber-misalignment ϕ_m is reduced from 5° to 2° .

A contour plot of the effective plastic strains in the matrix material during kink band

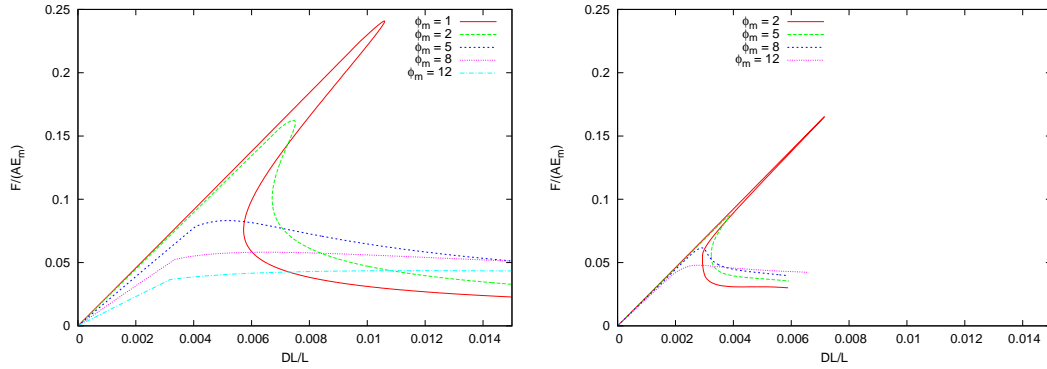


Fig. 4: Plastic deformation $E^f/E^m = 35$

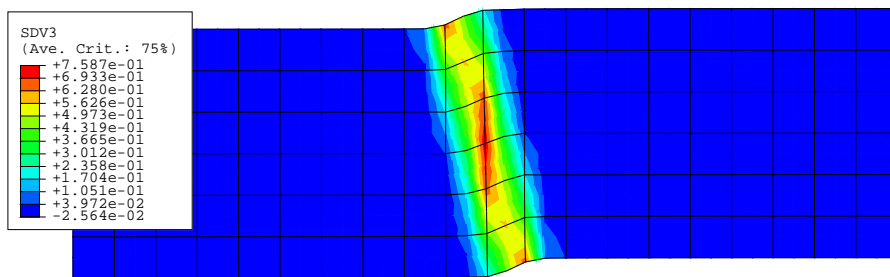


Fig. 5: Contour plot of effective plastic strain in the matrix material

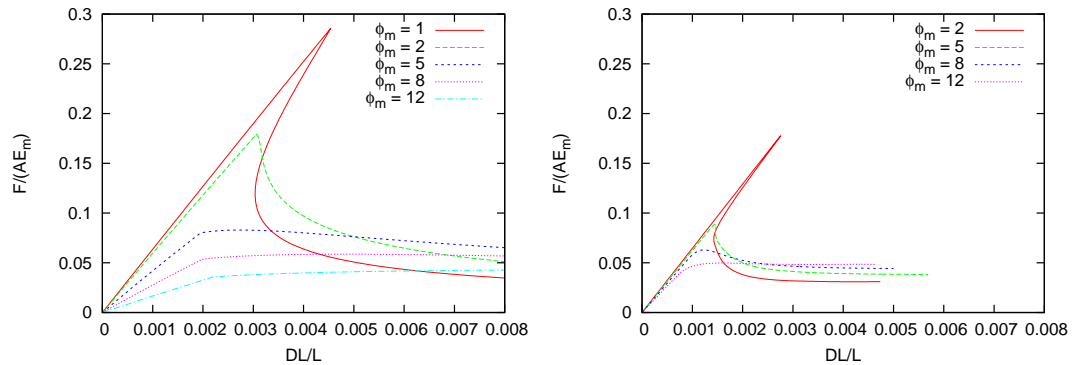


Fig. 6: Plastic deformation $E^f/E^m = 100$

formation is shown in Fig. 5.

The load-displacement curves for one single element and for a block of material, are shown in Fig. 6 for the stiffness ratio of the fiber/matrix system $E^f/E^m = 100$. These curves demonstrate a behavior similar to the one where $E^f/E^m = 35$. The implementation of the constitutive model does not include a material length-scale, and consequently the solutions show strong mesh dependency. This is illustrated in Fig. 7 which shows the load-displacement curves using four different meshes. All curves are found using the fiber misalignment variation (9) with $\phi_m = 8^\circ$. Similar to what is obtained by e.g. (Pamin, 1994) a more brittle post-localization behavior are obtained when the mesh is refined. From Fig. 8 it can be seen that the kink-band formation occurs in one row of elements. Not only the

post-necking behavior, but also the load carrying capacity is seen to be influenced by the mesh size.

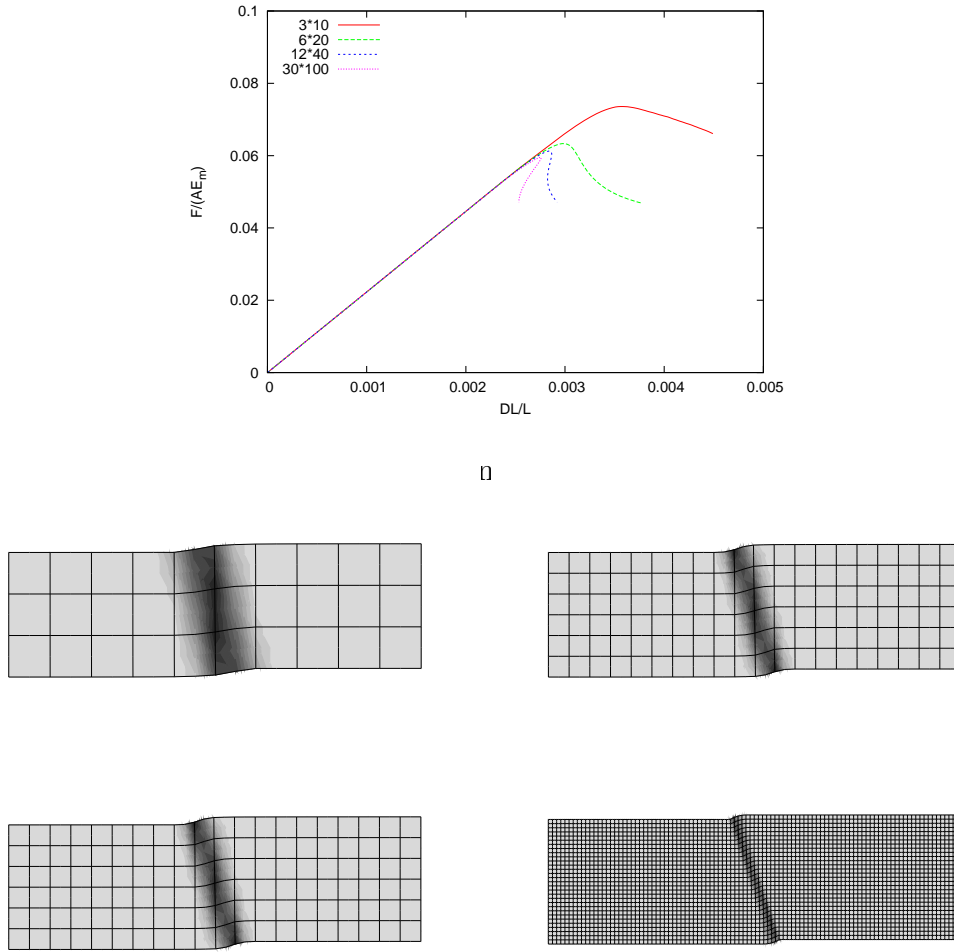


Fig. 8: Kink band mesh dependency

4. DISCUSSION

A plane constitutive model for fiber reinforced composites is implemented in ABAQUS as a user subroutine. It is demonstrated that the model qualitatively produces similar behavior as a micro-mechanical model, with regards to kink band development. The implementation of the model in ABAQUS does not include a material length-scale and therefore the kink-band will show strong mesh dependency. The implementation of the smeared-out composite material model in a finite element model has some immediately future applications, for instance kink-band development in more complex structures, such as a plate with a hole subject to compression. Other possible application is simulation of competing compressive failure mechanisms such as buckling and kink-band development in large fiber composite structures.

ACKNOWLEDGEMENT

The work has been financial supported by the Danish Technical Research Council through the project 'Interface Design of Composite Materials'.

REFERENCES

- Budiansky, B. (1993). Micromechanics. *Computers & Structures* 16, 3-12.
- Christoffersen, J., and Jensen, H.M. (1996). Kinkband analysis accounting for the microstructure of fiber reinforced materials. *Mechanics of Materials* 24, 305-315
- Dunne, F., and Petrinic, N. (2005). *Introduction to Computational Plasticity*. Oxford University Press.
- Hsu, S.-Y., Vogler, T.J., and Kyriakides, S. (1998). Compressive Strength Predictions for Fiber Composites. *Journal of Applied Mechanics* 65
- Jensen, H.M., and Christoffersen, J. (1997). Kink Band Formation in Fiber Reinforced Materials. *J. Mech. Phys. Solids* 45, 1121-1136.
- Kyriakides, S., Arseculeratne, R., Perry, E. J. and Liechti, K. M. (1995). On the compressive failure of fiber reinforced composites. *Int. J. Solids Struct.* 32, 689-738.
- Liu, D., Fleck, N. A., and Sutcliffe, M. P. F. (2004). Compressive Strength of Fibre Composites with Random Fibre Waviness. *J. Mech. Phys. Solids* 52, 1481-1505.
- Pamin, J.K. (1994). Gradient-dependent plasticity in numerical simulation of localization phenomena. PhD-thesis, Delft University Press, The Netherlands.
- Pane, I. and Jensen, H.M. (2004) Plane strain bifurcation and its relation to kinkband formation in layered materials. *European Journal of Mechanics A/Solids* 23, 359-371

EFFECT OF ACIDIC CONDITIONS ON INTERFACE AND STRENGTH OF CELLULOSE FIBRES

A. Thygesen ¹, B. Madsen ², A. B. Thomsen ¹ and H. Lilholt ²

¹Biosystems Department, Risø National Laboratory,
4000 Roskilde, Denmark

²Material Research Department, Risø National Laboratory,
4000 Roskilde, Denmark

ABSTRACT

Composites were made with furan as matrix and aligned hemp fibres as reinforcement to obtain a completely biodegradable material. Since it is a new matrix material it is important to characterize the interface between fibres and matrix and the fibre strength. The resulting composites had reasonable stiffness (12-20 GPa) corresponding to a fibre stiffness of 62 GPa. The images showed a good impregnation of the fibre bundle surface. The fracture surface was perpendicular to the fibre axis indicating a relatively strong interface. Separate experiments on fibre bundles under acidic conditions indicate that the strength of the fibres suffers severe reduction at pH below 2.

1. INTRODUCTION

In order to make composite materials reinforced with cellulose based fibres from hemp and flax it is important that a good interface is established and that the fibres are not degraded in the process. The process conditions may affect both the surface and the bulk of the fibres, leading to potential changes (reductions) in respectively fibre-matrix interface binding and in fibre strength and stiffness. A reduction in interface binding efficiency leads to lower composite strength and stiffness, and a reduction in fibre strength and stiffness leads to a general reduction in composite mechanical properties. It is therefore important to determine process conditions (e. g. pH-level) that the fibres can tolerate without severe degradation.

Composites were made with aligned hemp yarn in furan matrix at various fibre contents. These composites were tensile tested to determine the composite and fibre properties. Light microscopy was used to observe the impregnation of the fibres, and the composite fracture surfaces were used to determine composite failure mechanism. Fibre bundle tests were performed to determine the effect of pH level on the resulting fibre strength. Chemical analysis

was used to see if some components in the fibres were degraded.

2. MATERIALS AND METHODS

2.1. Treatment of hemp fibres at varied pH levels. Fibre sliver produced by alignment of hemp fibres was mixed with water at varied pH levels in the range pH = 1-7. The suspensions with fibres were incubated for 1 h at 30°C, 1 h at 50°C and finally 1 h at 80°C. The fibres were dried overnight at 60°C. The treated fibres were tested in fibre bundle tests and analysed for chemical composition.

2.2. Fibre bundle strength. Fibre bundles were tested at 23°C and 50% relative humidity. Tensile tests on fibre bundles (15 mm long l_f) were done with a 3 mm test span l_{span} at a strain rate of $3.4 \times 10^{-4} \text{ s}^{-1}$ (0.06 mm/min) using an Instron 5566 with pressley clamps [Type: Stelometer 654 from Zellweger Uster]. After fracture the fibre pieces of 15 mm were weighed w_f . The failure stress σ_{fu} was calculated based on the failure force F_{fu} and the fibre density ρ_f , which was 1.58 g/cm^3 for the investigated hemp fibres:

$$\sigma_{fu} = \frac{F_{fu}}{A_f} = F_{fu} \times \frac{l_f \times \rho_f}{w_f}$$

2.3 Chemical fibre analysis. The chemical composition of the fibre samples was determined using a gravimetric method (Browning, 1967; Thygesen et al., 2005). Fibres were initially milled in a knife mill and passed through a 1 mm sieve. Consecutively, degradation and extraction of wax, water-soluble components, pectin, lignin, and hemicellulose in the milled fibres was performed in the chemical analysis. The residual part was almost pure cellulose with a low content of minerals, estimated by ash determination.

2.4. Fabrication of furan-hemp fibre laminates. Aligned fibre assemblies were made from filament-winding of hemp yarn (47 tex). The hemp yarn has previously been studied for reinforcement of thermoplastics (Madsen, 2004). The fibre assembly was manually impregnated with two-component furan resin. A roller was used to distribute the furan uniformly within the fibre assembly. The furan impregnated fibre assembly was pressed to a fixed thickness (= 4 mm) between two press plates by using clamps. Prior to fabrication, the press plates were treated with a release agent (Zyvax Multishield). The curing of the composite laminate started at 30°C for 3 h, then at 60°C for 1.5 h and finally at 80°C for 1.5 h. After removal from the mould the laminates were post cured at 80°C for 18h and 110°C for 3 h. Laminate dimensions were approx. $300 \times 220 \text{ mm}^2$. The three levels of tested fibre volume fraction were 15 %, 25 % and 35 %.

3. RESULTS AND DISCUSSION

3.1. Results of the composite tests regarding mechanical properties. The tensile test of the laminates was performed in the fibre direction. The resulting stress-strain curve is shown in Figure 1. The calculated composite stiffness is shown in Figure 2.

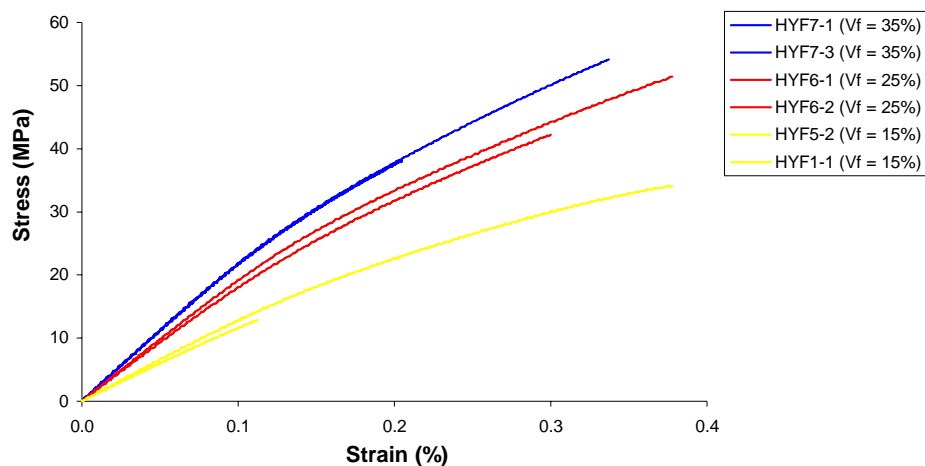


Figure 1. Tensile stress-strain curves of the fabricated aligned hemp fibre/furan composites with variable fibre volume fractions.

The results in Figure 1 show that the overall shape of the curves is the same for all composites irrespectively of their fibre content. The curves consist of an initial linear stress-strain relationship until a yielding point, which is followed by non-linear stress-strain relationship until failure.

The stress-strain performance of the composites is influenced by the content of fibres; the curves are clearly grouped according to the three levels of fibre volume fractions. The curves are shifted in an upward direction when the fibre content is increased, which means that stiffness and strength are increased correspondingly. The yielding point of the curves seems also to be increased with the fibre content. The failure strains were similar at the three levels of fibre content.

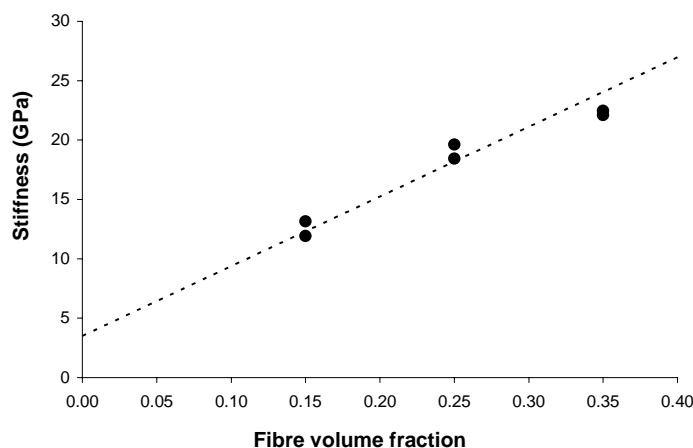


Figure 2. Stiffness of aligned hemp fibre/furan composites as a function of fibre volume fraction. Dotted line is model predictions.

The prediction line in Figure 2 is calculated by the rules-of-mixtures model traditionally used for unidirectional fibre composites. Previously, the stiffness of neat furan samples has been measured to be about 3.5 GPa (unpublished data), and this has been used in the model

calculations (at $V_f = 0$). The model predictions were fitted to the experimental data leading to an effective fibre stiffness of 62 GPa. The results in Figure 2 show also that stiffness of the composites is increased linearly as a function of the fibre volume fraction, which is as expected according to the model predictions. Thus, in terms of stiffness, the aligned hemp fibre/furan composites behave as normal composite materials.

The determined fibre stiffness of about 60 GPa has previously been found in a study of composites with the same type of fibres, but with other types of matrices like epoxy and PET (Madsen, 2004; Thygesen et al., 2007). The interface between fibres and matrix thereby seems to be as good for furan as for PET-resin and epoxy resin.

3.2. Results of the composite tests regarding micro structural properties. Two cross-sectional images of a furan matrix composite with aligned hemp yarn fibres are shown in Figure 3. The images are obtained by optical microscopy: (left) is high-magnification, and (right) is low-magnification.

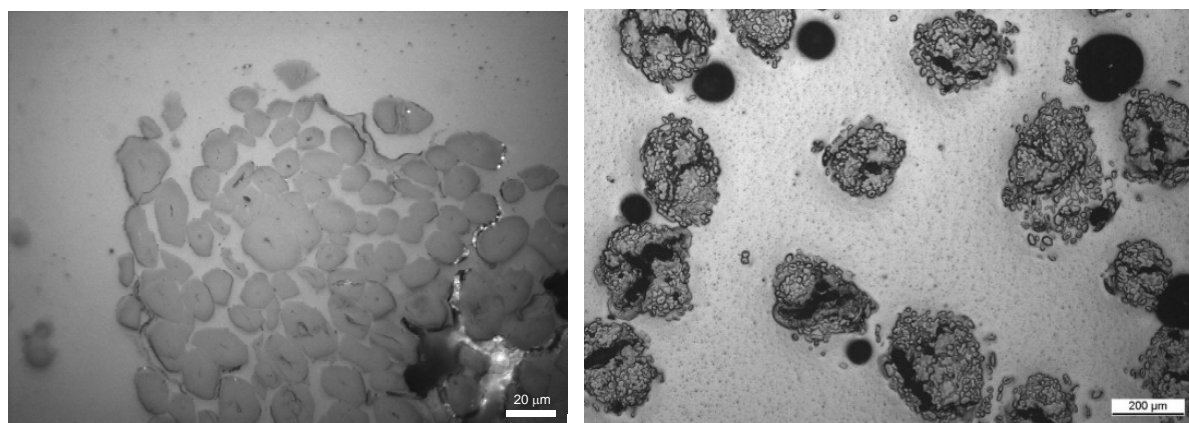


Figure 3. Cross sectional images of the hemp fibre composites with 15 volume-% fibres obtained by optical microscopy: (left) is high-magnification, and (right) is low-magnification.

The images demonstrate that the hemp yarn bundles are not perfectly impregnated with the furan resulting in porosities (i.e. black areas) located inside some of the bundles. Thus, future work must be focused at improvements of the fibre impregnation: e.g. by lowering the viscosity of the furan, and/or by increasing the available time for fibre impregnation before curing of the furan. However, the fibre impregnation may very well also be improved by using another composite fabrication method than compression moulding e.g. vacuum infusion. The compatibility between furan and hemp fibres seems to be good, since there are no (or only few) apparent interfacial gaps. This can be observed in the high-magnification image (left).

The test specimens after failure are shown in Figure 4. The fracture seems to occur along an almost straight line perpendicular to the fibre direction. This indicates that the interface is strong since fibres otherwise would be pulled out of the matrix resulting in a broad failure zone as observed with untreated fibres (Madsen, 2004). These fibres were roughly 7 times stronger so a stronger interface and better fibre impregnation were required.

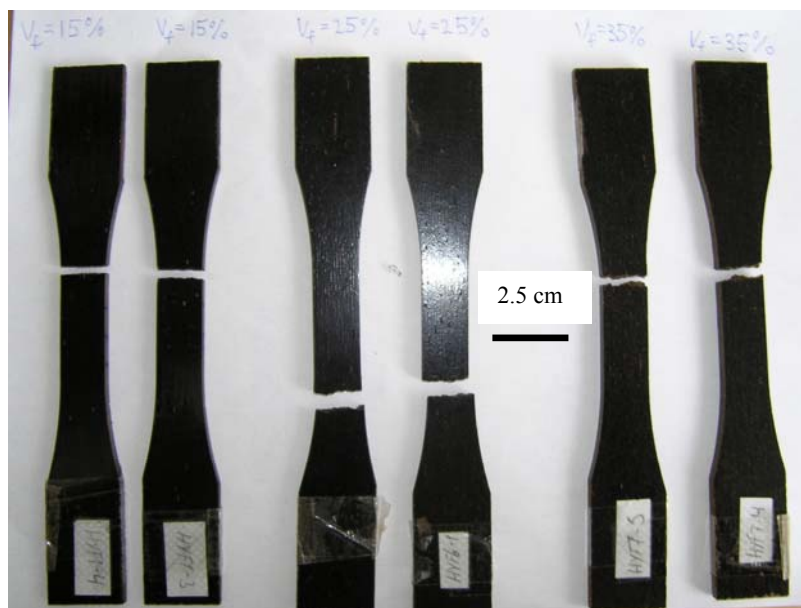


Figure 4. Tensile test specimens with varied fibre content and the furan matrix. The volume fraction of fibres were 15%, 25% and 35%, respectively.

3.3. Effect of the acidic conditions on the fibres. The effect of pH was tested since hydrolysis of cellulose and hemicellulose can occur at acidic conditions (Figure 5). Degraded bindings within the fibres are expected to reduce the fibre strength.

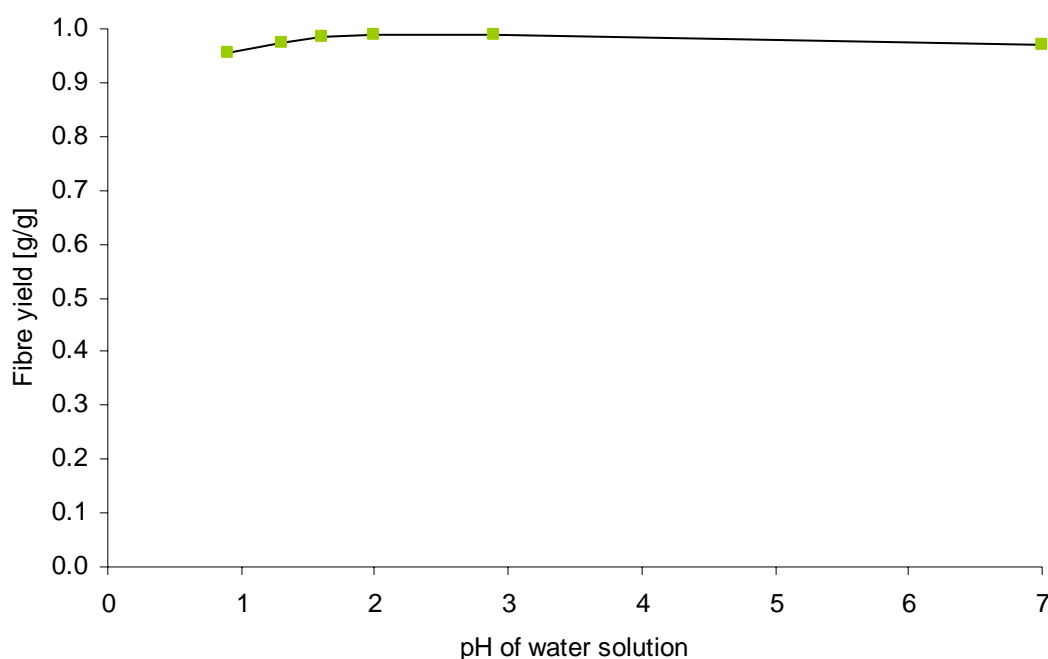


Figure 5. Effect of pH on fibre yield.

The yield of fibres was high during all treatments. The extraction of material is thereby low at these conditions. The chemical composition of the fibres after the treatments is shown in Table 1. The cellulose fraction in the fibres was not changed in the treatment. However since the fibre yield was 97-99 g/100 g raw fibres a small amount of cellulose was extracted (0-2 g/100 g

raw fibres). The other compounds that were partly extracted were lignin (2 g/100 g raw fibres), wax (2 g/100 g raw fibres) and ash (1-2 g/100 g raw fibres). Increases in contents were observed for hemicellulose (1-3 g/100 g raw fibres) and pectin (0-2 g/100 g raw fibres). The composition of the fibres is thereby slightly modified in the treatment and the hemicellulose remained solid even though low pH was used. The decrease in fibre strength is therefore probably due to acidic damage of cellulose chains and other chemical bindings in the fibres.

Table 1. Chemical composition of the hemp sliver after treatment at the varied pH levels.

Treatment hemp sliver	Cellulose % (w/w)	Hemicel. % (w/w)	Lignin % (w/w)	Pectin % (w/w)	Water ext. % (w/w)	Wax % (w/w)	Ash % (w/w)
Raw sample	73.4	14.6	4.3	2.4	0.0	3.2	2.1
pH = 7.0	74.1	16.3	2.6	3.7	2.9	0.0	1.4
pH = 2.0	75.3	15.1	2.6	2.9	2.2	1.1	0.8
pH = 1.6	73.7	16.4	2.8	2.5	2.8	1.5	0.4
pH = 1.3	73.0	17.4	2.6	4.2	1.2	1.2	0.3
pH = 0.9	73.6	17.4	2.0	4.5	1.3	0.9	0.4
Standard deviation	0.6	0.2	0.2	0.3	0.4	0.6	0.1

Fibre bundle stress-strain curves of the hemp fibres treated at different pH-values are shown in Figure 6. The slope of the curves for stress versus strain is highest when the fibres had been treated at high pH-values leading to high fibre stiffness and fibre strength. The fibres become weaker due to acidic hydrolysis at the low pH-level (0.9-1.2).

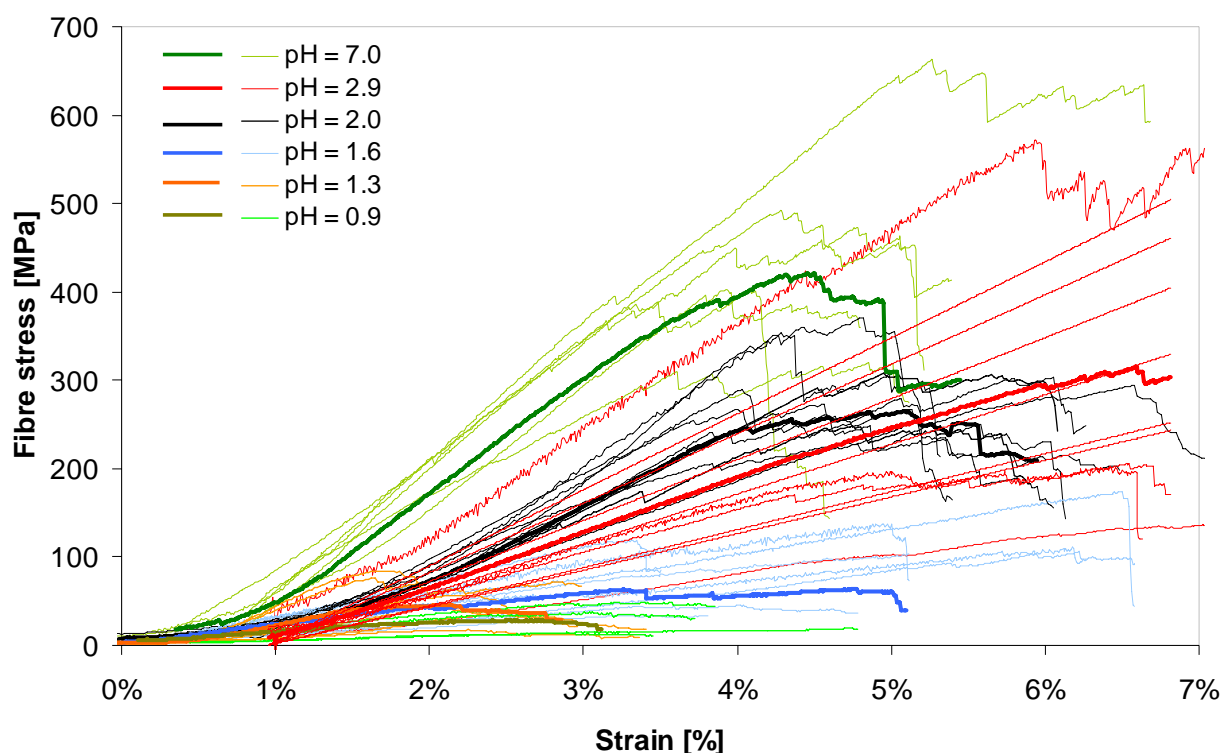


Figure 6. Fibre bundle tests on hemp sliver treated at different pH-values. The individual curves are shown (thin lines) and the average curves are shown (thick and darker lines).

Fibre bundle strength of the hemp fibres treated at variable pH-values is shown in Figure 7. Taking the large variability of the measurements into account, the strength seems to be in the

range 300-500 MPa at high pH-values. At lower pH-values, the fibre bundle strength is clearly decreased: the rate of acidic hydrolysis resulting in chemical fibre damage is thereby increasing versus decreasing pH.

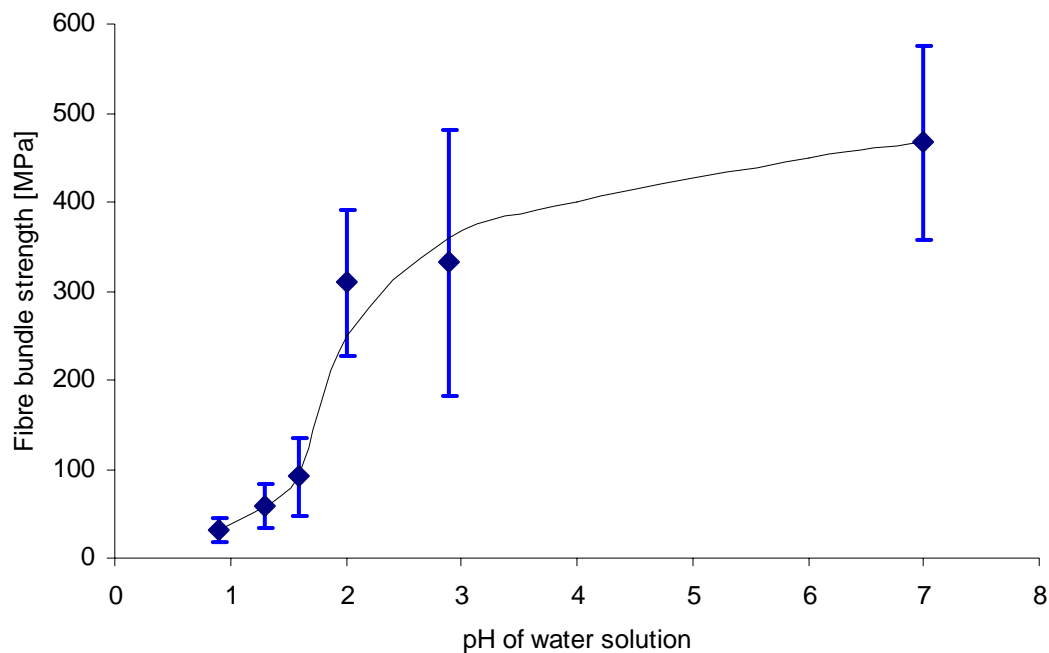


Figure 7. Fibre strength obtained versus pH of the water solution

4. CONCLUSION

The resulting composites have reasonable stiffness corresponding to a fibre stiffness of 60 GPa.

The images show a good impregnation of the fibre bundle surface. However there are areas within the fibre bundles that are not impregnated resulting in porosity at these sites. The failure seems to occur perpendicular to the fibre axis and the failure mechanism indicates a relatively strong interface.

The fibre strength is relatively unchanged at pH in the range 7 to 3 while severe reduction of fibre strength occurs at pH below 2.

ACKNOWLEDGEMENTS

The authors wish to thank Faculty of Life Sciences, University of Copenhagen for usage of the equipment for fibre bundle tests. The EU commission is acknowledged for supporting the BioComp project (EU 6th Framework Programme IP No 515769 (New Classes of Engineering Composite Materials from Renewable Resources, WP 3)).

REFERENCES

Browning, B. L. (1967). *Methods of wood chemistry*. New York: Interscience Publishers, A division of John Wiley & Sons.

- Madsen, B. (2004). Properties of plant fibre yarn polymer composites - An experimental study. Technical University of Denmark.
- Thygesen, A., Oddershede, J., Lilholt, H., Thomsen, A. B., and Ståhl, K. (2005). On the determination of crystallinity and cellulose content in plant fibres. *Cellulose* 12(6):563-576.
- Thygesen, A., Thomsen, A. B., Daniel, G., and Lilholt, H. (2007). Comparison of composites made from fungal defibrated hemp with composites of traditional hemp yarn. *Industrial Crops and Products* 25:147-159.

PREVIOUS PUBLICATIONS

Proceedings of the 1st Risø International Symposium on
“Recrystallization and Grain Growth of Multi-Phase and Particle Containing Materials”
Editors: N. Hansen, A.R. Jones, T. Leffers
Risø National Laboratory 1980

Proceedings of the 2nd Risø International Symposium on
“Deformation of Polycrystals: Mechanisms and Microstructures”
Editors: N. Hansen, A. Horsewell, T. Leffers, H. Lilholt
Risø National Laboratory 1981

Proceedings of the 3rd Risø International Symposium on
“Fatigue and Creep of Composite Materials”
Editors: H. Lilholt, R. Talreja
Risø National Laboratory 1982

Proceedings of the 4th Risø International Symposium on
“Deformation of Multi-Phase and Particle Containing Materials”
Editors: J.B. Bilde-Sørensen, N. Hansen, A. Horsewell, T. Leffers, H. Lilholt
Risø National Laboratory 1983

Proceedings of the 5th Risø International Symposium on
“Microstructural Characterization of Materials by non-Microscopical Techniques”
Editors: N. Hessel Andersen, M. Eldrup, N. Hansen, D. Juul Jensen, T. Leffers,
H. Lilholt, O.B. Pedersen, B.N. Singh
Risø National Laboratory 1984

Proceedings of the 6th Risø International Symposium on
“Transport-Structure Relations in Fast Ion and Mixed Conductors”
Editors: F.W. Poulsen, N. Hessel Andersen, K. Clausen, S. Skaarup, O. Toft Sørensen
Risø National Laboratory 1985

Proceedings of the 7th Risø International Symposium on
“Annealing Processes – Recovery, Recrystallization and Grain Growth”
Editors: N. Hansen, D. Juul Jensen, T. Leffers, B. Ralph
Risø National Laboratory 1986

Proceedings of the 8th Risø International Symposium on
"Constitutive Relations and Their Physical Basis"
Editor: S.I. Andersen, J.B. Bilde-Sørensen, N. Hansen, T. Leffers, H. Lilholt,
O.B. Pedersen, B. Ralph
Risø National Laboratory 1987

Proceedings of the 9th Risø International Symposium on
"Mechanical and Physical Behaviour of Metallic and Ceramic Composites"
Editors: S.I. Andersen, H. Lilholt, O.B. Pedersen
Risø National Laboratory 1988

Proceedings of the 10th Risø International Symposium on
"Materials Architecture"
Editors: J.B. Bilde-Sørensen, N. Hansen, D. Juul Jensen, T. Leffers, H. Lilholt,
O.B. Pedersen
Risø National Laboratory 1989

Proceedings of the 11th Risø International Symposium on
"Structural Ceramics - Processing, Microstructure and Properties"
Editors: J.J. Bentzen, J.B. Bilde-Sørensen, N. Christansen, A. Horsewell, B. Ralph
Risø National Laboratory 1990

Proceedings of the 12th Risø International Symposium on
"Metal Matrix Composites - Processing, Microstructure and Properties"
Editors: N. Hansen, D. Juul Jensen, T. Leffers, H. Lilholt, T. Lorentzen, A.S. Pedersen,
O.B. Pedersen
Risø National Laboratory 1991

Proceedings of the 13th Risø International Symposium on
"Modelling of Plastic Deformation and Its Engineering Applications"
Editors: S.I. Andersen, J.B. Bilde-Sørensen, N. Hansen, D. Juul Jensen, T. Leffers,
H. Lilholt, T. Lorentzen, O.B. Pedersen, B. Ralph
Risø National Laboratory 1992

Proceedings of the 14th Risø International Symposium on
"High Temperature Electrochemical Behaviour of Fast Ion and Mixed Conductors"
Editors: F.W. Poulsen, J.J. Bentzen, T. Jacobsen, E. Skov, M.J.L. Østergård
Risø National Laboratory 1993

Proceedings of the 15th Risø International Symposium on
“Numerical Predictions of Deformation Processes and the Behaviour of Real Materials”
Editors: S.I. Andersen, J.B. Bilde-Sørensen, T. Lorentzen, O.B. Pedersen, N.J. Sørensen
Risø National Laboratory 1994

Proceedings of the 16th Risø International Symposium on
“Microstructural and Crystallographic Aspects of Recrystallization”
Editors: N. Hansen, D. Juul Jensen, Y.-L. Liu, B. Ralph
Risø National Laboratory 1995

Proceedings of the 17th Risø International Symposium on
“High Temperature Electrochemistry: Ceramics and Metals”
Editors: F.W. Poulsen, N. Bonanos, S. Linderoth, M. Mogensen, B. Zachau-Christensen
Risø National Laboratory 1996

Proceedings of the 18th Risø International Symposium on
“Polymeric Composites – Expanding the Limits”
Editors: S.I. Andersen, P. Brøndsted, H. Lilholt, Aa. Lystrup, J.T. Rheinländer,
B.F. Sørensen, H. Toftegaard
Risø National Laboratory 1997

Proceedings of the 19th Risø International Symposium on
“Modelling of Structure and Mechanics of Materials from Microscale to Product”
Editors: J.V. Carstensen, T. Leffers, T. Lorentzen, O.B. Pedersen, B.F. Sørensen,
G. Winther
Risø National Laboratory 1998

Proceedings of the 20th Risø International Symposium on
“Deformation-Induced Microstructures: Analysis and Relation to Properties”
Editors: J.B. Bilde-Sørensen, J.V. Carstensen, N. Hansen, D. Juul Jensen, T. Leffers,
W. Pantleon, O.B. Pedersen, G. Winther
Risø National Laboratory 1999

Proceedings of the 21st Risø International Symposium on
“Recrystallization – Fundamental Aspects and Relations to Deformation
Microstructure”
Editors: N. Hansen, X. Huang, D. Juul Jensen, E.M. Lauridsen, T. Leffers, W. Pantleon,
T.J. Sabin, J.A. Wert
Risø National Laboratory 2000

Proceedings of the 22nd Risø International Symposium on
"Science of Metastable and Nanocrystalline Alloys – Structure, Properties and
Modelling"

Editors: A.R. Dinesen, M. Eldrup, D. Juul Jensen, S. Linderoth, T.B. Pedersen,
N.H. Pryds, A. Schrøder Pedersen, J.A. Wert

Risø National Laboratory 2001

Proceedings of the 23rd Risø International Symposium on

"Sustainable Natural and Polymeric Composites - Science and Technology"

Editors: H. Lilholt, B. Madsen, H.L. Toftegaard, E. Cendre, M. Megnis, L.P. Mikkelsen, B.F.
Sørensen

Risø National Laboratory 2002

Proceedings of the 24th Risø International Symposium on

"Superconductivity and Magnetism: Materials Properties and Developments"

Editors: N.H. Andersen, N. Bay, J.-C. Grivel, P. Hedegård, D. McMorro, S. Mørup,
L.T. Kuhn, A. Larsen, B. Lebech, K. Lefmann, P.-E. Lindelof, S. Linderoth, N.F. Pedersen

Risø National Laboratory 2003

Proceedings of the 25th Risø International Symposium on

"Evolution on Deformation Microstructures in 3D"

Editors: C. Gundlach, K. Haldrup, N. Hansen, X. Huang, D. Juul Jensen, T. Leffers, Z.J. Li,
S.F. Nielsen, W. Pantleon, J.A. Wert, G. Winther.

Risø National Laboratory 2004

Proceedings of the 26th Risø International Symposium on

"Solid State Electrochemistry"

Editors: S. Linderoth, A. Smith, N. Bonanos, A. Hagen, L. Mikkelsen, K. Kammer,
D. Lybye, P.V. Hendriksen, F.W. Poulsen, M. Mogensen, W.G. Wang

Risø National Laboratory 2005

Proceedings of the 27th Risø International Symposium on

"Polymer Composite Materials for Wind Power Turbines"

Editors: H. Lilholt, B. Madsen, T. L. Andersen, L. P. Mikkelsen, A. Thygesen

Risø National Laboratory 2006

AUTHOR INDEX

Almdal, K.	165, 221	Stadlbauer, W.	149
Almgren, K. M.	1	Ståhle, P.	273
Andersen, T. L.	207	Stigh, U.	265
Ayoub, P. N.	249	Tandy, Jr. W. D.	45
Biel, A.	143	Thomason, J. L.	75
Bjerkén, C.	273	Thomsen, A. B.	289
Brøndsted, P.	241	Thouless, M. D.	93
Burgstaller, C.	149	Thygesen, A.	289
Carlberger, T.	143	Tryding, J.	273
Coenen, V.	157	Tvergaard, V.	113
Day, R.	157	Walker, A.	157
Dibo, R. A.	249	West, K.	165
Drews, J.	165, 181	Wool, R. P.	125
Förtsch, W.	173	Zhang, J.	157
Fox, B. L.	157		
Franz, H. E.	173		
Friedrich, K.	173		
Gamstedt, E. K.	1		
Goutianos, S.	55, 165, 181		
Hansen, C. M.	191, 221		
Honein, E. V.	249		
Hvilsted, S.	165		
Jensen, L. R.	199, 257		
Jones, F. R.	21		
Kao-Walter, S.	273		
Kusano, Y.	207		
Laborie, M.-P. G.	213		
Launay, H.	221		
Liechti, K. M.	45		
Lilholt, H.	289		
Madsen, B.	289		
Marin, M.	227		
Michelsen, P. K.	207		
Mikkelsen, L. P.	55, 281		
Mishnaevsky, Jr. L.	241		
Nesbitt, A.	157		
Østergaard, R. C.	55		
Parmigiani, J. P.	93		
Pyrz, R.	199, 257		
Rai, H. G.	249		
Rauhe, J. C.	199, 257		
Salomonsson, K.	265		
Sørensen, B. F.	55, 207		
Sørensen, K. D.	281		